UNITED STATES DEPARTMENT OF THE INTERIOR

GEOLOGICAL SURVEY

PROCEEDINGS OF

WORKSHOP XXVII

MECHANICS OF THE MAY 2, 1983 COALINGA EARTHQUAKE

Convened under Auspices of

NATIONAL EARTHQUAKE PREDICTION AND HAZARDS PROGRAMS

13 - 15 June 1984

Editors and Convenors

Michael J. Rymer
U.S. Geological Survey
Menlo Park, California 94025

William L. Ellsworth
U.S. Geological Survey
Menlo Park, California 94025

OPEN-FILE REPORT 85-44

Compiled by
Muriel Jacobson

MENLO PARK, CALIFORNIA
1985

TABLE OF CONTENTS

ACKNOWLEDGEMENTS

The organization of this workshop benefitted greatly by the suggestions of Jack Boatwright. We thank the scientists who led the separate sessions of the workshop: Walter Mooney, Paul Somerville, and Donna Eberhart-Phillips. The logistics of gathering and keeping the participants at Asilomar were managed flawlessly by Wanda Seiders, Sheryl Johnson, and Lorraine Hollis-Alger. Their help and expertise helped the workshop proceed smoothly, allowing the participants to concentrate on other topics. The proceedings were compiled by Muriel Jacobson who substantially improved the appearance of the volume and corrected errors. Finally, we thank the participants for their interest in the workshop and their cooperation in spite of a short lead time. The participants eagerly entered into lively discussion, which furthered the understanding of the mechanics of the Coalinga earthquake and made the workshop a success.

LIST OF PARTICIPANTS

Mary C. Andrews
U.S. Geological Survey
345 Middlefield Road MS 977
Menlo Park, California 94025

Brian F. Atwater
U.S. Geological Survey
345 Middlefield Road MS 975
Menlo Park, California 94025

William H. Bakun
U.S. Geological Survey
345 Middlefield Road MS 977
Menlo Park, California 94025

George L. Choy
U.S. Geological Survey
Denver Federal Center
Box 25046, MS 967
Denver, Colorado 80225

Malcolm M. Clark
U.S. Geological Survey
345 Middlefield Road MS 977
Menlo Park, California 94025

Jerry P. Eaton
U.S. Geological Survey
345 Middlefield Road MS 977
Menlo Park, California 94025

Donna Eberhart-Phillips
U.S. Geological Survey
345 Middlefield Road MS 977
Menlo Park, California 94025

William L. Ellsworth
U.S. Geological Survey
345 Middlefield Road MS 977
Menlo Park, California 94025

Eric J. Fielding
Department of Geological Sciences
Cornell University
Ithica, New York 14853

E. J. Fowkes
West Hills College
Coalinga, California 93210

David R. Fuller
California Div. of Mines and Geology
107 S. Broadway, Room 1085
Los Angeles, California 90012

Thomas Heaton
U.S. Geological Survey
California Institute of Technology
Seismological Laboratory, 252-21
Pasadena, California 91125

David P. Hill
U.S. Geological Survey
345 Middlefield Road MS 977
Menlo Park, California 94025

Mason L. Hill
14067 E. Summit Drive
Whittier, California 90602

William R. Lettis
Bechtel Civil and Mineral Inc.
P.O. Box 3065
San Francisco, California 94119

Allan G. Lindh
U.S. Geological Survey
345 Middlefield Road MS 977
Menlo Park, California 94025

Arthur F. McGarr
U.S. Geological Survey
345 Middlefield Road MS 977
Menlo Park, California 94025

Walter D. Mooney
U.S. Geological Survey
345 Middlefield Road MS 977
Menlo Park, California 94025

Charles S. Mueller
U.S. Geological Survey MS 977
345 Middlefield Road MS 977
Menlo Park, California 94025

Benjamin M. Page
Department of Geology
Stanford University
Stanford, California 94305

Charles R. Real
California Div. Mines and Geology
1416 9th Street
P.O. Box 2980
Sacramento, California 95814

Paul A. Reasenberg
U.S. Geological Survey
345 Middlefield Road MS 977
Menlo Park, California 94025

Michael J. Rymer
U.S. Geological Survey
345 Middlefield Road MS 977
Menlo Park, California 94025

Paul Segall
U.S. Geological Survey
345 Middlefield Road MS 977
Menlo Park, California 94025

Roger Sherburne
California Div. Mines and Geology
1416 9th Street
P.O. Box 2980
Sacramento, California 95814

Paul Somerville
Woodward-Clyde Consultants
566 El Dorado Street, Suite 100
Pasadena, California 91101

Ross S. Stein
U.S. Geological Survey
345 Middlefield Road MS 977
Menlo Park, California 94025

Robert A. Uhrhammer
University of California
Department of Geology and Geophysics
Berkeley, California 94720

Allan W. Walter
U.S. Geological Survey
345 Middlefield Road MS 977
Menlo Park, California 94025

Carl M. Wentworth
U.S. Geological Survey
345 Middlefield Road MS 975
Menlo Park, California 94025

Robert F. Yerkes
U.S. Geological Survey
345 Middlefield Road MS 975
Menlo Park, California 94025

MECHANICS OF THE MAY 2, 1983, COALINGA, CALIFORNIA EARTHQUAKE: AN INTRODUCTION

Michael J. Rymer and William L. Ellsworth

U.S. Geological Survey
Menlo Park, California 94025

On May 2, 1983 our understanding of earthquake risk and mechanisms of crustal deformation in California were fundamentally altered by the occurrence of a magnitude 6.7 earthquake near the town of Coalinga. This earthquake occurred beneath a young fold on the western margin of the San Joaquin Valley, in an area where recent fault movement at the surface was unknown. While other significant California earthquakes have occurred in areas where faults were unknown, such as the Kern County earthquake of 1952, subsequent investigations have invariably revealed the causative fault, which could have been recognized before the event by careful or subsurface geologic studies.

The case of the Coalinga earthquake is fundamentally different, as extensive geological and geophysical investigations have all failed to find evidence for surface expression of the fault responsible for the earthquake. Instead, the earthquake is intimately associated with active folds on the western margin of the San Joaquin Valley.

Changes in surface elevation measured along a profile across Pleasant Valley, where Coalinga is located, and Anticline Ridge show that Pleasant Valley subsided and the anticline grew as a result of the earthquake. The recognition that the earthquake was related in a complex manner to surficial features has focused attention on a number of difficult questions regarding the nature of this event: the underlying tectonic process, the potential for similar or even larger events in similar tectonic settings, and the mechanisms of fold development as a seismically driven process.

In order to answer some of these questions and especially to focus attention on the mechanics of faulting in the 1983 Coalinga earthquake and styles of past deformation in the region, a conference on the mechanics of the Coalinga earthquake sequence was held from June 13 to 15, 1984, under the auspices of the Office of Earthquakes, Volcanoes, and Engineering of the U.S. Geological Survey. Its purpose was to bring together the results of recent interdisciplinary research on earthquakes and faulting in the Coalinga region. The papers submitted for this volume represent the diverse specialties of investigators who attended the meeting: the papers range in scope from detailed to broad, theoretical to descriptive, and range topically from geological to geophysical to seismological.

The papers in this volume present several important observations and conclusions concerning the mechanics of the Coalinga earthquake sequence, a few of which are summarized below. Of primary importance to understanding the

Coalinga sequence is an understanding of the geologic history and tectonic setting of the region. The dominant structural feature of the region is the San Andreas fault, which at its nearest point is about 33 km southwest of the main shock epicenter. Northeast of the San Andreas fault is the Diablo Range which is experiencing uplift relative to the San Joaquin Valley to the east that began about 3 m.y. ago. Locally along the western boundary of the San Joaquin Valley there are northwest-trending anticlines, indicative of a compressional regime normal to the San Andreas fault. The Coalinga main shock occurred near the axis of one of these anticlines, below Anticline Ridge. Seismic refraction and reflection studies across this anticline indicate lithological and structural complexity below 5 km. Lying at shallower depths a stack of sedimentary rocks is folded into the Anticline Ridge structure. The seismologic setting of the southern part of the Diablo Range, excluding activity along the San Andreas fault, is dominated by widely spaced clusters of earthquakes with reverse to thrust mechanisms; earthquakes farther north are aligned along strike-slip faults, primarily the Ortigalita fault (Eaton, this volume). Teleseismic observations by Choy (this volume) of the Coalinga earthquake suggest a double event, both events with northwest-trending strikes. The two events are inferred to be about 5 km and 3.2 s apart, the second event being more westerly and only half as strong.

An unusual and frustrating aspect of the Coalinga earthquake was the ambiguity as to which of the nodal planes corresponds to the fault plane of the main shock. The resultant two choices of faulting style are 1) a shallowly southwest-dipping thrust fault or 2) a steeply northeast-dipping reverse fault; both of these opposing faults (nodal planes) were supported by preliminary investigations and arguments for both are presented in this report. For many earthquakes of moderate to large magnitude, surface faulting reveals the style of faulting and restrains which of the nodal planes is represented. However, for the Coalinga main shock there was no related surface rupture (Clark and others, 1983). Another aspect of this seismic event was the complex and widespread distribution of aftershocks which, with only a relatively minor exception, were associated with previously unknown faults that have no surface expression. Studies of the main shock and more than 100 of the larger aftershocks by Eaton (this volume) and of more than 2000 large and small aftershocks by Eberhardt-Phillips and Reasenberg (this volume) indicate the presence of several intersecting fault planes, all of which were active during the Coalinga sequence, apparently reflecting complexity of the Diablo Range-San Joaquin Valley geologic boundary at depth. The sum of the evidence of both of these studies favors the thrust-fault solution for the main shock. Geodetic leveling data indicate uplift of 0.5 m at Anticline Ridge and depression of 0.25 m in adjacent Pleasant Valley (Stein, this volume). These data are fitted to fault dislocation models to infer the style of faulting for the Coalinga main shock, concluding that a steeply dipping reverse fault fits the geodetic data better than a gently dipping thrust fault.

McGarr and others (this volume) studied ground motion parameters relative to crustal strength in the seismogenic zone. They show considerable variation in crustal strength within the seismogenic zone, typical of compressional states of crustal stress, surrounded by zones of much lower implied strength. Two of the papers in this volume take advantage of information from the local densely spaced oil wells to investigate possible relations with the Coalinga earthquake. The paper by Seagall and Yerkes (this volume) investigates the likelihood of the region's long-term oil withdrawal on inducing the earth-

quake. Their analyses indicate that at hypocentral depths the driving stress decreased by less than 0.05 bars, which would slightly inhibit slip. The paper by Yerkes and others (this volume) looks into the distribution of naturally occurring abnormally high fluid pressures because they counteract the vertical load and significantly reduce the frictional strength of the rocks, thus enhancing the likelihood of thrust faulting. The one fault that did experience surface rupture during the earthquake sequence is the Nunez fault, a steeply east-dipping reverse fault which ruptured in association with an M 5.2 event 40 days after the main shock (Rymer and others, this volume). An interesting aspect of the surface rupture is the presence of afterslip that has enlarged the surface displacement as much as 60 percent of the coseismic slip, making the Nunez fault the first reported reverse fault to have significant afterslip at the ground surface.

The observations and results presented in this volume are undoubtedly applicable to potential earthquake sites in similar tectonic environments along the east margin of the Coast Ranges. Fortunately, studies of the 1983 Coalinga earthquake help focus attention on the area and should motivate further work towards the understanding of this complicated region.

REFERENCE CITED

Clark, M. M., Harms, K. K., Lienkaemper, J. J., Perkins, J. A., Rymer, M. J., and Sharp, R. V., 1983, The May 2, 1983 earthquake at Coalinga, California: The search for surface faulting, in Borcherdt, R. D., compiler, The Coalinga earthquake sequence commencing May 2, 1983: U.S. Geological Survey Open-File Report 83-511, p. 8-11.

GEOLOGIC BACKGROUND OF THE COALINGA EARTHQUAKE OF MAY 2, 1983

Benjamin M. Page

Department of Geology, Stanford University
Stanford, CA 94305

Introduction

The near-surface geology of the Coalinga region does not pinpoint the cause of the May 2, 1983 earthquake, but it does provide hints as to the kinds of structures and tectonics that may have been involved. Pre-1983 published background material includes descriptions of the rocks and structures of the Diablo Range, Coalinga area, Kettleman Hills, and San Joaquin Valley. The areal geology is shown in maps by Dibblee (1971, 1973), Jennings (1958, 1977), and Jennings and Strand (1958). The main near-surface features are represented in figure 1 of Wentworth and others (this volume).

Principal Rock Assemblages

Basement rocks Exposures of basement rocks in the region around Coalinga are confined to the southern Diablo Range, which is underlain by the Franciscan assemblage (Bailey and others, 1964). At the surface, the assemblage largely consists of melange(s) comprising blocks of graywacke, greenstone, and chert in a highly sheared argillaceous matrix. Few of the blocks have been dated, but they presumably range from Upper Jurassic to Upper Cretaceous in age, like similar Franciscan rocks in the central Diablo Range farther north. In some Franciscan areas (for example, around Mount Hamilton east of San Jose), large coherent tabular bodies of metagraywacke predominate over melanges. Conceivably, such bodies might occur at depth in the Coalinga region, although there is no indication of this at the surface. The vertical and eastward limits of the Franciscan assemblage are unknown.

Other basement rocks in the region include serpentinite that, unlike the ophiolite at the base of the Great Valley sequence, apparently stems from a source beneath the Franciscan. This serpentinite forms much of the New Idria diapir in an antiformal part of the Diablo Range 25-45 km northwest of Coalinga, and it contains many inclusions of high P/T blueschist facies Franciscan rocks (Coleman, 1957). The serpentinite mass is partly sheathed by Franciscan melange, which separates it from the flanking Great Valley sequence. Its enormous volume seems to preclude a source within the Franciscan, as the familiar serpentinite blocks in Franciscan melanges are inadequate in size. Cold intrusions and extrusions of serpentinite are conspicuous along faults in the Diablo Range south of Coalinga (Dickinson, 1966a and 1966b), and this serpentinite also may have risen from beneath the Franciscan. The cryptic parent body could be a thick ultramafic-mafic(?) layer or slab deep in the crust.

The Sierran basement extends westward beneath much of the San Joaquin Valley, and it must approach the Franciscan in the subsurface somewhere east of Coalinga. Existing drillholes are far too shallow to throw any light on the structure of the zone of closest approach of the two types of basement, or on the nature of the westernmost Sierran basement complex. The latter is

almost certainly not granitic like the exposed Mesozoic plutonic arc farther east; instead, it could be almost any kind of accreted assemblage, perhaps of island arc or ophiolitic character. If it is ophiolitic, it will be difficult to distinguish it from the Coast Range ophiolite on the basis of geophysical data. Indeed, it might be an extension of the Coast Range ophiolite, although this seems unlikely. Another possibility is that some assemblage that is unrelated to either the Coast Range rocks or the Sierran basement lies between the two.

Great Valley sequence (GVS) The Franciscan core of the Diablo Range is overlain tectonically by a partly eroded cover of the Upper Jurassic-Cretaceous Great Valley sequence (Bailey and others, 1964). The tectonic contact is possibly the Coast Range thrust (CRT) of Bailey and others (1970), or perhaps it consists of younger faults that have overprinted the CRT (Raymond, 1973). In any case, no verifiable depositional contact between the GVS and the Franciscan has been found.

Ideally, a complete GVS section would include a basal ophiolite ca. 160 m.y. old (Bailey and others, 1964; Hopson and others, 1981), pelagic chert above the ophiolite, and a great thickness of turbiditic clastic sediment representing most, or all, stratigraphic stages from Turonian (uppermost Jurassic) to Maastrichtian (uppermost Cretaceous). However, in the Coalinga region, little or no ophiolitic material, and no chert, remain at the base of the clastic sediments, probably because they were removed by faulting along the CRT. Although Turonian and Valanginian sediments are reported west of Coalinga, apparently most of the Lower Cretaceous stages are missing throughout the region. On the other hand, the Upper Cretaceous section (Cenomanian through Maastrichtian) is locally more than 6 km thick. The GVS in this region has been described by Ingersoll (1978), Marsh (1960), and Mansfield (1972), among others.

Cenozoic rocks The Cenozoic stratigraphic section in the Coalinga-Kettleman Hills area has been well-studied because of its importance in the oil fields. It locally attains a thickness of 5 km, all Cenozoic epochs being represented, from Paleocene to Pleistocene. Most of the sediments are marine clastics, but some upper Miocene formations are largely thin-bedded procelanite. Nonmarine tongues appear in the middle to upper Miocene section; the Pliocene strata are estuarine and nonmarine, and the Plio-Pleistocene Tulare Formation is almost wholly nonmarine except at the base, reflecting prevalent uplift. The Cenozoic section and near-surface structures have been described by many, including Arnold and Anderson (1910), Anderson and Pack (1915), Stewart (1946), and Woodring and others (1940).

Structure

Coast Range thrust (CRT) As mentioned above, the CRT or its counterpart separates the Franciscan and GVS. One such fault, now folded, was mapped by Dickinson (1966b) south of Coalinga. Although the CRT was originally believed to be subduction-related, I now think it most likely formed in the Paleocene after much of the Franciscan had been assembled. The folded thrust shown by Dickinson (1966b) evidently truncates Upper Cretaceous GVS rocks. Its activity may have caused the regional unconformity below the Paleocene sediments along the west side of the San Joaquin Valley. The main thrusting episode probably ended before the Salinian Block arrived at this latitude (i.e., before the Eocene), because the CRT-type thrusts occur just across the

San Andreas fault from the Salinian Block, but are not found within the latter.

The CRT or its counterpart, just described, is the principal exposed structural feature that might extend to seismogenic depths as a gently-dipping surface of potential slip. Any other low-angle faults that may exist deep in the crust have not been identified at the surface. Although it is a pre-Neogene structure, the CRT might respond to modern stresses wherever it is appropriately oriented.

Neogene structures The main structural elements are shown in figure 1 of Wentworth and others (this volume). North of Coalinga, the Diablo Range is a broad antiform which trends N.65°W. and which is pierced by the New Idria diapir of serpentinite and Franciscan rocks. The antiform encompasses subsidiary folds, one of which is the Joaquin Ridge anticline. From this latter fold, a discontinuous belt of anticlines extends southeastward past Coalinga and across the epicenter of May 2, 1983. The belt, unlike the N.65°W. structures to the northwest, trends about N.40°W. It is more than 90 km long and includes the Coalinga anticline (site of the epicenter); Guijarral Hills structure; Kettleman North, Middle, and South Domes; and Lost Hills anticline. Significantly, most of the folds and the belt as a whole are nearly parallel with the San Andreas fault, so they are not wrench-type structures, although the individual anticlines are slightly separated in a right-stepping en echelon manner. The trough of the San Joaquin Valley synform lies a few kilometers northeast of the Coalinga Nose-Kettleman Hills belt of anticlines, and is parallel with it. On the southwest, a syncline separates the belt from a narrow extension of the Diablo Range. This part of the range, south of Coalinga, contains a complicated variety of structures, including wrench-type folds trending about N.65°W. It is bounded by the San Andreas fault.

A rather traditional structural interpretation is shown in a cross section by Page and others (1977), and Page (1981, p. 337). The line of section crosses Kettleman North Dome 27 km southeast of the epicenter of May 2, 1983. The North Dome fold is depicted with a steep southwest limb (see also Woodring and others, 1940), and with small internal thrust faults dipping northeast, these being based on oil company data. The fold configuration, which is established by oil well logs, is such that it could hardly involve the basement. By implication, there must be a thrust fault or decollement surface beneath the fold, although this was not included in the cross section.

Neogene thrust faults and high-angle reverse faults have been mapped at the surface both to the west and south of Coalinga. Some, such as those near Orchard Peak (Marsh, 1960) trend east-west and can be explained as compressional effects related to wrench tectonics (Wilcox and others, 1973). Others, for example, the Maxey fault (Dickinson, 1966b), are more nearly parallel with the San Andreas fault and require some other explanation.

Age and origin of folds, faults, and Diablo Range uplift The Coalinga anticline-Kettleman Hills belt of folds is obviously young, as it is marked by arching of the Tulare Formation. The latter is mainly nonmarine, but is paralic at the base. The age range of the formation is probably mid-Pliocene to mid-Pleistocene. Northeast of Coalinga, the upper part of the Tulare Formation contains the tuffaceous Corcoran Clay, which is reported to be ca. 600,000 yr. old (Janda, 1965). The Tulare Formation is folded almost as much as the older strata beneath it. Apparently the Coalinga and Kettleman Hills

anticlines began to form in the Pliocene, developed rapidly in the Pleistocene, and are still growing. The Kettleman North Dome was eroded to a surface of low relief after it had reached structural maturity in the Pleistocene, but subsequent renewed movement has arched the erosion surface (Woodring and others, 1940). This suggests that anticlinal growth in the area proceeds haltingly.

The uplift of the Diablo Range in its present configuration likewise started in Pliocene time, most likely accelerated in the Pleistocene, and is probably still in progress. Along the east flank, the Tulare Formation is upturned; along the west flank of the central part of the range, the Plio-Pleistocene San Benito Gravels and age-equivalent Santa Clara Formation are deformed. The three Plio-Pleistocene formations locally contain coarse detritus from the Diablo core, whereas such material is not plentiful in pre-Pliocene formations. (An exception is the middle Miocene Big Blue unit, described by Casey and Dickinson, 1976, which contains serpentinite debris from the initial extrusion of the New Idria diapir). Admittedly, local uplift and incipient folding occurred here and there from time to time throughout the Cenozoic, as shown by unconformities, but these events contributed little or nothing to the outline and elevation of the present range.

Young compressional features oriented parallel with the plate boundary are being increasingly recognized (for example, Page, 1981, p. 403-406; Crouch and others, 1984). These features are widespread in west-central California from the foot of the continental slope to the San Joaquin Valley. Individual ranges are similarly oriented; these include the Diablo, Temblor, Gabilan, Santa Cruz, and Santa Lucia Ranges. The causes of compression transverse to the plate boundary are not fully understood. A misfit between the azimuth of the San Andreas fault vis-a-vis the direction of relative plate motion may be a factor, as well as extension in the Basin and Range province (Minster and Jordan, 1984). A change in Pacific plate motion 5 m.y. BP has been documented by Cox and Engebretson (in prep.), and this (perhaps in conjunction with the above-mentioned influences) seems to have played a critical role, judging from the timing of the tectonic activity in question. Possibly this is one of the ultimate causes of the Coalinga earthquakes.

Concluding Remarks

There is abundant evidence for recent (probably ongoing) compressional deformation, both oblique to, and normal to, the plate boundary. Structural geometry suggests that the surface of the basement cannot be folded in conformity with near-surface anticlines, thus implying decollement or low-angle thrusting. The tectonic contact (Coast Range thrust?) between the Franciscan Complex and Great Velley sequence is the principal exposed structural feature that might flatten at depth to become a major quasi-horizontal locus of slippage. Any other gently-dipping major faults that may exist at depth have not been identified at the surface. However, reverse faults and thrusts of moderate size offset Neogene and older rocks in many places. Several of these are nearly parallel with the San Andreas fault, like the unseen active faults interpreted from Coalinga earthquake focal mechanisms.

The widespread occurrence, and the youthfulness, of compressional features (some wrench-type and others that are parallel with the SAF) suggest that Coalinga-type earthquakes may occur in other parts of west-central California.

References

Anderson, R., and Pack, R. W., 1915, Geology and oil resources of the west border of the San Joaquin Valley north of Coalinga, California: U.S. Geological Survey Bulletin 603, 210 p.

Arnold, R., and Anderson, R., 1910, Geology and oil resources of the Coalinga district, California: U.S. Geological Survey Bulletin 392, 343 p.

Bailey, E. H., Irwin, W. P., and Jones, D. L., 1964, Franciscan and related rocks and their significance in the geology of western California: California Division of Mines and Geology Bulletin 183, 177 p.

Bailey, E. H., Blake, M. C., and Jones, D. L., 1970, On-land Mesozoic oceanic crust in California Coast Ranges: U.S. Geological Survey Professional Paper 700-C, p. C70-C81.

Casey, T. A. L., and Dickinson, W. R., 1976, Sedimentary serpentinite of the Miocene Big Blue Formation near Cantua Creek, California: in Fritsche, A. E., TerBest, H., and Wornardt, W. W., eds.: The Neogene Symposium, Society of Economic Paleontologists and Mineralogists, Pacific Section, p. 65-74.

Coleman, R. G., 1957, Mineralogy and petrology of the New Idria district, California (Ph.D. thesis): Stanford University, California, 166 p.

Cox, A., and Engebretson, D. C., in prep., Change in motion of Pacific plate at 5 Ma.

Crouch, J. K., Bachman, S. B., and Shay, J. T., 1984, Post-Miocene compressional tectonics along the central California margin, in Crouch, J. K., and Bachman, S. G., eds., Tectonics and sedimentation along the California margin: Society of Economic Paleontologists and Mineralogists, Pacific Section, p. 37-54.

Dibblee, T. W., 1971, Geologic maps of the Coalinga, Joaquin Rocks, New Idria, and Priest Valley 15-minute quadrangles, California: U.S. Geological Survey Open-File Report 71-87, scale 1:62,500.

_____1973, Regional geologic map of San Andreas and related faults in Carizzo Plain, Temblor, Caliente, and La Panza Ranges and vicinity, California: U.S. Geological Survey Miscellaneous Geological Investigations Map I-757, scale 1:125,000.

Dickinson, W. R., 1966a, Table Mountain serpentinite extrusion in California Coast Ranges: Geological Society of America Bulletin, v. 77, p. 451-472.

_____1966b, Structural relationships of San Andreas fault; system, Cholame Valley, and Castle Mountain Range, California: Geological Society of America Bulletin, v. 77, p. 707-726.

Hopson, C. A., Mattinson, J. M., and Pessagno, E. A., 1981, Coast Range ophiolite, western California, in Ernst, W. G., ed.: The geotectonic development of California, Englewood Cliffs, New Jersey, Prentice-Hall, p. 418-510.

Ingersoll, R. V., 1978, Paleogeography and paleotectonics of the late Mesozoic forearc basin of northern and central California, in Howell, D. G., and McDougall, K. A., eds., Mesozoic paleogeography of the western United States: Society of Economic Paleontologists and Mineralogists, Pacific Section, Pacific Coast Paleogeography Symposium 2, p. 417-482.

Janda, R., V., 1965, Quaternary alluvium near Friant, California: International Quaternary Association. Guidebook for Field Conference 1, Northern Great Basin and California, p. 128-133.

Jennings, C. W., 1958, Geologic map of California, San Luis Obispo sheet: California Division of MInes and Geology, scale 1:250,000.

_____1977, Geologic map of California: California Division of Mines and Geology,
scale 1:750,000.

Jennings, C. W., and Strand, R. G., 1958, Geologic map of California, Santa Cruz sheet: California Division of Mines and Geology, scale 1:250,000.

Mansfield, C. G., III, 1972, Petrography and sedimentology of the late Mesozoic Great Valley sequence near Coalinga, California (Ph. D. thesis): Stanford University, California.

Marsh, O. T., 1960, Geology of the Orchard Peak area, California: California Division of Mines and Geology Special Report 62, 42 p.

Minster, J. B., and Jordan, T. H., 1984, Vector constraints on Quaternary deformation of the western United States east and west of the San Andreas fault, in Crouch, J. K., and Bachman, S. B., eds., Tectonics and sedimentation along the California margin: Society of Economic Paleontologists and Mineralogists, Pacific Section, p. 1-16.

Page, B. M., 1981, The southern Coast Ranges, in Ernst, W. G., ed., The geotectonic development of California: Englewood Cliffs, New Jersey, Prentice-Hall, p. 329-417.

Page, B. M., Wagner, H. C., McCulloch, D. S., Silver, E. A., and Spotts, J. H., 1977, Geologic cross section of the continental margin off San Luis Obispo, the southern Coast Ranges, and the San Joaquin Valley, California: Geological Society of America Map and Chart Series MC-28G.

Raymond, L. A., 1973, Tesla-Ortigalita fault, Coast Range thrust fault, and Franciscan metamorphism, northeastern Diablo Range, California: Geological Society of America Bulletin, v. 84, p. 3547-3562.

Stewart, R., 1946, Geology of Reef Ridge, Coalinga district, California: U.S. Geological Survey Professional Paper 205-C, p. 81-115.

Wilcox, R. E., Harding, T. P., and Seely, D. R., 1973, Basic wrench tectonics: American Association of Petroleum Geologists Bulletin, v. 57, p. 74-96.

Woodring, W. P., Stewart, R., and Richards, R. W., 1940, Geology of the Kettleman Hills oil field, California: U.S. Geological Survey Professional Paper 195, 170 p.

Velocity Structure near Coalinga, California

by
Allan Walter
U. S. Geological Survey
345 Middlefield Road
Menlo Park, CA 94025

Seismic refraction traveltime data collected by the U.S.G.S. along two profiles (Figure 1) across the hypocentral region of the Coalinga earthquakes have been partially modeled by 2-D ray-tracing techniques. North of Coalinga, an E-W profile extends from the Diablo Range eastward into the San Joaquin Valley. East of Coalinga, a NW-SE profile extends south along State Highway 33. A brief description of the profiles including an interpretation of the first arrival data is available in Walter and Mooney (1983). Tables of the shot and station data, location maps, and record sections are all available in an open-file report (Colburn and Walter, 1984).

The velocity structure derived for the east-west profile (shotpoints 9-12) is presented in Figure 2. In the San Joaquin Valley the velocity of the Quaternary and Tertiary strata increases from 1.7 km/s at the surface to about 3.6 km/s at 3 km depth. Near the base of the Tertiary section, top of the Cretaceous Great Valley Sequence (GVS), the velocity increases abruptly to 4.0-4.3 km/s. With increasing depth of burial the velocity of the GVS in the valley increases to 4.9 km/s. Locally some thin units have lower velocities probably resulting from higher pore pressures. In the center of the San Joaquin Valley, the GVS overlies a basement with a velocity of 6.3-6.4 km/s, indicative of a mafic composition. Between shotpoints 9 and 10, the dip of the basement is less than 5 degrees. Westward of SP 10 the mafic basement plunges from 6.0 km depth to about 15 km depth beneath the Diablo Range; the location of this change in basement geometry coincides with the axis of the valley magnetic high.

In the Diablo Range a wedge of 5.7-6.0 km/s rocks, most probably Franciscan, lies between the GVS exposed at the surface and the mafic basement layer. The position of the boundary separating the GVS and Franciscan wedge beneath Anticline ridge is not well constrained by the data, but the depth to the top of the wedge, about 6 km at SP 12 (Figure 2), increases eastward to a junction with the mafic basement. The Franciscan wedge in the model does not extend east beneath the San Joaquin Valley. Just east of the anticline (SP11), travel time delays (Figure 5-8) require a basin containing several additional kilometers of 5.0 km/s strata probably associated with the GVS.

At equivalent depths of burial, the velocities of the lower GVS units in the Diablo Range (4.8-4.9 km/s) are higher than those found for the GVS farther east in the San Joaquin Valley (4.0-4.3 km/s). The east-west refraction data (Figure 3) do not show clear evidence for a low velocity zone (LVZ), however data recorded along the NW-SE profile (Figure 4) do show evidence for a LVZ located within the GVS beneath the Pleasant Valley syncline west of SP 11.

Figure 5 shows the velocity cross-section inferred for the NW-SE profile. This cross-section extends from SP 13 across Joaquin Ridge and down the axis of the syncline to SP 15 (Figure 1). The velocity structure is similar to that described for the east-west profile. The top of the Franciscan lies at about 7.5 km depth and the mafic basement is at 15 km depth. The refraction data from SP 13 and SP 14 show the presence of a

velocity inversion at 2.4 km depth in the GVS beneath Black Mountain on Joaquin Ridge. This LVZ correlates with a zone of high fluid pressure encountered in a nearby ARCO well (R. F. Yerkes, pers. comm.). The top of this LVZ plunges into the syncline to a depth of 3.4 km at the intersection with the E-W profile, thus, the LVZ may be stratigraph- ically controlled. The velocity within the LVZ is lower (4.2 km/s) south of axis of Joaquin Ridge. The LVZ is less than 2 km in thickness and does not appear to extend west of the Pleasant Valley syncline; it may extend east- ward at greater depths into the San Joaquin Valley.

Figures 6 and 7 show the locations of some of the larger Coalinga aftershocks (J. Eaton et. al., 1983) projected onto the plane of the respective velocity cross-sections. Note that the majority of earthquake locations lie within the Franciscan wedge near its eastern termination.

A better fit of the travel time data is possible, so the velocity model should not be taken literally as correct, but rather as suggesting the gross velocity structure. Overall, the Coalinga E-W velocity model (Figure 2) is strikingly similar to the preliminary E-W velocity model derived for a refraction profile recorded along reflection line SJ-6 across the San Joaquin Valley and the Diablo Range 50 km farther south (Wentworth et. al., 1983).

References Cited

Colburn, R. H. and A. W. Walter, 1984, Data Report for Two Seismic-Refraction Profiles crossing the Epicentral Region of the 1983 Coalinga, California Earthquakes, U. S. Geological Survey Open File Report, in press, pp. 1-57, 12 plates.

Eaton, J., R. Cockerham, F. Lester, 1983, Study of the May 2, 1983 Coalinga Earthquake and Its Aftershocks Based on the USGS Seismic Network in Northern California, Calif. Div. Mines and Geol., J. H. Bennett and R. W. Sherburne Eds., Spec. Pub. 66, pp. 261-274.

Walter, A. and W. Mooney, 1983, Preliminary Report on the Crustal Velocity Structure Near Coalinga, California, as Determined From Seismic Refraction Surveys in the Region, CDMG, J. H. Bennett and R. W. Sherburne Eds., Spec. Pub. 66, pp. 127-136.

Wentworth, C. M., A. Walter, J. A. Bartow, and M. D. Zoback,1983, Evidence on the Tectonic Setting of the 1983 Coalinga Earthquakes from Deep Reflecton and Refraction Profiles Across the Southeastern End of the Kettleman Hills, CDMG, J. H. Bennett and R. W. Sherburne Eds., Spec. Pub. 66, pp. 113-126.

COALINGA REFRACTION LINES - LOCATION MAP

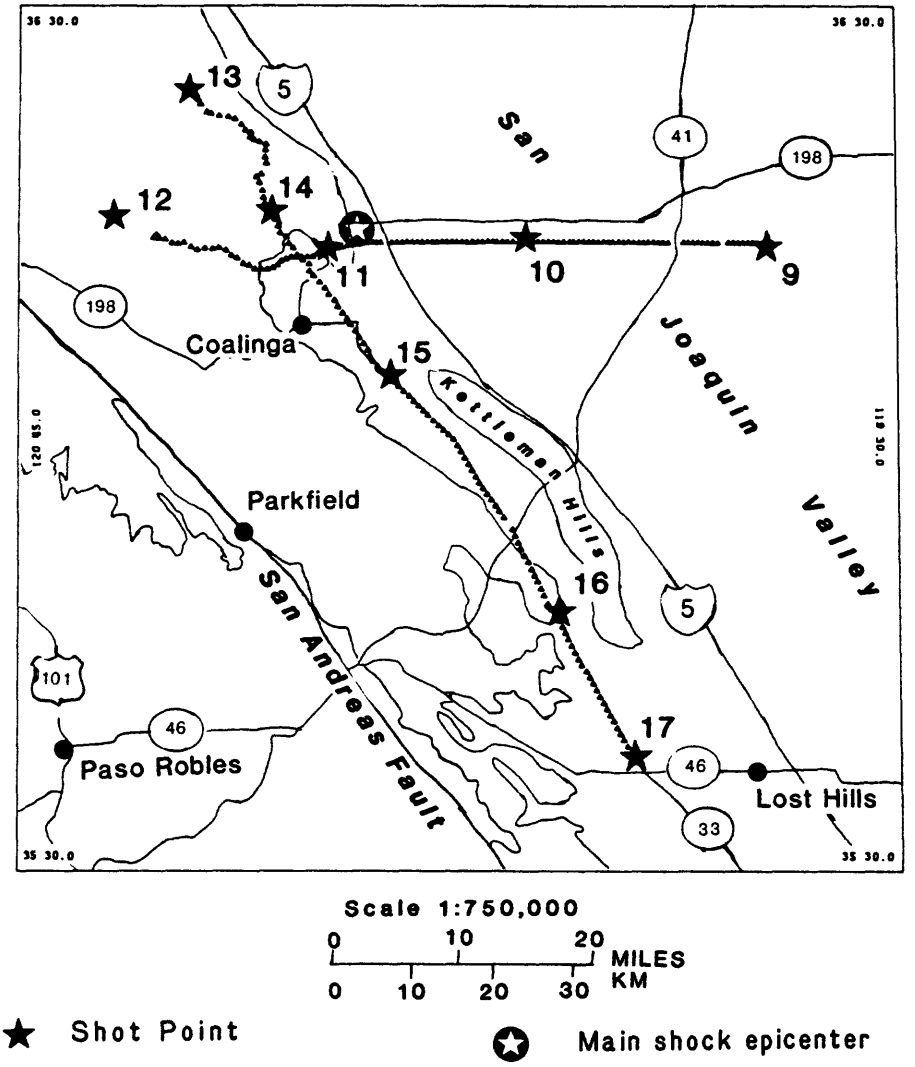

Fig. 1. Map of the geography and the shotpoint and station locations along the U.S.G.S. Coalinga refraction profiles.

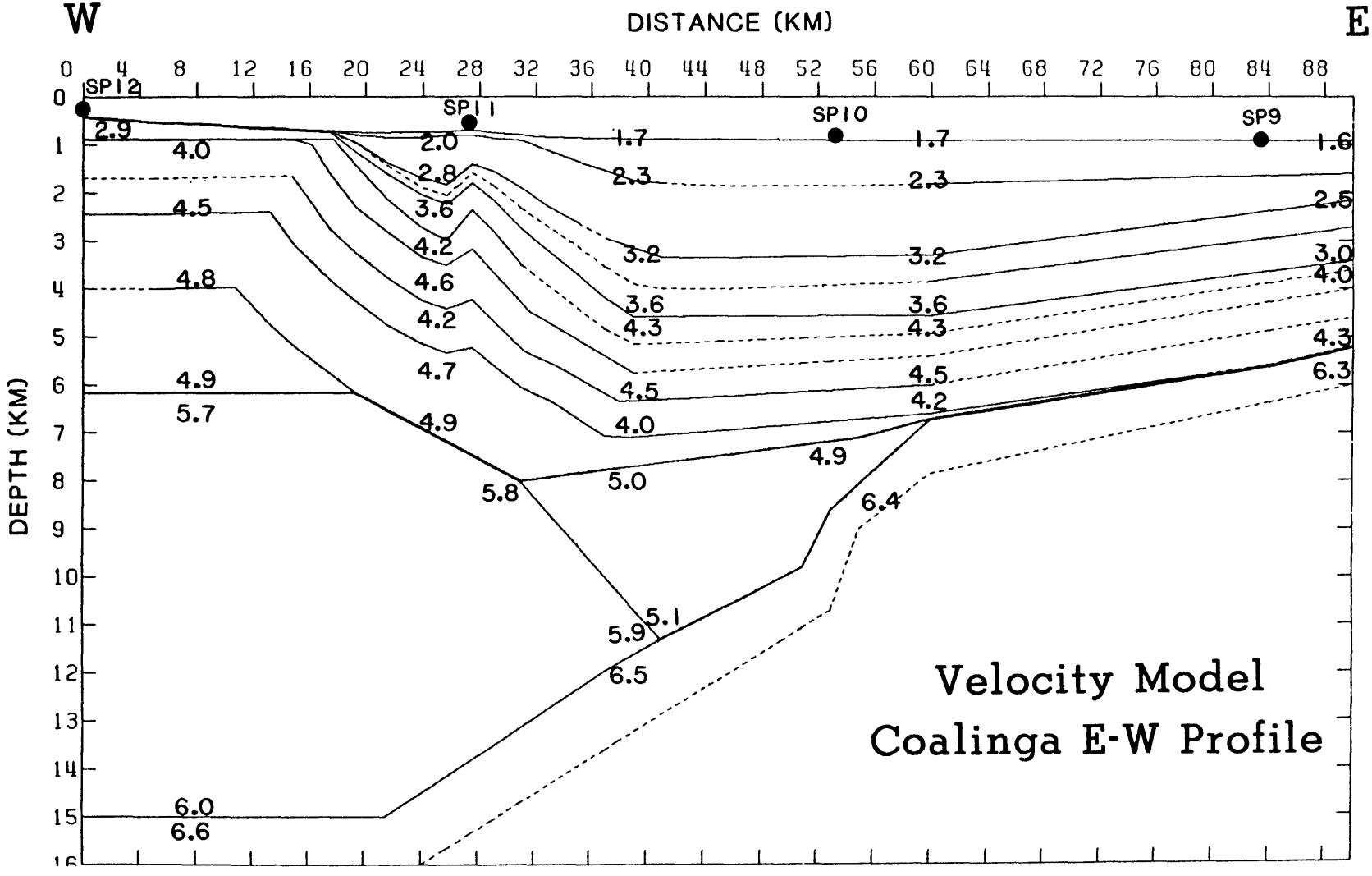

Fig. 2. Velocity cross-section along the E-W refraction profile. Shotpoint locations are labelled at top of figure.

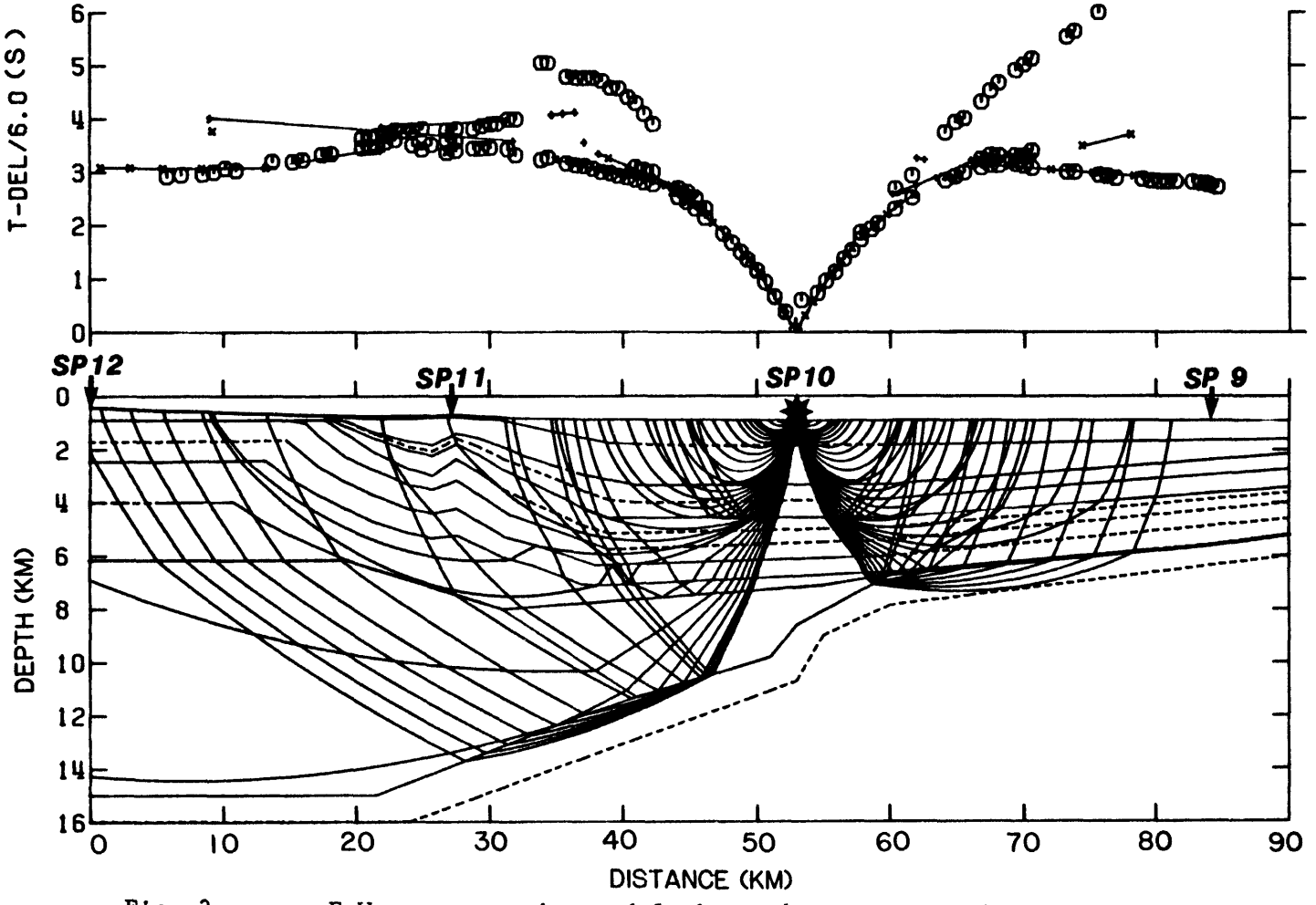

Fig. 3. E-W cross-section model shows the rays traced from shotpoint 10, (SP10). Travel-time plot shows both the observed travel times and the calculated ray times.

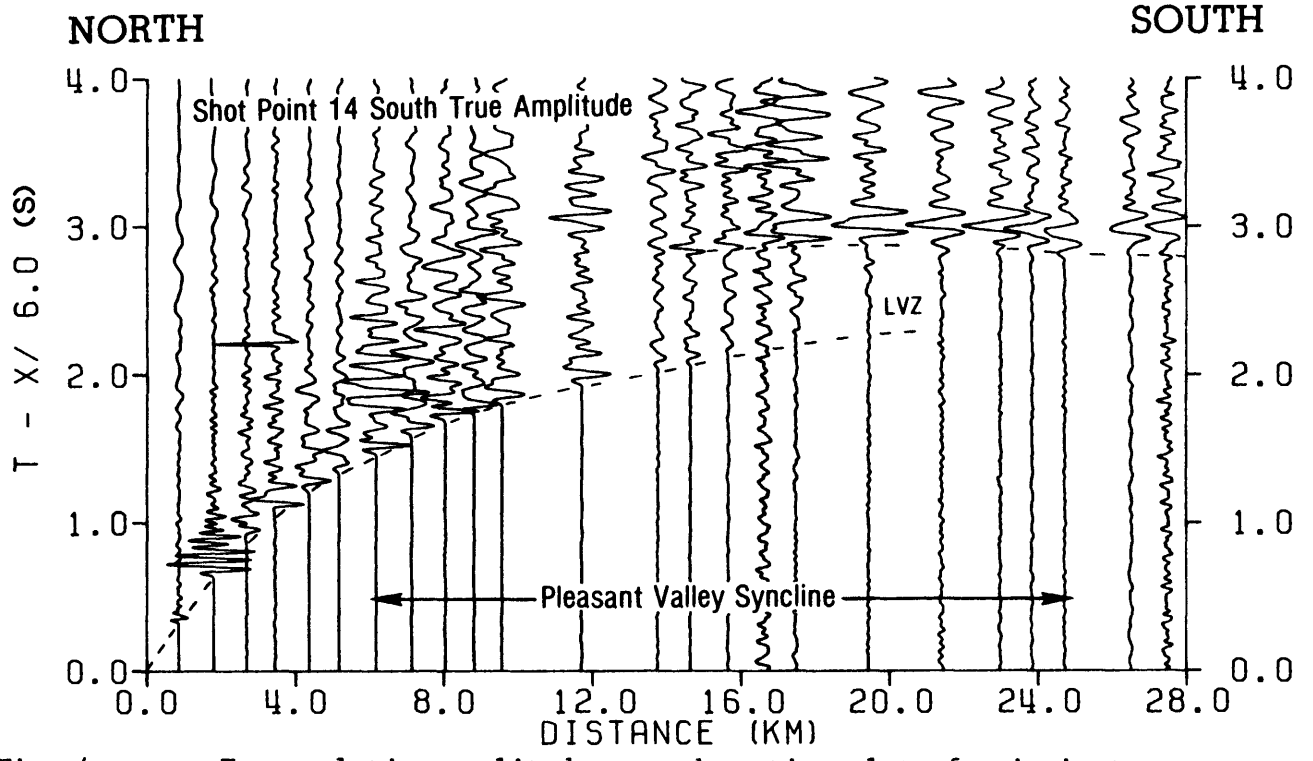

Fig. 4. True relative amplitude record section plot of seismic traces between 0 and 28 km distance south of SP 14. The disappearance of the first arrivals, the travel-time delay, and the large amplitude reflection indicate the presence of a low velocity zone within the Great Valley Sequence beneath the Pleasant Valley Syncline.

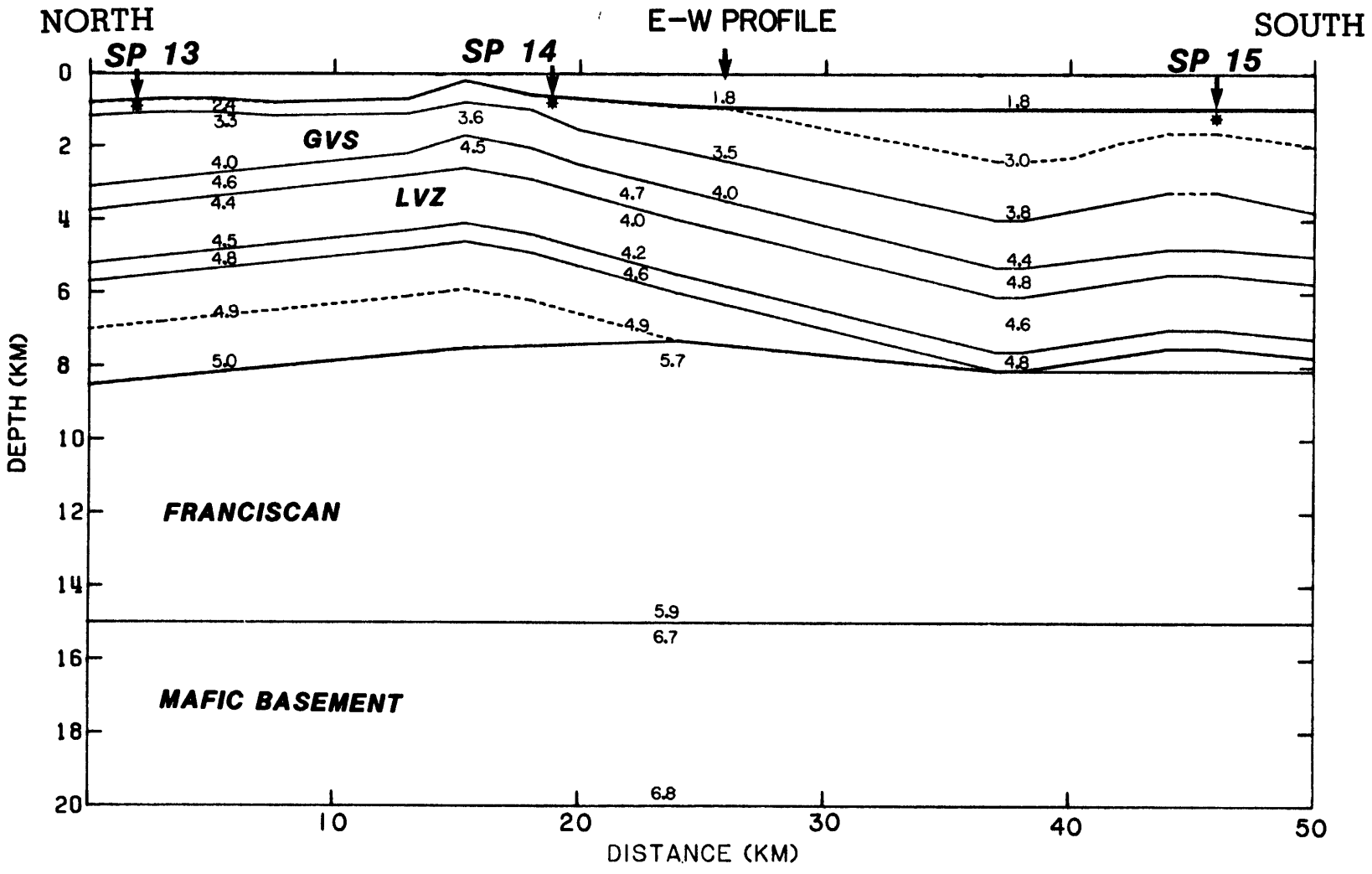

Fig. 5. Velocity cross-section along the NW-SE refraction profile between SP 13 and SP 15.

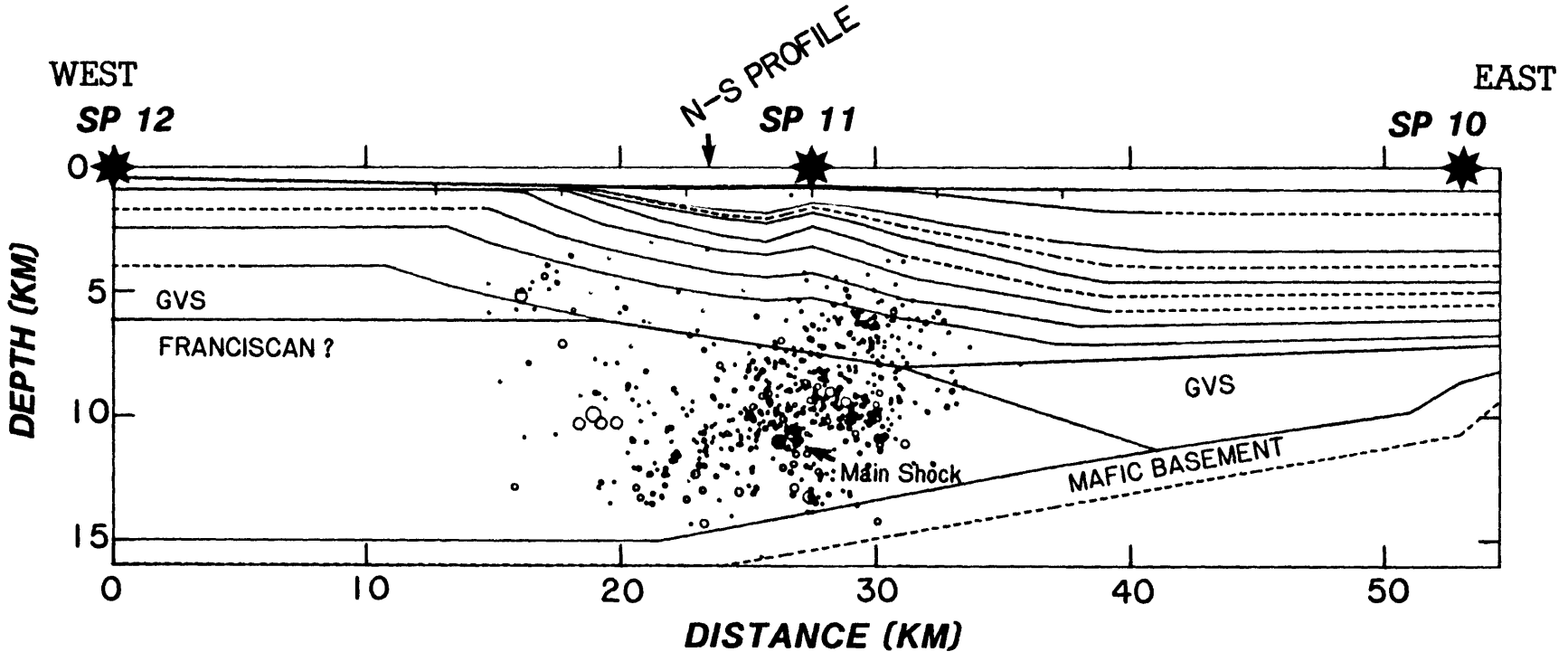

Fig. 6. E-W cross-section model with aftershock locations (Eaton, et. al., 1983) superimposed.

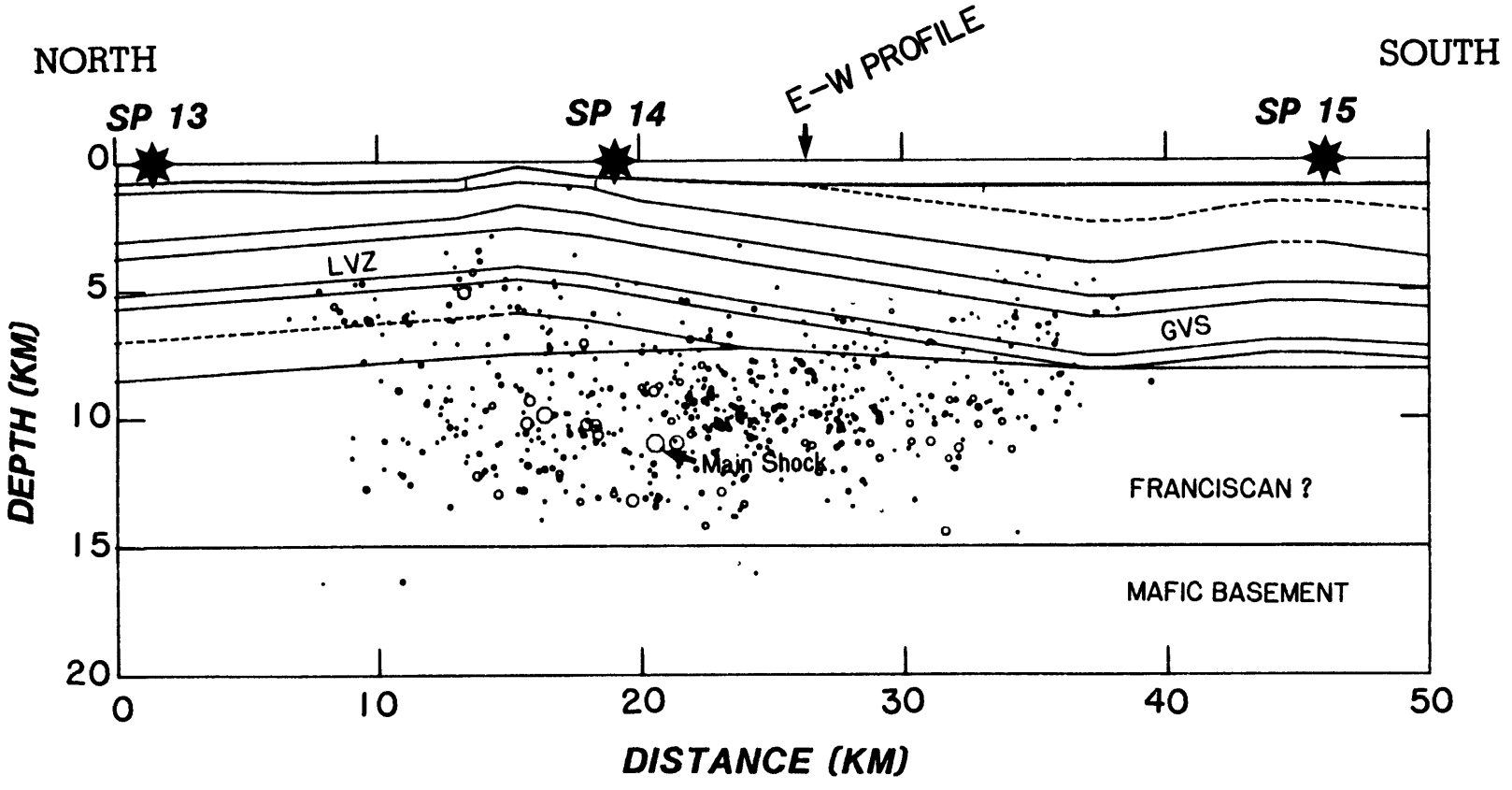

Fig. 7. NW-SE cross-section model with aftershock locations (Eaton, et. al., 1983) superimposed.

TECTONIC SETTING OF THE 1983 COALINGA EARTHQUAKES FROM SEISMIC REFLECTION PROFILES: A PROGRESS REPORT

Carl M. Wentworth, Mark D. Zoback and J. Alan Bartow

U.S. Geological Survey
Menlo Park, California 94025

INTRODUCTION

The 1983 Coalinga earthquakes occurred at the east margin of the uplifted Diablo Range where the range abruptly narrows southeastward and its bold east front is replaced by the Coalinga-Kettleman Hills-Lost Hills anticlinal trend. East-west seismic reflection profiles, recorded across both the Coalinga epicentral area and the Coast Range-Great Valley boundary 65 km to the southeast and 140 km to the northwest, all suggest eastward-directed thrusting at that boundary. This thrusting is inferred during emplacement (obduction?) of the Franciscan assemblage, near the beginning of the Tertiary, and subsequently, including considerable movement in the Plio-Quaternary.

Profiles SJ-6, SJ-19, and SJ-3 (see fig. 1 for locations) are 6-second, 24-fold, VIBROSEIS records that were purchased from Western Geophysical Company and reprocessed to 12-seconds. Profile CC-1 (located 73 km northwest of the northwest margin of fig. 1) is a 15-second, 133-fold, VIBROSEIS record collected for the USGS by Geophysical Systems Corporation, using 800 channel, sign-bit recording. Work is still underway on processing and interpreting the records.

COAST RANGE-GREAT VALLEY BOUNDARY

An abrupt and fundamental structural change occurs across the boundary between the Diablo Range and the San Joaquin Valley. Beneath the valley, a regional unconformity dips gently southwestward at the base of similarly dipping Upper Cretaceous and Cenozoic strata and reaches depths of 5-10 km at the west side. The thickness of Cretaceous strata beneath the west side of the San Joaquin Valley ranges from about 1.5 to 4 km. Immediately to the west in the Diablo Range, the Cretaceous (and locally Jurassic) Great Valley sequence stands nearly on edge, dips steeply northeastward toward the valley, and has a minimum stratigraphic thickness ranging from 3 to 8 km (exposed base is everywhere faulted). The Mesozoic sedimentary section is thus abruptly thickened and upturned westward across the boundary. Uplift of the Diablo Range associated with this upturning has raised the base of the Great Valley sequence as much as 8 km above its position beneath the west edge of the valley. The abrupt westward thickening of the Great Valley sequence remains a persistent and puzzling problem.

SOUTH END OF KETTLEMAN HILLS

An interpretation of reflection profile SJ-6 (fig. 2, and Wentworth and others, 1983) shows the prominent fold of Kettleman South Dome, with Pliocene and Quaternary strata thinned against its east flank as it grew. The base of the Great Valley sequence west of Kettleman Hills is repeated by eastward-directed thrusting that folded South Dome during the Pliocene-Quaternary. This folding required about 2 km of horizontal shortening. The configuration

of the thrust and the implied offset is uncertain. USGS experimentation with migration of the reflection record (J. Rector and R. Williams, written commun., 1984) suggests a steeper dip and smaller offset for the thrust and also clouds the evidence for the northeast-dipping reverse faults shown in figure 2 beneath the anticline.

Mafic basement (velocity of 6.5 km/s) plunges westward from 9 km at the valley margin to 15 km beneath the Diablo Range, with much of the space above occupied by a wedge of material having a velocity of about 5.7 km/s, which is appropriate for Franciscan rocks. This relation implies thrust emplacement of a wedge of Franciscan rock over the same basement that bears Great Valley sequence farther east and beneath the peeled up Great Valley sequence of the Diablo Range (Wentworth, Walter, Zoback, and Blake, 1983).

CENTRAL DIABLE RANGE

Preliminary interpretation of reflection profile CC-1 (fig. 3) also shows a simple, west-dipping valley basement, which reaches a depth of about 6 km at the structural trough (km 36, fig. 3) near the valley margin, where the upper Cretaceous section is 4 km thick. Farther west, the section bends upward slightly and extends beneath the leading edge of the Diablo Range (km 24, fig. 3), where steeply east-dipping Great Valley sequence is exposed at the surface. A prism of 5.6-5.8 km/s material, again inferred to be Franciscan rocks from the velocity, lies between this slightly upturned Great Valley sequence and faster underlying basement, in much the same fashion as the Franciscan(?) wedge in figure 2. The Great Valley sequence exposed here in the Diablo Range is 7-8 km thick, twice as thick as the upper Cretaceous section beneath the range front (km 24, fig. 3). At the surface, just north of the mouth of Garzas Creek where the reflection line runs (see Jennings, 1977), the attitude of the Eocene Kreyenhagen formation defines an abrupt hinge between 60° easterly dips in the range and 10° dips in front of the range. This hinge, faulted or not, must extend down and westward beneath the range to account for the penetration of flat dips beneath the range front.

The Ortigalita fault raises Franciscan rocks against Great Valley sequence, probably through eastward-directed thrust or reverse faulting. In a fashion somewhat similar to that shown in figure 2, this faulting should repeat the base of the Great Valley sequence, now eroded from the crest of the range.

In the core of the Diablo Range, strong, moderately east-dipping reflections beneath exposed Franciscan may lie within a thick Franciscan terrane, as suggested by the refraction interpretation of Walter and Mooney (1982), or may define the base of an unexpectedly thin Franciscan. Indistinct eastward continuation of these reflections in the record suggest that this east-dipping feature plunges to a depth of at least 15 km. Comparisons with the SJ-6 and SJ-19 sections (figs. 2 and 6) suggest that Franciscan rocks also extend to a depth of about 15 km here. The east-plunging feature would then probably represent a Cenozoic thrust that post-dates emplacement of the Franciscan(?) wedge.

COALINGA EPICENTRAL AREA

The Coalinga area marks the change from a wide, massive Diablo Range cored by exposed Franciscan rocks on the northwest to a narrow, complex Diablo Range flanked by the Coalinga-Kettleman Hills-Lost Hills anticlinal trend on the southeast (fig. 1). Coalinga anticline occurs at this transition, rising north-northwestward up onto the southern flank of the northwesterly trending Joaquin Ridge anticline (fig. 4). Like Kettleman South Dome (fig. 2), Coalinga anticline seems to have grown largely in Pliocene and Quaternary time, although Joaquin Ridge anticline has a longer history.

Interpretation of two reflection profiles that cross the nose, SJ-3 and SJ-19 (fig. 5), including correlation with the stratigraphy encountered in several nearby oil wells, reveals some of the details of structure and stratigraphy. A Cenozoic stratigraphic section that is about 4.5 km thick beneath the valley thins and is uplifted westward across the folds and into the Diablo Range. About 1.5 km of Upper Cretaceous strata (Moreno and Panoche formations) are present above crystalline basement in the San Joaquin Valley 40 km east of Coalinga anticline, compared to an exposed section of Great Valley sequence about 8 km thick in the range to the west. The records are difficult to interpret below the top of the Panoche formation: deep structure is only partly represented and simple layered reflections contain a major tectonic boundary. In concert with the nearby refraction velocity model (A. Walter, this volume; see fig. 4 for location), however, important deep structure can be extracted from the reflection profiles.

Partial interpretations of profiles SJ-3 and SJ-19, prepared without the aid of the refraction model, are shown in figure 5 to illustrate changes along strike. Figure 6 presents a more complete interpretation of SJ-19 that is based on reevaluation of the reflection record in the context of the reflection model. We assume, in comparing the reflection and refraction profiles, that strike is parallel to the axis of Coalinga anticline.

It is important to identify the base of the sedimentary section as a constraint in interpretation. The top of basement beneath the Panoche formation seems evident at the east end of SJ-19, where a strong reflection approximately coincides with the equivalent basement in the refraction model and with basement extrapolated from well control to the east. There are, however, discontinuous layered reflections below this horizon that define interval velocities of 4.5 to 5 km/s and extend to a depth of almost 10 km. The base of the Panoche here may thus be an unconformity within the Great Valley sequence, with more sedimentary rocks below, as implied by the interval velocities and the refraction results. The deep, half graben of Fielding and others (1984) may represent this underlying sedimentary prism, which probably is pre-Panoche Great Valley sequence.

At the west end of SJ-19 and SJ-3, concentric layered reflections about 3-seconds thick beneath the Panoche top extend eastward beneath Coalinga anticline. Using a velocity of 4.5 km/s, these layered reflections extend to at least 10 km and possibly as much as about 13 km. Thus there is more than sufficient space to accomodate the whole 8 km of Great Valley sequence that is exposed to the west. If the refraction model is even approximately correct, however, the base of the Great Valley sequence must lie well up in the interval represented by these layered reflections. The deeper reflections

must then be from Franciscan rocks. These relations make the Great Valley sequence only 3 km thick beneath the syncline and anticline, compared to a thickness of about 5 km east of the anticline (Panoche plus underlying 5 km/s prism).

The refraction model (fig. 6) defines in its west half an eastward thinning wedge of 5.8 km/s material that, because of its velocity, we infer to be Franciscan. The top of this wedge corresponds to a prominent reflection beneath Coalinga anticline in SJ-19. Steps in this reflection imply faults that can be fit by principal northeastward-directed thrusts and subordinate antithetic thrusts. These faults lie beneath, and are presumably associated with, the northwest-striking anticline (fig. 4).

Coalinga anticline changes amplitude dramatically along its length, as shown by the structure contour map (fig. 4) and by the two reflection profiles (fig. 5)--about 2.5 km on SJ-19 and almost 4 km on SJ-3, measured at the base of the Moreno formation between the crest of the fold and the base of its northeast limb. Relief across the fold is accomplished in two distinct steps or tiers, the lower of which shows about the same amplitude, 1.5 km, on both profiles. Pleasant Valley syncline expresses only the amplitude of the upper tier of the anticline, which probably developed separately from the lower tier. Each tier is probably associated with separate, underlying thrusts. Just how these thrusts and fold tiers relate to the northwest and north-northwest trends of folding is not clear: SJ-19 crosses northnorthwest-trending Coalinga anticline, whereas SJ-3 shows the lower tier on the nose of northwest-trending Joaquin Ridge anticline (fig. 4).

The position of the tip of the Franciscan(?) wedge beneath undeformed strata east of the anticline as shown in figure 6 seems inconsistent with folding of the anticline by thrusting associated with the wedge. One explanation, which would also account for the smaller thickness of Great Valley sequence beneath the folds than farther east, is that the Franciscan wedge splits the sedimentary section and overlies at least 2 km of Great Valley sequence.

RELATION TO 1983 COALINGA EARTHQUAKES

The 1983 Coalinga main shock is consistent with the northeast-directed thrusting inferred above. That earthquake involved northeast-southwest compression and rupture on a plane striking northwest and dipping either 67° NE or 23° SW (Eaton, Cockerham, and Lester, 1983). The hypocenter lies at a depth of about 10 km beneath the crest of the anticline (figs 4 and 6). Northeast-directed thrusting would require that the gently southwest-dipping focal plane of the main shock be selected (fig. 6), rather than the steeply northeast-dipping plane favored by Stein's modeling of co-seismic surface deformation (this vol., and 1984). If the thrusts in figure 6 flatten down dip to the southwest, a thrust drawn through the hypocenter would have a shape similar to that of the thrust alternative that most closely fits the surface deformation in Stein's modeling.

REFERENCES CITED

Eaton, J., Cockerham, R., and Lester, F., 1983, Study of the May 2, 1983 Coalinga earthquake and its aftershocks, based on the USGS seismic network in northern California, in Bennett, J. H., and Sherburne, R. W., eds., The 1983 Coalinga earthquakes: California Division of Mines and Geology Special Publication 66, p. 261-273.

Fielding, Eric, Barazangi, Muawia, Brown, Larry, Oliver, Jack, and Kaufman, Sidney, 1984, COCORP seismic profiles near Coalinga, California: Subsurface structure of the western Great Valley: Geology, v. 12, p. 268-273.

Jennings, C. W., 1977, Geologic map of California: California Division of Mines and Geology, Geologic Data Map 2, scale 1:750,000.

Stein R. S., and King, G. C. P., 1984, Seismic potential revealed by surface folding: 1983 Coalinga, California, earthquake: Science, v. 224, p. 869-872.

Walter, A. W., and Mooney, W. D., 1982, Crustal structure of the Diablo and Gabilan Ranges, central California: A reinterpretation of existing data: Bulletin of the Seismological Society of America, v. 72, no. 5, p. 1567-1590.

Wentworth, C. M., Walter, A. W., Bartow, J. A., and Zoback, M. D., 1983, Evidence on the tectonic setting of the 1983 Coalinga earthquakes from deep reflection and refraction profiles across the southeastern end of Kettleman Hills, in Bennett, J. H., and Sherburne, R. W., eds., The 1983 Coalinga, California earthquakes: California Division of Mines and Geolgy Special Publication 66, p.113-126.

Wentworth, C. M., Walter, A. W., Zoback, M. D., and Blake, M. C., Jr.,1983 Possible obduction of Franciscan assemblage, southeasternmost Diablo Range, California (abs.): Transactions, American Geophysical Union, EOS, v. 64, no. 45, Nov. 8, 1983, p. 868.

FIGURE CAPTIONS

Figure 1. Geologic map of the Kettleman Hills-Coalinga region. Locations of seismic reflection lines SJ-3, -6, and -19 are shown relative to the Coalinga-Kettleman Hills anticlinal trend, the uplifted Franciscan assemblage and Great Valley sequence exposed in the Diablo Range, and the 1983 main-shock epicenter.

Figure 2. Interpretation of reflection profile SJ-6 from Wentworth and others (1983). Basement and Franciscan assemblage based in part on associated refraction velocity model. Note the two-fold vertical exaggeration.

Figure 3. Preliminary interpretation of reflection profile CC-1. Profile lies 140 km northwest of profile SJ-19 along Garzas Creek and highway 140 (see Jennings, 1977). Velocity structure 6 km east of west end of profile taken from Walter and Mooney (1982); pi symbols mark deep boundaries in that velocity model, which crosses this profile at a high angle. Surface attitudes shown at range front (km 24). West-dipping queried faults and steeply east-dipping layering in Great Valley sequence not evident in reflection record.

Figure 4. Structure map on top of Kreyenhagen. The top of Eocene strata (Kreyenhagen formation) represents the deepest structural horizon for which drill-hole control is abundant. Similar structure extends downward at least another half kilometer to the top of the Cretaceous Panoche formation. Surface geology not shown above Kreyenhagen in contoured area. Epicenter location of the Coalinga main shock from Eaton and others (1983), reconfirmed July, 1984 (Eaton, oral commun.).

Figure 5. Interpretations of reflection profiles SJ-3 and 19, independent of refraction velocity model. Velocities shown are those used to correct time to depth and are based partly on reflection interval velocities and partly on geologic interpretation. Velocity structure in the upper 5 km fairly well constrained by reflection data.

Figure 6. Refraction velocity model and associated reflection interpretation along profile SJ-19. Refraction model from A. Walter (this vol.). Velocities above 5 km in reflection model are based on reflection interval velocities, those below are taken from refraction model. "Deepest event" marks deepest clear reflection in 12-s reflection record. Coalinga main-shock hypocenter and southwest-dipping focal plane (Eaton and others, 1983) projected to this W-E section parallel to the anticline axis.

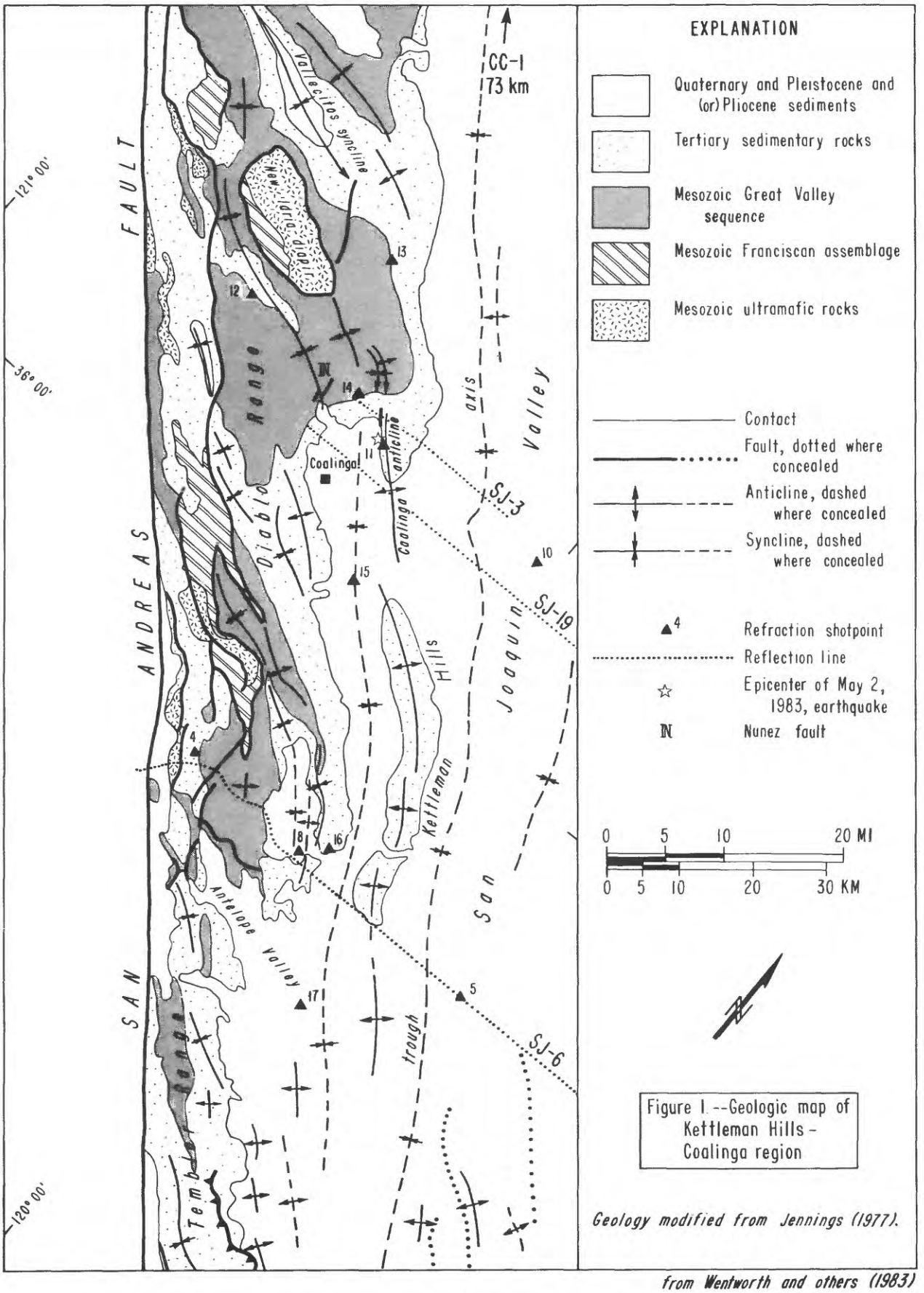

Figure 1.--Geologic map of Kettleman Hills - Coalinga region

Geology modified from Jennings (1977).

from Wentworth and others (1983)

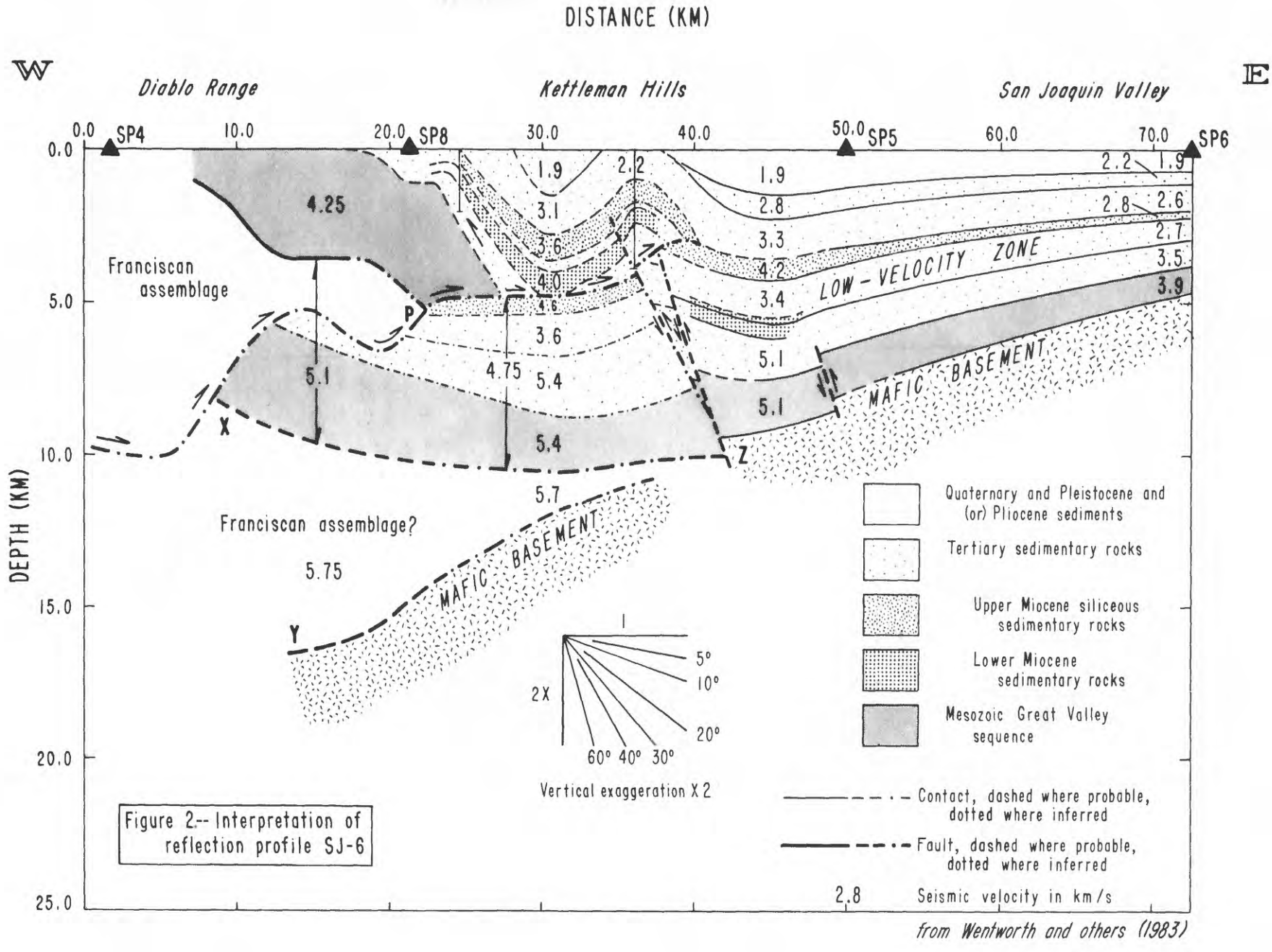

Figure 2.-- Interpretation of reflection profile SJ-6

from Wentworth and others (1983)

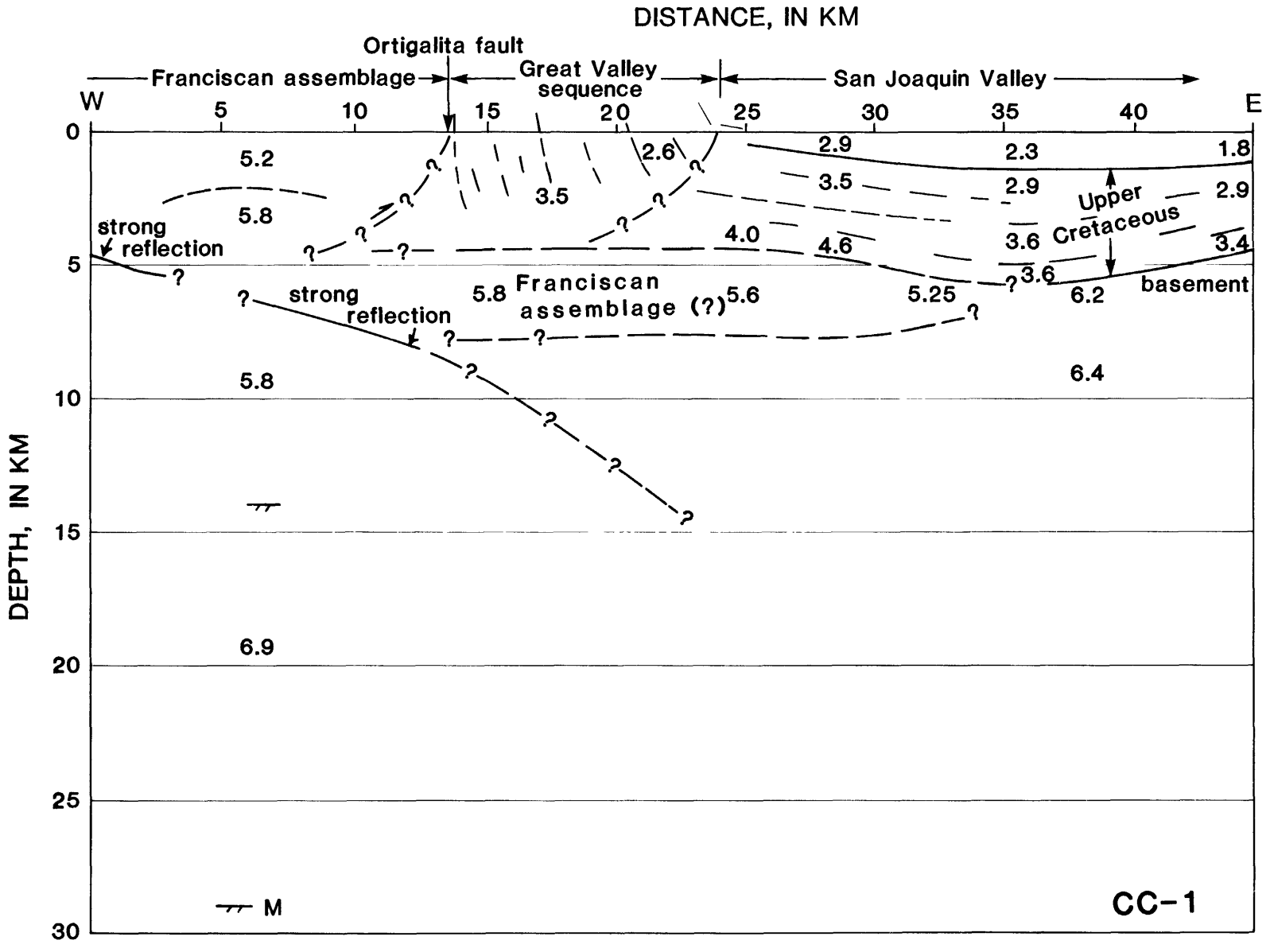
DISTANCE, IN KM
Ortigalita fault
Franciscan assemblage
Great Valley sequence
San Joaquin Valley
W
E
5
10
15
20
25
30
35
40
0
5
10
15
20
25
30
DEPTH, IN KM
5.2
5.8
strong reflection
2.6
3.5
2.9
2.3
1.8
3.5
2.9
2.9
Upper Cretaceous
4.0
4.6
3.6
3.4
3.6
5.25
6.2
basement
strong reflection
5.8 Franciscan assemblage (?) 5.6
5.8
6.4
6.9
M
CC-1

Figure 3

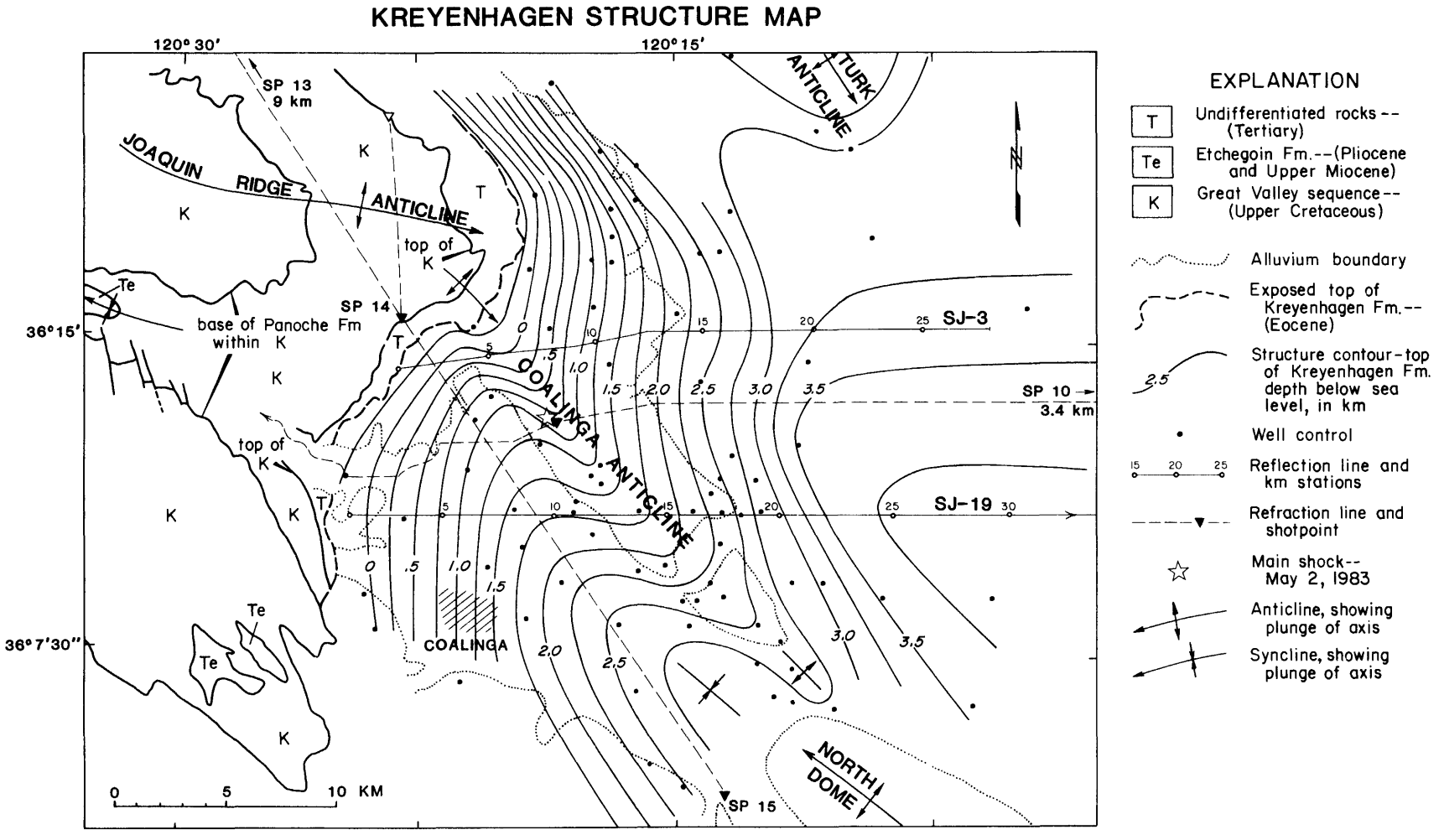
KREYENHAGEN STRUCTURE MAP
120° 30'
120° 15'
36° 15'
36° 7' 30"
SP 13
9 km
JOAQUIN RIDGE ANTICLINE
TURK ANTICLINE
top of K
SP 14
base of Panoche Fm within K
COALINGA ANTICLINE
SJ-3
SP 10
3.4 km
SJ-19
COALINGA
NORTH DOME
SP 15
0 5 10 KM
EXPLANATION
T Undifferentiated rocks -- (Tertiary)
Te Etchegoin Fm. -- (Pliocene and Upper Miocene)
K Great Valley sequence -- (Upper Cretaceous)
Alluvium boundary
Exposed top of Kreyenhagen Fm. -- (Eocene)
Structure contour - top of Kreyenhagen Fm. depth below sea level, in km
Well control
Reflection line and km stations
Refraction line and shotpoint
Main shock -- May 2, 1983
Anticline, showing plunge of axis
Syncline, showing plunge of axis

Figure 4

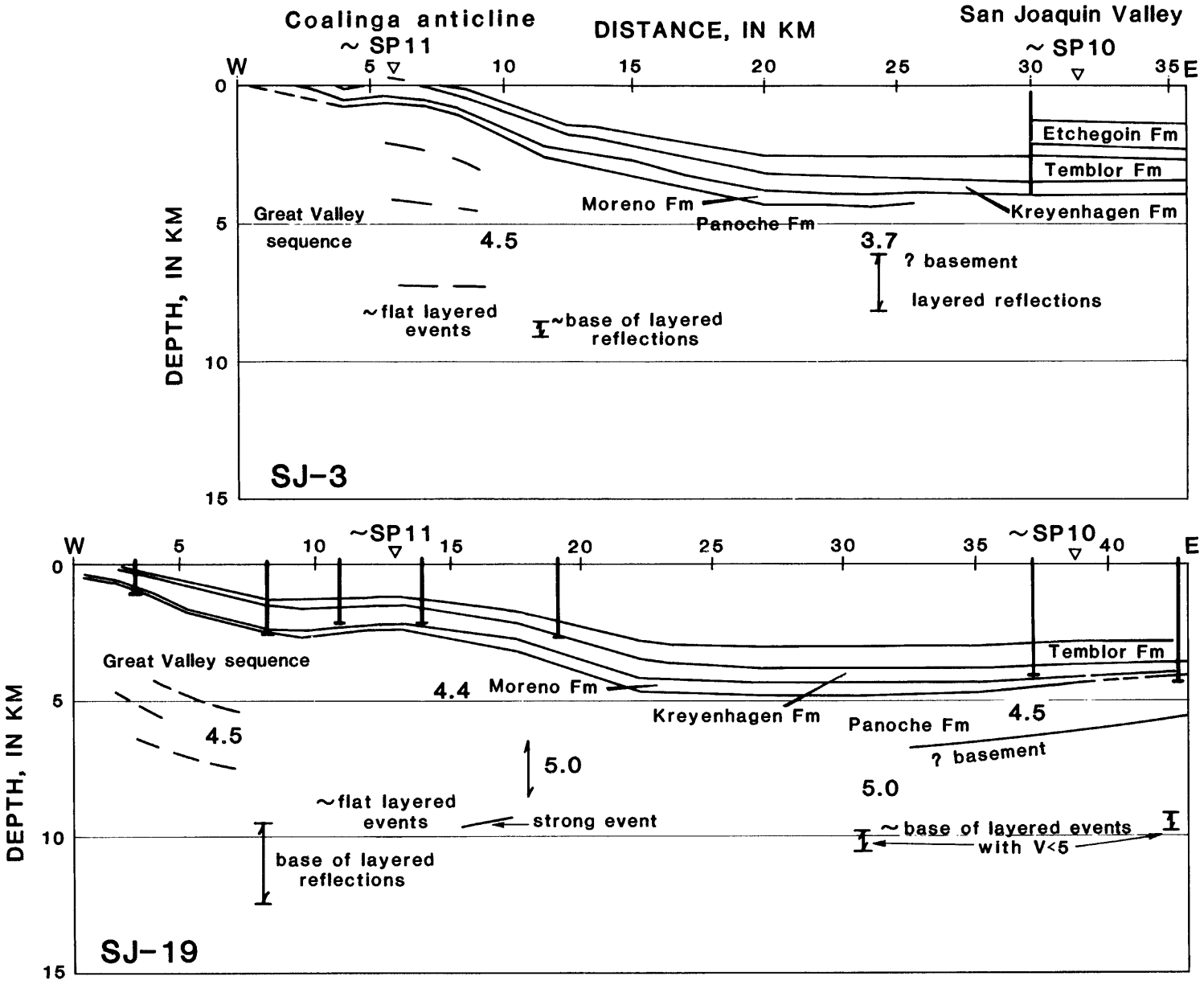
Coalinga anticline
~ SP11
DISTANCE, IN KM
San Joaquin Valley
~ SP10
W
E
DEPTH, IN KM
Etchegoin Fm
Temblor Fm
Great Valley sequence
Moreno Fm
Panoche Fm
Kreyenhagen Fm
4.5
3.7
? basement
layered reflections
~flat layered events
~base of layered reflections
SJ-3
~SP11
~SP10
Great Valley sequence
4.4
Moreno Fm
Kreyenhagen Fm
Panoche Fm
4.5
? basement
5.0
~flat layered events
strong event
base of layered reflections
~base of layered events with V<5
SJ-19

Figure 5

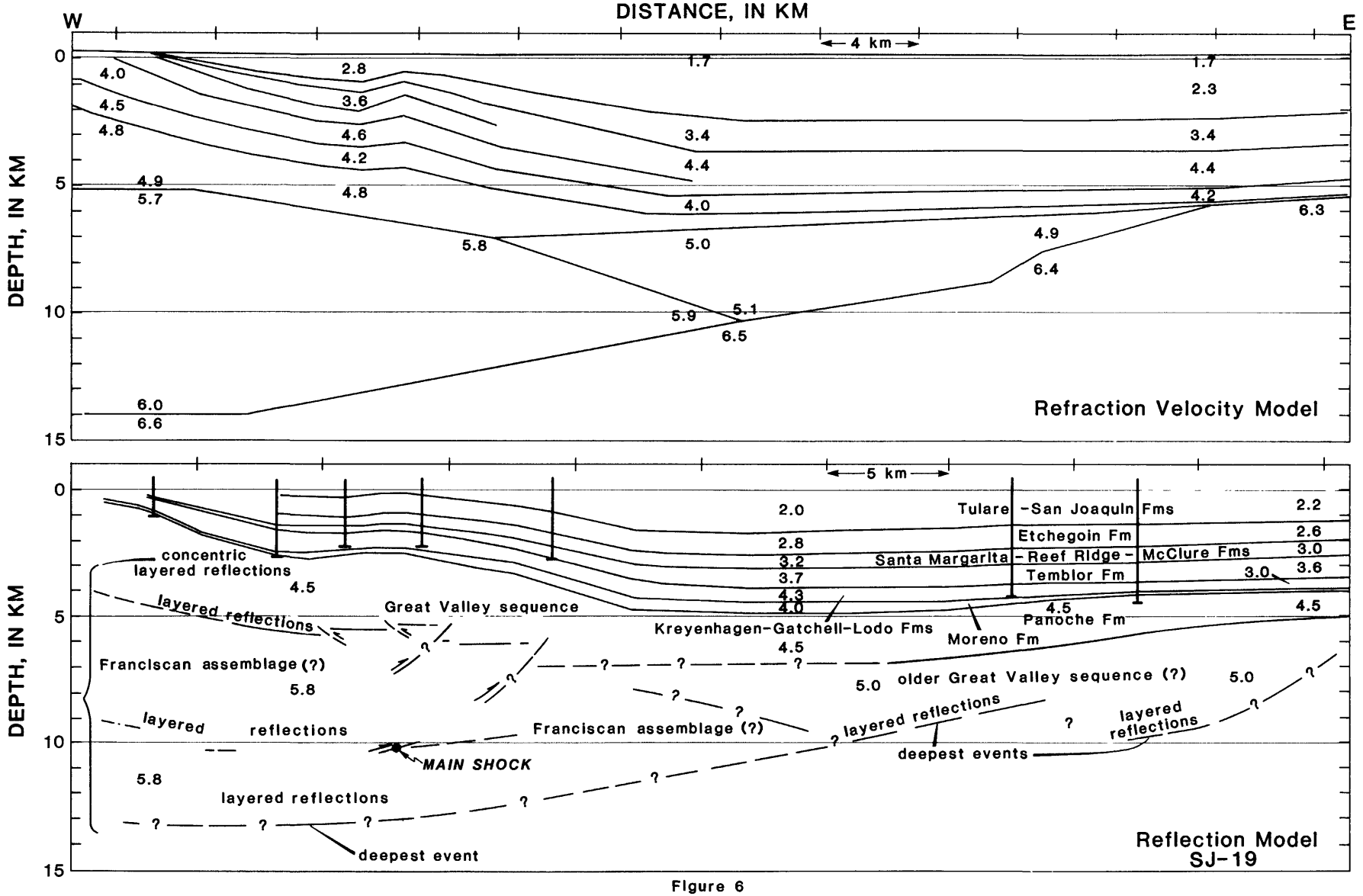
DISTANCE, IN KM
W
E
4 km
DEPTH, IN KM
0
5
10
15
4.0
4.5
4.8
2.8
3.6
4.6
4.2
4.8
1.7
3.4
4.4
4.0
5.0
4.9
5.7
5.8
5.9
5.1
6.5
6.0
6.6
1.7
2.3
3.4
4.4
4.2
6.3
4.9
6.4
Refraction Velocity Model
5 km
concentric
layered reflections
4.5
layered reflections
Great Valley sequence
Franciscan assemblage (?)
5.8
layered reflections
Franciscan assemblage (?)
MAIN SHOCK
5.8
layered reflections
deepest event
2.0
2.8
3.2
3.7
4.3
4.0
4.5
Kreyenhagen-Gatchell-Lodo Fms
Tulare -San Joaquin Fms
Etchegoin Fm
Santa Margarita - Reef Ridge - McClure Fms
Temblor Fm
Moreno Fm
4.5
Panoche Fm
5.0
older Great Valley sequence (?)
layered reflections
deepest events
layered
reflections
2.2
2.6
3.0
3.6
3.0
4.5
5.0
Reflection Model
SJ-19

Figure 6

Basement Faults Beneath the Western Great Valley of California Based on COCORP Seismic Reflection Profiles near Coalinga

Eric Fielding and Muawia Barazangi
Department of Geological Sciences
and
Institute for the Study of the Continents
Cornell University
Ithaca, New York 14853

Summary

COCORP, the Consortium for Continental Reflection Profiling, collected deep seismic reflection profiles along two lines in the Coalinga area of central California during May and June of 1977 (see Figure 1). These reflection data shed some light on the deep Cenozoic and Mesozoic structures in the subsurface and suggest the existance of basement faults beneath the 1983 Coalinga earthquake sequence, and the western San Joaquin Valley. The collection and processing of the reflection data are covered in more detail in Fielding and others (1983), and the geologic background and stratigraphic interpretation of the data are covered in Fielding and others (1984); these topics will be covered only briefly here.

The COCORP data are most consistant with faulting on the high-angle nodal plane of the May 2, 1983 main shock focal mechanism (see Figures 2, 4 and 5), and the continuity of reflections from the folded sedimentary layers across the axis of the Coalinga Nose-Kettleman Hills North Dome (KHND) anticline indicates that major movement on faults has not broken through about the upper 6 km of the sedimentary section at the latitude of the COCORP lines. The presence of low-angle, southwest-dipping thrust faults to the southwest of the Coalinga Nose anticline is ruled out in the upper 8-10 km by the continuity of reflections from presumed sedimentary layering (see Figures 2, 3 and 4). A southwest-dipping thrust fault deeper than 10 km cannot be ruled out, but there are no deeper reflections in the COCORP data to suggest such a fault.

We have interpreted and inferred several faults beneath the axis of the San Joaquin Valley, with significant movement during the Cretaceous, as high-angle normal faults that affected the basement and the overlying sediments. The Late Cenozoic and ongoing surface folding and subsurface reverse faulting, highlighted by the recent Coalinga earthquake sequence, may be the result of the reactivation of these

inferred high-angle basement faults; hence pre-existing faults may be controlling the compressional deformational style of the western Great Valley in the Coalinga area.

Discussion

Figure 1 shows the locations of the two COCORP Coalinga lines on a tectonic map of the area with structural contours, faults, fold axes, and the May 2, 1983 main shock location and focal mechanism and the preliminary spatial extent of the aftershock zone (Eaton, 1983; Reasenberg and others, 1983). The main, 50 km long, east-west Line 1 runs from the hills southwest of the city of Coalinga, due east across the Coalinga Nose-KHND anticline, and out into the San Joaquin Valley. It passes about 15 km to the southeast of the May 2 main shock epicenter along the strike of the Coalinga Nose anticline (also called Anticline Ridge), and crosses the southern end of the aftershock zone. Note that there is about 2 km of plunge and a considerable decrease in amplitude along the fold axis, as shown by the structural contours on the Eocene Kreyenhagen formation, derived from the closely spaced oil wells of the Coalinga and Kettleman Hills oil fields (Figure 1); this would suggest that the underlying fault offset is less and/or deeper than it is where the main shock occurred.

The short, 15 km north-south crossline, labelled Line 3, starts at the base of Reef Ridge, southeast of Coalinga, and runs due north across the end of the Kettleman Hills North Dome. Common depth point, or CDP, coverage on Line 3 extends only to vibration point 113, or VP 113--the station numbering used on this and the other figures--so the CDP stack does not quite cross Line 1. The results presented here are from extensive reprocessing done on the Megaseis computing facility at Cornell University during 1982 and 1983--before and after the May 2 main shock--and followed a standard processing sequence. A detailed stacking velocity (approximately equal to RMS velocity for shallowly dipping layers) analysis was performed; a plot of the interval velocities derived from the processing of Line 1, can be found in Fielding and others (1983).

Figure 2 shows the CDP stack for Line 1. The scale is approximately equal for the horizontal and vertical axes, assuming a velocity of 4 km/s (close to the average velocity of the sedimentary section) for the conversion of the two-way travel time to depth. There are several caveats to remember in the interpretation of these data. Because the dominant frequency of the reflections detected in these data is 10-15 Hz, with a wavelength of 200-400 m, the resolution of these

data is about 50-100 m. Fault offsets or other structures smaller than 50 m or 1/4 wavelength might not be detectable.

Figures 2 and 3 show unmigrated CDP stacks, which means that dipping reflections are apparently displaced down-dip, and appear to have shallower dips than the true position of the reflectors in the earth. In addition, Lines 1 and 3 cross the Coalinga Nose-KHND structure at about 40 and 50 degree angles, respectively, so that the reflection points are probably not directly below the surface traces of the lines. For Line 1, this means that the east-dipping reflections are actually bouncing somewhat south of the line, and appear to have slightly shallower dips than they would if they were in the plane of the section. The combined corrections for the migration and the off-strike section take reflections with apparent dips of 20 degrees to true dips of about 35 degrees.

Figure 3 shows the unmigrated CDP stack for Coalinga Line 3. This crossline runs from the steeply dipping strata of the Reef Ridge anticline, due north across the north end of the Kettleman Hills North Dome. The continuity and slight north dip of the sedimentary reflectors across the syncline here clearly rules out a southwest-dipping thrust fault, at least in the upper 5-6 s, or down to about 8-10 km depth. Subhorizontal reflections are assumed to be from the same sedimentary section as is interpreted beneath about VP 90 of Line 1.

Figure 4 shows the interpretation of Coalinga Line 1. The strong reflectors in the Tertiary section are shown in this figure with their identified ages only, derived from the exposed surface geology off the west end of the line, and from several nearby oil wells (see Fielding and others, 1984 for the geologic map and stratigraphic description). In the lower part of the section, consisting mostly of the Upper Jurassic through Cretaceous Great Valley Group, the seismic data have been abstracted as a line-drawing. No wells have penetrated deeply into the Cretaceous section, so the exposed thickness of 8-10 km has been projected down-dip from the hills west of Coalinga, placing the approximate bottom of the sedimentary section and the top of basement at the depth indicated by the dashed line, where projected down-dip, and the dotted line, where inferred from the deepest reflections received.

Notice the offset between event A and event B, which are correlated as the same stratigraphic horizon by their seismic expression; this offset requires about a kilometer of movement on an inferred fault. The best fit to the observed truncations, and to the folding of the overlying sediments is with a high-angle normal fault dipping to the east. The dip

and, especially the strike, are not well constrained. In addition, strike-slip movement on the basement faults cannot be detected in the seismic data.

To the west of events A and B on Line 1, there is a wedge-shaped package of reflectors which dip increasingly westward, extending to event C. A migrated version of this feature can be found in Fielding and others (1984). The tilting of the probably Cretaceous sediments in this wedge requires significant rotation of the underlying basement, at least 30 degrees, depending on the unconstrained strike of the dipping strata. The wedge has a seismic expression similar to half-grabens imaged on other reflection profiles, and occurs in the same position as a wedge of material with velocities near 5 km/s shown on the U.S.G.S. refraction line some 15 km to the north (Walter, this volume; Wentworth and others, this volume). The essentially undeformed overlying Tertiary section indicates that fault movement on both of the interpreted basement faults described above ended before the Tertiary (see Figures 2 and 3).

The fault beneath the Coalinga Nose anticline, shown in Figure 4, is inferred from several sources: from the COCORP data, the focal mechanism of the 1983 Coalinga main shock from Eaton (1983), and dislocation modelling of coseismic elevation changes by Stein and King (1984). COCORP lines 1 and 3 show continuous reflections from the apparently little deformed sedimentary layering of the Great Valley Group and the Tertiary section to the west and south, respectively, of the Coalinga Nose-KHND anticlinal axis to depths of about 6 seconds two-way travel time or 8 to 10 km (Figures 2 and 3). This rules out significant fault offsets greater than the approximate 50-100 m resolution of the reflection data within the observed sedimentary section. Beneath the sedimentary reflectors, extensive reprocessing of the reflection data revealed no evidence of any southwest dipping reflections, as might be expected if there were a low-angle fault zone at depth. Seismic reflection data has been very successful in imaging low-angle faults in other areas (e.g., Wentworth and others, 1983; and this volume; Allmendinger and others, 1984), so the absence of reflections here may be significant, assuming that some seismic energy is penetrating through the thick overlying sedimentary section.

The shape of the Coalinga Nose-KHND anticline both outcropping at the surface and revealed in the seismic reflection lines across the fold axis is quite similar to forced folds and drape folds seen on seismic lines in the Laramide province (e.g., Sacrison, 1978). Because there is good evidence for high-angle Cretaceous basement faults

beneath the sedimentary section just 10-15 km to the east of the CN-KHND axis, the simplest interpretation of the 1983 Coalinga main shock focal mechanism is that movement occurred on the high-angle northeast-dipping nodal plane determined by Eaton (1983; see Figure 1). As described in detail by Stein and King (1984), the repetition of about a thousand earthquakes of the magnitude of the 1983 earthquake would produce the observed fold amplitude and shape.

Reflections from a fault with a 50 or 60 degree dip would probably not be detected on a seismic reflection line, and if it were, it would appear displaced significantly down-dip to the northeast on the unmigrated seismic sections. As mentioned earlier, the continuity of reflections from the sedimentary layers folded over the anticlinal axis rules out large (> 50 m) fault displacements certainly in the upper 4 km, and probably in the upper 6 km, where the fold is crossed by COCORP line 1. This is consistent with the elastic dislocation modelling of the coseismic surface deformation measured on levelling lines and long-term deformation of terraces along streams which cross the Coalinga Nose (Stein and King, 1984).

Figure 5 shows two highly schematic cross-sections along Line 1, portraying two of many possible geometries of basement faults, which satisfy the observed structures in the overlying sedimentary section shown in the COCORP data. Cretaceous faults in the preferred figure 5a are high-angle normal faults, and would be similar to growth-fault adjustments seen in other deep sedimentary basins. Cretaceous listric reverse-faults and/or strike-slip faults could also explain the rotation and deformation of the Cretaceous strata, as shown in figure 5b. In both cases, the pre-existing faults may be controlling the deformational style of the Pliocene to Recent folding of the Coalinga Nose-KHND anticline.

It is not unreasonable to compare the general active deformational style of the Coalinga area, and possibly the whole western Great Valley, to the active deformation of the Zagros fold belt in western Iran. The Zagros orogenic belt is the result of the Miocene to present continental collision of the Arabian plate with the Iran crustal blocks at the edge of the Asian plate. Shortening of the Zagros belt is being accomodated both by folding of the relatively thick (6-10 km) sedimentary section, and by thrust faulting of the basement, as indicated by numerous medium-sized earthquakes. The basement faulting in the Zagros appears to be strongly decoupled from the overlying folded sedimentary section by a relatively thick (about 1 km) salt layer located at the base of the sedimentary cover. As appears to be the case in the

Coalinga earthquake sequence, the main shocks of medium-sized (M_S = 6-7) events in the Zagros are located in the uppermost part of the basement and are not associated with surface faulting; however, many aftershocks do occur within the overlying sedimentary section. Hence, it is tempting to speculate that numerous, and mostly unmapped, active faults may exist beneath the western edge of the Great Valley. The seismic hazard potential of such "blind" faults should be carefully evaluated.

Acknowledgements

Supported by COCORP National Science Foundation Grants EAR 82-12445 and EAR 80-25361. We thank L. Brown, C. Wentworth, and A. Walter for helpful discussions. The field data were collected by crew 404-48-02 of Compagnie Generale de Geophysique. Cornell contribution No. 813.

References Cited

Allmendinger, R., Sharp, J., von Tish, D., Serpa, L., Brown, L., Kaufman, S., Oliver, J., and Smith, R.B., 1983, Cenozoic and Mesozoic structure of the eastern basin and range from COCORP seismic reflection data: Geology, v. 11, p. 532-536.

Eaton, J.P., 1983, Seismic setting, location, and focal mechanism of the May 2, 1983 Coalinga earthquake, in Borcherdt, R.D., ed., The Coalinga earthquake sequence commencing May 2, 1983: U.S. Geological Survey Open-File Report 83-511, p. 20-26.

Eaton, J.P., Cockerham, R., and Lester, F., 1983, Study of the May 2, 1983 Coalinga earthquake and its aftershocks, based on the USGS seismic network in northern California, in The 1983 Coalinga, California Earthquakes: California Division of Mines and Geology Special Publication 66, p. 261-273.

Fielding, E.J., Barazangi, M., Brown, L., Oliver, J., and Kaufman, S., 1983, COCORP seismic reflection profiles near the 1983 Coalinga earthquake sequence: Deep structures, in The 1983 Coalinga, California Earthquakes: California Division of Mines and Geology Special Publication 66, p. 137-149.

Fielding, E.J., Barazangi, M., Brown, L., Oliver, J., and Kaufman, S., 1984, COCORP seismic profiles near Coalinga, California: Subsurface structure of the western Great Valley: Geology, v. 12, p. 268-273.

Reasenberg, P., Eberhart-Phillips, D., and Segall, P., 1983, Preliminary views of the May 2, 1983, Coalinga earthquake, in Borcherdt, R.D., ed., The Coalinga earthquake sequence commencing May 2, 1983: U.S. Geological Survey Open-File Report 83-511, p. 20-26.

Sacrison, W.R., 1978, Seismic interpretation of basement block faults and associated deformation, in Matthews, V., III, ed., Laramide folding associated with basement block faulting in the western United States: Geological Society of America Memoir 151, p. 39-49.

Stein, R.S., and King, G.C.P., 1984, Seismic Potential Revealed by Surface Folding: 1983 Coalinga, California, Earthquake: Science, v. 224, p. 869-872.

Walter, A., Velocity structure near Coalinga, California: this volume.

Wentworth, C.M., Zoback, M.D., and Bartow, J.A., Structure at the west side of the San Joaquin Valley, California, from seismic reflection profiles: this volume.

Figure Captions

Figure 1:
Generalized tectonic map of the Coalinga area, showing location of COCORP lines, major faults and fold axes, topographic contours (dashed), 500m structural contours on top of Eocene Kreyenhagen formation derived from wells in Coalinga and Kettleman Hills oil fields, location and focal mechanism of May 2, 1983 Coalinga earthquake main shock and its aftershock zone through June 12, 1983.

Figure 2:
COCORP Coalinga Line 1: time section is not migrated or deconvolved. Trace amplitude balancing with a window of 0.5 s applied before stack. High-amplitude, continuous reflections are from Lower Tertiary section. Note structures in Cretaceous section reflectors beneath the strong Tertiary reflections.

Figure 3:
COCORP Coalinga Line 3: time section is not migrated or deconvolved. Trace amplitude balancing with a window of 0.5 s applied before stack. Note sharp upwarping toward Reef Ridge on south end and limb of Kettleman Hills North Dome on north end. Relatively continuous, presumably unfaulted, reflectors can be seen down to 5-6 s (10-12 km) in syncline in the middle of the line.

Figure 4:
Interpretation of COCORP Line 1 (unmigrated), showing surface topography and geology, stratigraphic interpretation of reflections from the Cenozoic section, line drawing abstracted from deeper reflections intepreted as from the Great Valley Group, inferred basement faults and approximate location of basement (dashed where projected and dotted where inferred). Note offset between events A and B, and wedge-shaped package of reflectors extending to event C. Wells projected onto section are identified in Fielding (1984).

Figure 5:
Schematic drawings of two possible interpretations of the subsurface structure and tectonic setting of the Coalinga area, consistent with the COCORP data on the overlying sedimentary section. Basement faults deformed the Great Valley Group, and one may be reactivated under the Coalinga Nose anticline.

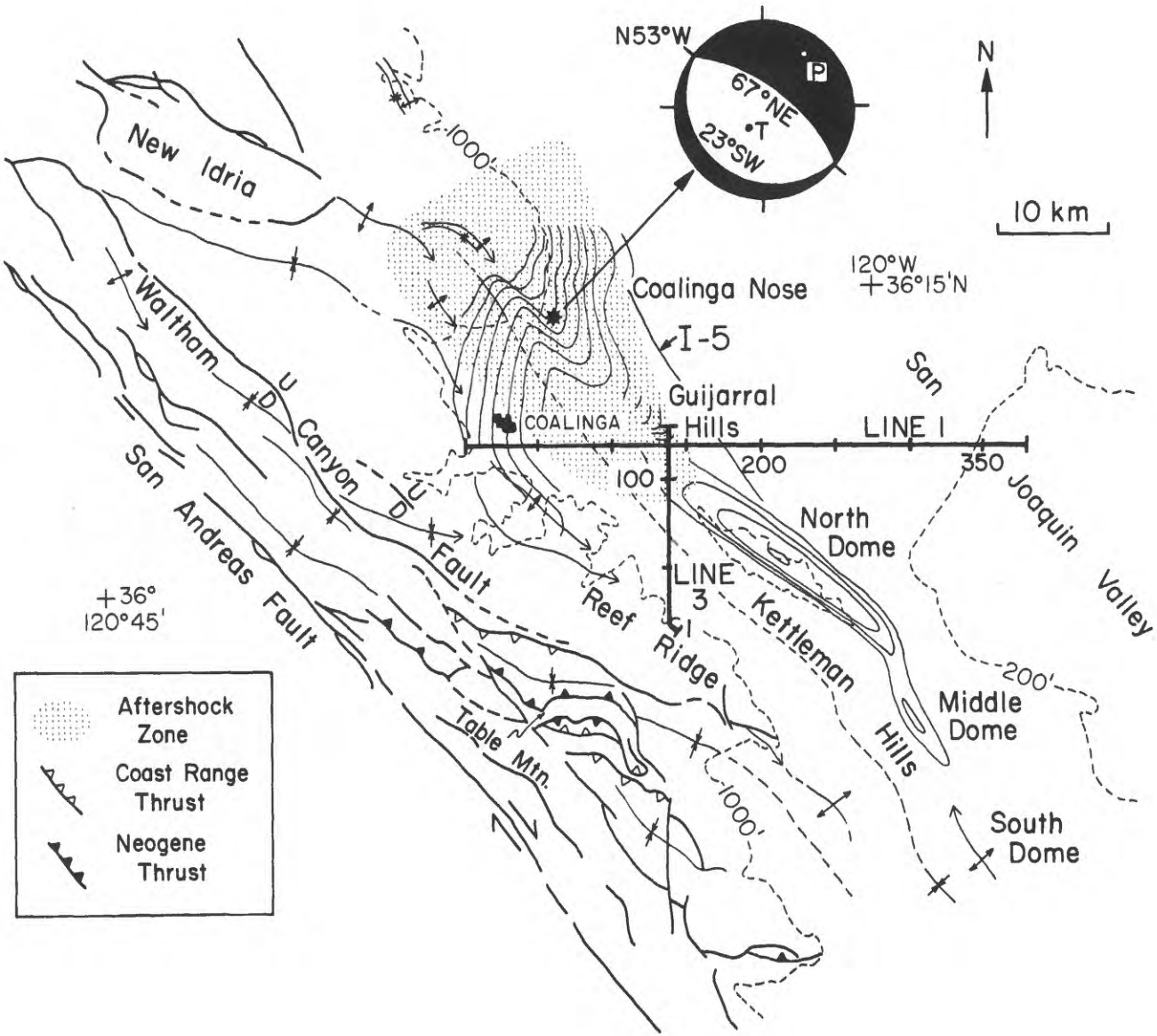
N53°W
67°NE
23°SW
P
T
N
10 km
120°W
+36°15'N
Coalinga Nose
I-5
New Idria
Waltham Canyon Fault
U
D
San Andreas Fault
COALINGA
Guijarral Hills
LINE 1
100
200
350
San Joaquin Valley
North Dome
LINE 3
Kettleman Hills
Middle Dome
South Dome
Reef Ridge
Table Mtn.
1000'
200'
+36°
120°45'
Aftershock Zone
Coast Range Thrust
Neogene Thrust

Fig. 1

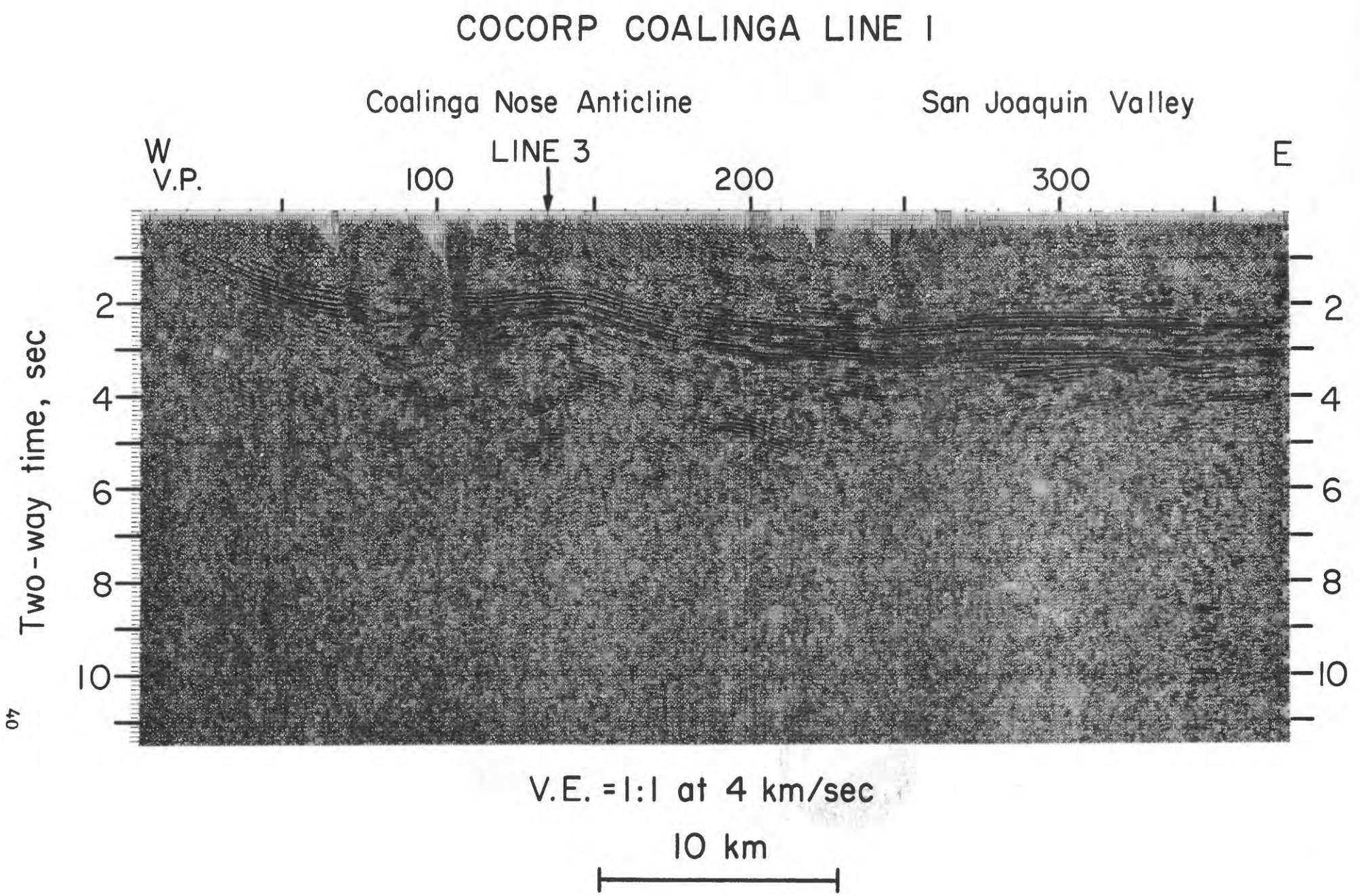
COCORP COALINGA LINE 1
Coalinga Nose Anticline
San Joaquin Valley
W
V.P.
LINE 3
E
100
200
300
2
4
6
8
10
Two-way time, sec
V.E. = 1:1 at 4 km/sec
10 km

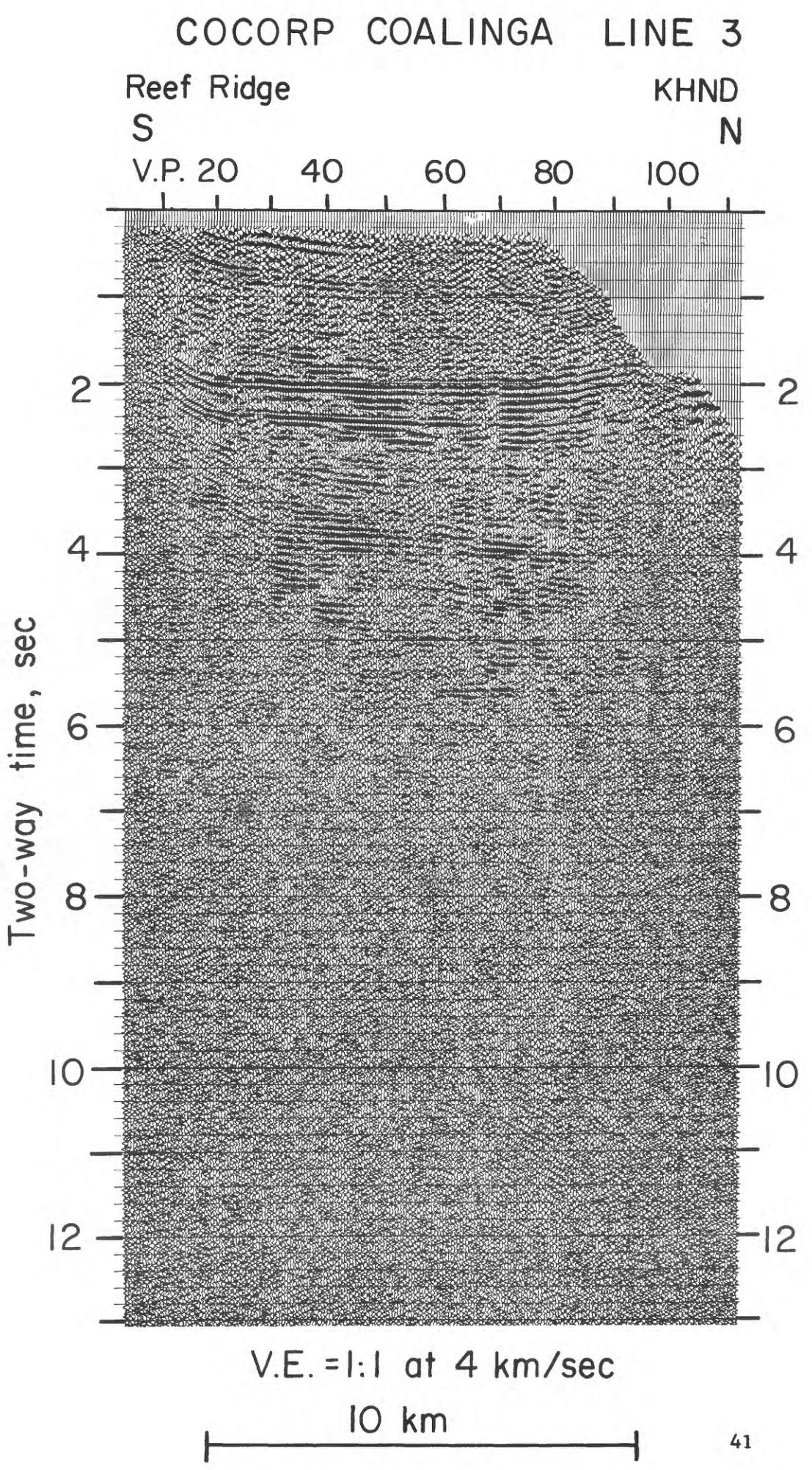
COCORP COALINGA LINE 3
Reef Ridge
KHND
S
N
V.P. 20
40
60
80
100
2
4
6
8
10
12
Two-way time, sec
V.E. = 1:1 at 4 km/sec
10 km

Fig. 3

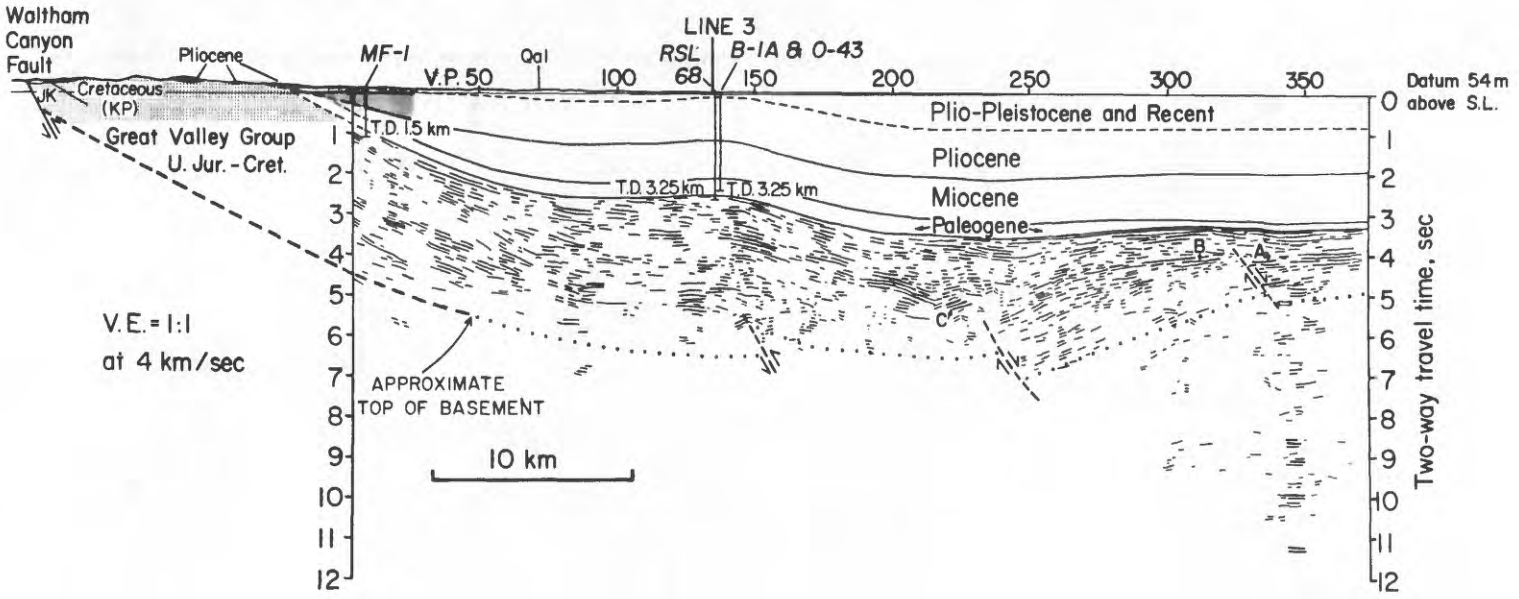
Waltham
Canyon
Fault
Pliocene
JK
Cretaceous
(KP)
Great Valley Group
U. Jur. - Cret.
MF-1
V.P. 50
Qal
LINE 3
RSL 68
B-1A & O-43
100
150
200
250
300
350
Datum 54 m
above S.L.
Plio-Pleistocene and Recent
Pliocene
Miocene
Paleogene
T.D. 1.5 km
T.D. 3.25 km
T.D. 3.25 km
A
B
C
V.E. = 1:1
at 4 km/sec
APPROXIMATE
TOP OF BASEMENT
10 km
Two-way travel time, sec
0
1
2
3
4
5
6
7
8
9
10
11
12

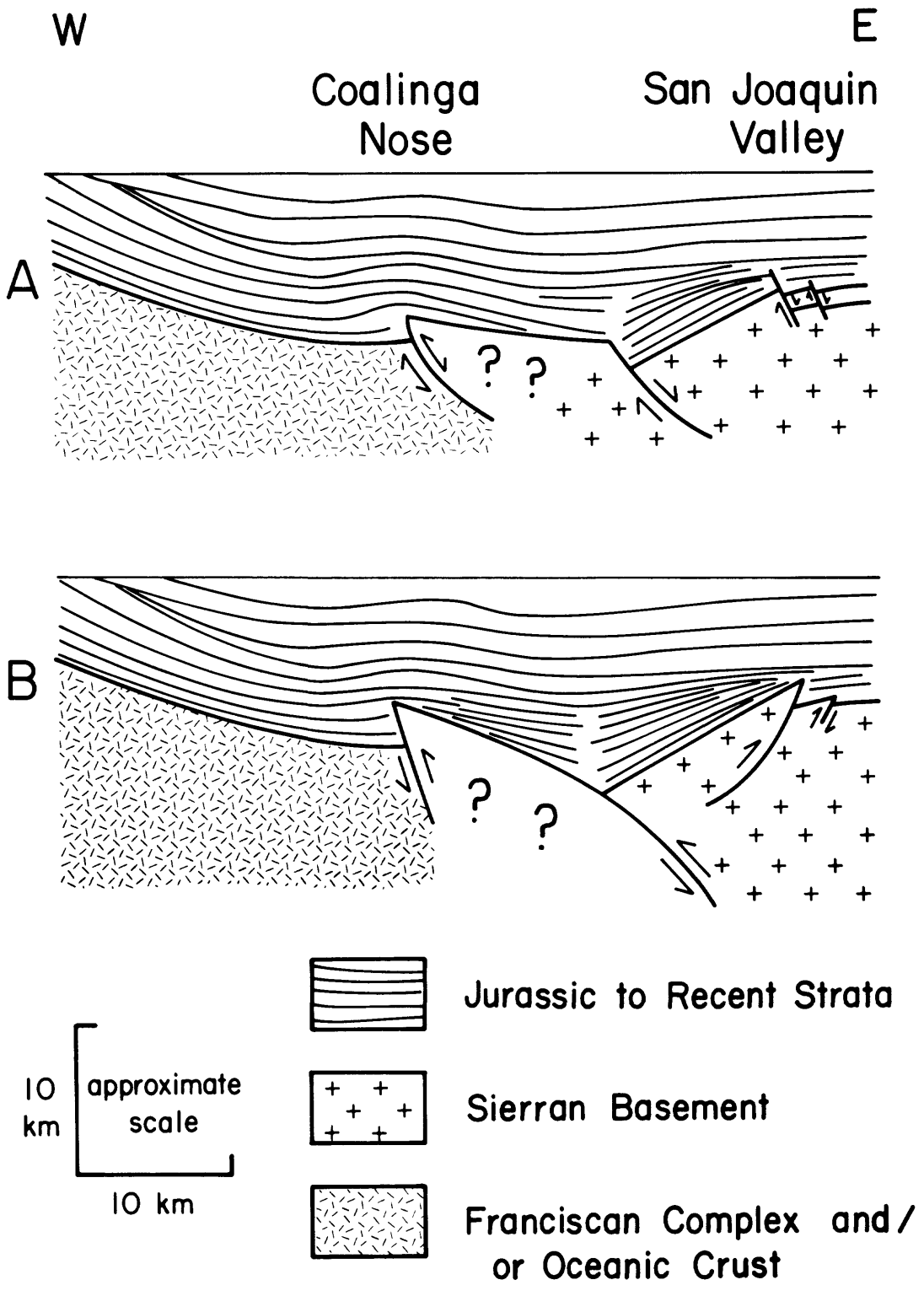
W
E
Coalinga Nose
San Joaquin Valley
A
B
? ?
? ?
Jurassic to Recent Strata
Sierran Basement
Franciscan Complex and/ or Oceanic Crust
10 km
approximate scale
10 km

Fig. 5

REGIONAL SEISMIC BACKGROUND OF THE MAY 2, 1983 COALINGA EARTHQUAKE

J. P. Eaton

U.S. Geological Survey
Menlo Park, California 94025

ABSTRACT

Seismicity in the central and southern Coast Ranges for the 11 years prior to the 1983 Coalinga earthquake is examined along with focal mechanisms of selected large recent earthquakes in the region. A preliminary model is proposed for the process that generates reverse and thrust fault earthquakes along east and west flanks of the Coast Ranges. The cause of such earthquakes appears to be a component of convergent displacement across the San Andreas transform system in the southern Coast Ranges. The earthquakes with reverse and thrust focal mechanisms are found in regions with a distinctive cluster pattern of seismicity, along the flanks of the southern Coast Ranges, that are separated from the San Andreas fault by regions of relative quiescence. The reverse and thrust fault earthquakes occur where detachment zones that lie within a ductile lower crust beneath the center of the transform system pass upward into the brittle crust along its margins. Convergence of the transform system, together with regions of unusually strong materials in the brittle upper crust flanking the San Andreas fault southeast of Cholame, may play an important role in producing such large earthquakes in that region.

INTRODUCTION

The occurrence of the 1983 Coalinga earthquake was a surprise for several reasons: no fault capable of producing an M6.7 event had been mapped in the Coalinga region, the historical record does not place such a large earthquake near Coalinga, and the pattern of recent seismicity in the region had not been interpreted to indicate the presence of an active, undiscovered fault capable of producing such an event. We shall pursue the last point by examining the seismicity in the central Coast Ranges during the 11 years prior to the Coalinga earthquake to determine whether an uninterpreted warning lay hidden in the seismicity data.

The primary data set we examine is the catalog of earthquakes located by the USGS telemetered seismic network from January 1972 through April 1983. Because the network was reinforced and extended during these years the catalog is not uniform in either spatial or temporal coverage. The numbers of stations in the northern subregion (Carquinez to San Benito) and the southern subregion (San Benito to Santa Margarita) were, respectively, 54 and 24 in 1972, 73 and 52 in 1975, and 87 and 68 in 1982. Critical stations near Coalinga, including Anticline Ridge (PAR), were installed in 1975, and critical stations near San Luis Obispo, including Santa Margarita (PMG), were installed

in 1978. Because the network was initially designed to study the San Andreas, Hayward, and Calaveras faults, station density was high near these faults and low elsewhere, particularly along the edge of the Great Valley and along the coast. Consequently, the ability of the network to detect and locate small events in these last two regions, particularly in their southern parts, lagged seriously behind the capability of the network elsewhere in the central Coast Ranges during the entire period, 1972 to 1983. Moreover, the persistent concentration of small earthquakes along slipping segments of the major faults noted above permits these segments to be delineated by seismicity in a relatively short recording interval, whereas the intermittent, sparse earthquakes in other parts of the region must be recorded over a much longer period to accumulate a sufficient number of earthquakes to delineate the active structures from which they emanate.

Our presentation consists of an examination of three seismicity maps of the central Coast Ranges and two maps portraying focal mechanisms of selected large recent earthquakes in the Coast Ranges and Transverse Ranges. The first seismicity map, figure 1, covers the period January 1982-April 1983 and shows the regional distribution of earthquakes relatively unbiased by the evolution of the network. The second and third seismicity maps cover the period January 1972-April 1983 and show the cumulative distribution of earthquakes in the central Coast Ranges (figure 2) and the central Coast Ranges east of the San Andreas fault (figure 3), respectively. These two figures are biased by the loss of smaller earthquakes along the coast and along the edge of the Great Valley. The first focal mechanism map (figure 4) shows first motion solutions and P-axis orientations; the second (figure 5) shows the orientation and dip of the focal planes believed to correspond to the fault planes as well as the corresponding relative displacements on the faults.

SHORT-TERM SEISMICITY PATTERN

Central Coast Range earthquakes for the 16 months preceding the Coalinga earthquake are plotted in figure 1. The 500' elevation contour is the approximate boundary between the Coast Ranges and the Great Valley. The directions N41°W and N35°W correspond, respectively, to the average strike of the San Andreas fault between Cholame and Hollister and the relative motion between the Pacific and North American plates in the same region derived by Minster and Jordan (1978) from a global inversion of plate motions from which data on the San Andreas fault were excluded.

In its general appearance, the short-term pattern of seismicity shown in figure 1 is very similar to that for any comparable time interval from 1970 onward. Such maps for earlier times, however, are relatively poorer in events in the southern parts of the coastal and Great Valley margin regions because of the inadequacy of the network in those regions in earlier years. The pattern of seismicity revealed by comparison, in 1978, of yearly plots from 1970 through 1977 suggested (Eaton, 1985) that they were composed of several types of epicenter distributions:

1) linear concentrations of epicenters of rather uniform density, along selected portions of the principal faults of the region, which are repeated with little variation from year to year,
2) episodes of seismicity that spring up suddenly and then die out slowly over a period of a year or more; these episodes are moderate, isolated earthquakes and their aftershocks, and they occur both on and off well

recognized faults,
3) scattered epicenters throughout seismically active portions of the Coast Ranges from the Pacific shoreline to the western edge of the Great Valley.

In figure 1 the principal linear concentrations of epicenters along mapped faults are: 1) along the San Andreas fault from Parkfield to Corralitos, 2) along the Hayward fault east of San Francisco Bay, 3) along the Calaveras fault from Hollister to the south end of San Francisco Bay, and 4) along the Sargent fault. The cluster of events southeast of Idria on figure 1 represents the aftershock zone of the October 25, 1982 Idria earthquake (M5.5). The scattered epicenters away from the principal mapped faults on figure 1 show more clearly defined trends and clusters than was evident on earlier maps. Such trends include one that lies east of Hollister and extends from San Benito on the south to the junction of the Calaveras and Hayward faults north of Hollister, another that parallels the coast from Pt. Sur to west of Bryson, and another that extends from the southeast end of the Ortigalita fault to the Idria aftershock cluster. Broader trends of activity composed of diffuse patches of epicenters lie along the coast from Bryson to Santa Margarita, along the western edge of the Great Valley from Idria to Devils Den, and east of the Calaveras fault.

LONG-TERM SEISMICITY PATTERN

Coast Range earthquakes for the 11-year period January 1972-April 1983 are shown on figure 2, where nearly 13,000 events are plotted. The short-term features that were evident in figure 1 are reinforced and extended in the long term pattern; additional features well expressed in the long-term pattern were not visible in figure 1. Such new features include the linear zones of epicenters along the San Andreas fault between Corralitos and San Francisco and between Parkfield and Cholame, along the Palo Colorado-San Gregorio fault between Pt. Ano Nuevo and Pt. Sur, along other faults that are parallel to and east of the Hayward fault in the region east of San Francisco Bay, and (probably) along a zone that runs diagonally across the Salinian block from Monterey to Cholame.

Another striking feature of the overall pattern is the virtual absence of activity along the San Andreas fault southeast of Cholame and along the edge of the Great Valley southeast of Devils Den. Other regions of very low seismicity include the San Francisco Bay block between the San Andreas and Hayward faults, a large quiet region east of the southern half of the Calaveras fault, and most of the Salinian block between the San Andreas fault and the zone of epicenters along the coast.

For a more detailed look at the long-term pattern of seismicity in the Coalinga region we turn to figure 3, which is an enlarged version of the southeast quarter of figure 2. Here, we are interested primarily in the region east of the San Andreas fault. As in the earlier figures, the 500' contour marks the approximate boundary between the Coast Ranges and the Great Valley. The main shock and aftershock zone of the 1983 Coalinga earthquake are shown with dashed lines, and the dates of occurrence of the more prominent clusters are also indicated. Northwest of Idria seismicity drops off abruptly east of a medial line striking N34°W that lies parallel to and just east of the Ortigalita fault. West of the medial line northwest of Idria, epicenters

are broadly scattered and clusters are not prominent. Southeast of Idria clusters of events are prominent and most of the epicenters lie east of the medial line. The Coalinga earthquake sequence was almost entirely contained between the medial line and the 500' contour. The aftershocks filled in a region of relative quiescence that was framed by the clusters of 1976, 1980, and 1982. Another quiet zone of comparable size lies just east of Idria. It is framed by the 1983 aftershock region and the clusters of 1975, 1974, and 1982. An even larger quiet zone lies between the 1983 aftershock zone and the San Andreas fault.

If the medial line suggested by the distribution of epicenters east of the San Andreas fault in figure 3 is extended to the northwest as shown with a dashed line in figure 2, it passes through the easternmost linear concentration of epicenters (near Livermore) east of San Francisco Bay. The medial line is very nearly parallel to the direction of relative motion between the Pacific and North American plates. The pattern of seismicity in the central and northern parts of figure 2 appears to be dominated by the branching of the Calaveras and other faults off of the San Andreas. This process appears to be responsible for the complexity of the seismicity pattern along and near the major faults from San Benito northward and in the region east of the Hayward fault. Other processes appear to dominate the pattern along the coast southeast of Pt. Sur and in the southeastern Coast Ranges southeast of the San Luis Reservoir. In a general way the seismicity patterns in these two regions are similar. The most prominent features in the northern halves of these regions are linear concentrations of epicenters in northwest-trending zones, between Pt. Sur and Cape San Martin along the coast and between San Luis Reservoir and Idria along the edge of the Great Valley. The most prominent features of the southern halves of these regions are the broad clusters of epicenters between Cape San Martin and Santa Margarita along the coast and between Idria and Devils Den along the edge of the Great Valley. We suspect that these changes in the pattern of seismicity in the regions bordering the San Andreas fault are related to the change in behavior of the San Andreas itself from the region northwest of Parkfield to the region southeast of Cholame: the transition from creep accompanied by frequent small earthquakes (unlocked) to no creep with virtually no small earthquakes (locked).

FOCAL MECHANISMS IN THE SOUTHERN COAST RANGES AND TRANSVERSE RANGES

To search for the reasons underlying the changes in seismicity pattern from northwest to southeast in the central Coast Ranges we turn to data on focal mechanisms of 20, mostly recent, earthquakes in the southern Coast Ranges and western Transverse Ranges. Except for the composite solution for 1966 Parkfield aftershocks, the first motion solutions are for individual, mostly fairly large, events that were played back from magnetic tape for analysis. The earthquakes were sufficiently well recorded at distances in excess of 100 km that many Pn arrivals at a broad range of azimuths, as well as refractions from shallower crustal boundaries and direct arrivals, were used in the solutions. Most of the solutions are very well determined, although some events along the San Andreas had many systematically discordant arrivals as a consequence of a horizontal contrast in velocity across the fault. Details of the seven new solutions worked out for this paper are shown in figure 6; details of the remaining solutions are given in the references cited in table 1.

Four of the events studied were on the San Andreas fault between Parkfield and Corralitos, two were on the Calaveras fault north of Hollister, six were along the coast between Santa Barbara and Monterey, three were from the region along the edge of the Great Valley near Coalinga and preceded the Coalinga earthquake, and five were from the Coalinga sequence itself. First motion diagrams and P-axis orientations are shown in figure 4, and fault plane orientations and slip directions are shown in figure 5.

The six solutions along the San Andreas and Calaveras faults indicate right-lateral strike slip on near-vertical fault surfaces with strike and slip directions that parallel the sections of the faults on which the earthquakes occurred.

The six solutions along the coast show a progressive change from northwest to southeast: Point Sur (840123), right-lateral strike-slip displacement on a near-vertical fault with a location and orientation corresponding to the Palo Colorado-San Gregorio fault; San Simeon (830829), right-oblique reverse slip on a fault parallel to the coast (and the nearby offshore Hosgri Fault) and dipping 55°NE; Point Sal (800529), thrust displacement on a fault striking N62°W and dipping 34°NE; Santa Barbara (780813), left oblique reverse slip on a fault striking N64°W and dipping 32°NE.

The solutions for the Coalinga region indicate a preponderance of reverse faulting, but, otherwise, they are remarkably diverse. Inferred P-axis azimuths of the main Coalinga earthquake and of two of the three pre-Coalinga earthquakes are nearly perpendicular to the San Andreas fault. The inferred P-axis orientations of the Coalinga aftershocks vary systematically across the aftershock zone: nearly east-west in the northwestern part to nearly north-south in the southeastern part.

DISCUSSION

Effective use of seismicity data to predict the location of future earthquakes requires that such data be interpreted within the context of a specific model that organizes and explains the existing data and provides a vehicle for predicting future events in the modelled systems. Broadly, the global plate tectonic model and the seismic gap approach to predicting earthquakes provide a framework for the model we need, but they are not sufficiently specific to be of practical use. On a gloabal scale the San Andreas fault system is a simple transform fault along which the Pacific and North American plates move past one another parallel to the fault. On a regional scale, that transform is an extended zone of interaction between the Pacific and North American plates, and it is very complex. It has a width that is a significant fraction of its length, a complex internal structure that varies with position within it, poorly understood transitions to other global structures at its ends, and a poorly known variation of elastic properties with depth. Moreover, the northern and southern parts of the zone are dissimilar, and there is a large left-stepping offset in its longitudinal axis where it crosses the Transverse Ranges.

We shall to outline a preliminary model for the central Coast Ranges that encompasses (1) the seismicity and focal mechanism data presented above, (2) the gross geologic features of the region, and (3) the general results of detailed studies of earthquakes and crustal structure in the region. The most

important of these results are that, with rare exceptions, the deepest earthquakes in the central Coast Ranges are only about 12-15 km deep (Eaton, this volume; Sibson, 1984) and that P-wave velocities appear to increase from near 6 km/sec to about 6.5 km/sec at that depth (Walter and Mooney, 1982; Walter, this volume). The depth to the mantle and the velocity of P-waves in the upper mantle appear to vary across the region from less than 25 km and about 8.1 km/sec, respectively, along the coast to nearly 30 km and 7.9 to 8.0 km/sec, respectively, along the edge of the Great Valley (Oppenheimer and Eaton, 1984).

The zone of interaction between the Pacific and North American plates appears to extend entirely across the Coast Ranges. Earthquakes at depths of a few km to about 12 km occur throughout the region, which implies that the crust is being deformed and is both brittle and elastic in that depth range. The heaviest concentration of small earthquakes is along sections of the major strike-slip faults that currently are undergoing continuous or intermittent creep. Along sections of these faults that are not presently creeping, earthquakes are sparse and somewhat scattered or they are virtually absent. At intervals of a century or more, however, large sudden offsets accompanied by major earthquakes occur when these locked sections of the faults move.

Studies of the distribution of earthquakes with depth on the major strike-slip faults, using both large earthquakes and their aftershocks and the long-term background of smaller earthquakes, show that the transition from the seismic zone to the aseismic zone is abrupt (Sibson, 1984; Eaton and others, 1970; Cockerham and Eaton, 1984). A similar abrupt cutoff of seismicity below about 12 km was observed for the Coalinga earthquake sequence, which occurred near the edge of the Great Valley more than 30 km northeast of the San Andreas fault and consisted almost entirely of reverse-fault events (Eaton, this volume).

We interpret the foregoing observations to indicate that there is an abrupt transition from brittle elastic behavior to ductile behavior at a depth of about 12-15 km, at or near a transition from upper to lower crustal velocities (and materials?) throughout the central Coast Ranges (see also Sibson, 1982, 1984). Present evidence is insufficient to determine whether the ductile zone is limited to the lower crust or whether it extends through the upper mantle into the asthenosphere. In the former case, the relative motion between the Pacific and North American plates in the upper mantle would, presumably, occur along an earthquake-free (creeping) fault or along a narrow ductile shear zone. In either case, the relative motion between the plates would not be communicated directly to the brittle upper crust and expressed at the surface as a major fault rooted in the interface between the two plates at depth. The ductile lower crust would provide sufficient decoupling between the upper mantle and the brittle upper crust so that the pattern of deformation in the heterogeneous upper crust would be strongly influenced by its local physical properties and by the character of structures within it.

Particularly strong sections of the crust would resist internal deformation, and earthquakes would be concentrated along their boundaries. Weaker portions of the crust could undergo internal deformation and generate earthquakes internally as well as along their boundaries. Once established as zones of relative weakness, major throughgoing faults could remain active even when the pattern of intra-crustal stresses was no longer optimum for their

development. The entire brittle upper crust might indeed be rotated or pushed laterally along subhorizontal zones of detachment in the lower crust without symptomatic earthquakes except where the detachment surface might pass upward into the brittle crust.

Several features of the seismicity and focal mechanism maps for the central Coast Ranges suggest the presence of a detachment zone beneath the upper crust. Such features include the complex branching of major faults northwest of San Benito and the mismatch between the strike of the San Andreas fault and the direction of relative plate motion (N41°W versus N35°W) between San Benito and Cholame. More important with regard to the Coalinga earthquake is the evidence for reverse and thrust faulting along the flanks of the Coast Ranges southeast of Cape San Martin and southeast of Idria (see also Crouch, 1984; Eaton, this volume). These are the two regions where the seismicity maps show scattered large clusters of epicenters rather than the linear concentrations which might suggest the presence of strike-slip faulting. Focal mechanisms of large recent earthquakes in these regions are predominantly thrust or reverse faults. We suggest that the distinctive pattern of seismicity in these regions maps out reverse fault provinces. Earthquakes scattered over a subhorizontal fault cutting upward through the crust would appear as a cluster of epicenters rather than a linear zone, as for a vertical fault. The reverse faults along the margins of the southern Coast Ranges may be rooted in detachment zones below 12 km depth, which may extend for some distance back toward the San Andreas fault in the middle of the range. Crouch and others (1984) suggested a detachment zone below about 12-15 km depth on the basis of seismic reflection profiles across faults offshore, between Point San Luis and Santa Barbara.

The presence of zones of thrusting along both flanks of the southern Coast Ranges suggests that there is a component of convergent movement between the Pacific and North American plates across this part of the transform. Minster and Jordan (1984) concluded that there is between 4 and 13 mm/yr compression normal to the San Andreas fault across the fault system. The paucity of earthquakes between the San Andreas fault and the flanking zones of reverse faulting indicates that the crust is sufficiently strong and sufficiently decoupled from the plates beneath it that it can resist internal deformation while sustaining the compressive forces required to push its outer margins out over the edges of the contracting transform zone. Looking farther south toward the Carrizo plains and the locked "Fort Tejon" section of the San Andreas fault, we may wonder whether the same process is responsible for the behavior of that section of the fault: abnormally strong crustal rocks pinned together along the San Andreas fault by an abnormally large normal component of stress resulting from convergence of the plates along that section of the transform. The existence of a tentative model for a region, like that sketched above for the southern Coast Ranges, does not lead us directly to believable earthquake predictions. It does, however, provide a specific vehicle that can be tested against additional existing data and modified and improved by new observations and insights. The model that evolves through this process can be expected to optimize the value of historical seismicity data as well as the stream of current seismicity observations for the prediction of earthquakes.

The model of the earthquake generating process that is undergoing the most vigorous evaluation in California is applicable to the major strike-slip

faults of the San Andreas system, and relatively little attention has been paid to potential earthquake sources along the flanks of the Coast Ranges. The relatively high level of background seismicity and the occurrence of several M5+ earthquakes along the edge of the Great Valley between Idria and Devils Den from 1975 through 1982 did cause some concern, but the seismicity data for this region had not been organized in a manner to support thoughtful interpretation. Moreover, the monitoring and evaluation of earthquakes along the flanks of the southern Coast Ranges was not being pursued vigorously because of limited resources and the higher priority assigned to the nearby San Andreas fault. We must conclude that the surprise that accompanied the occurrence of the Coalinga earthquake was, at least in part, due to neglect. However, a larger part was due to the lack of a plausible model to explain the occurrence of earthquakes in such regions and to place them in the broader context of processes at work in the transform zone.

The occurrence of the Coalinga earthquake has stimulated increased concern over large earthquakes along the flanks of the Coast Ranges, and the post-earthquake analysis of the instrumental record of seismicity in the central Coast Ranges during the 11 years prior to the earthquake has led to a tentative model of the process that generates events like the Coalinga earthquake. Further development of the model and its effective application to the earthquake prediction task will both require improved monitoring and analysis of earthquakes along the edges of the Coast Ranges. The same effort should lead to a better understanding of the process that generates great earthquakes along the section of the San Andreas southeast of Cholame.

Acknowledgements

M. J. Rymer reviewed the manuscript and made important contributions to the discussion section.

REFERENCES CITED

Cockerham, R. S., and Eaton, J. P., 1984, The April 24, 1984 Morgan Hill earthquake and its aftershocks: April 24 through September 30, 1984: California Division of Mines and Geology Special Publication 66.

Crouch, J. K., Bachman, S. B., and Shay, J. T., 1984, Post-Miocene compressional tectonics along the central California margin, in Crouch, J. K., and Bachman, S. B., eds., 1984, Tectonics and sedimentation along the California margin: Pacific Section Society of Economic Paleontologists and Mineralogists, v. 38, p. 37-54.

Eaton, J. P., 1984a, Focal mechanisms of near-shore earthquakes between Santa Barbara and Monterey, California: U.S. Geolgical Survey Open-File Report 84-477.

_____ 1984b, The May 2, 1983 Coalinga earthquake and its aftershocks: a detailed study of the hypocenter distribution and of the focal mechanisms of the larger aftershocks: this volume.

_____ 1985, Temporal variation in the pattern of seismicity in Central California, in Earthquake prediction: Proceedings of the international symposium of earthquake prediction (Paris, April 2-6, 1979), UNESCO.

Eaton, J. P., O'Neill, M. E., and Murdock, J. N., 1970, Aftershocks of the 1966 Parkfield-Cholame, California, earthquake: A detailed study: Bulletin Seismological Society of America, v. 60, p. 1151-1197.

Minster, J. B., and Jordan, T. H., 1978, Present-day plate motions: Journal of Geophysical Research, v. 83, p. 5331-5354.

_____ 1984, Vector contraints on Quaternary deformation of the western United States east and west of the San Andreas fault, in Crouch, J. K., and Bachman, S. B., eds., Tectonics and sedimentation along the California margin: Pacific Section Society of Economic Paleontologists and Mineralogists, v. 38, p. 1-16.

Oppenheimer, D. H., and Eaton, J. P., 1984, Moho orientation beneath central California from regional earthquake travel times: Journal of Geophysical Research, v. 89, p. 10,263-10,282.

Sibson, R. H., 1982, Fault zone models, heat flow, and the depth distribution of earthquakes in the continental crust of the United States: Bulletin Seismological Society of America, v. 72, p. 151-163.

_____ 1984, Roughness at the base of the seismogenic zone: Contributing factors: Journal of Geophysical Research, v. 89, p. 5791-5799.

Walter, A. W., and Mooney, W. D., 1982, Crustal structure of the Diablo and Gabilan Ranges, central California: Bulletin Seismological Society of America, v. 72, p. .

Table 1. Summary of hypocentral and focal mechanism data for the earthquakes in figures 4 and 5. Abbreviations in the table heading are: LAT = latitude; LON = longitude; MAG = local magnitude, NS = number of stations used in hypocentral solution; GAP = maximum azimuthal gap, in degrees, of stations used in hypocentral solution; DMIN = epicentral distance, in kilometers, to nearest seismic statin; RMS = root mean square of traveltime residuals; ERH and ERZ = estimated errors, in kilometers, in the epicenter and focal depth, respectively; Q = hypocentral solution quality; P-AX/AZ DP = P-axis azimuth and dip (plunge); FAULT PLN/STR DIP = strike and dip of the fault plane; AUX PLN/STR DIP = strike and dip of the auxiliary plane; POL FP/STR DP = strike and dip of the pole of the fault plane, POL AP/STR DP = strike and dip of the pole of the auxiliary plane; DISP TYPE/FLT AUX = displacement type corresponding to slip on the fault plane and auxiliary plane, respectively; RF = reference showing first motion plot - 1 = this paper, 2 = Eaton (1984a), 3 = Eaton (1984b), 4 = Cockerham and Eaton (1984), 5 = Eaton and others (1970).

														P-AX		FAULT PLN		AUX PLN		POL FP		POL AP		DISP	TYPE	
DATE	TIME	LAT	LON	DEPTH	MAG	NS	GAP	DMIN	RMS	ERH	ERZ	Q	AZ	DP	STR	DIP	STR	DIP	STR	DP	STR	DP	FLT	AUX	RF
750803	635 17.32	36-27.03	120-26.43	10.33	4.9	31	209	35.0	0.18	1.1	1.1	C	50	51	N31W	6NE	N31W	84SW	239	84	59	6	N	N	1
760114	2143 59.15	36-04.48	120-14.62	11.94	4.7	26	225	17.3	0.19	0.9	0.6	C	215	26	N 5W	42NE	N86W	83SW	264	48	4	7	RS-R	LS-R	1
780813	2254 51.80	34-23.18	119-42.60	11.34	5.9	14	116	2.1	0.11	0.6	0.4	B	228	15	N64W	32NE	N30W	62SW	208	58	59	28	T-LS	R-RS	2
790806	1705 22.28	37-06.15	121-30.80	7.79	5.9	80	101	5.9	0.20	0.4	0.5	B	15	4	N30W	84SW	N60E	90	60	6	330	0	RS	LS-N	1
800529	0338 47.51	34-58.65	120-42.37	9.17	5.1	10	200	28.1	0.17	1.5	1.2	C	202	11	N62W	34NE	N72W	57SW	208	56	17	33	T-RS	R-LS	2
820625	0358 22.97	35-57.43	120-33.11	9.06	4.2	51	63	2.9	0.21	0.4	0.6	B	184	7	N39W	80NE	N51E	90	231	10	321	0	RS	LS-N	1
820811	0746 43.04	36-37.64	121-18.16	11.62	4.8	45	38	2.1	0.19	0.5	0.8	B	187	13	N37W	85NE	N51W	76NW	233	5	141	13	RS-N	LS-N	1
820818	0843 49.50	37-01.49	121-44.63	12.21	4.3	51	38	3.6	0.15	0.4	0.6	B	353	2	N52W	80NE	N40E	77SE	218	10	310	13	RS-R	LS-R	1
820923	2042 50.60	34-52.19	120-21.76	4.77	4.0	24	66	19.1	0.15	0.4	1.0	C	55	8	N54W	56NE	N12W	42SW	216	34	78	48	R-LS	T-RS	2
821025	2226 03.67	36-19.31	120-30.44	10.95	5.5	40	144	12.5	0.10	0.3	0.3	B	12	24	N72E	26SE	N64W	70NE	343	64	205	20	T-LS	R-RS	1
830502	2342 38.14	36-13.96	120-18.57	10.01	6.7	30	214	3.4	0.05	0.3	0.2	C	37	23	N53W	23SW	N53W	67NE	37	67	217	23	T	R	3
830522	0839 21.74	36-09.03	120-12.09	10.48	4.2	47	61	8.8	0.13	0.2	0.4	A	356	6	N74E	40SE	N85W	52NE	344	50	185	38	T-LS	R-RS	3
830611	0309 52.21	36-15.33	120-27.01	2.40	5.2	45	67	6.0	0.12	0.2	0.4	B	107	5	N17E	50SE	N17E	40NW	287	40	107	50	R	T	3
830721	0123 32.97	36-09.17	121-32.64	5.24	3.9	34	144	15.0	0.10	0.3	0.5	B	176	4	N49W	90	N41E	84NW	41	0	131	6	RS-N	LS	2
830722	0239 54.07	36-14.44	120-24.53	7.37	6.0	36	48	6.1	0.09	0.2	0.2	A	260	7	N 5W	38NE	N21W	53SW	265	52	69	37	T-RS	R-LS	3
830829	1010 30.90	35-50.17	121-21.70	6.57	5.4	32	177	8.6	0.11	0.4	0.4	B	198	2	N39W	55NE	N77E	58SE	231	35	347	32	RS-R	LS-R	2
830909	0916 13.47	36-13.91	120-15.90	6.69	5.3	34	71	7.2	0.06	0.2	0.2	B	22	1	N26W	75NE	N68E	72SE	244	16	338	18	RS-R	LS-R	3
840123	0540 19.88	36-22.13	121-52.74	7.74	5.2	31	195	18.2	0.12	0.9	1.2	D	194	9	N30W	78NE	N62E	84SE	242	12	332	6	RS-R	LS-R	2
840424	2115 18.78	37-18.56	121-40.68	8.42	6.2	39	58	5.8	0.25	0.3	0.9	B	191	3	N34W	84SW	N57E	80NW	56	6	147	10	RS-R	LS-R	4
660627		35-47.70	120-20.50	7.0	5.5	(COMPOSITE)							4	3	N41W	88SW	N49E	84SE	319	6	49	2	RS	LS	5

FIGURE CAPTIONS

Figure 1. Central Coast Range earthquakes from January 1982 through April 1983. The 500' contour (shown only along the west side of the Great Valley) marks the approximate boundary between the Coast Ranges and the Great Valley. The locations of selected cities are marked with X's. Selected faults and geographic features are identified for reference. N41°W and N35°W are the average strike of the San Andreas fault between Cholame and Hollister and the direction of relative motion of the Pacific plate to the North American plate in the same region, respectively.

Figure 2. Central Coast Range earthquakes from January 1972 through April 1983. The 500' contour marks the approximate boundary between the Coast Ranges and the Great Valley. The locations of selected cities are marked with X's. Selected geographic features are identified for reference.

Figure 3. Central Coast Range earthquakes east of the San Andreas fault for January 1972 through April 1983. The 500' contour marks the approximate boundary between the Coast Ranges and the Great Valley. The locations of selected cities are marked with X's. The main shock and aftershock region of the 1983 Coalinga earthquake as well as the dates of occurrence of the larger earthquake clusters are indicated on the map.

Figure 4. First motion diagrams and P-axis orientations for selected earthquakes in the Coast Ranges and Transverse Ranges. Individual earthquakes are identified by their dates of occurrence. First motion diagrams of earthquakes of the 1983 Coalinga sequence are shown at an expanded scale. On the inset showing P-axis orientations, events of the Coalinga sequence are plotted with dashed lines. Hypocentral and focal mechanism data are summarized in table 1.

Figure 5. Fault plane orientations and slip directions for selected earthquakes in the Coast Ranges and Transverse Ranges. Strike directions are indicated by the line segment drawn through the epicenter symbols. Dip angles and directions are shown by each solution. Slip sense and direction for strike-slip solutions are indicated by the half-barbed pairs of arrows. For events with appreciable dip-slip displacement, an arrow indicates the direction of slip of the upper plate relative to the lower plate and the + and - signs indicate the relative vertical displacement of the two plates. Events of the 1983 Coalinga sequence are shown at an expanded scale.

Figure 6. First motion plots and focal plane solutions for selected events shown on figures 4 and 5. Solid circles and open circles represent unambiguous compressional and dilatational first wave onsets, respectively. Less certain compressional and dilatational first wave onsets are indicated by + and -, respectively. The inferred axes of maximum and minimum compressional stress (pressure axis and tension axis) are marked by P and T, respectively.

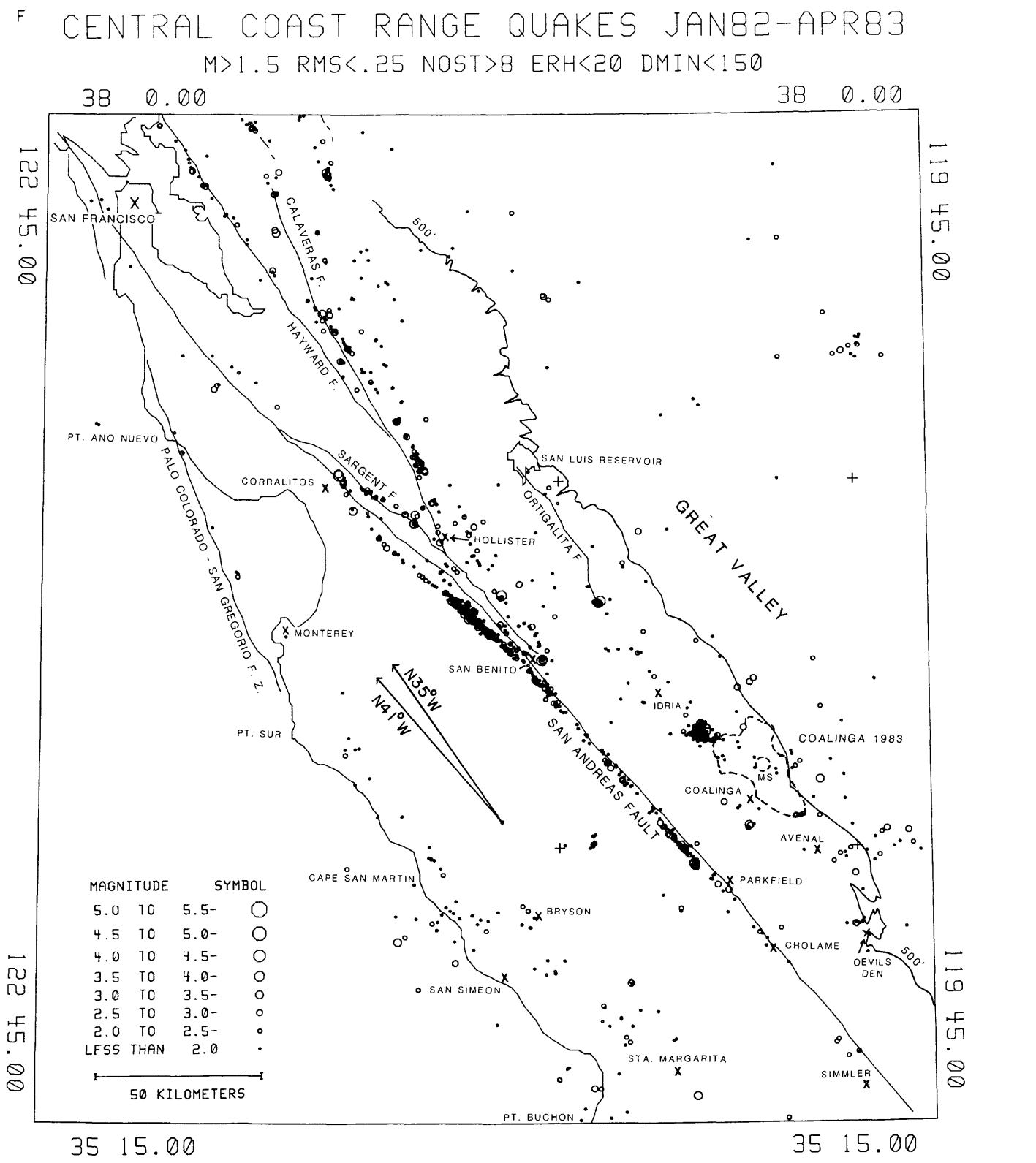
F
CENTRAL COAST RANGE QUAKES JAN82-APR83
M>1.5 RMS<.25 NOST>8 ERH<20 DMIN<150
38 0.00
38 0.00
122 45.00
119 45.00
122 45.00
119 45.00
35 15.00
35 15.00
SAN FRANCISCO
CALAVERAS F.
HAYWARD F.
500'
PT. ANO NUEVO
PALO COLORADO - SAN GREGORIO F. Z.
SARGENT F.
CORRALITOS
SAN LUIS RESERVOIR
ORTIGALITA F.
GREAT VALLEY
HOLLISTER
MONTEREY
SAN BENITO
N35°W
N4°W
IDRIA
COALINGA 1983
MS
COALINGA
AVENAL
SAN ANDREAS FAULT
PT. SUR
CAPE SAN MARTIN
BRYSON
PARKFIELD
CHOLAME
DEVILS DEN
500'
SAN SIMEON
STA. MARGARITA
SIMMLER
PT. BUCHON
MAGNITUDE SYMBOL
5.0 TO 5.5-
4.5 TO 5.0-
4.0 TO 4.5-
3.5 TO 4.0-
3.0 TO 3.5-
2.5 TO 3.0-
2.0 TO 2.5-
LESS THAN 2.0
50 KILOMETERS

Figure 1

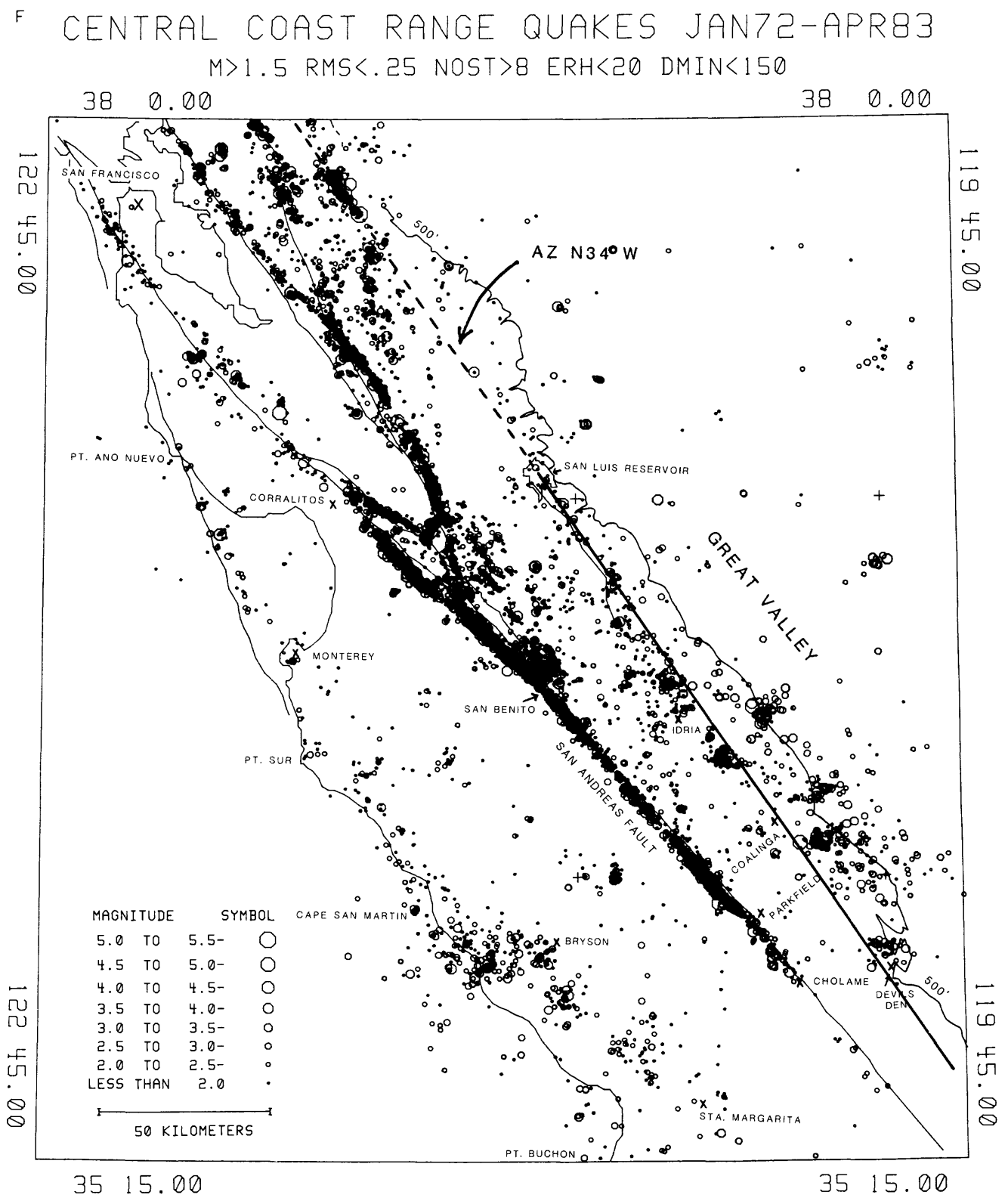
CENTRAL COAST RANGE QUAKES JAN72-APR83
M>1.5 RMS<.25 NOST>8 ERH<20 DMIN<150
38 0.00
38 0.00
122 45.00
119 45.00
122 45.00
119 45.00
35 15.00
35 15.00
SAN FRANCISCO
500'
AZ N34°W
PT. ANO NUEVO
CORRALITOS
SAN LUIS RESERVOIR
GREAT VALLEY
MONTEREY
SAN BENITO
IDRIA
PT. SUR
SAN ANDREAS FAULT
COALINGA
PARKFIELD
CAPE SAN MARTIN
BRYSON
CHOLAME
DEVILS DEN
500'
STA. MARGARITA
PT. BUCHON
MAGNITUDE SYMBOL
5.0 TO 5.5-
4.5 TO 5.0-
4.0 TO 4.5-
3.5 TO 4.0-
3.0 TO 3.5-
2.5 TO 3.0-
2.0 TO 2.5-
LESS THAN 2.0
50 KILOMETERS

Figure 2

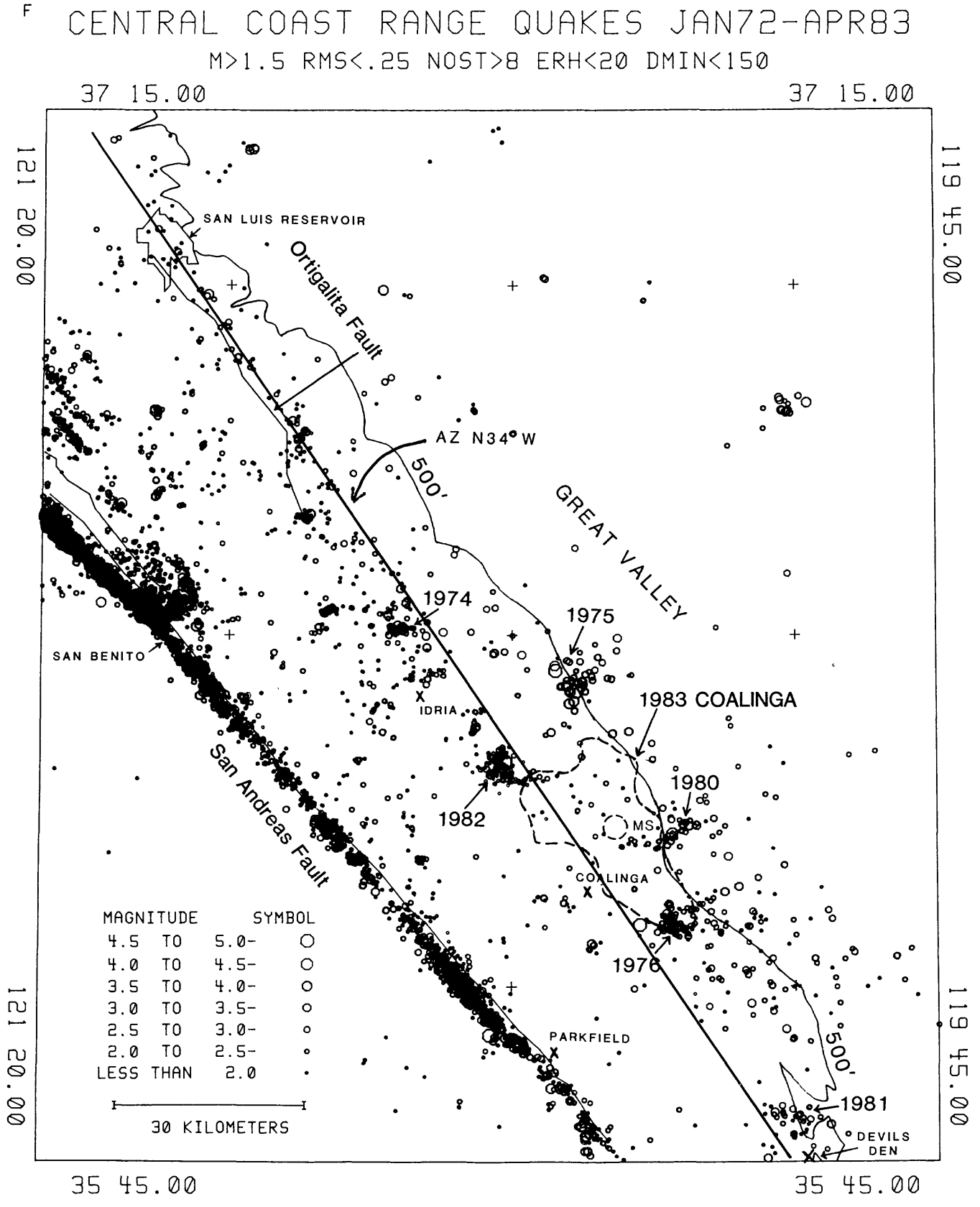
CENTRAL COAST RANGE QUAKES JAN72-APR83
M>1.5 RMS<.25 NOST>8 ERH<20 DMIN<150
37 15.00
37 15.00
121 20.00
119 45.00
SAN LUIS RESERVOIR
Ortigalita Fault
AZ N34°W
500'
GREAT VALLEY
1974
1975
SAN BENITO
IDRIA
1983 COALINGA
1980
San Andreas Fault
1982
MS
COALINGA
1976
PARKFIELD
500'
1981
DEVILS DEN
MAGNITUDE SYMBOL
4.5 TO 5.0-
4.0 TO 4.5-
3.5 TO 4.0-
3.0 TO 3.5-
2.5 TO 3.0-
2.0 TO 2.5-
LESS THAN 2.0
30 KILOMETERS
35 45.00
35 45.00

Figure 3

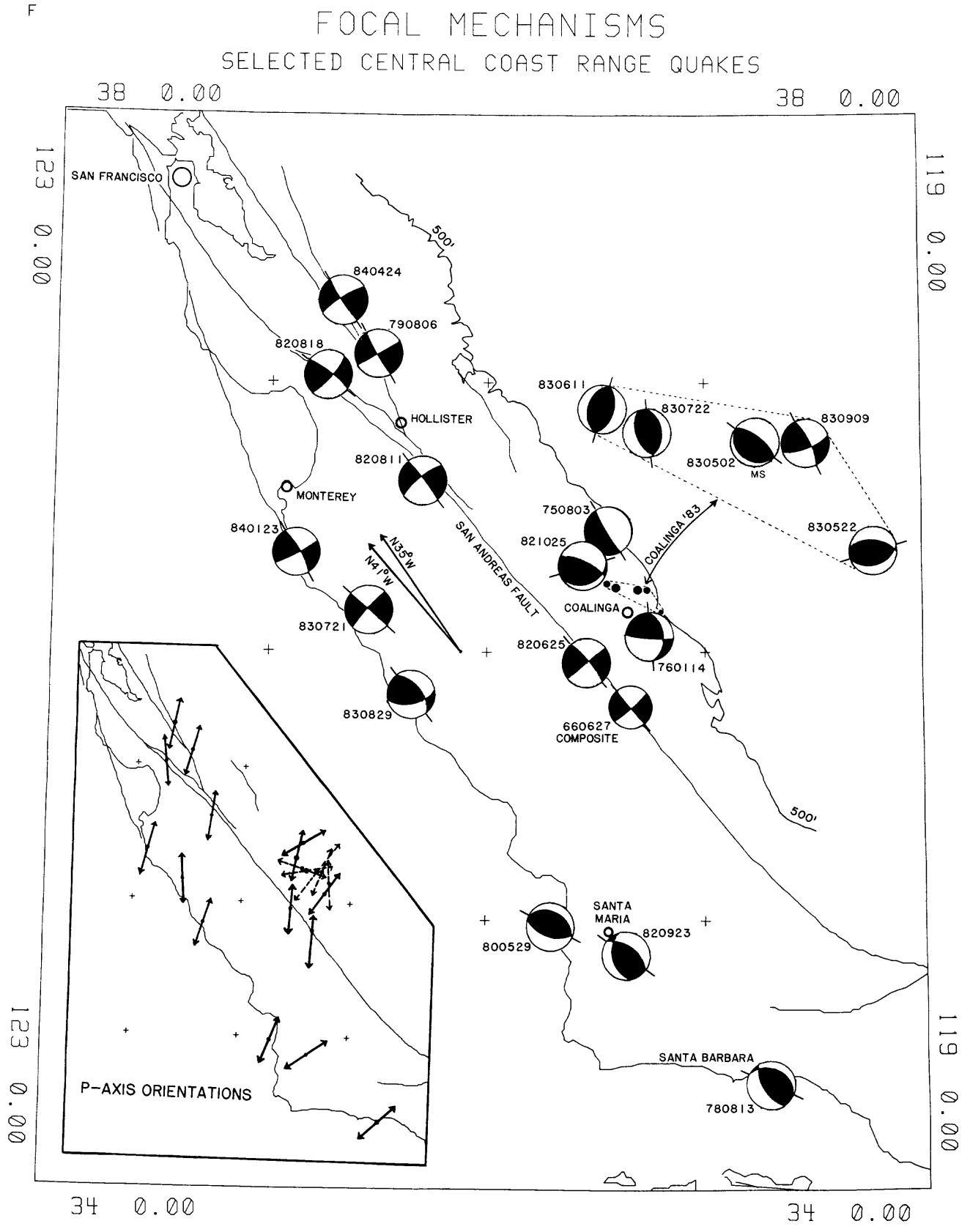
FOCAL MECHANISMS
SELECTED CENTRAL COAST RANGE QUAKES
38 0.00
38 0.00
123 0.00
119 0.00
SAN FRANCISCO
500'
840424
790806
820818
HOLLISTER
820811
MONTEREY
840123
N35°W
N41°W
SAN ANDREAS FAULT
830721
830829
830611
830722
830909
830502
MS
750803
821025
COALINGA 83
830522
COALINGA
820625
760114
660627
COMPOSITE
500'
SANTA MARIA
820923
800529
SANTA BARBARA
780813
P-AXIS ORIENTATIONS
123 0.00
119 0.00
34 0.00
34 0.00

Figure 4

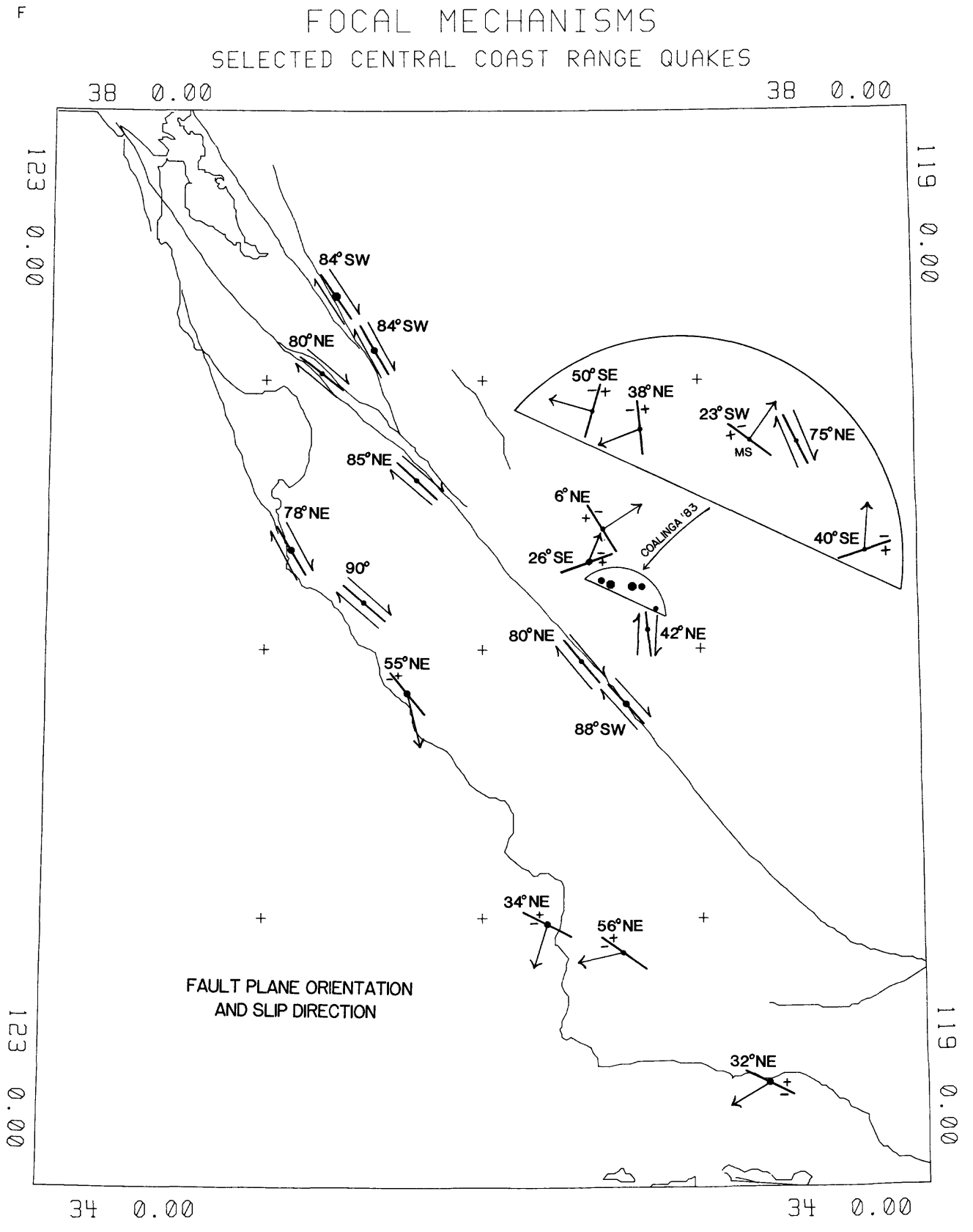
FOCAL MECHANISMS
SELECTED CENTRAL COAST RANGE QUAKES
38 0.00
38 0.00
123 0.00
119 0.00
84°SW
84°SW
80°NE
85°NE
78°NE
90°
55°NE
50°SE
38°NE
23°SW
MS
75°NE
6°NE
26°SE
COALINGA '83
40°SE
80°NE
42°NE
88°SW
34°NE
56°NE
32°NE
FAULT PLANE ORIENTATION
AND SLIP DIRECTION
123 0.00
119 0.00
34 0.00
34 0.00

Figure 5

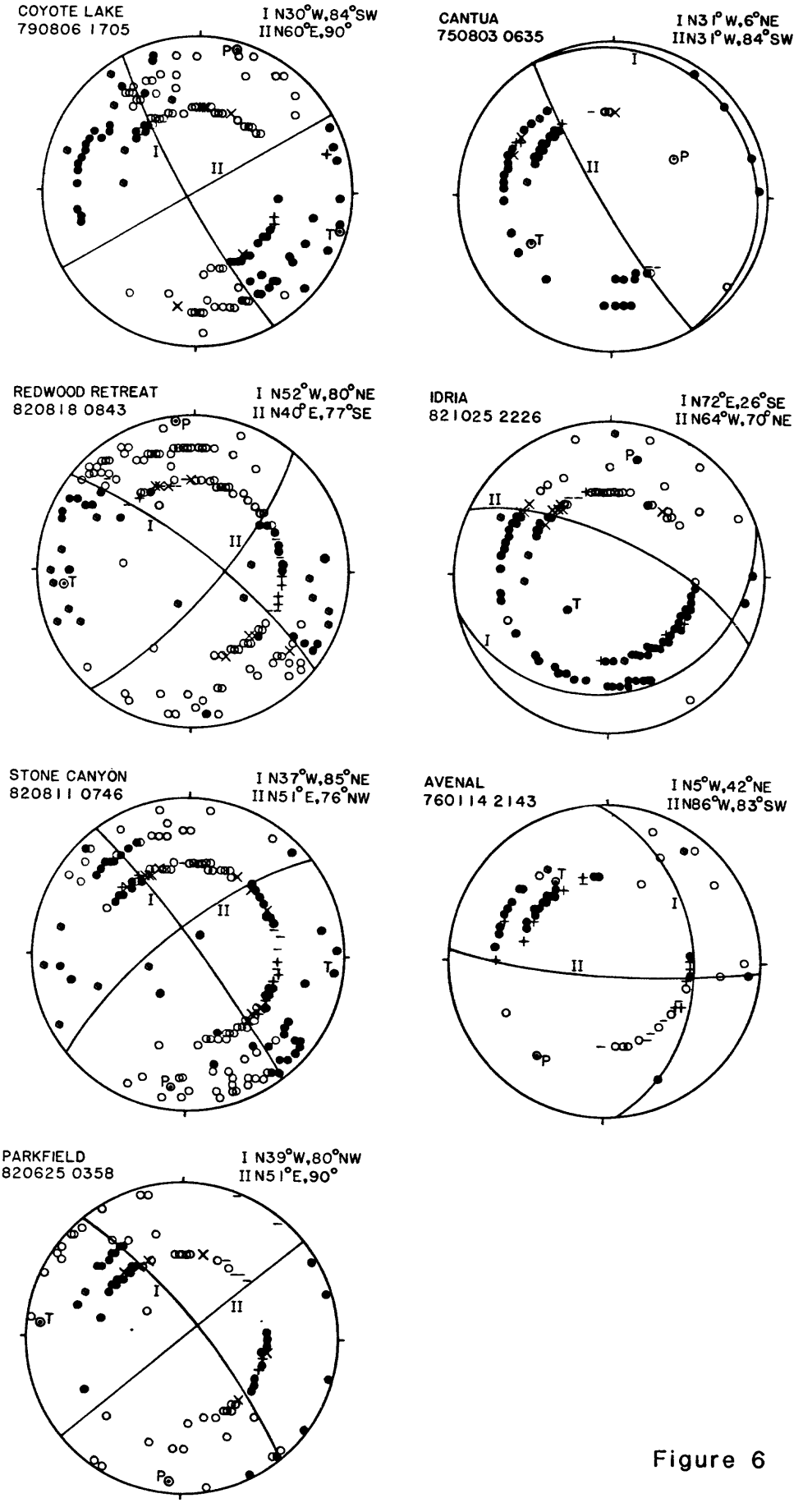
COYOTE LAKE
790806 1705
I N30°W,84°SW
II N60°E,90°
CANTUA
750803 0635
I N31°W,6°NE
II N31°W,84°SW
REDWOOD RETREAT
820818 0843
I N52°W,80°NE
II N40°E,77°SE
IDRIA
821025 2226
I N72°E,26°SE
II N64°W,70°NE
STONE CANYON
820811 0746
I N37°W,85°NE
II N51°E,76°NW
AVENAL
760114 2143
I N5°W,42°NE
II N86°W,83°SW
PARKFIELD
820625 0358
I N39°W,80°NW
II N51°E,90°

Figure 6

The May 2, 1983 Coalinga Earthquake and Seismicity Rates and Strain Energy in the Central Coast Ranges, California

Robert A. Uhrhammer

Seismographic Station
University of California, Berkeley
Berkeley, California 94720

ABSTRACT

The cumulative rate of seismicity for the Central Coast Ranges in California ($\log N = 2.287 - 0.811 M_L$; normalized to earthquake sequences per year per $1000 km^2$) is determined from a 132 year historical seismicity record (1851-1982; $3.0 \leqslant M_L \leqslant 7.3$ or $MM \geqslant VII$). The spatial distribution of the seismicity ($3.0 \leqslant M_L \leqslant 5.6$; 1953-1982) indicates that the average interoccurrence time for a $M_L \geqslant 6.7$ (Coalinga sized) earthquake, centered to the northeast of the San Andreas fault zone, is 690 ± 180 years. The probability of a $M_L \geqslant 6.7$ earthquake occurring in the vicinity of Coalinga, in a 132 year interval, is 20 percent. Therefore the M_L 6.7 Coalinga mainshock of May 2, 1983 is not an unexpected event in either size or general location.

The coseismic strain release in the Central Coast Ranges has averaged $0.40 \pm 0.12 \mu strain/year$ from 1953 to 1982 over a zone $100 km$ wide, centered approximately on the San Andreas Fault. A strain energy glut has been accumulating for at least the past 30 years at an average rate of $1 \times 10^{19} ergs/year$ in a $30 km$ wide zone, transverse to the axis of the Central Coast Ranges, centered in the vicinity of the Coalinga mainshock. The implication is that the presence of a significant strain glut is indicative of the approximate size and general position, but not the time of occurrence, of an impending earthquake.

A comparison between the average rate of strain accumulation ($0.56 \pm 0.03 \mu strain/year$), in a $100 km$ wide segment of the Central Coast Ranges, and the average rate of coseismic strain release implies that the largest magnitude earthquake which can occur in the region between approximately Hollister and Parkfield is $M_L^{max} = 7.46 \pm 0.14$.

The difference in azimuth between the relative tectonic plate motion vector and the strike of the San Andreas Fault is $5.4° \pm 2.0°$. Decomposing the plate motion vector into orthogonal components yields a right-lateral strike-slip motion of $5.6 \pm 0.3 cm/year$ parallel to the fault and a compressive motion of $0.53 \pm 0.20 cm/year$ perpendicular to the fault. The tectonic compression is compatible with the reverse faulting mechanism for the Coalinga mainshock.

Introduction

The historical record of seismicity in a 250*km* long segment of California's Central Coast Ranges, from approximately Monterey to Santa Maria, extends in more-or-less complete form back to 1830 (Townley and Allen, 1928) with only one event reported prior to 1851. During the 1850's many newspapers were established in California and written records of widely felt and damaging earthquakes became common (*e.g.*, Toppozada *et al.*, 1981). This paper analyzes the historical seismicity record from 1851 to 1982 for the Central Coast Ranges. The aim is to give a broad seismicity setting to the occurrence of the 1983 Coalinga sequence. The May 2 mainshock had a mean local magnitude $M_L = 6.7 \pm 0.16$ determined from maximum trace amplitudes measured on 5 Wood-Anderson records from the U. C. Berkeley network. Its seismic moment was $M_o = (2.3 \pm 1.2) \times 10^{25} dyne-cm$ estimated from the Berkeley and Jamestown broad-band recordings (Uhrhammer *et al.*, 1983).

The historical record is sufficient to determine the average cumulative rate of seismicity for $3.0 \leqslant M_L \leqslant 7.5$. Since the occurrence of the Coalinga sequence (see Figure 1), there has been much speculation about the earthquake potential in the region of the Central Coast Ranges on the northeast side of the San Andreas fault zone. This problem is addressed in light of the spatial variation in the rate of seismicity, parallel to and perpendicular to the San Andreas fault zone, from a 30 year seismicity sample (1953-1982; $3.0 \leqslant M_L \leqslant 5.6$; 455 earthquake sequences). Descriptively the spatial distribution of seismicity perpendicular to the San Andreas fault zone is trimodal and one of the peaks, accounting for approximately 20 percent of the earthquake sequences, occurs over a 40*km* wide zone, parallel to the San Andreas Fault and centered in the vicinity of Coalinga.

The analysis of the spatial variation in the rate of strain energy release is one way to consider mechanical aspects of the regional seismo-tectonics. In this paper it is calculated as a function of position, parallel to and perpendicular to the San Andreas fault zone, from the 30 year seismicity sample (1953-1982; $3.0 \leqslant M_L \leqslant 5.6$; 660 earthquakes) including foreshocks and aftershocks. The likelihood of earthquake occurrence is assumed to be inversely proportional to the rate of coseismic strain energy release. The size and relative position of coseismic strain energy gluts in the region are determined to test the hypothesis that such gluts may be indicative of the approximate size and relative position of an impending earthquake. The 1983 Coalinga mainshock did occur in an area of a strain energy glut and the earthquake essentially dissipated the accumulated excess strain energy in the region.

In addition a comparison between the cumulative rate of seismicity and the net rate of overall strain energy accumulation, for the Central Coast Ranges, provides an upper bound on the magnitude of earthquakes which can occur in the region. The rate of high coseismic strain energy release transverse to the San Andreas fault occurs over a zone approximately 100*km* wide.

Historical Rate of Seismicity

The rate of seismicity in the Central Coast Ranges of California (shown in Figure 1) was determined by combining information from three primary sources: 1) Townley and Allen (1928); 2) Bolt and Miller (1974) supplemented with the semiannual Bulletins of the Seismographic Stations (1974-1982) (the "UCB catalog"); and 3) Hileman *et al.* (1973) (the "CIT catalog"). A search was made using these sources to list all earthquakes reported in a 250*km* segment of the central coast centered in the vicinity of Coalinga. All earthquakes centered within a 47,700km^2 quadrangle, defined by the coordinate points (37.40°N, 120.53°W); (35.68°N, 118.88°W); (34.58°N, 120.48°W); and (36.27°N, 122.22°W), were selected. One hundred ninety earthquakes occurring between 1851 and 1927 were selected from the Townley and Allen Catalog (1928), 2352 earthquakes occurring between 1910 and 1982 were selected from the UCB catalog, and 213 earthquakes occurring between 1932 and 1973 were selected from the CIT catalog. All earthquakes in the region (excluding foreshocks and aftershocks) with local magnitude (M_L) $\geqslant$ 5.5, with area shaken at Modified Mercalli (MM) $\geqslant$ V in excess of 16,000km^2, or with maximum MM intensity $\geqslant$ VII are listed in Table 1. The Rossi-Forrel

intensities given by Townley and Allen (1928) have been changed to the equivalent Modified Mercalli intensities, based on the description of felt reports and damage, for in-house use at Berkeley (B. A. Bolt, personal communication).

The local magnitude (M_L) given in Table 1 is determined by: 1) instrumental records; 2) area shaken with MM$\geqslant$V; or 3) maximum MM intensity. For most earthquakes, occurring in the region after 1911, instrumental records are available (kept on store at Berkeley) for determining M_L. When instrumental records were not available, M_L was estimated from the area (A) in km^2 shaken with MM $\geqslant$ V. When felt reports were not sufficiently detailed to determine the area shaken with MM $\geqslant$ V, the maximum reported MM intensity was used to estimate M_L.

The largest magnitude earthquake which has occurred in the region since 1851 is the M_L 7.3 Lompoc earthquake of November 4, 1927 (Byerly, 1930). There is some uncertainty about the location of this earthquake and recent reanalyses by Gawthrop (1978) and Hanks (1979) agree at least in placing the epicenter closer to shore (approximately $25\,km$ west of Pt. Arguello) which reduces the magnitude slightly to M_L 7.2-7.3 (this agrees with the moment-magnitude estimate by Hanks and Kanamori (1979)). Four earthquakes, with an M_L of 5.9 or larger, occurred in the 132 year interval from 1851 to 1982 (see Table 1). The local magnitude for the 1885 and 1901 earthquakes is determined from the area shaken with MM $\geqslant$ V and M_L for the 1922 and 1952 earthquakes is determined from instrumental records.

The number and MM intensities of felt earthquakes reported in the Townley and Allen catalog (1928) (excluding aftershocks) are given in Table 2. Note that the number of earthquakes reported felt (listed in Table 1) at the MM$\geqslant$VII intensity level is probably complete back to 1850 because the number of earthquakes per decade does not fluctuate significantly. However, the number of earthquakes reported felt at the MM$\geqslant$IV intensity level is not constant and it increases rapidly after 1900 which implies that either all earthquakes capable of being felt with MM$\geqslant$IV are not accounted for or the rate of seismicity is not stationary with time. The former explanation seems more likely.

The earthquakes reported felt, within the Central Coast Ranges, prior to 1915 do not have instrumentally determined local magnitudes. The M_L for 5 earthquakes occurring between 1882 and 1916 was determined from the area (A) shaken with MM $\geqslant$ V using the relation: $M_L = 0.86 + 1.09\log A$, where A is in km^2 (Toppozada, 1975). The uncertainty in M_L, determined from the area of MM $\geqslant$ V shaking, is about 0.3 magnitude units. Prior to 1880 the felt reports are insufficient to estimate the area of MM $\geqslant$ V shaking. In order to estimate the rate of seismicity from the longest possible seismicity record, the equivalency between the maximum reported intensity (MM) and local magnitude (M_L) must be determined. The estimated correlation, sufficiently accurate for the present purpose, between MM and M_L is given in Table 3. From 1932 to 1972 the UCB catalog gives both MM and M_L for many earthquakes which occurred on the Central Coast Ranges in the region shown in Figure 1. A maximum reported MM intensity of VII is equivalent to $M_L = 5.5 \pm 0.40$ and 11 earthquakes occurred between 1851 and 1982 with either MM VII (prior to 1930) or $5.5 \leqslant M_L < 5.9$ (after 1930). The earthquakes with MM = VII (see Table 1) occurred in 1852, 1853, 1882, 1902, 1915, 1916, 1926, 1952, 1961 and 1966. As discussed above, the list is probably complete. There is considerable scatter in M_L for earthquakes which are assigned a given MM intensity and the standard error is about half a magnitude unit. Note that the earthquakes have a tendency to cluster together in time which suggests that a stationarity assumption may not be valid.

The cumulative number of earthquake sequences N (number of sequences with magnitude $\geqslant M_L$) and the inferred rate (normalized to earthquake sequences per year per $1000\,km^2$) is given in Table 4. The uncertainty in magnitude (σ_{M_L}) is taken to be the precision to which the magnitude is determined. The area is $33{,}750\,km^2$ (the area of the map in Figure 1) for $M_L \leqslant 5$ and $47{,}700\,km^2$ for $M_L > 5$ (as described earlier in the text). The reason for using two different areas is to provide the largest possible portion of the Central Coast Ranges (centered around Coalinga, where the San Andreas fault trace is relatively straight) which is compatible with the completeness of the available seismicity record at each magnitude level. The standard

error in the rate is calculated assuming that the earthquakes follow a Poisson distribution.

Prior to estimating the rate of seismicity for $M_L \geqslant 5$ and $M_L \geqslant 4.5$ the CIT catalog (Hileman et.al., 1973) was compared with the UCB catalog (Bolt and Miller, 1974). No additional earthquakes centered within the area of Figure 1 were found listed in the CIT catalog which were not listed in the UCB catalog. The magnitude of an earthquake which occurred, prior to the development of the M_L scale in the 1930's, was not determined from instrumental records unless there was a special interest in the earthquake. For $M_L \geqslant 5$, 17 earthquakes occurred between 1932 and 1982 in the region shown in Figure 1, and, for $M_L \geqslant 4.5$, 51 earthquakes were observed in the same time interval.

The rate of seismicity for $M_L \geqslant 3.0$, $M_L \geqslant 3.5$, and $M_L \geqslant 4.0$ is estimated from the UCB catalog for the 30 year interval from 1953 to 1982. From approximately 1950 on, the seismicity record for $M_L \geqslant 3.0$ in the region (excluding foreshocks and aftershocks) stabilized at an average rate of approximately 15 earthquake sequences per year. Ranges of time and distance windows, for identifying members of a sequence, were tried and a 14 day time and 30 *km* distance window was adopted as about optimal. Earthquakes which occur within 14 *days* and 30 *km* of each other are assumed to be members of the same sequence. Fourteen days is 0.13 percent of the 30 year sample time and the area of a 30 *km* circle is 8.4 percent of the 33,750 km^2 sample area. The probability of two unrelated earthquakes in the 660 earthquake sample occurring within the criteria for a single sequence is only 6.1 percent (assuming that the sequences follow a Poisson distribution). The 455 earthquake sequences ($3.0 \leqslant M_L \leqslant 5.6$) observed from 1953 to 1982 are plotted in Figure 1. At the $M_L \geqslant 3.0$, $M_L \geqslant 3.5$, and $M_L \geqslant 4.0$ level, 455, 152, and 61 earthquake sequences, respectively, were observed in the 30 year interval shown in Table 4. Note that the original 660 earthquake seismicity sample reduces to 445 earthquake sequences so that, on the average, two-thirds of the earthquakes with $M_L \geqslant 3$ will be associated with a sequence of two or more earthquakes. The distribution of earthquakes within the sequences is not considered in this paper.

Below M_L 3.0 the cumulative rate of seismicity is not reliably estimated for two principal reasons (dealing primarily with the southern part of the region shown in Figure 1). First, the earthquakes listed in the UCB catalog are not complete for $2.5 \leqslant M_L < 3.0$ due to few high-magnification seismographic stations in the region and because the selection criteria for inclusion in the UCB catalog has changed since 1953. The southern most station in the Berkeley network (PRI; 14.7kg vertical Benioff; magnification 80K at 1 sec; established in 1961) is located on Priest Mountain (near 2 in Figure 1) which is 50-100 *km* from the earthquakes occurring along the southern part of the region. Second, the local magnitude, of earthquakes occurring in the region, can not be estimated from the maximum trace amplitudes recorded on the relatively low-gain Wood-Anderson torsion seismograms for $M_L < 3$. The two Wood-Anderson seismographs nearest to Coalinga are located at Mt. Hamilton (MHC; 180 *km* northwest) and Isabella (ISA; 180 *km* east-southeast). For internal consistency, it is preferable to use only magnitudes determined from the maximum trace amplitudes recorded on Wood-Anderson seismograms.

The cumulative rate of seismicity data given in Table 4 was fit to the standard form $\log N = a - bM_L$ by a weighted least-squares procedure and the result is (normalized, as before, to earthquake sequences per year per 1000 km^2):

$$\log N = 2.287 - 0.881 M_L. \tag{1}$$

The associated variance is:

$$\sigma^2_{\log N} = 0.2422 - 0.1362 M_L + 0.01991 M_L^2 \tag{2}$$

where N is the number of earthquake sequences which have a magnitude $\geqslant M_L$. The seismicity in the Central Coast Ranges is assumed to be stationary with time in order that the data from the different time intervals in Table 4 can be combined to solve for (1) and (2). The weighting is by inverse variance which is equivalent to the maximum likelihood solution. Equations (1) and (2) are considered valid for $3.0 \leqslant M_L \leqslant 7.5$. From (2), the linear correlation

(ρ_{ab}) is -0.98 so the coefficients in (1) have a high negative linear correlation (there may be higher order correlations present which are not taken into account in the form of (1)). The cumulative rate of seismicity is plotted in Figure 2 where (1) is an excellent fit to the observations and there are no significant discrepancies in the rates estimated from the 30, 51, and 132 year sample times given in Table 4. There is no graphical indication that the stationarity assumption is violated, however the observed cumulative number of earthquakes would have to deviate, from the theoretical value given by (1), by a factor of two or more before it would become noticeable. The average cumulative rate of seismicity from (1) and its corresponding uncertainty from (2) are given in Table 5 along with the average interoccurrence time and its corresponding uncertainty (all entries are normalized to a $1000\,km^2$ area).

From (1), the rate of occurrence of a $M_L \geqslant 6.7$ earthquake sequence (such as the May 2, 1983 Coalinga mainshock; Uhrhammer *et al.*, 1983) along a $100\,km$ segment (centered on Coalinga) of the Central Coast Ranges on the northeast side of the San Andreas Fault (excluding earthquakes centered within $10\,km$ of the San Andreas Fault) is $0.0019 \pm 0.00026\,earthquakes/year$ in a $8375\,km^2$ area. This corresponds to an average interoccurrence time for $M_L \geqslant 6.7$ earthquakes of 515 ± 70 years and the 95 percent confidence interval spans from 390 to 650 years. This estimate assumes that (1) is appropriate everywhere in the region and, as shown in the next section, there is evidence that in fact it underestimates the interoccurrence time for $M_L \geqslant 6.7$ earthquakes.

For comparison, the rate in the same area, as estimated from a much shorter 1962 - 1982 seismicity sample ($M_L \geqslant 3$), is 0.0062 ± 0.0030 earthquakes per year with $M_L \geqslant 6.7$ (Uhrhammer *et al.*, 1983) which corresponds to an average interoccurrence time of 161 ± 78 years. The two estimates of the interoccurrence time differ by a factor of 3 and the difference can be traced to the relatively low b-value (0.67 ± 0.065) estimated for the shorter time interval.

Spatial Variation in the Rate of Seismicity

The distribution of the 455 epicenters ($3.0 \leqslant M_L \leqslant 5.6$; 1953-1982) plotted in Figure 1 shows that the rate of seismicity is not uniform throughout the Central Coast Ranges. The rate of seismicity strikingly varies as a function of position along and perpendicular to the San Andreas Fault. Given a cumulative rate of seismicity of the form:

$$\log N = a - bM_L, \tag{3}$$

the problem is to determine the variation in a and b as a function of position, parallel to and perpendicular to the San Andreas Fault. The San Andreas Fault was chosen as the coordinate reference frame since more than one-half (260) of the earthquake sequences plotted in Figure 1 are within $10\,km$ of the trace of the fault. Note that the seismicity, in the vicinity of the San Andreas Fault, tends to cluster approximately $3\,km$ to the southwest of the surface trace of the fault. The offset is attributed to a 10 to 20 percent lateral velocity contrast across the fault zone which is not taken into consideration when locating the earthquakes. The seismicity extends approximately 90 km on either side of the San Andreas Fault towards the continental shelf on the southwest and towards the San Joaquin Valley on the northeast. The distribution of seismicity is such that 140 (30.7%) of the earthquake sequences are located on the southwest side of the San Andreas Fault and 86 (18.9%) are located on its northeast side.

In order to determine whether or not there is a significant spatial variation in the b-value in (3), the b-value was computed for three cases. First, on the southwest side of the fault ($>10\,km$ SW), fitting (3) to 140 earthquakes ($3.0 \leqslant M_L \leqslant 5.2$) gives $b = 1.02 \pm 0.087$. Along the San Andreas Fault (within 10 *km*), fitting (3) to 230 earthquakes ($3.0 \leqslant M_L \leqslant 5.6$) yields $b = 0.86 \pm 0.073$. On the northeast side of the fault ($>10\,km$ NE), fitting (3) to 86 earthquakes ($3.0 \leqslant M_L \leqslant 5.4$) gives $b = 0.87 \pm 0.14$. None of these b-values differ significantly, at the 95 percent confidence level, from b determined from the historical seismicity. The sample size is just not sufficiently large to detect, with statistical significance, fine variations in the b-value. Therefore the historically derived b-value of 0.88 ± 0.14 is adopted for use in all subsequent calculations.

The variation of the a-value in (3) is estimated as a function of position (x) for cross-sections A-A' and B-B' (see Figure 1) which are perpendicular and parallel, respectively, to the San Andreas Fault. The normal distribution function is used as an averaging kernel to estimate:

$$a(x_o,\sigma) = bM + \log\left\{\frac{\sum_{i=1}^{n}\exp\left\{-(x_i-x_o)^2/2\sigma^2\right\}}{\sqrt{2\pi\sigma^2}}\right\}, \tag{4}$$

where b = 0.88, M = 3.0 (*minimum* M_L), x_o is the position, and 2σ is the averaging width. In computing $a(x_o,\sigma)$ a range of averaging widths were tried and a width of $2\sigma=10\,km$ was chosen as about optimal. A larger width smooths out detail in $a(x_o,\sigma)$ and a smaller width causes a large increase in the variance of $a(x_o,\sigma)$. The uncertainty in $a(x_o,\sigma)$ is given by:

$$\sigma_a^2 = \frac{2\pi\sigma^2\log^2 e}{\sum_{i=1}^{n}\exp\left\{-(x_i-x_o)^2/2\sigma^2\right\}}. \tag{5}$$

The value of $a(x_o,\sigma)$ normalized to per year per $1000\,km^2$ for $2\sigma=10\,km$ along cross-section A-A', perpendicular to the San Andreas Fault, is given in Figure 3. The cross-hatched region represents the 95 percent confidence level in $a(x_o,\sigma)$. Note that the spatial distribution of $a(x_o,\sigma)$ is trimodal with the main peak corresponding to the San Andreas fault zone. The right-hand peak at $x_o=33\,km$ northeast of the San Andreas Fault corresponds to the relative increase in seismicity observed in Figure 1 in a rather diffuse zone which runs from the Ortigalita fault through the vicinity of Coalinga. The left-hand peak at $x_o=-65\,km$ corresponds to a general increase in seismicity in the vicinity of the coastline shown in Figure 1. The cumulative rate of seismicity for magnitude $\geqslant M_L$ is determined from the value of $a(x_o,\sigma)$ plotted in Figure 3 using

$$\log N = a(x_o,\sigma) - 0.88M_L, \tag{6}$$

and the corresponding uncertainty is:

$$\sigma^2_{\log N} = (1.232 - 0.6930M_L + 0.1013M_L^2)\,C^2, \tag{7}$$

where C is the 95 percent confidence level (the height of the shaded region in Figure 3). The coefficients in (7) were derived by scaling the coefficients given in (2).

As an example of estimating the rate of seismicity, using $a(x_o,\sigma)$ from Figure 3, consider the location of the 1983 Coalinga mainshock, shown as a star in Figure 1 and as an arrow in Figure 3. The width of the peak in a at $x_o=33\,km$ is $40\,km$ ($x_o=13\,km$ to $x_o=53\,km$ as estimated from the width where the rate decreases to one-fourth of the peak value). The average a-value ($\bar{a}$) for the region is given by:

$$\bar{a}(x_o,\sigma) = \log\left\{\frac{1}{x_2-x_1}\int_{x_1}^{x_2} 10^{a(x,\sigma)}\,dx\right\}. \tag{8}$$

The associated uncertainty $\sigma_{\bar{a}}$ is given by the standard method for finding the variance of an arbitrary function. Equation (8) is used to find the average value of a ($\bar{a}$) when the area is greater than $1000\,km^2$. Solving for $\bar{a}(x_o,\sigma)$ where $x_1=13\,km$ and $x_2=53\,km$ yields $\bar{a}=2.46$ and $\sigma_{\bar{a}}=0.106$. The rate of seismicity is then $0.00146\pm0.000382\,earthquakes/year$ with $M_L\geqslant 6.7$ in a $4000\,km^2$ area in the vicinity of Coalinga. Note that the size of the area is arbitrary and $4000\,km^2$ was chosen based on the approximate width of the zone of seismicity occurring on the northeast side of the San Andreas Fault ($40\,km$, from Figure 1) and the length was normalized to $100\,km$. It follows that the average interoccurrence time for $M_L\geqslant 6.7$ earthquakes in the same region is 690 ± 180 years. Table 6 gives the rate of seismicity and the corresponding

average interoccurrence time for the region of the Coalinga mainshock. On the assumption that $M_L \geqslant 6.7$ earthquakes exhibit a Poisson probability distribution, $\lambda = rt = 0.00146 \times 132 \approx 0.2$, so that the probability of one or more $M_L \geqslant 6.7$ earthquakes occurring in the vicinity of Coalinga in a 132 year interval is approximately one in five. The inference is that the May 2, 1983 M_L 6.7 Coalinga mainshock is not an unexpected event in either size or general location. Remember that the Coalinga mainshock was not included in the seismicity sample for determining the rate of seismicity. Including the Coalinga mainshock in the seismicity sample does not appreciably change the results.

The value of $a(x_o,\sigma)$ normalized to per year per $1000 km^2$ for $2\sigma = 10 km$ along cross-section B-B' (see Figure 1), parallel to the San Andreas Fault, is given in Figure 4. The peak in the a-value of 3.25 at $x_o = -92 km$ is associated with the high rate of seismicity along the Bear Valley - Stone Canyon segment of the San Andreas Fault (number 1 on Figure 1). The low in the a-value of 2.08 at $x_o = -50 km$ is due to the rapid decrease (by a factor of 5) in the observed seismicity along the San Andreas fault zone southeast of Parkfield (bottom of Figure 1). South of Parkfield is the "locked" Carrizo Plain segment of the San Andreas Fault where the rate of seismicity is low and the potential for the occurrence of a large earthquake is relatively high (Lindh, 1983). For approximately $100 km$ along the cross-section the a-value fluctuates around 2.8 with significant lows near the projection of the Coalinga mainshock location (arrow on Figure 4) and approximately $50 km$ to the northwest ($x_o = 50 km$). The significance of these lows in the a-value is discussed below.

Spatial Variation in the Rate of Strain Energy Release

Cumulative coseismic strain release from a 30 year sample of seismicity (1953-1982; 660 earthquakes; $3.0 \leqslant M_L \leqslant 5.6$) may be estimated from the square-root of the seismic wave energy (Benioff, 1955). The strain is plotted as a function of position (x) along the two cross-sections A-A' and B-B' (in Figure 1) in Figures 5 and 6, respectively. The coseismic strain energy release (E) for each earthquake is estimated from the local magnitude M_L where:

$$\frac{1}{2}\log_{10}E = 5.9 + 0.75 M_L. \tag{9}$$

The form of the normal distribution function was again used as an averaging kernel to estimate the cumulative strain energy release $E_s(x_o,\sigma)$ where:

$$E_s(x_o,\sigma) = \frac{1}{\sqrt{2\pi\sigma^2}} \sum_{i=1}^{n} E_i \exp\left\{-(x_i - x_o)^2 / 2\sigma^2\right\} \tag{10}$$

as a function of position x_o and averaging width 2σ. In computing $E_s(x_o,\sigma)$ a width of $2\sigma = 10 km$ was chosen after test trials (same as averaging width for the estimation of $a(x_o,\sigma)$ in the previous section). The largest earthquake in the seismicity sample is M_L 5.6 which has a source dimension approximately the same as the averaging width ($10 km$). If the largest earthquake in the seismicity sample has a source dimension which is much larger than the averaging width, the rapid variations in the plotted strain energy at the location of the large earthquake may be misleading. The uncertainty σ_{E_s} for $E_s(x_o,\sigma)$ in (10) is calculated assuming that the uncertainty in the M_L estimate is $\sigma_{M_L} = 0.15$ (a typical observed value for earthquakes which occur in the Central Coast Ranges).

The strain energy release rate (normalized to per year per $1500 km^3$ volume) for the cross-section A-A' (see Figure 1) perpendicular to the San Andreas fault is given in Figure 5. The $1500 km^3$ volume comes from a zone $1 km$ wide by $100 km$ long by $15 km$ deep. The $15 km$ depth is estimated from the observed range of focal depth ($0-15 km$) for earthquakes which have occurred in the Central Coast Ranges (Bolt and Miller, 1971). Below a depth of $15 km$ it is assumed that strain is relieved by plastic flow and elastic strain energy is not accumulated. The maximum in Figure 5 (9.6) corresponds to a strain energy release rate of $(1.6 \pm 0.7) \times 10^{19} ergs/year$ which coincides with the San Andreas Fault and the width of the zone of high strain energy release rate is approximately $100 km$ (from $40 km$ southwest to $60 km$

northeast of the San Andreas fault).

The average strain release ϵ (Bullen, 1963) is estimated from the strain energy release by:

$$\epsilon = \sqrt{\frac{E_s}{\mu V}} \tag{11}$$

where μ is the average shear modulus ($3\times10^{11} dynes/cm^2$) and V is the crustal volume under strain. The average strain release rate in the $40\,km$ wide zone on the southwest side of the San Andreas fault is $0.46\pm0.15\mu\, strain/year$. Also, the average strain release rate in the $60\,km$ wide zone on the northeast side of the fault is $0.38\pm0.09\mu\, strain/year$. The average for the whole $100\,km$ wide zone is $0.40\pm0.12\mu\, strain/year$ (averaged over 30 years). Assuming that the average rate of crustal distortion in a $100\,km$ wide region across the San Andreas fault zone is equivalent to the relative motion across the Pacific-North American plate boundary, $5.6\pm0.3\,cm/year$ (Minster and Jordan, 1978), the average rate of shear strain accumulation in the region is $0.56\pm0.03\mu\, strain/year$. Therefore, for the past 30 years, the rate of strain accumulation due to relative plate motion has exceeded the rate of coseismic strain dissipation due to earthquakes, occurring in the $180\,km$ long segment of the Central Coast Ranges, by $0.16\pm0.087\mu\, strain/year$. The conclusion is that the rate of strain accumulation has exceeded the rate of coseismic strain dissipation by approximately 40 percent during the past 30 years (1953-1982), assuming that all of the strain is accumulated in the Central Coast Ranges and that μ and V (combined as μV) are not in error as much as (1). This strain accumulation suggests an increasing potential for the occurrence of a large earthquake with time. Other mechanisms for dissipating the strain energy, such as aseismic creep, mountain building, and tectonic folding are not considered in this calculation so it clearly represents an overestimate of the potential.

On the southwest side of the San Andreas Fault, the average strain accumulation rate has exceeded the average coseismic strain dissipation rate by $0.10\pm0.11\mu\, strain/year$ which is not statistically significant. Thus almost all of the strain energy accumulation on the southwest side of the fault, during the past 30 years, has been dissipated by the earthquakes which have occurred in the region. On the other hand, on the northeast side of the fault, the average rate of strain accumulation has exceeded the average rate of coseismic strain dissipation by $0.18\pm0.067\mu\, strain/year$ which is statistically significant. Therefore, on the northeast side of the fault, a strain energy glut has been accumulating over at least the 30 year interval from 1953 to 1982. One inference is that the potential for the occurrence of a large earthquake is increasing more rapidly on the northeast (Coalinga) side of the fault than on the southwest side of the fault.

The strain energy released by the 1983 Coalinga mainshock, M_L 6.7, is approximately $7\times10^{21} ergs$ (from (9)). The aftershocks were distributed over a $20\,km$ by $25\,km$ zone to a depth of $15\,km$ which implies that the volume of the source region is approximately $7500\,km^3$. Consequently, from (11), the average strain release by the Coalinga mainshock is approximately $56\mu\, strain$.

The coseismic strain energy release rate (normalized to per year per 100km length) for the cross-section B-B' (see Figure 1) parallel to the San Andreas Fault is given in Figure 6. The maximum in the strain energy release rate (9.58) at $x_o=-100\,km$ ($1.4\times10^{19} ergs/year$) is associated with the high rate of seismicity along the Bear Valley - Stone Canyon segment of the San Andreas Fault (1 in Figure 1). The second highest strain energy release rate (9.50) at $x_o=9\,km$ ($1.0\times10^{19} ergs/year$) is associated with the relatively high rate of seismicity along the Parkfield segment of the San Andreas fault (2 in Figure 1). Note that to the southeast of Parkfield ($x_o>40\,km$ in Figure 6 and bottom of Figure 1) the rate of strain energy release due to earthquakes decreases by a factor of approximately 20. Assuming that the overall tectonic strain rate is uniform along the Central Coast Ranges when averaged over a long period of time, the coseismic strain energy release rate in Figure 6 is inversely proportional to the earthquake potential. Thus the highest potential for the occurrence of a large earthquake is to the southeast of Parkfield. There are two other significant lows in Figure 6, at $x_o=-8\,km$ (where

the M_L 6.7 Coalinga mainshock occurred) and at x_o=−50km. The relative position of the epicenter of the Coalinga mainshock is shown by the arrow in Figure 6. Assuming that the strain energy released by the M_L 6.7 Coalinga mainshock is $7\times10^{21}ergs$ (from (9)) and that an event this size or larger occurs every 690±180 years, the average annual coseismic strain energy release per year in a 30km wide zone is $10^{2\times(9.51\pm0.056)}ergs/year$ (given by the dashed line in Figure 6). It follows that the low in the rate of strain energy release (i. e., the strain energy glut) at x_o=−8km in Figure 6 disappeared when the M_L 6.7 Coalinga mainshock occurred.

The source dimensions of the Coalinga mainshock are of the same order as the 30km distance between the peaks at x_o=−22km and x_o=8km. There is a suggestion that it may be possible to predict the general size and relative position of a maximum sized earthquake in the region, but not the time of occurrence, from the relative rate of strain energy release along the Central Coast Ranges (based on relatively short, 30 year, seismicity sample). Consider the low at x_o=−50km in Figure 6. This low in the rate of strain energy release is approximately 80km wide which is of the same order as the fault rupture length associated with a M_L 7½ earthquake. The strain energy release for a M_L 7½ earthquake is $1\times10^{23}ergs$ (from (9)) and the corresponding rate of occurrence along the San Andreas Fault is $0.00066\pm0.00026 earthquakes/year$ (from Figure 3). The average interoccurrence time is 1500±500 years. The low in the rate of strain energy release at x_o=−50km will accumulate strain energy at a rate of $(5.6\pm2.6)\times10^{19}ergs/year$ and at this rate it can accumulate $1\times10^{23}ergs$ in 1700±830 years. Thus the average interoccurrence time of 1500±500 years for a M_L 7½ earthquake and the strain accumulation time of 1700±830 years in a 80km segment of the San Andreas fault zone are quite compatible.

Discussion and Conclusions

The average annual rate of seismicity, (1), and its variance, (2), for earthquakes which occur in a 180km segment of the Central Coast Ranges of California, centered around Coalinga, are estimated for earthquakes with $3.0\leqslant M_L\leqslant7.5$ from the 132 year record of historical seismicity (1851-1982). It is assumed that the rate of seismicity is stationary in time as there are no statistically significant fluctuations in the observed number of earthquakes per decade. The results show a clear spatial variation in the rate of seismicity (from Figure 1) which can be assigned to either variation in the a-value or the b-value (or both) in (3) with position. A b-value of 0.88±0.14 does not vary significantly with position perpendicular to the San Andreas Fault.

The spatial distribution in the rate of seismicity in the transverse cross-section A-A' (Figure 3) is trimodal with the highest a-value associated with the San Andreas Fault. The broad peak at x_o=−65km (in Figure 3) is associated with the numerous, relatively small magnitude, earthquakes which occur in the vicinity of the coastline in Figure 1. Note that the rate of strain energy release in the same region (see Figure 5) is relatively low. This is in agreement with the relative lack of larger earthquakes in the region and it implies that the appropriate b-value for the vicinity of the coastline may in fact be larger than the adopted b-value of 0.88±0.14. The peak in the a-value at x_o=33km is associated with the seismicity occurring in a rather diffuse zone, which extends from the Ortigalita fault (Figure 1) through the vicinity of Coalinga. Assuming that large earthquakes exhibit a Poisson probability distribution, a $M_L\geqslant6.7$ earthquake (such as the May 2, 1983 Coalinga mainshock) will occur on the average every 690±180 years (in a 4000km^2 area) in the vicinity of Coalinga. The probability of one or more $M_L\geqslant6.7$ earthquakes occurring in a 132 year interval is approximately 20 percent (1 chance in 5). The M_L 6.7 Coalinga mainshock is therefore not an unexpected event in either size or general location.

Elastic strain energy accumulates in the crust due to the $5.6\pm0.3 cm/year$ relative motion between the Pacific and North American plates. The San Andreas fault zone is the boundary between the two plates and the overall strain energy is dissipated primarily by earthquakes which occur within a 100km wide zone (see Figure 5) centered approximately on the San Andreas fault. The average rate of strain accumulation in the 100km wide zone

($0.56 \pm 0.03 \mu$ *strain/year*) exceeds the average rate of coseismic strain dissipation ($0.40 \pm 0.12 \mu$ *strain/year*; averaged over 30 years) by $0.16 \pm 0.087 \mu$ *strain/year*. This strain energy glut indicates increased likelihood for the occurrence of large earthquakes with time.

On the northeast side of the fault zone, approximately 70 percent of the strain energy is dissipated within 13 *km* of the San Andreas fault and the other 30 percent of the strain energy is dissipated over a zone extending from 13 *km* to 60 *km* northeast of the fault. This is compatible with the difference between the average motion across the San Andreas Fault (3.7 ± 0.3 *cm/year*; Hall and Sieh, 1977) and the average relative motion of the Pacific and North American plates (5.6 ± 0.3 *cm/year*; Minster and Jordan, 1978). The annual rate of strain accumulation over the past 30 years (1953-1982) in the zone from 13 *km* to 60 *km* northeast of the San Andreas fault is $0.045 \pm 0.033 \mu$ *strain/year*. The M_L 6.7 Coalinga earthquake had an estimated strain release of 56μ *strain* and it would take 1200 ± 910 years to accumulate this amount of strain. Thus the strain accumulation time, although it is not well determined, is compatible with the interoccurrence time of 685 ± 178 years for M_L 6.7 earthquakes estimated in this paper from the seismicity record.

An upper bound for the magnitude of an earthquake (M_L^{max}), which can occur in a region, is reached when the average rate of coseismic strain release is equal to the average rate of tectonic strain accumulation ($0.56 \pm 0.03 \mu$ *strain/year*). The average rate of coseismic strain release for $3.0 \leqslant M_L \leqslant M_L^{max}$ is determined from the cumulative rate of seismicity (1), the strain energy release (9), and the strain release (11). The resulting upper magnitude bound for the Central Coast region is $M_L^{max} = 7.46 \pm 0.14$. In estimating M_L^{max} the cross-sectional area perpendicular to the San Andreas fault zone is limited to a maximum of $1500\,km^2$ ($100\,km \times 15\,km$). There are two basic assumptions in determining this value for M_L^{max}. First, the rate of strain accumulation is stationary. Some support for this assumption in recent geologic times comes from the similarity of slip rates, along the San Andreas Fault in central California, determined by geologic evidence (Hall and Sieh, 1977; 3.7 ± 0.3 *cm/yr* over the past 3 millennia) and geodetic evidence (Thatcher, 1975). Second, the source volume of large earthquakes increases linearly with the largest source dimension (length) as opposed to small earthquakes where the source volume increases with the cube of the source dimension. This assumption is fundamental in limiting the size of M_L^{max} because it implies that the larger earthquakes, which behave like line sources, will release proportionally more elastic strain. Some examples of coseismic strain release are: the M_L 5.9 Coyote Lake earthquake of August 6, 1979 relieved $\approx 23 \mu$ *strain* (Uhrhammer, 1980); the M_L 6.7 Coalinga mainshock relieved $\approx 56 \mu$ *strain* (this paper); and the M_s 8.3 San Francisco earthquake of April 18, 1906 relieved $\approx 115 \mu$ *strain* (Thatcher, 1975). Thus above $M_L \approx 6$ the coseismic strain release increases with M_L at a rate of approximately 40μ *strain*/ M_L and M_L^{max} corresponds to a balance between the rates of strain accumulation and strain release.

Note that the average annual rate of strain energy release transverse to the San Andreas fault zone (Figure 5) exhibits a periodicity of 25 ± 4.4 *km* between peaks. For comparison, the median spacing between Quaternary age faults, parallel to the San Andreas Fault, in the region (Jennings, 1975) is 28 ± 3 *km*. The upper part of the crust which accumulates and dissipates elastic strain energy is assumed to be approximately 15 *km* thick (the depth to which earthquake foci are observed in the Central Coast Ranges). The aspect ratio between the inter-strain peak distance and the elastic crustal thickness is approximately 1.8. One possible explanation for the similarity and the regularity in the spacing of peaks in the rate of coseismic strain energy release and in the spacing of the Quaternary age faults is as follows. First, the regularity in the spacing of the existing Quaternary age faults is mechanically controlled by the width of a crustal cross-section (perpendicular to the relative plate motion) required to accumulate sufficient strain energy to fracture the entire thickness of the elastic portion of the crust. Second, the coseismic strain energy release is controlled by the lateral variation in the strength of the elastic upper crust and the higher rates of strain energy release will occur along existing faults where the crust is presumably weaker.

The RM2 model of Minster and Jordan (1978) predicts a rate of relative motion between

the Pacific and North American plates, in the Central Coast Ranges, of $5.6 \pm 0.3\,cm/year$ in a direction N35°W±2.0°. The strike of the surface trace of the San Andreas Fault is N40.4°W±0.23° in the region shown in Figure 1 (Jennings, 1975). The difference in the azimuth between the relative motion of the plates and the strike of the fault is 5.4°±2.0° which is statistically significant. Decomposing the relative plate motion vector into orthogonal components which are parallel and perpendicular, respectively, to the strike of the San Andreas Fault, yields a right-lateral strike-slip motion of $5.6 \pm 0.3\,cm/year$ parallel to the fault and a compressive motion of $0.53 \pm 0.20\,cm/year$ perpendicular to the fault. Hall and Sieh (1977) estimate a slip rate of $3.7 \pm 0.3\,cm/year$ along the San Andreas Fault in Central California, thus $1.9 \pm 0.4\,cm/year$ of right-lateral strike-slip motion and the compressive motion are not absorbed by the San Andreas Fault. These motions must be taken up, in part, by active orogenic processes which are occurring in the Central Coast Ranges. The tectonic compression is compatible with the reverse slip mechanism for the Coalinga mainshock as evidenced from geodetic elevation changes (Stein, 1983).

Acknowledgements

The author would like to acknowledge B. A. Bolt and T. V. McEvilly for several enlightening discussions during the course of this work and for critically reading the manuscript. The research was sponsored, in part, by the Field Investigation Fund of the Seismographic Station.

References

Benioff, H., "Seismic Evidence for Crustal Structure and Tectonic Activity", Geol. Soc. Am., Special Paper 62, 61-74, 1955.

Bakun, W. H. and T. V. McEvilly, "Recurrence Models and Perkfield, California, Earthquakes", J. Geophys. Res., in press, 1984.

Bolt, B. A. and R. D. Miller, "seismicity of Northern and Central California, 1965-1969", Bull. Seism. Soc. Am., 61, 1831-1847, December 1971.

Bolt, B. A. and R. D. Miller, "Catalog of Earthquakes in Northern California and Adjoining Areas (1 January 1910 - 31 December 1972)", Seismographic Station, University of California, pp. 567, 1975.

Bullen, K. E., "Introduction to the Theory of Seismology", Third Edition, Cambridge Univ. Press, pp. 381, 1963.

Byerly, P., "The California Earthquake of November 4, 1927", Bull. Seism. Soc. Am., 20, 53-66, June 1930.

Ellsworth, W. L., A. G. Lindh, W. H. Prescott and D. G. Herd, "The 1906 San Francisco Earthquake and the Seismic Cycle", Am. Geophys. Union, Maurice Ewing Monogr. 4, pp. 126-140, 1981.

Gawthrop, W., "The 1927 Lompoc, California Earthquake", Bull. Seism. Soc. Am., 68, 1705-1716, December 1978.

Hall, N. T. and K. E. Sieh, "Late Holocene Rate of Slip on the San Andreas Fault in the Northern Carrizo Plane, San Louis Obispo County, California", (abstract), Geol. Soc. Amer. Abstr. Programs, 9, 428, 1977.

Hanks, T. C., "The Lompoc, California, Earthquake (November 4, 1927; M=7.3) and its Aftershocks", Bull. Seism. Soc. Am., 69, 0451-0462, April 1979.

Hanks, T. C. and H. Kanamori, "A Moment Magnitude Scale", J. Geophys. Res., 84, pp. 2348-2350, 1979.

Hileman, J. A., C. R. Allen and J. M. Nordquist, "Seismicity of the Southern California Region, 1 January 1932 to 31 December 1972", Seismological Laboratory, California Institute of Technology, pp. 487, 1973.

Jennings, C. W., "Fault Map of California", California Geologic Data Map Series, Map 1, Calif. Div. of Mines and Geol., 1975.

Lindh, A. G., "Preliminary Assessment of Long-Term Probabilities for Large Earthquakes Along Selected Fault Segments of the San Andreas Fault System in California", U. S. Geological Survey, Open-File Report 83-63, 1983.

Majer, E. L. and T. V. McEvilly, "Seismological Investigation at the Geysers Geothermal Field", Geophysics, 44, No. 2, pp. 246-269, February 1979.

Minster, J. B. and T. H. Jordan, "Present-Day Plate Motions", J. Geophys. Res., 83, 5331-5354, 1978.

Stein, R. S., "Reverse Slip on a Buried Fault During the 2 May 1983 Coalinga Earthquake: Evidence from Geodetic Elevation Changes", California Division of Mines and Geology, Special Publication 66, pp. 151-163, 1983.

Thatcher, W.,"Strain Accumulation on the Northern San Andreas Fault Zone Since 1906", J. Geophys. Res., 80, 4873-4880, 1975.

Thatcher, W., "Crustal Deformation Studies and Earthquake Prediction Research", Am. Geophys. Union, Maurice Ewing Monogr. 4, pp. 394-410, 1981.

Toppozada, T. R., "Earthquake Magnitude as a Function of Intensity Data in California and Western Nevada", Bull. Seism. Soc. Am., 65, pp. 1223-1238, October 1975.

Toppozada, T. R., C. R. Real and D. L. Parke, "Preparation of Isoseismal Maps and Summaries

of Reported Effects for Pre-1900 California Earthquakes", U. S. Geological Survey, Open File Report 81-11 SAC, 1981.

Toppozada, T. R. and D. L. Parke, "Areas Damaged by California Earthquakes, 1900-1949", U. S. Geological Survey, Open File Report 82-17 SAC, 1982.

Townley, S. D. and M. W. Allen, "Descriptive Catalog of Earthquakes of the Pacific Coast of the United States, 1769 to 1928", Bull. Seism. Soc. Am., 29, February 1939.

Uhrhammer, R. A., "Observations of the Coyote Lake, California Earthquake Sequence of August 6, 1979", Bull. Seism. Soc. Am., 70, 559-570, April 1980.

Uhrhammer, R. A., R. B. Darragh and B. A. Bolt, "The 1983 Coalinga, California Earthquakes", California Division of Mines and Geology, Special Publication 66, 221-231, 1983.
USCGS Earthquake Reports, "Abstracts of Earthquake Reports for the Pacific Coast and the Western Mountain Region, April 1, 1934 to June 30, 1934, pp. 39, 1934.

Table 1.

Earthquakes with MM ⩾ VII or M_L⩾5.5							
Date	Time (UTC)	Lat °N	Long °W	MM	M_L	Felt Area[1]	Region
12/17/1852		35.3	120.7	VII	5.5[2]		San Louis Obispo
02/01/1853	21:00	35.7	121.2	VII	5.5[2]		San Simeon
03/06/1882	21:45	36.9	121.2	VII	5.5[3]	17	Quien Sabe Valley
04/12/1885	04:05	36.4	121.0	VIII	6.2[3]	72	Bitterwater
03/03/1901	07:45	36.0	120.5	VIII-IX	5.9[3]	38	Stone Canyon
07/28/1902	06:57	34.8	120.4	VII	5.5[3]	18	Los Alamos
01/12/1915	04:31	34.8	120.3	VII	5.5[4]	16	Los Alamos
08/06/1916	19:38	36.7	121.3	VII	5.5[3]	15	Paicenes
03/10/1922	11:21	35.8	120.3	VIII-IX	5.6[5]	22	Parkfield
07/25/1926	17:57	36.6	120.8	VII	5.5[2]		Idria
11/04/1927	13:50	34.6	120.9	VIII-IX	7.3[6]	130	W of Pt. Arguello
06/08/1934	04:47	35.8	120.8	VIII	5.6[5]	25	Parkfield
11/24/1952	07:46	35.7	121.2	VII	5.9[4]	45	San Simeon
04/09/1961	07:23	36.7	121.3	VII	5.6[4]	18	Paicines
06/28/1966	04:26	36.0	120.5	VII	5.6[5]	23	Parkfield

1 - area in $10^3 km^2$ with MM⩾V
2 - estimated from max MM intensity
3 - estimated from area with MM⩾V
4 - determined from seismograms kept on store at Berkeley
5 - from Bakun and McEvilly (1984)
6 - from Byerly (1930)

Table 2.

Number of Felt Earthquakes (excluding aftershocks)								
Date	MM Intensity						N	Population
	IV	V	VI	VII	VIII	IX		*people/ km²*
1850								0.128
		1	1	2			4	
1860								0.378
		1					1	
1870								0.848
	2						2	
1880								1.25
		1			1		2	
1890								2.00
		1					1	
1900								2.04
	1		2		1	1	5	
1910								2.47
	8	7	1	2	1		19	
1920								2.82
	7		1	1		2	11	
1930								4.02

Table 3.

Maximum MM Intensity versus M_L		
MM	M_L	σ_{M_L}
IV	3.7	0.54
V	4.1	0.52
VI	4.6	0.48
VII	5.5	0.40
VIII	6.0	0.32

Table 4.

Observed Cumulative Rate of Seismicity						
$M_L \geqslant$	σ_{M_L}	Area ($10^3 km^2$)	Time (yr)	n	r (eq/yr)	σ_r (eq/yr)
3.0	.05	33.75	30	455	.449	.0211
3.5	.05	33.75	30	152	.150	.0122
4.0	.05	33.75	30	61	.0603	.00771
4.5	.05	33.75	51	51	.0210	.00294
5.0	.05	33.75	51	17	.00699	.00170
5.5	.10	47.7	132	15	.00242	.000625
5.9	.15	47.7	132	4	.000635	.000318
7.3	.15	47.7	132	1	.000161	.000161

Table 5.

Calculated Cumulative Rate of Seismicity				
$M_L \geqslant$	r (eq/yr)	σ_r (eq/yr)	T (yr)	σ_T (yr)
3.0	.441	.114	2.27	.586
3.5	.160	.0356	6.25	1.39
4.0	.0580	.0168	17.2	4.99
4.5	.0210	.00870	47.5	19.7
5.0	.00763	.00426	131.	73.2
5.5	.00277	.00197	361.	257.
6.0	.00100	.000867	996.	867.
6.5	.000364	.000373	2750.	2820.
6.7	.000243	.000264	4120.	4470.
7.0	.000132	.000156	7570.	8950.
7.5	.0000479	.0000644	20900.	28100.

Table 6.

Cumulative Rate of Seismicity (Coalinga Region)				
$M_L \geqslant$	r (eq/yr)	σ_r (eq/yr)	T (yr)	σ_T (yr)
3.0	2.64	.160	.38	.023
3.5	.959	.0494	1.0	.054
4.0	.348	.0238	2.9	.20
4.5	.126	.0124	7.9	.78
5.0	.0459	.00612	22.	2.9
5.5	.0167	.00284	60.	10.
6.0	.00605	.00125	170.	34.
6.5	.00220	.000539	450.	110.
6.7	.00146	.000382	690.	180.
7.0	.000798	.000226	1300.	350.
7.5	.000299	.0000961	3500.	1100.

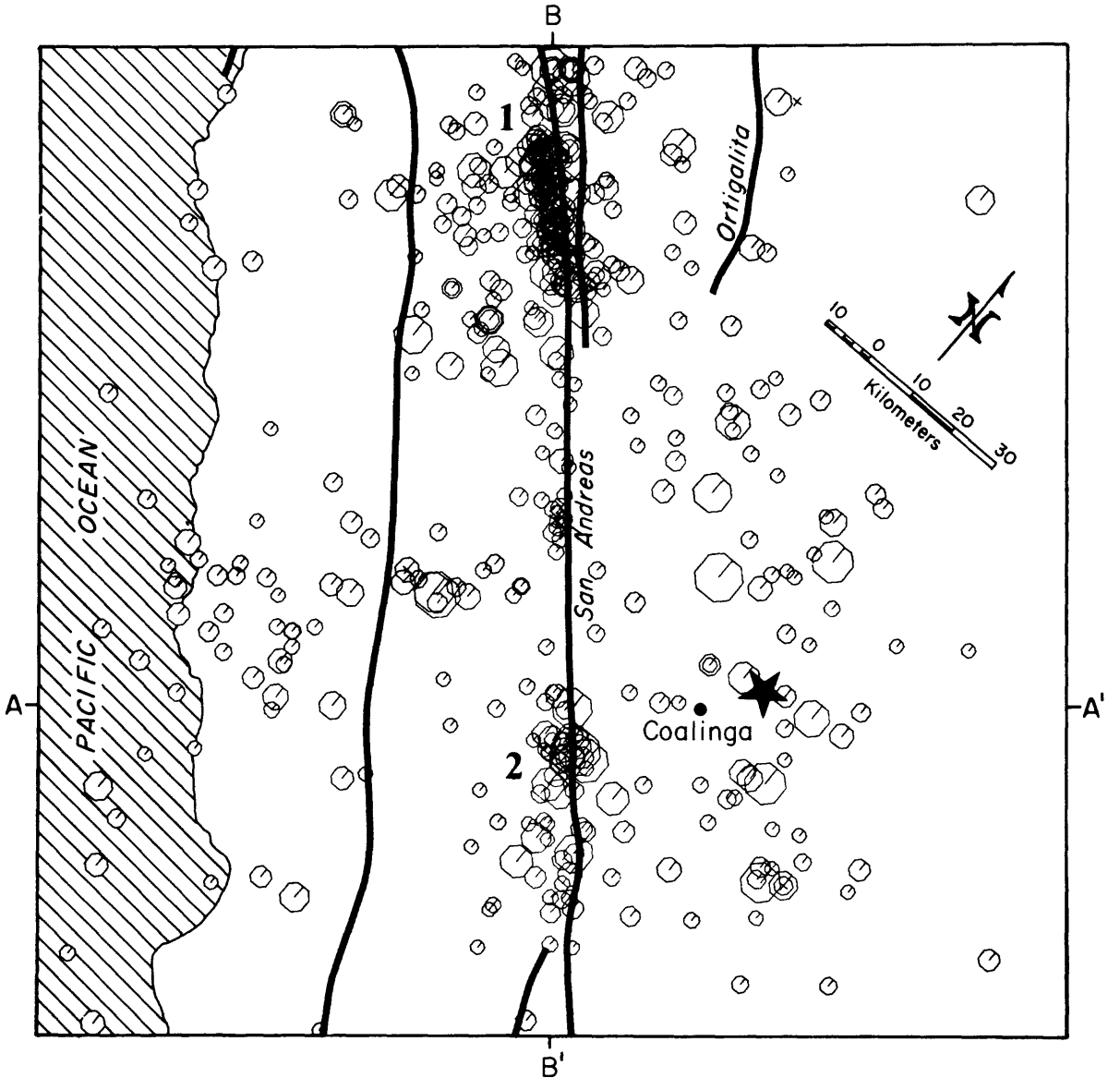

Figure 1. Map of Central Coast Ranges of California from approximately Monterey to Santa Maria. The positions of the major faults are indicated by the heavy lines. Thirty years of seismicity (455 earthquake sequences; $3.0 \leqslant M_L \leqslant 5.6$; 1953-1982) are plotted in octagons which are scaled to the size of the earthquakes. The star is the location of the M_L 6.7 Coalinga mainshock of May 2, 1983. The large numbers 1 and 2 indicate the Bear Valley-Stone Canyon and Parkfield segments, respectively, of the San Andreas Fault. The area is 33,750km (180km×187.5km) and cross-sections A-A' and B-B' are used in Figures 3 to 6.

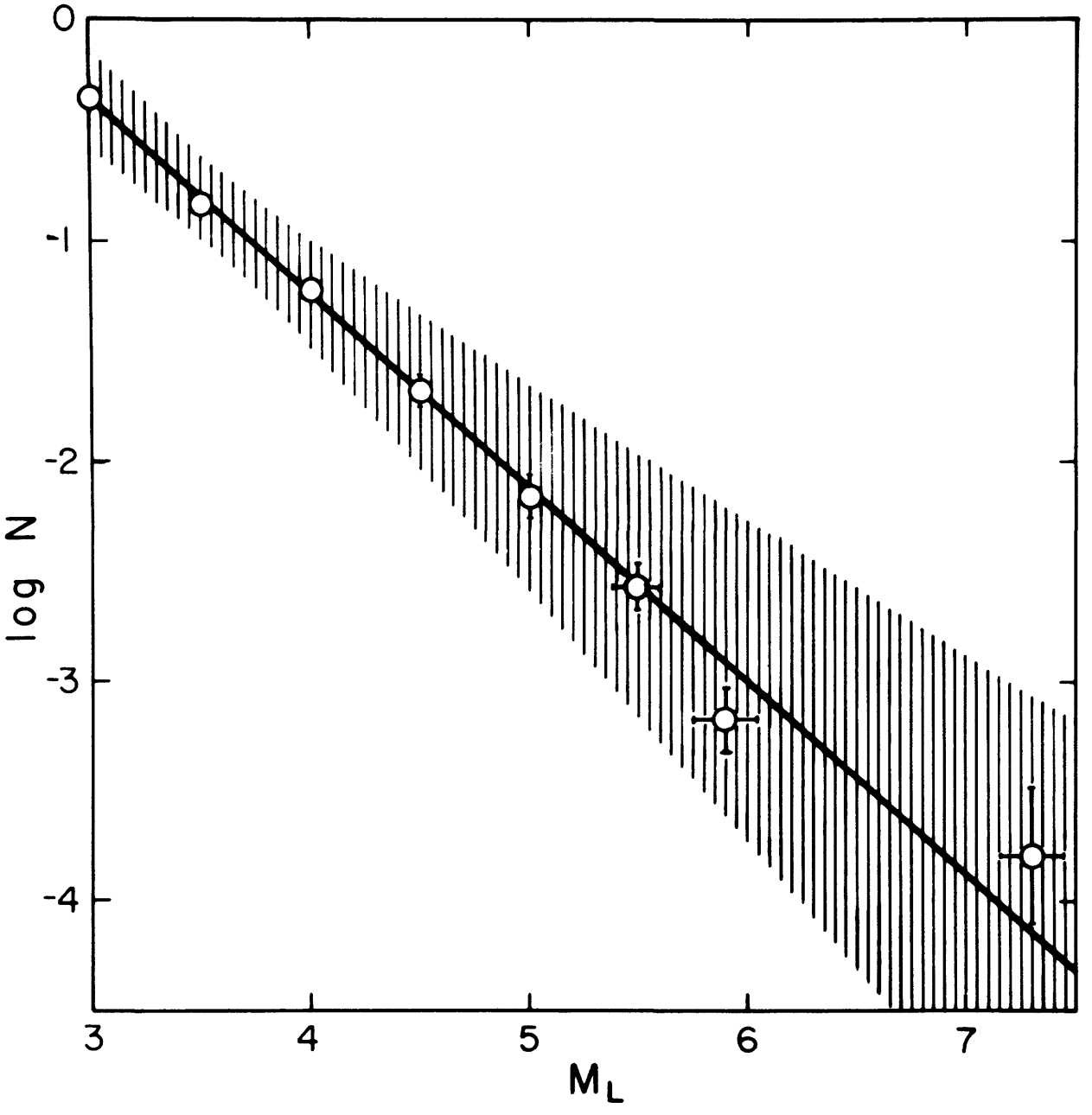

Figure 2. Cumulative rate of seismicity for the Central Coast Ranges where N is normalized to earthquake sequences per year per $1000 km^2$. The shaded band represents the 95 percent confidence interval for $\log N$ and the open circles with error bars are the observed data.

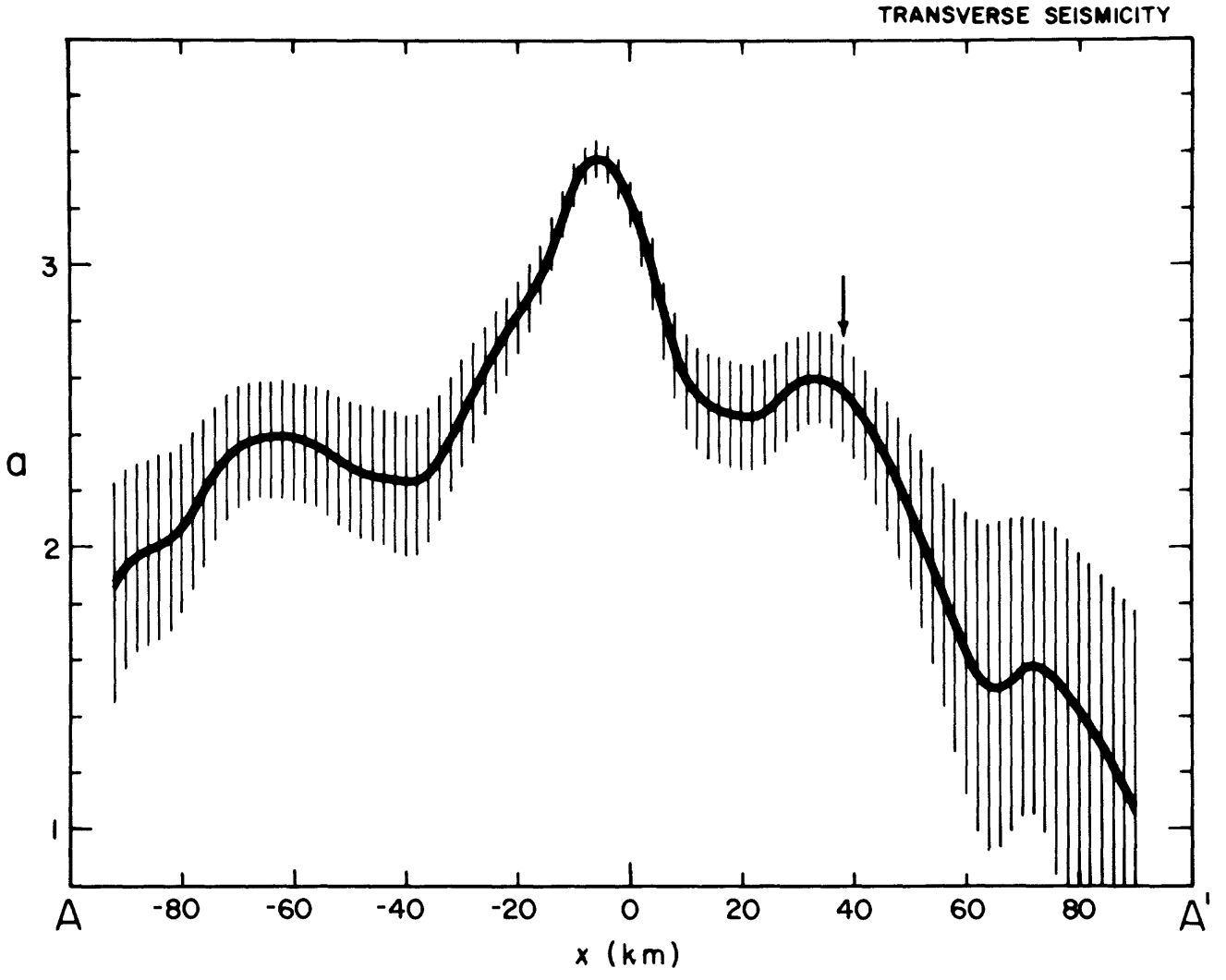

Figure 3. The a-value is plotted as a function of position perpendicular to the San Andreas Fault (cross-section A-A' in Figure 1). The a-value is normalized to per year per $1000\,km^2$ and the shaded region is the 95 percent confidence level. The arrow indicates the position of the Coalinga mainshock.

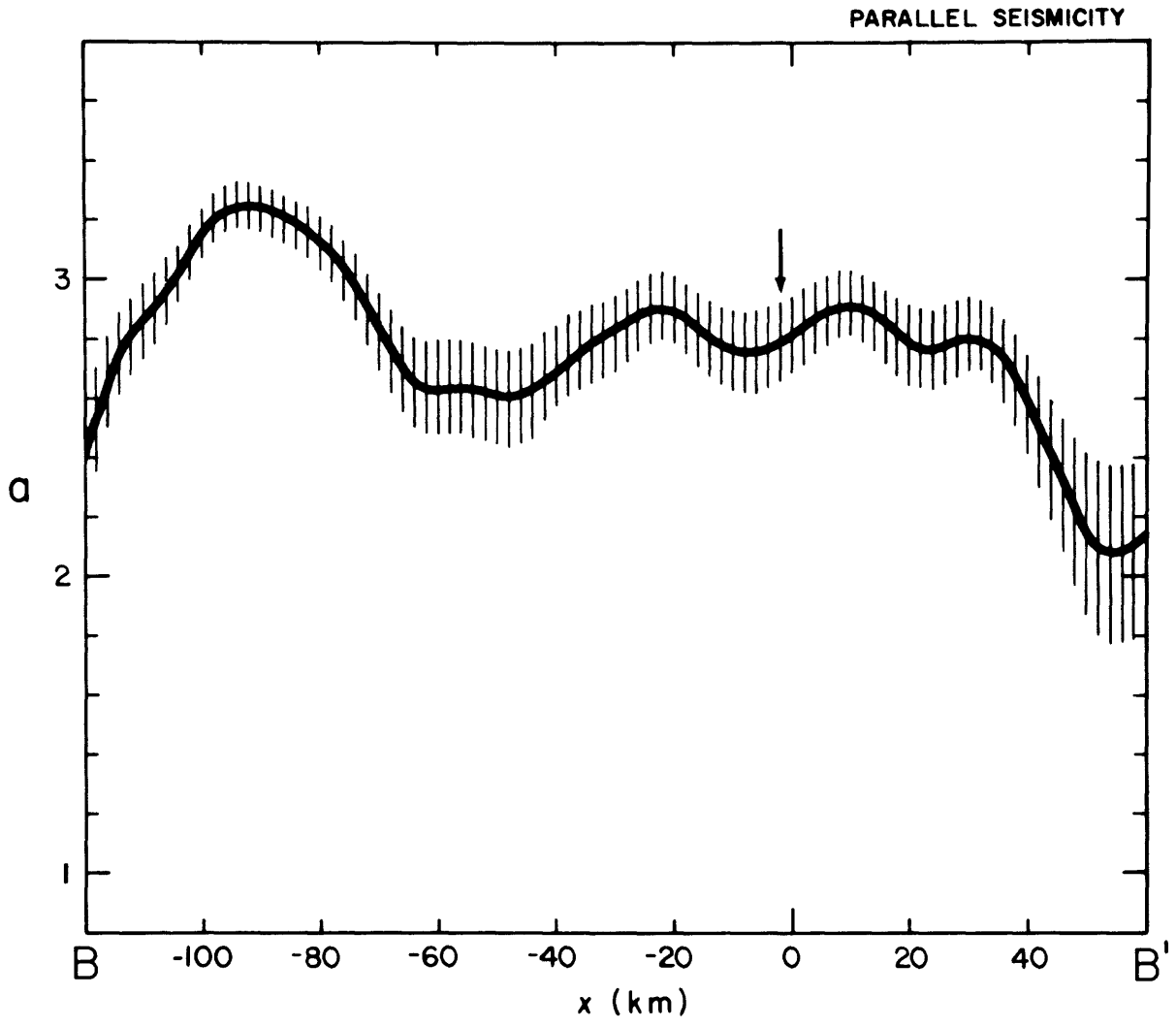

Figure 4. The a-value is plotted as a function of position parallel to the San Andreas Fault (cross-section B-B' in Figure 1). The a-value is normalized to per year per 1000 km^2 and the shaded region is the 95 percent confidence level. The arrow indicates the position of the Coalinga mainshock.

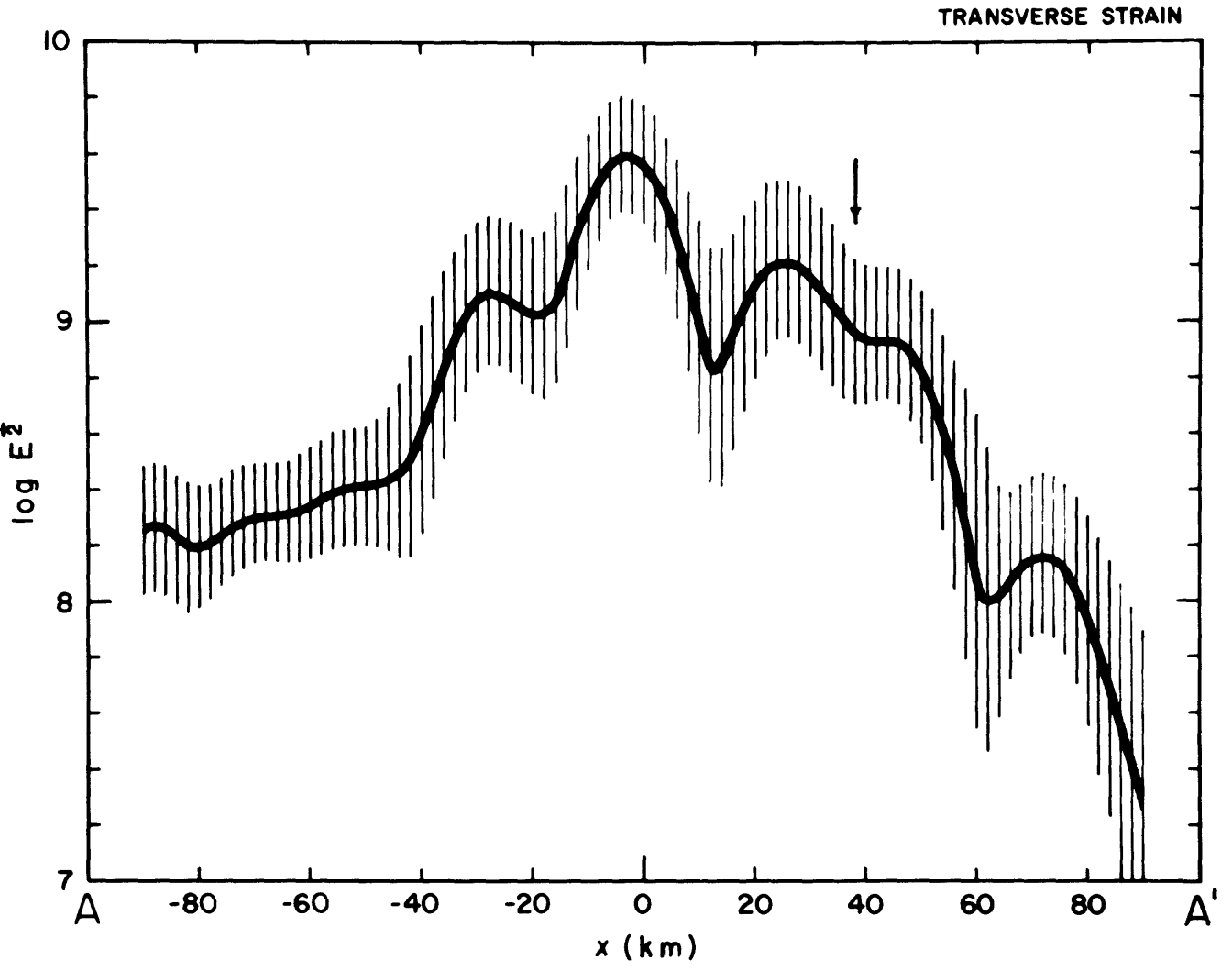

Figure 5. The square-root of the coseismic strain energy release (proportional to strain) is plotted as a function of position perpendicular to the San Andreas fault zone (cross-section A-A' in Figure 1). The strain energy is normalized to ergs per year per $1500\,km^3$. The shaded region is the 95 percent confidence level and the arrow indicates the position of the Coalinga mainshock.

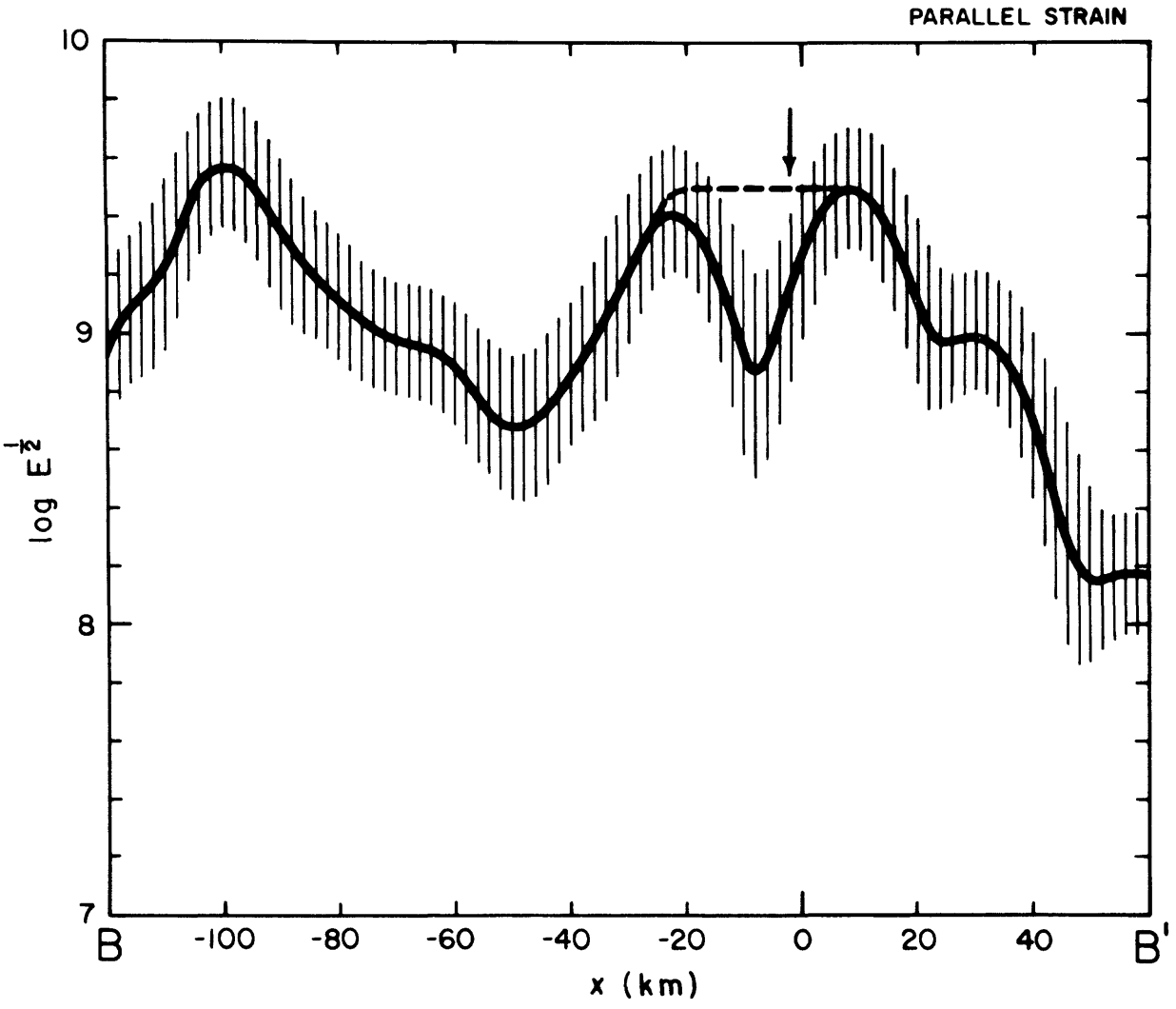

Figure 6. The square-root of the coseismic strain energy release (proportional to strain) is plotted as a function of position along the San Andreas fault zone (cross-section B-B' in Figure 1). The strain energy is normalized to ergs per year per $1500\,km^3$. The shaded region is the 95 percent confidence level and the arrow indicates the position of the Coalinga mainshock. The dashed line indicates the strain energy release due to the Coalinga mainshock.

Source Parameters of the Coalinga, California Earthquake of May 2, 1983 Inferred from Broadband Body Waves

by

George L. Choy

U. S. Geological Survey
Box 25046, MS 967
Denver Federal Center
Denver, CO 80225

ABSTRACT

Source characteristics of the Coalinga earthquake of May 2, 1983 (m_b 6.2, M_S 6.5) have been determined from analysis of teleseismic data that were digitally recorded by the Global Digital Seismograph Network. Broadband displacement and velocity records of P waves have sufficient frequency content to determine that the mainshock was a complex rupture consisting of two events that occurred about 3.2 seconds apart. By fitting the broadband pulse shapes with synthetics, we find that the first event had a depth of 9.5 km and a predominantly thrust focal mechanism with strike 300°, dip 65° and rake 85°. The hypocenter of the second event has a depth of 5.6 km. Its fault plane solution with strike 300°, dip 80° and rake 80° is similar to the solution of the first event. The moments of the first and second events are 1.9×10^{25} and 0.8×10^{25} dyne-cm, respectively. By inverting P-wave arrival time differences at each station, we find the second hypocenter is located on a separate en echelon fault southwest of the first hypocenter. The surface projections of these faults bracket a substantial portion of the aftershock zone. From an inversion of P-wave pulse durations, the rupture geometries of each event could be estimated. The rupture geometries are nearly circular with a radius of about 6.0 km for the first event and 4.7 km for the second event. Assuming a circular rupture geometry, the static stress drop of the first event is about 34 bars. The static stress drop of the second event is about 19 bars. An estimate of the dynamic stress drop could be obtained only for the first event because of the waveform complexity. A lower bound for this parameter is 24 bars or 31 bars depending on whether the steep or shallow dipping nodal plane is chosen as the fault plane. Inverting the energy flux in the velocity waveforms, we find the energy radiated by earthquake is 1.6×10^{21} dyne-cm. This implies an average apparent stress of 18 bars.

The complexity of the mainshock and of the aftershock sequence indicate that strain could have accumulated on a system of strongly interdependent faults. As the region became critically loaded, the effect of a major rupture was to critically stress faults adjacent to the initial nucleation. The ensuing stress release reflects the complexity of the fault system, occurring in a rapid mode (the second event of the mainshock) and in a slow mode (the aftershock sequence).

INTRODUCTION

The use of theoretical seismograms to model teleseismically recorded body waves has significantly enhanced the ability of seismologists to describe the dynamics of the rupture process in earthquakes. Recent papers (e.g., Choy and Boatwright, 1981; Choy et al., 1983) have demonstrated that broad bandwidth data, data with spectral information from several Hz to tens of seconds, can provide greater resolution of the rupture process. These papers demonstrated that variations in pulse shape about the focal sphere could be readily quantified and related to dynamic and static properties of the source, including estimates of associated stress drops and the rupture geometry. The variations in pulse shape were relatively easy to quantify for the earthquakes studied in these papers, however, because the direct phases of the events were well-separated from depth phases. Unfortunately, body waves generated by shallow earthquakes generally are not well-separated. In the P-waves from such earthquakes, the direct phase, surface-reflected phases and phases arising from a complex source all may interfere with one another. The purpose of this paper is to demonstrate that even for a shallow earthquake, broadband data can be used to great advantage in interpreting the dynamics of the rupture process.

As an example of such an analysis, this paper describes the modelling of broadband body waves from the Coalinga earthquake of May 2, 1983 (OT 23h 42m 37.85s; m_b 6.2; M_S 6.5). The teleseismically inferred source parameters are derived entirely from properties of the body waves. The resulting rupture history provides an independent complement to aftershock and strong motion data for understanding the earthquake.

DATA PROCESSING

To study the rupture complexity of teleseismically recorded earthquakes it is necessary to have phase and amplitude information about and above the

corner frequency. For moderate-sized earthquakes (i.e., events with $5.5 \leq m_b \leq 6.5$), the frequency band of interest ranges from 0.1 to 5 Hz. Although such broadband data are not yet routinely recorded by any global network, they can be obtained by data processing techniques in which seismograms from bandlimited instruments at a single station are combined to give a record with overall broadband response. Because of the difficulty in preserving accurately information at intermediate and high frequencies by hand-digitization of analog records, we use data from the Global Digital Seismograph Network (GDSN). The high quality and digital format of the data recorded by the GDSN permits the easy and accurate retrieval of original broadband ground displacements and velocities by the recombination of long- and short-period seismograms. A method for doing this with GDSN data is described by Harvey and Choy (1982). A comparison of typical broadband data with conventional bandlimited data is shown in Figure 2. At the top, the broadband displacement from station COL (solid line) is superimposed on the original long-period record (dashed line). Compared to the displacement pulse, the long-period record is significantly spread out in time and the waveform is devoid of high frequency details. The bottom part of Figure 2 compares the original short-period record with the broadband velocity record. Short-period instruments often emphasize energy in a narrow bandwidth near 1 Hz, producing a ringing appearance in seismograms so that arrivals from a complex source or from depth phases are very difficult to discern. The velocity records are generally better than the displacement records for identifying the onsets of arrivals. All the broadband P-waves in this report have flat response to displacement or velocity between 0.02-5 Hz.

Our analysis of the Coalinga earthquake will emphasize the simultaneous use of broadband displacement and velocity to quantify source parameters. The distribution of GDSN stations which provided usable broadband records with

respect to the epicenter of the Coalinga earthquake is shown in Figure 1. The P-wave data for the mainshock (Figures 3a-3h) are shown in three ways. The top trace shows the original short-period recording. The next trace shows the broadband ground displacement. The bottom trace shows the corresponding broadband ground velocity.

COMPUTATION OF BODY WAVE SYNTHETICS

The basic procedure in inverting for details of the rupture is to compare observed records of displacement with synthetics generated by a source model. The comparison is repeated until by trial and error the best possible fit to the suite of waveforms about the focal sphere is obtained. Observed body waves from a complex source are synthesized by the summation of simple sources. For a single shallow source, the far-field P-wave may be written as the sum of the direct P-wave and the depth phases,

$$u(\underline{x},t) = \frac{g_p(\Delta,t) * \Omega_p(\underline{x},t)}{R(\vartheta_p,\varphi_p)} + \frac{g_{pP}(\Delta,t-t_{pP}) * \Omega_{pP}(\underline{x},t)}{R(\vartheta_{pP},\varphi_{pP})} + \frac{g_{sP}(\Delta,t-t_{sP}) * \Omega_{sP}(\underline{x},t)}{R(\vartheta_{sP},\varphi_{sP})} \quad (1)$$

Here, $g_p(\Delta,t)$ is the propagation operator for a point source for a distance Δ for the direct P wave. $\Omega_p(\underline{x},t)$ is the undistorted body wave pulse shape radiated by the source toward a receiver at $\underline{x}$. $R(\vartheta_p,\varphi_p)$ is the radiation pattern coefficient for the body wave with takeoff angle ϑ_p relative to the fault normal and azimuth φ_p relative to the slip direction. Similarly, g_{pP}, g_{sP} and Ω_{pP} and Ω_{sP} are the propagation and source operators for pP and sP; t_{pP} and t_{sP} are the delays of the depth phases. Note that eq. 1 implies that the direct and surface-reflected pulses are expected to be sufficient to describe the rays radiated by the source to receiver. The variety of crustal models that have been proposed for the Coalinga region (e.g., Wentworth et al., 1983; Walter and Mooney, 1983; Fielding et al., 1983; Eaton et al., 1983; and Sherburne et al., 1983). indicates that the

refractors that are present are either weak and/or inconsistent. Although most of these papers use flat-layers to present their crustal models, the velocity-depth functions for Coalinga can be represented equally well by velocity gradients. This can be seen in the detailed model of Fielding et al. (1983) which used high-angle reflections from a COCORP signal source. The COCORP data indicate that the crust can consist of fine laminations, too small to be resolved by refraction data, rather than thick layers with homogenous velocities. While the discretization of velocity gradients into layers is justified and useful for simplifying the inversion of travel-time data, it may be less appropriate for modelling waveforms. For teleseismic body waves propagating through the gradient at relatively steep angles of incidence, no significant secondary arrivals would be generated.

For body waves between approximately $30°<\Delta<90°$, the effects of propagation consist primarily of geometrical spreading and attenuation. Our propagation operator is computed using the full wave method (Richards, 1973; Choy, 1977; and Cormier and Richards, 1977). For earth structure, the JB earth model is used except near the source. Near the source we use the velocity profile at the intersection of lines 1 and 3 in the COCORP study of Fielding et al. (1983). The COCORP model, derived from high-angle reflection data, is probably more applicable to modelling teleseismic waveforms than models derived from refraction data. The attenuation operator we use has a t^* of about 0.8 secs.

The crustal response at the receiver can be easily calculated using the matrix method of Haskell (1962), but it is not necessary in our analysis. At teleseismic distances (>30°), the angles of incidence are very steep. For most commonly used earth models (where there are no high-impedance velocity contrasts other than the crust-mantle interface), crustal reverberations on the vertical component seismograms are unimportant. Models with intracrustal

low-velocity layers that have been suggested for some pathogenic stations (Rial and Brown, 1984) predict a significant arrival about 15 seconds after the first P-arrival. This late arrival may have to be considered in long-period and moment-tensor inversions because, owing to the phase response of typical long-period seismographs, rather long time windows must be processed even for a simple impulse response. The broadband body waves of the Coalinga earthquake, however, have a typical duration of about 12 seconds (see Figures 2 and 3a-h).

The source pulse is a triangular function. We do not constrain the depth phases to have the same time function as the direct body wave because, in general, for any given station P, pP and sP have different takeoff angles with respect to the fault plane. Any significant variation in the pulse durations can be used to constrain the source geometry (Boatwright, 1984).

For a complex earthquake, the synthetics are obtained by summing a number of simple sources, lagged in time to account for the different travel times of spatially separated foci. Although this strategy is similar to that described by other analyses of earthquakes (e.g., Langston and Helmberger, 1975; Rial, 1978), we emphasize one major difference with previous studies. Our primary emphasis is on the synthesis of broadband displacements rather than long-period records.

DATA ANALYSIS

Seismogram synthesis

We begin by modelling the broadband waveforms with a single source. If the best synthetic waveforms still disagree systematically with the data, waveforms from additional events are superimposed on the data until it is clear that the fit between observed and synthetic records can no longer be improved. For the Coalinga earthquake, it turns out that two rupture events are required to satisfy

the complexity in the observed waveforms. The focal mechanism of the first event is shown in Figure 4 by the solid lines. The nodal planes for the second event are shown by dashed lines. Distributed about the focal sphere are the velocity waveforms from stations used to derive the rupture histories. To illustrate the procedure used to model the earthquake, we detail the construction of the synthetic for the displacement at COL. The same procedure is followed for the construction of the synthetic displacements for the other stations.

The first step is to model the observed displacement with the best-fitting single source using a focal mechanism consistent with observed P-wave first motions. As is evident in Figure 5a, the first-motion data are sufficient to clearly define one nodal plane. The resolution of the rake requires additional information which can be provided by seismogram synthesis of the observed interference pattern of P, pP and sP at the GDSN stations. The synthesis requires some knowledge of the depth of the event and the time function of each body wave. We enumerate these constraints for the COL displacement pulse. The analysis is similar for the data at the other stations. The first positive pulse of the COL displacement (Figure 3a) is interpreted as the direct P-wave from the first event. This pulse corresponds to the first cycle in the velocity record. Because the velocity pulse is nearly complete, the triangular function approximating the P-wave is well constrained. Before the P-wave velocity pulse completely returns to the zero baseline, it is reversed by a sharp negative pulse (indicated by the line in Fig. 3a). This sharp pulse can be seen about 4.0-4.2 secs behind the initial P-arrival across the entire suite of velocity records except possibly at HON and AFI where the microseism levels are rather high. Identifying this arrival as pP yields a depth of 9.5±0.6 km. The corresponding sP phase should arrive 5.8 secs after the P-wave. Although we expect this phase to

be masked by the pP waveform, some energy can be seen on the velocity records at the appropriate time at several stations (COL, KEV, SCP, MAJO and AFI). At this point we have the following information. Knowing depth, we know the arrival time of sP as well as pP; knowing the strike, dip and to a lesser extent the rake of the focal mechanism, we know fairly well the relative amplitudes of the body waves; and we know the time function of P very well. In order to proceed with the modelling, we impose an a priori constraint on the duration of the pP and sP displacement pulses: their durations must be less than or roughly equal to the duration of the P-wave. This constraint corresponds to the physical condition that the direction of rupture is upward rather than downward. Note that the depth of the mainshock is near the bottom of the zone defined by the aftershocks located by Eaton et al. (1983)

The best fit to the displacements that can be obtained using a single rupture event has a focal mechanism with strike 300°, dip 65° and rake 85°. The uncertainties in strike and dip are constrained to better than ±5° by the relative amplitudes and polarities of the P and pP waveforms with takeoff angles in the proximity of the steeply dipping nodal plane. The uncertainty in rake is ±10°. Rake is constrained by the amplitudes and polarities of the sP phases, which have takeoff angles near a nodal line of the SV radiation pattern (Figure 5b). The rake is also constrained by the first motions of the digitally recorded long-period SH body waves. The moments and time functions derived from the body waves for each station are listed in Table 1. The average weighted moment for the source is 1.9×10^{25} dyne-cm. Before we describe the extent to which we can derive other source parameters such as stress drop and rupture geometry, we must complete the analysis of the waveforms.

A typical fit using the single rupture event model is shown in Figure 6 (top) for station COL. The first cycle of displacement, consisting predominantly of P

and pP, is fit rather well. However, there is a large discrepancy in the match of the last (positive) backswing of the synthetic and observed waveforms, which is dominated by the sP contribution. The peak in the last backswing of the synthetic arrives earlier than the corresponding peak of the actual record. The total duration of the synthetic displacement is also much shorter than that of the observed waveform. As previously discussed, neither receiver structure nor source structure is likely to account for such a discrepancy. That this feature of the waveform is associated with the rupture process is further corroborated by an examination of body waves from the largest aftershock that followed the Coalinga earthquake (July 22, 1983 0T 02 39 53.7; m_b 6.0). Its location is very well constrained by data from the northern California network to be within a few kilometers of the the mainshock (Eaton et al., 1983). In contrast to the mainshock, we find that the two displacement waveforms available for this event could be easily modeled using a single source (Figure 7a) having a focal mechanism that agrees with the P-wave first motion data from local and teleseismic data (Eaton et al., 1983; R. Needham, written commun., 1984). One of the stations, KEV, recorded both the mainshock and the aftershock. The P-waves of these two earthquakes would have traversed nearly identical propagation paths to that station. Thus, the large difference in the P-waves generated by the two earthquakes arises from properties of the rupture processes. We also note that long-period waveform inversions require significant complexity in the source. Sipkin and Needham (1984) found a 28% non-double couple component in the moment tensor while Dziewonski and Woodhouse (pers. commun., 1984) found a 40% non-double couple component.

In describing how the second rupture event is modelled, it is useful to refer again to Figure 6. The synthetic seismogram at the top is the waveform predicted by the best-fitting single rupture event. We cannot merely double the

duration of the synthetic sP just to match the duration of the observed wavetrain. As we noted previously, a sP duration that is twice that of the P duration implies a rupture that proceeds in the unlikely direction downdip. Furthermore, in order to conserve moment, stretching the duration would require halving the amplitude of the displacement pulse. The resulting synthetic fits the data very poorly. Instead, we strip the synthetic displacement from the observed record. Then we proceed to fit a second rupture event to the remainder of the waveform. The synthetic waveform that best fits the data at COL is shown in the middle of Figure 6. The sum of the synthetics from the two rupture events is our final synthetic (Figure 6, bottom). The strike, dip and rake of the second event are 300°, 80° and 80°, respectively. The depth of nucleation is 5.6 km. The moments, time functions and delay times with respect to the initial P-arrival at each station for the second event are given in Table 1. The average weighted moment of the second event is 0.8×10^{25} dyne-cm.

Although the uniqueness of the parameters describing the second event is not easy to quantify, one measure is the difficulty in finding other solutions that match the waveform. This is illustrated in Figure 8, which compares the best-fitting waveform for COL with synthetics computed using slight perturbations in the source parameters of the second event. The perturbations are for a change in depth of 1 km; a change in delay time relative to the first event of 0.5 sec; and a change in strike of 15°. The sensitivity of the synthetics to these perturbations is very evident. Note that the final solution must satisfy the suite of waveforms distributed about the focal sphere (Figure 4) with takeoff angles and azimuths that straddle both sides of a P-nodal plane and an SV-nodal line. Based on synthetics computed for perturbations of our solution, we estimate our uncertainties in depth as ±0.8 km; in strike and dip as ±5°; in rake as ±15°; and in delay time as ±0.3 sec.

The location of the hypocenter of the second event relative to the hypocenter of the first event can be computed by inverting the P-wave arrival-time differences at each station. Typical techniques for doing this are discussed in Spence (1980). The location and axes of the error ellipse are shown in Figure 9. Its hypocenter is significantly to the southwest of the first event. Our analysis has also shown that the second hypocenter had a more shallow depth. The second event occurred 3.2 seconds after the first event. (Note that the P-wave delays in Table 1 are between 3.5 and 4.2 seconds. The variation is due both to the azimuth of a particular station and the difference in depth between the events.) The extent of the vertical and lateral separation in hypocenters indicates that the events occurred on separate fault planes, regardless of whether rupture occurred on the steep or shallow set of nodal planes. In the next section, the computation of some source parameters (viz., dynamic stress drop and rupture geometry) requires that a fault plane be chosen. Where this is necessary, the parameters are computed for both possibilities.

CHARACTERISTICS OF THE RUPTURE PROCESS

Associated stresses and radiated energy

Assuming an event grows as a self-similar crack, the dynamic stress drop can be measured from the initial slope of the velocity waveforms using the relation given by Boatwright (1980)

$$\tau_e = \frac{[\rho(\xi_0)\,\rho(x)\,c(x)]^{\frac{1}{2}}\,c(\xi_0)^{\frac{5}{2}}}{C(\frac{v}{\beta})\,v^2\,\beta(\xi_0)} \left[\frac{R(\xi_0,x)}{F(\vartheta,\varphi)}\right] (1-\zeta^2)^2 \left[\frac{\dot{u}(x,t)}{t}\right] \qquad (2)$$

where ρ and c are density and wave velocity at coordinates ξ_0 and x, the source and receiver coordinates, respectively; $C(v/\beta)$ is the Kostrov function; v is the rupture velocity; β is the shear-wave velocity; and $\zeta = v \sin\vartheta / c(\xi_0)$ where ϑ is the takeoff angle relative to the fault normal. $R(\xi_0,x)$ is the ray-theory coefficient

describing the geometrical spreading between source and receiver, including appropriate free-surface corrections. F is the radiation pattern coefficient for the body wave with takeoff angle ϑ relative to the fault normal and azimuth φ relative to the slip direction. The last term in brackets is the average initial slope after correcting for attenuation. Because of the complexity of the rupture, only the slope of the P-wave of the first event can be measured. No estimate can be made of the dynamic stress drop of the second event. Using the direct P-waves, we obtain a dynamic stress drop of 24±16 bars or 31±16 bars depending on whether the steep or shallow dipping nodal plane is chosen as the fault plane, respectively. However, because the takeoff angles of the direct P-waves sample only a small solid angle of the focal sphere in a downdip direction, these values of dynamic stress drop should be considered as lower limits. The effect of sampling a rupture in the direction away from the direction of rupture is to bias the estimate of stress drop to a smaller value.

Where the velocity pulses of P, pP and sP are not well separated, the expression relating radiated energy to the energy flux of the P-wave group is given by Boatwright and Choy (1984) as

$$E_s = \frac{8\pi}{5}(1+q)\left(\frac{R^P}{F^{gP}}\right) I^* \qquad (3)$$

where I^* is the integral of the velocity squared of the P-wave group, corrected for attenuation. R^P is the P-wave geometrical spreading factor. The factor q is the ratio of S-wave energy to P-wave energy. From Boatwright and Fletcher (1984), q is taken to be 13.5. F^{gP} is the generalized radiation pattern term defined as

$$F^{gP} = (F^P)^2 + (F^{pP})^2 + \frac{2q}{3}\left(\frac{\alpha}{\beta}\right)(F^{sP})^2 \qquad (4)$$

where F^i are the radiation pattern coefficients, corrected for free-surface reflection if necessary, for i=P, pP and sP. For dip-slip motion on a 65° dipping fault plane, F^{gP} varies only weakly with variations in the mechanism. The energy

radiated by the earthquake is $1.6\pm0.3\times10^{21}$ dyne-cm.

The apparent stress can be computed using $\tau_a=\mu E_s/M_0$ (Wyss and Brune, 1968), where μ is the average rigidity at the hypocenter. The average apparent stress for the earthquake computed from the total radiated energy and the total moment is 18 bars.

Rupture geometry

Displacement pulses about the focal sphere can be used to invert for the rupture geometry of each event. If the fault plane and rupture direction for each event are known, we can employ a simplification of the method used by Boatwright (1984). The rise time (or the rupture phase of Boatwright's (1981) rupture model) is first corrected for attenuation. We then minimize the χ^2 error

$$\chi^2 = \sum_{i=1}^{N} \frac{[\tau_i-(1-e)\tau_c(\frac{a}{v}) -e\tau_u (\frac{a}{v},\varphi_r)]^2}{\sigma_i^2} \qquad (5)$$

where τ_i and σ_i are the durations of the rupture phase and its standard deviation measured from N body wave arrivals, e is the per cent unilateral rupture, $\tau_c(\frac{a}{v})$ is the pulse duration expected from a circular rupture of radius a and rupture velocity v and $\tau_u(\frac{a}{v},\varphi_r)$ is the pulse duration expected from a unilateral rupture of length a in the direction φ_r. Formulae for τ_c and τ_u are derived in the appendix of Boatwright (1984). We assume a rupture velocity of 0.75β. For a particular rupture direction, the best-fitting rupture length and per cent unilateral rupture can be computed from eq. 5. The rupture half-width is estimated from the rupture length and percent unilateral rupture as

$$w = \frac{a[1 + (1-e^2)^{\frac{1}{2}}]}{2(1+e)} \qquad (6)$$

The static stress drop is then estimated as

$$\Delta\sigma = \frac{(1+e)}{2aw^2} M_0 \qquad (6)$$

Any directivity in the waveforms that may have enabled us to favor one nodal plane over another as the fault plane for either event is masked by the interference of waveforms. Thus, we estimate the source dimensions by carrying out the the inversion for both the steep and shallow dipping nodal planes of the mechanism for each event. We also do not know a priori the direction of rupture. However, the mainshock is located in the midst of the aftershocks laterally, but deeper than most of the aftershocks (Eaton et al., 1983). For each possible fault plane we compute the best-fitting source geometries for a suite of directions ±60° from the updip direction.

For the first event, it turns out that the rupture geometry is independent of the choice of fault plane and the direction of rupture. The best-fitting rupture geometries for either plane for directions ±60° about the updip direction are all approximately circular with rupture radius of 6.0±2.0 km. The corresponding static stress drop assuming either nodal pane as the fault plane is 34 bars. Seismic slip can be estimated as 52 cm from $d=M_0/\mu A$, where μ is the rigidity (3.2×10^{11} dyne-cm) and A is the rupture area.

The inversion for the rupture geometry of the second event is significantly less certain than for the first event because the durations of the P-waves are inferred and not directly measured. We can only obtain an idea, albeit crude, of the rupture length by making an arbitrary assumption about the rupture geometry. Assuming, for instance, that the geometry is circular, we obtain a radius of 4.7±2.0 km, a static stress drop of 19 bars and slip of 36 cm. As with the first event, the source radius is basically unchanged whether the steep or shallow dipping nodal plane is used as the fault plane. As no surface faulting was found for the mainshock (Clark et al. 1983), the source radius is probably smaller. Note the uncertainty in fault length is about 40%. The source radius can also be reduced if a smaller rupture velocity is assumed. This is possible for

secondary or triggered events which may release stress less coherently than the initial event.

In plan view the aftershock zone from Eaton et al. (1983) covers a complex and broad zone (Figure 9). In this figure the fault lengths of the two events are drawn using the strikes of the steep nodal planes of the focal mechanisms and projecting them to the surface. (For the shallow dipping planes, the trace of the first event would be nearly the same as shown in Figure 9; the strike of the second event would be rotated clockwise 35° with respect the strike of the steep plane.) For the first event, we use the location determined by Eaton et al. (1933) for the mainshock. Although the location of the second event has some uncertainty, Figure 9 shows that the en echelon fault traces bracket a subtantial portion of the aftershock area. Figure 10 shows this is true whether one chooses as the fault planes for each event the set of steep dipping nodal planes, the set of shallow-dipping nodal planes or one shallow-dipping and one steep-dipping plane. Figure 10 shows the aftershock activity of the northern region in a vertical cross-section as obtained by Eaton et al. (1983). Drawn on this figure are traces representing the steep and shallow nodal planes for each event. These traces are slightly distorted because the cross-section (line NT-NT' in Figure 9) is not exactly perpendicular to the strike of the focal mechanism solutions of the two events. If the azimuth of the cross-section were perpendicular to the strike of the first event, then most of the seismicity would be bounded by the shallow plane of the first event and the steep plane of the second event.

Although we cannot from the waveform data choose one configuration of fault planes over another, we note that the choice of a shallow fault plane for the first event is somewhat favored by aftershock studies (Eaton et al., 1983; Eberhart-Phillips and Reasenberg, 1983) which show the predominant clustering of the earlier and larger aftershocks on a shallow southwest dipping surface. A

choice of the steep-dipping nodal plane for the fault plane of the second event would indicate conjugate faulting. Such an explanation has been suggested, for instance, by Wetmiller et al. (1984) for the New Brunswick earthquake of January 9, 1982 and its aftershocks. The existence of steeply dipping faults in the epicentral region is known from reflection data (e.g., Wentworth et al., 1983; Fielding et al., 1983). This configuration of fault planes is also consistent with the geological arguments of Fuller and Real (1983) for a steeply dipping fault plane.

DISCUSSION

The Coalinga earthquake occurred in a portion of the Californian Coast Ranges characterized by a variety of geological structures including numerous folds that are punctuated by several high-angle reverse faults (e.g., Wentworth et al., 1983; Fielding et al., 1983). The complexity of the mainshock and the aftershock sequence may reflect this geological complexity. The process of strain accumulation in the region could have occurred in such a way as to critically load the entire region. That is, in the presence of a system of faults of nearly equal strength, strain accumulates on all faults. The state of stress on each fault segment becomes dependent on the state of stress of adjacent faults. The effect of a major rupture on any fault may result in the rupture of any critically stressed adjacent faults. If this interpretation is applied to our source model of the mainshock, it implies that the first rupture event activated the second fault. The subsequent aftershock activity represents a slower response to the stress release.

The complexity of the rupture history explains many of the characteristics of the aftershock distribution, despite the uncertainty in the choice of fault planes. There is, as expected, a concentration of activity in the vicinity of the fault plane of the first event. There is also a concentration of events at the

southeastern end of the second fault. These events define a diffuse lineation with the same strike as the second event. The fault plane solution of a large aftershock in this region (event F of Eaton et al., 1983) has high-angle reverse faulting similar to the second event. It is possible that the second event of the mainshock and these aftershocks lie on the same fault plane.

The epicenters of several moderate-sized aftershocks ($5.4<m_b<6.0$) that occurred on June 11, July 9, 22 and 25, 1983 (indicated by solid circles in Figure 9), are located within a couple of kilometers of the northern end of the second event of the mainshock. Hart et al. (1983) found surface faulting associated with some of these aftershocks. Rymer et al. (1984) have inferred from the surface faulting and observed displacements that these events could be related to steep east-dipping reverse faults that could be associated with the Nunez fault. However, fault plane solutions of these events from Eaton et al. (1983) have different strikes and dips than the mechanism of the second event. Thus, the second event is probably not associated with the Nunez fault. However, the proximity of the Nunez fault to the rupture plane of the second event suggests that the Nunez fault could have been critically loaded by the occurrence of the second event.

Our source model might also explain why damage was so severe in the town of Coalinga (about 10 km southwest of the epicenter) but relatively light near the epicenter. The hatched area of Figure 9 represents the boundary of Coalinga. It is obvious that the fault trace of the second rupture event falls much closer to the town of Coalinga than does any part of the first fault. We also note that accelerograms at the Pleasant Valley Pumping Plant, which had the nearest accelerographs, exhibit complexity. These records were processed by Maley et al. (1983). On both the corrected acceleration and velocity records from the 45° horizontal component (Figure 3c of Maley et al.), two relatively

distinct arrivals can be identified. The time separation of the two arrivals, slightly less than four seconds, is about what we would expect from our two-event rupture model. Note that the peak acceleration identified by Maley et al. is associated with the second event of the mainshock.

CONCLUSIONS

Very often, as was the case with the Coalinga earthquake, both the mainshock and the ensuing aftershock sequence are complex. A detailed rupture history of the main shock is critical to understanding the mechanics of rupture and the tectonic activity of a region. Given high quality digital data with broadband content, we have shown that body waves can be used to obtain details of the rupture process of moderate-sized shallow earthquakes. Except for the choice of fault plane, these details have been derived entirely from characteristics of the waveforms. They provide an independent but complementary source of information from which to obtain an overall picture of the earthquake process. A summary of the source parameters we have obtained for the Coalinga earthquake is in Table 2.

The description of the Coalinga earthquake has important implications for estimating seismic hazards in California. We have found that the Coalinga mainshock consisted of two events. The second event had roughly one-half the moment of the first event and was located to the southwest of the first event. The complexity of the rupture suggests that strain may accumulate on many faults in a geologically complex region. Once critically loaded, the state of stress on each fault becomes dependent on the state of stress of adjacent faults. The effect of a major rupture would result in the rupture of any critically stressed adjacent faults. There is the possibility that damage can arise from faults other than the one which initially failed.

ACKNOWLEDGMENTS

The author expresses his gratitude to Jack Boatwright for rousing and beneficial discussions. The author benefited from critical reviews by Stuart Sipkin and Stephen Hartzell. Madeleine Zirbes provided valuable help in the data processing.

Table 1. The time functions of P, pP, and sP at each station for each event of the mainshock in seconds. The first number is the rise time of the triangular function. The number in parentheses is the total duration. Also given is the moment computed from each body wave. For event 2, the delay time of the P̄-wave with respect to the first P-wave is also given.

Event 1

	Time Function			Moment
	P	pP	sP	(10^{25}dyne·cm)
COL	1.6(3.6)	1.8(3.6)	1.8(3.6)	1.6
KEV	1.6(3.8)	1.9(3.8)	1.9(3.8)	1.9
ANTO	1.8(3.8)	1.9(3.8)	1.9(3.8)	1.1
SCP	2.0(4.5)	2.5(4.5)	2.5(4.5)	0.8
ZOBO	3.0(4.5)	3.0(4.0)	3.0(4.0)	1.6
HON	1.2(3.7)	1.8(3.7)	1.8(3.7)	1.8
AFI	2.1(4.2)	2.1(4.2)	2.1(4.2)	2.4
MAJO	2.0(4.3)	2.0(4.3)	2.0(4.3)	2.3

Event 2

	Time Function			Moment	Delay Time
	P	pP	sP	(10^{25}dyne·cm)	(secs)
COL	1.7(3.4)	1.7(3.4)	1.7(3.4)	0.8	4.2
KEV	2.0(2.2)	2.0(4.0)	2.3(4.0)	4.0	4.1
ANTO	2.0(4.0)	2.0(4.0)	2.0(4.0)	0.5	4.2
SCP	2.5(5.0)	2.5(5.0)	2.5(5.0)	2.0	4.0
ZOBO	2.0(4.0)	2.0(4.0)	2.0(4.0)	0.6	4.0
HON	1.5(3.0)	1.5(3.0)	1.5(3.0)	0.6	3.5
AFI	2.0(4.0)	2.0(4.0)	2.0(4.0)	1.1	3.6
MAJO	1.8(3.6)	1.8(3.6)	1.8(3.6)	0.9	3.6

Table 2. A summary of the rupture characterisitics inferred from the broad-band analysis of the Coalinga earthquake of May 2, 1983. For dynamic stress drop and rupture radius, a rupture velocity of .75β was used.

Parameter	Event 1	Event 2
Depth	9.5 ± 0.6 km	5.5 ± 0.8 km
Strike	300° ± 5°	300° ± 5°
Dip	65° ± 5°	80° ± 5°
Rake	85° ± 10°	80° ± 15°
Rupture radius	6.0 ± 2.0 km	4.7 ± 2.0 km
Moment ($\times 10^{25}$dyne·cm)	1.9 ± 0.3	0.8 ± 0.4
Dynamic stress drop		
steep plane	24 ± 16 bars	-
shallow plane	31 ± 16 bars	-
Static stress drop	34 ± 18 bars	19 ± 10
Seismic slip	52 ± 40 cm	36 ± 36 cm
Total Moment	2.7 ± 0.7 $\times 10^{25}$dyne·cm)	
Radiated energy	1.6±0.3$\times 10^{21}$dyne·cm	
Apparent stress	18 bars	

REFERENCES

Boatwright, J., 1981, Quasi-dynamic models of simple earthquakes: an application to an aftershock of the 1975 Oroville, California earthquake: Bull. Seism. Soc. Am., v. 71, p. 1-27.

Boatwright, J., 1984, The effect of rupture complexity on estimates of source size: J. Geophys. Res., v. 89, p. 1132-1146.

Boatwright, J. and Choy, G. L., 1984, Teleseismic estimates of the energy radiated by shallow earthquakes: in preparation.

Boatwright, J., and J. B. Fletcher, 1984, The partition of radiated energy between P-waves and S-waves: J. Geophys. Res., in press.

Choy, G. L., 1977, Theoretical seismograms of core phases calculated by a frequency dependent full wave theory, and their interpretation: Geophys. J., v. 51, p. 275-312.

Choy, G. L. and Boatwright, J., 1981, The rupture characteristics of two deep earthquakes inferred from broadband GDSN data: Bull. Seism. Soc. Am., v. 71, p. 691-711.

Choy, G. L., Boatwright, J., Dewey, J. W. and Sipkin, S. A., 1983, A teleseismic analysis of the New Brunswick earthquake of January 9, 1982: J. Geophys. Res., v. 88, p. 2199-2212.

Clark, M., Harms, K., Lienkaemper, J., Perkins, J., Rymer, M. and Sharp, R., 1983, The search for surface faulting: in Coalinga earthquake sequence commencing May 2, 1983, U. S. Geological Survey Open-file Report 83-511, p. 8-11.

Cormier, V. F. and Richards, P. G., 1977, Full wave theory applied to a discontinuous velocity increase: J. Geophys., v. 43, p. 3-31.

Cormier, V. F., 1982, The effect of attenuation on seismic body waves: Bull. Seism. Soc. Am., v. 72, p. S169-S200.

Der, Z. A., McElfresch, T. W. and O'Donnell, A., 1982, An investigation of the regional variations and frequency dependence of anelastic attenuation in the United States in the 0.5-4 Hz band: Geophys. J., v. 69, p. 67-100.

Eaton, J., Cockeram, R., and Lester, F., 1983, Study of the May 2, 1983 Coalinga earthquake and its aftershocks, based on the USGS seismic network in Northern California: in the 1983 Coalinga, California earthquakes, California Div. of Mines and Geol. Special Publication 66, p. 261-273.

Eberhart-Phillips, D. and Reasenberg, P., 1984, Hypocenter locations and constrained fault-plane solutions for Coalinga aftershocks, May 2-24, 1983: this volume.

Fielding, E., Barazangi, M., Brown, L., Oliver, J. and Kaufman, S., 1983, COCORP seismic reflection profiles near the 1983 Coalinga earthquake sequence: Deep structures: in the 1983 Coalinga, California earthquakes, California Div. Mines and Geol. Special Publication 66, p. 137-149.

Fuller, D. R. and Real, C. R., 1983, High-angle reverse faulting, a model for the 2 May 1983 Coalinga earthquake: in the 1983 Coalinga, California earthquakes, California Div. of Mines and Geology Special Publication 66, p. 177-184.

Hart, E. W. and McJunkin, R. D., 1983, Surface faulting northwest of Coalinga, California June and July 1983: in the 1983 Coalinga, California earthquakes, California Div. Mines and Geol. Special Publication 66, p. 201-219.

Harvey, D. and Choy, G. L., 1982, Broadband deconvolution of GDSN data: Geophys. J. R. astr. Soc., v. 69, p. 659-668.

Haskell, N. A., 1962, Crustal reflection of P and SV waves: Bull. Seism. Soc. Am., v. 61, p. 4751-4767.

Langston, C. A. and Helmberger, D. V., 1975, A procedure for modelling shallow dislocation sources: Geophys. J., v. 42, p. 117-130.

Maley, R., Brady, G., Etheredge, E., Johnson, D. Mork, P. and Switzer, J., 1983,

Analog strong motion data and processed main event records: in Coalinga earthquake sequence commencing May 2, 1983, U. S. Geological Survey Open-file Report 83-511, p. 38-60.

Rial, J. A., 1978, The Caracas, Venezuela earthquake of July 1967; A multiple source event, J. Geophys. Res., 83 5405-5414.

Rial, J. A. and E. Brown, 1983, Waveform modeling of long-period P-waves from the Coalinga earthquake of May 2, 1983: in the 1983, Coalinga California earthquakes, California Div. Mines and Geol. Special Publication 66, p. 247-259.

Richards, P. G., 1973, Calculation of body waves for caustics and tunnelling in core phases, Geophys. J., 35, 1575-1588.

Rymer, M. J., Harms, K. K., Lienkaemper, J.J., and Clark, M. M., 1984, Relations of surface rupture along the Nunez fault to fault processes in the Coalinga earthquake sequence: this volume.

Sherburne, R., McNally, K., Brown, E., and Aburto, A., 1983, The mainshock-aftershock sequence of 2 May 1983: Coalinga, California: in the 1983 Coalinga, California earthquakes, California Div. Mines and Geol. Special Publication 66, p. 275-292.

Sipkin, S. A. and Needham, R. E., 1984, Kinematic source parameters of the 2 May 1983 Coalinga earthquake determined by time-dependent moment tensor inversion and an analysis of teleseismic first motions: this volume.

Spence, W., 1980, Relative epicenter determination using P-wave arrival-time differences, Bull. Seism. Soc. Am., 70, 171-183.

Walter, A. W. and Mooney, W. D., 1983, Preliminary report on the crustal velocity structure near Coalinga, California, as determined from seismic refraction survey in the region: in the 1983 Coalinga California earthquakes, California Div. Mines and Geol. Special Publication 66, p. 127-135.

Wentworth, C. M., Walter, A. W., Bartow, J. A. and Zoback, M. D., 1983, Evidence on the tectonic setting of the 1983 Coalinga earthquakes from deep reflection and refraction profiles across the southeastern end of Kettleman Hills: in the 1983 Coalinga, California earthquakes, California Div. Mines and Geol. Special Publication 66, p. 113-126.

Wetmiller, R. J., Adams, J., Anglin, F.M., Hasegawa, H.S., and Stevens, A. E., 1984, Aftershock sequences of the 1982 Miramichi, New Brunswick, earthquakes: Bull. Seism. Soc. Am., v. 74, p. 621-653.

Wyss, M. and Brune, J., 1968, Seismic moment, stress, and source dimensions for earthquakes in the California-Nevada region: J. Geophys. Res., v. 73, p. 4681-4694.

Figure 1. Stations of the Global Digital Seismograph Network that are used in this study. They are plotted on an azimuthal equi-distant projection centered on the epicenter of the Coalinga earthquake of May 2, 1983.

Figure 2. (Top) The digitally recorded long-period, vertical-component P-wave (dashed line) at station COL. The broadband displacement of the P-wave is also plotted (solid line) for comparison. The apparently later arrival of the long-period P-wave is a consequence of the strong phase delay in the long-period instrument response. The Nyquist frequency of the broadband records is 10 Hz. (Bottom) The short-period P-wave at COL (dashed line) is compared to the broadband velocity record. (Note that the time scale is different from the top part of the figure.)

Figure 3a. (Top) The original short-period record of the P-wave at COL (Δ 33.1°; Θ or azimuth 338.9°). (Middle) The broadband ground displacement. Response is flat to displacement from 0.02-5 Hz. The dashed line is the synthetic. The synthetic is derived in greater detail in Figure 6. (Bottom) The broadband ground velocity. An inflection in the displacement record is a strong pulse in velocity (indicated by the vertical line) and is interpreted as the onset of pP.

Figure 3b. The original short-period record of the P-wave at KEV (Δ 71.7°; Θ 11.4°) and its corresponding displacement and velocity records.

Figure 3c. The short-period, displacement and velocity records of the P-wave recorded at ANTO (Δ 100.3°; Θ 20.7°).

Figure 3d. The short-period, displacement and velocity records of the P-wave recorded at SCP (Δ 33.3°; Θ 69.0°).

Figure 3e. The short-period, displacement and velocity records of the P-wave recorded ZOBO (Δ 71.8; Θ 127.0).

Figure 3f. The short-period, displacement and velocity records of the P-wave

recorded at HON (Δ 36.0°; Θ 256.0).

Figure 3g. The short-period, displacement and velocity records of the P-wave recorded at AFI (Δ 69.6°; Θ 234.1°).

Figure 3h. The short-period, displacement and velocity records of the P-wave recorded at MAJO (Δ 77.3°; Θ 306.0°).

Figure 4. Focal mechanisms of the two rupture events comprising the mainshock on a lower hemisphere projection. The strike, dip and rake of the first event (solid lines) are 300°, 65° and 85°. The strike, dip and rake of the second event (dashed lines) are 300°, 80° and 80°. Distributed about the focal sphere are the velocity waveforms used in our analysis. The takeoff angles of four stations (COL, KEV, ANTO and SCP) are well-located to provide constraints on the change in dip of the steeply dipping nodal planes.

Figure 5. (a) Lower hemisphere projection with polarities of teleseismically recorded P-wave data (R. Needham, written commun.) for the Coalinga earthquake of May 2, 1983. The nodal planes of the first rupture event are also plotted on the focal sphere. First motion data are insufficient to constrain the shallow-dipping fault plane. (b) The P, SV and SH radiation patterns for the focal mechanism of the first event. Polarities are indicated by solid circles (compression) or open circles (dilatation). Both P and pP takeoff angles used in our analysis are plotted in the focal sphere for the P-radiatio pattern. Takeoff angles of sP are plotted in the SV-pattern. The polarities of the first motion SH body waves read from rotated long-period GDSN records are indicated in the SH-pattern.

Figure 6. An example of the construction of synthetic displacement records using the P-wave from COL. The observed waveform is the dashed line;

the synthetic waveforms are solid lines. (Top) The best fit for a single rupture satisfies the initial part of the waveform. It does not. however, match the last (positive) backswing. (Middle) The synthetic pulse shape of the best-fitting second event, found through forward modelling. (Bottom) The sum of the waveforms from the two rupture events compared with the actual displacement waveform.

Figure 7. Broadband P-wave displacements (solid lines) from the aftershock of July 22, 1983. The data are easily matched by synthetics (dashed lines) employing one rupture event. The focal mechanism used in the synthetics has a strike, dip and rake of 340°, 45° and 90°, respectively. The best-fitting depth is 9 km.

Figure 8. Examples of how the uncertainties of the source parameters of the second event are determined. Synthetic displacements for COL are computed using the source parameters of the first event, but perturbing the source parameters of the second event. The synthetic which best fits the data is shown by the solid line. The other synthetics are computed using the parameters of the best-fitting second event but in each case changing one parameter. The changes shown are for a change in depth of 1 km; in delay time by 0.5 sec; and in strike by 15° The sensitivity of the waveform to these changes is evident.

Figure 9. Epicenter plots of the Coalinga earthquake and aftershocks with m_b>2.5 from May 2 through July 31 (from Eaton et al., 1983). Superimposed on this plot are the fault lengths of the two events of the mainshock (heavy lines) projected to the surface. The location error ellipse of the second event is indicated by the error bars. The hatched area represents the location of the town of Coalinga. Darkened circles are epicenters of some large aftershocks associated with the Nunez

fault.

Figure 10. Seismicity plot on a vertical cross-section of data in the northern subregion of Figure 9 (modified from Eaton et al., 1983). Drawn on the figure are traces (solid lines) representing the fault lengths of the steep and shallow nodal planes for the two events. For the location of the first event, we use the location of the mainshock (A) from Eaton et al. Events E and H are relatively large aftershocks related to the Nunez fault. Note that there is some distortion because the azimuth of the cross-section (line NT-NT' of Figure 9) is not quite perpendicular to the strike of the fault planes of the mainshock.

FIGURE 1

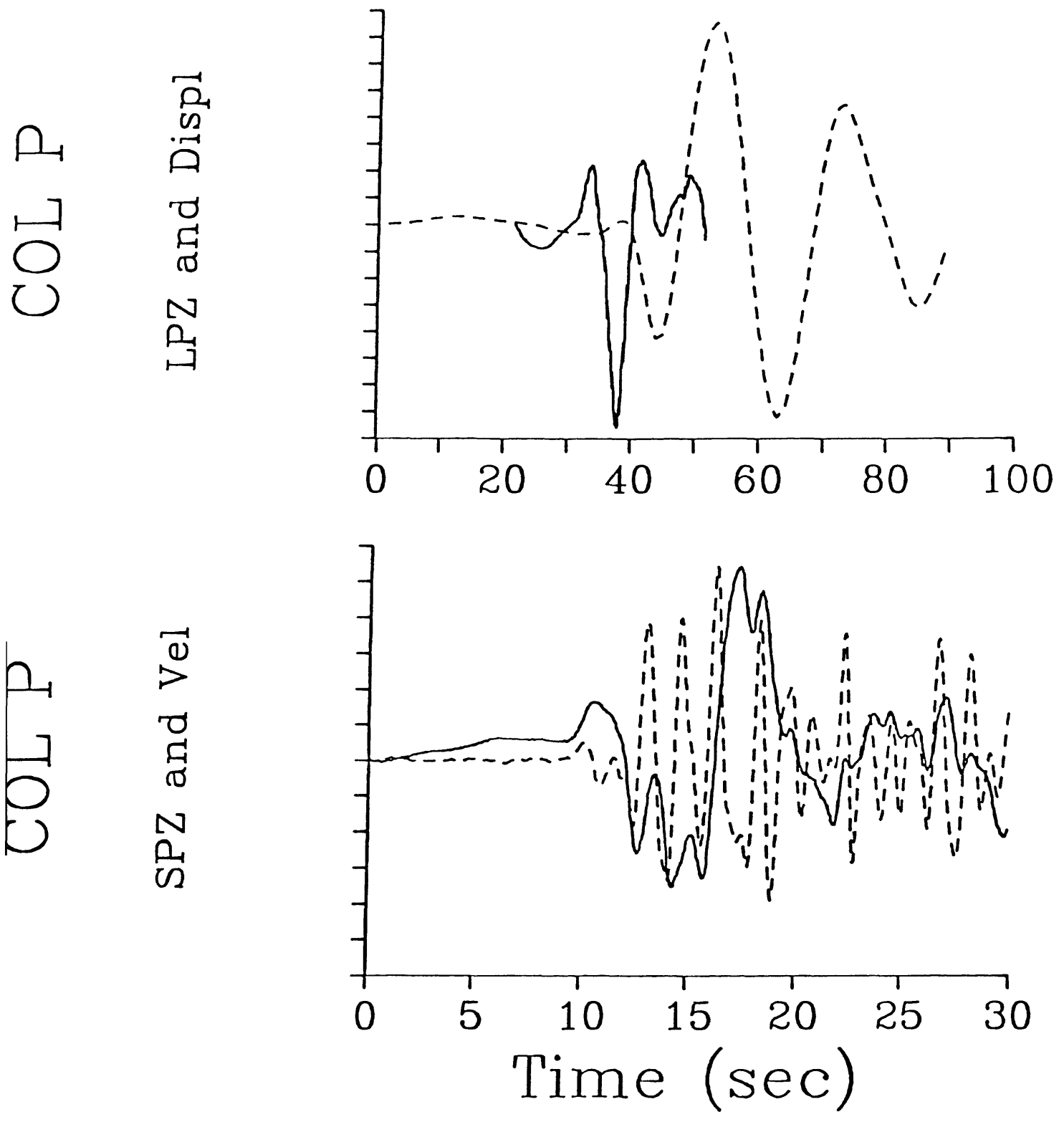
COL P
LPZ and Displ
0
20
40
60
80
100
COL P
SPZ and Vel
0
5
10
15
20
25
30
Time (sec)

FIGURE 2

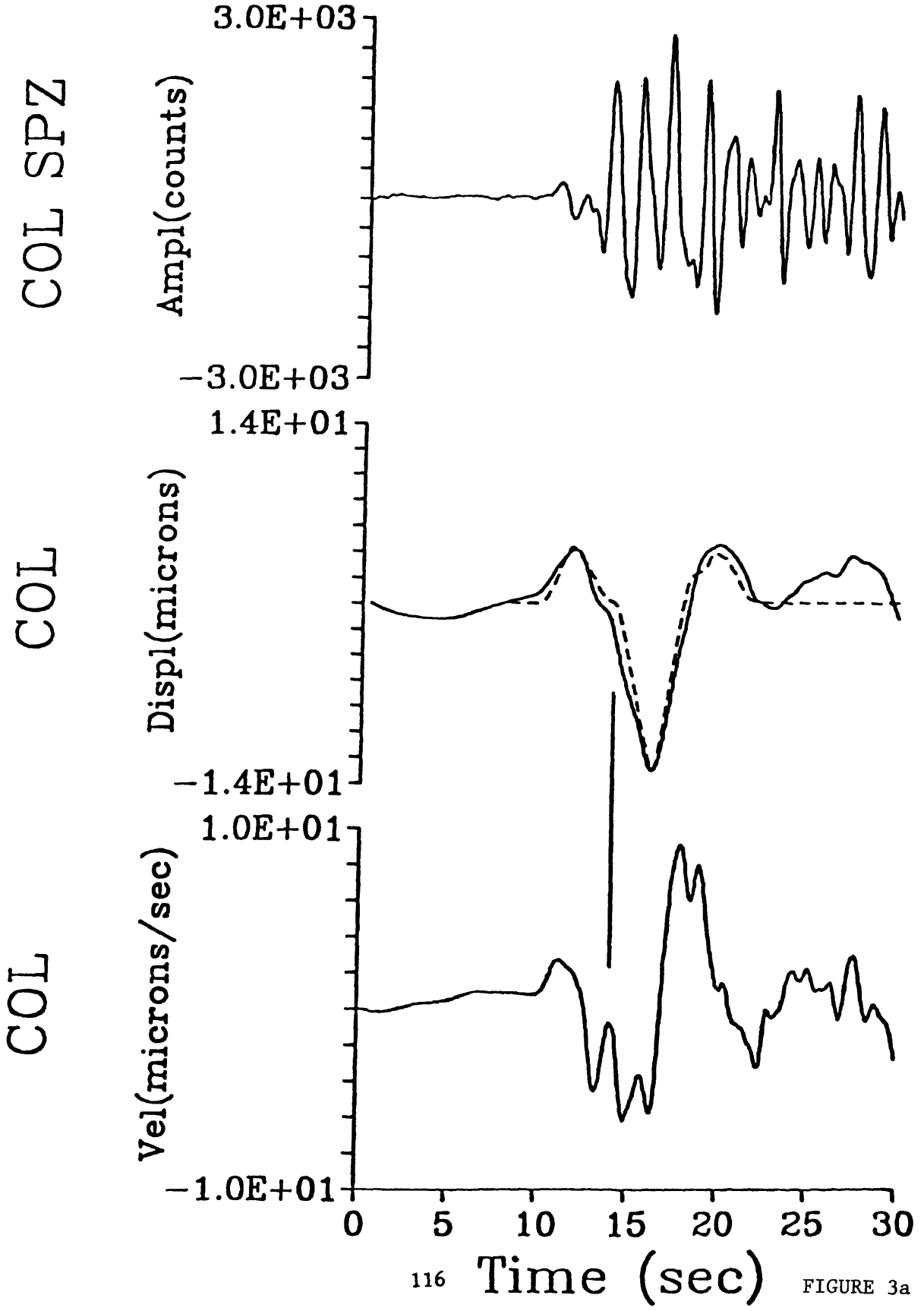
COL SPZ
Ampl(counts)
3.0E+03
-3.0E+03
COL
Displ(microns)
1.4E+01
-1.4E+01
COL
Vel(microns/sec)
1.0E+01
-1.0E+01
0
5
10
15
20
25
30
Time (sec)

FIGURE 3a

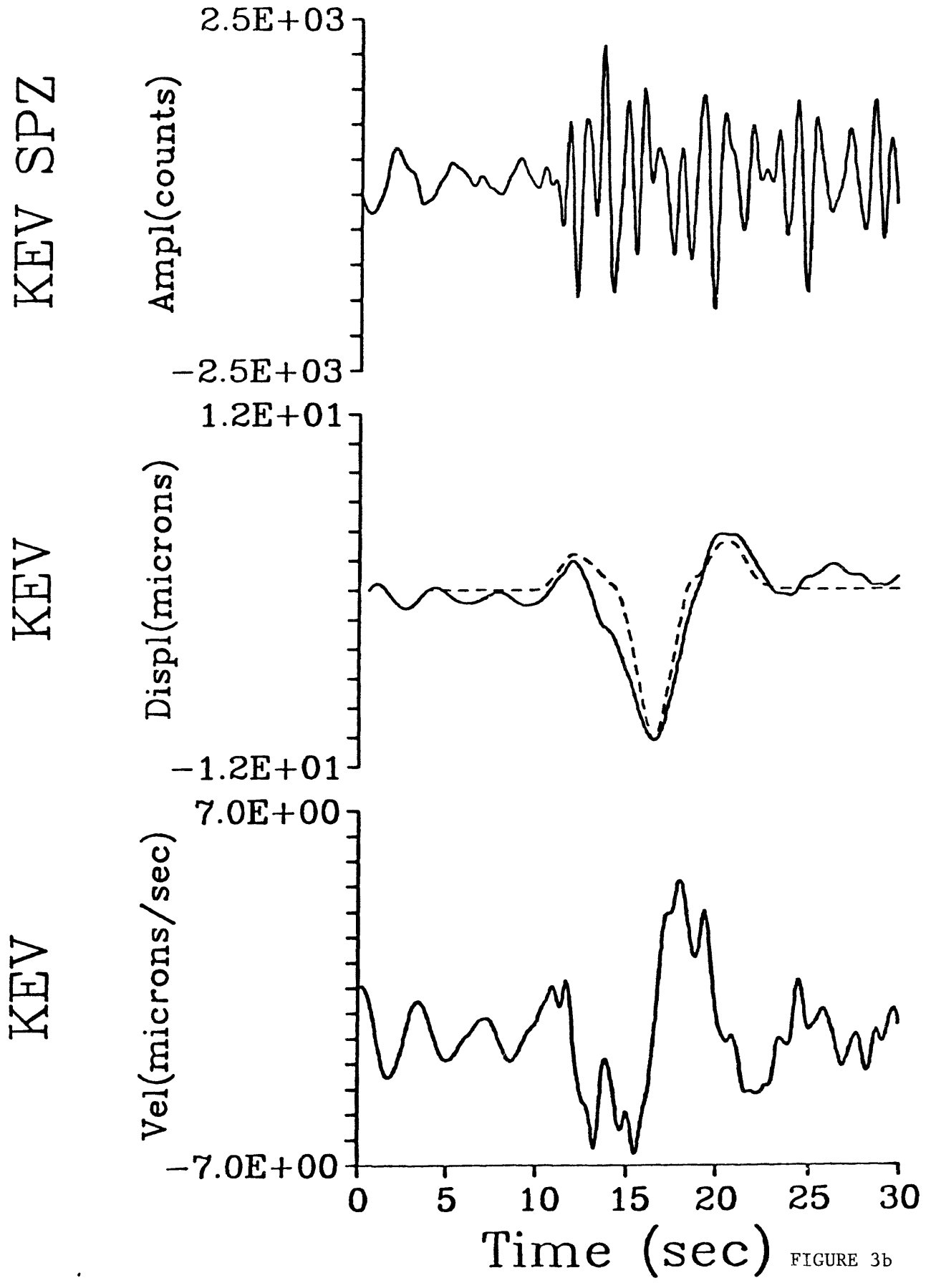
KEV SPZ
Ampl(counts)
2.5E+03
-2.5E+03
KEV
Displ(microns)
1.2E+01
-1.2E+01
KEV
Vel(microns/sec)
7.0E+00
-7.0E+00
0
5
10
15
20
25
30
Time (sec)

FIGURE 3b

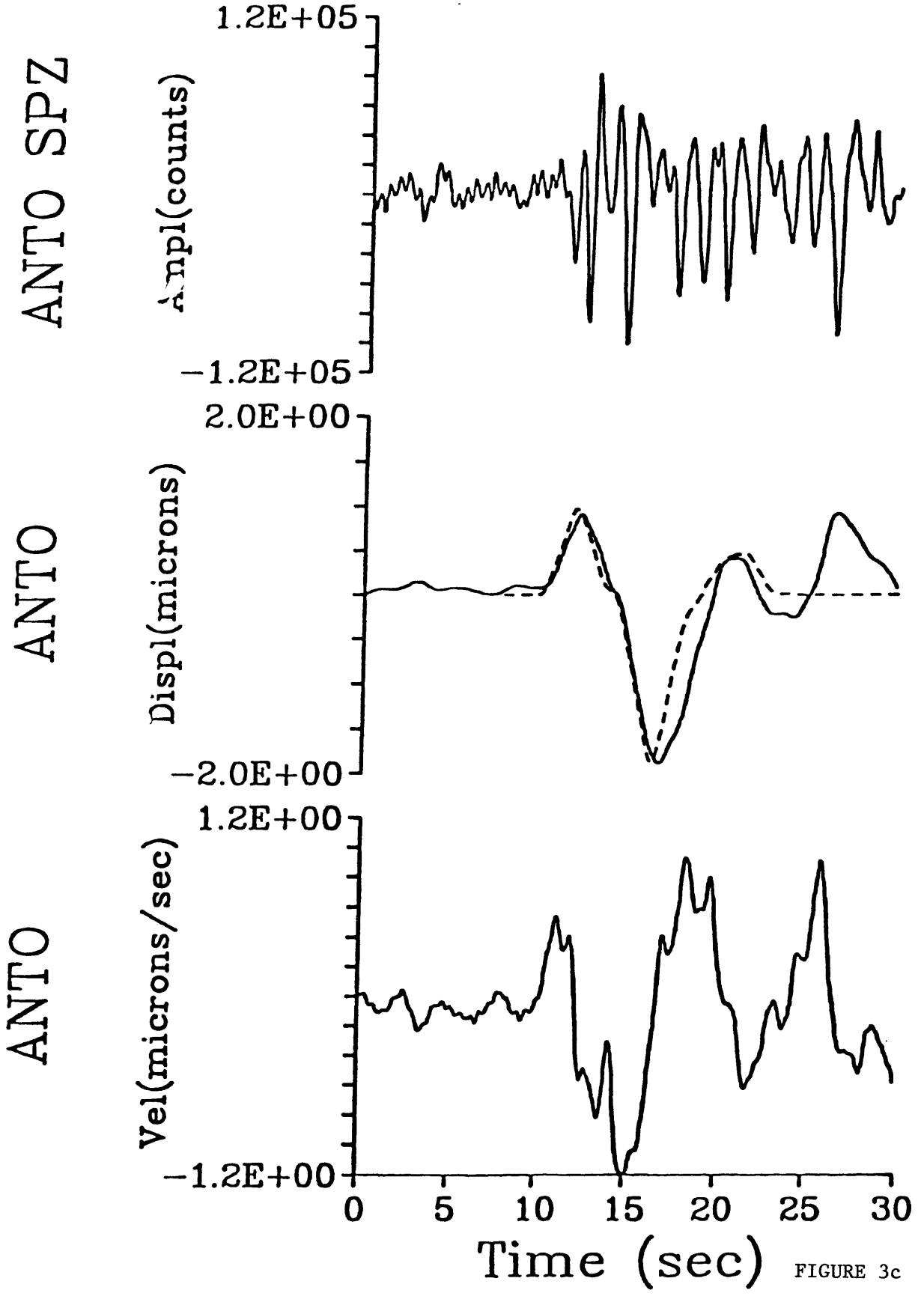
ANTO SPZ
1.2E+05
Ampl(counts)
-1.2E+05
ANTO
2.0E+00
Displ(microns)
-2.0E+00
ANTO
1.2E+00
Vel(microns/sec)
-1.2E+00
0
5
10
15
20
25
30
Time (sec)

FIGURE 3c

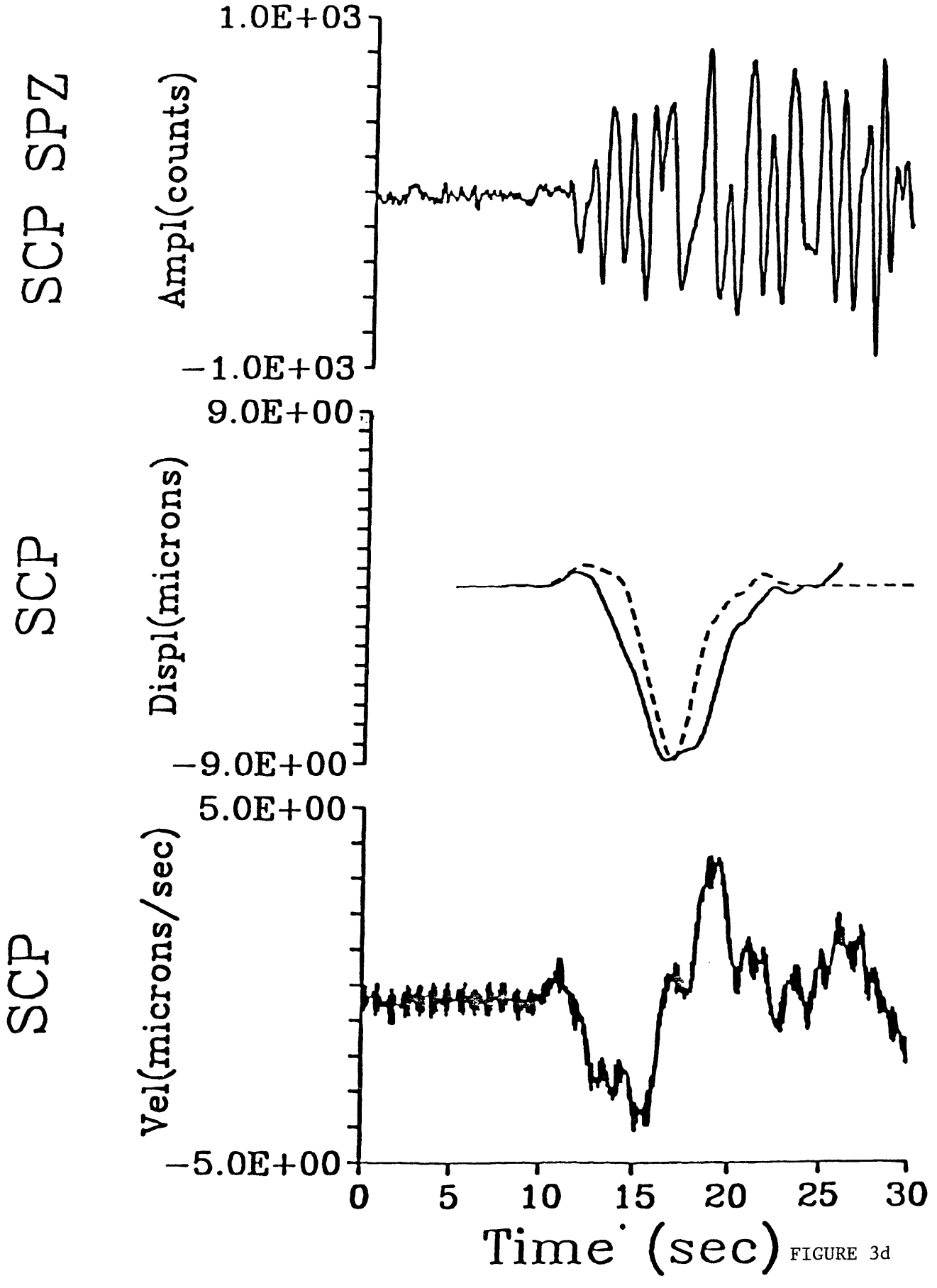
SCP SPZ
1.0E+03
Ampl(counts)
-1.0E+03
SCP
9.0E+00
Displ(microns)
-9.0E+00
SCP
5.0E+00
Vel(microns/sec)
-5.0E+00
0
5
10
15
20
25
30
Time (sec)

FIGURE 3d

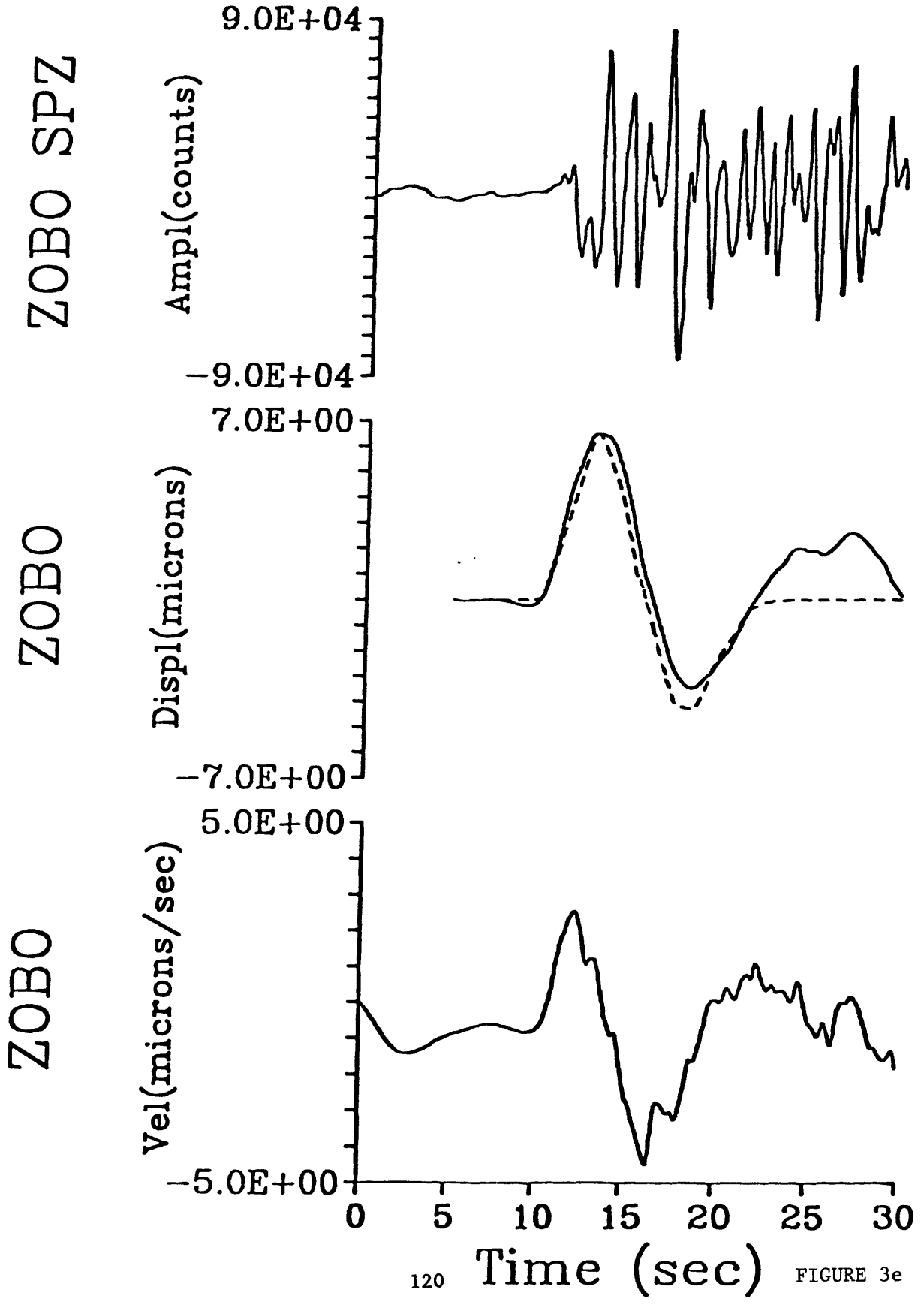
ZOBO SPZ
9.0E+04
Ampl(counts)
-9.0E+04
ZOBO
7.0E+00
Displ(microns)
-7.0E+00
ZOBO
5.0E+00
Vel(microns/sec)
-5.0E+00
0
5
10
15
20
25
30
Time (sec)

FIGURE 3e

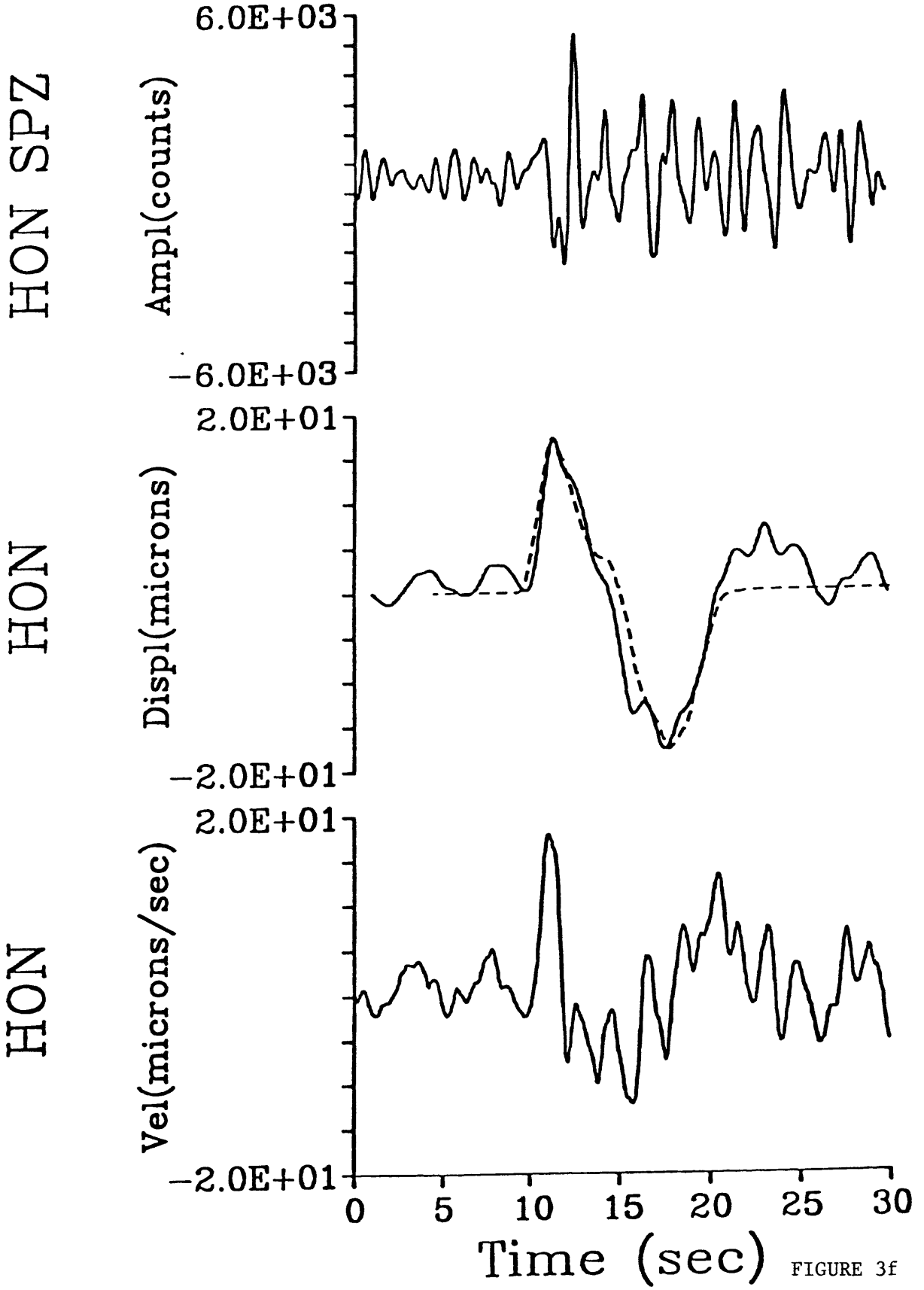
HON SPZ
6.0E+03
Ampl(counts)
-6.0E+03
HON
2.0E+01
Displ(microns)
-2.0E+01
HON
2.0E+01
Vel(microns/sec)
-2.0E+01
0
5
10
15
20
25
30
Time (sec)

FIGURE 3f

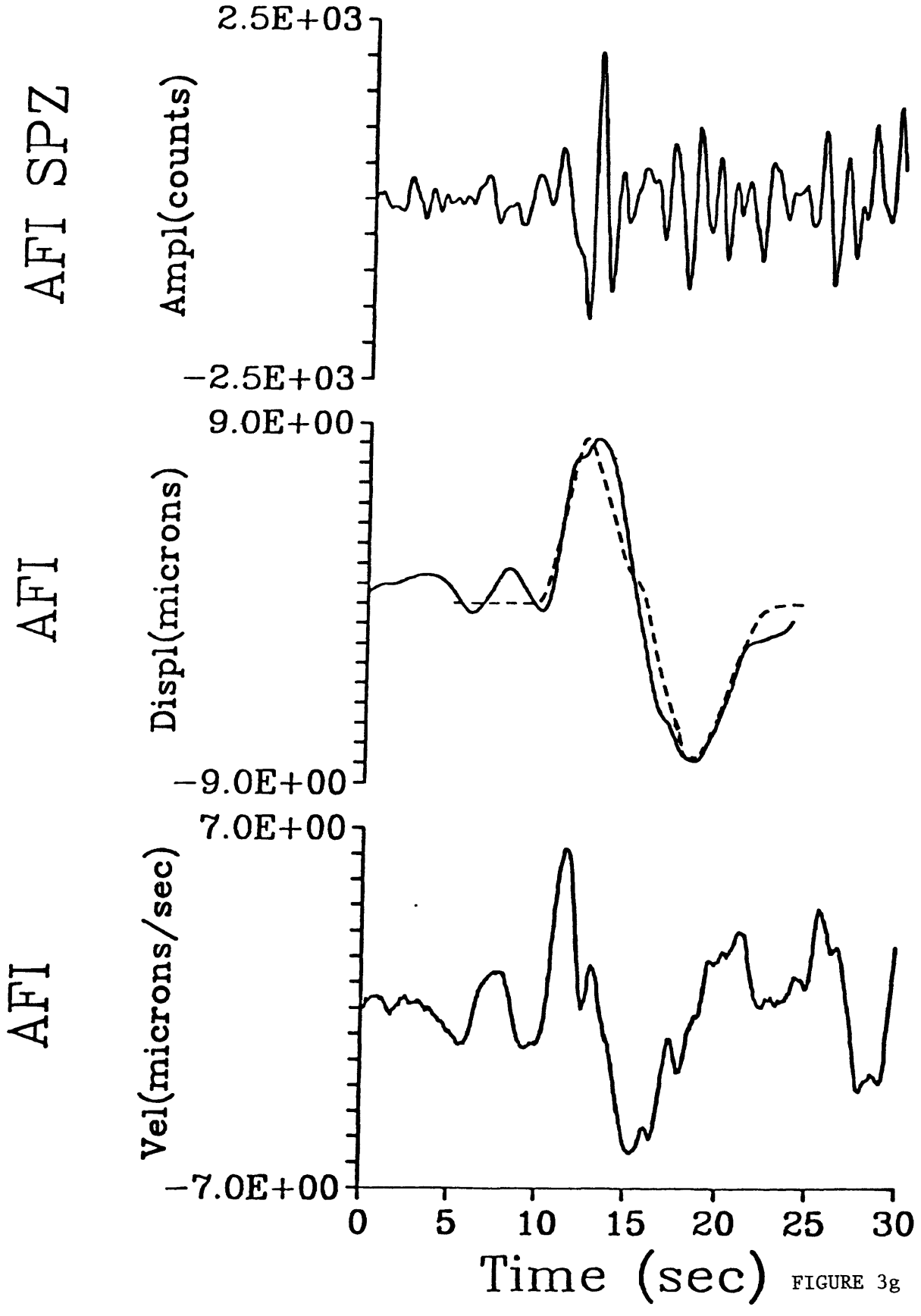
AFI SPZ
2.5E+03
Ampl(counts)
-2.5E+03
AFI
9.0E+00
Displ(microns)
-9.0E+00
AFI
7.0E+00
Vel(microns/sec)
-7.0E+00
0
5
10
15
20
25
30
Time (sec)

FIGURE 3g

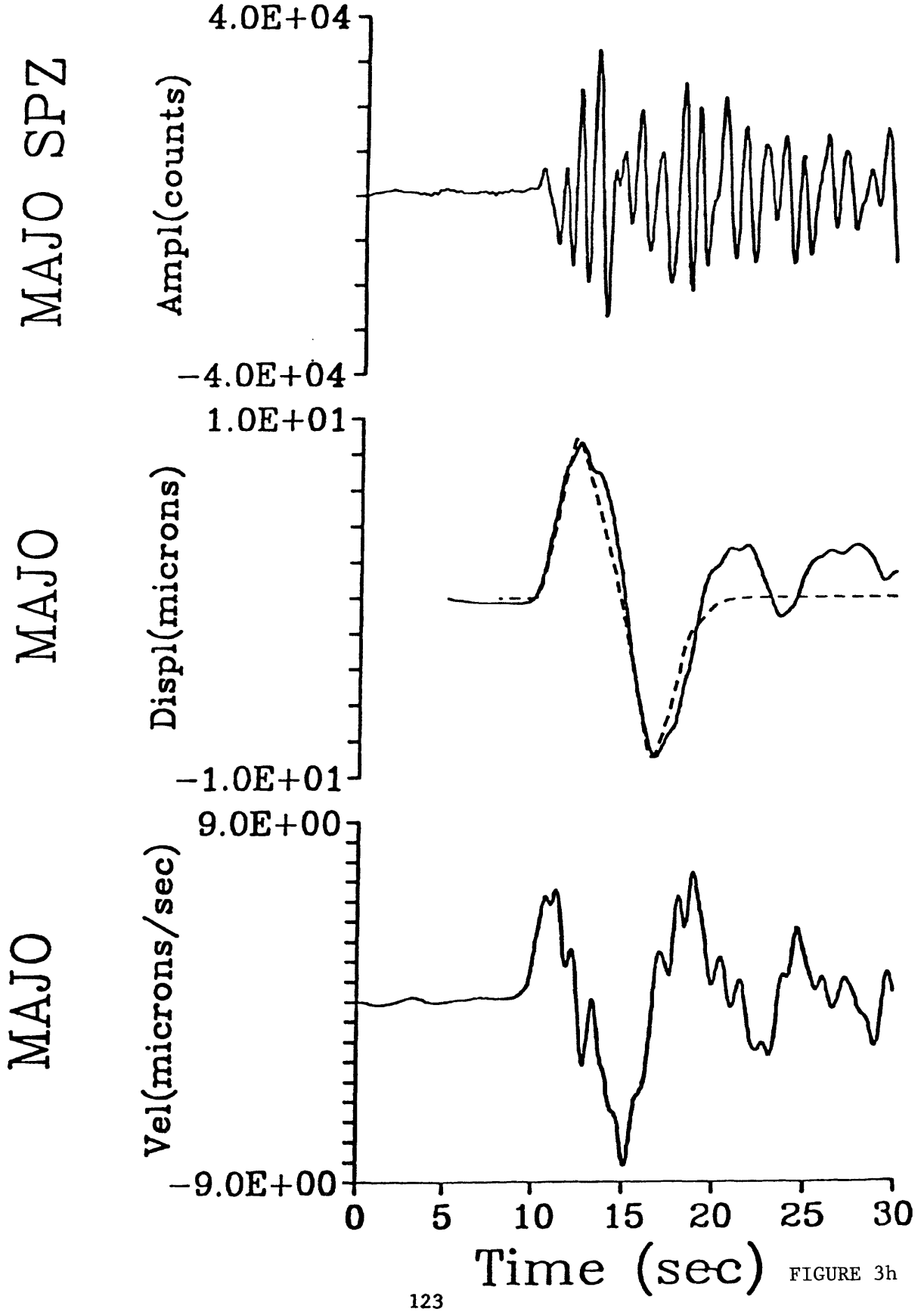
MAJO SPZ
4.0E+04
Ampl(counts)
-4.0E+04
MAJO
1.0E+01
Displ(microns)
-1.0E+01
MAJO
9.0E+00
Vel(microns/sec)
-9.0E+00
0
5
10
15
20
25
30
Time (sec)

FIGURE 3h

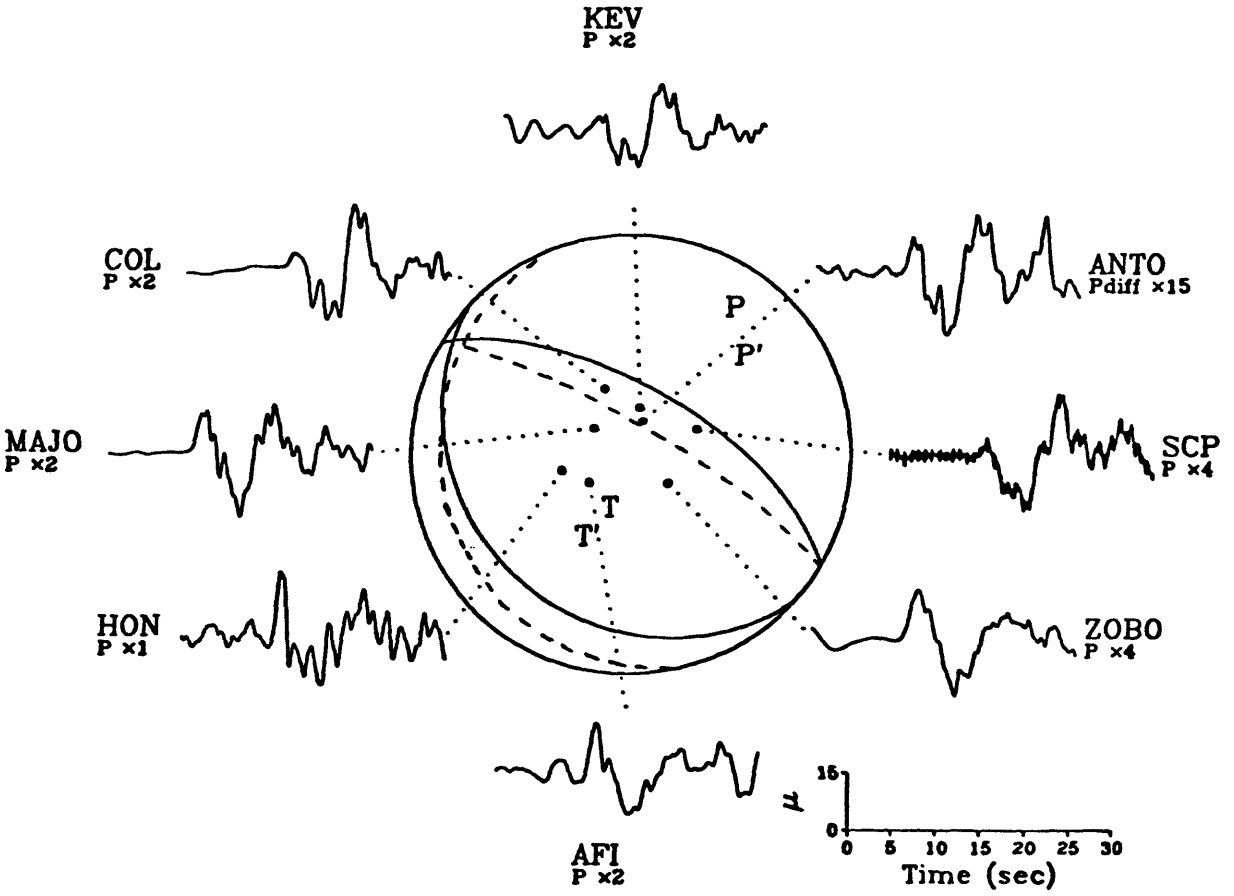
02 May 1983 23:42:37.70
Central California
KEV
P ×2
COL
P ×2
ANTO
Pdiff ×15
P
P'
MAJO
P ×2
SCP
P ×4
T
T'
HON
P ×1
ZOBO
P ×4
AFI
P ×2
15
0
0 5 10 15 20 25 30
Time (sec)

FIGURE 4

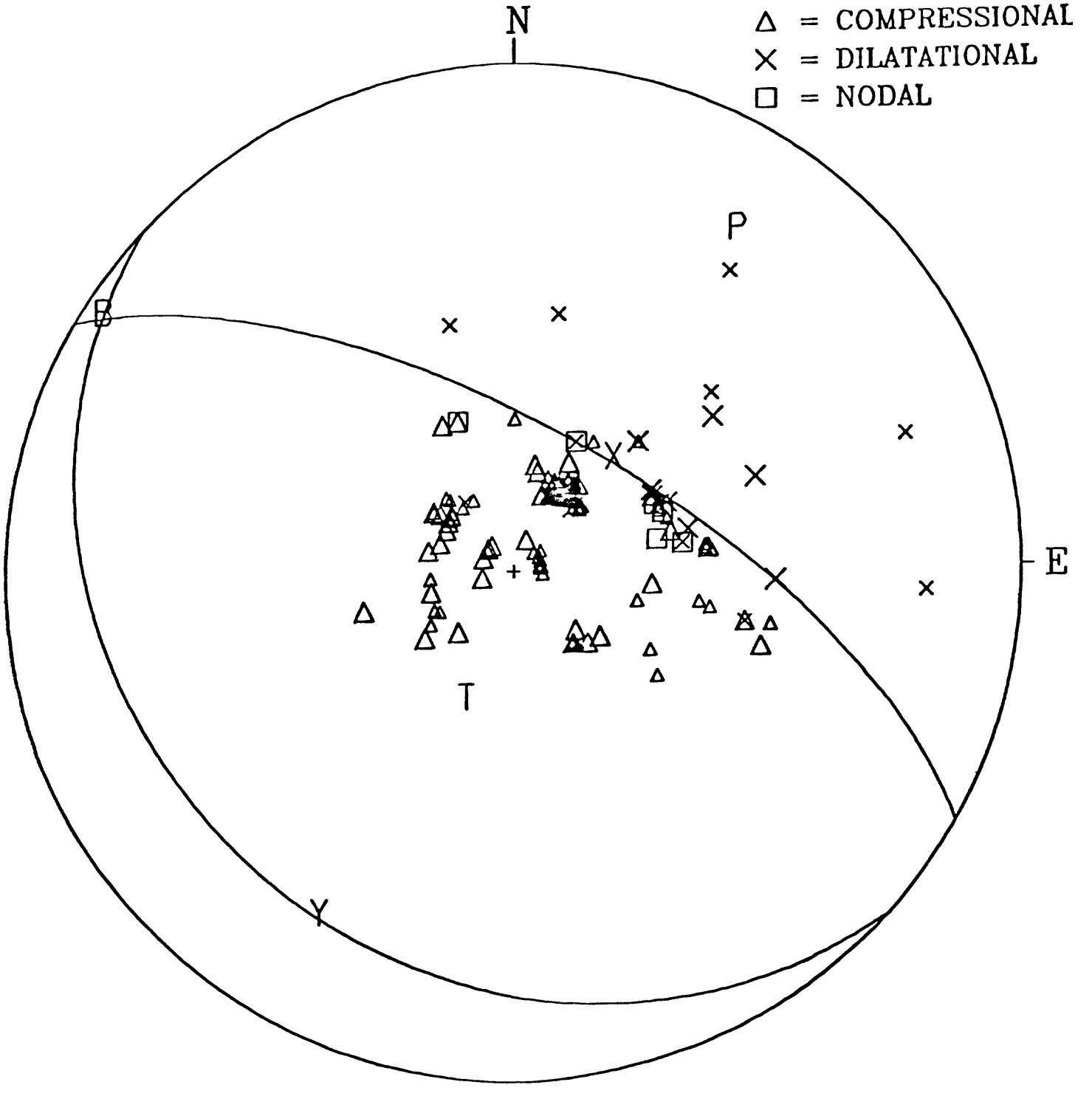

FIGURE 5a

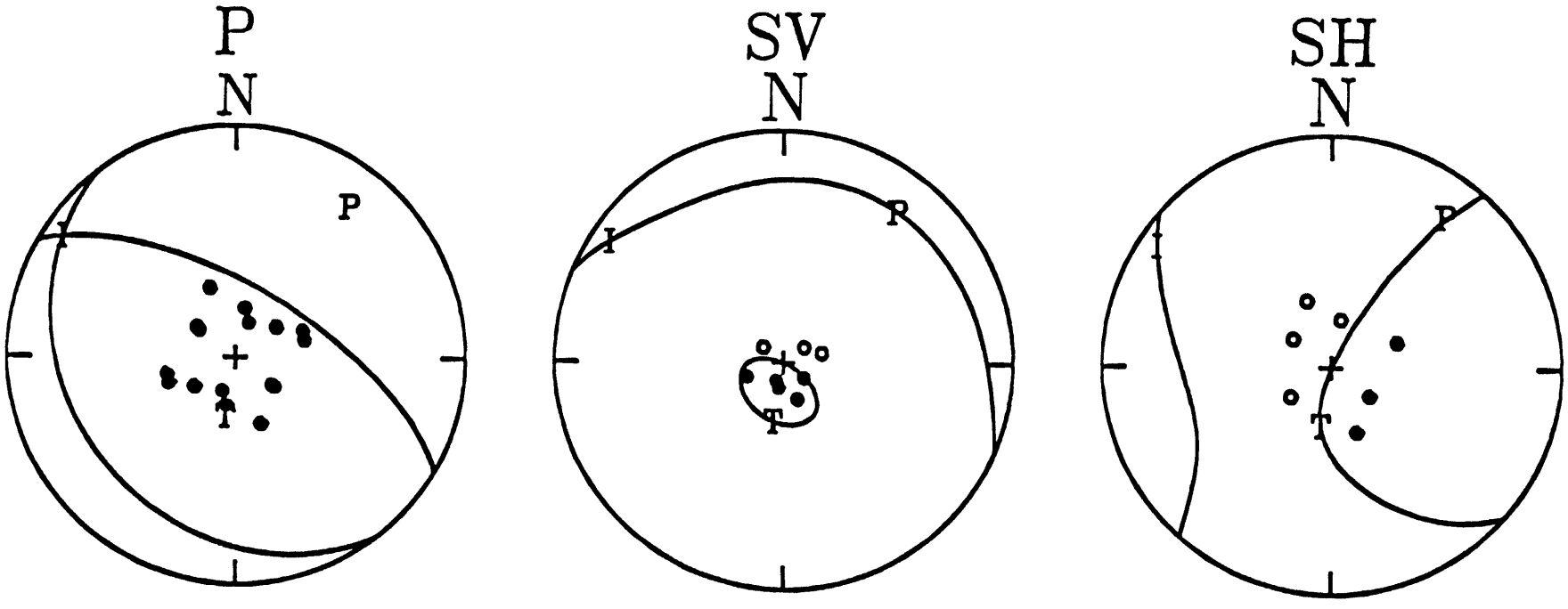

FIGURE 5b

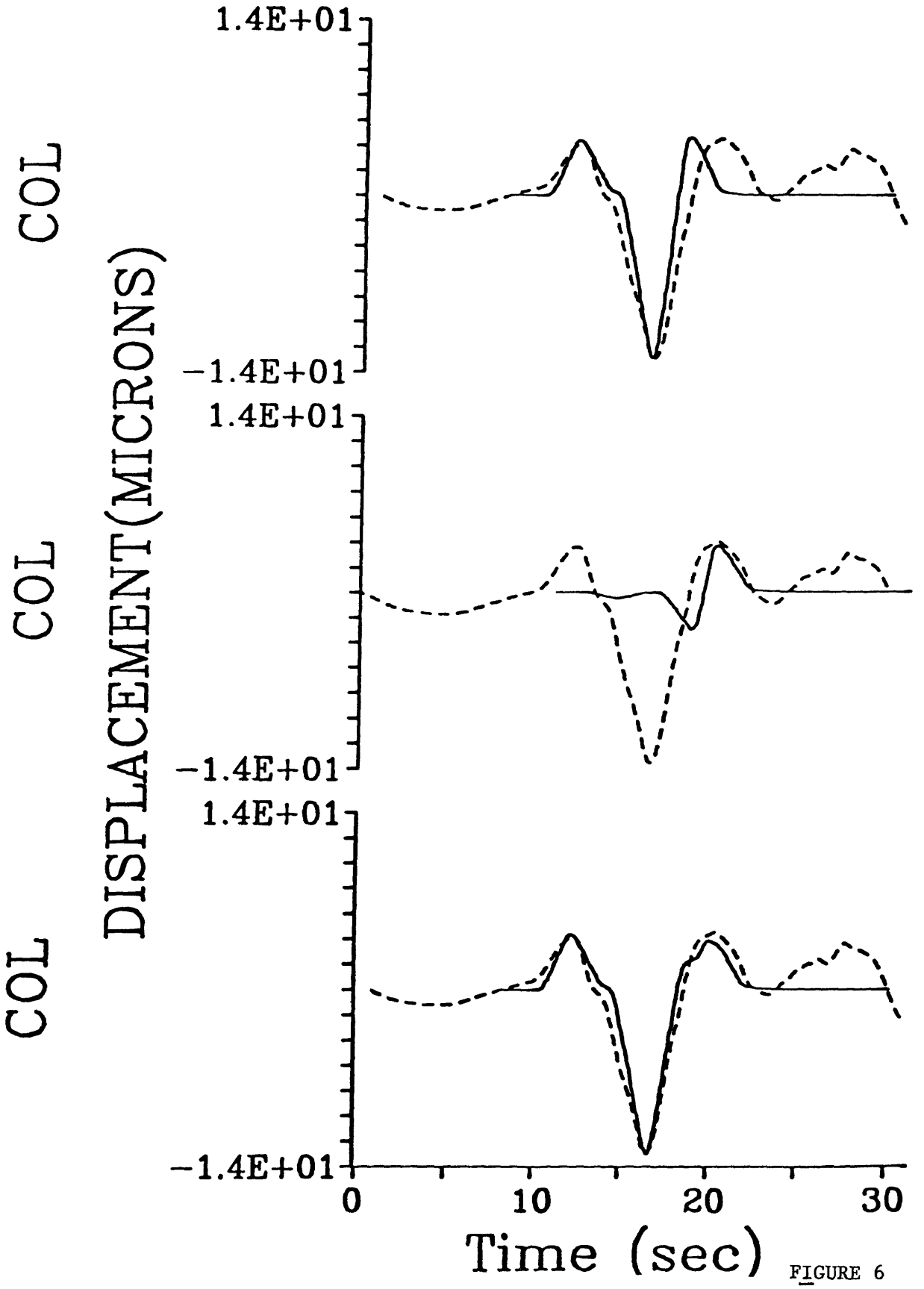
COL
COL
COL
DISPLACEMENT(MICRONS)
1.4E+01
-1.4E+01
1.4E+01
-1.4E+01
1.4E+01
-1.4E+01
0
10
20
30
Time (sec)

FIGURE 6

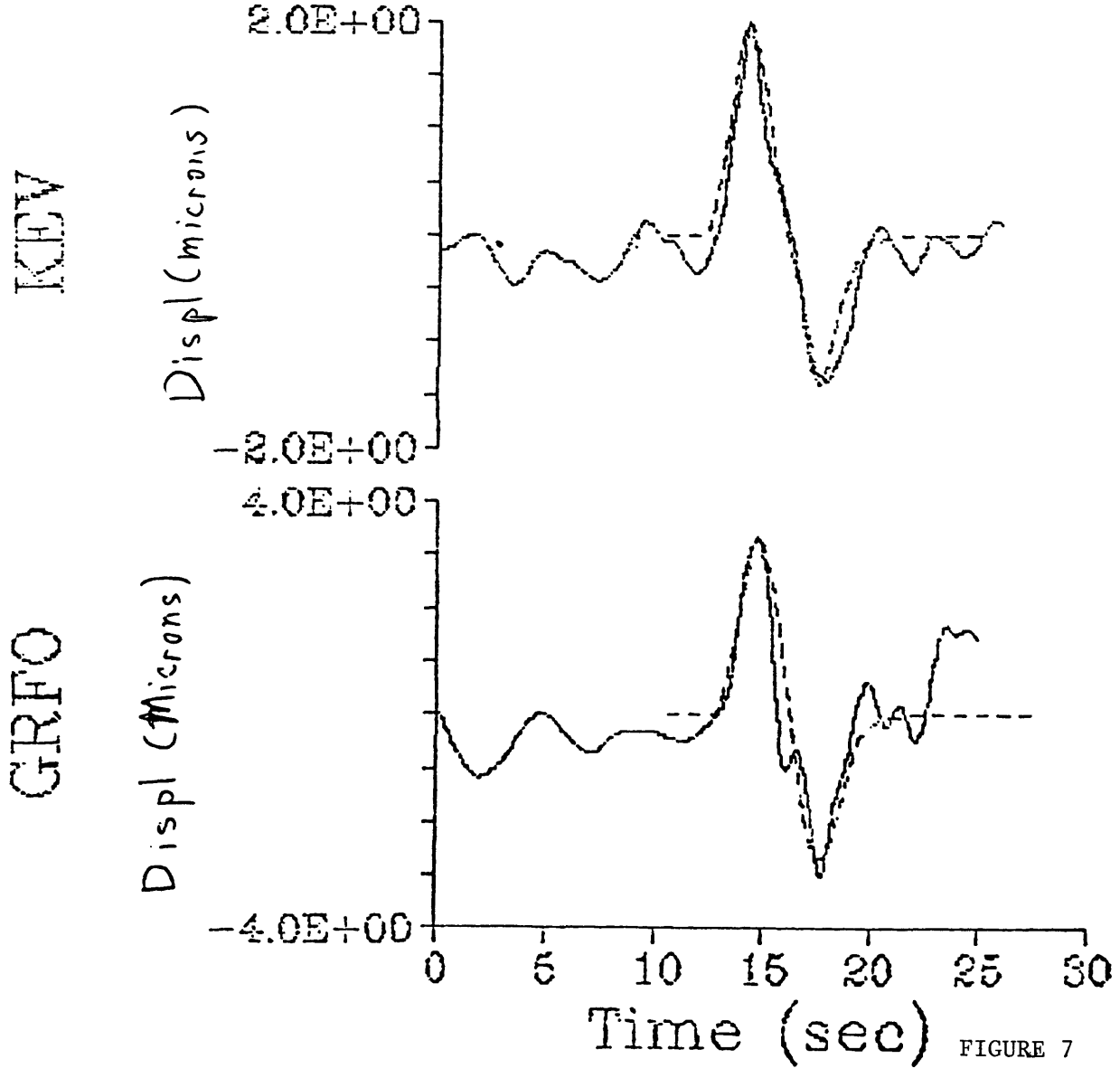
KEW
GRFO
2.0E+00
-2.0E+00
4.0E+00
-4.0E+00
Displ (microns)
Displ (Microns)
0
5
10
15
20
25
30
Time (sec)

FIGURE 7

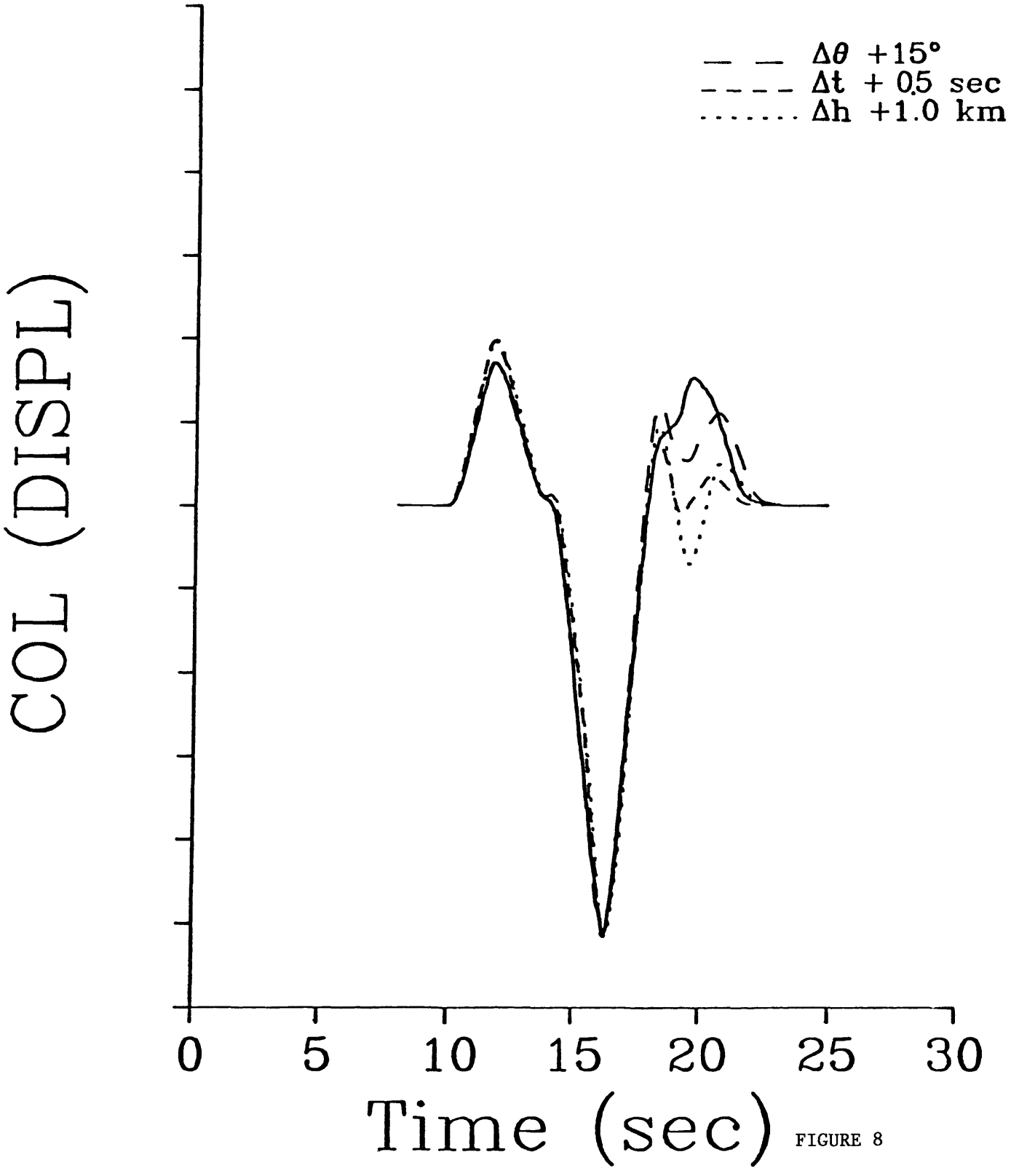

FIGURE 8

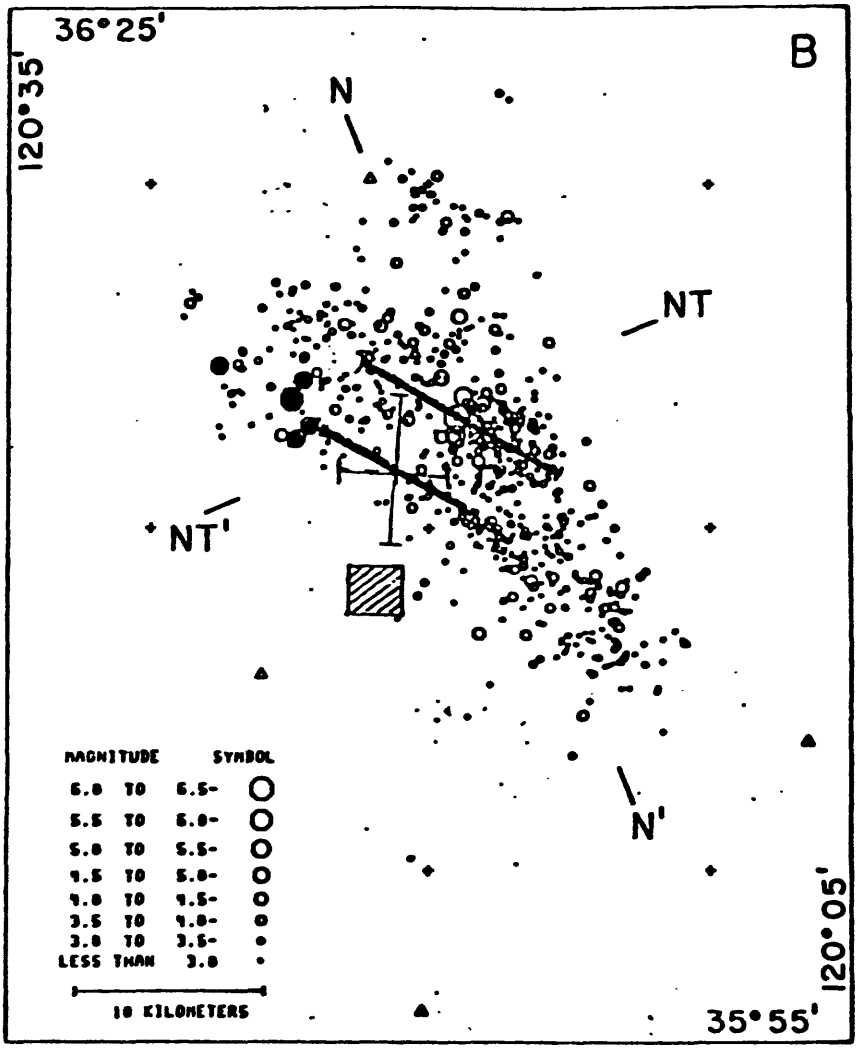
36°25'
B
120°35'
N
NT
NT'
N'
MAGNITUDE
SYMBOL
6.0 TO 6.5-
5.5 TO 6.0-
5.0 TO 5.5-
4.5 TO 5.0-
4.0 TO 4.5-
3.5 TO 4.0-
3.0 TO 3.5-
LESS THAN 3.0
10 KILOMETERS
120°05'
35°55'

FIGURE 9

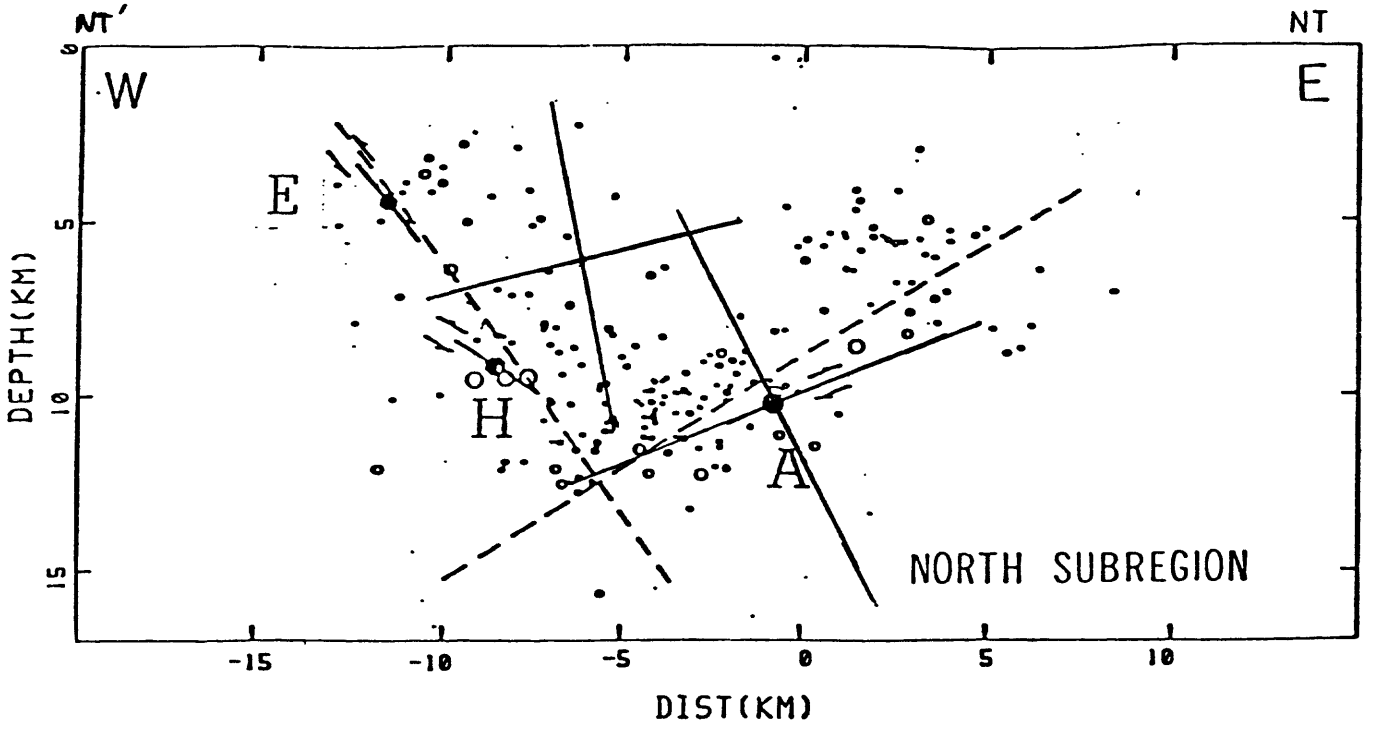

N-36-22.0 120-23.0 N'-36-02.0 120-12.7 May02-Jul31 M>2.5

FIGURE 10

THE MAY 2, 1983 COALINGA EARTHQUAKE AND ITS AFTERSHOCKS: A DETAILED STUDY OF THE HYPOCENTER DISTRIBUTION AND OF THE FOCAL MECHANISMS OF THE LARGER AFTERSHOCKS

J. P. Eaton

U.S. Geological Survey
Menlo Park, California 94025

ABSTRACT

Analysis of the Coalinga earthquake sequence based on the Allen/Ellis RTP (real time processor) automatic P-phase onset time and event duration measurements provides hypocentral and magnitude determinations for several thousand events from May 2, 1983 through Sept. 30, 1983. Maps and cross sections of the nearly 800 best-located M2.5+ events show the spatial distribution and temporal evolution of the sequence and provide some clues to the nature of the faulting that produced the sequence. Focal mechanism studies of the main shock and 10 of its largest aftershocks offer two choices for the main shock fault, a thrust fault striking N 53°W and dipping 23°SW or a high angle reverse fault striking N 53°W and dipping 67°NE, and show that the predominant focal mechanism of the larger aftershocks is reverse faulting. These materials, however, are insufficient for making a clear choice between the two possibilities for the main shock fault.

More detailed studies of the main shock and more than 100 of its M3.2 and larger aftershocks, from records played back from magnetic tape, further clarify the sequence. Maximum pressure axis orentations deduced from first-motion plots for these earthquakes vary systematically from one part of the aftershock region to another. Stereo-pair plots of the fault planes of the aftershocks permit several intersecting fault surfaces to be mapped out. The sum of the evidence strongly favors the thrust fault solution for the main shock.

INTRODUCTION

The Coalinga earthquake sequence presents a rare opportunity to study a large non-San Andreas earthquake in the central Coast Ranges. An understanding of the faulting that produced it may provide insight into the relationship of Coast Range structures to the San Andreas fault and to the underlying tectonic processes that produce earthquakes on the San Andreas as well as throughout the Coast Ranges. The large size of the main shock and its location adjacent to the Parkfield section of the San Andreas at the transition from the slipping portion of the fault northwest of Parkfield to the locked portion of the fault in the Carrizo Plains and beyond toward the southeast raise the question of whether such earthquakes may play a role in locking or unlocking the Fort Tejon section of the San Andreas.

Excellent records of the main shock were obtained on 29 telemetered seismographs within 80 km of its epicenter, including one station on Anticline Ridge near the center of the aftershock region. Nonetheless, azimuthal station coverage for the main shock was poor because it occurred just east of

the dense network around Parkfield and just west of the seismically noisy Great Valley, which had no nearby stations on May 2. Beginning about 24 hours after the main shock, the network was augmented by a portable network of 12 stations; and four permanent stations were installed along the western edge of the Great Valley to close the network gap northeast of the main shock within the first week.

The complex geology at the Coast Range-Great Valley interface where the sequence occurred and our poor knowledge of the velocity structure of the crust in that region were serious impediments to determining reliable, accurate hypocenters for earthquakes of the Coalinga sequence. Determination of a suitable structure from the earthquake data was therefor undertaken in conjunction with the determination of the earthquake hypocenters. In this process possible structures were constrained by the requirement that they yield first-motion plots corresponding to double couple focal mechanisms as well as that they result in hypocentral solutions with suitably small traveltime residuals. The requirement that the first-motion plots correspond to a double couple focal mechanism places constraints on the ratios of the velocity at the focus to velocities at the various refractors from which first motion data are recorded. To suppress the systematic bias in hypocenter location that is introduced by the rapid lateral variation in velocity in the upper crust at the Coast Range-Great Valley boundary, station delays derived by an interative procedure beginning with Pn timeterm differences were used with the crustal velocity model that met the requirements stated above.

This paper represents a second phase in the analysis of the Coalinga data. The first, reported by Eaton, Cockerham and Lester (1983) in CDMG Special Publication 66, was based primarily on the analysis of arrival times for several thousand earthquakes that were detected and timed by the Allen/Ellis RTP (real time processor) in Menlo Park (Allen, 1982) and on detailed studies of the main shock and nine aftershocks played back from magnetic tape. Only the results of that study will be summarized here. The present study is based on the detailed analysis of the main shock and 110 of its largest aftershocks from magnetic tape playbacks. This study's goals are, first, to refine the crustal model and station delays to permit more reliable hypocentral determinations and, second, to help resolve major features of the faulting that produced the earthquakes of the sequence through a joint study of focal mechanisms and the hypocentral distribution of its largest aftershocks.

SEISMIC RECORDS AVAILABLE FOR THE STUDY OF THE COALINGA EARTHQUAKE SEQUENCE

The Coalinga earthquake occurred about 5 km west of the Great Valley-Coast Range boundary and about 3 km SE of the nearest station of the telemetered central California seismic net (figure 1). Although there were 3, 17, and 29 network stations within 25, 50, and 80 kms, respectively, of the epicenter, they all were in the Coast Ranges, enitrely on one side of the epicenter. The records we have used for the first 24 hours of the aftershock sequence came exclusively from stations of the original (May 2) telemetered network, which were recorded on magnetic tape and film as well as processed automatically by the RTP in Menlo Park. Beginning about 24 hours after the main shock, 12 portable 3-component 5-day-tape-recorder stations recording at two gain levels for each component were installed rapidly around the main shock epicenter to

provide improved near-in and azimuthal station coverage of the aftershock region (solid squares, figure 1). Four new permanent stations of the telemetered network, at locations chosen to complement the original telemetered network in the Coalinga region (open triangles inside circles), began recording on May 6. Except for the portable station at Domingine Ranch, which was removed when the new permanent station was installed nearby, the original 5-day-tape network was operated until the end of June. Its number was then reduced to eight, and it was operated in its diminished form until the end of July. The four new telemetered stations have remained in operation until the present.

The earlier study of the Coalinga earthquake and its aftershocks by Eaton, Cockerham, and Lester was based almost entirely on P-phase onset times from thousands of aftershocks determined by the RTP from stations of the telemetered network, including the new stations after they were placed in operation. Those data were augmented by magnetic tape playbacks from the telemetered network for the main shock and 10 of its largest aftershocks. No systematic use was made of records from the portable network.

The present study is based on magnetic tape playbacks from the telemetered network and from the portable network of the main shock and 110 of its aftershocks. Events included in this study were selected from the list of M3+ earthquakes of the earlier study. For the first 24 hours of the aftershock sequence, for which only telemetered network data were available, only aftershocks greater than M3.75 were selected. For the rest of the study period, i.e. from May 4 through Sept. 30, the threshhold for selection was reduced to M3.4; and records from the portable network as well as the permanent network were used in their analysis.

Although only stations at distances of 80 km or less were used for hypocentral calculations, more distant stations were used for determining magnitudes and focal mechanisms. The low-gain multi-component subset of telemetered network stations were particularly useful for magnitude determinations, and telemetered network stations at distances between 80 km and 300 km and at a wide range of azimuths were indispensable for the focal mechanism determinations.

The magnetic tapes were played out on a calibrated strip-chart recorder to produce records with a time base of 1 inch/second (telemetered net) or 0.5 inch/second (portable net). P-wave onset times and first-motion directions were measured from high-gain vertical components, and when S-wave onsets were distinct their times were measured, generally, from low-gain horizontal compenents. Maximum amplitudes and associated periods were measured from unclipped traces. The unclipped traces generally were from low-gain channels, although high-gain channels produced usable records for moderate earthquakes at epicentral distances of several hundred kilometers.

DEVELOPMENT OF CRUSTAL MODELS, P-WAVE STATION DELAYS, AND MAGNITUDE CORRECTIONS

The region of the Coalinga earthquake and its aftershocks lies at the eastern edge of the dense seismic network in central California and just west of the boundary between the Coast Ranges and the Great Valley; and the velocity model routinely used by the USGS for central California earthquakes

gives poor results there. Also, crustal structure varies abruptly from east to west across the region, particularly the thickness of low velocity material in the upper crust (Walter, this volume). Although recent refraction profiles provide better information along selected profiles (Walter, this volume; Wentworth, Zoback, and Bartow, this volume), they do not yet cover a sufficiently broad region to provide an adequate model for earthquake hypocenter determinations.

We have employed data from particularly well recorded, well distributed Coalinga "calibration" events to develop a more appropriate model and associated set of station delays. Starting with an initial model and set of station delays, layer depths and velocities were varied systematically during a succession of relocations of the calibration events to minimize the r.m.s. of traveltime residuals for the individual events and to comply with the constraint that the first-motion plots be separable into distinct fields of compressions and dilatations by the two orthogonal focal planes of a double couple earthquake source. The average station traveltime residuals for the best-fitting model were then added to the station delays used with the model to obtain an improved set of station delays. The calibration events were then relocated using the best-fitting model and the improved station delays. Finally, the average station residuals resulting from this last relocation were added to the station delays employed for the relocation to obtain the final set of station delays for use with the best-fitting model.

The delays so determined embody traveltime variations due to purely local (near surface) structural anomalies at the individual stations as well as possible systematic errors due to a mismatch of the crustal model to the earth. It can be argued that the use of station delays obtained in this manner improves the relative locations of hypocenters, particularly of events that were not well recorded by the entire set of stations used for the location of the calibration events; but absolute location errors resulting from gross regional variations in structure, such as the transition from the Coast Ranges to the Great Valley, are not removed.

This deficiency can be offset partially by use of an initial set of station delays that reflects the gross regional variation in traveltimes due to the anomalous structure. We have used a set of initial station delays based on Pn timeterm differences determined from well recorded events at appropriate distances and azimuths from the network around Coalinga. This procedure is valid to the extent that the relative delays at the stations are due primarily to variations in the shallow structure beneath the stations that is traversed both by Pn waves from regional earthquakes and by the direct or refracted waves from the local Coalinga earthquakes that we wish to locate. Thus, these delays are only first-order estimates of the delays experienced by waves traversing the anomalous structures at angles of incidence different from that of Pn.

In our earlier study of the Coalinga earthquake (Eaton, Cockerham and Lester, 1983) we employed Pn timeterm-difference data that were rather weak in the Coalinga region. They were determined prior to the installation of telemetered network stations in the Great Valley east of Coalinga; values for the new Great Valley stations were estimated from very meager data at stations along the eastern edge of the Sacramento Valley, far to the north. Since the earlier study, however, four additional well recorded, well located

earthquakes in central California have provided good Pn data in the part of the network used to locate the Coalinga earthquakes. These new data have been used, together with data from the earlier Pn travelterm-difference study, to establish an improved set of initial station delays for the Coalinga region.

Beginning with the final crustal model (CM4) from our previous study and the improved set of initial station delays discussed above, we have repeated the procedure described above to obtain a crustal model (CM5) and station delay set that should more adequately suppress the bias in hypocenter locations resulting from the east-to-west variation in crustal structure across the Coalinga region. This model and station delay set have been used for hypocentral determinations of the 111 quakes analyzed further in this study.

Maximum amplitudes and associated periods were read from unclipped records of both the telemetered network and the portable network to provide a basis for computing local magnitudes. In order to reduce the dependence of computed magnitudes of individual events on the subset of stations used to determine them we have computed station magnitude corrections in a manner analogous to the determination of station traveltime delays discussed above.

With all station magnitude corrections set to zero, all 111 events in this study were located with crustal model CM5 and its associated set of station delays, and magnitudes were determined for each event for each station reporting maximum amplitude and associated period data. Magnitude residuals were then computed for each reporting station (average of all station magnitudes subtracted from that of the reporting station) for each event; and the average magnitude residual (for all events) at each station was determined. These residuals were then subtracted from the initial station magnitude corrections (all zero in this case). This procedure was repeated once more, and the resulting average station magnitude residuals were subtracted from the previous station magnitude corrections to obtain the set of station magnitude corrections applied in this study.

Crustal models 4 and 5 are compared in Table 1. The station delays used with crustal models 4 and 5, as well as the station magnitude corrections applied in this study, are presented in Table 2.

DISTRIBUTION OF HYPOCENTERS OF M2.5 AND LARGER EVENTS OF THE COALINGA SEQUENCE AND FOCAL MECHANISM OF THE MAIN SHOCK

Our first analysis of the Coalinga sequence was based largely on P-phase onset times and durations, from the telemetered network, determined by the RTP in Menlo Park. The procedures used to refine the RTP data and the results for the Coalinga sequence through the end of July, 1983, have been described previously (Eaton, Cockerham and Lester, 1983). The same methods were used to extend the data and results through the end of September, 1983.

To avoid clouding the analysis with poorly located events we consider only events with $M \geq 2.5$, RMS ≤ 0.20 sec., NOST ≥ 12, ERH ≤ 3km, and DMIN ≤ 30 km, where M is local magnitude, RMS is the root mean square of traveltime residuals, NOST is the number of the stations used in the hypocenter determination, DMIN is the epicentral distance of the nearest station, and ERH is the estimated error in epicenter location. The 771 events satisfying these

criteria are shown in figure 2, where they are superposed on a map showing the principal topographic features of the region. From the location of the main shock and the location and orientation of its aftershock region, the Coalinga earthquake appears to be closely related to the Anticline Ridge-Guijarral Hills structure. Details of the aftershock pattern are more clearly seen in figure 3, which shows all aftershocks satisfying the selection criteria listed above for the first day of the sequence (figure 3A) and for the entire 5 months of the sequence reported here (figure 3B). Nearly the entire area of the aftershock zone as well as most of its principal features were clearly marked out during the first day of the sequence. The aftershock zone of the first day was nearly 30 km long from NW to SE and 10 km wide from NE to SW, and the main shock was 3 to 4 km N of the center of the zone. The aftershocks were grouped into rather distinct clusters, which persisted, with reinforcement, throughout the sequence. From north to south these features were:

1) Domingine cluster - a detached cluster of small events near the Domingine Ranch, about 5 km north of the main aftershock zone;

2) northwest triangle - a triangular patch, about 10 km on a side, of rather evenly spaced aftershocks at the northwestern end of the aftershock region;

3) quiet band - a narrow band with practically no aftershocks that cut across the aftershock zone from SW to NE just northwest of the main shock;

4) main shock cluster - a dense elliptical patch of aftershocks about 8 km long extending southeastward from the main shock, which lay at its NW end;

5) southern cluster - a broad, 15-km-long, NW-SE trending patch of aftershocks lying south of the main shock cluster. This cluster is separated from the main shock cluster by a low density band of predominantly small earthquakes.

Modification of this pattern during the next 5 months consisted primarily of 1) an approximate 3-fold increase of the number of aftershocks in the patches described above, 2) the appearance of a new cluster (Nunez extension) during June and July along the western edge of the northwest triangle, and 3) the appearance of several distinct subclusters in the southern cluster.

Longitudinal sections (figure 4) along the line R-R' (figure 3) show the distribution of the aftershocks as a function of depth and longitudinal (NW-SE) position in the aftershock zone. The pattern for the first day (figure 4A) is a lower density version of the pattern for the first 5 months of the sequence (figure 4B). Northwest of the main shock a distinct cluster at 3 to 6 km depth marks the Domingine cluster and shallow events of the Nunez extension. The deeper events northwest of the main shock are rather evenly distributed between 7 and 13 km depth. Southeast of the main shock there is a concentration of aftershocks at 8 to 10 km depth superposed on a fairly uniform background of activity from 3 to 13 km, except for more than 10 km SE of the main shock, where the aftershocks cut off at about 11 km depth.

Transverse sections (figures 5 and 6) along the line T-T' (figure 3) show the distribution of aftershocks as a function of depth and transverse (NE-SW) position in the aftershock zone. During the first day aftershocks northwest of the main shock cluster (figure 5A) were concentrated in a zone that passes through the main shock and dips about 40° toward the SW. Southeast of the main shock (figure 5B), aftershocks were clustered in three sub-horizontal bands dipping about 10° toward the SW that are centered approximately on the main shock and step upward from the depth of the main shock to a depth of about 5 km.

The transverse sections for the first 5 months of the aftershock sequence are shown in figure 6. Northwest of the main shock (figure 6A), the SW-dipping band of aftershocks through the main shock has intensified and broadened, and a new NE-dipping zone that joins the former zone several km NE of the main shock has appeared. The latter represents the Nunez extension aftershocks of June and July. Together, these dipping zones of aftershocks form a "V", with its vertex a few km SW of the main shock; very few aftershocks occur in the central space between the arms of the V. Southeast of the main shock (figure 6B) the number of aftershocks in the subhorizontal bands has increased and the bands have almost coalesced. A prominent zone of aftershocks dipping northeastward below the main shock has appeared as well as a diffuse zone of deep aftershocks southwest of the main shock.

Because a layered model was used to deterine the hypocenters of the aftershocks we cannot be sure that the subhorizontal banding of the aftershock distribution is not an artifact of the location procedure.

The focal mechanism of the main shock determined from a plot of first motion directions (Eaton, Cockerham, and Lester, 1983) defined two focal planes, the first striking N 53° W and dipping 23° SW and the second striking N 53° W and dipping 67° NE. Comparison of these planes with the cross sections of the M 2.5+ aftershocks does not determine clearly which is the fault plane and which is the auxiliary plane. Geodetically determined coseismic changes in elevation of the ground surface, measured along a road that crosses Anticline Ridge near the main shock, provide important constraints on the style and extent of faulting that produced the earthquake. Stein (this volume) finds that the simplest fault that can explain the level changes would correspond closely to the high angle reverse fault indicated by the second focal plane described above. Somewhat more complex faulting, based on a thrust fault similar to that indicated by the first focal plane described above, can explain the level changes almost as well, however.

LOCATIONS, FOCAL MECHANISMS, AND DISTRIBUTION OF THE LARGER AFTERSHOCKS

The first phase analysis of the Coalinga earthquakes and its aftershocks was largely reconnaissance in nature because it relied so heavily on analysis of phase data picked by the RTP. We have seen that analysis of the distribution of the best-located hypocenters gives only vague clues to the processes embodied in the sequence. Supplemental studies of the main shock and its largest aftershocks have shown that reverse faulting is the dominant deformation process at work, but the great variation in those solutions indicates that several different faults are involved.

In an attempt to improve the resolution of the seismic results, we have undertaken a more detailed study of about 100 additional aftershocks. These aftershocks were selected from the summary list of the original study. The selection threshhold was set at M 3.75 for the first 24 hours and at M 3.4 thereafter. Some smaller events were also selected on the basis of the number of phases used in the hypocenter determination, wich depends on the size and onset clarity of the earthquakes.

The data for these aftershocks were read from paper playbacks from magnetic tape. All available portable network records were used. Records were read from the telemetered network from stations out to about 150 km, as well as from low noise stations in critical azimuths out to several hundred km.

P-wave onset times and first-motion directions were read from high-gain vertical components, and clear S-wave onsets were read when available, generally from low-gain horizontal components. Maximum amplitudes and associated periods were read from unclipped traces, which were generally from low-gain recording channels.

For hypocenter determinations, the improved model (M 5) and station corrections derived from the improved Pn timeterm differences were used with program HYP071 (Lee and Lahr, 1975). Magnitudes were computed from maximum amplitude and associated period data, with the station magnitude corrections described above. For this calculation HYP071 reduces the recorded maximum amplitude to the corresponding Wood-Anderson amplitude and uses the Richter log amplitude-vs-distance zero-magnitude earthquake reference curve.

Focal mechanisms were determined by hand fitting nodal lines (with a Wulff net) to a lower hemisphere equal area projection of the first-motion data on a printer plot. The program that prepared the plot corrects known reversed stations and permits individual data points to be down-weighted or eliminated on the basis of the analyst's quality estimate of the phase pick and on the basis of epicentral distance of the recording station.

A summary list of the Coalinga earthquake and its larger aftershocks, showing origin times, locations, focal depths, magnitudes, and the focal planes deduced from first motion plots, is presented in Table 3. First motion plots for the 108 largest events of the Coalinga sequence are presented in figure 24.

The epicenters of the main shock and its larger aftershocks are plotted in figure 7, where they are superposed on a map showing the principal physiographic features of the Coalinga region. The earthquake symbols are coded for depth and scaled by magnitude. The spicenters shown on figure 7 are shifted about 1.5 km toward the NNW relative to those on fig. 2 because of the different crustal model and station delays used to located them (CM5 instead of CM4, etc.). Although there are far fewer epicenters on figure 7 than figure 2, the same general features in their patterns are evident. However, the southwestern cluster of the aftershock region is more poorly represented on figure 7 because of the high ratio of small to large earthquakes in that region.

Focal mechanisms are plotted in figure 8 on the same map base used in figure 7. Some small events on figure 7 are not plotted on figure 8 because

they coincided with larger events, and other events have been shifted slightly to avoid excessive overlap with their neighbors. The M3.2+ aftershocks show the same clustering as the M2.5+ shocks in figure 3: Domingine cluster in the north, combined NW triangle and Nunez extension, the quiet band just NW of the main shock, the main shock cluster just NE of Anticline Ridge, and the southern cluster. The most notable feature of the focal mechanism map is the preponderance of thrust and reverse solutions over strike slip solutions.

Though few in number, the strike-slip solutions are very interesting in their distribution. Their greatest concentration is along the southeastern edge of the NW triangle, near the 1000' elevation contour, just northwest of the quiet band. These solutions are interpreted to be right-slip faults. The largest strike-slip solution is for the magnitude 5.3 earthquake at 0916 on Sept. 9. It is interpreted as a right-slip fault and lies along the eastern edge of the main shock cluster. There is one strike-slip solution at the southern edge of the main shock cluster, one stike-slip solution in the Domingine cluster, and several strike-slip solutions in the southern cluster, near the Guijarral Hills.

The preponderant strike direction of the reverse fault solutions is approximately NW; but in the Nunez extension region the average strike direction is a few degrees W of north, and in the Guijarral Hills region most solutions have strike directions nearly due west.

The regional variation in orientation of the focal mechanisms is shown more clearly in figure 9, where inferred maximum pressure axis directions are plotted on the same map base used in figures 7 and 8. Arrows indicating pressure axis directions are scaled according to magnitude and point along the pressure axis in its downdip direction. Most pressure axes are nearly horizontal. Their orientation for events in the main shock cluster and, for deeper events throughout the aftershock region, is NE-SW. In the Nunez extension west of the main shock the most prevalent P-axis orientation is nearly due E-W. In the southern cluster, the most prevalent P-axis orientation is NNE-SSW.

This widespread systematic variation in P-axis orientation of all but the deepest aftershocks suggests that stresses in the aftershock region were profoundly altered by the main shock. The possibility that this stress pattern existed before the main shock cannot be ruled out by the present data, however. These variations are symmetrical relative to a vertical plane through the main shock epicenter and parallel to its P-axis direction, which is also its slip direction. In the Nunez Canyon region the presure axes are rotated clockwise relative to the P-axis of the main shock, while the P-axis south of the main shock are rotated counter-clockwise. These changes may be diagnostic of the style and amplitude of faulting accompanying the main shock.

To determine whether a group of earthquakes with thrust or reverse focal mechanisms were generated on the same extended fault surface we should project the earthquakes onto a vertical plane (or cross section) that is parallel to the slip direction of the focal mechanisms. For a pure thrust or reverse fault (with no strike slip component), the slip vector lies in the same plane as the pressure axis. Thus the viewing direction (which is prependicular to the projection plane) should be perpendicular to the slip direction and P-axes of the earthquakes to be examined. A line perpendicular to the average

presure axis orientation of events in the Nunez extension region has an azimuth about 347°. On a broader scale, a line perpendicular to the average P-axis orientation of the earthquakes in the main shock cluster and at the bottom of the active zone across the whole aftershock region has an azimuth of about 317°.

In figure 10 we show transverse cross sections, centered on the main shock, relative to viewing azimuths of 347° (A), 333° (B), and 317° (C). The cross section in figure 10A (AZ 347°) is oriented to test whether the aftershocks in the Nunez extension lie on a plane that is perpendicular to the plane of the section. The hypocenters at the far left of the section, which correspond to those aftershocks, appear to be closely grouped on a plane dipping about 60° toward the ENE. The cross section in figure 10C (AZ 317°) is oriented to test whether the earthquakes in the main shock cluster and at depths greater than 11 to 12 km throughout the region are aligned on planes perpendicular to the plane of the section. On this section the earthquakes deeper than the main shock suggest two planes, one dipping 30° to 35° toward the southwest and the other dipping 30° to 35° toward the northeast, that cross about 1 1/2 km SW of the main shock. The cross section in figure 10B (AZ 333°) is about midway between the other two, and on it the alignments suggested on the other two cross sections are mixed or blurred. For the cross sections in figures 11 and 12 we have gone one step further and separated the group of aftershocks with E-W pressure axes in the Nunez extension from the rest of the data. Transverse (T-T') and logitudinal (R-R') sections, relative to a viewing azimuth of 347°, of the Nunez events are plotted in figure 11, and corresponding sections, relative to a viewing azimuth of 317°, of the remaining earthquakes are plotted in figure 12. On the transverse sections in these two figures, the dip directions of the planes we have selected as the fault planes for the M 3.5+ earthquakes are indicated by short lines drawn through the symbols representing the hypocenters.

On the transverse section of the Nunez events (figure 11A) dip directions are nearly parallel to the dip of the fault plane inferred from the spatial alignment of the hypocenters. On the transverse section, relative to a viewing azimuth of 317°, of the remaining earthquakes the picture is more complex (figure 12A). Dip angles have been indicated only for thrust or reverse solutions with strikes that are approximately perpendicular to the plane of the section. Strike-slip events have been labelled R or L according to whether they are right-slip or left-slip events, respectively. The best correspondence between dip angle and spatial alignment is for the NE-dipping zone of events beneath the main shock. This zone appears to be truncated by the more diffuse band of hypocenters dipping toward the southest that passes through (or just above) the main shock. The SW-dipping zone contains many strike-slip events (solid symbols) and reverse fault events with strikes that are far from perpendicular to the plane of the section (symbols with dots at their centers). For events that are in neither of these groups there is little basis for choice of the fault plane.

The 317° azimuth is nearly parallel to the axis of Anticline Ridge, and the apex of the inverted V formed by the intersection of the two zones of hypocenters described above lies about 1 1/2 km SW of the main shock, approximately beneath the axis of Anticline Ridge. On the longitudinal section (figure 12B), the strike-slip events are labelled R or L, as on the transverse section. Events that lie more than 1 1/2 km SE of the plane of the

section, i.e. SW of the axis of Anticline Ridge, are shown as solid octagons and the events NE of that plane are shown as open octagons. Although the longitudinal and transverse sections in figure 12 provide some support for visualizing patterns in the distribution of the hypocenters plotted on them, they appear to fall far short of what is needed to explore the relationship between focal mechanisms and spatial distribution of the Coalinga earthquakes and its larger aftershocks.

STEREO PLOTS OF FOCAL PLANES OF THE LARGER AFTERSHOCKS

Maps and cross sections are inadequate to unravel the complex geometry of the distribution and focal planes of the Coalinga sequence; so we shall resort to a 3-dimensional analysis based on stereo-pair plots of the fault planes determined from the focal mechanism solutions. The specific questions we hope to answer are: 1) is there evidence that will permit us to decide which of the focal planes of the main shock (a SW-dipping thrust or a NE-dipping high angle reverse fault) is the fault plane, 2) what is the relationship of events in the Nunez area to the main shock, 3) to what extent do the M 3.2+ events map out the principal fault surfaces associated with the Coalinga sequence.

For preparation of the stereo plots the aftershock region was divided into three zones (north, central and south) based on groupings of events on the epicenter map. The north zone contains the Domingine and NW clusters as well as the Nunez region. The central zone contains the main shock cluster and the northern tip of the southern cluster. The south zone contains most of the south cluster. The outlines of these zones are shown on figure 9.

To show the temporal evolution of the aftershock pattern and to separate the relatively poor data from the first two days of the sequence from the rest of the data, plots were prepared for several different time intervals and combinations thereof.

May 2 - May 4: during this period prior to significant augmentation of the net and while the background noise was unusually high, hypocenter and focal mechanism determinations were substandard,

May 5 - June 10: following augmentation of the network and after the background noise subsided, high quality hypocenter and focal mechanism determinations of a large part of the sequence were obtained,

June 11 - Sept. 30: from the occurrence of the Nunez earthquake on June 11 to the end of our study period on Sept. 30, high quality hypocentral and focal mechanism solutions were obtained for the ongoing Coalinga sequence as well as for the secondary Nunez sequence, which had its largest events in June and July.

The stereo plot program is from Paul Reasenberg (personal commun., 1984) who augmented an earlier program written by German and Johnson (1981). The Reasenberg program enables one to plot surface features (contours, etc.) and a 3-dimensional reference framework as well as to depict earthquake focal mechanisms and hypocentral locations with different symbols that are scaled according to magnitude. The symbol for a focal mechanism is a circle centered at the hypocenter and lying in one of the nodal planes with a diameter-line to show the direction of slip. The position of the viewing point can be adjusted to obtain clear views of the data that are plotted. The three reference frames that are used correspond to the three regions outlined on figure 9.

The central axis that runs through all three frames has a direction N 45° W. In separate plots of the data in the north, central, and south regions, the corresponding frames are used. In plots of data for the entire epicentral region, the central frame only is used for reference, and the data extend out both ends of the frame.

To facilitate comparison of the plotted focal mechanisms with that of the main shock, a reference plane is depicted by a gridwork of points projected vertically downward onto the reference plane from a 1 km by 1 km gridwork of points on the earth's surface. The rectangular surface region chosen to approximate the thrust fault solution for the main shock has a long axis trending N 53° W and a length and width corresponding roughly to the distribution of epicenters on figure 7. This region is probably larger than the rupture surface of the main shock, particularly in its width.

Because the focal mechanism solution does not distinguish between the fault plane and the axiliary plane, the identification of the fault plane must be based on other considerations. For the plots that follow, the selection was made so that the focal mechanism fault plane corresponds, where possible, to the fault plane suggested by the spatial distribution of hypocenters near the event in question. The number of events for which we have focal mechanism solutions is relatively small, considering the size of the region through which they are distributed and the apparent complexity of the faulting associated with the Coalinga sequence; so the evidence for choosing the fault plane is not compelling in many cases.

For practical considerations, nodal planes with southwestward dips were chosen as fault planes for the first stereo plots. Upon examination of the stereo plots, choices for individual events were altered to fulfill the criterion stated above. In the final plots presented here we judge that the evidence for the choice of fault plane is strong where the data points are relatively dense and describe portions of structures that are somewhat isolated from intersecting structures. For isolated events or for events in regions of great complexity, the evidence for the choice of fault plane is weak.

We shall begin with a sequence of plots that show the development of the aftershock pattern in space and time and enable us to evaluate the early, substandard data separately from the higher quality data obtained during most of the sequence. The reference plane strikes N 53° W and dips 25° W (compared with N 53° W and 23° W for the thrust solution for the main shock). Each figure contains two stereo pairs, one viewing the data from the NW and the other, from the SE. The whole aftershock zone is included in the plots, but only the central zone stereo frame is used for reference. The viewing point is at a depth of 5 km, above the reference plane. Contours depicting topography on the earth's surface appear to float overhead. In the view from the SE (upper pair) the viewing point is beneath Kettleman Hills and the line of sight is northwestward along the axis of Anticline Ridge, which can be seen in the contours just right of the center of the reference frame. The city of Coalinga lies on the near edge of the reference frame just to the right of the left hand side of the frame. The frame is 15 km high and has horizontal lines marking 2 1/2 km depth internals along one side. The spacing of the grid points, referred to a horizontal surface, on the reference plane is 1 km in each direction. In the view from the NW (bottom pair) the viewing point is

northwest of Anticline Ridge and the line of sight is southeastward along the axis of Anticline Ridge. The northwest end of Kettleman hills is in the distance at the center of the frame. Coalinga appears on the far boundary of the reference frame just to the left of the right hand side of the frame. In all plots containing the central section of the aftershock zone the main shock is shown for reference, whether or not it occurred in the time interval shown in the plot. It lies near the northwest edge of the central reference frame and is "pierced" by the 4th and 5th highest horizontal rows of points on the reference plane.

While viewing the plots recall that the circle depicting an event lies in one of the possible fault planes deduced from its focal mechanism and that the diameter-line shows the direction of slip.

May 2 - May 4, figure 13: Aftershocks are spread widely across the aftershock region, but in the southern part of it they are not close to the reference plane. Station coverage was particularly poor for the southern part of the aftershock zone during this interval.

May 5 - June 10, figure 14: Many events throughout the aftershock region cluster around the reference plane and have fault planes that parallel it. Along the NE edges of the northern and central zones, clusters of events suggest NE-dipping reverse faults extending from the reference plane to a depth of about 12 km. In the main shock cluster southeast of the main shock and in the southern cluster farther south there are events several kilometers above the reference plane as well as on it.

May 2- June 10, figure 15: This combined plot of the previous two intervals covers the entire sequence prior to the onset of large earthquakes in the Nunez extension. The plot closely resembles that for May 5 - June 10, with a modest enhancement of aftershocks lying above the reference plane. A few aftershocks have appeared in the Domingine cluster and at the western edge of the Nunez extension at shallow depths.

June 11 - Sept. 30, figure 16: This interval covers the development of the Nunez extension and the continuation of activity throughout the Coalinga aftershock region. Its principal features are 1) the north-trending fault surface extending from the reference plane upward to the June 11 Nunez Canyon quake beneath the zone of surface breakage that accompanied it, 2) the wide distribution of aftershocks that practically coincide with the reference plane, and 3) the M 5.3 right slip earthquake that occurred at the eastern edge of the main shock cluster on Sept. 9. Several additional aftershocks occurred in the Domingine cluster and several more occurred beneath the reference place.

May 2 - Sept. 30, figure 17: (Thrust fault reference) These plots show the entire sequence in all its complexity. Note the large number of aftershocks that lie on or near the reference plane and have fault planes that are parallel to it. Note, also, that the Nunez fault surface and the NE-dipping fault segments beneath the reference plane appear to be truncated by it.

May 2 - Sept. 30, figure 18: (Thrust fault reference) In these plots we shift the line of sight from parallel to the aftershock zone to perpendicular to it. In the upper plot, where the aftershock region is viewed from the northeast, we can see the solutions that lie below the reference plane. These events lie near a line that descends from the reference plane, at about 10 km depth, on its northern end to a depth of about 12 km beneath the main shock. They have been interpreted as northeast-dipping reverse fault earthquakes lying along the downdip edge

of a fault that extends downward from the reference plane. In the alternate interpretation (southwest-dipping reverse faults) they would define a zone of faulting parallel to the reference plane that joins it on the northwest and drops away from it towards the main shock.
In the lower plot, from the SW, we can see the solutions that are above or near the reference plane.
May 2 -Sept. 30, figure 19: (Reverse fault reference) In these plots the entire aftershock sequence is shown with a reference plane representing the high angle reverse fault solution for the main shock (strike N 53° W, dip 67° NE). The line of sight is parallel to the long axis of the aftershock zone.
May 2 - Sept. 30, figure 20: (Reverse fault reference) In these plots we again show the entire aftershock sequence with the high angle reverse fault reference plane, but with the line of sight perpendicular to the long axis of the aftershock zone.

In the previous two figures there is a poor correspondence between the reference plane and the aftershock distribution.

In the next three figures we shall examine the aftershock sequence, section by section, in more detail. The reference plane corresponds to the thrust solution for the main shock and the line of sight is parallel to the long axis of the aftershock region.

May 2 - Sept. 30, (North region), figure 21: Aftershocks in the northern region are separated into well defined, distinct groups that appear to trace out the faults that produced them. The clearest of these are:

1) aftershocks in the Nunez extension that trace out an east-dipping reverse fault that extends upward from the reference plane to the June 11 Nunez Canyon earthquake that lies beneath the zone of surface cracking associated with it.
2) aftershocks beneath the reference plane that trace out a northeast-dipping reverse fault with a northwest strike that extends from the reference plane to a depth of about 12 km.
3) aftershocks of the Domingine cluster that appear to trace out a northeastward dipping reverse fault beneath the boundary between the Great Valley and Coast Range,
4) a line of aftershocks with right-lateral strike-slip solutions that trace out the southeast-boundary of the northern region along the NE-SW-trending quiet band. Most of these solutions lie very near the reference plane although their fault planes are nearly perpendicular to the reference plane.
5) a number of widely scattered aftershocks, including most of the ones with strike-slip solutions, lie very near the reference plane.

May 2 - Sept. 30 (Central region), figure 22: The central region contains the main shock and several structures that surround it. The reference plane is marked by several events downdip and south of the hypocenter of the main shock. It also contains a dense row of small events updip and southeast of the main shock. A group of aftershocks above and parallel the reference plane appears to define a 5 x 5 km thrust fault about 2 to 3 km above the reference plane in the region of the main shock cluster. Another concentration of aftershocks beneath the main shock suggests a northeast-dipping reverse fault beneath the main shock that extends from the reference plane to a depth of about 12 km.
May 2 - Sept. 30, (Southern region), figure 23: In the southern region

several small groups of aftershocks lie on or near the reference plane. The most distinctive feature of this region, however, is the set of aftershocks that lie several kilometers above the section of the reference plane that is marked out by events that are on or near it.

CONCLUSION

From a study of the stereo plots and the focal mechanism map (for sense of motion on the faults) we believe that the data support the following conclusions:

1) The distribution and focal mechanisms of the aftershocks we have studied are more compatible with the intrepretation of the main shock mechanism as a thrust fault striking N 53° W and dipping 23° toward the southwest than as a high-angle reverse fault striking N 53° W and dipping 67° toward the northeast for the following reasons:
   a) aftershock focal planes lie on or near the thrust plane over a large part of the early aftershock region (figure 3B) in what we may call the axial concordant zone.
   b) prominent secondary structures that rise above or dip below the thrust surface appear to root in or terminate against it.
   c) most out-of-plane events lie in the upper plate above the concordant zone.

2) The sequence developed in two phases:
   a) May 2 - June 10, The spatial pattern of events established on the first day was filled in and intensified by events with the same basic distribution,
   b) June 11 - Sept. 30 The Nunez fault break developed over a period of 6 to 8 weeks while activity in the first phase aftershock region continued.

3) The axial concordant zone is cut by northeast-trending right-slip faulting along the northwest edge of the quiet zone northwest of the main shock.

4) The detached cluster of events north of the main epicentral region appears to define a northeast-dipping reverse fault.

5) Except for the events in the Nunez extension and the Domingine cluster, there are few events between the thrust surface and the earth's surface in region N, northwest of the quiet zone.

6) South of the quiet zone, in regions C and S, aftershocks between the concordant zone on the thrust and the earth's surface are plentiful, but the style of faulting above the thrust in the southern region is not well established by the present data.

7) There appears to be an abrupt cutoff in activity at about 13 km depth in the Coalinga region. This depth is essentially the same as the cutoff depth of earthquakes on the San Andreas in the Parkfield region 30 km to the southwest. The reverse faults outlined by the Coalinga aftershocks do not appear to merge with a basal detachment zone above 13 km depth.

We offer the following speculation on the cause and progress of the Coalinga sequence.

The Coalinga earthquake was generated by movement on a southwest-dipping thrust fault underlying the epicentral zone of the M 2.5+ aftershocks of the first day of the sequence. The upper plate was driven northeast against resisting rocks beneath the western edge of the Great Valley and was abruptly shortened, in the NE-SW direction, by an amount equal to the slip on the thrust. Initial rupture of the NE-dipping reverse fault along the NE edge of the north zone and of both the NE-dipping reverse fault beneath the main shock and the SW-dipping thrust above it probably also occurred at this time. The upper plate north of the quiet zone appears to have been stronger than south of the quiet zone. South of this zone the upper plate yielded to the sudden application of NE-SW compression, caused by motion on the thrust, by faulting and folding in a narrow zone beneath Anticline Ridge and Guijarral Hills. North of the quiet zone the stiff upper plate above the slipped zone on the thrust resisted internal deformation elastically and distributed the NE-SW stress over a broad region, which resulted in the shallow earthquakes beneath the Domingine region and near Nunez Canyon.

For the next 5 weeks continued forward creep on the thrust generated aftershocks along the initial slip surfaces and extended their areas, and it continued to load the upper plate, which responded with additional aftershocks in the regions brought to life by the main shock. Northeast movement of the upper plate in the region north of the quiet zone relative to that to the south was accompanied by right-lateral strike-slip faulting in the upper plate along a NE-SW-trending zone along the northwest edge of the quiet zone.

Beginning on June 11 and accelerating in mid-July, the additional stored elastic strain in the upper plate north of the quiet zone was relieved by reverse faulting on the east-dipping fault that extended from Nunez canyon to the original thrust surface. From June 11 through the end of September, continuing forward creep on the thrust and relaxation of stored strain in the upper plate continued to produce aftershocks in the regions that were active prior to June 11 as well as on the Nunez fault.

By Sept. 9, deformation of the upper plate in the main shock cluster had sufficiently reduced the compressive forces perpendicular to Anticline Ridge that a NNW-trending strike slip fault at the NE edge of the main shock cluster came unpinned by the reduction in the normal component of stress across it, and it moved (right slip) to produce the last M 5+ aftershock of the sequence.

REFERENCES

Allen, R., Automatic phase pickers: their present use and future prospects: Seismol. Soc. Amer. Bull., v 74, p. S225-S242, 1982.

Eaton, J., R. Cockerham, and F. Lester, Study of the May 2, 1983 Coalinga earthquake and its aftershocks, based on the USGS seismic network in northern California, in The 1983 Coalinga, California Earthquakes, Special Publ. 66, Calif. Div. of Mines and Geology, p. 261-273, 1983.

German, Peter, and Carl Johnson, STEREO, A Computer Program for Projecting and Plotting Stereograms, U.S. Geological Survey Open-File Report 82-726, 1981.

Lee, W. H. K., and J. C. Lahr, HYPO71(Revised): A computer program for determining hypocenter, magnitude, and first motion pattern of local earthquakes, U.S. Geological Survey Open-File Report 75-311, 1975.

FIGURE CAPTIONS

Figure 1
Map showing the location of the Coalinga earthquake (open circle labelled MS), the San Andreas Fault (S.A.F.), the Coast Ranges-Great Valley boundary (500' contour), the seismograph stations of the portable network (solid squares), the pre-May 2 telemetered network (solid triangles), and the post-May 2 additions to the telemetered network (open triangles inside circles).

Figure 2
Map of the Coalinga earthquake and its aftershocks of M 2.5 and greater, from May 2 through Sept. 30, superposed on a simplified map of the principal physiographic features in the Coalinga region. Contours below 400' and above 1000' are omitted. Aftershock screening parameters were: magnitude $\geq$ 2.5, r.m.s. of traveltime residuals $<$ 0.20 sec, number of stations used in the hypocenter determination $\geq$ 12, distance to nearest station $\leq$ 30 km, estimated epicentral error $\leq$ 3 km.

Figure 3
Maps of the Coalinga earthquake and its aftershocks for the first day (fig. 3A) and for the first five months (fig. 3B) of the aftershock sequence. Screening parameters were the same as for figure 2. Various aftershock clusters discussed in the text are identified on figures 3A and 3B, and lines of section shown in figures 4, 5, and 6 are shown as R-R' (longitudinal) and T-T' (transverse) on figure 3B.

Figure 4
Longitudinal sections of the aftershock sequence for the first day (fig. 4A) and the first five months (fig. 4B) along the line R-R' shown on figure 3B. The aftershock screening parameters are the same as for figure 2.

Figure 5
Transverse cross sections of the first day of the aftershock sequence, along the line T-T' shown on figure 3B, for the region northwest of the main shock (figure 5A), southeast of the main shock (fig. 5B), and the entire aftershock region (fig. 5C). The aftershock screening parameters are the same as for figure 2.

Figure 6
Transverse cross sections of the first five months of the aftershock sequence, along the line T'T shown on figure 3B, for the region northwest of the main shock (fig. 6A), southeast of the main shock (figure 6B), and the entire aftershock region (fig. 6C). The aftersock screening parameters are the same as for figure 2.

Figure 7
Map of the Coalinga earthquakes and its larger aftershocks for May 2 through Sept. 30 superposed on a simplified map of the principal physiographic features of the Coalinga region. Contours below 400' and above 1000' are omitted. The plotting symbols are scaled according to mangitude and coded for depth according to the following scheme: A = 0 to 1 km, B = 1 to 2 km, C = 2 to 3 km,..., O = 14 to 15 km. The main shock

is represented by the letter "K" and lies about 1 1/2 km northeast of the word "ANTICLINE".

Figure 8
Map of focal mechanisms of the Coalinga earthquake and its larger aftershocks. The map base is the same as in figure 7. On the focal mechanism symbol dark areas represent compressional first arrivals and white areas, dilatational first arrivals. The symbols are not scaled according to magnitude.

Figure 9
Map of inferred pressure-axis directions of the Coalinga earthquake and its larger aftershocks from May 2 through Sept. 30. The arrows showing the orientation of the P-axes are scaled according to magnitude and point along the P-axes in their downdip directions. The map base is the same as in figure 7. The boxes labelled N, C, and S divide the aftershock region into three subregions that are discussed with the stereo plots in what follows.

Figure 10
Transverse cross sections, relative to the viewing azimuths (AZ) indicated on the plots, of the Coalinga earthquake and its larger aftershocks.

Figure 11
Transverse (Fig. 11A) and longitudinal (Fig. 11B) cross sections, relative to a viewing azimuth of 347°, of aftershocks in the Nunez extension with nearly E-W P-axes. The origin of horizontal coordinates is the main shock epicenter. On the transverse section, the fault plane dip angles are shown by short line segments across the hypocenter symbol.

Figure 12
Transverse (fig. 12A) and longitudinal (fig. 12B) cross sections, relative to a viewing azimuth of 317°, of aftershocks of the Coalinga sequence excluding the Nunez extension events plotted in figure 11. The origin of horizontal coordinates is the main shock epicenter. On the transverse cross section (fig. 12A) the fault plane dip angles of the larger reverse fault solutions are indicated by short line segments across the hypocenter symbols. Strike slip events (solid symbols) are labelled R (right slip) or L (left slip) according to their sense of slip, and events with strikes that are far from perpendicular to the section are shown as octagons with dots at their centers. On the longitudinal cross section (fig. 12B) the solid symbols show events with transverse coordinates (see fig. 12A) smaller than -1.5 km. Such events lie southwest of the longitudinal axis of Anticline Ridge. Strike-slip solutions are labelled as in figure 12A.

Figure 13
Stereo-pair plots of the fault planes of the Coalinga earthquake and its aftershocks of May 2 through May 4. Views from the SE (top) and NW (bottom). Reference frame C (fig. 9). Thrust fault reference plane: strike N 53°W, dip 25°SW. Horizontal spacing of points on the reference plane is 1 km x 1 km. See text for explanation of plots.

Figure 14
Stereo-pair plots of the fault planes of the Coalinga earthquake and its

aftershocks of May 5 through June 10. Views from the SE (top) and NW (bottom). Reference frame C (fig. 9). Thrust fault reference plane: strike N53°W, dip 25°SW. Horizontal spacing of points on the reference plane is 1 km x 1 km. See text for explanation of plots.

Figure 15
Stereo-pair plots of the fault planes of the Coalinga earthquake and its aftershocks of May 2 through June 10. Views from the SE (top) and NW (bottom). Reference frame C (fig. 9). Thrust fault reference plane: strike N 53°W, dip 25°SW. Horizontal spacing of points on the reference plane is 1 km x 1 km. See text for explanation of plots.

Figure 16
Stereo-pair plots of the fault planes of the Coalinga earthquake and its aftershocks of June 11 through Sept. 30. Views from the SE (top) and NW (bottom). Reference frame C (fig. 9). Thrust fault reference plane: strike N 53°W, dip 25°SW. Horizontal spacing of points on the reference plane is 1 km x 1 km. See text for explanation of plots.

Figure 17
Stereo-pair plots of the fault planes of the Coalinga earthquake and its aftershocks of May 2 through Sept. 30. Views from the SE (top) and NW (bottom). Reference frame C (fig. 9). Thrust fault reference plane: Strike N 53°W, dip 25°SW. Horizontal spacing of points on the reference plane is 1 km x 1 km. See text for explanation of plots.

Figure 18
Stereo-pair plots of the fault planes of the Coalinga earthquake and its aftershocks of May 2 through Sept. 30. Views from the NE (top) and SW (bottom). Reference frame C (fig. 9). Thrust fault reference plane: strike N 53°S, dip 25°SW. Horizontal spacing of points on the reference plane is 1 km x 1 km. See text for explanation of plots.

Figure 19
Stereo-pair plots of the fault planes of the Coalinga earthquake and its aftershocks of May 2 through Sept. 30. Views from SE (top) and NW (bottom). Reference frame C (fig. 9). High angle reverse fault reference plane: strike N 53°W, dip 67°NE. Horizontal spacing of points of the reference plane is 1 km x 1 km. See text for explanation of the plots.

Figure 20
Stereo-pair plots of the fault planes of the Coalinga earthquake and its aftershocks of May 2 through Sept. 30. Views from the NE (top) and SW (bottom). Reference frame C (fig. 9). High angle reverse fault reference plane: strike N 53°W, dip 67° NE. Horizontal spacing of points on the reference plane is 1 km x 1 km. See text for explanation of plots.

Figure 21
Stereo-pair plots of fault planes of aftershocks of the Coalinga earthquake in region N (fig. 9) from May 2 through Sept. 30. Views from the SE (top) and NW (bottom). Reference frame N (fig. 9). Thrust fault reference plane: Strike N 53°W, dip 25° SW. Horizontal spacing of points on the reference plane is 1 km x 1 km. See text for explanation of plots.

Figure 22

Stereo-pair plots of fault planes of the Coalinga earthquake and its aftershocks in region C (fig. 9) from May 2 through Sept. 30. Views from the SE (top) and NW (bottom). Reference frame C (fig. 9). Thrust fault reference plane: strike N 53°W, dip 25°SW. Horizontal spacing of points on the reference plane is 1 km x 1 km. See text for explanation of plots.

Figure 23

Stereo-pair plots of fault planes of aftershocks of the Coalinga earthquake in region S (fig. 9). Views from the SE (top) and NW (bottom). Reference frame S (fig. 9). Thrust fault reference plane: strike N 53°W, dip 25°SW. Horizontal spacing of points on the reference plane is 1 km x 1 km. See text for explanation of plots.

Figure 24a-r

First motion plots and fault-plane solutions for the Coalinga earthquake and 107 of its largest aftershocks. On the plots the letters C, B, and A represented 1, 2, and 3 compressional first arrivals, respectively, and D, E, F represent 1, 2, and 3 dilatational first arrivals, respectively. Conflicting first arrivals are represented by the letter X. P and T denote the inferred axes of maximum and minimum compressional stress (Pressure and Tension axes). Strikes and dips of the two nodal planes and the azimuth of the P-axis are shown on the diagrams and are listed in table 3.

Table 1

Crustal models used with the Coalinga earthquakes. Model 4 was used with RTP data to locate earthquakes larger than about M 1.7, including those shown in figures 2 through 6. Model 5 was used to located the larger events, for which focal mechanisms were determined, that are shown in figures 7 through 24.

Table 2

Station list with station delays for model 4 (DLY4) and model 5 (DLY5) and with station magnitude corrections (MCOR). Stations farther than 120 km from the main Coalinga earthquake are flagged with an asterisk. The standard values for MCOR are 0.0 for horizontal component instruments (xxxN or xxxE) and +0.25 for vertical component instruments (xxx or xxxZ). CALIB is proportional to the magnification of the seismic system and indicates the relative magnifications of different stations.

Table 3

List of larger Coalinga aftershocks showing hypocentral parameters and focal mechanisms. DATE, TIME, LAT, LON, DEPTH, and MAG are the date, time, latitude, longitude, depth, and local magnitude of the event. NS is the number of phases used in the hypocenter determination. GAP is the largest azimuthal gap in station coverage. DMIN is the distance in kilometers to the nearest station. RMS is the root mean square of arrival time residuals. ERH and ERZ are the estimated erros in epicenter and focal depth, respectively, in kilometers. AZM PAX is the azimuth of the Pressure-axis FLT PLN STR and FLT PLN DIP are the strike and dip of the fault plane, respectively. AUX PLN STR and AUX PLN DIP are the strike and dip of the auxiliary plane, respectively. (POLE F PLN) AZ, DP, and TYP are the azimuth and dip of the pole of the fault plane and the type of fault motion associated with the fault plane, respectively. (POLE A PLN) AZ, DP and TYP are the azimuth and dip of the pole of the auziliary plane and the type of faulting that would be associated with the auxiliary plane if it were the fault plane, respectively. T = thrust, R = reverse, RS = right slip, and LS = left slip.

TABLE 1 Crustal models used with the Coalinga earthquakes

MODEL 4		MODEL 5	
VELOCITY	DEPTH TO LAYER	VELOCITY	DEPTH TO LAYER
2.50km/sec	0.00km	2.50km/sec	0.00km
4.50	2.00	4.30	1.50
5.60	7.00	4.70	3.50
5.70	10.00	5.60	7.00
6.40	14.00	5.80	9.00
7.90	28.00	6.30	14.00
		6.60	15.50
		7.95	28.00

TABLE 2 Station list with station delays for model 4 (DLY4), model 5 (DLY5), and magnitude station corrections (MCOR). Stations farther than 120 km from the main shock are flagged with an asterisk.

	STN	LAT	LON	EL	DLY4	DLY5	MCOR	CALIB
*	ADW	3826.35N	12050.89W	251	0.	0.58	-0.02	11.152
*	ALA	3834.00N	12057.37W	293	0.	0.56	0.13	23.300
*	AOD	3836.89N	12043.71W	520	0.	1.38	0.21	11.152
*	ARJ	3841.19N	12057.38W	460	0.	0.77	0.14	11.152
	BAV	3638.75N	121 1.79W	604	-0.43	-0.47	0.82	23.300
	BAVE	3638.75N	121 1.79W	604	-0.43	-0.47	0.34	0.353
	BAVN	3638.75N	121 1.79W	604	-0.43	-0.47	0.33	0.353
	BAVZ	3638.75N	121 1.79W	604	-0.43	-0.47	0.46	0.353
	BBG	3635.48N	121 1.52W	1216	0.09	0.02	0.37	11.152
	BBN	3630.60N	121 4.53W	448	-0.09	-0.26	0.25	23.300
	BCG	3642.55N	12120.60W	305	-0.05	-0.01	0.34	5.590
	BEH	3639.88N	12110.45W	342	-0.13	-0.26	0.29	5.590
	BEM	3639.68N	121 5.76W	488	-0.09	-0.28	0.36	11.152
	BHR	3643.67N	12115.83W	213	-0.09	-0.25	-0.19	5.590
	BHS	3621.35N	12132.39W	646	-0.34	-0.25	2.04	5.590
	BJC	3632.82N	12123.53W	207	-0.60	-0.62	0.84	23.300
	BJO	3636.65N	12118.81W	1052	-0.49	-0.58	0.52	11.152
	BLR	3639.96N	12116.36W	232	0.12	0.07	0.25	11.152
	BMS	3639.78N	12047.51W	811	-0.08	-0.05	0.36	5.590
*	BPC	3634.32N	12137.56W	183	-0.32	-0.25	0.13	11.152
*	BPCN	3634.32N	12137.56W	183	-0.32	-0.25	-0.49	0.353
*	BPF	3613.80N	12146.30W	349	-0.49	-0.61	0.26	5.590
*	BPFN	3613.80N	12146.30W	349	-0.49	-0.61	-0.25	0.353
	BPI	3629.40N	12110.41W	329	-0.66	-0.75	0.58	23.300
	BPP	3610.12N	12122.68W	1591	-0.45	-0.59	0.17	11.152
	BRM	3650.70N	12049.42W	372	0.01	0.16	0.11	5.590
	BRV	3625.49N	121 1.10W	541	-0.01	-0.32	0.30	5.590
	BSC	3638.50N	12115.59W	323	-0.22	-0.37	0.37	11.152
	BSCE	3638.50N	12115.59W	323	-0.22	-0.37	0.11	0.353
	BSCN	3638.50N	12115.59W	323	-0.22	-0.37	0.19	0.353
	BSCZ	3638.50N	12115.59W	323	-0.22	-0.37	0.28	0.353
	BSG	3624.83N	12115.22W	192	-0.65	-0.78	0.47	5.590
	BSGE	3624.83N	12115.22W	192	-0.65	-0.78	0.08	0.353
	BSGN	3624.83N	12115.22W	192	-0.65	-0.78	-0.02	0.353
	BSGZ	3624.83N	12115.22W	192	-0.65	-0.78	0.30	0.353
	BSR	3639.99N	12131.12W	395	-0.37	-0.38	0.52	11.152
	BSRE	3639.99N	12131.12W	395	-0.37	-0.38	-0.23	0.353
	BSRN	3639.99N	12131.12W	395	-0.37	-0.38	-0.18	0.353
	BSRZ	3639.99N	12131.12W	395	-0.37	-0.38	0.13	0.353
	BVL	3634.51N	12111.34W	510	-0.29	-0.39	0.57	23.300
	BVY	3644.96N	12124.80W	585	-0.27	-0.26	0.63	23.300
*	CAL	3727.07N	12147.95W	265	0.	-0.25	0.57	23.300
*	CALE	3727.07N	12147.95W	265	0.	-0.25	-0.27	0.353
*	CALN	3727.07N	12147.95W	265	0.	-0.25	0.38	0.353
*	CALZ	3727.07N	12147.95W	265	0.	0.25	0.37	0.353
*	CAO	3720.96N	12131.96W	628	-0.42	-0.17	0.40	23.300
*	CAOE	3720.96N	12131.96W	628	-0.42	-0.17	0.22	0.353
*	CAON	3720.96N	12131.96W	628	-0.42	-0.17	0.19	0.353
*	CAOZ	3720.96N	12131.96W	628	-0.42	-0.17	0.29	0.353
*	CDV	3733.98N	12140.81W	250	0.	-0.11	0.73	11.152
*	CDVE	3733.98N	12140.81W	250	0.	-0.11	0.26	0.353
*	CDVN	3733.98N	12140.81W	250	0.	-0.11	0.17	0.353

*	CDVZ	3733.98N	12140.81W	250	0.	-0.11	0.24	0.353
*	CMP	3721.46N	12118.51W	799	-0.60	-0.44	0.45	5.590
	EAQ	3621.31N	12014.80W	97	0.20	0.65	0.16	4.504
	EAQE	3621.31N	12014.80W	97	0.20	0.65	-0.11	4.504
	EAQN	3621.31N	12014.80W	97	0.20	0.65	-0.14	4.504
	ECT	3624.09N	12026.14W	232	0.35	0.38	0.78	17.930
	ECTE	3624.09N	12026.14W	232	0.35	0.38	0.66	17.930
	ECTN	3624.09N	12026.14W	232	0.35	0.38	0.41	17.930
	EDQ	3620.15N	12021.25W	296	0.35	0.28	0.54	17.930
	EDQE	3620.15N	12021.25W	296	0.35	0.28	0.55	17.930
	EDQN	3620.15N	12021.25W	296	0.35	0.28	0.35	17.930
	EDN	3615.00N	12023.04W	415	0.30	0.08	0.46	17.930
	EDNE	3615.00N	12023.04W	415	0.30	0.08	0.33	17.930
	EDNN	3615.00N	12023.04W	415	0.30	0.08	0.24	17.930
	EGR	3606.53N	12004.47W	101	0.26	0.32	-0.16	4.504
	EGRE	3606.53N	12004.47W	101	0.26	0.32	-0.25	4.504
	EGRN	3606.53N	12004.47W	101	0.26	0.32	-0.37	4.504
	EPM	3613.12N	12017.07W	250	0.35	0.05	0.31	4.504
	EPME	3613.12N	12017.07W	250	0.35	0.05	0.02	4.504
	EPMN	3613.12N	12017.07W	250	0.35	0.05	-0.04	4.504
	ESK	3617.58N	12018.41W	256	0.35	0.15	0.41	8.990
	ESKE	3617.58N	12018.41W	256	0.35	0.15	0.28	8.990
	ESKN	3617.58N	12018.41W	256	0.35	0.15	0.16	8.990
	ETK	3622.42N	12005.04W	77	0.04	0.38	0.18	4.504
	ETKE	3622.42N	12005.04W	77	0.04	0.38	-0.16	4.504
	ETKN	3622.42N	12005.04W	77	0.04	0.38	-0.29	4.504
	ETM	3624.06N	12005.04W	72	0.04	0.25	-0.17	2.256
	ETME	3624.06N	12005.04W	72	0.04	0.25	-0.48	2.256
	ETMN	3624.06N	12005.04W	72	0.04	0.25	-0.59	2.256
	ETU	3609.09N	12017.95W	186	0.30	0.07	0.10	4.504
	ETUE	3609.09N	12017.95W	186	0.30	0.07	-0.05	4.504
	ETUN	3609.09N	12017.95W	186	0.30	0.07	-0.16	4.504
	EVV	3615.89N	12001.78W	88	0.07	0.44	-0.08	8.990
	EVVE	3615.89N	12001.78W	88	0.07	0.44	-0.34	8.990
	EVVN	3615.89N	12001.78W	88	0.07	0.44	-0.35	8.990
	EWH	3629.44N	12015.11W	76	0.10	0.61	-0.06	2.256
	EWHE	3629.44N	12015.11W	76	0.10	0.61	-0.20	2.256
	EWHN	3629.44N	12015.11W	76	0.10	0.61	-0.38	2.256
	EYU	3612.83N	12010.63W	128	0.27	0.23	-0.04	8.990
	EYUE	3612.83N	12010.63W	128	0.27	0.23	-0.22	8.990
*	HFE	3659.00N	12124.09W	323	-0.13	-0.09	0.19	5.590
	HFP	3645.22N	12129.43W	705	-0.51	-0.48	0.60	23.300
*	HGS	37 5.75N	12126.83W	778	-0.35	0.01	0.25	11.152
*	HJQ	3647.88N	12134.43W	171	-0.41	-0.36	0.47	11.152
	HJS	3648.99N	12117.92W	215	-0.45	-0.24	0.35	11.152
	HLT	3653.07N	12118.49W	183	-0.13	-0.05	0.41	11.152
*	HMQ	3636.03N	12155.06W	192	-0.52	-0.42	0.31	5.590
*	HPL	37 3.13N	12117.40W	152	-0.31	-0.16	0.25	5.590
*	HPLE	37 3.13N	12117.40W	152	-0.31	-0.16	-0.04	0.353
*	HPLN	37 3.13N	12117.40W	152	-0.31	-0.16	0.24	0.353
*	HPLZ	37 3.13N	12117.40W	152	-0.31	-0.16	0.38	0.353
	HQR	3650.02N	12112.76W	536	-0.15	-0.06	0.44	11.152
	HQRE	3650.02N	12112.76W	536	-0.15	-0.06	-0.05	0.353
	HQRN	3650.02N	12112.76W	536	-0.15	-0.06	-0.03	0.353
	HQRZ	3650.02N	12112.76W	536	-0.15	-0.06	0.24	0.353
	HSL	37 1.16N	121 5.13W	520	-0.58	-0.44	0.14	5.590
*	HSP	3706.91N	12130.94W	850	-0.30	-0.34	0.30	11.152
*	JSF	3724.31N	12210.55W	143	0.	-0.11	0.07	2.800
*	JSFE	3724.31N	12210.55W	143	0.	-0.11	-0.12	0.353
*	JSFN	3724.31N	12210.55W	143	0.	-0.11	0.01	0.353

*	JSFZ	3724.31N	12210.55W	143	0.	-0.11	0.18	0.353
*	KMPE	4025.04N	12407.21W	957	0.	-0.20	-0.15	0.353
*	KMPN	4025.04N	12407.21W	957	0.	-0.20	-0.19	0.353
*	LTCN	4012.50N	122 7.45W	257	0.	-0.20	-0.62	0.353
*	MAT	3752.40N	11952.00W	1353	-0.50	0.87	-0.02	5.590
*	MCH	38 1.12N	12030.57W	475	0.	0.47	0.16	11.152
	MHD	37 7.18N	11954.97W	146	-1.46	-1.22	0.71	11.152
*	MNH	38 8.75N	12048.82W	219	0.	0.03	0.32	23.300
*	MNP	3724.88N	11943.68W	1000	-0.59	-0.20	0.39	11.152
*	MNPN	3724.82N	11943.51W	975	-0.59	0.87	-0.31	0.353
*	MOY	3754.00N	12034.04W	176	0.	0.09	0.24	11.152
*	MRF	3814.72N	12031.24W	799	0.	0.94	0.03	11.152
*	MST	3754.27N	12024.29W	366	0.	0.35	0.10	11.152
*	NMHN	3840.17N	12237.93W	1311	0.	-0.20	-0.22	0.353
*	NVE	3822.36N	12226.17W	707	0.	-0.22	0.26	2.800
*	NVEN	3822.36N	12226.17W	707	0.	-0.22	-0.27	0.353
	PAD	3538.36N	12051.86W	471	-0.12	-0.44	0.26	5.590
	PAG	3543.92N	12014.96W	482	-0.26	-0.68	0.07	5.590
	PAN	3546.78N	12054.44W	451	-0.11	-0.48	0.25	11.152
	PAP	3554.77N	12121.70W	1015	-0.21	-0.43	0.54	11.152
	PAR	3614.95N	12020.52W	485	0.24	0.10	0.25	5.590
	PAV	3510.55N	12037.95W	133	-0.13	-0.07	-0.08	2.800
*	PBI	35 9.68N	12028.42W	561	0.11	0.02	0.25	11.152
	PBR	3532.91N	12100.54W	85	0.03	-0.31	-0.03	5.590
	PBW	3618.90N	12055.75W	381	-0.16	-0.41	0.52	5.590
	PBY	3548.90N	12104.89W	335	-0.29	-0.56	0.25	5.590
	PCA	3555.90N	12020.22W	1189	0.17	-0.26	1.36	11.152
	PCG	3525.52N	12044.34W	314	-0.08	-0.45	0.60	11.152
	PCR	36 5.63N	12026.08W	296	-0.14	-0.58	0.25	11.152
	PDR	3620.14N	12022.12W	488	0.15	0.22	0.25	0.
	PGH	3549.86N	12021.17W	433	-0.08	-0.52	0.76	11.152
	PHA	3550.16N	12023.91W	455	0.20	-0.26	0.25	11.152
	PHB	3614.93N	12004.96W	100	0.47	0.55	0.25	0.
	PHC	3540.93N	121 9.15W	514	-0.12	-0.34	0.67	11.152
	PHG	3552.56N	12029.01W	792	0.25	-0.19	1.52	11.152
	PHGE	3552.56N	12029.01W	792	0.25	-0.19	-0.19	0.353
	PHGN	3552.56N	12029.01W	792	0.25	-0.19	-0.26	0.353
	PHGZ	3552.56N	12029.01W	792	0.25	-0.19	0.01	0.353
	PHR	3622.38N	12049.10W	732	-0.23	-0.40	0.25	11.152
	PHRN	3622.38N	12049.10W	732	-0.23	-0.40	0.16	0.353
	PIV	3554.39N	12040.94W	497	0.20	-0.26	0.25	2.800
	PJL	36 5.39N	121 9.33W	290	-0.24	-0.45	0.94	11.152
	PJLE	36 5.39N	121 9.33W	290	-0.24	-0.45	-0.14	0.353
	PJLN	36 5.39N	121 9.33W	290	-0.24	-0.45	-0.11	0.353
	PJLZ	36 5.39N	121 9.33W	290	-0.24	-0.45	0.06	0.353
	PKE	36 3.69N	120 6.54W	288	0.26	0.06	0.25	0.
	PLO	3614.79N	121 2.55W	308	-0.40	-0.70	0.07	5.590
	PMC	3543.48N	12022.23W	488	0.	-0.39	0.25	11.152
	PMCE	3543.48N	12022.23W	488	0.	-0.39	0.02	0.353
	PMCN	3543.48N	12022.23W	488	0.	-0.39	-0.06	0.353
	PMCZ	3543.48N	12022.23W	488	0.	-0.39	0.11	0.353
	PMG	3525.79N	12031.22W	529	-0.54	-0.81	0.43	11.152
	PMP	3612.91N	12047.69W	784	0.05	-0.24	0.25	11.152
	PMPN	3612.91N	12047.69W	784	0.05	-0.24	0.02	0.353
	PMR	3547.09N	12014.14W	512	-0.03	-0.44	0.25	11.152
	PPF	3552.91N	12024.81W	469	0.25	-0.20	0.25	11.152
	PPR	3538.86N	12042.04W	279	-0.19	-0.63	0.22	2.800
	PPT	36 6.50N	12043.27W	506	-0.04	-0.33	0.25	5.590
	PRC	3615.37N	12037.20W	623	-0.12	-0.28	0.25	11.152
	PRCN	3615.37N	12037.20W	623	-0.12	-0.28	0.08	0.353

	PSA	36 1.52N	12053.30W	184	-0.25	-0.66	0.30	2.800
	PSE	3514.71N	12045.88W	201	-0.30	-0.45	0.17	11.152
	PSH	3535.45N	12024.92W	390	-0.05	-0.41	0.83	11.152
	PSM	36 4.18N	12035.68W	988	0.34	0.01	0.25	11.152
	PSR	3551.47N	12016.81W	552	0.22	-0.18	0.25	11.152
	PST	3556.48N	12031.53W	616	0.33	-0.09	0.25	11.152
	PTR	3539.28N	12012.67W	643	-0.13	-0.53	0.45	5.590
	PWK	3548.87N	12030.67W	503	0.16	-0.25	0.25	11.152
	PWM	3625.97N	12012.66W	72	0.61	0.75	0.25	0.
*	SCC	3456.38	12010.32	610	-0.26	0.05	0.59	11.152
*	SLC	3429.79	11942.81	1190	0.	0.02	0.06	5.590
*	SLP	3433.57	12024.02	134	0.	-0.35	0.18	5.590
	TBH	3511.10	12005.05	1140	-0.54	-0.56	0.80	23.300
*	TBM	3508.15	11835.81	1237	0.	-0.66	0.63	23.300
*	TCG	3514.53	11943.40	1204	0.20	-0.51	0.25	5.590
*	TTR	3505.24	11932.08	1021	0.30	-0.67	-0.21	2.800
	TYG	3526.18	11957.56	939	-0.46	-0.82	0.55	11.152
*	WAS	3544.29N	11833.42W	1871	-0.59	-0.29	0.49	11.152
*	WBR	3536.48	11753.40	925	0.	1.03	-0.18	11.152
*	WBS	3532.22N	11808.37W	1932	0.	1.76	-0.05	11.152
*	WCH	3552.98N	11804.48W	2475	0.	1.04	0.20	11.152
*	WCO	3537.35N	11826.25W	1609	0.	-0.07	0.67	23.300
*	WCS	36 1.58N	11746.01W	1143	0.	0.93	0.32	23.300
*	WCX	3542.63N	11735.98W	671	0.	0.28	0.31	23.300
*	WHF	3541.77N	11820.91W	902	0.	0.18	0.11	11.152
*	WHS	36 6.30N	11745.67W	1448	0.	0.94	-0.01	23.300
*	WHV	3530.60N	11831.07W	1006	0.	-0.50	0.15	11.152
*	WKT	3547.64N	11826.55W	890	0.	-0.17	0.01	11.152
*	WNM	3550.57N	11754.29W	951	0.	1.11	-0.03	11.152
*	WOF	3532.14N	11842.75W	1341	-1.10	-0.95	0.10	11.152
*	WOR	3541.79N	11814.52W	837	0.	0.38	0.09	11.152
*	WRC	3557.04N	11738.89W	945	0.	1.13	-0.02	23.300
*	WSH	3537.96	11729.50	780	0.	0.41	-0.37	11.152
*	WSN	3541.51	11744.96	698	0.	1.04	-0.45	5.590
*	WTO	3548.50	11745.90	314	0.	1.22	-0.62	5.590
*	WWP	3544.13N	11805.22W	1151	0.	0.81	0.45	23.300
*	CLK	3735.44N	11849.45W	2576	0.	1.58	0.	0.
*	DOE	3738.25N	11850.00W	1700	0.	1.96	0.	0.
*	EMH	3740.00N	11856.35W	2451	0.	1.86	0.	0.
*	LCC	3736.65N	11854.92W	2511	0.14	1.52	0.	0.
*	LMC	3743.70N	11856.71W	2530	0.	2.16	0.	0.
*	MQN	3748.80N	11841.73W	2472	0.	2.37	0.	0.
*	MLK	3739.88N	11858.53W	2671	0.	1.83	0.	0.
*	MMC	3821.65N	119 7.70W	2548	0.	2.25	0.	0.
*	ORC	3738.12N	11839.36W	2301	0.	2.02	0.	0.
*	SCH	3721.95N	11841.22W	2365	0.68	1.49	0.	0.
*	SHL	3737.05N	11857.25W	2499	0.	1.50	0.	0.
*	TAC	3737.93N	11857.91W	2398	0.	1.67	0.	0.

TABLE 3 List of larger Coalinga aftershocks. In addition to the usual hypocentral parameters the azimuth of the P-axis, the strikes and dips of the fault and auxiliary planes, and the azimuths and dips of the poles of the fault and auxiliary planes are given.

DATE	TIME	LAT	LON	DEPTH	MAG	NS	GAP	DMIN	RMS	ERH	ERZ		AZM PAX	FLT PLN STR	FLT PLN DIP	AUX PLN STR	AUX PLN DIP	POLE F PLN AZ	POLE F PLN DP	TYP	POLE A PLN AZ	POLE A PLN DP	TYP
830502	2342 38.14	36-13.96	120-18.57	10.01	6.70	30	214	3.4	0.05	0.3	0.2	CC	37	N53W	23SW	N53W	67NE	217	23	T	37	67	R
830503	039 46.01	36-13.81	120-20.93	11.33	4.52	31	152	2.2	0.06	0.3	0.2	BC	254	N24E	70NW	N58W	68NE	212	22	RS-R	114	20	LS-R
830503	057 44.25	36-16.23	120-20.07	8.13	5.08	31	214	2.5	0.07	0.4	0.3	CC	257	N13W	54SW	N13W	36NE	257	54	R	76	36	T
830503	141 45.96	36- 8.54	120-13.12	6.73	4.54	27	221	16.2	0.11	0.7	2.9	CC	18	N46W	45SW	N86E	56NW	176	34	R-RS	44	45	R-LS
830503	155 46.44	36-13.93	120-17.93	6.90	4.00	30	216	4.3	0.14	0.8	0.5	CC	16	N45W	44SW	N83E	59NW	177	31	T-RS	45	46	R-LS
830503	215 14.90	36-14.29	120-17.08	8.81	4.08	30	218	5.3	0.07	0.4	0.3	CC	196	N75W	10SW	N75W	80NE	195	19	T	15	80	R
830503	226 8.83	36-17.44	120-22.19	9.85	3.30	36	194	5.2	0.13	0.5	0.4	CC	66	N24W	32SW	N24W	58NE	246	32	T	66	58	R
830503	431 11.58	36-18.08	120-24.29	11.10	3.78	35	177	8.1	0.08	0.3	0.2	BC	33	N30W	17NE	N49W	74SW	41	17	T-RS	240	73	R-LS
830503	6 4 46.18	36-16.22	120-23.72	10.08	4.51	34	155	5.3	0.09	0.3	0.3	BC	265	N16W	31NE	N 0W	60 W	254	59	R-RS	90	30	T-LS
830503	612 50.35	36-15.31	120-22.23	8.34	3.78	35	145	2.6	0.18	0.8	0.7	CC	208	N62W	10SW	N62W	80NE	208	10	T	28	80	R
830503	635 3.23	36-12.99	120-17.20	12.80	4.25	32	216	6.2	0.07	0.4	0.2	CC	46	N65W	60NE	N15W	42SW	75	48	R-LS	205	30	T-RS
830503	855 1.99	36- 8.84	120-16.01	10.31	4.70	27	206	13.2	0.08	0.4	0.4	CC	358	N80E	41SE	N84W	50NE	186	40	T-LS	350	49	R-RS
830503	939 45.70	36-16.14	120-16.28	9.87	4.11	33	222	6.7	0.18	0.8	0.7	CC	57	N32W	53NE	N34W	37SW	56	53	R	238	37	T
830503	1510 35.74	36-17.24	120-20.27	8.20	3.95	32	215	4.2	0.07	0.4	0.3	CC	239	N 2E	70NW	N72W	52NE	198	38	RS-R	92	20	LS-R
830503	1541 41.56	36-14.13	120-18.15	7.89	4.78	30	215	3.9	0.10	0.5	0.4	CC	34	N61W	44SW	N48W	47NE	222	43	T-LS	29	46	R-RS
830503	2346 4.35	36- 9.09	120-20.19	13.88	3.96	39	148	10.9	0.12	0.4	0.4	BC	263	N 2E	48NW	N17W	44NE	253	46	R-RS	92	42	T-LS
830504	818 8.54	36-14.11	120-15.92	8.76	2.93	41	94	2.5	0.12	0.3	0.2	BC	70	N31W	30SW	N14W	61NE	256	29	T-LS	59	60	R-RS
830504	848 53.12	36-13.48	120-16.68	12.94	3.48	43	96	0.9	0.10	0.2	0.2	BC	244	N30W	20NE	N24W	70SW	66	20	T-LS	240	70	R-RS
830504	1329 15.91	36- 6.54	120-13.23	9.96	3.39	37	134	8.5	0.13	0.4	0.5	BC	180	N90W	22 N	N90W	68 S	0	22	T	180	68	R
830504	1559 13.99	36-14.62	120-17.47	7.13	3.78	42	84	2.8	0.10	0.2	0.3	AC	241	N28W	48SW	N28W	42NE	214	48	R	180	68	R
830504	1611 19.63	36-16.89	120-20.93	11.67	4.39	47	53	3.6	0.07	0.2	0.1	AC	216	N69W	47NE	N36W	48SW	54	42	R-LS	201	43	R-RS
830504	1945 2.86	36- 7.19	120-16.15	7.44	3.44	38	121	4.4	0.17	0.4	0.7	BC	202	N87W	60SW	N41W	40NE	229	50	R-LS	3	30	T-RS
830505	027 50.83	36-13.76	120-16.13	8.93	3.48	42	48	1.8	0.09	0.2	0.2	AC	62	N58W	19SW	N17W	76NE	253	14	T-LS	32	71	R-RS
830505	156 42.39	36-13.19	120-17.14	7.96	3.36	45	45	0.2	0.12	0.2	0.3	AC	61	N40W	18SW	N26W	72NE	244	18	T-LS	50	72	R-RS
830505	437 48.59	36- 8.06	120-12.21	11.22	4.01	41	77	8.8	0.15	0.3	0.5	AC	338	N44E	34SE	N81E	62NW	171	28	T-LS	314	56	R-RS
830505	8 6 26.69	36- 9.02	120-13.37	8.70	3.73	40	70	6.9	0.12	0.3	0.4	AC	14	N63W	40SW	N87E	54NW	177	36	T-RS	27	50	R-LS
830505	1020 44.09	36-17.13	120-22.10	11.49	4.61	43	46	4.7	0.05	0.1	0.1	AC	42	N64W	49NE	N31W	46SW	59	44	R-LS	206	41	R-RS
830505	1133 40.67	36-15.49	120-21.82	10.46	3.69	50	39	2.2	0.10	0.2	0.2	AC	73	N33W	8NE	N19W	82SW	71	8	N-RS	237	82	N-LS
830505	1150 49.98	36-10.88	120-17.08	10.52	3.47	44	61	3.6	0.09	0.2	0.2	AC	9	N82E	27SE	N73W	66NE	197	24	T-LS	352	63	R-RS
830505	1242 15.72	36-15.34	120-23.92	11.85	3.89	52	54	5.1	0.08	0.2	0.2	AC	164	N53E	52SE	N85W	46NE	185	44	R-LS	323	38	R-RS
830505	2246 12.38	36-18.08	120-25.15	10.10	3.36	54	64	6.5	0.10	0.2	0.3	AC	213	N44W	50SW	N70W	43NE	200	47	R-RS	46	40	T-LS
830506	457 9.43	36-12.09	120-17.39	10.79	3.38	50	55	2.0	0.09	0.2	0.2	AC	13	N65W	28SW	N82W	63NE	188	27	T-RS	25	62	R-LS
830506	943 38.98	36-11.67	120-20.31	12.77	3.71	47	57	6.1	0.08	0.2	0.2	AC	20	N71W	76SW	N76W	14NE	194	76	N-LS	19	14	N-RS
830506	1151 44.39	36-16.47	120-22.41	10.76	3.33	49	38	2.9	0.07	0.1	0.2	AC	80	N 3E	48SE	N24W	46SW	66	44	R-RS	273	42	R-LS
830507	017 15.90	36-16.09	120-19.32	8.92	3.88	48	47	2.8	0.06	0.1	0.1	AC	86	N48E	58NW	N47W	82SW	43	8	RS-R	138	32	LS-R
830507	543 57.33	36-14.11	120-16.62	8.92	3.47	45	47	2.0	0.07	0.2	0.2	AC	57	N39W	28SW	N26W	63NE	244	27	T-LS	51	62	R-RS
830507	1242 30.37	36-18.11	120-24.46	10.56	3.62	50	65	6.1	0.07	0.2	0.2	AC	64	N38W	10NE	N29W	80SW	61	10	N-RS	232	80	N-LS
830508	120 14.74	36-12.73	120-18.15	8.42	3.46	51	48	1.8	0.09	0.2	0.2	AC	249	N38W	50SW	N 3W	46NE	267	44	R-LS	52	40	R-RS
830508	147 25.90	36-12.34	120-16.68	8.09	3.03	52	38	1.5	0.14	0.2	0.2	AC	65	N38W	46SW	N12W	47NE	258	43	R-LS	52	44	R-RS
830508	345 33.89	36-15.43	120-26.17	1.80*	3.37	52	32	4.7	0.15	0.2	0.3	AC	269	N 9W	28NE	N 2E	62NW	92	28	T-LS	261	62	R-RS
830508	738 11.57	36-15.81	120-16.78	5.03	3.31	51	42	4.1	0.13	0.2	0.2	AC	57	N24W	27SW	N37W	64NE	233	26	T-RS	66	64	R-LS
830508	1037 21.12	36-13.10	120-21.27	11.59	3.27	58	30	3.6	0.09	0.1	0.2	AC	76	N30E	82NW	N58W	84NE	212	6	R8-R	120	10	LS-R
830508	1523 32.93	36-11.52	120-20.00	6.58	3.34	55	31	5.3	0.13	0.2	0.2	AC	273	N24W	60SW	N36E	49SE	306	41	R-LS	66	30	R-RS
830508	1918 24.22	36-17.59	120-28.27	11.61	3.72	56	42	9.2	0.08	0.2	0.2	AC	58	N48W	30SW	N23W	62NE	247	28	T-LS	42	60	R-RS
830508	2025 40.01	36-12.72	120-18.15	7.67	3.60	49	39	1.8	0.09	0.2	0.2	AC	237	N35W	64SW	N28W	26NE	242	64	R-RS	55	26	T-LS
830509	249 11.55	36-14.74	120-17.97	12.04	5.30	46	32	3.3	0.05	0.1	0.1	AC	34	N67W	48NE	N44W	44SW	46	46	R-LS	203	42	T-RS
830509	319 11.25	36-14.31	120-17.90	12.31	3.62	55	32	2.5	0.09	0.2	0.1	AC	224	N60W	43NE	N33W	50SW	67	40	T-LS	210	47	R-RS
830509	326 37.42	36-14.39	120-17.96	12.43	4.60	47	39	2.7	0.09	0.2	0.2	AC	18	N82W	52NE	N61W	40SW	29	50	R-LS	188	39	T-RS
830509	1324 33.75	36-12.06	120-16.39	9.48	3.29	49	55	2.2	0.08	0.1	0.2	AC	204	N23W	58NE	N77E	74SE	247	32	R-LS	347	16	R-RS
830510	1326 29.44	36-19.79	120-18.97	4.79	3.85	50	56	3.5	0.10	0.2	0.2	AC	228	N 6W	37NE	N63W	68SW	27	22	T-RS	264	54	R-LS
830510	1522 43.36	36-20.12	120-19.53	4.13	2.85	44	59	2.6	0.17	0.3	0.3	BC	232	N49W	46NE	N27W	46SW	221	44	R-RS	63	44	R-LS
830510	1522 45.53	36-19.49	120-18.76	4.05	3.37	42	55	3.6	0.13	0.3	0.3	AC	230	N56W	35NE	N27W	58SW	63	32	T-LS	214	55	R-RS
830511	814 47.25	36- 9.30	120-15.21	11.85	3.48	51	49	4.1	0.11	0.2	0.3	AC	232	N15W	54SW	N61W	46NE	209	44	R-RS	75	36	R-LS

830512	1341	6.82	36-10.00	120-16.10	10.98	4.50	48	66	3.2	0.09	0.2	0.2	AC	46	N60W	26SW	N35W	66NE	235	24T-LS	30	64R-RS
830513	1422	15.91	36- 7.26	120-12.55	11.29	3.29	51	51	8.8	0.16	0.3	0.5	BC	35	N17W	76NE	N80E	62SE	350	28RS-R	253	14LS-R
830514	5 2	3.11	36-16.51	120-18.46	11.18	3.90	49	48	4.2	0.07	0.1	0.2	AC	26	N87W	53NE	N40W	48SW	50	42R-LS	183	37R-RS
830514	1715	17.02	36-11.09	120-17.36	11.30	2.60	47	44	3.8	0.11	0.2	0.2	AC	39	N22W	18SW	N60W	76NE	210	15T-RS	68	72R-LS
830514	1715	35.70	36-10.43	120-16.89	8.88	3.49	42	45	2.9	0.18	0.4	0.4	BC	127	N68E	24NW	N24E	72SE	294	18T-RS	158	66R-LS
830516	131	37.65	36- 8.48	120-15.00	12.03	3.61	41	51	4.6	0.08	0.2	0.2	AC	170	N32E	60NW	N59W	88SW	31	2LS-R	122	30RS-R
830516	1217	42.99	36- 7.14	120-12.55	9.68	3.15	43	55	8.9	0.17	0.4	0.7	BC	220	N78W	75SW	N 5W	44NE	265	46R-LS	12	15T-RS
830516	1421	48.38	36- 9.55	120-16.48	9.15	3.90	41	104	2.4	0.09	0.2	0.3	BC	209	N56W	70SW	N76W	21NE	194	69R-RS	34	20T-LS
830517	2222	13.18	36-13.89	120-21.63	8.06	3.49	49	37	2.6	0.08	0.2	0.2	AC	251	N28W	60SW	N 5W	32NE	265	58R-LS	62	30T-RS
830519	11 5	30.15	36-13.79	120-16.28	12.95	4.16	48	48	1.7	0.11	0.2	0.2	AC	233	N37W	40NE	N37W	50SW	53	40T	233	50R
830519	2326	6.55	36-15.44	120-26.08	1.84	3.48	46	35	4.6	0.13	0.2	0.3	AC	262	N22W	30NE	N 0W	62 W	90	28T-LS	248	60R-RS
830521	10 5	41.05	36-11.15	120-14.57	11.09	3.21	48	54	5.2	0.11	0.2	0.2	AC	24	N29E	32SE	N30W	72SW	60	18N-LS	359	58N-RS
830522	839	21.74	36- 9.03	120-12.09	10.48	4.24	47	61	8.8	0.13	0.2	0.4	AC	356	N74E	40SE	N85W	52NE	185	38T-LS	344	50R-RS
830524	9 2	17.70	36-15.24	120-19.00	8.86	4.70	45	39	2.3	0.05	0.1	0.1	AC	58	N14W	18SW	N36W	74NE	234	16T-RS	76	72R-LS
830524	9 3	56.56	36-15.82	120-18.96	8.01	3.44	15	83	3.4	0.09	0.3	0.5	AC									
830524	1226	7.72	36-11.44	120-17.96	10.91	3.24	54	58	3.4	0.10	0.2	0.2	AC	210	N53W	46SW	N67W	45NE	203	45R-RS	37	44R-LS
830526	854	55.06	36-14.18	120-16.61	8.12	3.16	44	57	2.1	0.13	0.3	0.3	AC	78	N36W	19SW	N 4W	74NE	266	16T-LS	54	71R-RS
830527	2040	49.22	36-14.54	120-22.56	12.68	3.81	50	30	1.1	0.08	0.2	0.1	AC	230	N20W	50SW	N61W	48NE	209	42R-RS	70	40R-LS
830529	124	3.43	36-14.45	120-22.42	12.54	3.49	44	42	1.4	0.09	0.2	0.2	AC	230	N20W	49SW	N59W	48NE	211	42R-RS	70	41R-LS
830530	321	52.45	36-15.00	120-22.65	11.50	3.33	45	39	0.6	0.07	0.2	0.1	AC	71	N58W	15SW	N 9W	80NE	269	10T-LS	32	75R-RS
830607	518	37.78	36- 9.47	120-13.42	11.59	4:13	41	84	6.8	0.10	0.3	0.2	AC	338	N20E	42SE	N81W	80NE	189	10T-LS	290	48R-RS
830611	3 9	52.21	36-15.33	120-27.01	2.40	5.20	45	67	6.0	0.12	0.2	0.4	BC	107	N17E	50SE	N17E	40NW	107	50R	287	40T
830611	1427	5.56	36-14.50	120-26.73	4.13	3.22	54	60	5.6	0.18	0.3	0.4	BC	264	N 6W	40NE	N 7W	50SW	83	40T	264	50R
830611	23 2	19.83	36-15.50	120-26.37	3.53	3.37	49	64	5.1	0.15	0.3	0.4	BC	66	N24W	52NE	N24W	38SW	66	52R	246	38T
830612	131	27.54	36- 7.55	120-17.71	14.49	4.03	39	59	2.9	0.12	0.3	0.3	AC	66	N26E	44NW	N56W	82NE	214	8T-RS	116	46R-LS
830616	1737	23.60	36-14.52	120-21.52	10.59	3.54	52	39	1.7	0.08	0.1	0.2	AC	81	N 6W	20SW	N10W	70NE	260	20T-RS	84	70R-LS
830629	641	7.80	36- 9.56	120-11.47	13.06	3.55	45	74	6.2	0.15	0.4	0.3	AC	7	N86E	32SE	N76W	59NE	194	31T-LS	356	58R-RS
830705	2210	14.38	36-20.41	120-19.79	4.61	3.26	36	84	3.5	0.14	0.4	0.4	AC	65	N 2E	52SE	N50W	52SW	40	38R-RS	272	38R-LS
830707	030	33.66	36-13.25	120-16.77	12.45	3.65	30	218	6.4	0.08	0.4	0.2	CC	228	N70W	50NE	N14W	56SW	76	34R-LS	200	40R-RS
830709	740	51.30	36-15.04	120-24.01	9.02	5.39	39	50	5.2	0.11	0.3	0.4	AC	269	N18E	41SE	N15W	54SW	75	36T-RS	288	49R-LS
830714	1525	35.65	36-13.13	120-18.49	9.73	2.52	28	60	4.5	0.07	0.2	0.3	AC	244	N38W	48SW	N15W	44NE	255	46R-LS	52	42R-RS
830714	1525	41.48	36-13.22	120-18.38	6.70	3.69	26	115	18.2	0.11	0.4	1.1	BC	210	N58W	0SW	N58W	90	210	0T	30	90R
830717	2158	8.20	36-16.93	120-19.77	12.00*	3.66	35	67	3.8	0.15	0.2	0.2	AC	110	N66E	80NW	N26W	76SW	64	14RS-N	156	10LS-N
830718	1928	5.45	36-10.82	120-16.79	10.91	4.16	31	64	9.5	0.07	0.2	0.3	AC	6	N68E	28SE	N70W	68NE	200	22T-LS	338	62R-RS
830722	239	54.07	36-14.44	120-24.53	7.37	6.04	36	48	6.1	0.09	0.2	0.4	AC	260	N 5W	38NE	N21W	53SW	69	37T-RS	265	52R-LS
830722	249	9.97	36-13.31	120-24.77	6.78	4.14	37	45	7.1	0.11	0.2	0.4	BC	226	N78W	40NE	N21W	69SW	69	25T-LS	192	50R-RS
830722	3 3	41.55	36-13.55	120-24.29	7.68	3.19	38	44	6.2	0.09	0.2	0.4	AC	102	N57E	84NW	N35W	68SW	55	22RS-N	147	5LS-N
830722	311	42.69	36-20.67	120-20.90	4.01	2.36	26	89	2.1	0.14	0.4	0.4	AC	0	N90W	67 N	N90W	23 S	180	23T	0	67R
830722	311	47.62	36-19.93	120-19.96	1.80*	3.31	30	82	15.6	0.14	0.4	0.8	BC	206	N18W	70NE	N74E	84SE	344	6RS-R	252	20LS-R
830722	343	1.01	36-13.31	120-24.37	7.89	5.02	35	43	6.5	0.09	0.2	0.4	AC	255	N18W	30NE	N13W	60SW	77	30T-LS	252	60R-RS
830722	430	27.21	36-21.13	120-19.71	7.50*	3.61	37	89	4.0	0.24	0.5	0.8	BC	51	N42W	54NE	N35W	36SW	55	54R-RS	228	36T-LS
830722	712	10.86	36-16.58	120-24.18	7.06	3.35	39	56	6.3	0.12	0.3	0.6	AC	255	N12W	44NE	N16W	46SW	74	44T	258	46R
830722	2152	32.67	36-15.86	120-23.96	7.98	3.32	36	51	5.4	0.10	0.2	0.4	AC	256	N 2W	44NE	N24W	48SW	268	46R-LS	66	42T-RS
830725	2231	39.57	36-13.76	120-23.87	8.42	5.33	36	42	5.5	0.09	0.2	0.3	AC	258	N12W	38NE	N12W	52SW	78	38T	258	52R
830731	1643	52.54	36-13.84	120-15.88	9.50	3.54	34	71	7.2	0.08	0.2	0.4	AC	58	N73W	28SW	N13W	75NE	257	14T-LS	17	62R-RS
830731	1724	10.15	36- 9.43	120-13.93	11.03	3.55	29	220	14.2	0.11	0.5	0.4	CC	39	N73E	16SE	N39W	84NE	343	75R-RS	231	6T-LS
830731	1754	20.30	36-13.84	120-15.60	9.84	3.36	33	72	7.7	0.09	0.3	0.4	AC	76	N40W	24SW	N 4W	70NE	266	20T-LS	50	66R-RS
830805	10 6	1.00	36-14.13	120-26.55	4.87#	3.26	43	58	9.2	0.12	0.3	0.3	BC	52	N24W	54NE	N54W	40SW	36	50R-RS	246	36T-LS
830812	114	41.14	36-17.46	120-24.04	9.79	4.04	44	62	5.7	0.10	0.2	0.3	AC	50	N22W	40SW	N55W	55NE	215	35T-RS	68	50R-LS
830812	22 2	34.71	36-10.97	120- 8.16	8.68	4.10	29	153	8.8	0.09	0.4	0.6	BC	80	N26W	32SW	N 0W	60 E	270	30T-LS	64	58R-RS
830814	1243	35.74	36-17.32	120-24.67	9.64	4.30	41	67	6.5	0.10	0.2	0.3	AC	60	N19W	44SW	N40W	48NE	230	42T-RS	71	46R-LS
830826	321	17.25	36-18.00	120-28.40	11.98	4.04	47	85	10.2	0.10	0.2	0.2	AC	41	N42W	42SW	N54W	48NE	216	42T-RS	48	48R-LS
830826	1957	40.64	36-12.65	120-22.42	11.78	3.83	43	47	5.1	0.07	0.2	0.2	AC	63	N17E	80NW	N71W	80NE	199	10RS-R	107	10LS-R
830907	23 7	26.19	36-16.74	120-27.61	11.98	3.81	47	80	10.4	0.10	0.2	0.2	AC	47	N24W	40SW	N58W	55NE	212	35T-RS	66	50R-LS
830909	916	13.47	36-13.91	120-15.90	6.69	5.30	34	71	7.2	0.06	0.2	0.2	BC	22	N26W	75NE	N68E	72SE	338	18RS-R	244	16LS-R
830909	921	31.81	36-14.38	120-16.73	6.27	3.89	36	71	5.8	0.09	0.2	0.3	AC	245	N12W	50SW	N38W	43NE	232	47R-RS	78	40T-LS
830911	1148	6.60	36-14.53	120-22.99	10.04	4.48	41	42	3.8	0.07	0.2	0.2	AC	267	N10W	32NE	N 0W	58SW	90	32T-LS	260	58R-RS
830918	1434	32.04	36-16.68	120-20.65	9.16	3.45	41	63	3.2	0.09	0.2	0.3	AC	33	N32W	32SW	N72W	64NE	198	26T-RS	58	58R-LS

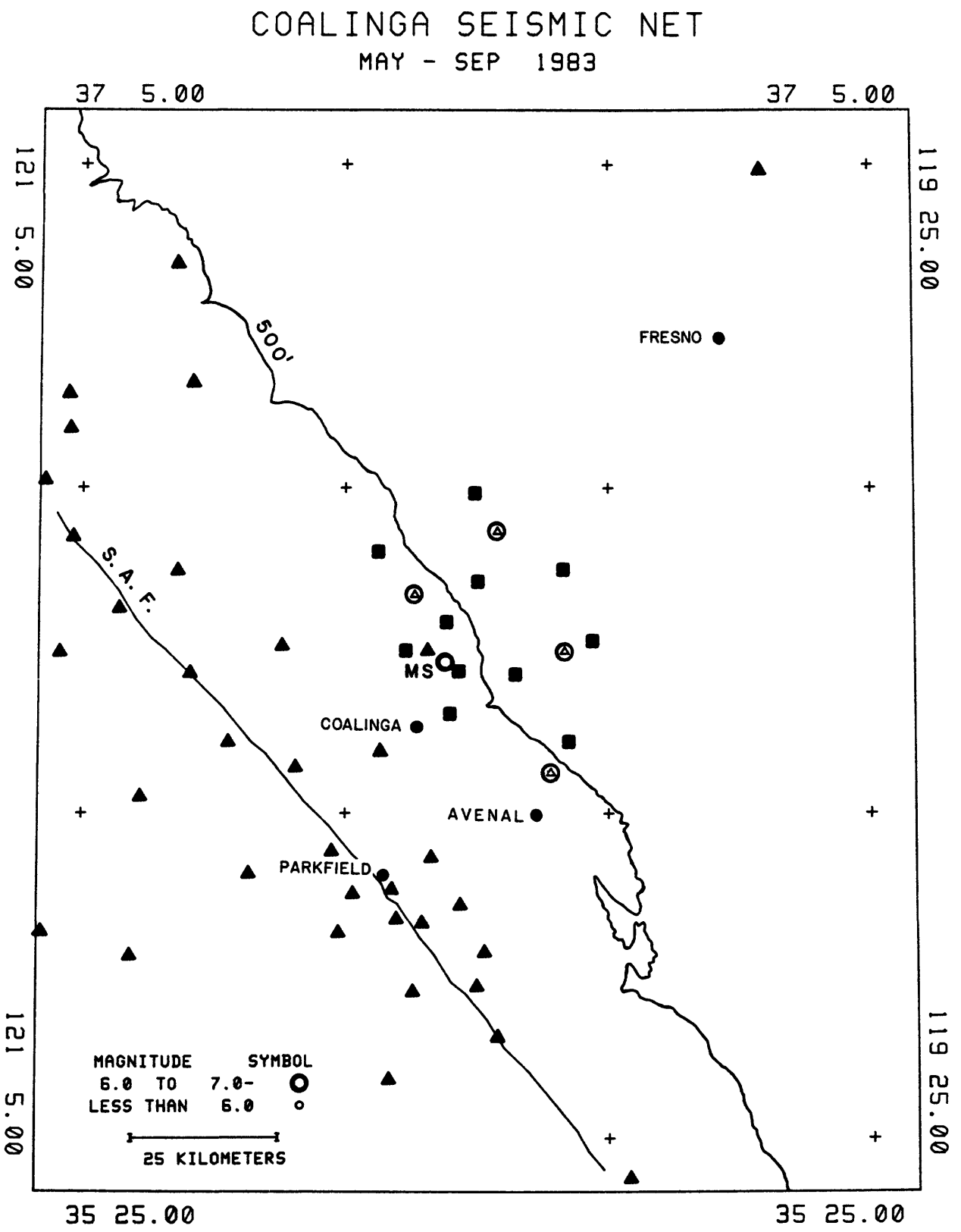
COALINGA SEISMIC NET
MAY - SEP 1983
37 5.00
37 5.00
121 5.00
119 25.00
500'
FRESNO
S.A.F.
MS
COALINGA
AVENAL
PARKFIELD
MAGNITUDE SYMBOL
6.0 TO 7.0-
LESS THAN 6.0
25 KILOMETERS
121 5.00
119 25.00
35 25.00
35 25.00

FIGURE 1

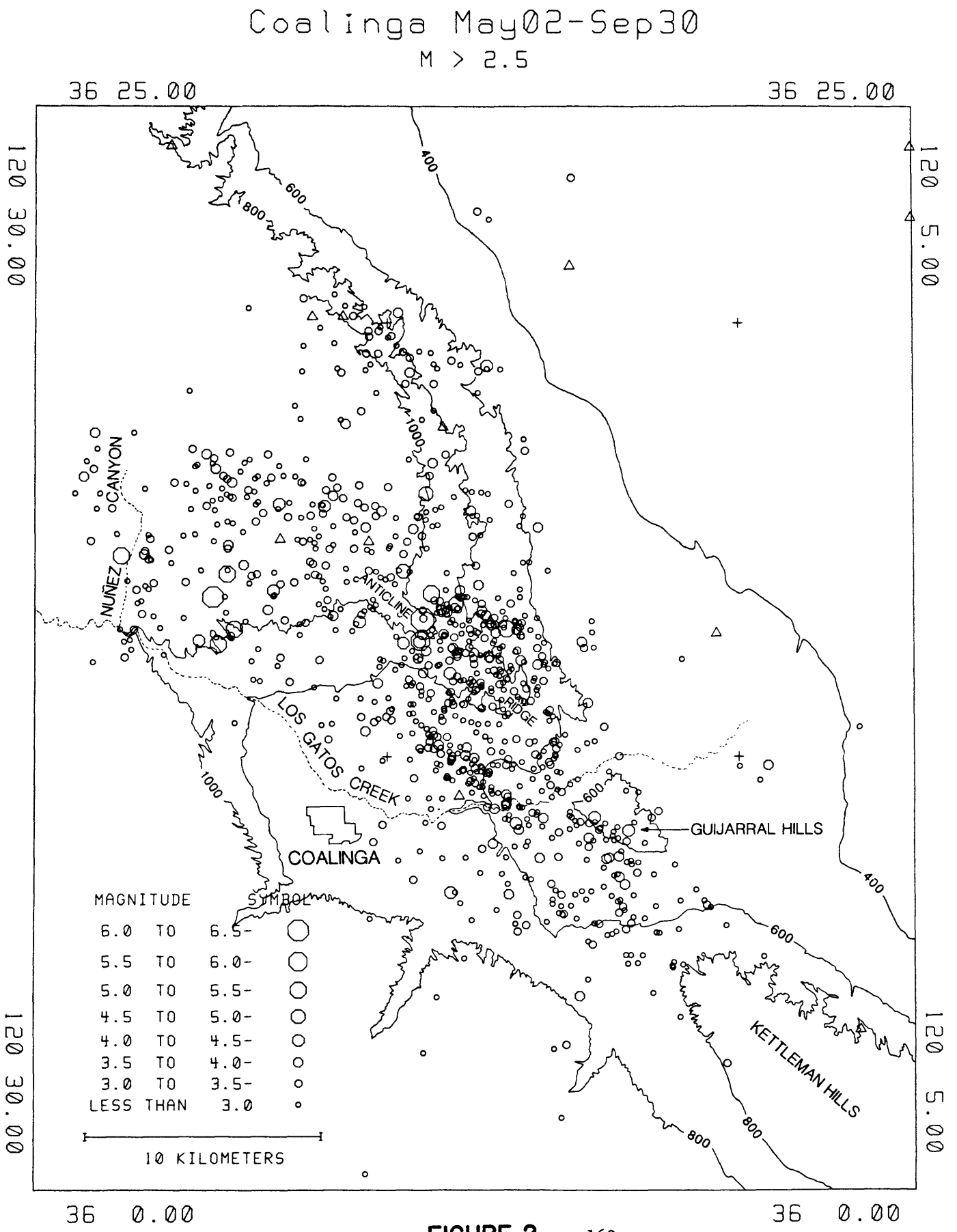
Coalinga May02-Sep30
M > 2.5
36 25.00
36 25.00
120 30.00
120 5.00
120 30.00
120 5.00
36 0.00
36 0.00
400
600
800
1000
1000
600
400
600
800
800
CANYON
NUÑEZ
ANTICLINE
RIDGE
LOS GATOS CREEK
COALINGA
GUIJARRAL HILLS
KETTLEMAN HILLS
MAGNITUDE
SYMBOL
6.0 TO 6.5-
5.5 TO 6.0-
5.0 TO 5.5-
4.5 TO 5.0-
4.0 TO 4.5-
3.5 TO 4.0-
3.0 TO 3.5-
LESS THAN 3.0
10 KILOMETERS

FIGURE 2

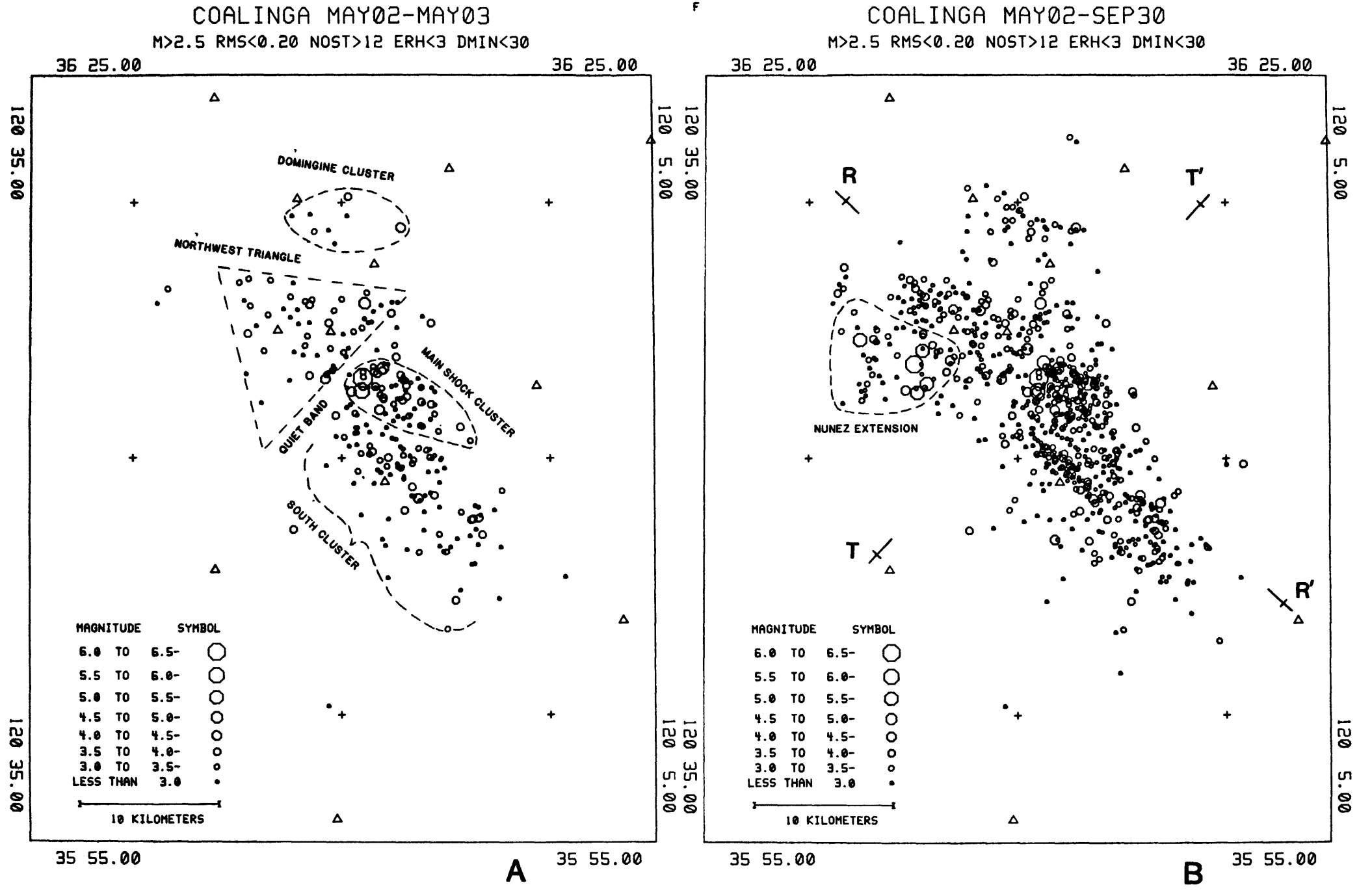
COALINGA MAY02-MAY03
M>2.5 RMS<0.20 NOST>12 ERH<3 DMIN<30
36 25.00
35 55.00
120 35.00
120 5.00
DOMINGINE CLUSTER
NORTHWEST TRIANGLE
QUIET BAND
MAIN SHOCK CLUSTER
SOUTH CLUSTER
MAGNITUDE SYMBOL
6.0 TO 6.5-
5.5 TO 6.0-
5.0 TO 5.5-
4.5 TO 5.0-
4.0 TO 4.5-
3.5 TO 4.0-
3.0 TO 3.5-
LESS THAN 3.0
10 KILOMETERS
A
COALINGA MAY02-SEP30
M>2.5 RMS<0.20 NOST>12 ERH<3 DMIN<30
R
T'
T
R'
NUNEZ EXTENSION
B

FIGURE 3

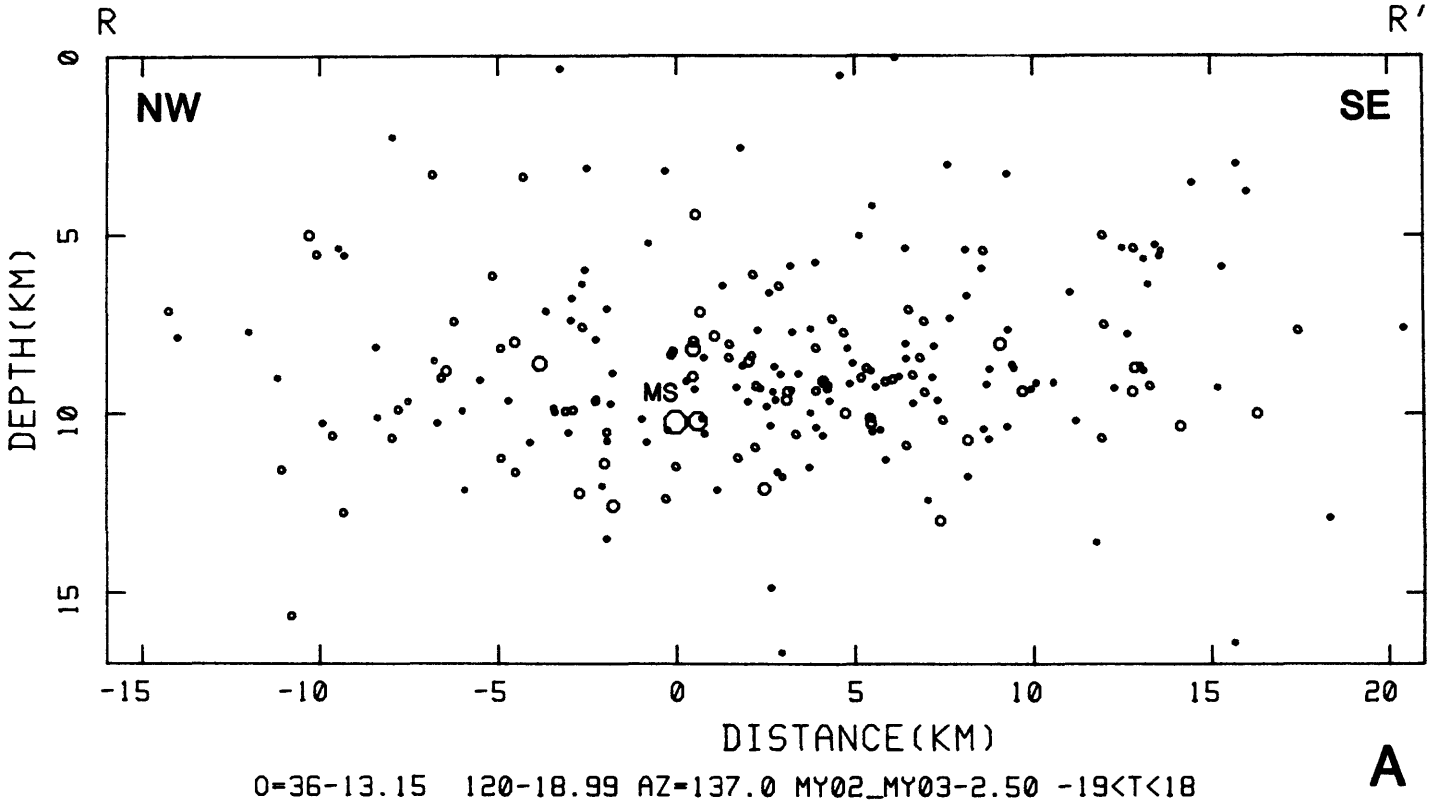
R
R'
NW
SE
MS
DEPTH(KM)
0
5
10
15
-15
-10
-5
0
5
10
15
20
DISTANCE(KM)
A
0=36-13.15 120-18.99 AZ=137.0 MY02_MY03-2.50 -19<T<18

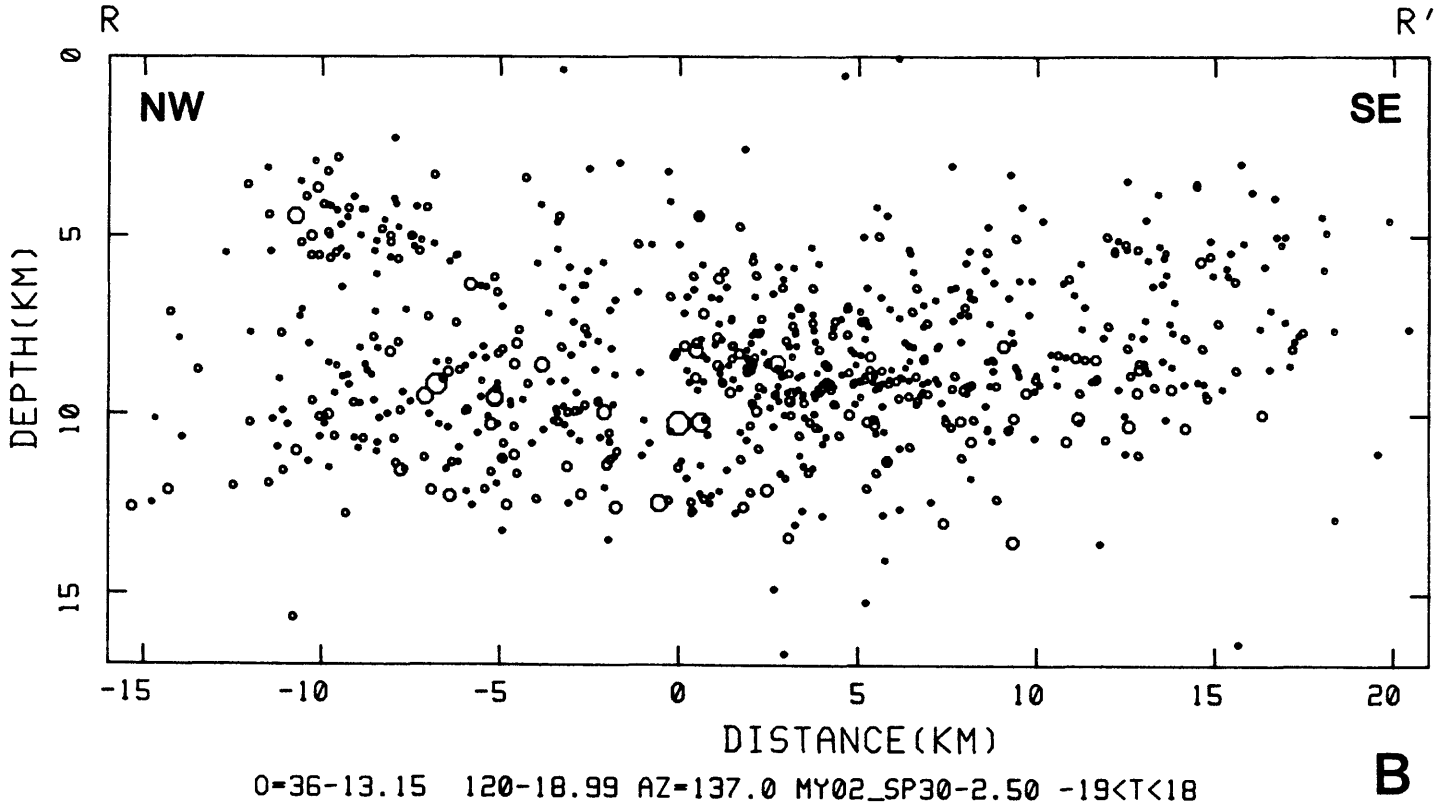
R
R'
NW
SE
DEPTH(KM)
0
5
10
15
-15
-10
-5
0
5
10
15
20
DISTANCE(KM)
B
0=36-13.15 120-18.99 AZ=137.0 MY02_SP30-2.50 -19<T<18

FIGURE 4

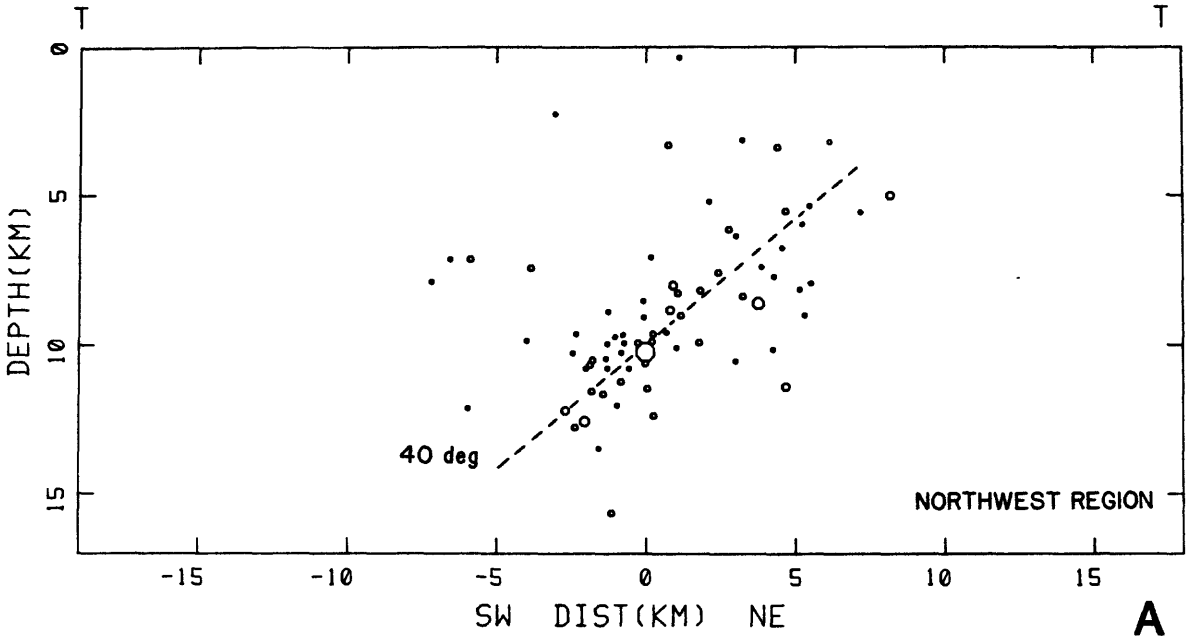

0=36-13.15 120-18.99 AZ=317.0 MY02_MY03-2.50 -0.1<R<21

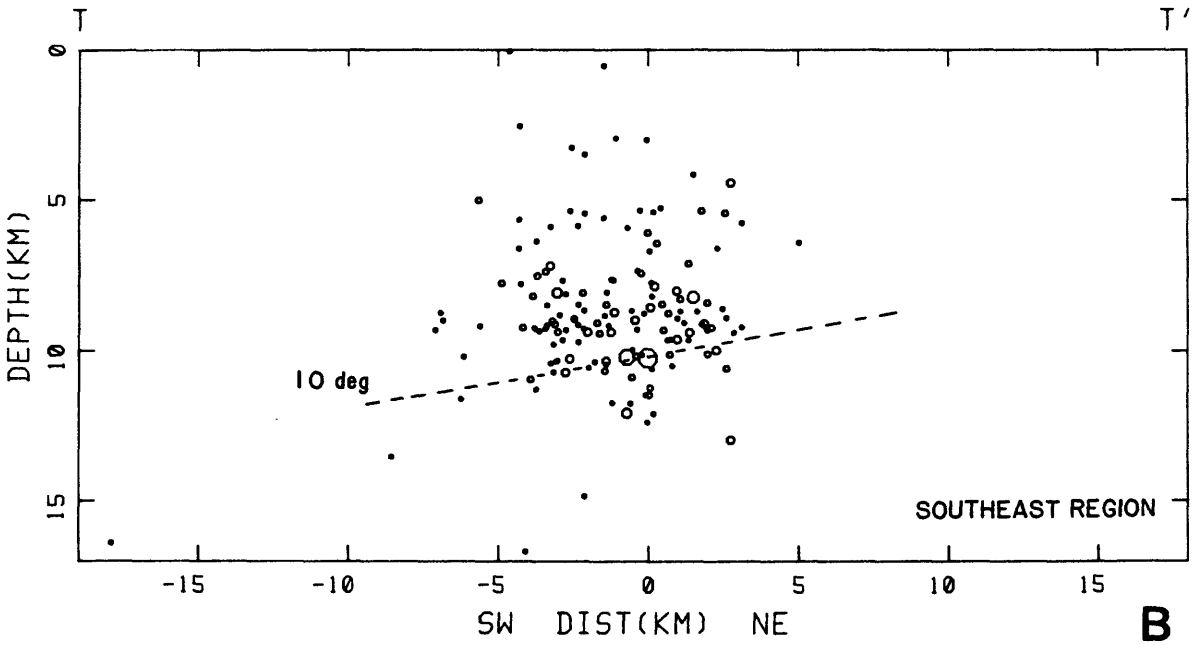

0=36-13.15 120-18.99 AZ=317.0 MY02_MY03-2.50 -16<R<0.1

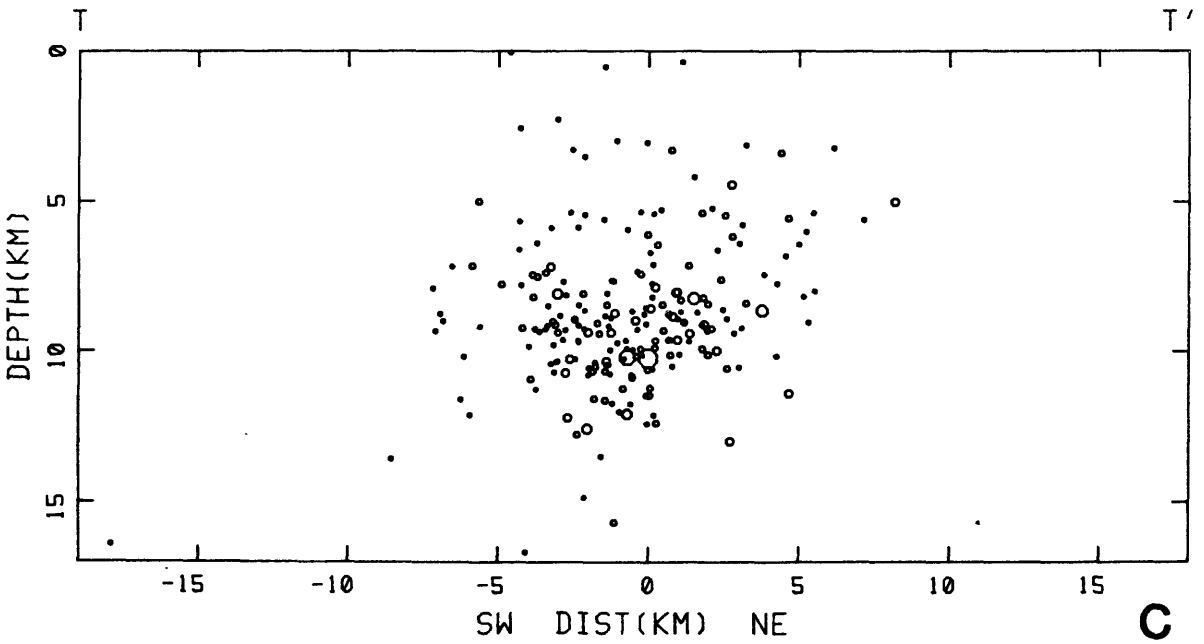

165 0=36-13.15 120-18.99 AZ=317.0 MY02_MY03-2.50 -16<R<21

FIGURE 5

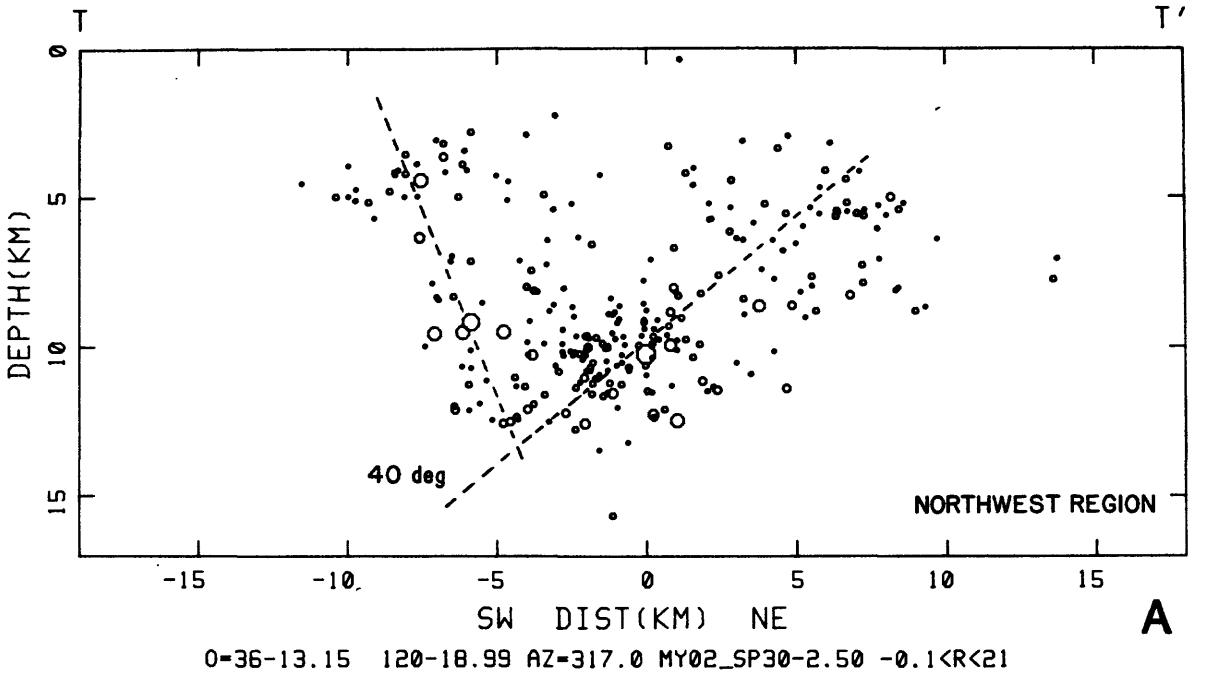
T
T'
DEPTH(KM)
0
5
10
15
40 deg
NORTHWEST REGION
-15
-10
-5
0
5
10
15
SW DIST(KM) NE
A
0=36-13.15 120-18.99 AZ=317.0 MY02_SP30-2.50 -0.1<R<21

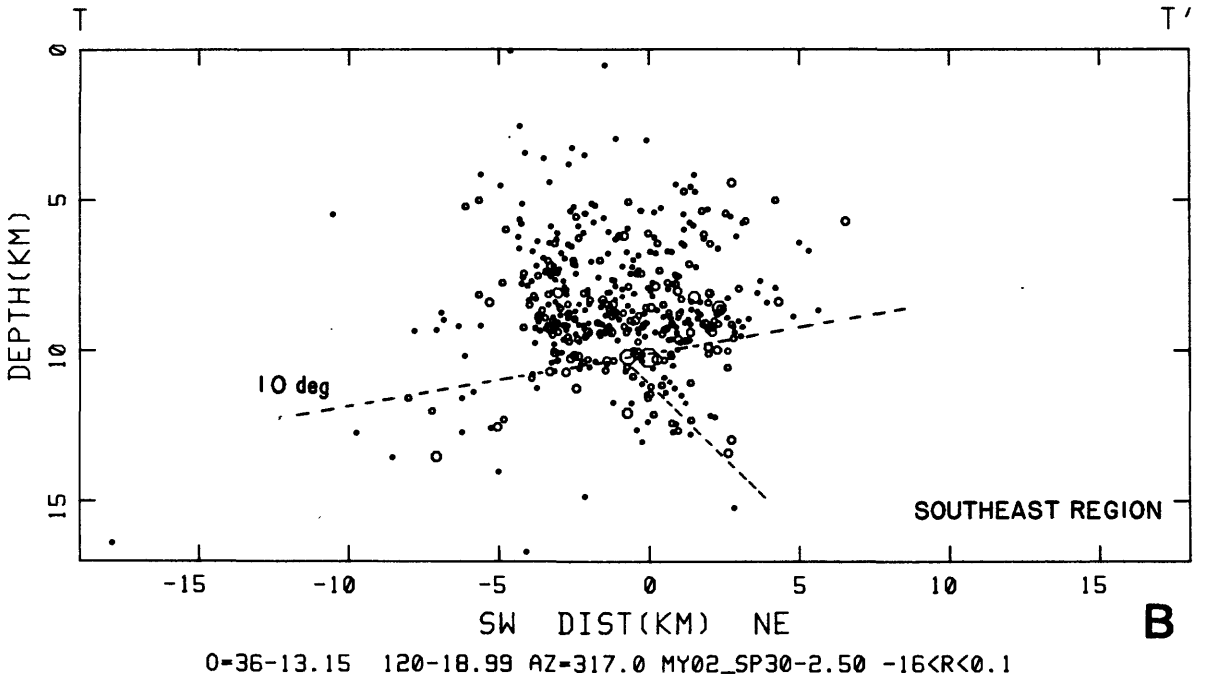
T
T'
DEPTH(KM)
0
5
10
15
10 deg
SOUTHEAST REGION
-15
-10
-5
0
5
10
15
SW DIST(KM) NE
B
0=36-13.15 120-18.99 AZ=317.0 MY02_SP30-2.50 -16<R<0.1

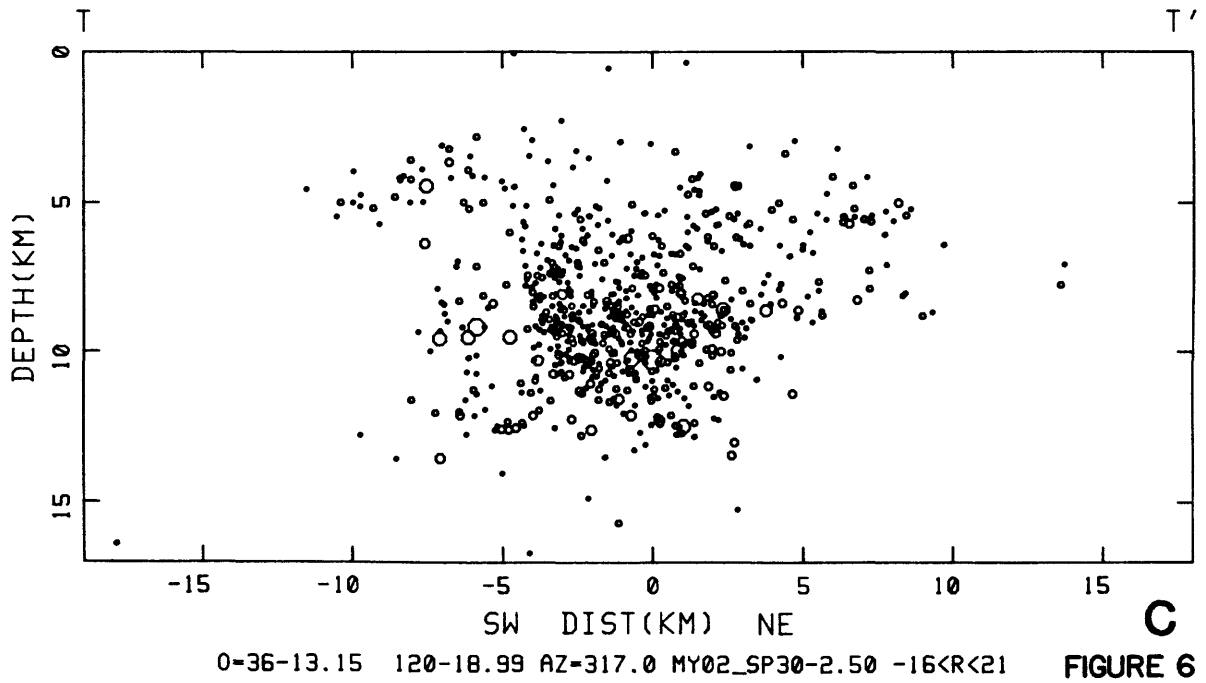
T
T'
DEPTH(KM)
0
5
10
15
-15
-10
-5
0
5
10
15
SW DIST(KM) NE
C
0=36-13.15 120-18.99 AZ=317.0 MY02_SP30-2.50 -16<R<21

FIGURE 6

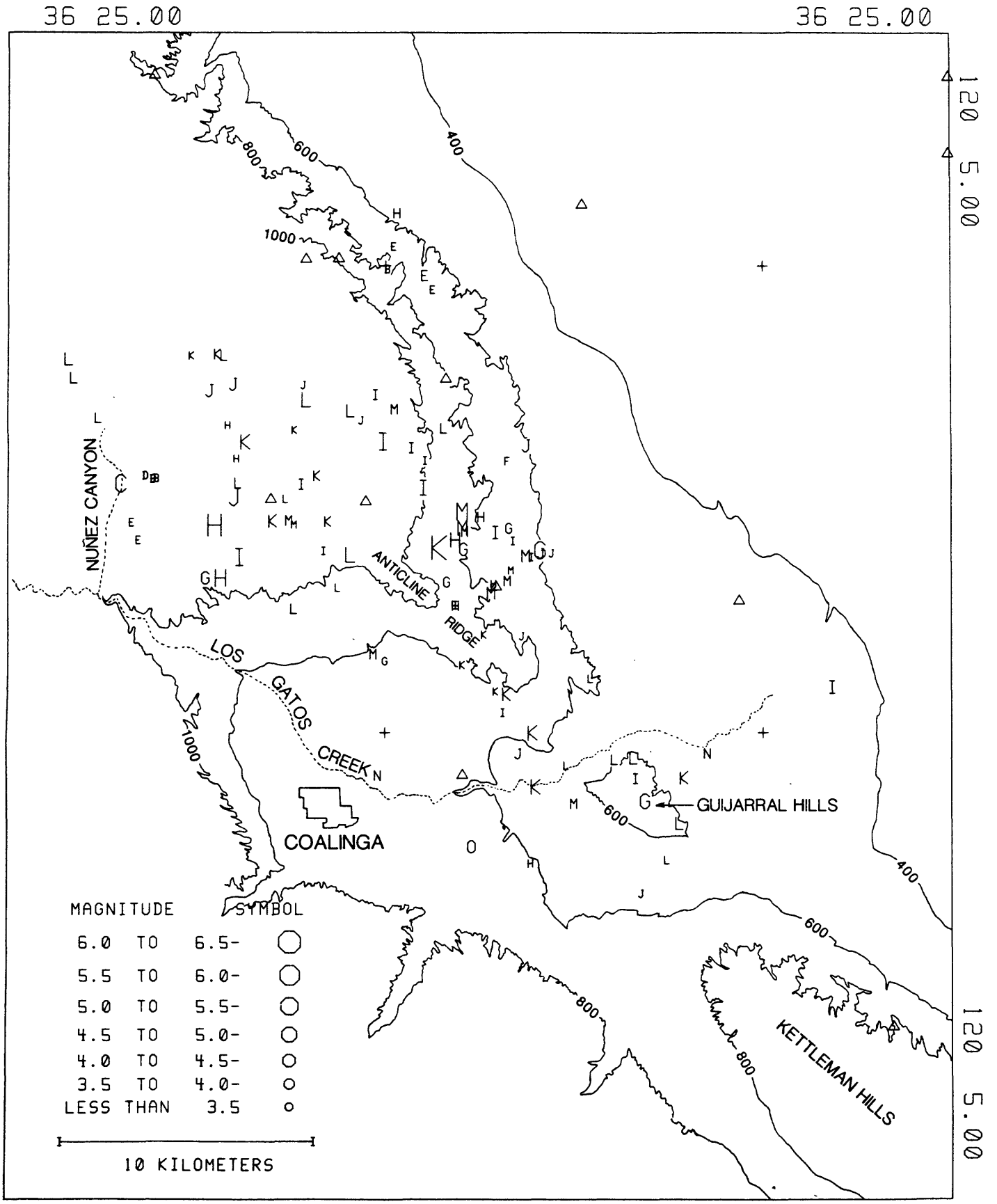
Coalinga May02-Sep30
M > 3.2
36 25.00
36 25.00
120 5.00
120 5.00
36 0.00
36 0.00
NUÑEZ CANYON
ANTICLINE
RIDGE
LOS GATOS CREEK
COALINGA
GUIJARRAL HILLS
KETTLEMAN HILLS
400
600
800
1000
MAGNITUDE SYMBOL
6.0 TO 6.5-
5.5 TO 6.0-
5.0 TO 5.5-
4.5 TO 5.0-
4.0 TO 4.5-
3.5 TO 4.0-
LESS THAN 3.5
10 KILOMETERS

FIGURE 7

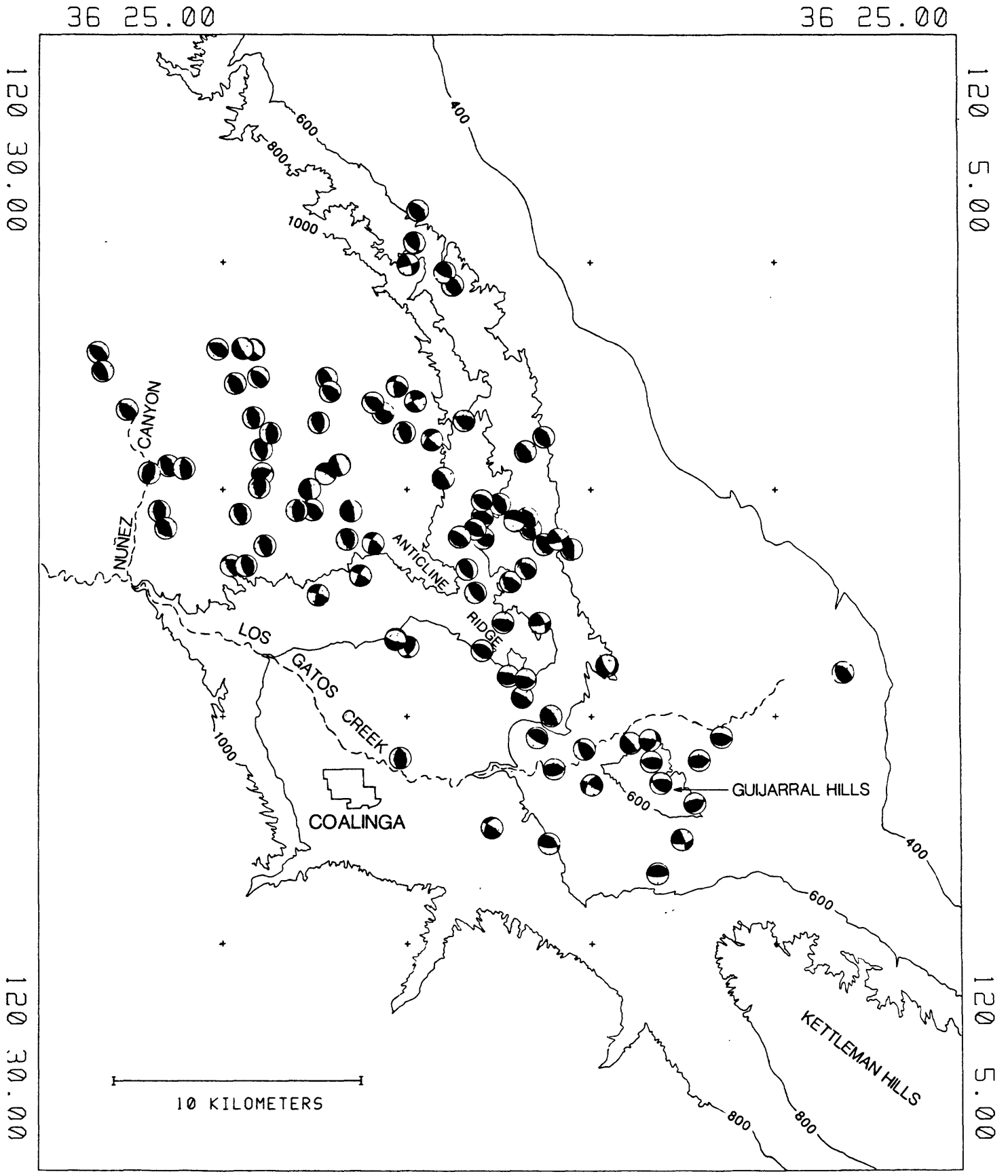
COALINGA MAY02-SEP30
FOCAL MECHANISMS M>3.2
36 25.00
36 25.00
120 30.00
120 5.00
600
800
1000
400
CANYON
NUÑEZ
ANTICLINE
RIDGE
LOS
GATOS
CREEK
1000
COALINGA
GUIJARRAL HILLS
600
400
600
KETTLEMAN HILLS
800
800
10 KILOMETERS
36 0.00
36 0.00
120 30.00
120 5.00

FIGURE 8

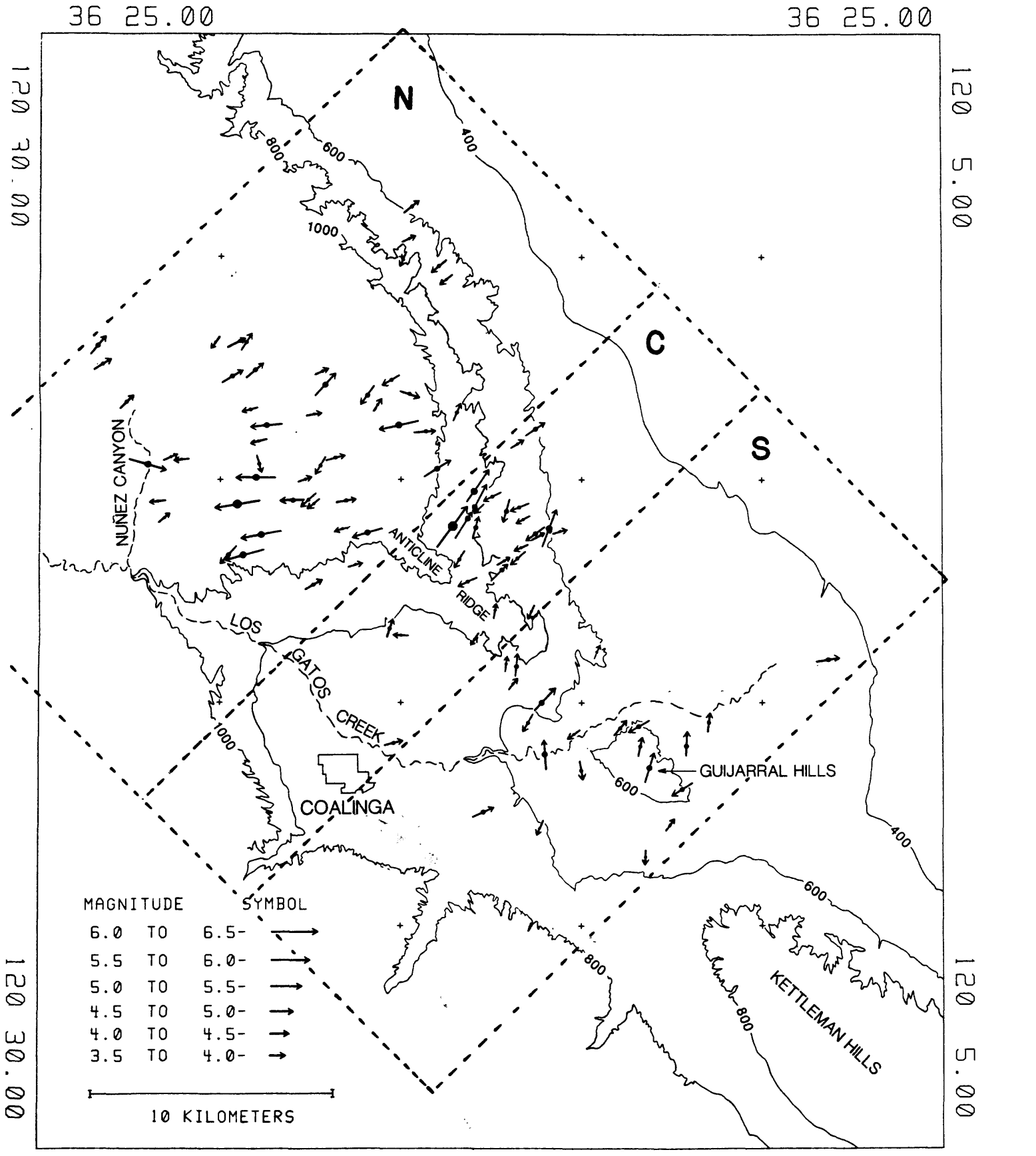
Coalinga May02-Sep30
M > 3.2
36 25.00
36 25.00
120 30.00
120 5.00
N
C
S
800
600
400
1000
NUÑEZ CANYON
ANTICLINE
RIDGE
LOS
GATOS
CREEK
COALINGA
GUIJARRAL HILLS
KETTLEMAN HILLS
MAGNITUDE SYMBOL
6.0 TO 6.5-
5.5 TO 6.0-
5.0 TO 5.5-
4.5 TO 5.0-
4.0 TO 4.5-
3.5 TO 4.0-
10 KILOMETERS
36 0.00
36 0.00
120 30.00
120 5.00

FIGURE 9

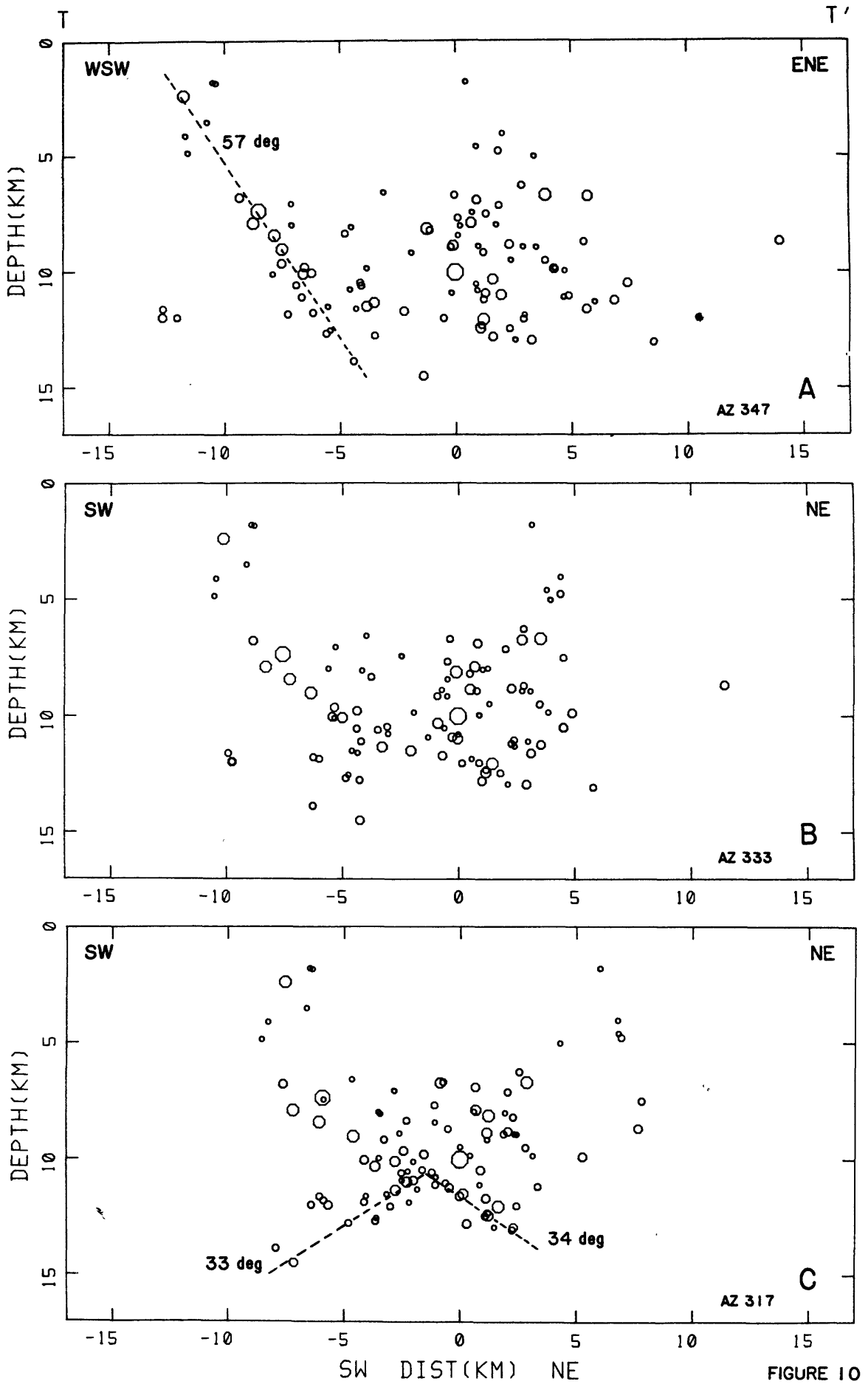

FIGURE 10

0=36-13.96 120-18.57 MY02_SP30-3.20 -17<R<17 sum

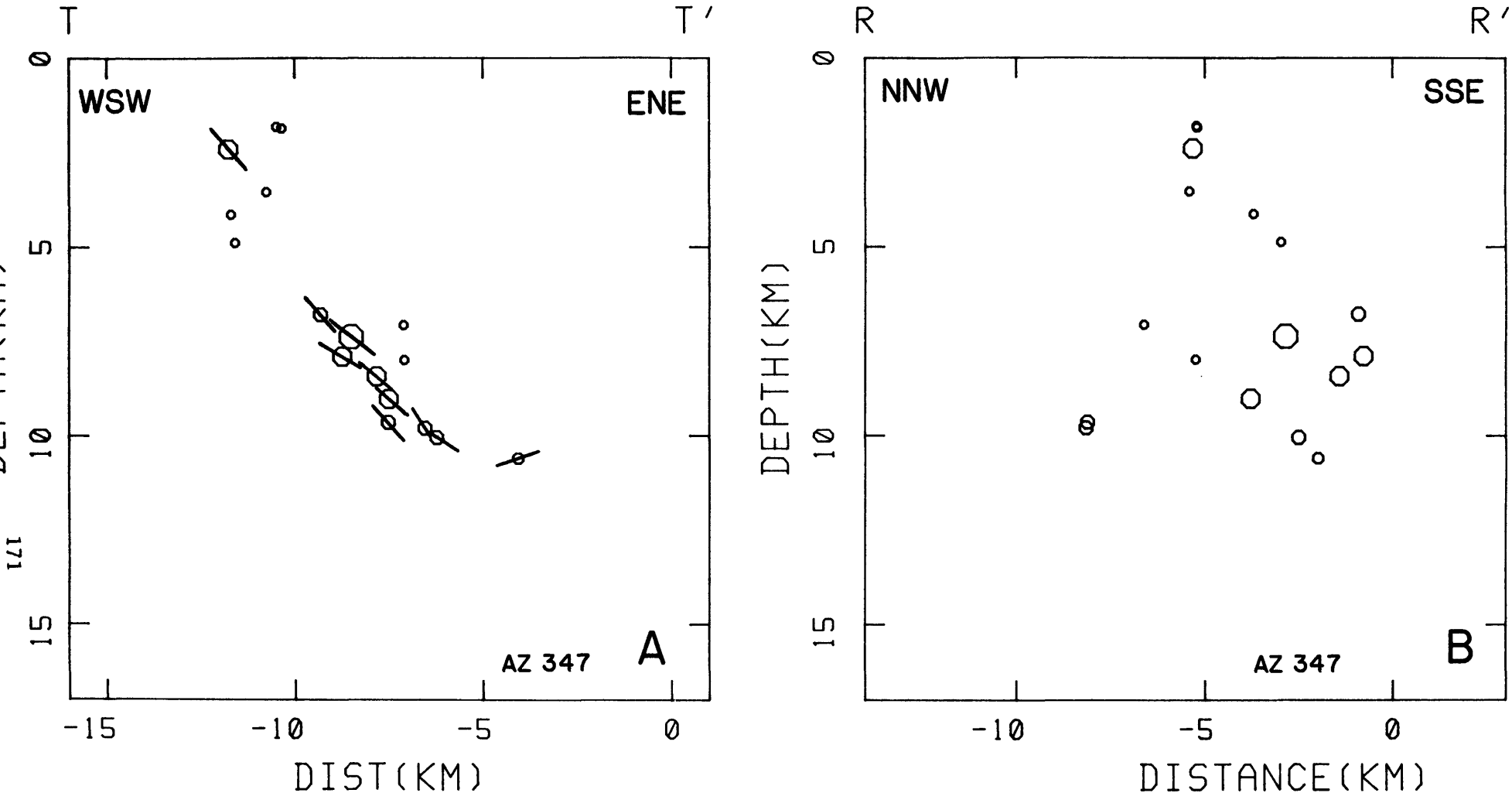

0=36-13.96 120-18.57 AZ=347.0 MY02_SP30-3.20

FIGURE 11

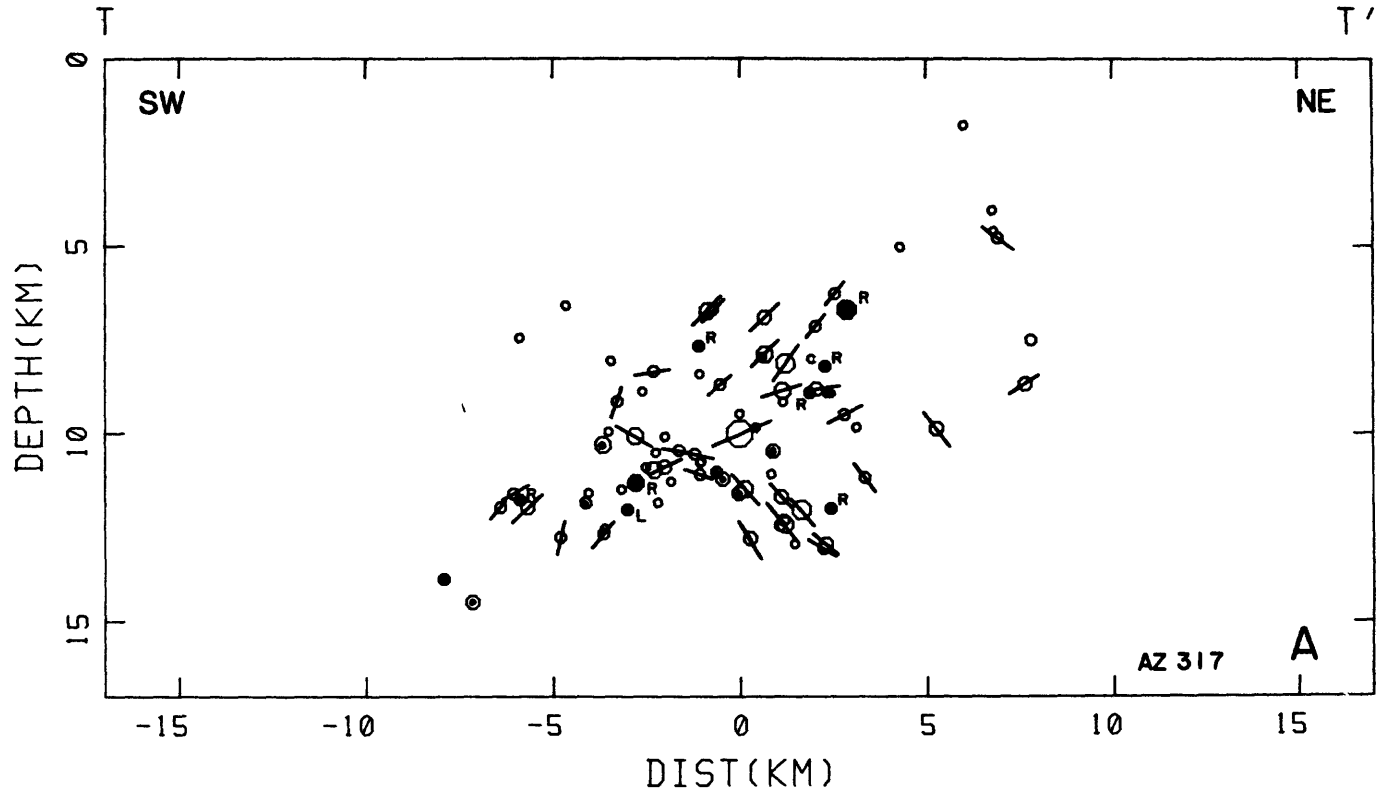

0=36-13.96 120-18.57 MY02_SP30-3.20 -17<R<17 summ

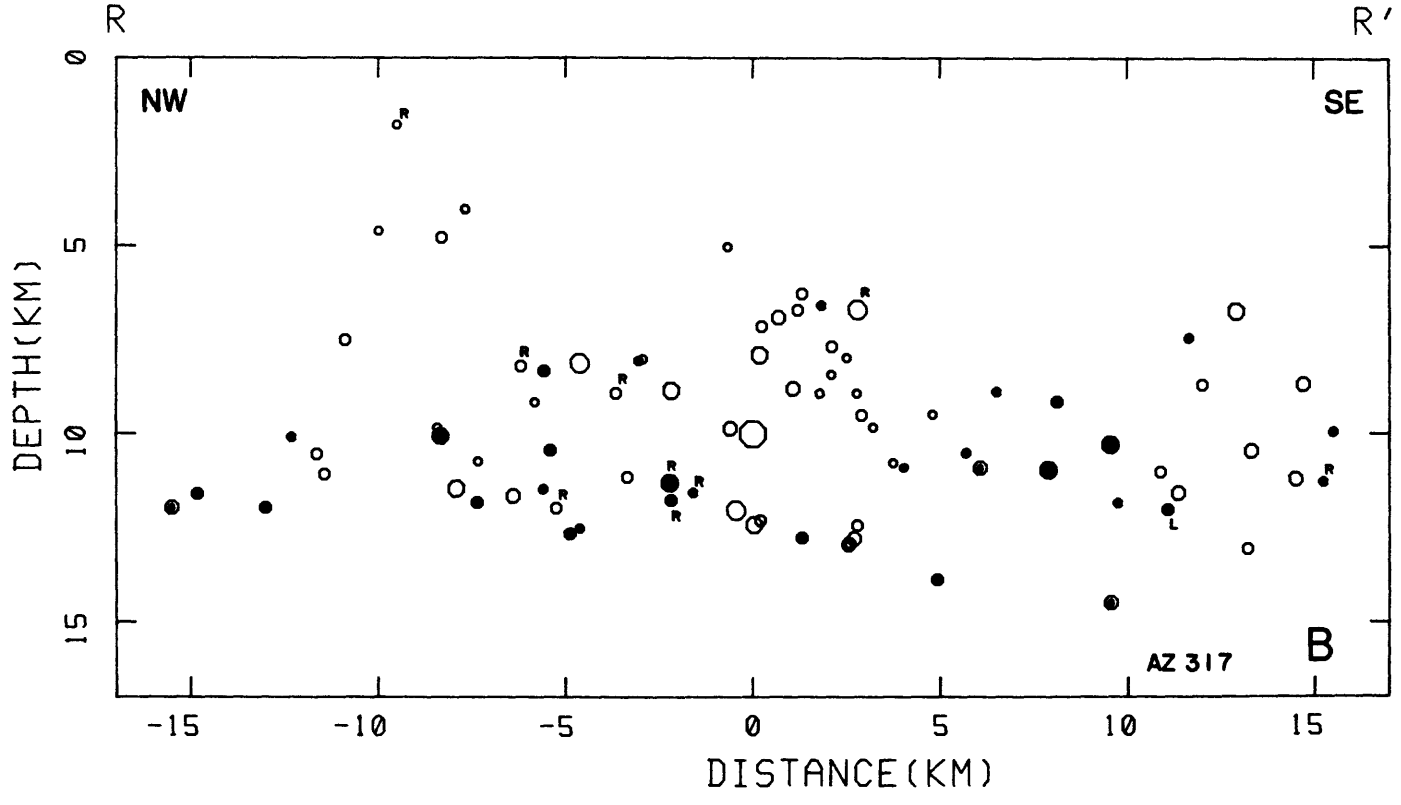

0=36-13.96 120-18.57 AZ=137.0 MY02_SP30-3.20 -17<T<17 summ

FIGURE 12

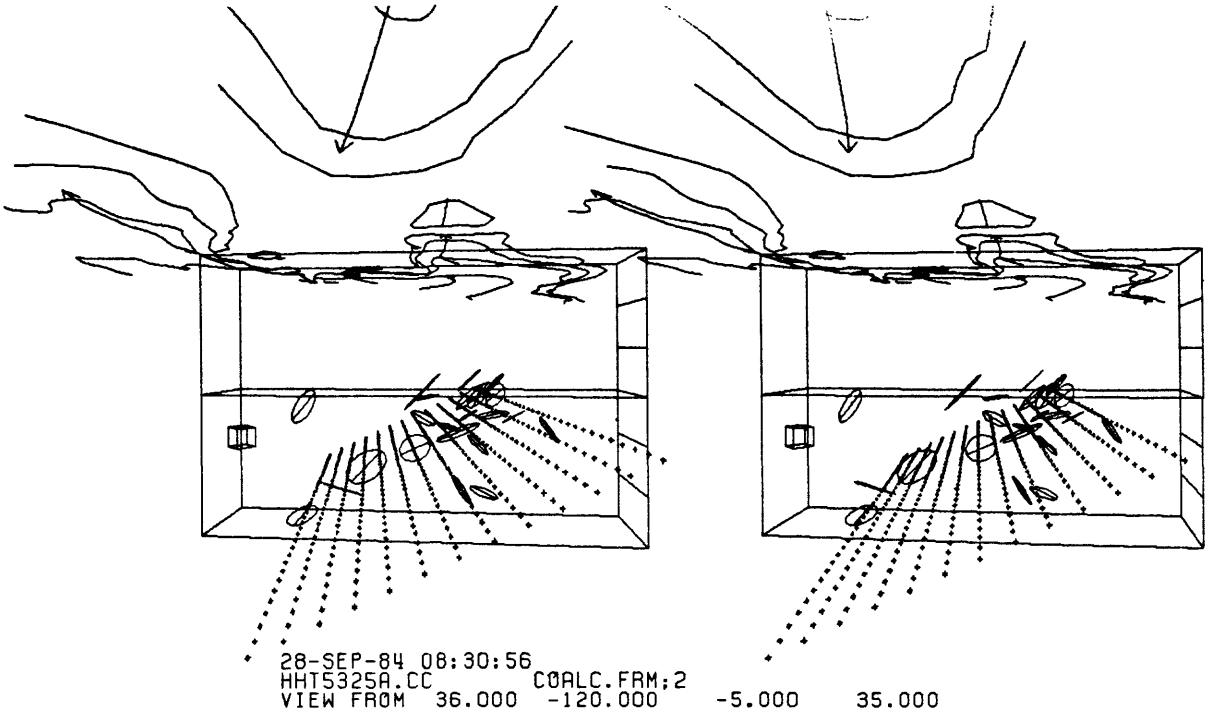

MY02-MY04 NCS FROM SE

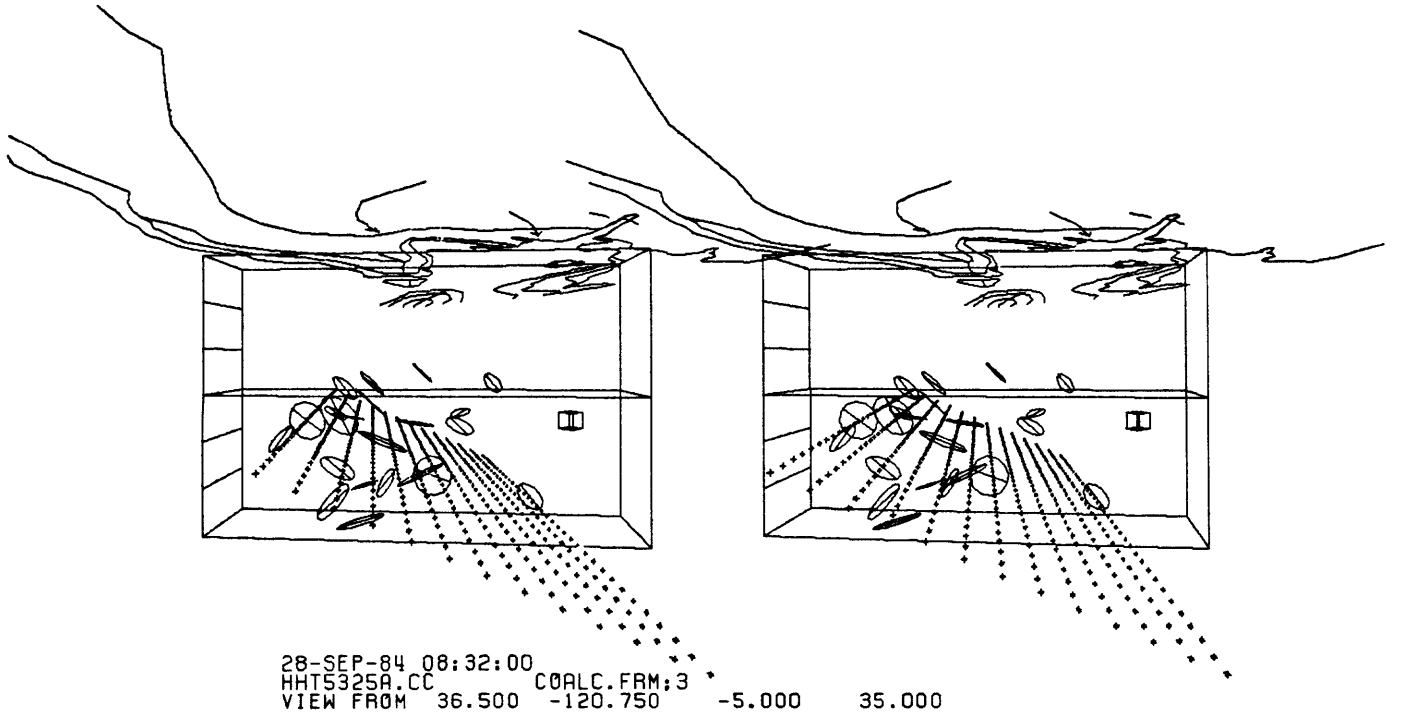

MY02-MY04 NCS FROM NW

FIGURE 13

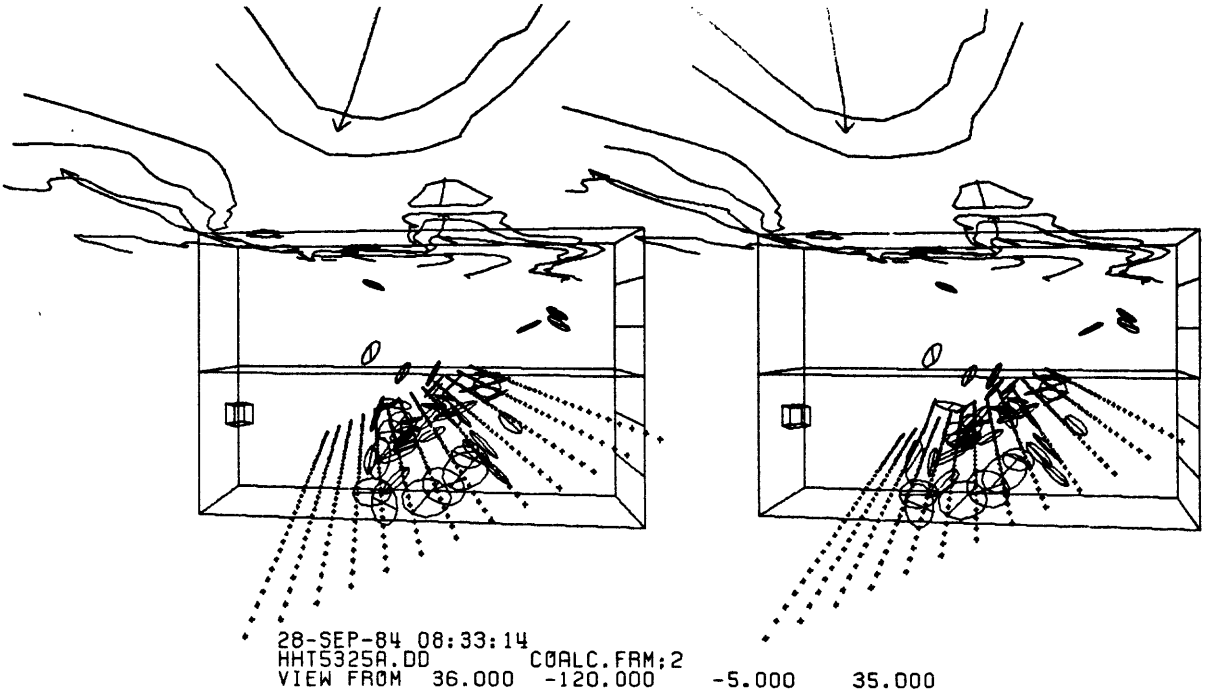

MYO5-JN10 NCS FROM SE

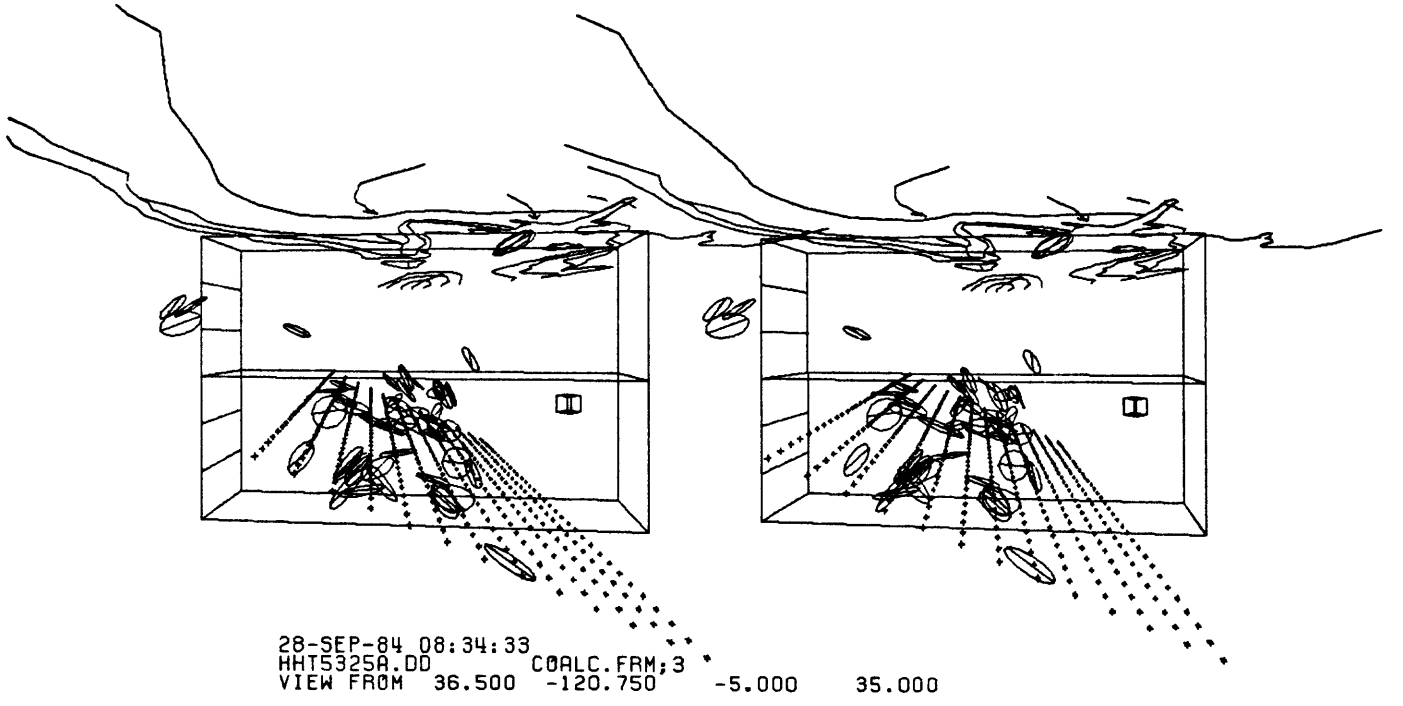

MYO5-JN10 NCS FROM NW

FIGURE 14

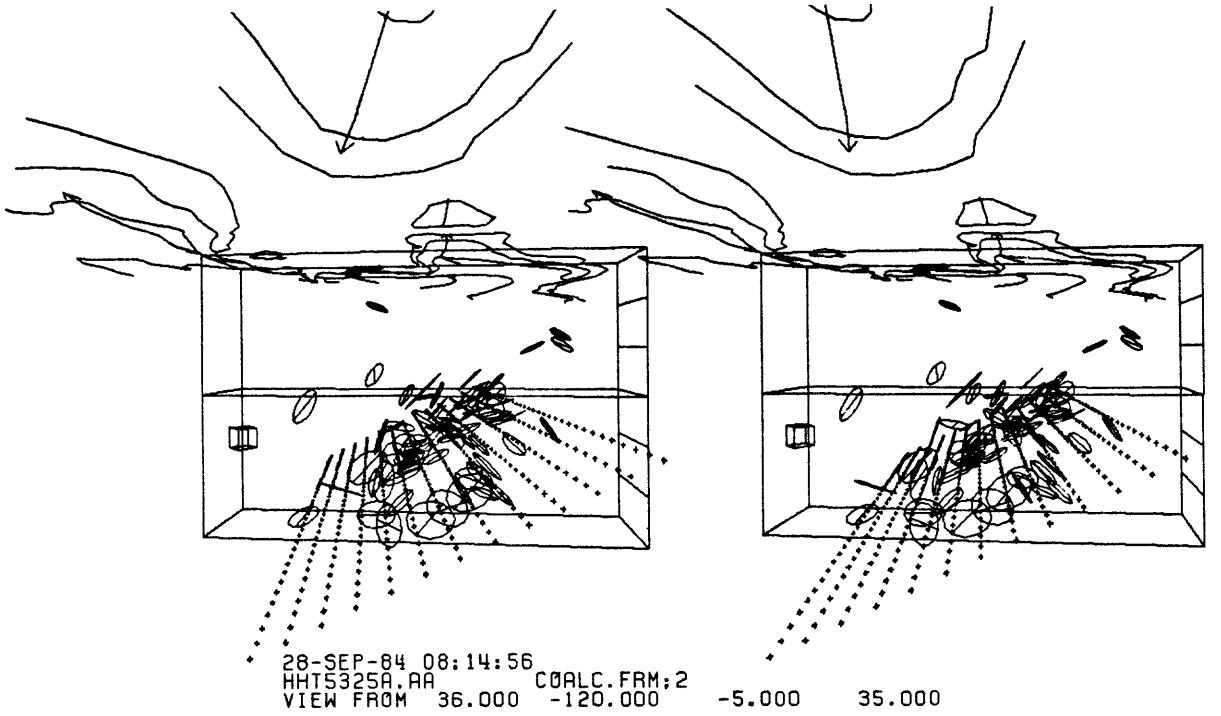

MY02-JN10 NCS FROM SE

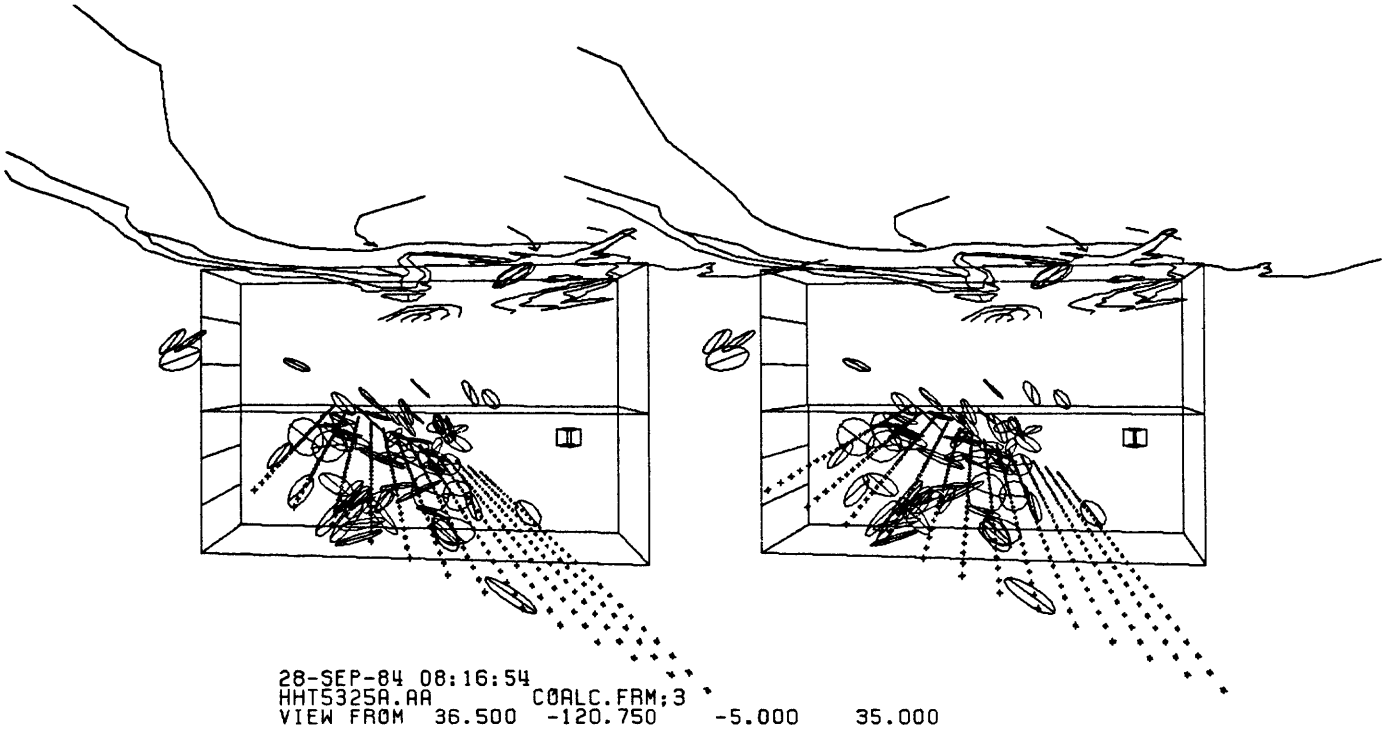

MY02-JN10 NCS FROM NW

FIGURE 15

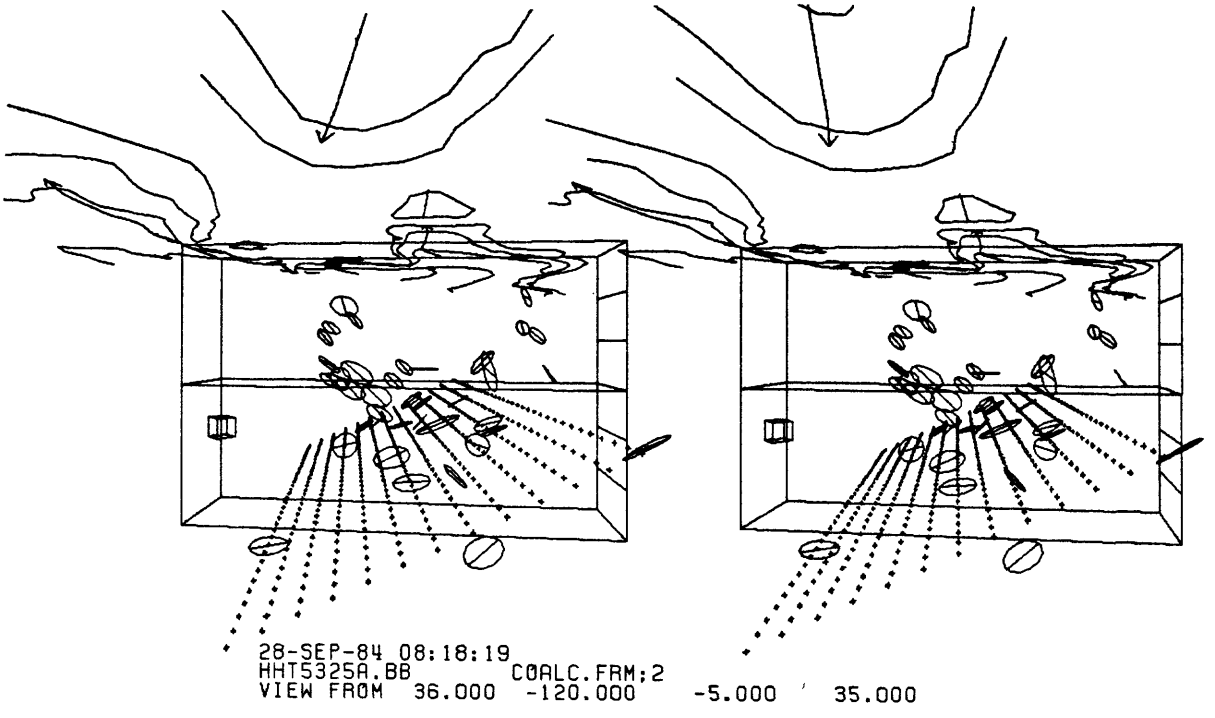

JN11-SP30 NCS FROM SE

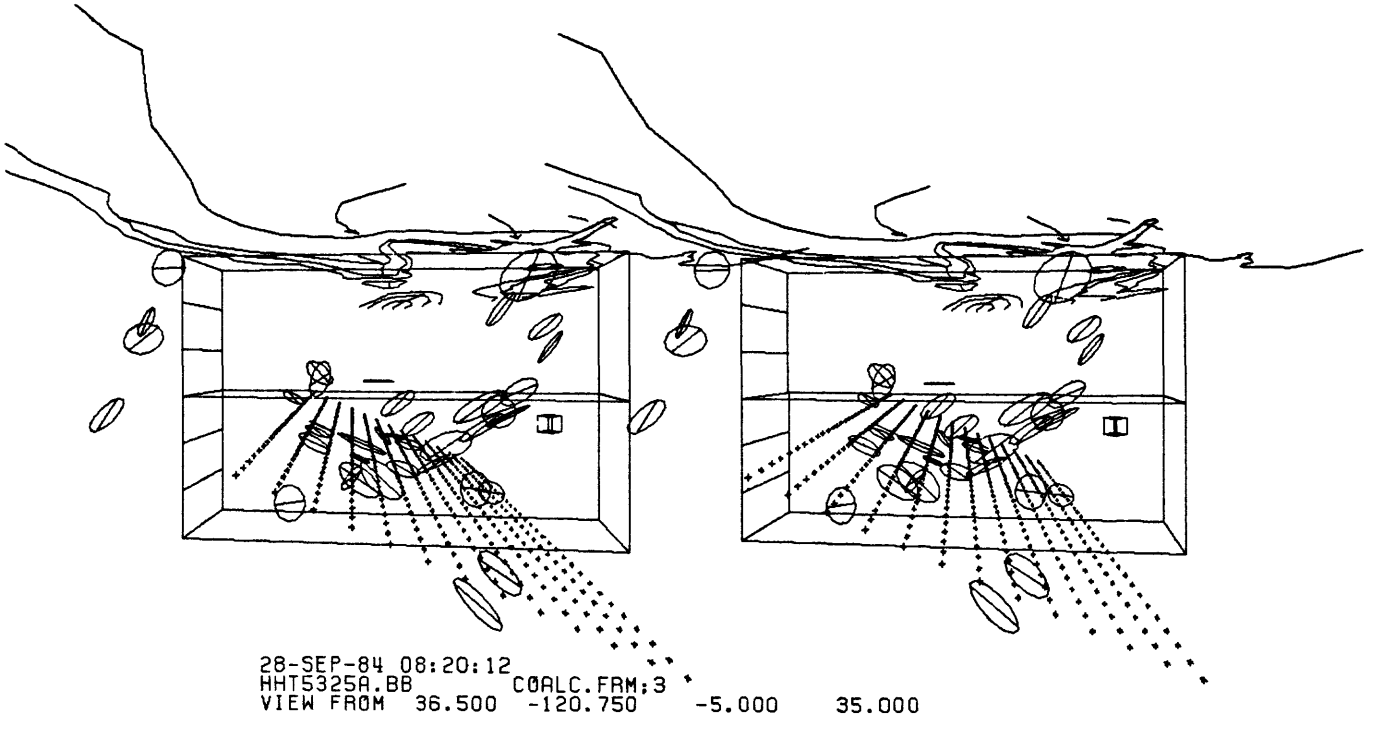

JN11-SP30 NCS FROM NW

FIGURE 16

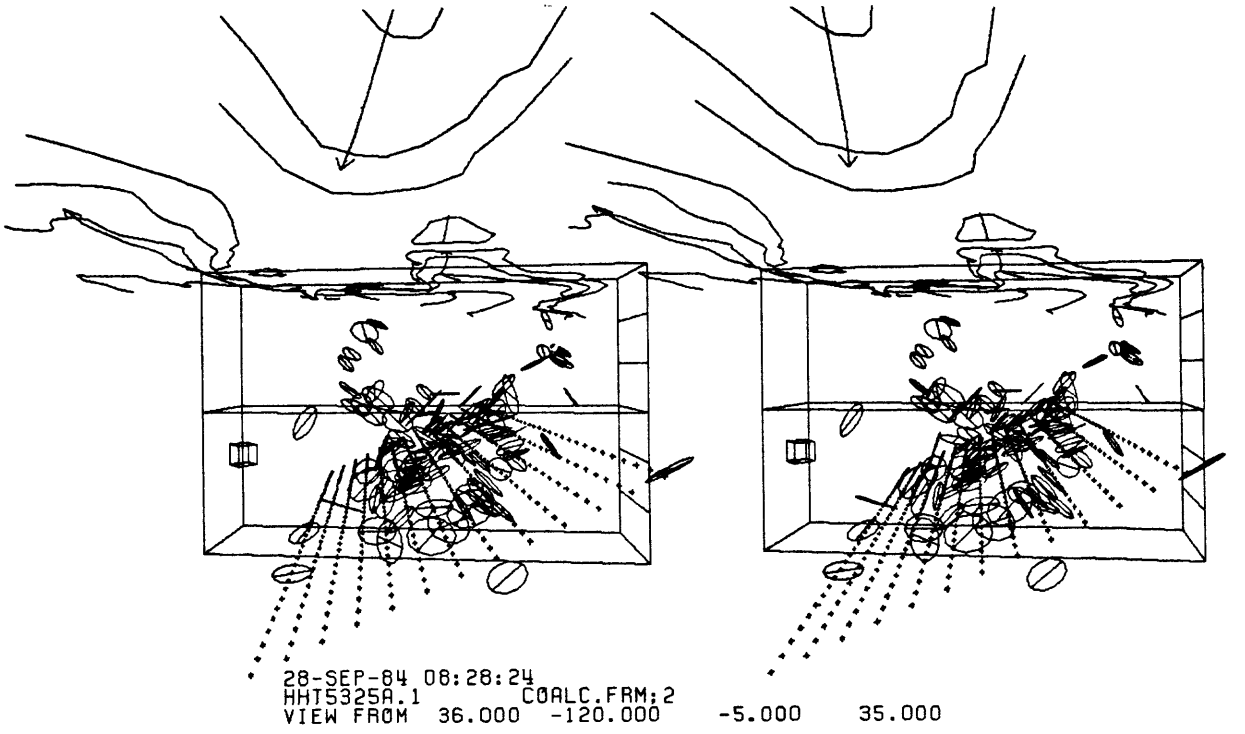

MY02-SP30 NCS FROM SE

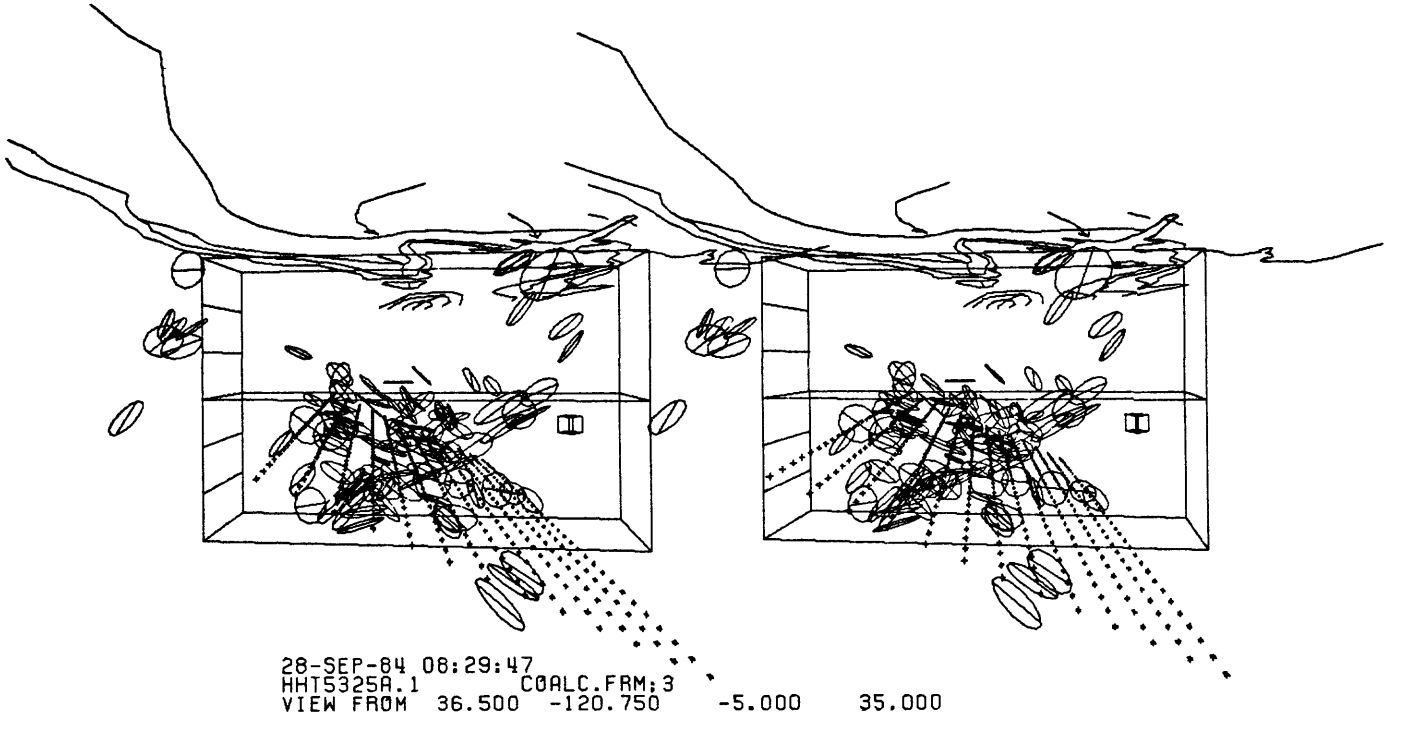

MY02-SP30 NCS FROM NW

FIGURE 17

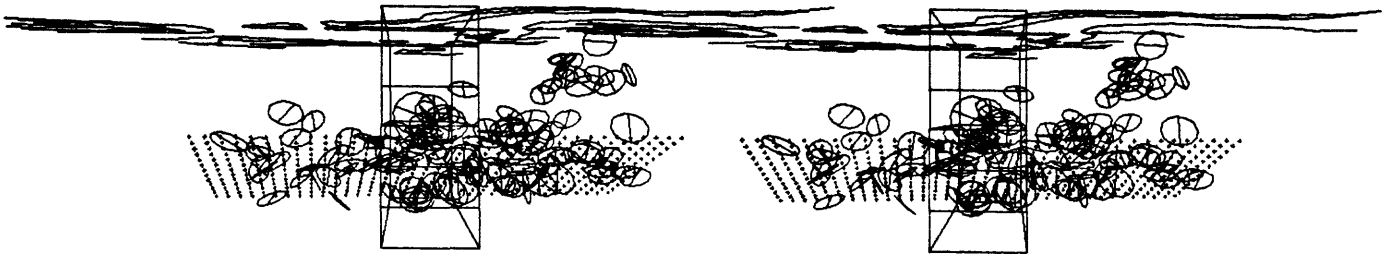

28-SEP-84 08:02:50
HHT5325A.1 COALC.FRM;7
VIEW FROM 36.780 -119.600 -7.500 50.000

MY02-SP30 NCS FROM NE

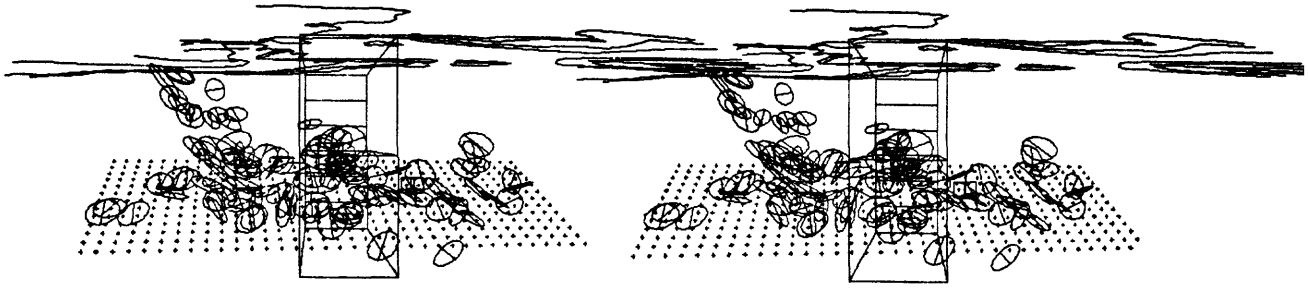

28-SEP-84 08:01:10
HHT5325A.1 COALC.FRM;6
VIEW FROM 35.650 -121.000 -7.500 50.000

MY02-SP30 NCS FROM SW

FIGURE 18

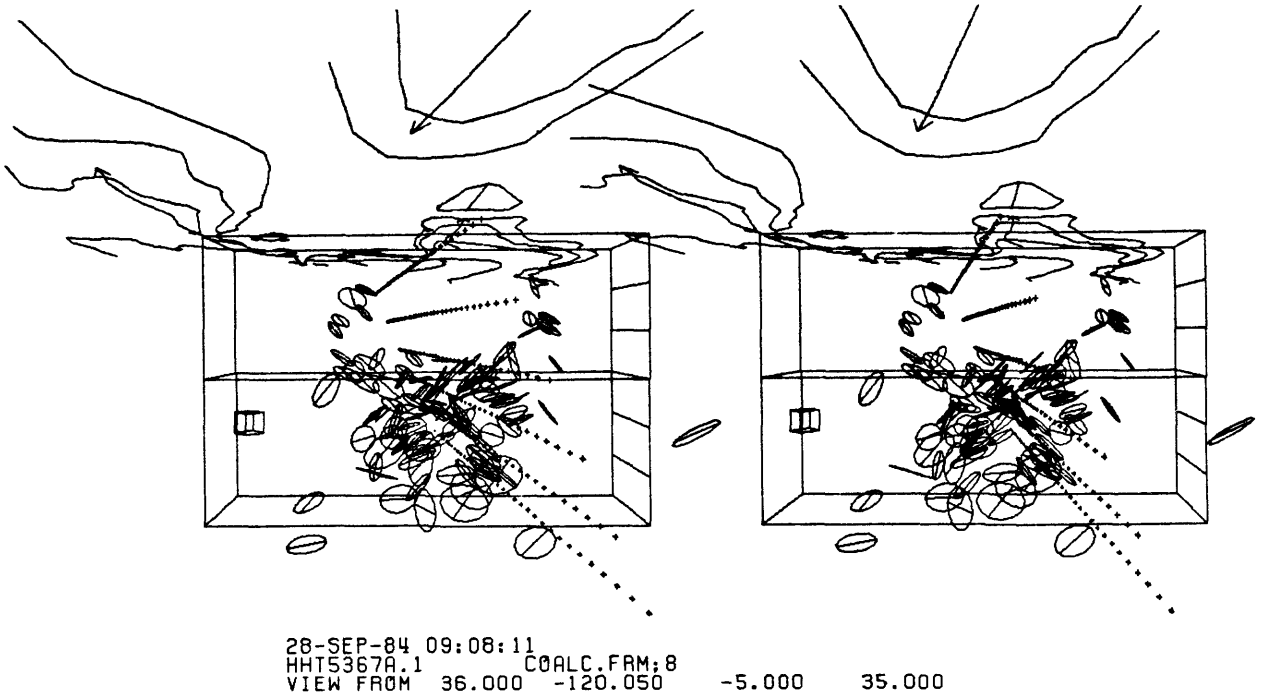

MY02- SP30 NCS FROM SE

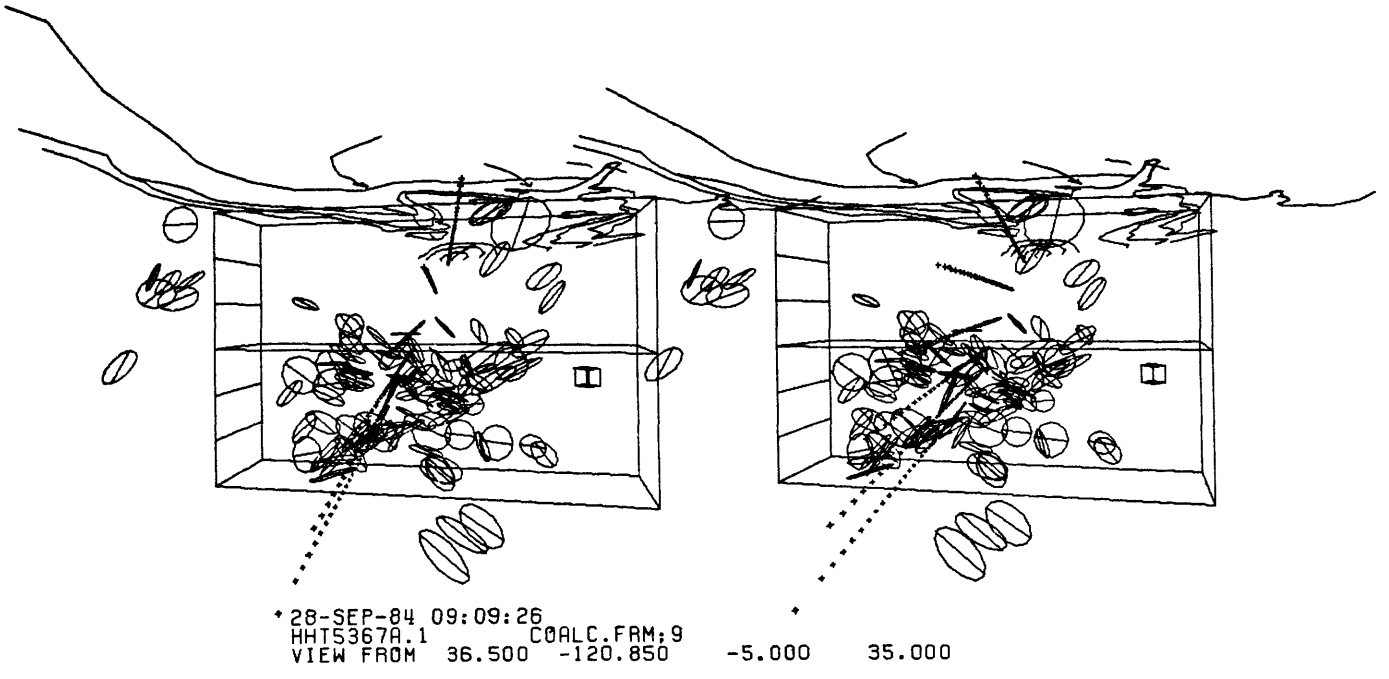

MY02-SP30 NCS FROM NW

FIGURE 19

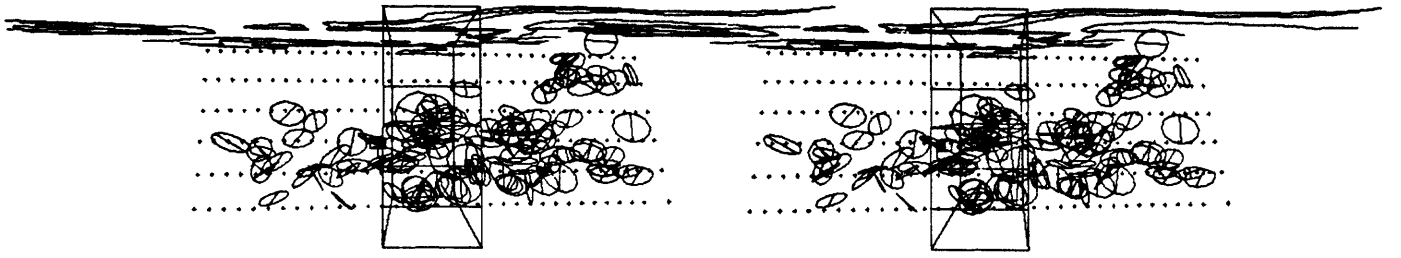

28-SEP-84 09:14:18
HHT5367A.1 COALC.FRM;7
VIEW FROM 36.780 -119.600 -7.500 50.000

MY02-SP30 NCS FROM NE

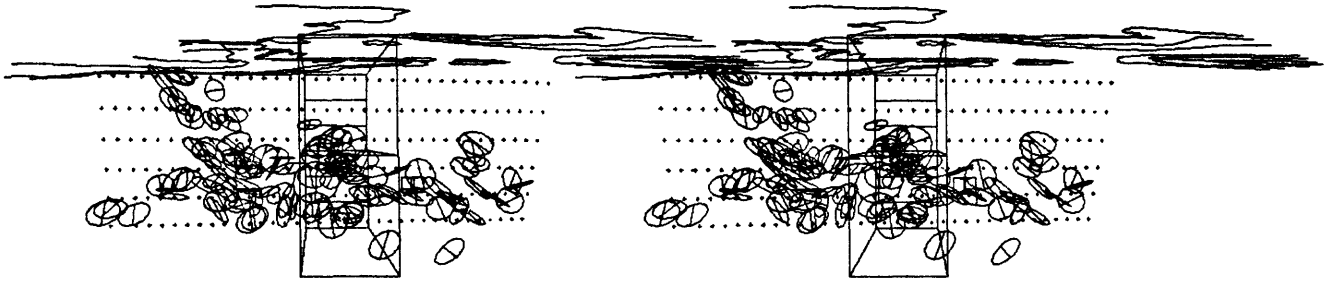

28-SEP-84 09:11:12
HHT5367A.1 COALC.FRM;6
VIEW FROM 35.650 -121.000 -7.500 50.000

MY02-SP30 NCS FROM SW

FIGURE 20

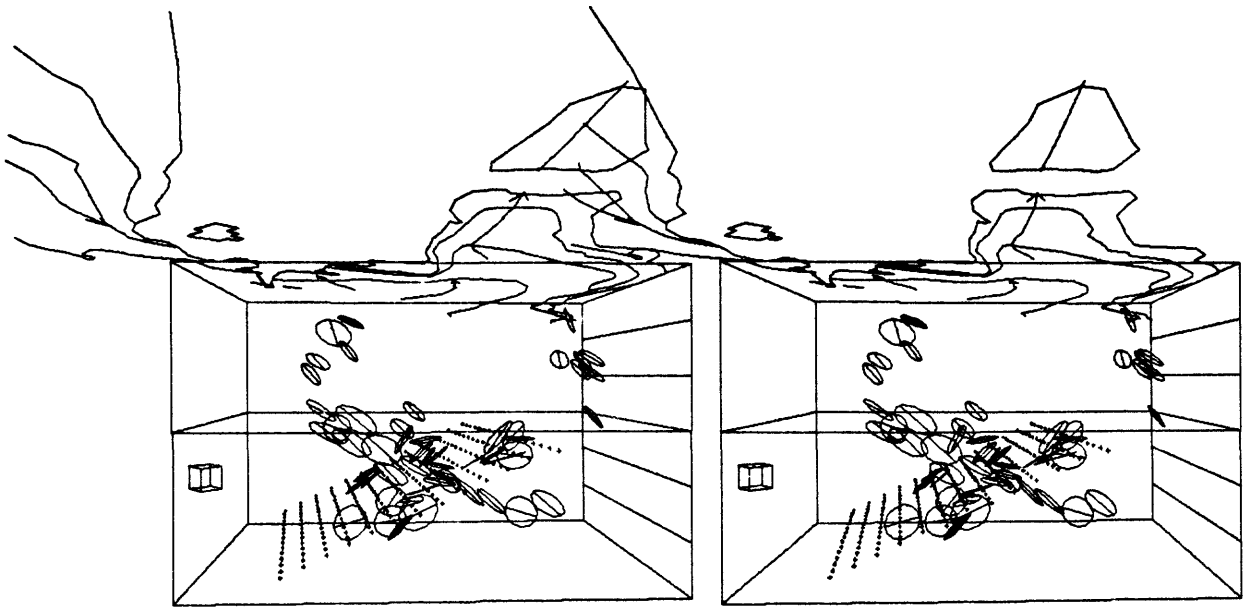

28-SEP-84 07:52:47
HHT5325A.N COALN.FRM;2
VIEW FROM 36.220 -120.330 -5.000 35.000

MY02-SP30 N FROM SE

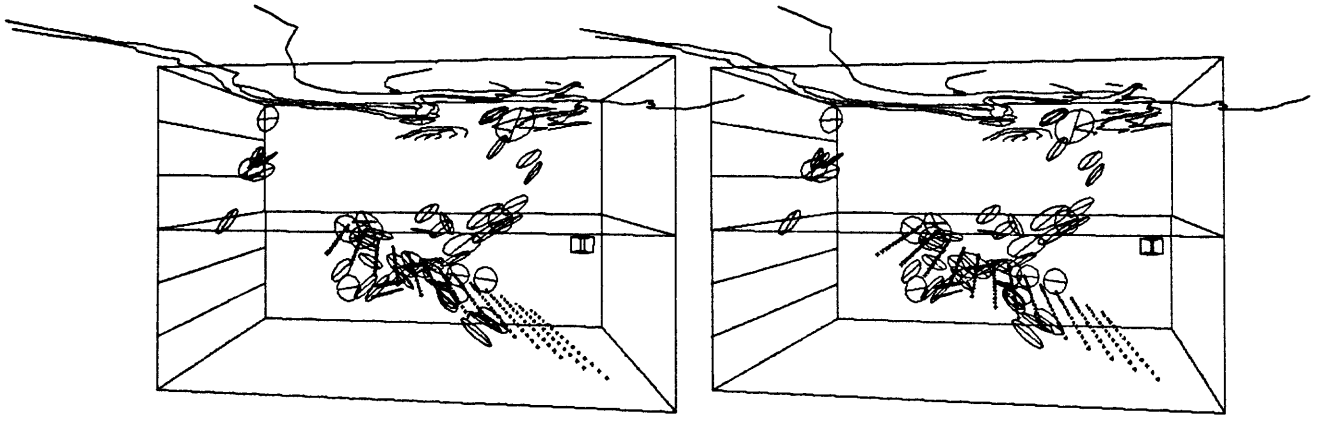

28-SEP-84 07:53:47
HHT5325A.N COALN.FRM;3
VIEW FROM 36.500 -120.750 -5.000 35.000

MY02-SP30 N FROM NW

FIGURE 21

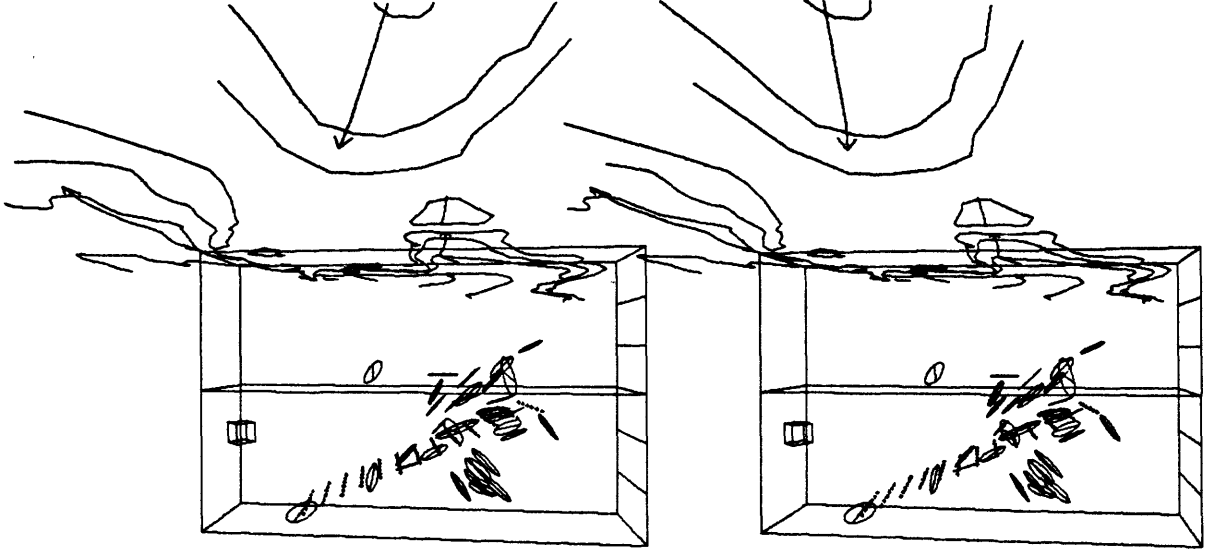

28-SEP-84 08:12:49
HHT5325A.C COALC.FRM;2
VIEW FROM 36.000 -120.000 -5.000 35.000

MY02-SP30 C FROM SE

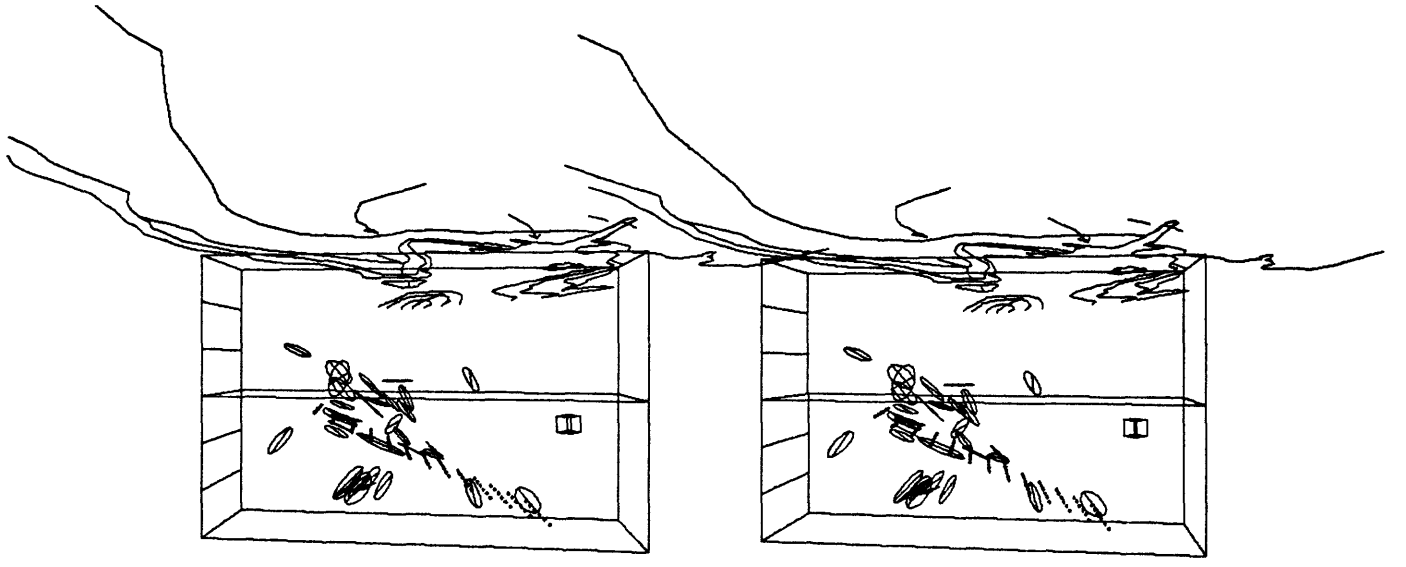

28-SEP-84 08:13:37
HHT5325A.C COALC.FRM;3
VIEW FROM 36.500 -120.750 -5.000 35.000

MY02-SP30 C FROM NW

FIGURE 22

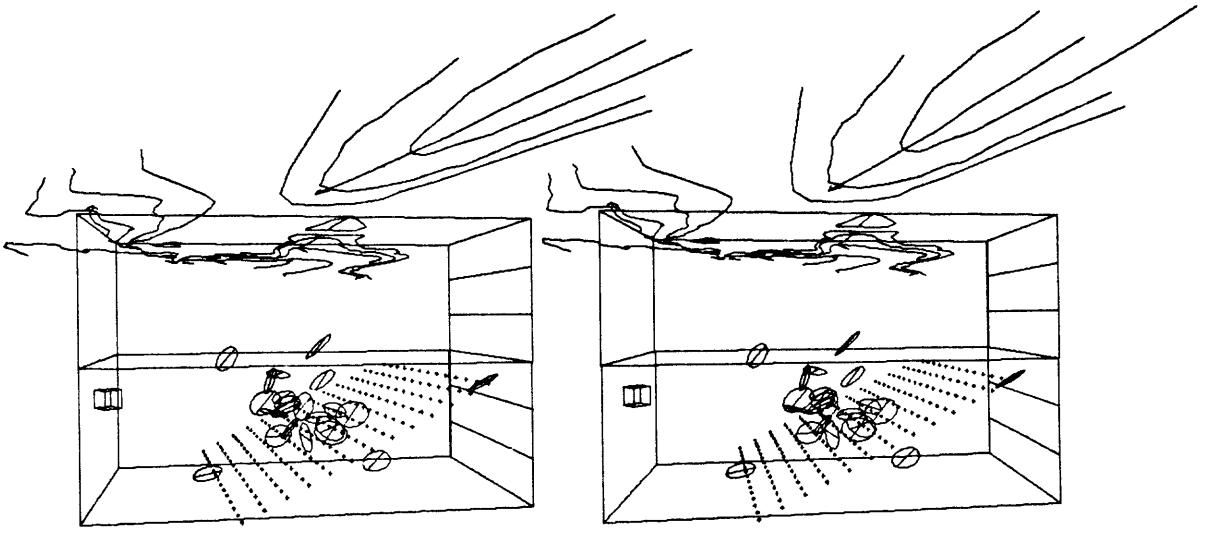

28-SEP-84 07:57:45
HHT5325A.S COALS.FRM;2
VIEW FROM 36.030 -120.120 -5.000 35.000

MY02-SP30 S FROM SE

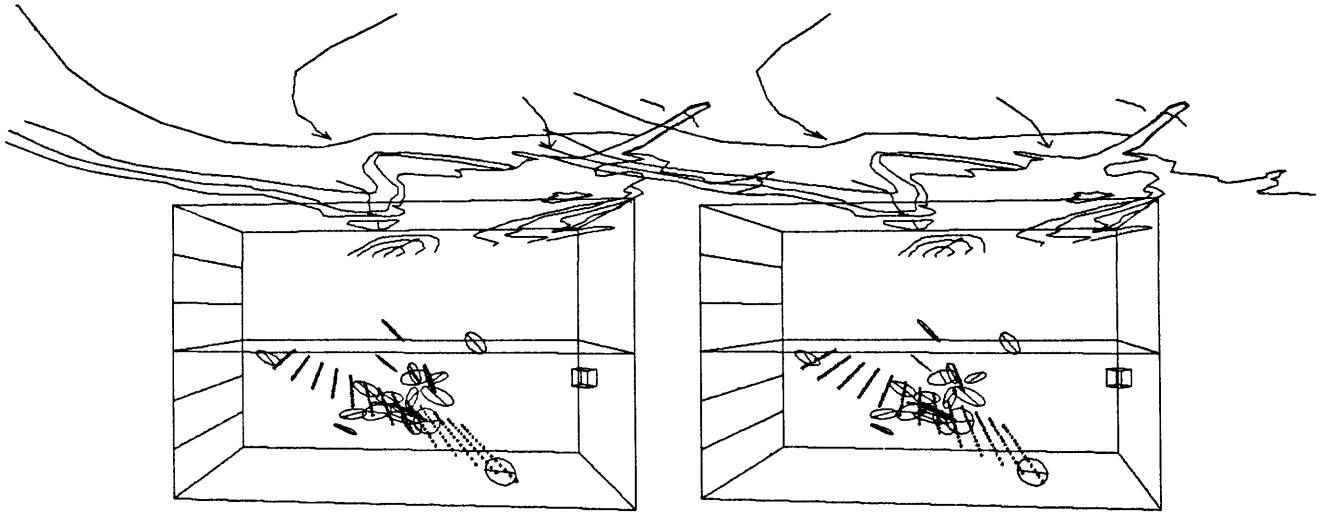

28-SEP-84 07:59:03
HHT5325A.S COALS.FRM;3
VIEW FROM 36.500 -120.750 -5.000 35.000

MY02-SP30 S FROM NW

FIGURE 23

830502 2342 H 10.1 M 6.7

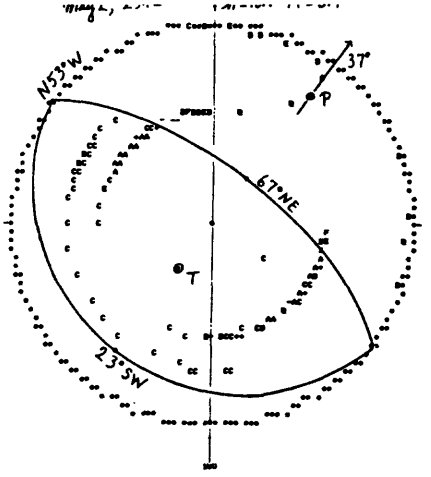

830503 0141 H 6.7 M 4.5

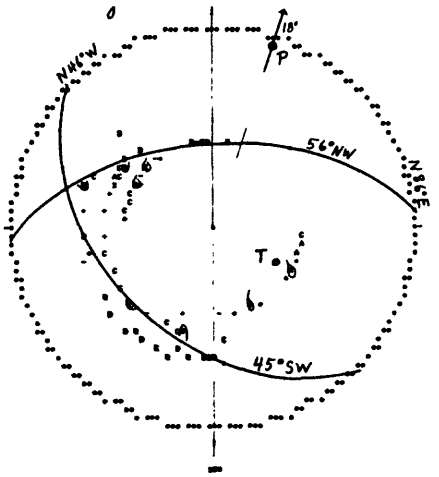

830503 0039 H 11.3 M 4.5

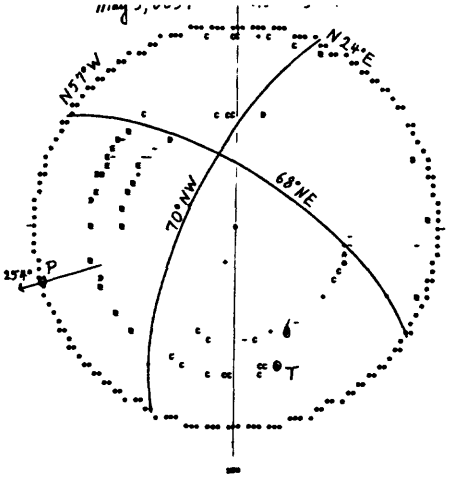

830503 0155 H 6.9 M 4.0

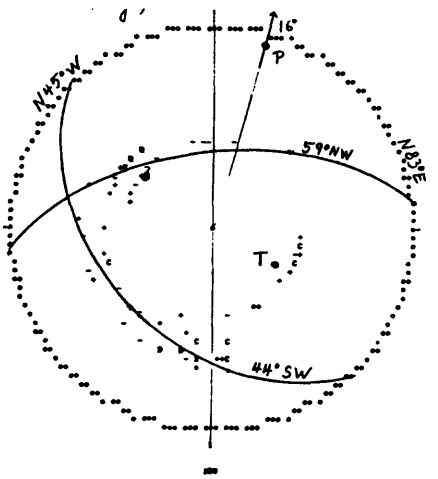

830503 0057 H 8.1 M 5.1

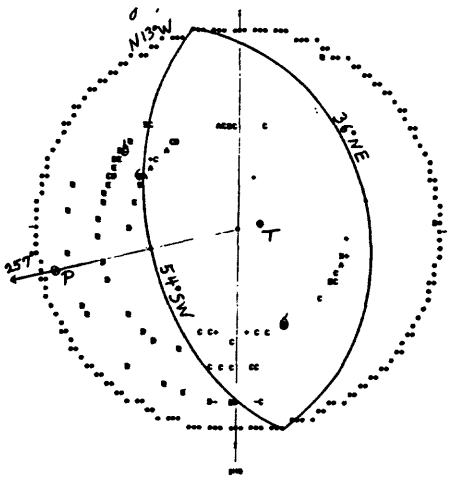

830503 0215 H 8.8 M 4.1

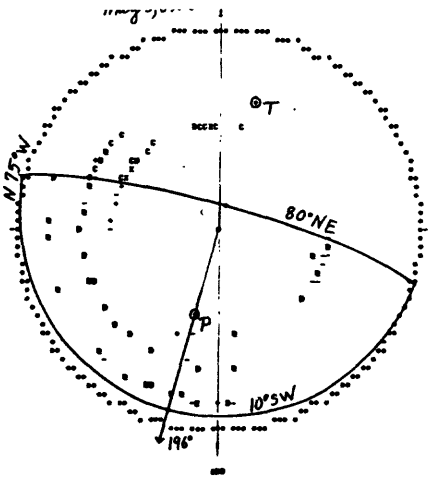

FIGURE 24—a

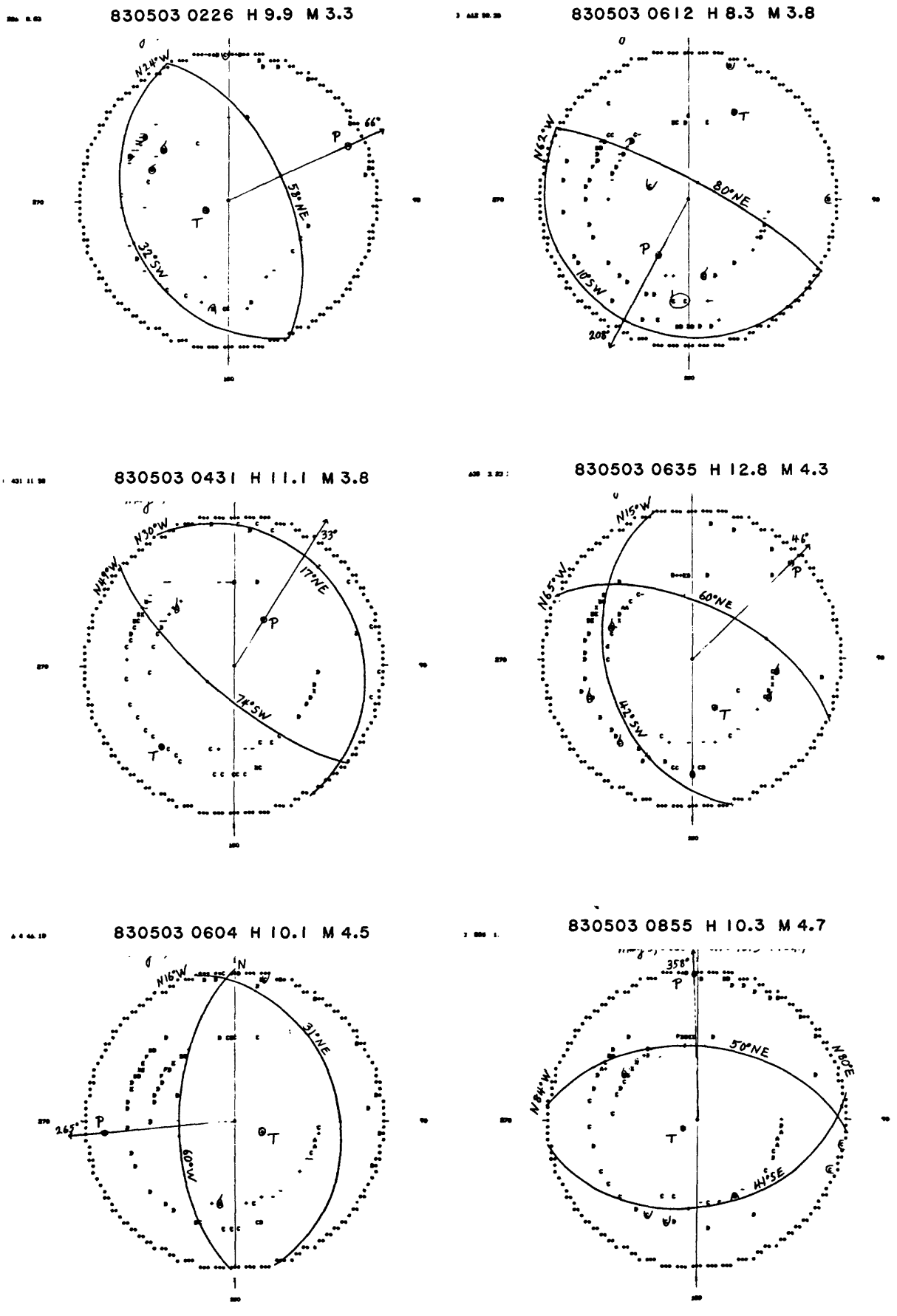
830503 0226 H 9.9 M 3.3
N24°W
66°
P
52°NE
T
32°SW
830503 0612 H 8.3 M 3.8
N42°W
T
80°NE
P
105°SW
205°
830503 0431 H 11.1 M 3.8
N30°W
33°
17°NE
P
74°SW
T
830503 0635 H 12.8 M 4.3
N15°W
46°
P
N65°W
60°NE
42°SW
T
830503 0604 H 10.1 M 4.5
N16°W
N
31°NE
265°
P
T
60°W
830503 0855 H 10.3 M 4.7
358°
P
50°NE
N80°E
N84°W
T
41°SE

FIGURE 24-b

830503 0939 H 9.9 M 4.1

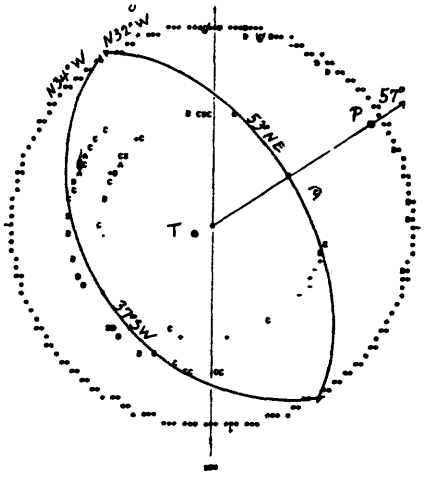

830503 2346 H 13.9 M 4.0

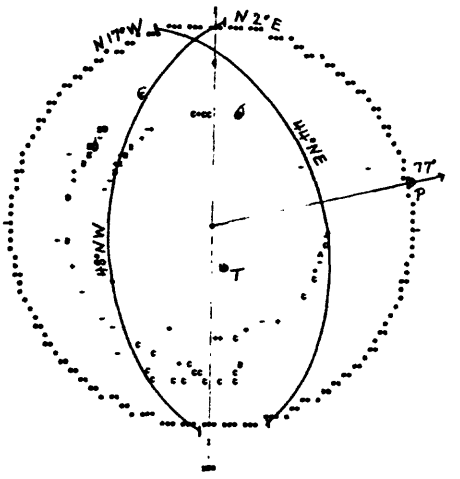

830503 1510 H 8.2 M 4.0

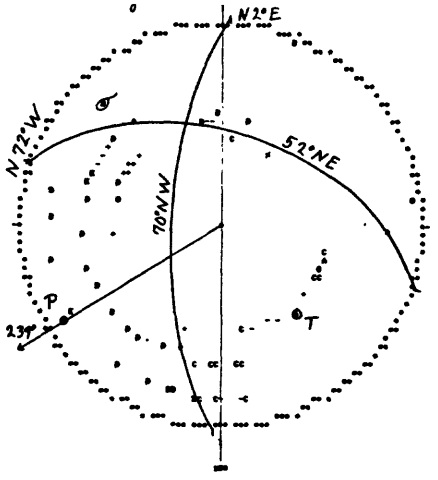

830504 0818 H 8.8 M 2.9

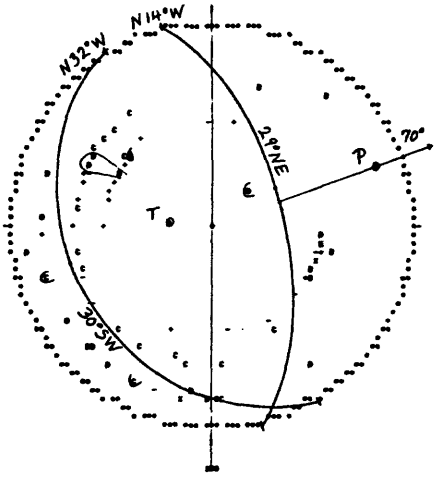

830503 1541 H 7.9 M 4.8

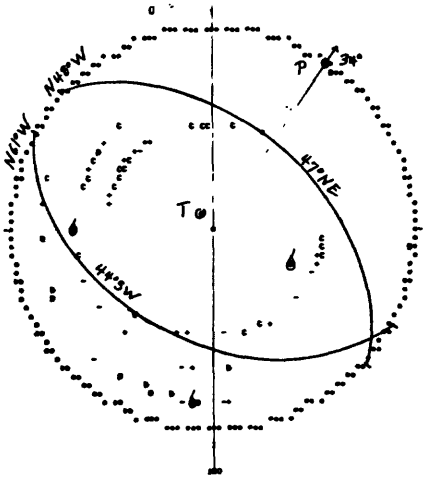

830504 0848 H 12.9 M 3.5

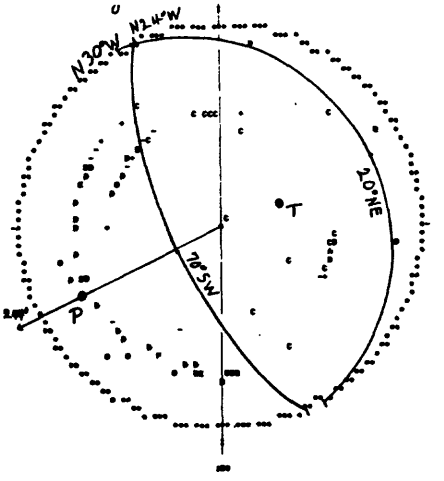

FIGURE 24-c

830504 1329 H 10.0 M 3.4

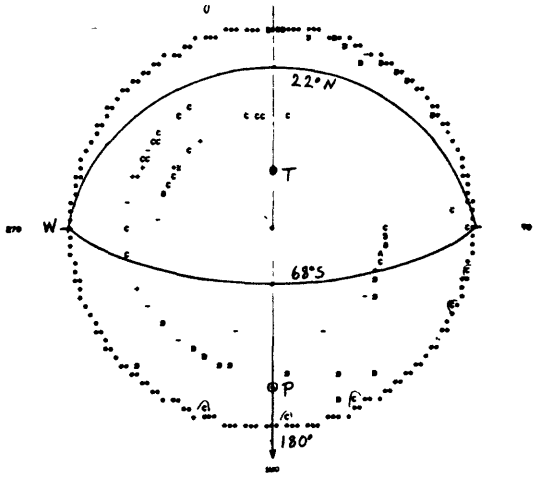

830504 1945 H 7.4 M 3.4

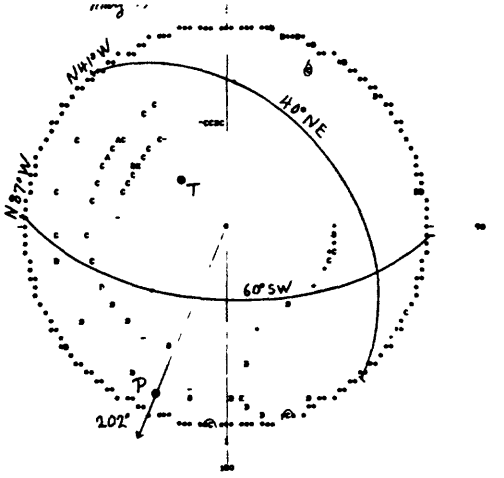

830504 1559 H 7.1 M 3.8

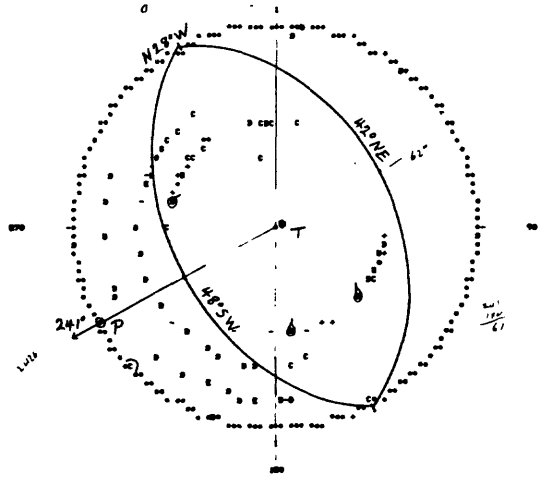

830505 0027 H 8.9 M 3.5

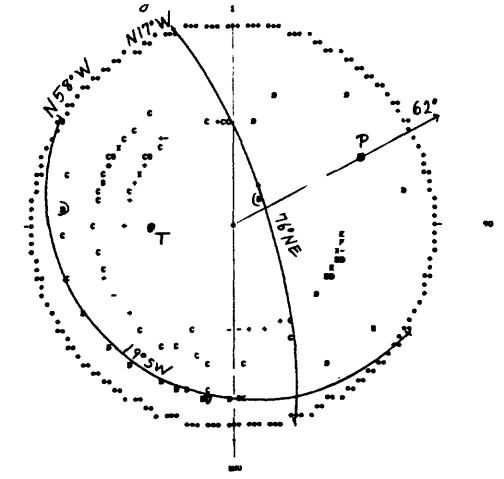

830504 1611 H 11.7 M 4.4

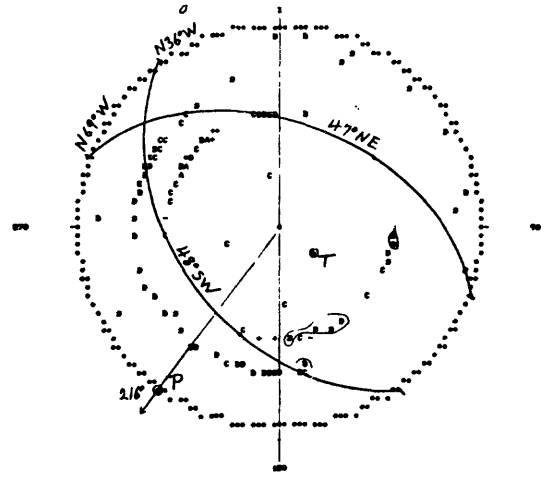

830505 0156 H 8.0 M 3.4

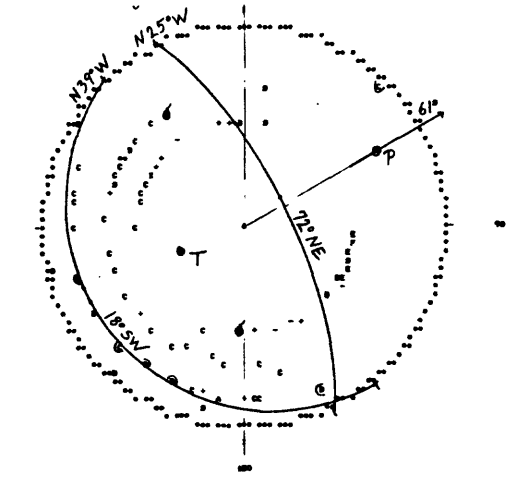

FIGURE 24-d

830505 0437 H 11.2 M 4.0

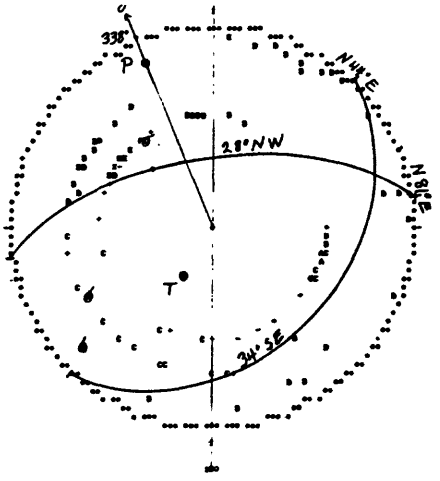

830505 1133 H 10.5 M 3.7

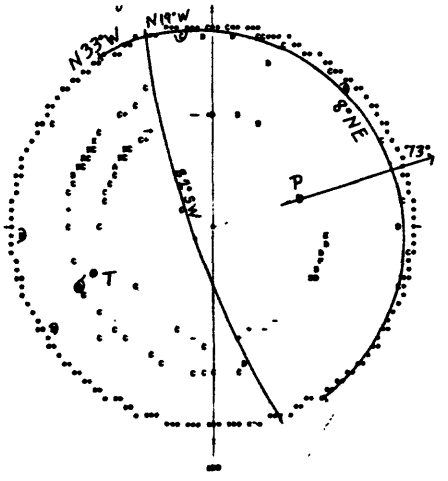

830505 0806 H 8.7 M 3.7

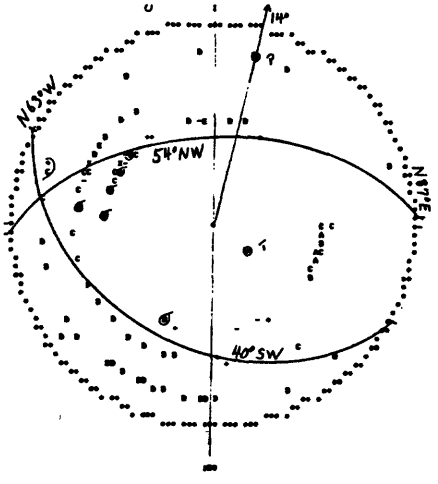

830505 1150 H 10.5 M 3.5

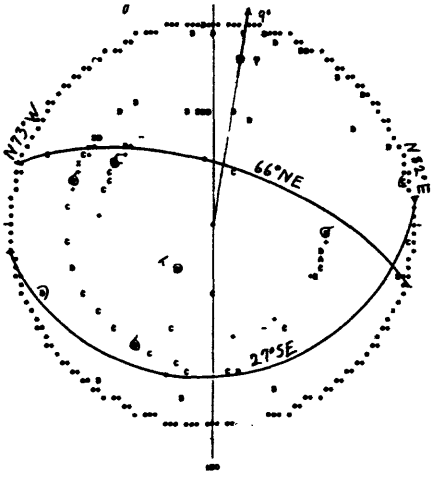

830505 1020 H 11.5 M 4.6

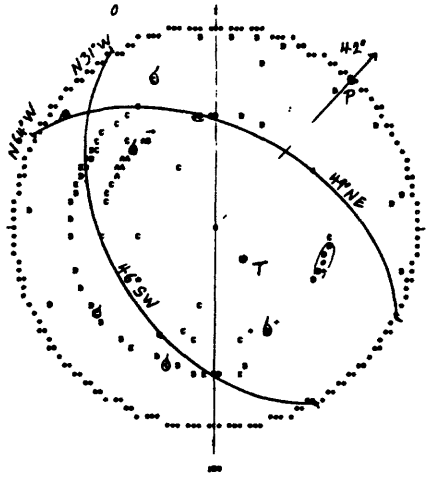

830505 1242 H 11.9 M 3.9

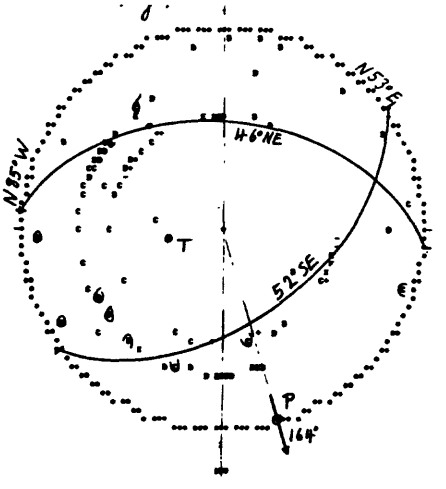

FIGURE 24–e

830505 2246 H 10.1 M 3.4

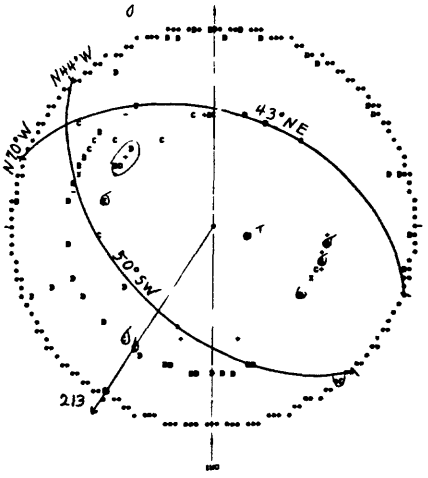

830506 1151 H 10.8 M 3.3

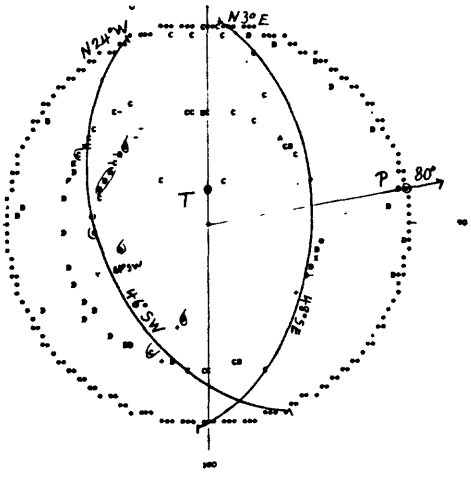

830506 0457 H 10.8 M 3.4

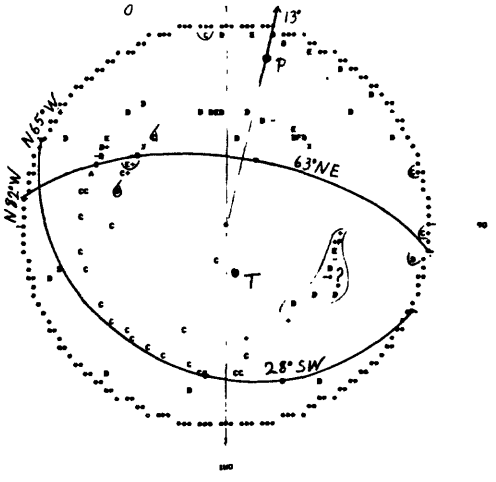

830507 0017 H 8.9 M 3.9

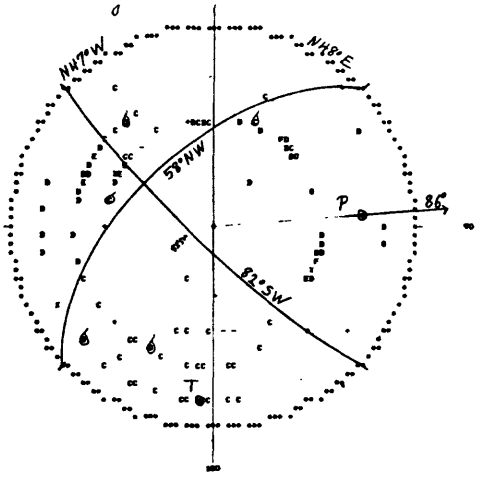

830506 0943 H 12.8 M 3.7

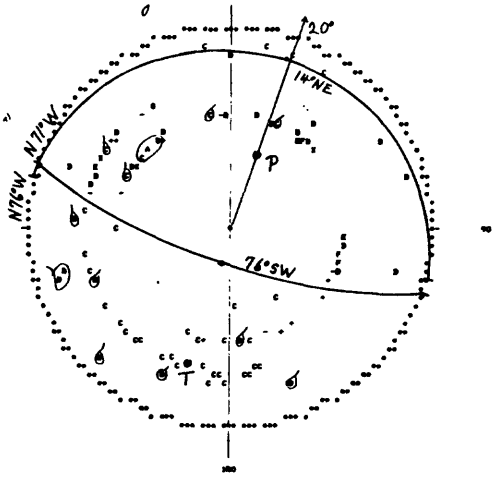

830507 0534 H 9.2 M 3.5

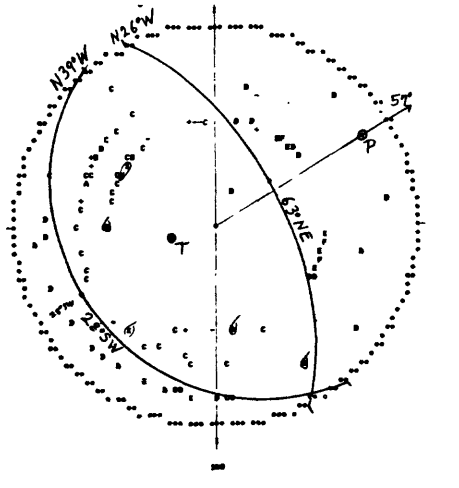

FIGURE 24-f

830507 1242 H 10.6 M 3.6

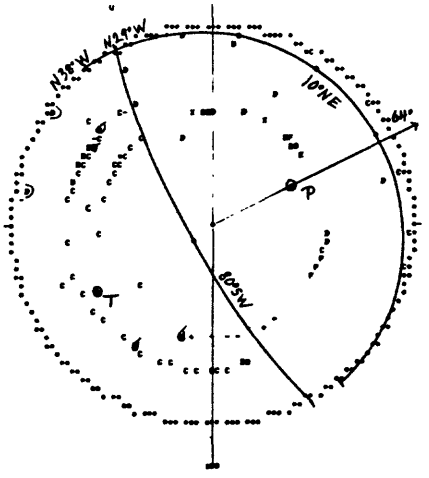

830508 0345 H 1.8 M 3.4

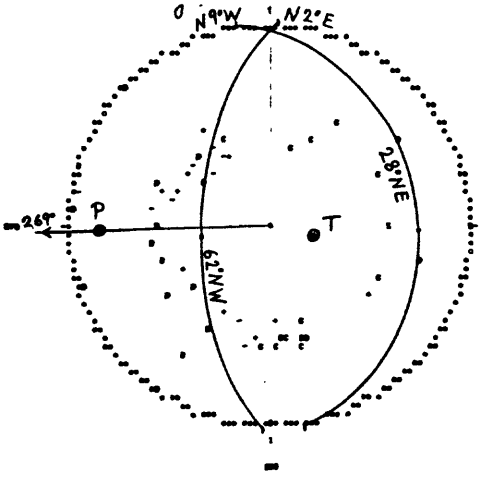

830508 0120 H 8.4 M 3.5

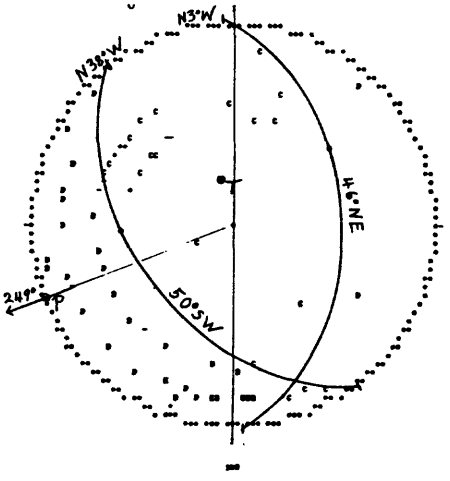

830508 0738 H 5.0 M 3.3

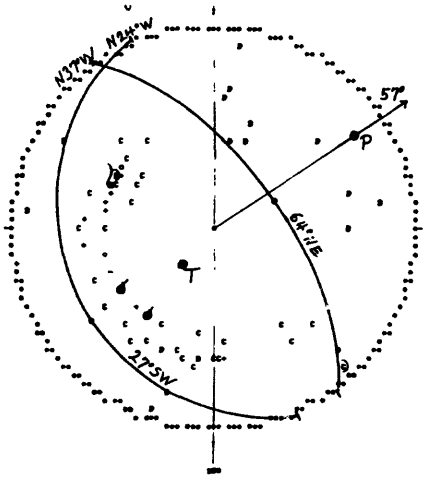

830508 0147 H 8.1 M 3.0

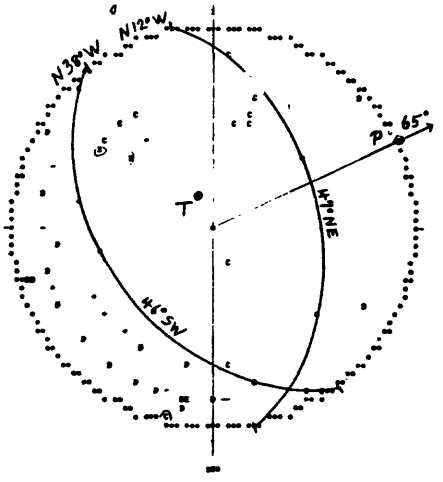

830508 1037 H 11.6 M 3.3

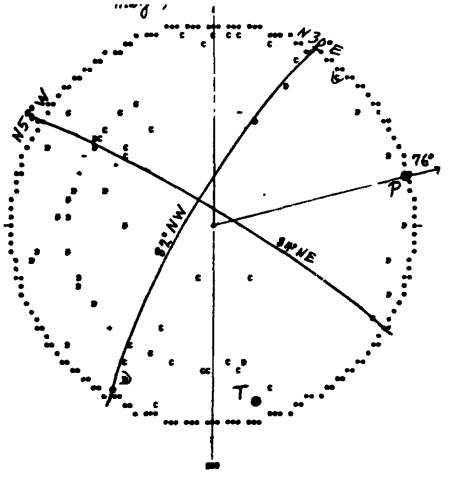

FIGURE 24-g

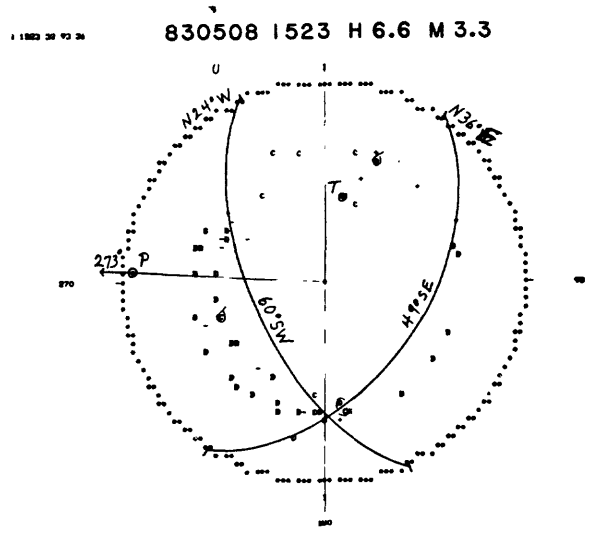
830508 1523 H 6.6 M 3.3
N24°W
N36°E
273°
P
T
60°SW
49°SE

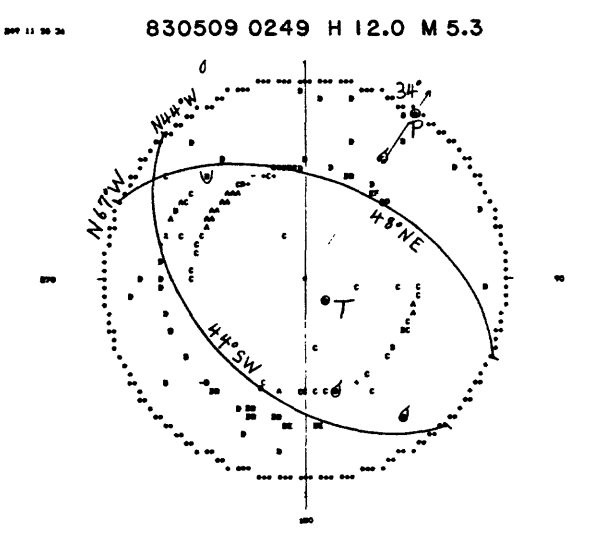
830509 0249 H 12.0 M 5.3
N44°W
N67°W
34°
P
T
48°NE
44°SW

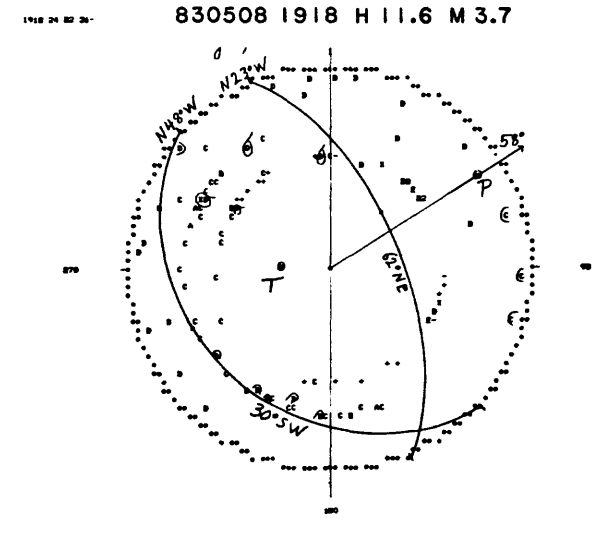
830508 1918 H 11.6 M 3.7
N23°W
N48°W
58°
P
T
62°NE
30°SW

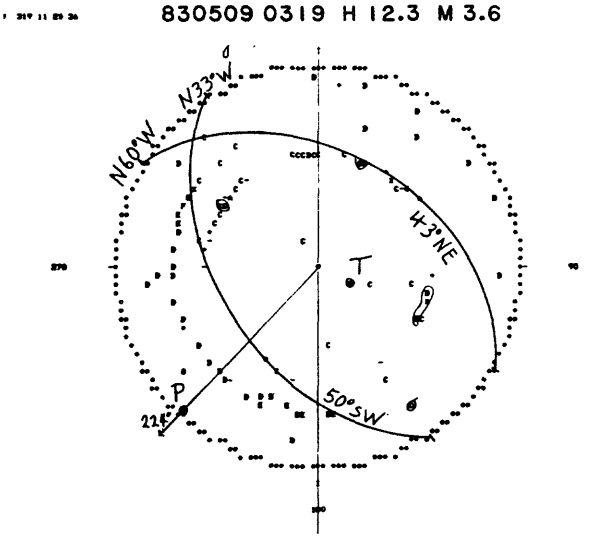
830509 0319 H 12.3 M 3.6
N33°W
N60°W
43°NE
T
P
225°
50°SW

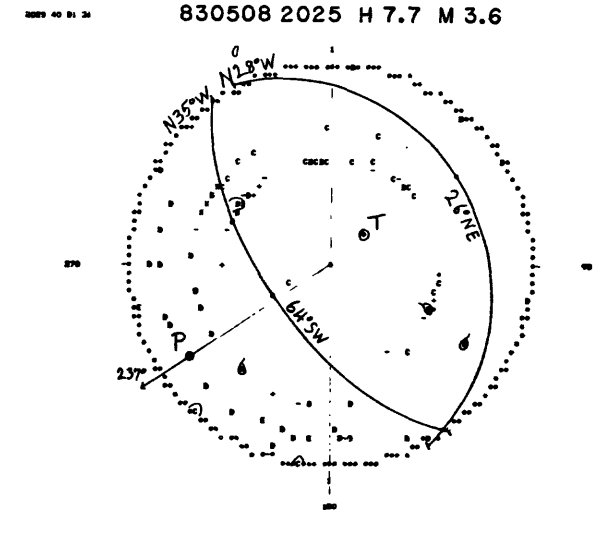
830508 2025 H 7.7 M 3.6
N28°W
N35°W
26°NE
T
64°SW
P
237°

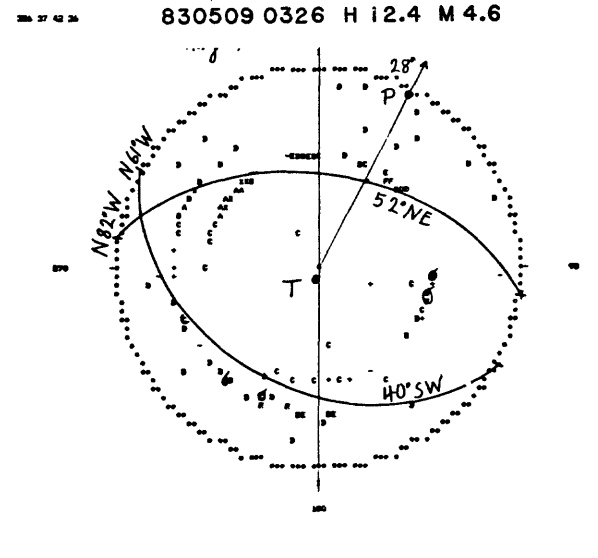
830509 0326 H 12.4 M 4.6
28°
P
N61°W
N82°W
52°NE
T
40°SW

FIGURE 24-h

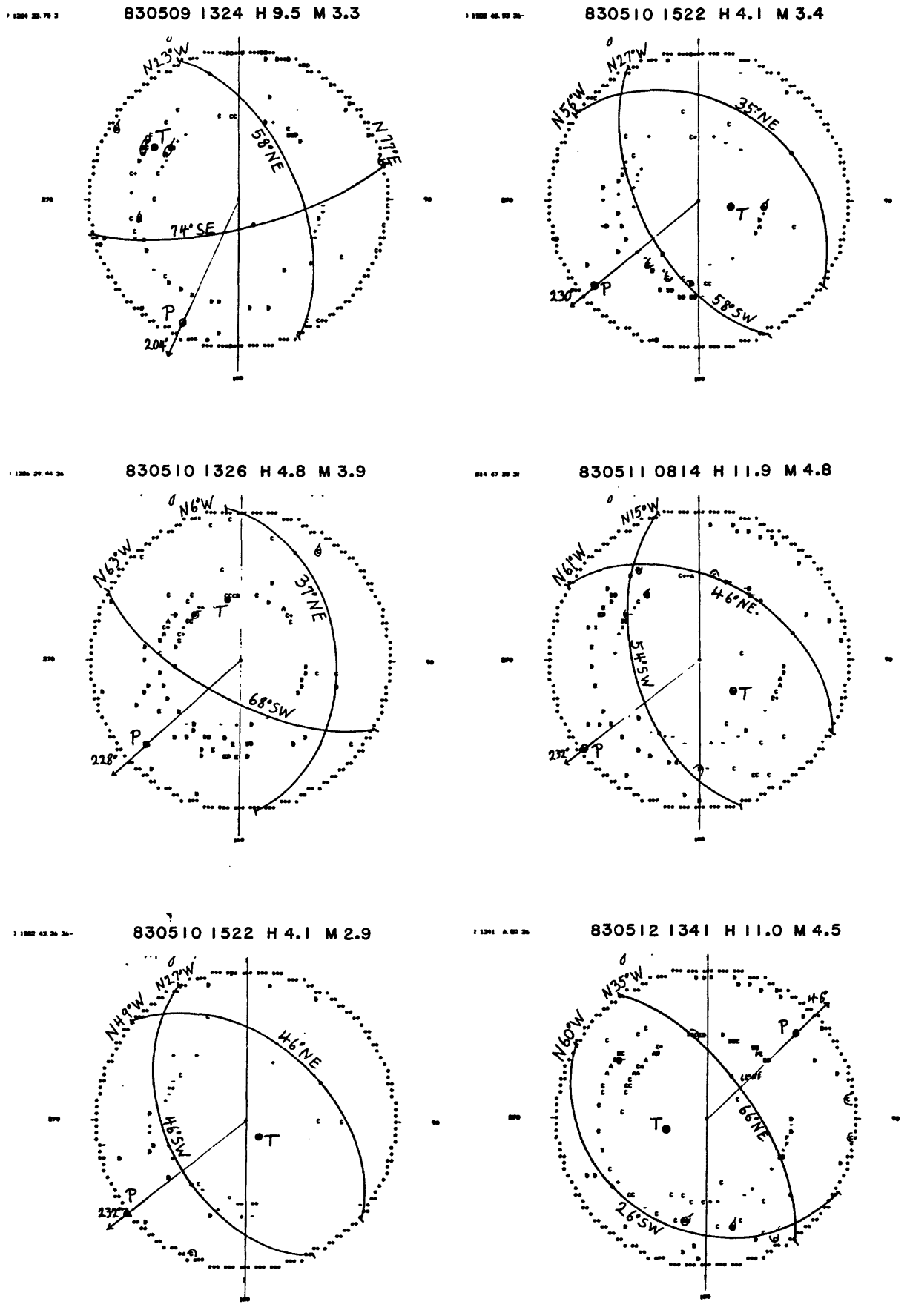
830509 1324 H 9.5 M 3.3
N23°W
58°NE
N77°E
74°SE
T
P
204°
830510 1522 H 4.1 M 3.4
N27°W
N56°W
35°NE
T
P
230°
58°SW
830510 1326 H 4.8 M 3.9
N6°W
N63°W
37°NE
T
68°SW
P
228°
830511 0814 H 11.9 M 4.8
N15°W
N61°W
46°NE
54°SW
T
P
23°
830510 1522 H 4.1 M 2.9
N27°W
N49°W
46°NE
49°SW
T
P
232°
830512 1341 H 11.0 M 4.5
N35°W
N60°W
P
T
66°NE
26°SW

FIGURE 24–i

830524 0902 H 8.9 M 4.7

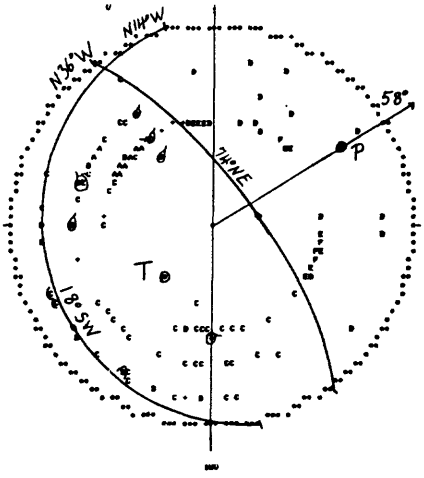

830527 2040 H 12.7 M 3.8

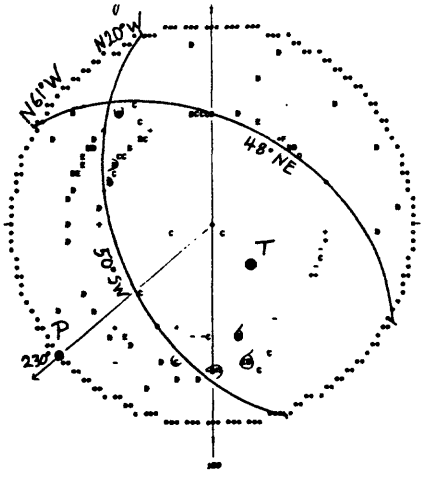

830524 1226 H 10.9 M 3.2

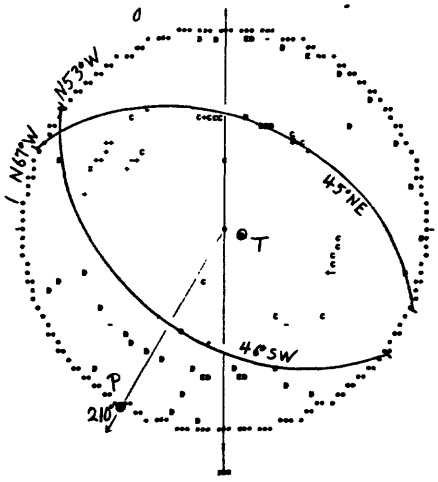

830529 0124 H 12.5 M 3.5

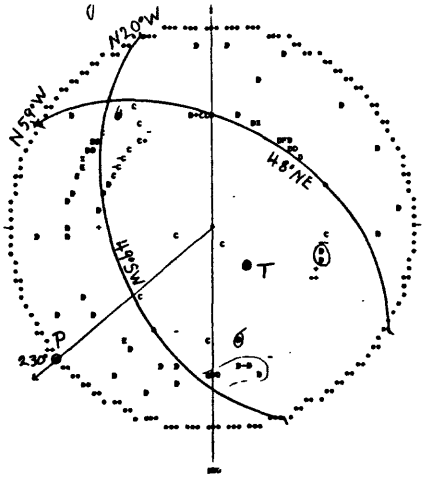

830526 0854 H 8.1 M 3.2

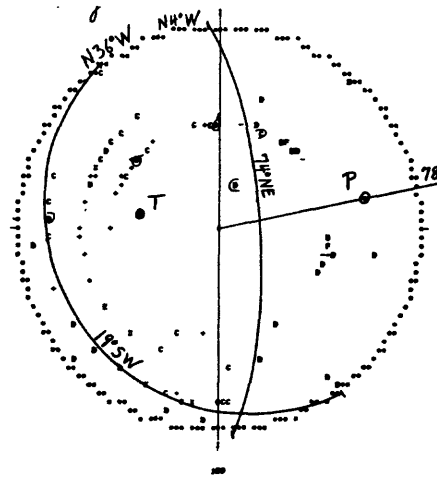

830530 0321 H 11.5 M 3.3

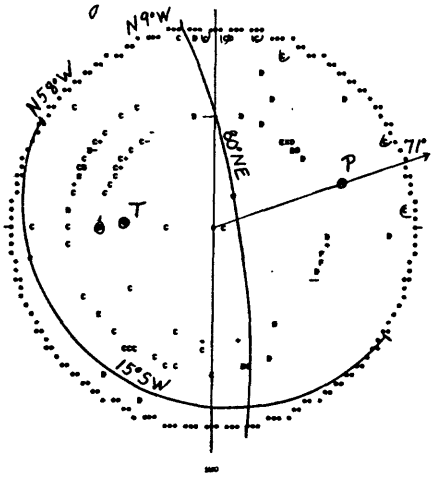

FIGURE 24-j

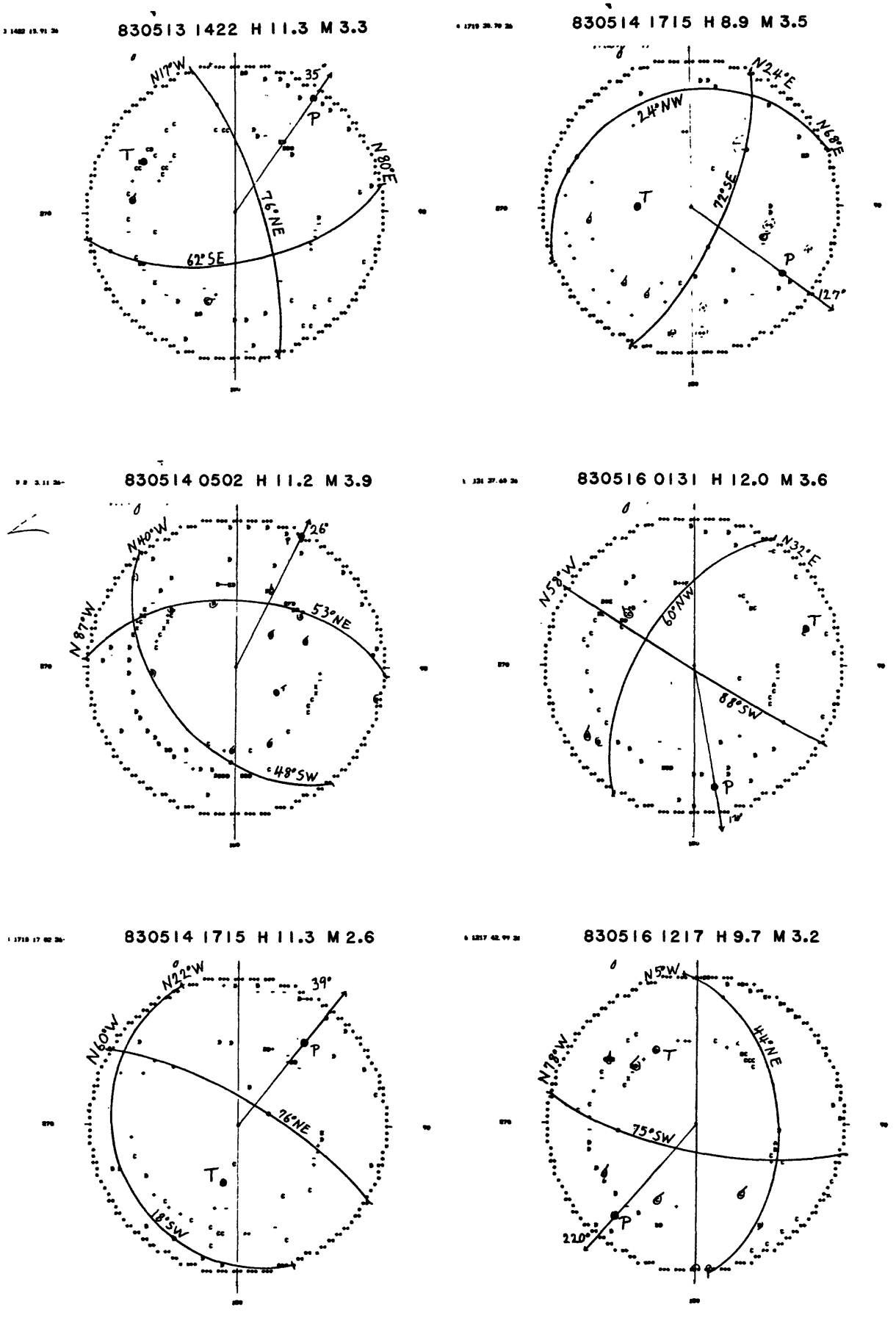
830513 1422 H 11.3 M 3.3
N17°W
35°
P
T
N80°E
76°NE
62°SE
830514 1715 H 8.9 M 3.5
N24°E
N68°E
24°NW
72°SE
T
P
127°
830514 0502 H 11.2 M 3.9
N40°W
26°
N87°W
53°NE
48°SW
830516 0131 H 12.0 M 3.6
N32°E
N53°W
60°NW
T
88°SW
P
830514 1715 H 11.3 M 2.6
N22°W
39°
N60°W
P
76°NE
T
18°SW
830516 1217 H 9.7 M 3.2
N5°W
N78°W
T
44°NE
75°SW
P
220°

FIGURE 24-k

830516 1421 H 9.2 M 3.9

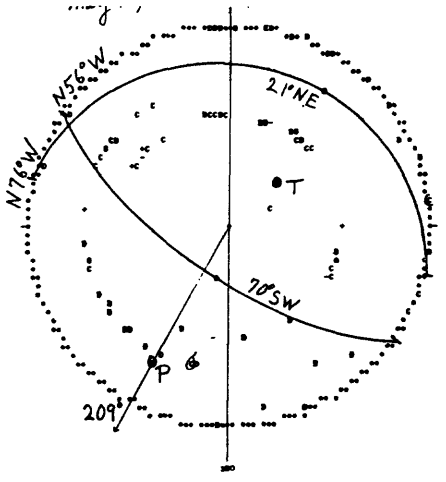

830519 2326 H 1.8 M 3.5

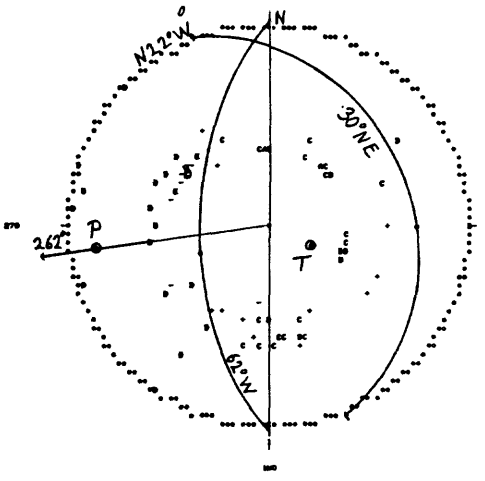

830517 2222 H 8.1 M 4.5

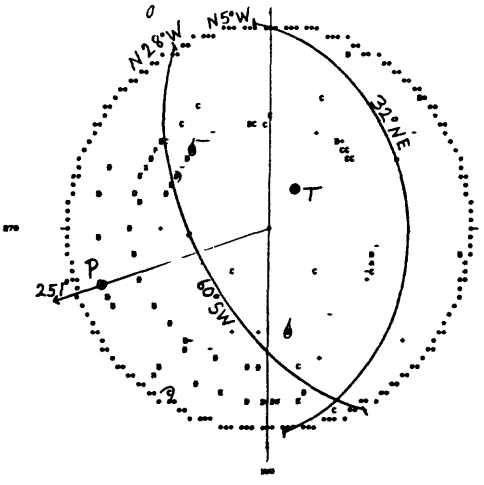

830521 1005 H 11.1 M 3.2

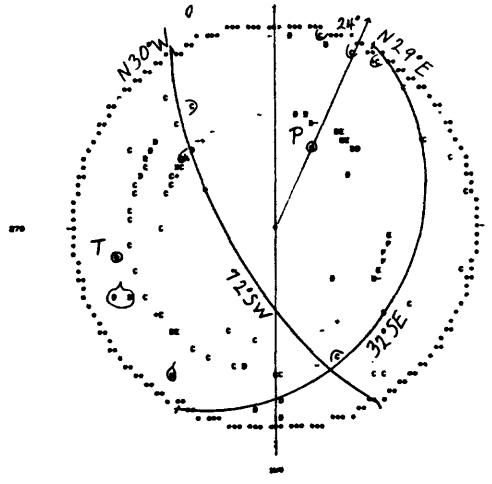

830519 1105 H 13.0 M 4.2

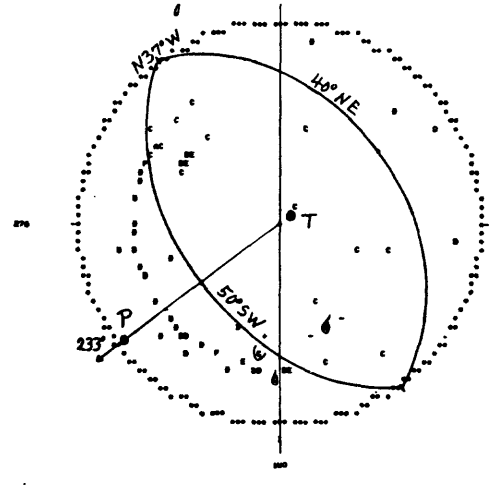

830522 0839 H 10.5 M 4.2

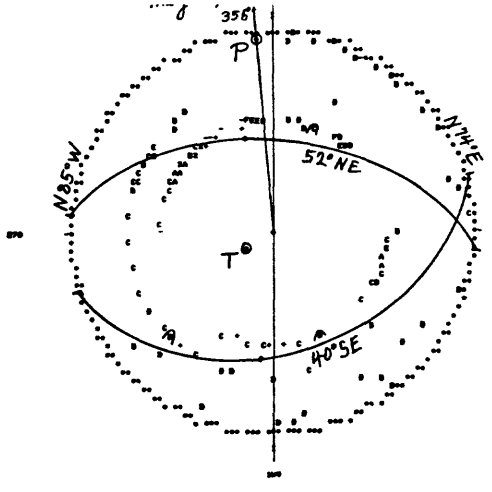

FIGURE 24-1

830607 0518 H 11.6 M 4.1

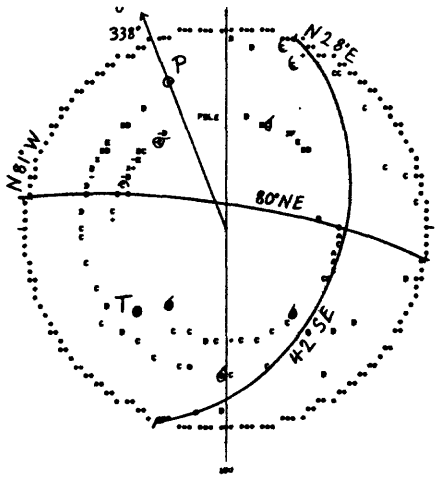

830611 2302 H 3.5 M 3.4

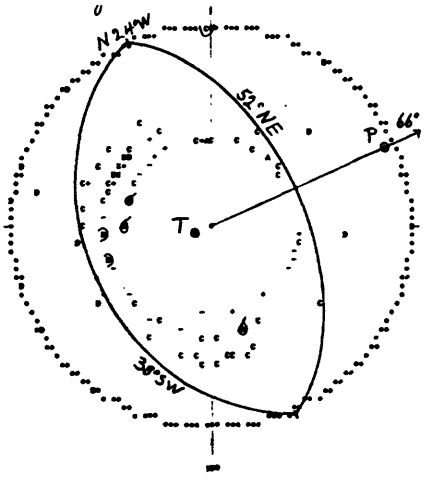

830611 0309 H 2.4 M 5.2

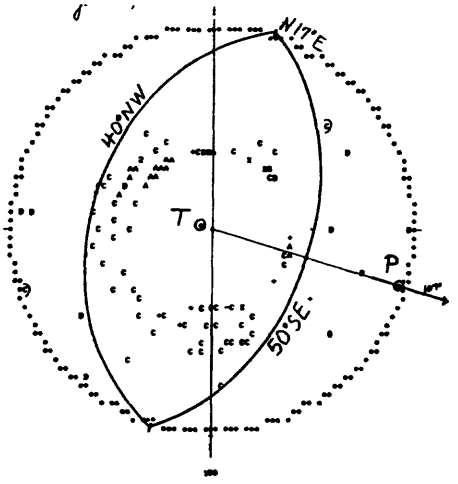

830612 0131 H 14.5 M 4.0

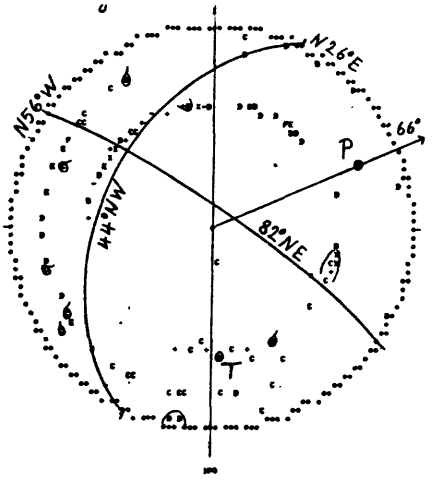

830611 1427 H 4.1 M 3.2

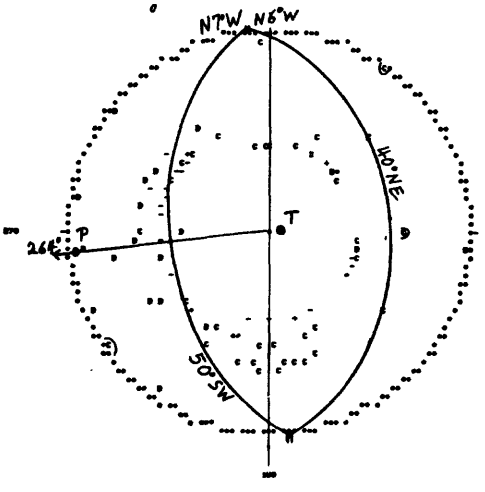

830616 1737 H 10.6 M 3.5

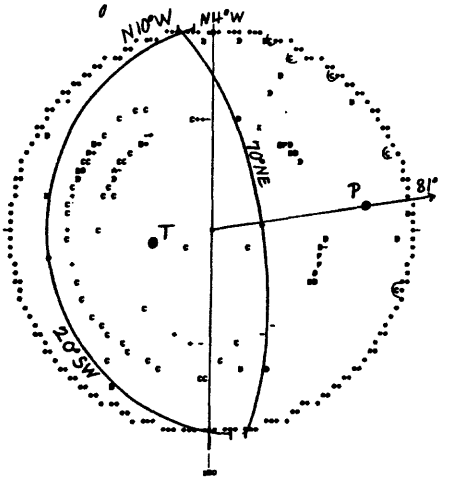

FIGURE 24-m

830629 0641 H 13.1 M 3.6

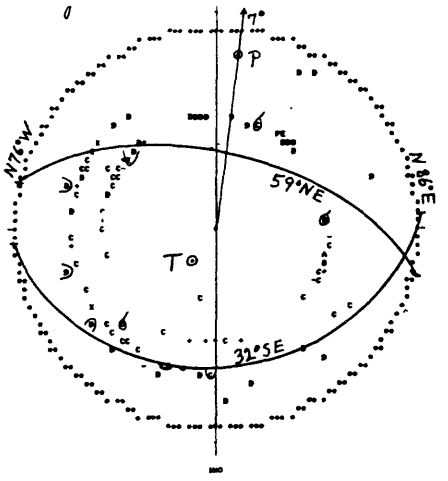

830709 0740 H 9.0 M 5.4

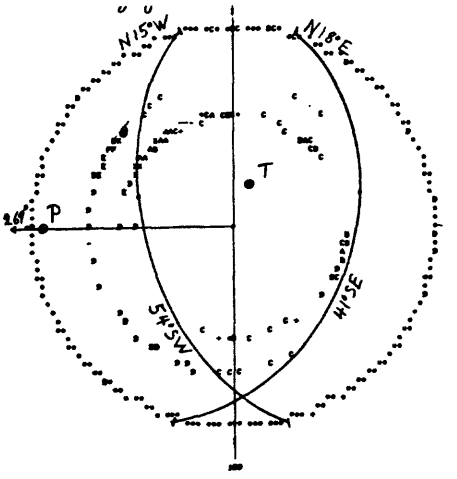

830705 2210 H 4.6 M 3.3

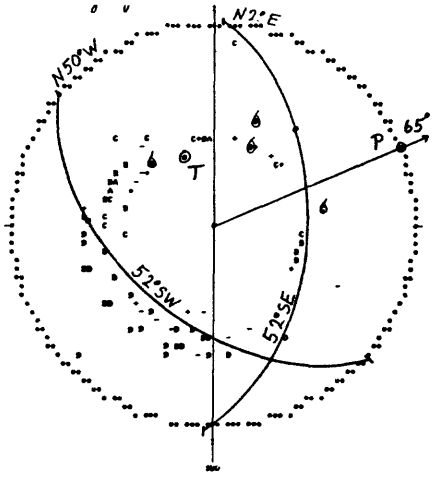

830714 1525 H 6.7 M 3.7

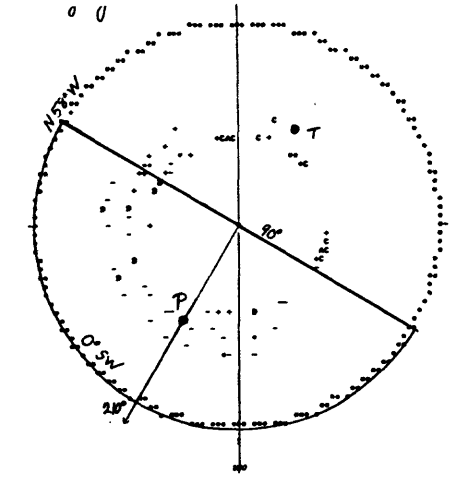

830707 0030 H 12.5 M 3.7

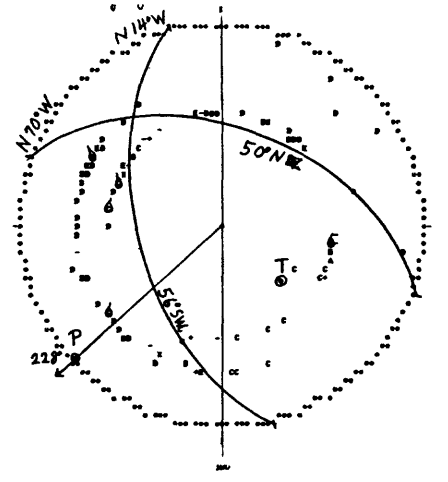

830717 2158 H 12.0 M 3.7

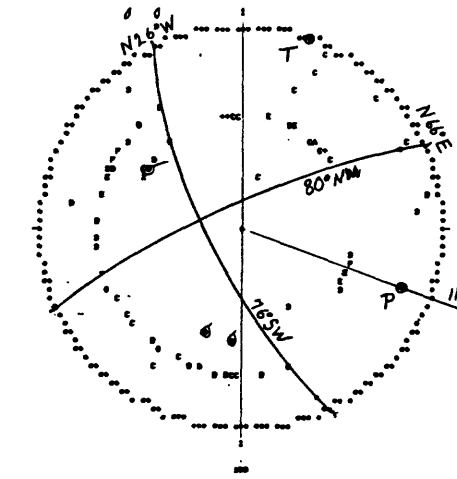

FIGURE 24-n

830718 1928 H 9.1 M 4.2

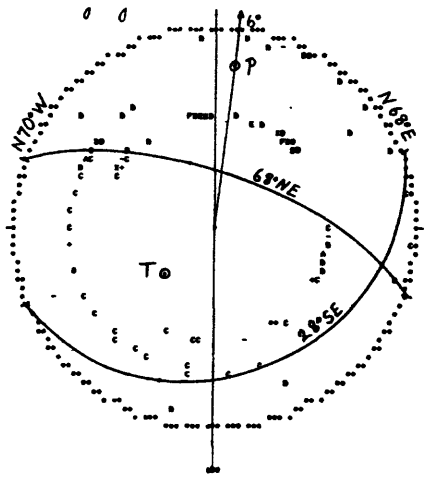

830722 0303 H 6.7 M 3.2

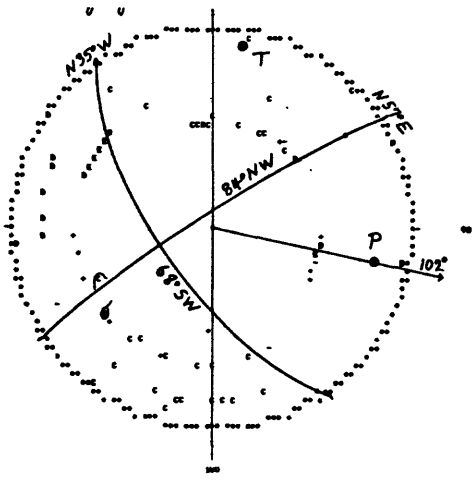

830722 0239 H 7.4 M 6.0

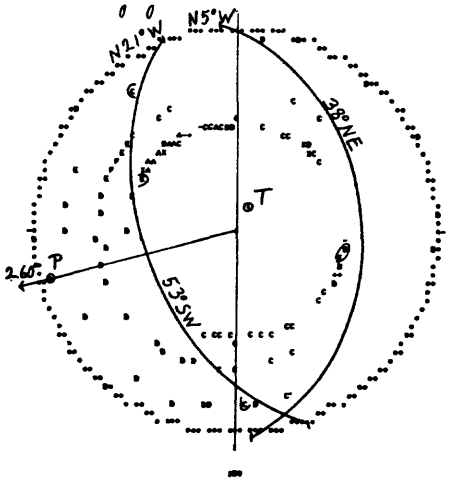

830722 0311 H 1.8 M 3.3

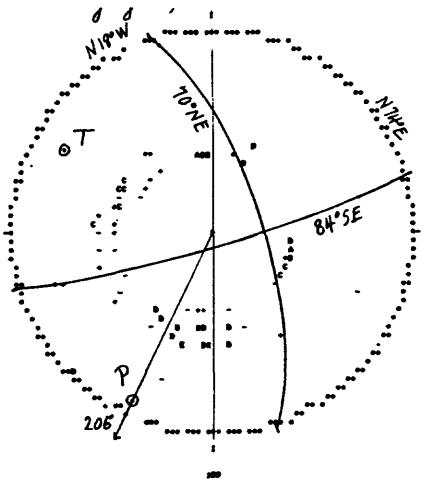

830722 0249 H 6.8 M 4.1

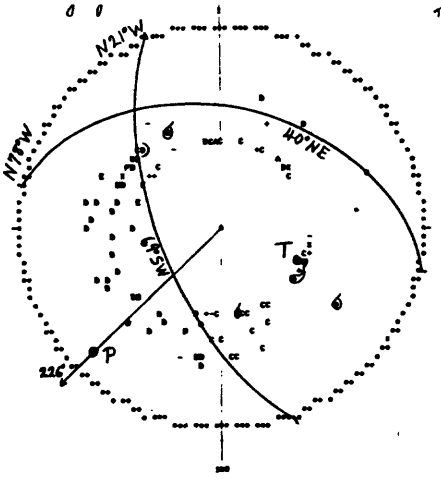

830722 0343 H 7.9 M 5.0

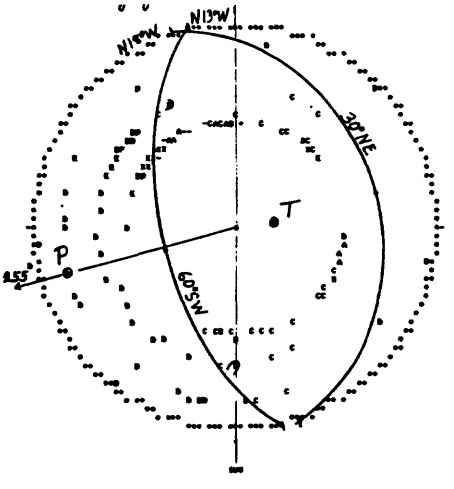

FIGURE 24–0

830722 0430 H 7.5 M 3.6

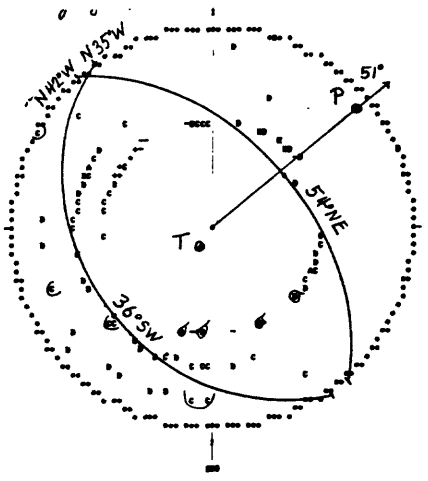

830725 2231 H 8.4 M 5.3

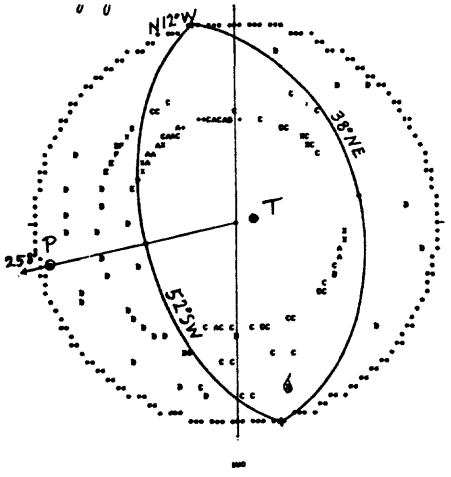

830722 0712 H 7.1 M 3.4

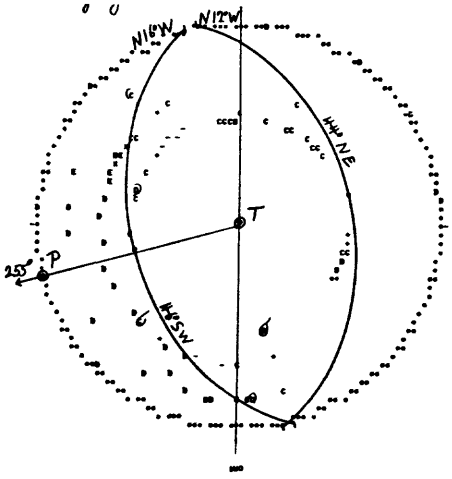

830731 1643 H 9.5 M 3.5

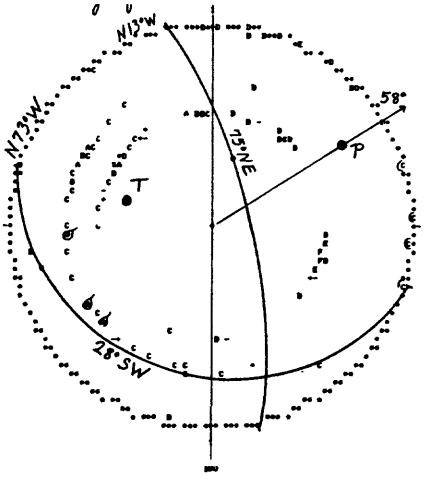

830722 2152 H 8.0 M 3.3

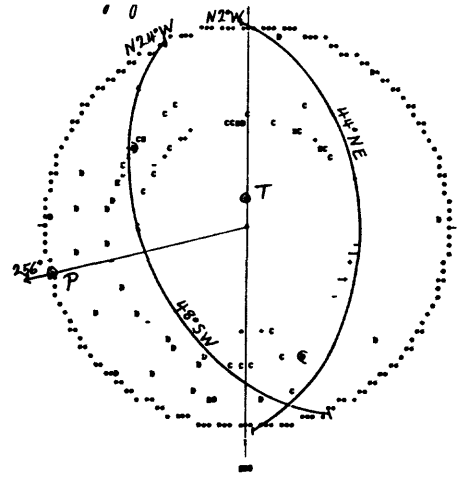

830731 1724 H 11.0 M 3.6

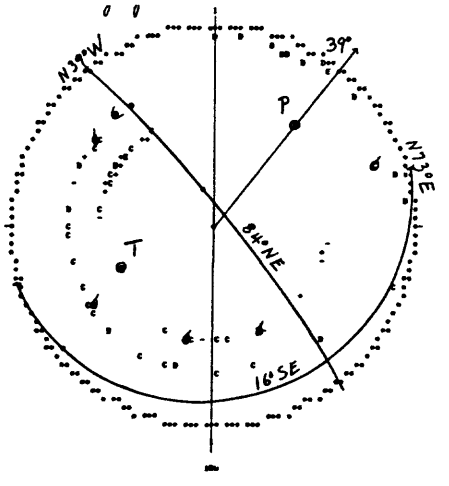

FIGURE 24-p

830731 1754 H 9.8 M 3.4

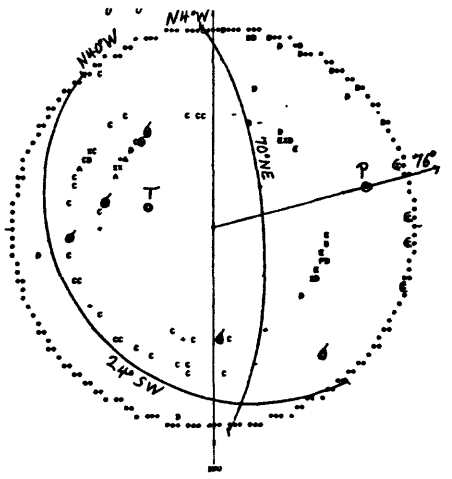

830812 2202 H 8.7 M 4.1

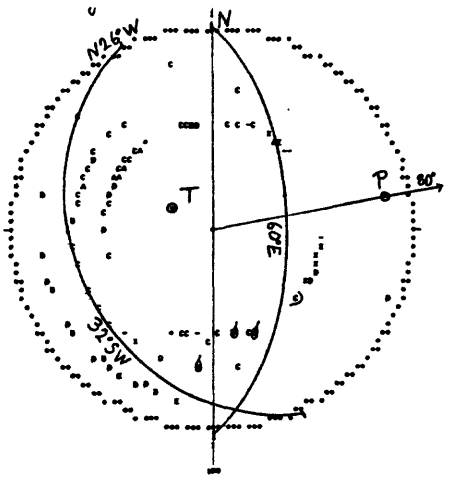

830805 1006 H 4.9 M 3.3

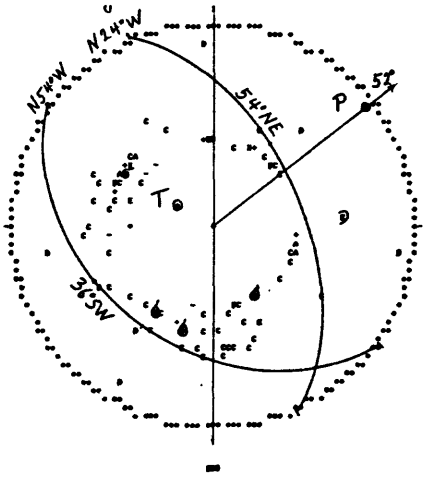

830814 1243 H 9.6 M 4.3

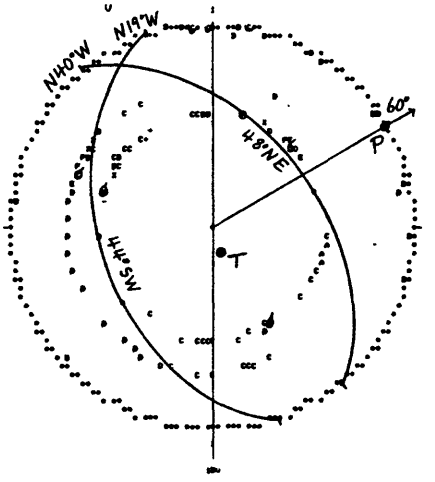

830812 0114 H 9.8 M 4.0

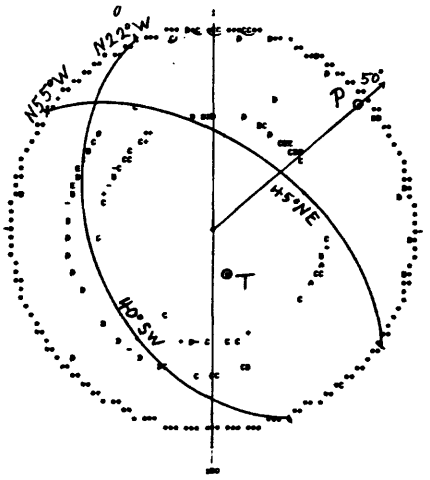

830826 0321 H 12.0 M 4.0

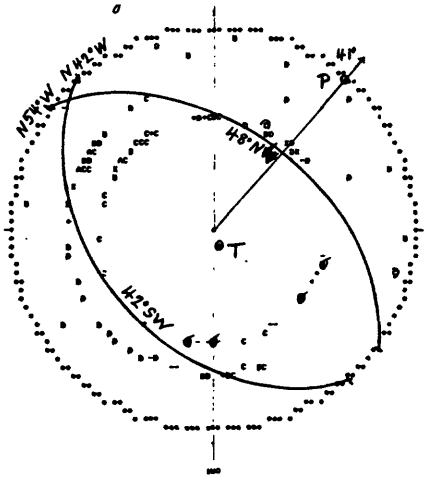

FIGURE 24-q

830826 1957 H 11.8 M 3.8

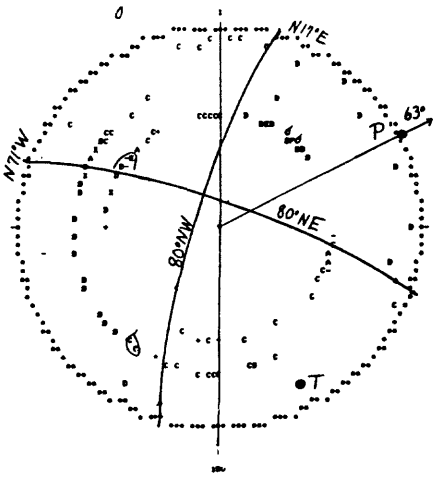

830909 0921 H 6.3 M 3.9

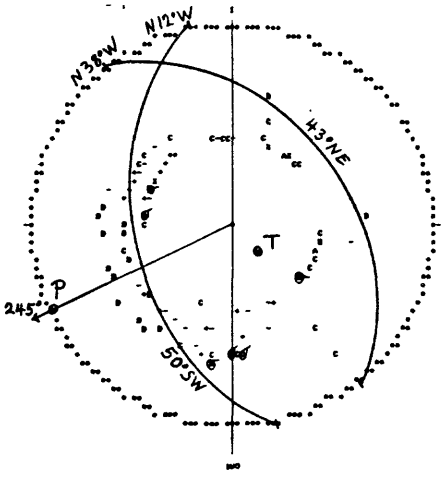

830907 2307 H 12.0 M 3.8

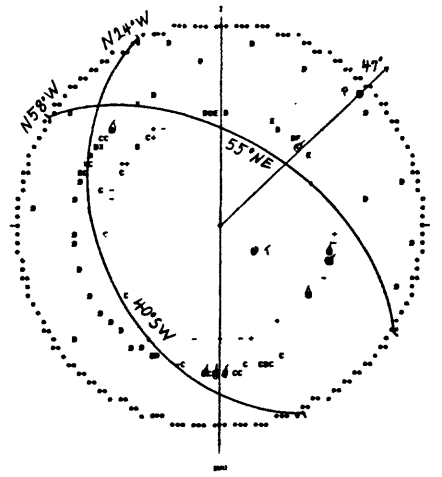

830911 1148 H 10.0 M 4.5

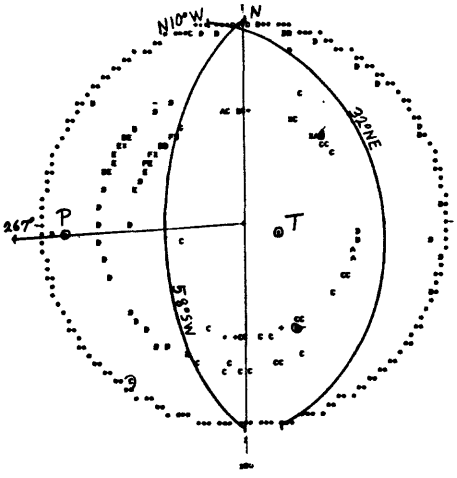

830909 0916 H 6.7 M 5.3

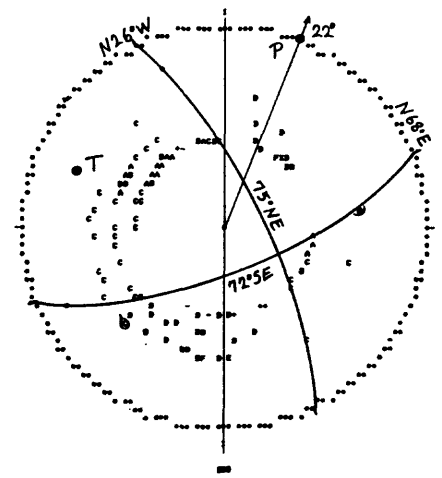

830918 1434 H 9.2 M 3.5

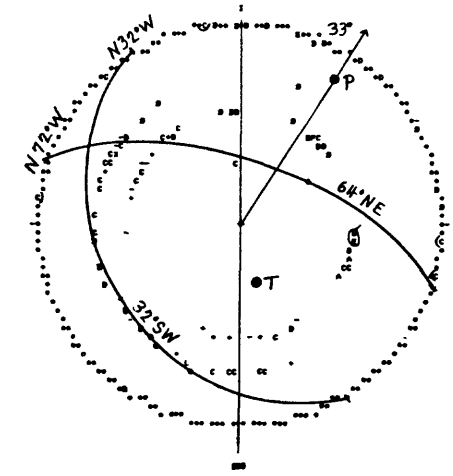

FIGURE 24-r

HYPOCENTER LOCATIONS AND CONSTRAINED FAULT-PLANE SOLUTIONS FOR COALINGA AFTERSHOCKS, MAY 2-24, 1983: EVIDENCE FOR A COMPLEX RUPTURE GEOMETRY

Donna Eberhart-Phillips and Paul Reasenberg

U.S. Geological Survey
Menlo Park, California 94025

ABSTRACT

The 1983 Coalinga, California earthquake (M_L = 6.7) consisted of a complex rupture on two, or possibly three, planes of slip. These planes all strike approximately parallel to the axis of Coalinga Anticline, but vary widely in dip. The distribution of 2060 hypocenters, and the alinement of 550 nodal planes for aftershocks occuring between May 2 and May 24, 1983 enable this detailed inference of rupture geometry to be drawn. The identified planes dip 70-80 degress NE, 45-55 degrees SW and 5-10 degrees SW. The two steeper planes intersect at the mainshock hypocentral depth (10 km), and define a wedge-shaped buried horst between 5 and 11 km depth that may have been uplifted during the earthquake by slip on both planes. The distribution of early aftershocks suggests that the first and largest mainshock displacement was probably on the SW dipping fault.

Co-seismic surface elevation changes are consistent with slip distributed on the multiple-plane structure proposed here. A teleseismic body-wave model portraying the mainshock as a double event is also consistent with the proposed structure. Evidence for secondary faulting in the form of bedding plane slip is found in the hypocentral distribution and nodal plane orientation of aftershocks at the north edge of the aftershock zone, along the northeast flank of the anticline. Considered together, these observations are consistent with a complex mainshock rupture between 5 and 11 km depth, with passive folding accomodating the seismic displacement in the overlying 5 km of rock.

Introduction

The 1983 Coalinga earthquake sequence produced a vast quantity of high quality recorded seismic data. Conventional methods for processing this data set, including the hand-fitting method for modeling fault-plane solutions, have resulted in the analysis to date of fewer than 100 of the largest aftershocks (Eaton, this volume). It is realistic to expect that no more than one hundred additional events will ultimately be modeled by hand. In addition, this earthquake sequence is presenting somewhat of a challenge to seismologists, as its seismicity apparently does not conform to patterns of main rupture surface and aftershock geometry seen in comparable sequences. For example, the ambiguity in identification of one of the mainshock nodal planes as the rupture plane is not definitively resolved by the early aftershock pattern (Reasenberg, et al., 1983). We believe the

difficulty being encountered in analysis of the seismicity is primarily due to complexity of the deformation geometry present in this earthquake sequence. Thus it may be necessary to study in detail an ususually large number of aftershocks to get a correct model of the deformation. We have applied some unconventional methods designed to automatically process the seismic data for a large number of aftershocks. Using these methods, some 3612 aftershocks have been timed and relocated, and constrained fault plane solutions were determined for 2397 of them. The resulting distribution of hypocenters is considered together with observed alinements in the modeled fault plane solutions, in order to form a unified model of the deformation geometry.

The data used in this study are a) CALNET local P-wave arrivals at 24 stations within an 80-km radius of the mainshock; b) P-wave arrivals from 12 portable 3-component seismographs (known as "5-day recorders") installed within 4 days after the mainshock within a 30-km radius; c) S-P times read from 11 portable digital (GEOS) wideband seismographs located directly above the aftershock zone (Figure 1). The period of coverage is May 2 to May 24, 1983.

Hypocenter Locations

The P-arrival times, first-motion polarities, and coda lengths for the CALNET stations were identified and picked in real-time by a computer processor (RTP) system (Allen, 1982). For the 5-day tapes, a similar system was developed to read and pick the vertical component seismic signal from tape at twenty times real time. System timing for both data sets are tied to WWVB. Total absolute timing error is estimated to be less than 0.1 s. For the GEOS stations, P and S arrivals were hand-timed from 3-component traces with a reading accuracy of approximately 0.02 s (M. Andrews, personal communication). However, because of problems in calculating time corrections for these stations, only S-P times were used in the locations.

A 1-dimensional velocity model with station corrections for the CALNET and 5-day data was obtained by inversion of 2000 observations for a spatially distributed set of 83 well-recorded aftershocks. The initial model was Eaton's (1983) 6-layer crustal velocity model M4. Velocities in the final model are within 2 percent of those for M4. The rms residual for these 83 events using the resulting model is 0.125 s. 69 events, for which GEOS data are available, were individually located with HYP071 (Lee and Lahr, 1975) using this model. The average residual for each GEOS station was taken as the station correction for subsequent locations. These station corrections and those for the CALNET and 5-day stations contour smoothly, in general agreement with the shape of the anticline, suggesting that they reflect local lateral crustal structure.

Uncertainty in the resulting hypocenter locations is approximately 1 km (horizontal) and 2 km (vertical). The absolute depth of the hypocenter set is less well determined. In all, 2060 aftershocks were relocated with HYP071 A or B quality solutions. The mainshock hypocenter obtained with our final model is 36o 12.72' latitude, 120o 17.61' longitude, 10.0 km depth.

Modeling constrained fault plane solutions from RTP first motion polarities

In order to obtain fault plane solutions for the large volume of seismic data obtained for this earthquake sequence we have utilized, as much as

possible, the available RTP arrival times and first-motion polarities, and applied an automated model-and-fit technique. While the accuracy of the RTP P-wave arrival times has been shown to equal or exceed that of the routine network handpicks (Reasenberg, 1980; Allen, 1982), no comparable assessment of the RTP first-motion polarities has yet been made. To assess their fidelity we compared polarities for P-phases from 10 events hand-picked by Eaton (personal communication, 1984) with those reported by the RTP. For 152 Ø-weight RTP picks with HYPO71 parameter PWT $\geq$ 1.0, the rate of agreement in polarity is 80 percent. First-motion data used in the following analysis was similarly selected and is presumed to be of comparable quality. The quality of the first-motion data used is lower than normal, for studies of this kind, by modern CALNET standards. Hence, one's ability to constrain the fault planes is diminished. This adversity is partly compensated by the high density of station coverage, which provides redundancy in the observations.

A fault plane solution was estimated for each event by repeatedly fitting the first-motion polarities to the radiation pattern calculated for a suite of double-couple source models that uniformly span a selected portion of source- parameter space. Based on preliminary modeling of fault plane solutions by Eaton et al. (1983) for some of the larger aftershocks, we have constrained our source models to be pure reverse dip-slip, striking W to NNE (270° to 20° azimuth). Dip and, within the above range, strike of the nodal planes are free parameters. These constraints are pragmatically motivated; available data for many of the smaller events are inadequate to distinguish a pure dip-slip mechanism from an oblique-slip mechanism.

The fitting scheme compares the observed polarity at each observed point on the focal sphere with that calculated for a given source model. The fit-function, F, is defined as

$$F = \frac{\sum \left| P_o - P_t \right| w_o w_t}{N_W} \qquad (1)$$

and

$$N_W = \sum w_o w_t \qquad (2)$$

where P_o and P_t are terms representing the observed and theoretical first motion polarities (0.5 for compressions and -.5 for dilatations). The observation weight, w_o, is set equal to the HYPO71 parameter PWT, and the theoretical weight, w_t, is equal to the square root of the theoretical radiation amplitude for the given source model. This weighting scheme downweights observations near nodal planes, thereby minimizing the effect of inconsistencies near the nodal planes, such as those caused by unmodeled refractions.

For each source model in the suite, F is calculated. The model in the suite that minimizes F ($F = F_{min}$) is adopted as the fault-plane solution. An assessment of quality is made for each adopted solution based on the degree to which the observations fit the model, the weighted number of observations used in the solution, N_W, and the uncertainty in the parameters of the adopted solution. The uncertainty in strike and dip are the ranges for which solutions fit the data five percent worse than does the

adopted solution ($F \leq F_{min} + .05$). For example, if the adopted solution uses 40 rays and the polarities observed at 4 of them are "wrong", then $F_{min} = .10$ (ignoring radiation pattern weighting) and the ranges ΔS and ΔD correspond to solutions for which $F < .15$, or 6 polarity discrepancies out of 40. Using the algorithm in Table 1, quality code A, B, C or D is assigned to each solution. Figure 2 illustrates the range of typical of the A and B quality solutions obtained in this study. Only A and B quality fault plane solutions are shown and analyzed in this study. In general, the dip is better determined than the strike, reflecting the favorable position of rays on the focal sphere for resolving the dip of NW striking thrust mechanisms. Events that are not well fit by any mechanism within the suite considered are not included in this report. Of those included, 550 are A or B quality, and of these 163 are A quality (Table 1).

Epicentral distribution of aftershocks

Figure 3 shows the relocated epicenters for the period May 2-24, the first day and the next 3 weeks. The distribution is divided into three epicentral zones (Figure 3a) that are considered separately in the next section. The zones are perpendicular to the longitudinal trend of the aftershock zone and approximately perpendicular to the Coalinga anticline. Zones 1 and 2 include Stein's modeled mainshock fault. Zone 2 includes the mainshock epicenter. Zone 3 extends from the SE end of the modeled fault to Kettleman Hills, where the surface expression of anticlinal folding undergoes a change in strike of approximately 10 - 15 degrees and an offset of 4 km. The outlined area in Figure 3b depicts the surface projection of the mainshock thrust plane modelled by Stein (fig. 1b, this volume). The epicenters surrounding and southeast of the mainshock form an elongate concentration with major axis striking 320 $\pm$ 5°. To the northeast a band relatively devoid of aftershocks separates the main bulk of the distribution from an arm of shallow seismicity that wraps around the northeast flank of Joaquin Ridge Anticline and roughly follows the trace of mapped stratigraphic contacts on the anticline's NE flank. During the first day of the sequence the aftershocks are largely confined to Zone 2 (Figure 3b). Over the next 20 days the distribution fills in to the northwest (especially the shallow arm in Zone 1), and extends to the southeast (Figure 3c).

Hypocentral distribution and fault plane solutions

Figures 4, 5 and 6 show separately the hypocentral distribution and orientation of nodal planes obtained for the aftershocks in zones 1, 2 and 3, respectively. In these figures each fault plane solution is represented by a circle oriented in either the southwest-dipping or northeast-dipping nodal plane. Circle radius is proportional to event coda magnitude, up to magnitude approximately 3.7. For the larger magnitude events, the RTP codas (and hence magnitudes and symbol sizes) are clipped at the M 3.7 value. Most of the circle symbols are considerably larger than the rupture areas associated with them. For example, assuming a 30 bar stress drop, M 2-4 events are approximately 6 to 1.5 times smaller than their corresponding symbol. The diameter drawn in each circle represents the slip vector, and, because these solutions are constrained to be pure dip-slip, the slip is necessarily up-dip and normal to strike. The box surrounding the hypocentral zone in each stereo view corresponds to one of the zones in

Figure 3a, and extends from the surface to 15 km depth, with a mid-depth line at 7.5 km drawn for reference. Views are toward the northwest from a point located 7.5 km below the surface. The surface features drawn are generalized contacts between mapped stratigraphic units, as in Figure 3. A one-km cube is shown for scale, and the city of Coalinga is drawn on the surface.

The hypocenters in zone 2 extend from approximately 3-4 km to 13-14 km depth (Figure 5a). Their spatial distribution suggest a "V" or "X" shaped pattern formed by two intersecting planes - both striking approximately parallel to the axis of Coalinga Anticline. The mainshock hypocenter is located in this zone at 10 km depth approximately 3 km east of the intersection of these planes. Northeast-dipping fault plane solutions aline with the 70o-80o northeast-dipping plane (A in Figure 5b), but generally crosscut the 45o-55o southwest-dipping plane (B in Figure 5b). Southwest-dipping fault plane solutions (Figure 5c) aline with plane B. Plane B is colocated with the plane identified by Reasenberg et al. (1983) from hypocenters for 14 $M \geq 3$ earthquakes during the first 21 hours of the sequence. An alinement of shallow angle (10-15o) southwest-dipping fault plane solutions at 9-11 km depth suggests a third plane (C in Figure 5c) roughly bisecting planes A and B, near the mainshock hypocenter, and dipping approximately 5^{o} - 10^{o} southwest. These shallow angle solutions are largely confined to the depth range 7-11 km (Figure 7). Seismicity at 4 - 7 km depth on the northeast side of zone 2 appears as a separate cluster (D in Figure 5). Northeast-dipping fault plane solutions (Figure 5b) are in better alinement with this cluster's hypocentral distribution than southwest-dipping solutions (Figure 5c) which tend to crosscut it.

In zone 1, aftershock hypocenters extend from approximately 3-4 km to 14-15 km depth (Figure 4a). The greatest concentration of aftershocks occurs at 9-11 km depth in the center of the distribution. In the southwest portion of this zone, under the northeast side of Pleasant Valley, the distribution of hypocenters suggests a continuation of plane A from zone 2, extending up to 2-3 km depth. Northeast dipping fault plane solutions aline with this plane, while southwest dipping solutions crosscut it. An extension of plane C from zone 2 is suggested by the presence of very shallow angle (15o) thrust planes at 9-11 km depth (Figure 4c). Seismic expression of plane B in zone 1 is relatively weak or absent. A separate cluster of hypocenters to the north, at 3-8 km depth extends cluster D in zone 2 northwest and deeper, and corresponds to the "arm" of epicenters on the northeast flank of Coalinga Anticline (Figure 3a). Northeast dipping fault plane solutions aline with the hypocentral distribution in this cluster better than southwest-dipping solutions (Figures 4b, c).

The hypocenters in zone 3 extend from approximately 3 km to 12-13 km depth (Figure 6a). Their spatial distribution suggests two steeply northeast-dipping planes between 4 and 10 km depth, one an extension of plane A from zone 2, and the other parallel and located approximately 2-3 km to the northeast. This structure can be seen in the epicentral distribution (Figure 3a) as two parallel linear concentrations of epicenters trending northwest in this zone. Northeast-dipping fault plane solutions aline with these planes somewhat better than southwest-dipping ones do (Figures 6b, c).

Early development of the aftershock zone

Hypocenters in zones 1 and 2 during the first 12 hours of the sequence are shown together with the reverse faulting and thrust nodal planes obtained for the mainshock by Eaton (1983) in Figures 8a and 8b respectively. This period precedes the installation of the 5-day and GEOS portable seismographs, and also precedes the augmentation of the CALNET telemetered network with two key stations (PHB and PWM) to the north and east of the aftershock zone (Figure 1). As a result, azimuthal coverage is relatively poor for this period and the resulting locations are relatively degraded. All solutions in Figures 8a and 9a are HYPO71 C quality owing to the large azimuthal gap to the northeast, while Figures 4a, 5a and 6a include only A and B quality solutions. The mainshock fault plane symbol (Eaton, 1983) is drawn centered on the hypocenter, with radius 6 km corresponding to the source dimension obtained from teleseismic body waves by Choy (this volume). The distribution of hypocenters during the first 12 hours is better alined with the mainshock thrust plane than the reverse fault plane (Figures 8a, b). Similarly, southwest-dipping nodal planes for aftershocks during this period (Figure 8d) aline with the hypocentral distribution, while the northeast-dipping nodal planes (Figure 8c) crosscut the distribution.

Figures 9a and 9b show hypocenters during the first 3 hours of the sequence in zones 1 and 2, together with Eaton's northeast and southwest dipping nodal planes, respectively. Identification of the distribution of hypocenters during the early hours of the aftershock sequence with the mainshock rupture favors the southwest over the northeast-dipping nodal plane. These earliest aftershocks are mainly located in zone 1, northwest of the mainshock hypocenter, suggesting that the mainshock's southwest-dipping rupture propagated northwest.

Discussion

The observations presented above raise a basic question. What is actually being represented by the observed structure in the aftershock distribution? Recent detailed studies of aftershock sequences suggest that aftershock hypocenters and fault plane solutions in some cases define the geometry of the mainshock rupture surfaces (e.g., Reasenberg and Ellsworth, 1982), and in others reveal secondary faulting off the main rupture (e.g., Stein and Lisowski, 1983). Certainly it is safe to say that in the Coalinga aftershock sequence the distribution of hypocenters and alinement of nodal planes suggests a complex geometry consisting of up to three planar structures. Ultimately, the interpretation of apparent structure in the aftershock sequence must take into account all the available geophysical and geologic evidence. However, at the present stage in the study of this earthquake sequence, some assumptions are required in order to formulate a working hypothesis or interpretation. In the following discussion we have assumed that the observed structure in the aftershock distribution reveals both a complex mainshock rupture surface and secondary faulting. The basis for this assumption lies in the fact that the resulting model is consistent with several independent geophysical and geologic observations of this earthquake sequence, reported in this volume, and discussed below.

The distribution of hypocenters and alinements in orientation of nodal planes suggest that the mainshock was a complex event consisting of up to

three principal planes of failure, all striking approximately parallel to Coalinga Anticline but with widely differing dips. Distribution of aftershocks in zones 1 and 2 during the first 12 hours of the sequence, and particularly during the first 3 hours, favors the southwest-dipping plane B and suggests that this plane was the principal displacement surface in the mainshock rupture. The same conclusion was reached by Reasenberg et al. (1983), based on early observation of the spatial distribution of $M \geq 3$ aftershocks occuring during the first 21 hours of the sequence. However, the complexity in the distribution of aftershocks presented in Figures 4-6 strongly suggests to us that a complex rupture occurred, with slip distributed on planes A and B, and possibly C. (The role of plane C in the earthquake sequence is not understood at present, however.) The distribution of early aftershocks does not preclude a complex model, but perhaps suggests that if the main rupture was complex the first and largest displacement was on plane B. Indeed, a simple southwest-dipping planar mainshock is inconsistent with observed coseismic surface elevation changes (Stein, this volume).

There also exists evidence for secondary faulting in the earthquake sequence, in the presence of a cluster of relatively shallow aftershocks (Feature D in Figures 4 and 5), and its apparent northeast-dipping structure. The fact that this cluster developed largely after the first 24 hours of the sequence also suggests secondary faulting. Discontinuity between this cluster and the main bulk of the aftershock zone further suggests that the events in this cluster are located off the mainshock fault structure. While dipping more steeply than the mapped stratigraphic contacts above them, these events correspond in location and strike to the buried northeast flank of the anticline, suggesting that they may be associated with slip on northeast- dipping bedding planes. Their depths place them within the layered Great Valley sequence (Wentworth et al., Walter and Mooney, this vol.) which is a more likely location for bedding plane slip than the underlying Franciscan assemblage.

A multiple slip plane hypothesis is consistent with other observations of this earthquake sequence. First, slip distributed on planes A, B and C could be well fit to surface leveling data for a variety of slip distributions (R. Stein, personal communication). Reverse or thrust movement on planes A and B would result in uplift of the wedge of rock between and above them, producing a buried horst beneath Coalinga Anticline. The measured co-seismic surface uplift is maximum at a point directly above the mainshock, approximately 3 km east of the intersection of planes A and B. Thrust on plane B or C would contribute an assymmetric distribution of surface elevation change similar to that observed by Stein (this volume), with greater uplift to the northeast than depression to the southwest. Namson, et al. (manuscript in preparation), using balanced cross-sections, also conclude that several fault planes (a southwest-dipping thrust with west-verging back thrusts in the hanging wall) are required to account for the Pliocene and Quarternary Coalinga uplift.

Secondly, Choy (this volume) models the mainshock rupture process from teleseismic body waves as two events on separate rupture planes striking northwest and dipping either steeply northeast or shallowly southwest. If Choy's first event is associated with our plane B, then his source model is in first-order agreement with the structure revealed by the aftershock distribution (compare Choy's Figure 10 with Figure 5). His smaller,

shallower second event, located a few kilometers southwest of the first event is possibly associated with plane A, dipping northeast.

Thirdly, the mainshock fault plane solution obtained by Eaton (this volume) agrees with our interpretation of aftershock locations if his southwest dipping nodal plane is identified as the mainshock fault. By assuming that the distribution of aftershock hypocenters and orientation of aftershock nodal planes during the first 12 hours, and especially during the first 3 hours of the sequence, map the mainshock rupture plane, we infer that the mainshock's first motions resulted from slip on a southwest dipping thrust plane. Eaton's mainshock thrust plane is the obvious candidate for plane B, but its dip is approximately 20° too shallow. Figure 5c suggests that plane B is less steeply dipping below 8 km. Perhaps plane B is better described as two faults, one dipping 23°, in accord with the mainshock, and a shallow one dipping 45°. Such a geometry approximates a thrust that flattens with depth. Slip on a fault model with this geometry was shown by Stein (this volume) to fit the coseismic elevation changes fairly well, and is consistent with the faulting model inferred by Wentworth et al. (this volume) from seismic reflection profiles.

Conclusions

The distribution of hypocenters and fault plane orientations for the May 1983 Coalinga earthquake sequence suggests the presence of planar structures which we interpret as both mainshock and secondary faulting surfaces. The rupture during the mainshock was probably complex with slip distributed on two or possibly three planes, each parallel to the axis of Coalinga Anticline, but having widely differing dips. The first and greatest slip probably took place on a southwest-dipping plane, with rupture propagating northwest. The 6 km source dimension obtained from teleseismic body waves by Choy (this volume) agrees with the distribution of aftershocks during the first 3 hours of the sequence. Slip on a second, steeply northeast-dipping, plane is suggested by the aftershock pattern in zones 2 and 3, and this plane is consistent with the second source event modeled by Choy. A third near-horizontal southwest thrust plane is also indicated by the aftershocks. Its part in the earthquake sequence is not understood, however.

These planes form a buried horst under Coalinga Anticline that is being uplifted by thrust and reverse fault displacements on them. Coseismic elevation changes across Coalinga Anticline are qualitatively consistent with this model (R. Stein, personal communication). The seismic deformation occurs at depths below approximately 4-5 km, while passive folding is largely confined to the upper 4-5 km of the crust. Inferred secondary faulting on the northeast limb of the anticline is associated with bedding-plane slip there, as the uppermost crust folds in response to the brittle deformation below. Thus, a change in style of deformation occurs at approximately 4-5 km. depth (deeper on the anticline flank) with tectonic faulting below, and passive folding above.

ACKNOWLEDGMENTS

This study would not have been possible without the careful work of Mari Kauffmann in extracting and organizing the phase data from the 5-day tapes, the rapid and accurate work of USGS seismic field crews in deploying temporary stations, and the persistence of Jerry Eaton in building and maintaining the USGS central California seismic network. We also thank Mary Andrews for sharing the GEOS S-P data with us, and Carl Wentworth and David Oppenheimer for spirited and careful reviews of the manuscript.

References

Allen, R. V., 1982, Automatic phase pickers: Their present use and future prospects: Bulletin Seismological Society of America, v. 72, no. 6, p. S225-S242.

Eaton, J., R. Cockerham, and F. Lester, 1983, Study of the May 2, 1983 Coalinga earthquake and its aftershocks, based on the USGS seismic network in northern California: in The 1983 Coalinga California Earthquakes, Special Publ. 66, Calif. Div. of Mines and Geology, p 261-273.

Lee, W. H. K., and Lahr, J. C., 1975, HYPO71 (Revised): A computer program for determining hypocenter, magnitude and first motion pattern of local earthquakes: U.S. Geological Survey Open-File Report 75-311.

Reasenberg, P., 1980, Comparison of performance of automatic and human p-picking systems using a common data set (abstract): EOS, Trans. A. G. U., 61, no. 46.

Reasenberg, P., D. Eberhart-Phillips and P. Segall, 1983, Preliminary views of the aftershock distribution: in The Coalinga earthquake sequence commencing May 2, 1983, U.S. Geological Survey Open File Report 83-511.

Reasenberg, P., and W. L. Ellsworth, 1982, Aftershocks of the Coyote Lake, California, Earthquake of August 6, 1979: A detailed study, J. Geophys. Res., v. 87, p. 10637-10655.

Stein, R. S., 1983, Reverse slip on a buried fault during the 2 May 1983 Coalinga earthquake: evidence from geodetic elevation changes: in The 1983 Coalinga, California Earthquakes, Special Publ. 66, Calif. Div. of Mines and Geology, p 151-163.

Stein, R. S., and Lisowski, M., 1983, The 1979 Homestead Valley earthquake sequence, California: control of aftershocks and postseismic deformation, J. Geophys. Res., v. 88, p. 6477-6490.

Figure Captions

Figure 1. Seismograph stations used in this study.

Figure 2. Fit of fault plane solution for an earthquake is illustrated by this diagram depicting the region of parameter space considered for the model. The "x" indicates the dip and strike of the best fitting solution ($F=F_{min}$). Shaded area contains all solutions with slightly worse fit ($F=F_{min}$ + .05). For each solution, ΔS and ΔD are the uncertainty in strike and dip of the adopted solution. a) typical A-quality solution; b) typical B quality solution.

Figure 3. Relocated epicenters for the Coalinga earthquake sequence shown with simplified geology from Stein (fig. 1a, this volume). Included are solutions with 6 or more observations and HYPO71 quality A, B, or C. Mainshock epicenter indicated by star. (a) May 2 through May 24. Outlined areas indicate zones 1, 2, and 3 shown separately in Figures 4, 5, and 6, respectively. (b) First 24 hours (May 2 - 3). Outlined area is projection of a modeled fault for the mainshock (Stein, 1983). (c) Next 3 weeks (May 4-24).

Figure 4. Stereoscopic views of aftershocks occuring May 2 - May 24, 1983. a) relocated hypocenters with HYPO71 quality A or B solutions, b) fault plane solutions with quality A or B, represented by circles oriented in northeast-dipping nodal planes (see text), c) same as (b), but with southwest-dipping nodal planes represented. Data shown lies within zone 1 shown in Figure 3a. Box extends from surface to 15 km depth. Simplified geology from Stein (fig. 1a, this volume) is drawn on the surface. View is from the southeast toward azimuth 315°, from a point located 7.5 km below the surface. A 1 km cube is shown for scale.

Figure 5. Same as Figure 4, but for epicentral zone 2 of Figure 3a. Planes A, B and C and cluster D are indicated (see text).

Figure 6. Same as Figure 4, but for epicentral zone 3 of Figure 3a.

Figure 7. Distribution of A and B quality fault plane solutions with respect to dip angle, shown separately for hypocentral depth ranges 0-7 km, 7-11 km, and greater than 11 km. Total of 550 solutions for events between May 2 and May 22, 1983 are represented. All three depth ranges have a preferred dip angle of 30-40 degrees SW (50-60°NE). However, only the mid-depth group has a significant population of 10-15° SW (75-80°NE) dipping solutions.

Figure 8. Distribution of hypocenters and orientation of nodal planes for aftershocks in zones 1 and 2 during the first 12 hours of the sequence. a) HYPO71 quality A-C hypocenters, shown with Eaton's (1983) northeast-dipping nodal plane for the mainshock (circle symbol). Mainshock symbol is centered on its hypocenter, and is plotted with 6 km radius; b) same hypocenters, shown with southwest-dipping mainshock nodal plane; c) northeast-dipping nodal planes for aftershocks; d) southwest-dipping nodal planes for aftershocks.

Figure 9. Distribution of hypocenters for aftershocks in zones 1 and 2 during the first 3 hours of the sequence. a) HYPO71 quality A-C hypocenters shown with Eaton's northeast-dipping nodal plane for the mainshock; b) same hypocenters shown with the corresponding southwest-dipping nodal plane. See Figure 8 caption for further explanation.

TABLE 1

QUALITY PARAMETER FOR CONSTRAINED

FAULT PLANE SOLUTIONS

QUALITY	F	N_W	ΔS	ΔD	Number of solutions
A	≤ 0.2	≥ 6	≤ 20	≤ 20	163
B	≤ 0.3	≥ 5	≤ 35	≤ 30	387
C	≤ 0.4	≥ 4	≤ 45	≤ 40	551
D	>0.4	<4	>45	>40	1296

Solutions of a given quality code satisfy all four inequalities shown for that code.

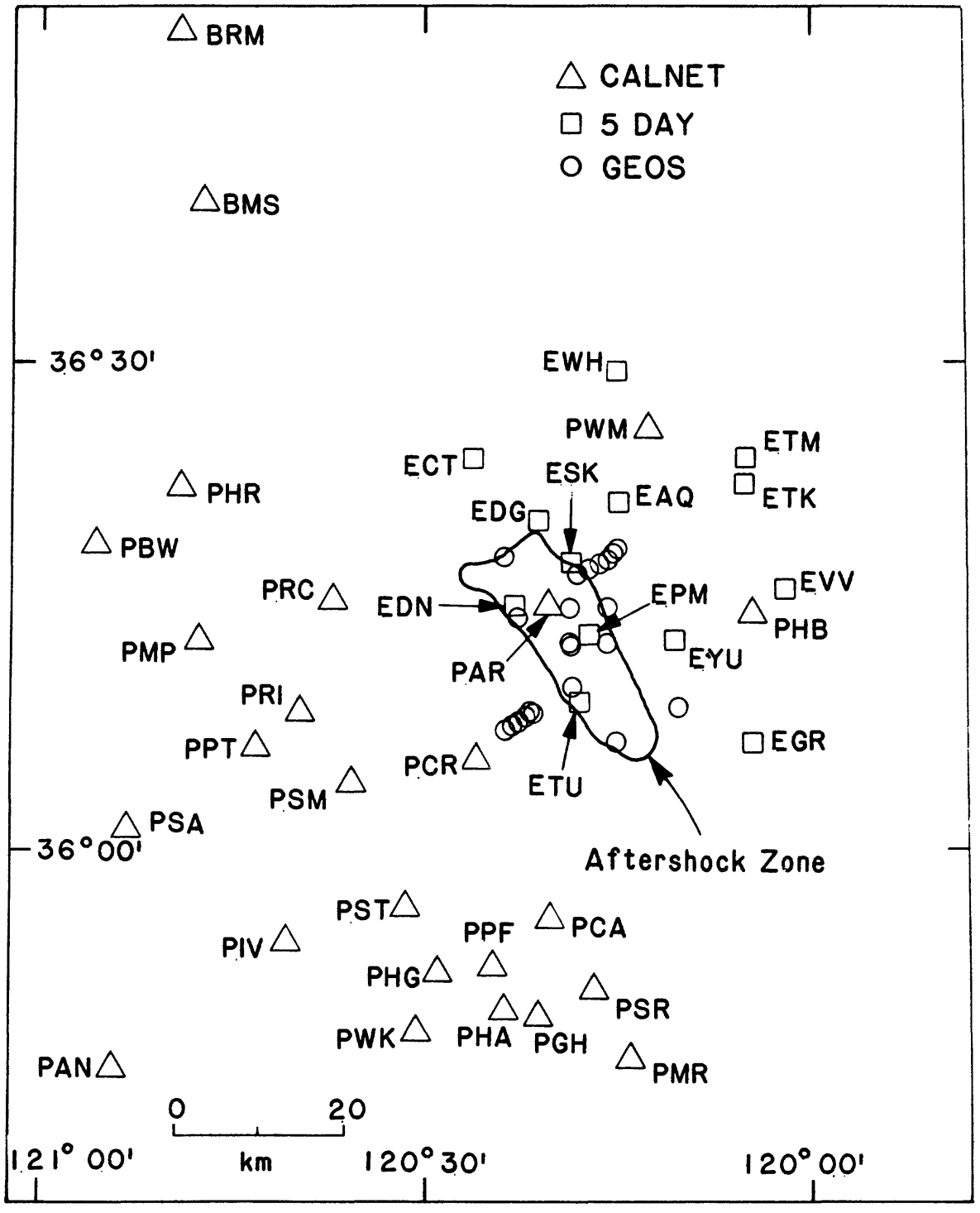
BRM
CALNET
5 DAY
GEOS
BMS
36° 30'
EWH
PWM
ETM
ECT
ESK
PHR
EAQ
ETK
EDG
PBW
PRC
EDN
EPM
EVV
PHB
PMP
EYU
PAR
PRI
PPT
EGR
PCR
ETU
PSM
PSA
36° 00'
Aftershock Zone
PST
PPF
PCA
PIV
PHG
PSR
PWK
PHA
PGH
PAN
PMR
0
20
km
121° 00'
120° 30'
120° 00'

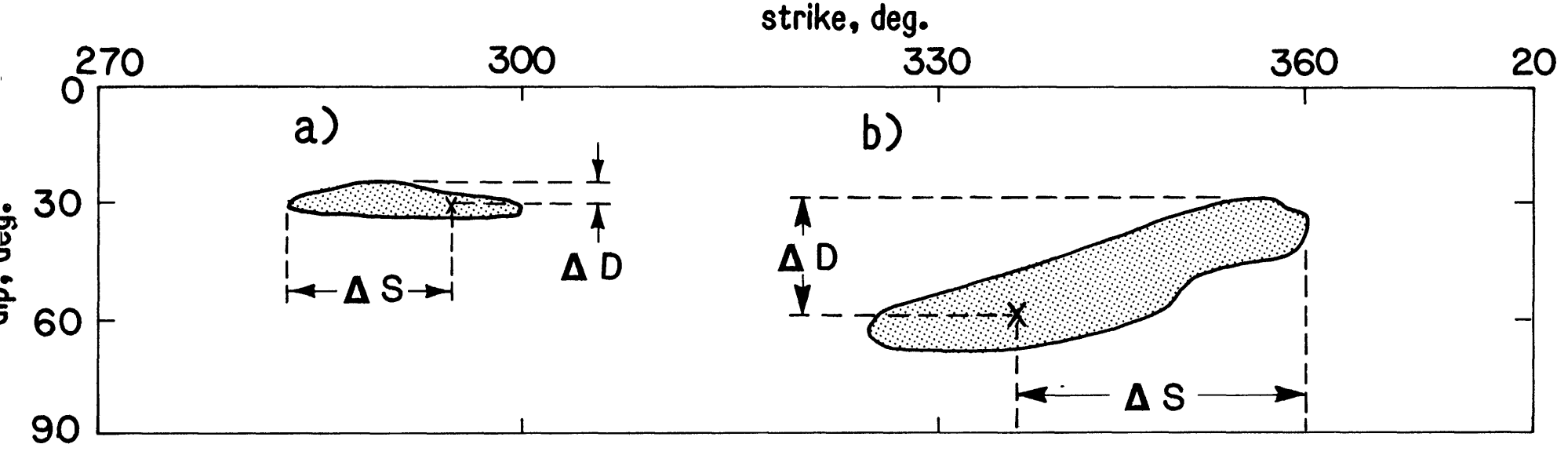
strike, deg.
270
300
330
360
20
0
30
60
90
a)
b)
Δ S
Δ D
Δ D
Δ S

Figure 3a

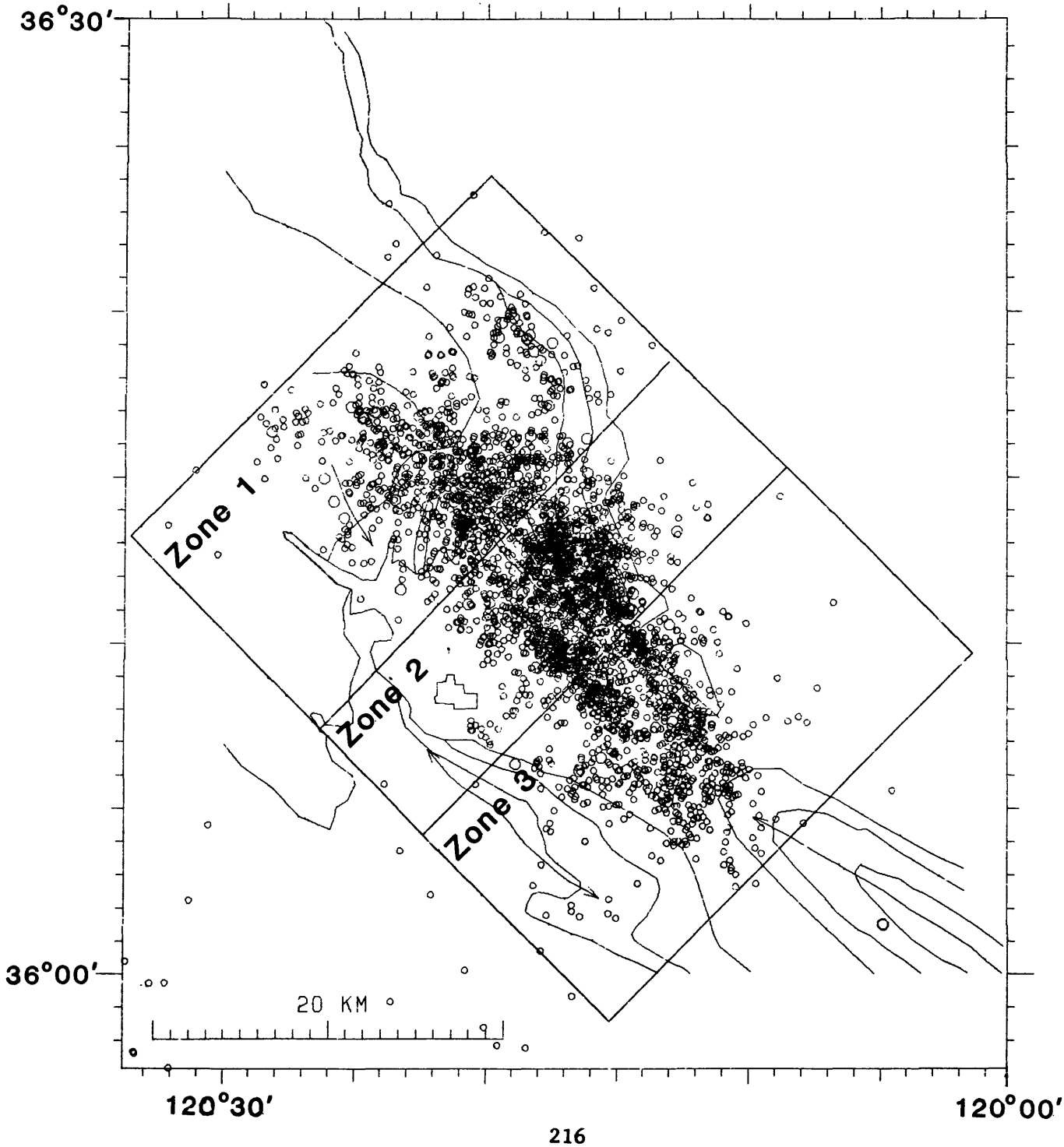

Figure 3b

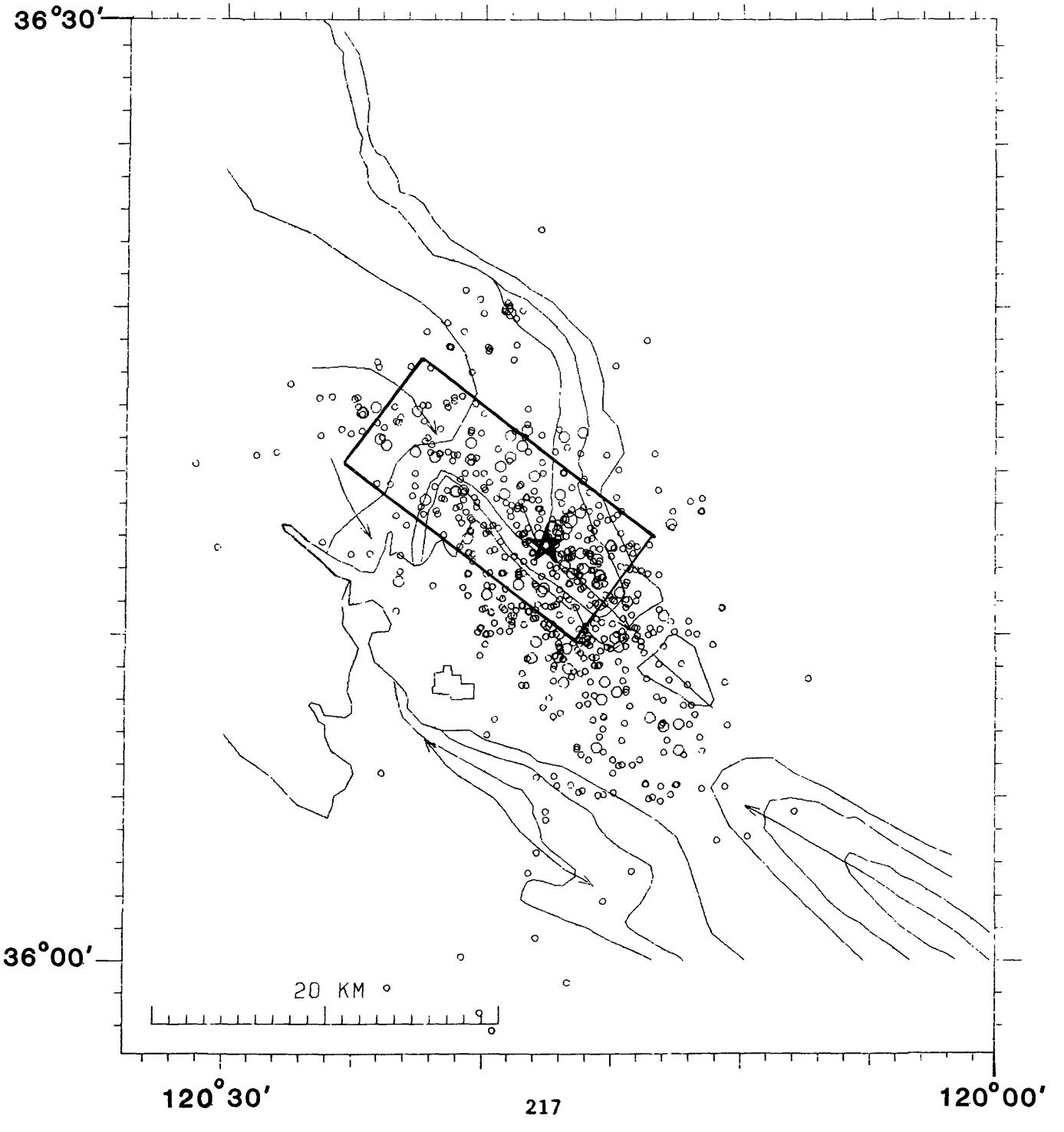

Figure 3c

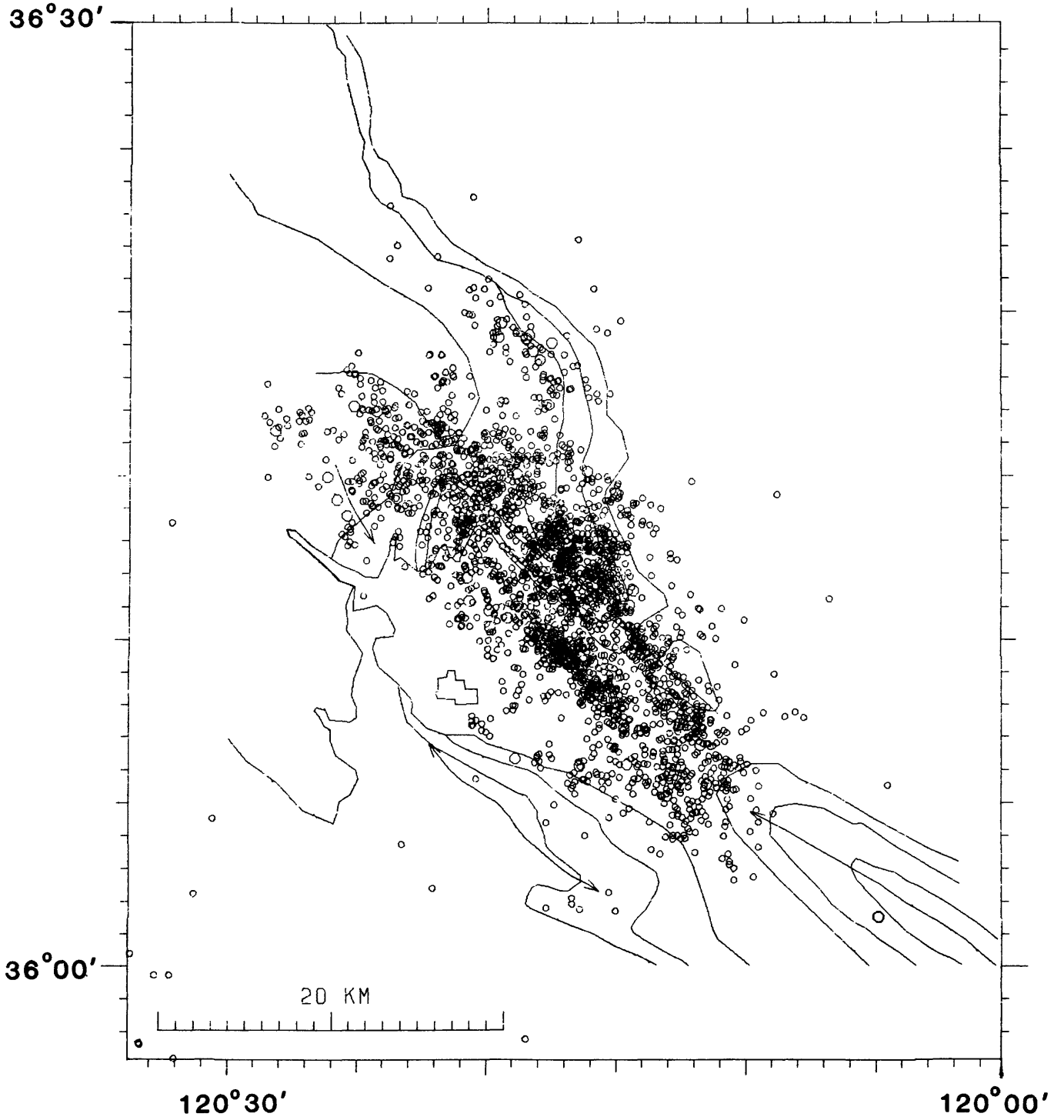

Zone 1

Fig. 4a

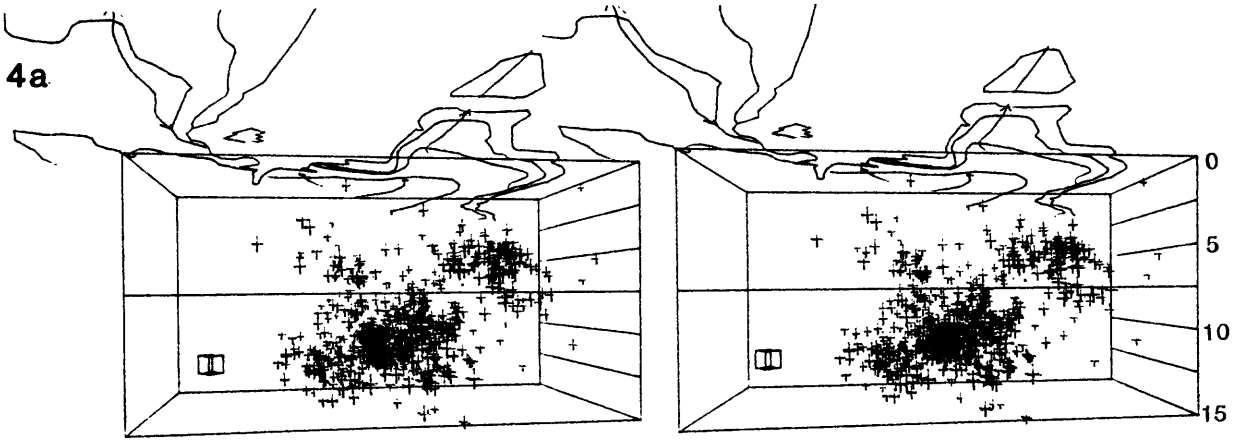

Fig. 4b

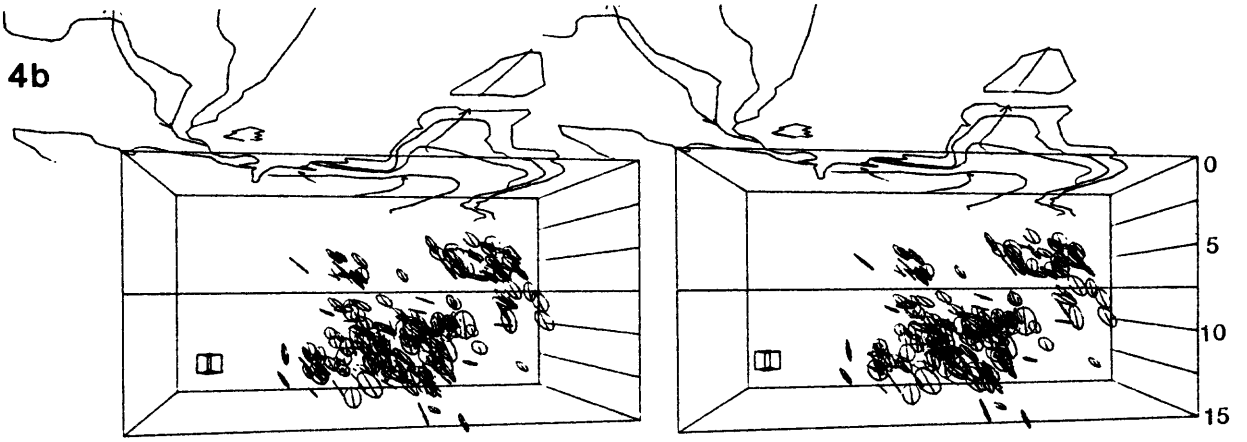

Fig. 4c

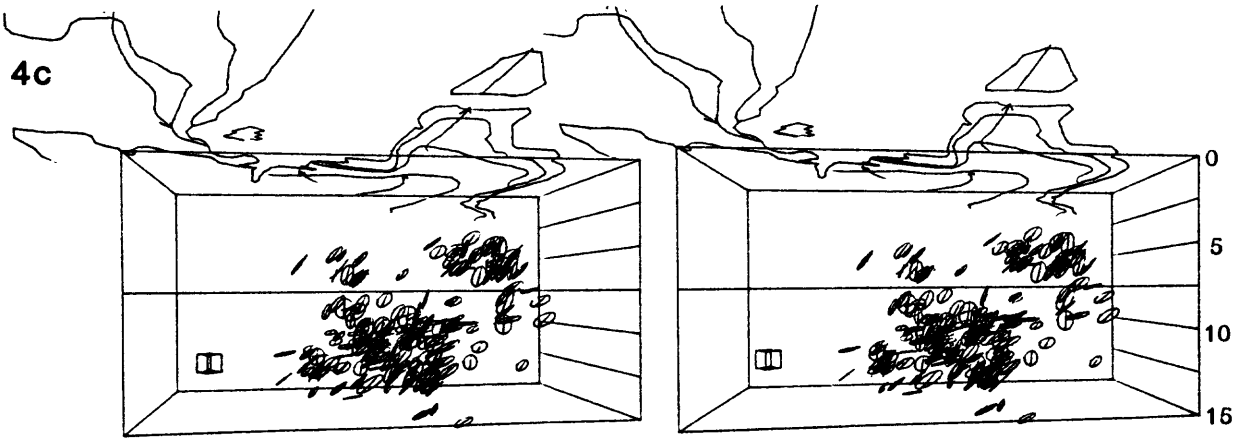

Zone 2

Fig. 5a

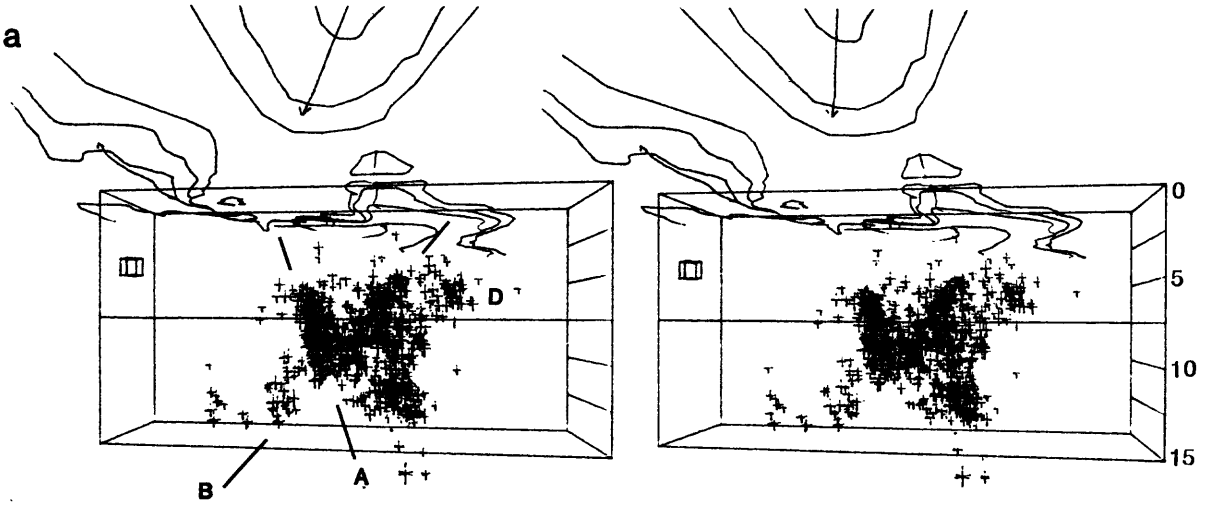

Fig. 5b

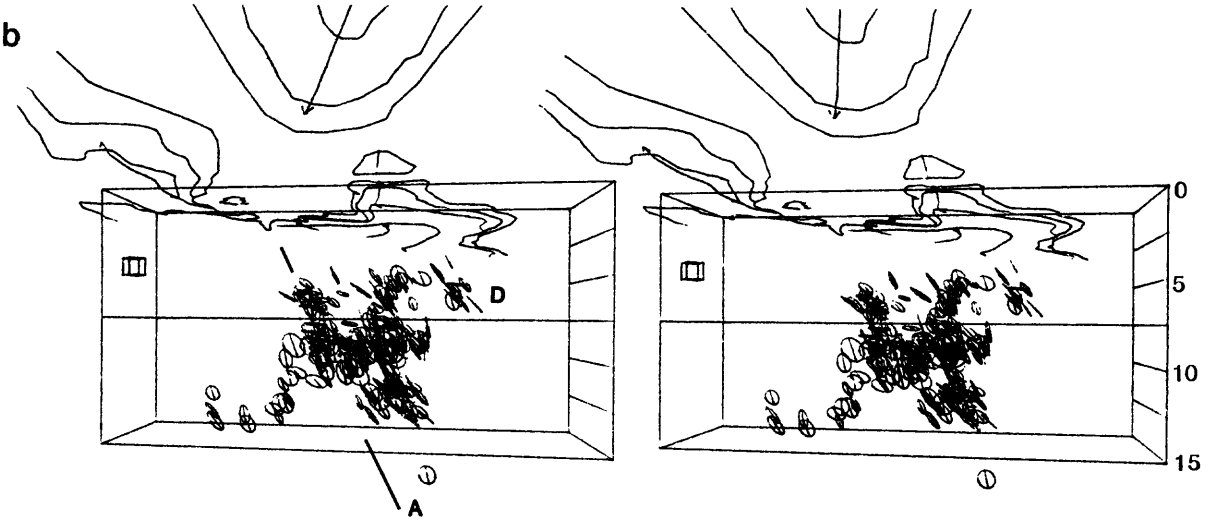

Fig. 5c

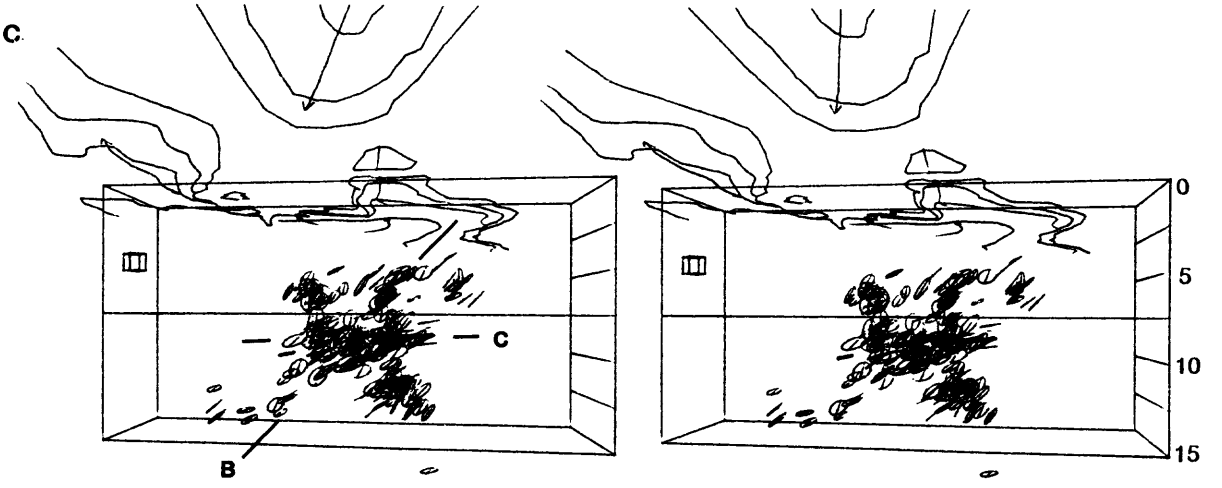

Zone 3

Fig. 6a

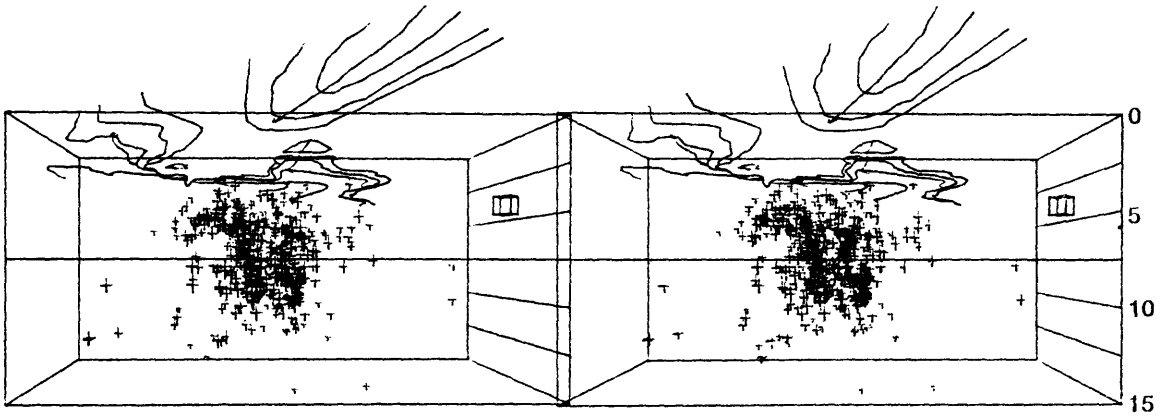

Fig. 6b

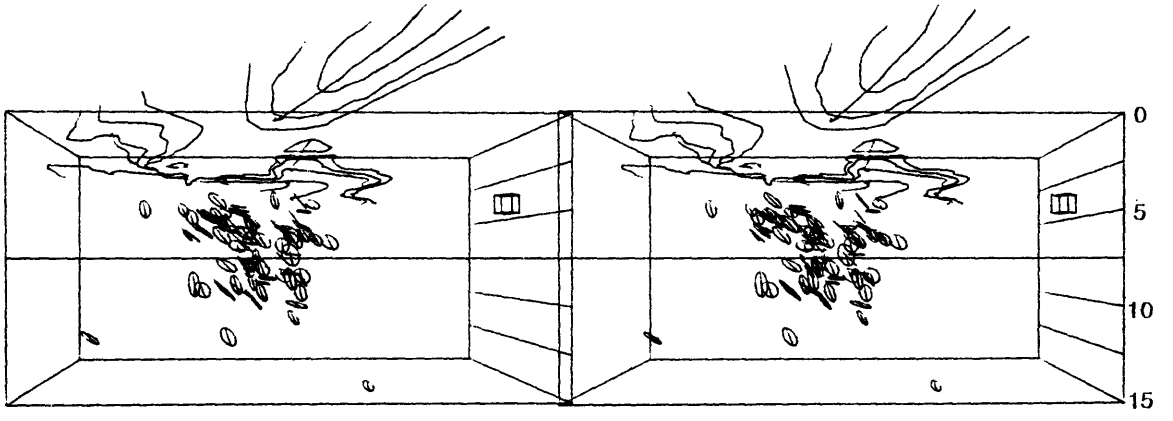

Fig. 6c

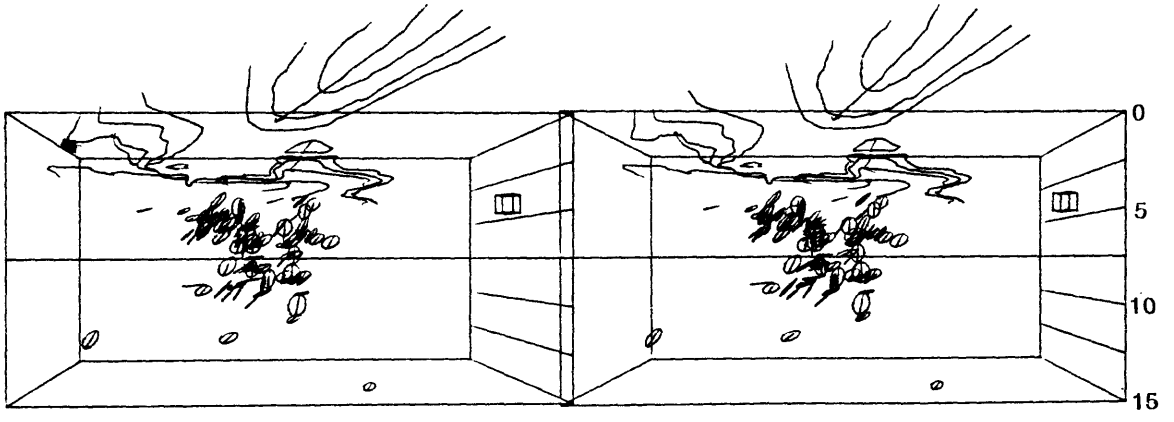

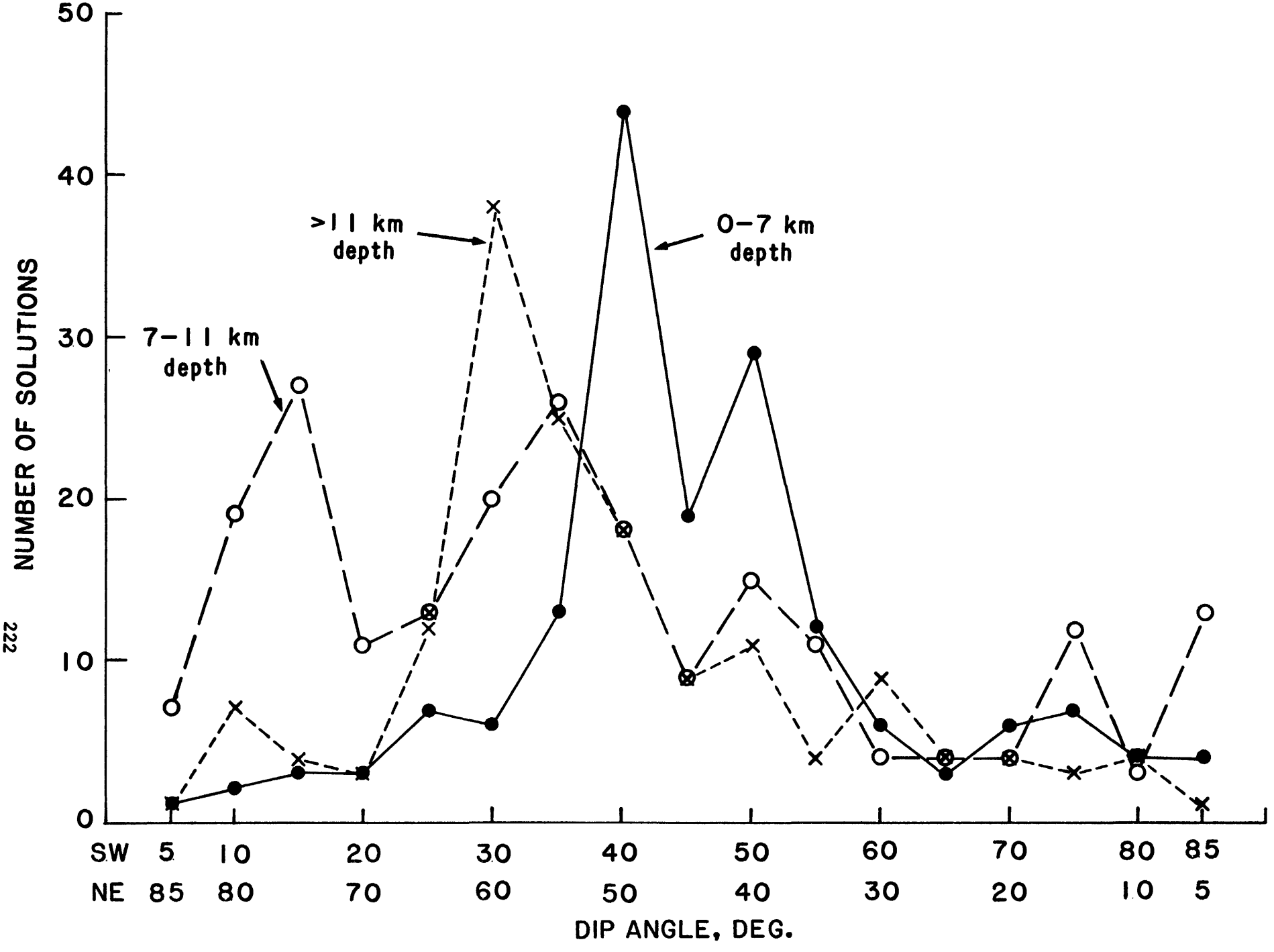
50
40
30
20
10
0
NUMBER OF SOLUTIONS
>11 km depth
0-7 km depth
7-11 km depth
SW 5 10 20 30 40 50 60 70 80 85
NE 85 80 70 60 50 40 30 20 10 5
DIP ANGLE, DEG.

First 12 Hours

Fig. 8a

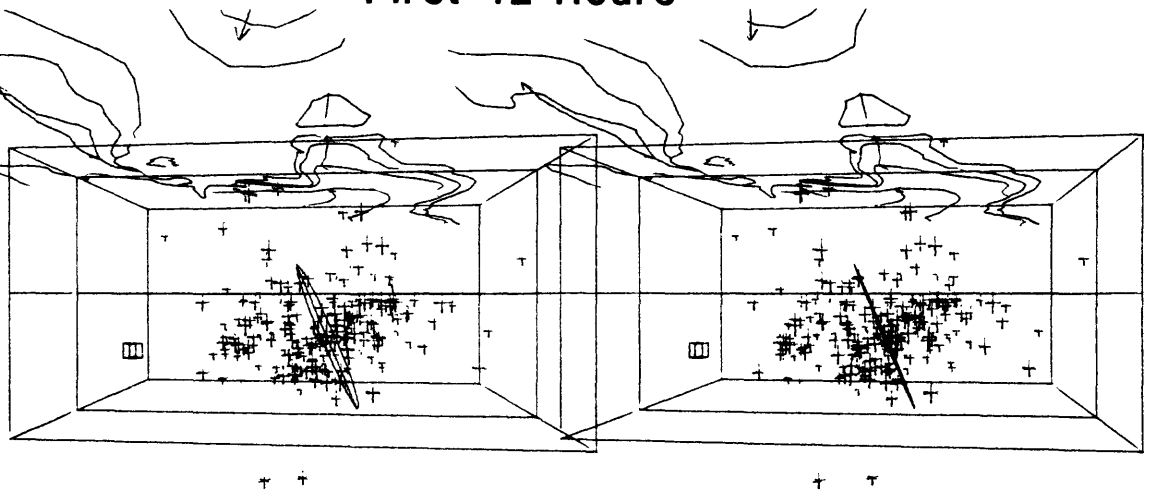

Fig. 8b

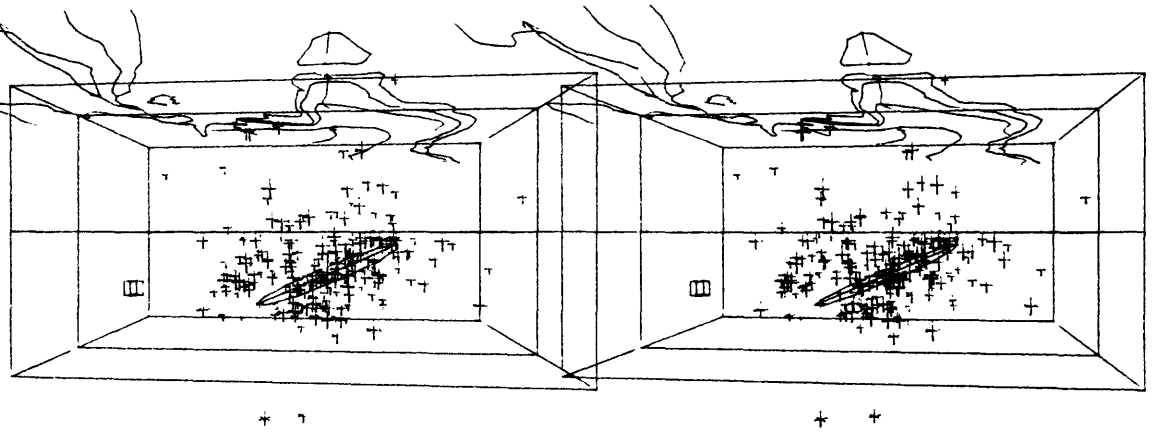

Fig. 8c

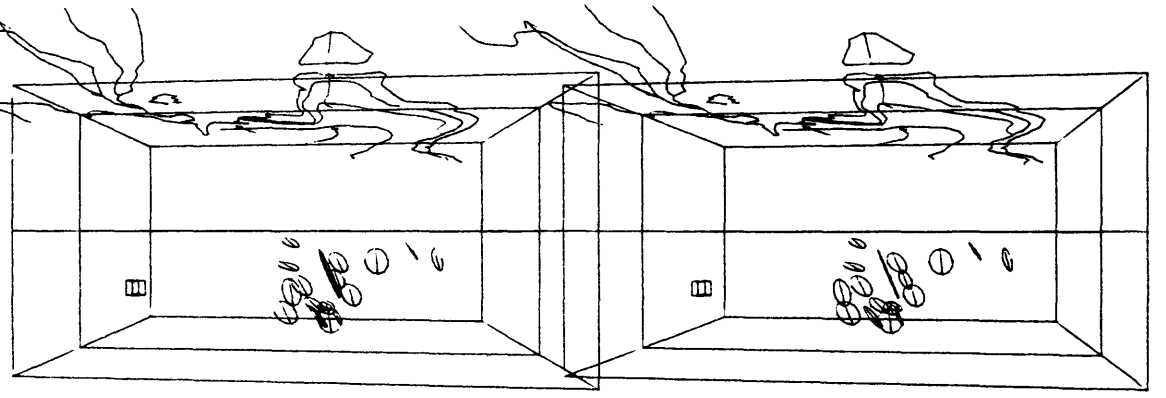

Fig. 8d

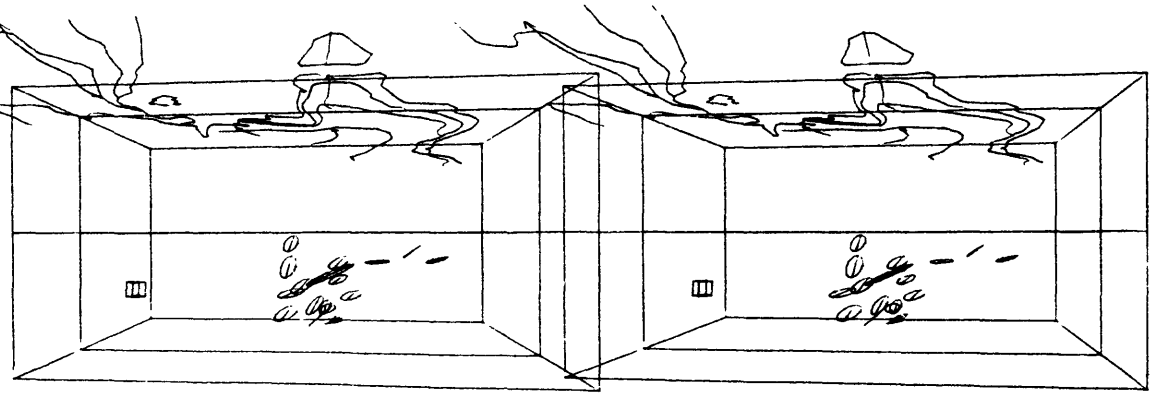

First 3 Hours

Fig. 9a

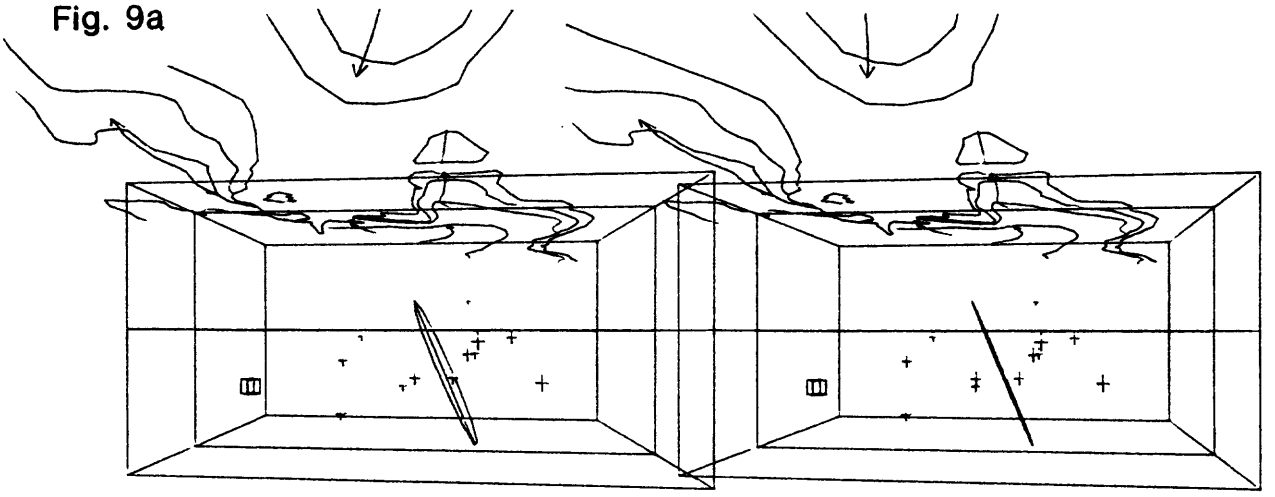

Fig. 9b

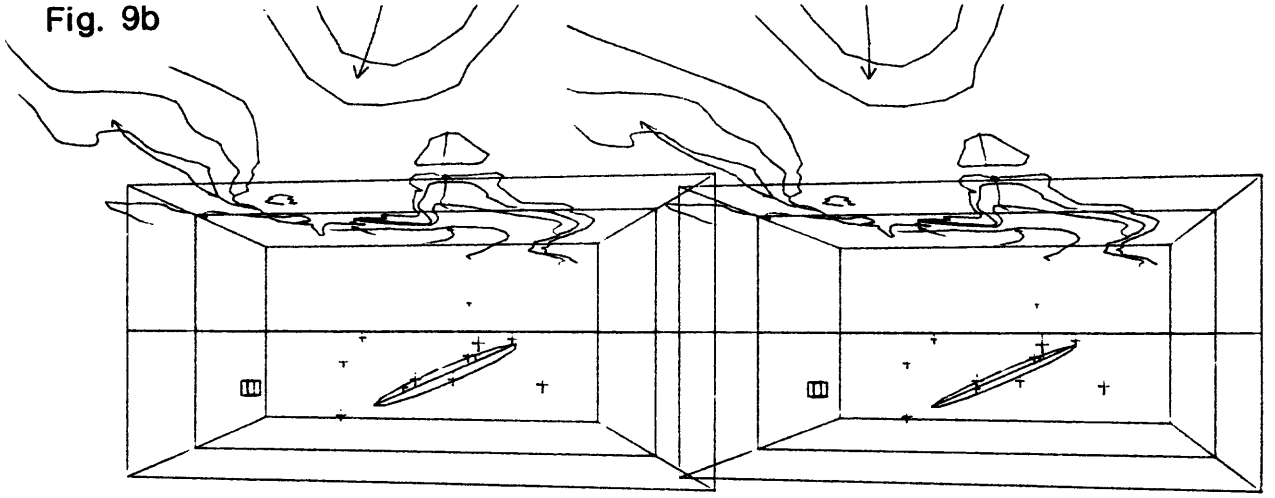

EVIDENCE FOR SURFACE FOLDING AND SUBSURFACE FAULT SLIP FROM GEODETIC ELEVATION CHANGES ASSOCIATED WITH THE 1983 COALINGA, CALIFORNIA, EARTHQUAKE

Ross S. Stein
U.S. Geological Survey
Menlo Park, California 94025

ABSTRACT

The Coalinga earthquake (M_L = 6.7) uplifted Anticline Ridge 0.5 m and depressed the adjacent Pleasant Valley syncline 0.25 m, but caused no fault rupture at the ground surface. Coseismic elevation changes are used to estimate of the attitude, geometry, and slip of the concealed fault. Small topographic relief over the route minimizes systematic leveling errors. Deep-well compaction monitors and the record of fluid pumping are used to correct for and remove artificial subsidence due to fluid withdrawal. A steeply dipping reverse fault fits the geodetic and seismic data better than a gently dipping thrust fault. Using the N53°W strike and a 67°NE dip determined for the mainshock focal mechanism, the best-fit earthquake parameters are: 1.7 ± 0.5 m of dominantly reverse dip slip on a fault extending from a hypocentral depth of 12 ± 1.5 km to within 4 ± 1 km from the ground; M_o = 6-7 x 10^{25} dyne-cm. Equivalence of the geodetic and seismically determined moments requires that most of the slip occurred during the mainshock. The deformation caused by the 1983 earthquake strikingly resembles the structural relief of the Pleistocene Tulare Formation on Anticline Ridge and in Pleasant Valley. About 2 km of cumulative concealed fault slip would account for this similarity, yielding a Quaternary slip rate of 1-4 mm/yr. Well documented examples of anticlinal uplift associated with large thrust earthquakes, and the similarity between Anticline Ridge and adjacent structures, argue that the earthquake potential along the eastern California Coast Ranges is greater than previously recognized.

INTRODUCTION

The 2 May 1983 Coalinga earthquake struck beneath Anticline Ridge, a low ridge bounding the San Joaquin Valley syncline to the east and the California Coast Ranges to the west (Figure 1a). In order to evaluate the repeat time and the cumulative displacement on the fault, as well as its tectonic role in the Coast Ranges geology, knowledge of the fault attitude and slip is necessary. This paper presents an investigation of the fault geometry and displacement consistent with the permanent vertical deformation and earthquake mainshock, and an estimate of the slip rate based on the resemblance between the coseismic and Pleistocene deformation.

Spirit leveling is a technique designed to measure the height of permanent bench marks (BM's) in the ground. To estimate changes in elevation caused by the earthquake, the elevations of BM's surveyed largely 11 years before the 2 May 1983 earthquake were subtracted from the elevations measured one to four months after the mainshock. Leveling errors due to random and systematic sources prove to be negligible in comparison to the magnitude of the coseismic deformation. Artificial subsidence caused by water and oil withdrawal is more substantial. Uncertainties in the proper removal of these contaminants limit the ability to construct definitive models of the fault slip.

Dislocations embedded in an elastic half-space are used to model the earthquake rupture. This is equivalent to making a cut within an elastic body, displacing the faces of the cut a prescribed amount, and bonding the faces back together. The entire elastic body as well as its surface will be deformed, and the surface deformation is matched to the observations. Dislocation models are inherently non-unique: One pattern of surface deformation can be satisfied by more than one dislocation source. Here models are kept as simple as possible, limited by the constraints imposed by the mainshock hypocenter and fault plane solution. Because the leveling route is oriented across the geologic structure and passes over the mainshock, the pattern of surface deformation allows the fault-plane to be distinguished with fair confidence from the auxiliary plane. Subject to a poorly constrained fault length along strike, the seismic moment (M_o) can be estimated for comparison with the moment measured from seismic waves.

DATA

Leveling Network

The 2 May 1983 Coalinga earthquake occurred within a leveling network established to study compaction of unconsolidated deposits in response to ground-water withdrawal [Bull, 1975]. The network has been affected by bench mark subsidence caused by ground-water withdrawal in Pleasant Valley and in the San Joaquin Valley, and by oil withdrawal beneath Anticline Ridge (Figure 1a and 1b). Subsidence is evident on the 1966-72 profile of elevation change before the earthquake occurred (Figure 2a). However, the network is ideally located with respect to the 2 May 1983 mainshock and aftershocks (Figure 1c). The network, with 82 km of leveling routes, was surveyed in 1960, 1966, 1969, and 1972 by the National Geodetic Survey (NGS) for the U.S. Geological Survey (USGS). The NGS releveled the central network during 8-24 June 1983 (the bench marks are denoted by circles, triangles, and squares; Figure 1a), the Los Gatos Creek route (hexagons, Figure 1a) on 6-19 September 1983, and the Guijarral Hills spur (diamonds; Figure 1a) on 30 August-6 September 1983, at the request of the USGS. The 22-km long leveling route up Los Gatos Creek was previously surveyed in 1939 by the USGS, using less accurate 3rd Order specifications (hexagons; Figure 1). Because of the lower quality of the pre-earthquake elevations there, and the low density of BM's, no further discussion of elevation changes along the upper Los Gatos Creek will be made.

Leveling Errors

Sources of measurement uncertainty in leveling are dominated by slope dependent systematic errors. These include improper calibration of the graduated leveling rods and atmospheric refraction of the line of sight between the rods and the level, a horizontal telescope. Typical errors in the length of leveling rods used during the period 1953-1979 are less than 25 ppm at the 95% level of confidence [Strange, 1980; Stein, 1981]. Because the maximum elevation difference along the leveling route is 200 m (see Figure 2d), rod errors of 5 mm are possible. Elevation changes shown in Figure 2 have been corrected for refraction error using the method of Holdahl [1981]. Most of the refraction error that accumulated along a 50 km-long test route in southern California was removed by this method. The test involved procedures and climatic conditions similar to those that prevail in Coalinga [Holdahl, 1982; Whalen and Strange, 1983]. Residual refraction error should be less than 5 mm, assuming a 100% error in estimating the mean temperature gradient along the line of sight and a 50% error in estimating the mean distance between the level and rods for the 1972 survey.

Random errors grow with the square root of the distance leveled. All of the 1960, 1966, and 1983 leveling reported here was performed to (4.0 mm) double-run First-Order standards [Federal Geodetic Control Committee, 1980] while the 1969 and 1972 leveling was run to (8.4 mm) single-run Second-Order standards. The random error should amount to less than 15 mm over the 35-km distance between the southwest and northeast ends of the route. Leveling errors from all sources thus sum to less than 20 mm, equal to the size of the bench mark symbols in Figure 2.

COSEISMIC DEFORMATION

Non-tectonic elevation change between the pre-earthquake 1972 survey and the post-quake 1983 survey must be removed before reconstructing the coseismic deformation. The subsidence rate during 1966-72 is used for this purpose, modified by the record of surficial compaction and fluid extraction during 1972-83. Prior to 1983, bench marks in consolidated Cretaceous rocks, farthest from the sites of known artificial subsidence, (F1046-J944, Figure 1; BM's 1-6, Figure 2a) are assumed to have been stable. During the coseismic period this assumption is no longer valid, as no bench mark is more than 20 km from the mainshock epicenter. Therefore the position of the zero-elevation-change datum in Figures 2b and 2c (the thin horizontal line) is arbitrary.

San Joaquin Valley Subsidence

Subsidence caused by artesian-head decline along the western margin of the San Joaquin Valley reached its peak rate during the mid-1950's. After construction of the California Aqueduct in 1970, pumping from deep aquifers decreased [Bull, 1975]. During the period 1970-80, the aqueduct delivered 93% of the water used for irrigation [Ireland, et al., 1982]. Because of the reduced rate of head decline after 1970, the rate of subsidence during 1966-72 (Figure 2a) provides an upper bound on the rate for the ensuing decade.

Poland et al. [1975] and Bull [1975] report on deep-well compaction recorders installed to measure the vertical strain or shortening caused by compaction of surface deposits within the most intensively pumped aquifers. Compaction well 33A1, 313 m deep, is located at the northeast end of the main leveling route (marked by an X in Figure 1a). From March 1966, a year after its installation, through January 1980, the end of the published record, the well recorded 275 mm of compaction [Ireland et al., 1982]. The California Department of Water Resources releveled the northeast segment of the route from BM Y998 USGS, adjacent to the recorder well, to BM E929 atop Anticline Ridge in February 1982 (the BM's are shown as circles in Figure 1a; BM's 27-37 in Figure 2a). Subsidence of BM Y998 USGS from March 1966 to February 1982 was 300 mm. Therefore the compaction recorder measured at least 90% of the total subsidence. The rate of compaction during the period 1972-1980 is 30% of the 1966-72 rate, suggesting that the subsidence rate also decreased by about 30%. Compaction well 23P2, 670 m deep, operated through 1974 Figure 1a). During 1966-72 the well recorded 100% of the subsidence measured at nearby BM Z888. During the succeeding two years the rate of compaction was 40% of the rate during 1966-72. Under the assumption that the aquifer continued to recharge after 1974 with a concomitant decrease in compaction rate, the projected 1972-83 subsidence rate would be about 30% of the 1966-72 rate. The elevation changes from well 23P2 south to the Guijarral Hills was corrected using 30% of the 1969-1972 rate, as no 1966 survey exists there.

The compaction history of wells with recorders therefore suggests that the elevation of bench marks surveyed during 1972 should be corrected for 1972-83 subsidence at a rate equal to 30% of the 1966-72 rate. Bench marks in Holocene alluvium (east of the subsidence boundary in Figure 1b) have been corrected for subsidence in Figure 2c. Probable error in the correction should be less than 50% of the estimated 1972-83 subsidence rate, or 45 mm at the end of the north spur where the 1972-83 subsidence rate is estimated to be 8 mm/yr (squares in Figure 1; BM E927), 55 mm at the end of the east spur where the rate is 10 mm/yr (triangles; BM H927), and only a few mm at the end of the main route where the 1982-83 rate of subsidence is 6 mm/yr (circles in Figure 1; BM Q1195).

Pleasant Valley Subsidence

The rate of subsidence in Pleasant Valley during 1960-68 was about one-third of the rate in the San Joaquin Valley [Propokovitch and Magleby, 1968], but subsidence in Pleasant Valley after 1972 is more uncertain because no wells record compaction there, and because no releveling was conducted there during 1973-83. Aqueduct deliveries to the Coalinga township during 1972-82 comprised 30% of the total water consumption, whereas the aqueduct supplied only 2% of the water useage for the township during 1970-71 [unpub. Bureau of Reclamation Water Delivery Records for 1983]. Estimated ground-water pumpage (for Township/Range 20S/15E) decreased by 40% from 1966-71 to 1975-77 [Mitten, 1972, 1976, 1980]. No pumping records are available for the years 1972-74 and 1978-83, but continued water-table decline increased the cost of pumping for irrigation, which probably reduced pumpage after 1977. Here it is assumed that the subsidence rate during the period 1972-83 was about 50% of the rate during 1966-72. The maximum 1972-83 subsidence rate in the Valley, at BM's 12 and 17 in Figure 2b, would then be 9 mm/yr - roughly equivalent to the rate in

the San Joaquin Valley - with an uncertainty of perhaps 4 mm/yr, or 45 mm.

Anticline Ridge Subsidence

The net liquid production rate beneath Anticline Ridge has declined slightly since 1966, from 29 to 26 million bbl/yr [4.6-4.1 million m^3/yr; Conservation Committee of California Oil Producers, 1967-1982]. These values include the combined pumping of oil and water, minus re-injected water and steam, in the Coalinga and East Extension fields that are traversed by the leveling route. The 1966-72 subsidence rate, about 5 mm/yr, is therefore employed to correct the earthquake elevation changes of BM's W944 - W237 and J929 - Y156 in Figure 1a (BM's 22-26 and 46-49 in Figure 2a). North of the oil fields and south of the recent alluvium, BM's Y662 - X662 showed no subsidence during 1960-72 (Figure 1; BM's 37-42, Figure 2a); therefore no corrections were made to these BM's in Figure 2c. Segall [1984] modelled the subsurface stress changes and surface elevation changes at Anticline Ridge caused by fluid withdrawal. He predicted a nearly linear subsidence rate of 3.3 ± 0.7 mm/yr for 1966-1983, in fair agreement with the observed rate during 1966-72, and the rate projected for 1972-83.

To summarize, subsidence corrections are generally small in comparison to the total observed elevation changes during the earthquake period; corrections nowhere exceed 110 mm. The largest corrections are made to the main leveling route in Pleasant Valley, and to the north, east and southern spurs in the San Joaquin Valley. A portion of the main route in the San Joaquin Valley was leveled only 1.5 years before the earthquake, and thus sustained little artificial subsidence. Contoured coseismic elevation changes are presented in Figure 2e.

DISLOCATION MODELS

The earthquake elevation changes are modeled by dislocations in an elastic half-space using expressions of Mansinha and Smylie [1971] and with Poisson's ratio set to 1/4. The half-space is a body with infinite depth and with a flat upper surface corresponding to the ground. The fault rupture is modeled as a rectangular plane with uniform slip on its surface. The actual rupture is probably neither rectangular nor planar, and the assumption of uniform slip produces an unrealistic infinite stress at the perimeter. However, these simplifications do not modify the vertical deformation at the ground surface enough to warrant the use of other more plausible geometries.

Testing of candidate fault models was simplified by adherence to the fault-plane solution of Eaton, et al. [1983] from first motion of P-waves at 39 stations less than 100 km from the epicenter. The model fault strike was therefore fixed to be N53°W. A N37°E ± 20° axis of maximum compression suggests reverse dip slip. This means that up to a 20° right-lateral or left-lateral slip component is permissible. With one exception, model fault planes were constrained to pass within 1.5 km of the mainshock hypocenter, which is located at 36°13.99' N. lat., 120°17.59' W. long., at a depth of 10.5 km. One nodal plane dips 67°NE, and the other dips approximately 23°SW. Model faults are shown in Figure 3 with aftershocks $M_L \geq 2.5$ during 2 May - 31 July from

Eaton et al. [1983]. In the absence of primary ground-surface rupture [Clark et al., 1983; Hart and McJunkin, 1983] both planes were tested.

Northeast-Dipping Reverse Fault

The general characteristics of the earthquake deformation limit the suitable choices for the fault location and attitude. For a reverse-fault plane with uniform slip, the peak uplift occurs above the upper edge or top of the fault, and the elevation change is zero where the fault plane, if extended to the surface, would intersect the ground (see Figure 3a). For a fixed fault dip and depth to the center of the fault, the product of the slip times the fault width (the down-dip fault dimension) is the same for all acceptable models. The fault length is poorly determined by the data, since observations are sparse northwest of the mainshock (Figure 3e), where aftershocks are distributed over a large area (Figure 1c).

Uplift across the southern end of the aftershock zone (see Figures 1c, 2c, and 2e) is only one-third of that across Anticline Ridge at the 2 May epicenter. This deformation pattern can be approximately satisfied if the fault terminates at the southern end of Anticline Ridge, or if the fault extends beneath the Guijarral Hills with slip diminished to about one quarter that at the center of the fault. A M_L = 4.0 aftershock beneath Guijarral Hills has a fault plane solution indistinguishable from the mainshock [see Earthquake "F" in Figure 2 of Eaton, et al., 1983] Some continuity of the structures beneath Anticline Ridge and the Guijarral Hills is thus likely. A fault length of 14-16 km thus appears consistent with the decay of elevation change at southeastern end of the leveling network but is poorly constrained to the northwest. All models with pure reverse slip show M_o = 6.0-6.5 x 10^{25} dyne-cm (6.0-6.5 x 10^{18} Nm), where $M_o = G \cdot U \cdot A$, G is the shear modulus, here assumed to be about 3 x 10^{11} dyne/cm^2 (3 x 10^{10} N/m^2), U is the slip, and A is the fault area, and M_o is the geodetic moment.

For a 67°NE dip, the vertical depth to the top of the fault (the depth of burial of the fault's upper edge) is equal to about two-thirds the width of the peak-to-trough elevation change. The uncertainty in the depth of burial stems from the deformation near Coalinga, 10 km southwest of the epicenter, where the BM's display inconsistent elevation changes and where the artificial subsidence is most uncertain. The surface projection of the fault models represented by a dotted line and by a dashed line in Figure 3a is shown in Figure 1b. The geodetic data permit up to a 20° left-lateral departure from pure dip slip on the steeply dipping reverse fault, causing a slight increase in M_o (Figure 3b). A 20° right-lateral slip component is less compatible with the southeastern elevation changes, but cannot be confidently rejected.

If reverse fault slip tapered from a depth of 5 to 3 km, the vertical deformation would look similar to that if rupture terminated at 4 km. Similarly, if slip was distributed on the reverse fault over a fault thickness of 1 km rather than confined to a plane, the dislocation models would overestimate the upper fault depth. Thus the depth-of-burial values should be considered maximum estimates.

Southwest-Dipping Thrust Fault

The peak uplift along the leveling route occurs near the mainshock epicenter. Because the uplift must locate above the top of the fault, the upper edge of a gently dipping model fault must lie at a depth of about 10 km (the dot-dash line in Figure 3c). The fit to the observed elevation changes is poor. The deeply buried fault also requires more slip than the steeply dipping fault to uplift the ground surface the same amount. For a fault length of 14 km, the southwest dipping fault has $M_o = 9 \times 10^{25}$ dyne-cm. The hypocenter of mainshock at the upper edge of a fault in this model, which implies that seismic rupture was in the down-dip direction.

A good fit to the observations using a southwest-dipping thrust plane can be accomplished with more complex models. A thrust fault at a shallow depth with slip increasing down-dip provides an excellent fit to the leveling data (dotted line in Figure 3c). However, the mainshock would not locate on the fault plane unless its epicenter were relocated 6.5 km to the southwest and its depth were reduced from 10.5 km to 7.5 km. In order to satisfy the condition that the model fault should pass through the mainshock, a listric fault is required, one in which the fault becomes more gently dipping with depth beneath the hypocenter (Figure 3d). The steeply dipping segment with 1 m of reverse slip brings the predicted elevation change at the northeast end of the leveling route into better agreement with the data. Some misfit remains in the region from the epicenter extending for 10 km to the southwest. The surface projection of this fault model is shown by a solid line in Figure 1b. The parameters of all the fault models shown in Figure 3 are presented in Table 1.

INTERPRETATION OF THE COSEISMIC DEFORMATION

Steeply Dipping Reverse Fault vs. Gently Dipping Thrust

The leveling data alone do not permit selection between the two nodal planes of the mainshock. When the interpretation of the leveling observations is constrained by the depth and location of the mainshock, then the earthquake elevation changes are best fit by a northeast-dipping thrust extending from a depth of 3-5 km to 10-13 km, with 1.3-2.3 m of reverse dip slip. A southwest-dipping thrust plane can only fit the data as well if it is sufficiently shallow, and if the fault slip increases down-dip. However, the depth of seismicity argues against the likelihood that such a shallow thrust fault produced the elevation changes. Both the mainshock and the larger immediate aftershocks in the epicentral area lie beneath the 4-7 km depth of the candidate thrust fault (Figure 3c). The earthquake could have ruptured the curved or two-plane thrust fault shown in Figure 3d. However, the fit to the leveling data is inferior to the reverse-fault models, and the non-double couple component of the mainshock is small, indicative of a coplanar rupture

[Hartzell and Heaton, 1983]. The apparent absence of seismic radiation from a steeply dipping upper portion of such a listric fault could be explained by seismic rupture from 10 to 14 km in the down-dip direction, preceded or followed by aseismic slip from a depth of 10 to 5 km. Barring significant relocation of the mainshock and aftershocks, though, the steeply dipping reverse plane provides the most straightforward fit to the geodetic and seismic evidence. The uncertainty of bench mark subsidence in Pleasant Valley does not permit rejection of the two-plane model.

Down-dip rupture of the mainshock, if established from the earthquake accelerograms, could resolve the nodal plane dispute. Up-dip rupture is by far more common, but at least one case of down-dip rupture is well documented, the 1946 M_s = 7.4 Aleutian earthquake [Sykes, 1971]. Choy [this volume] argues for two main events separated by 3.5 sec. If there are distinct sources, then their relative location could prove essential to the selection of the nodal plane.

Namson et al. [1983] have argued that stratigraphic relations require a southwest dipping thrust plane beneath Joaquin Ridge, 15 km northwest of the 2 May 1983 mainshock (Figure 2a). Such a structure would lie considerably deeper than the Coalinga mainshock if it was projected down the southeast plunging anticline to the epicentral region. Whether such a thrust sheet slips seismically or by creep is crucial to the question of its role during the earthquake. The structural necessity of a thrust plane, to uplift the Coast Ranges with respect to the San Joaquin Valley, does not guarantee its role as a seismic source.

Flexural slip has been advanced by Hill [this volume] as an alternative seismic source. While flexural slip may be associated with the aftershocks, the double-couple component of the mainshock precludes a highly curved source. Without a more detailed picture of the deep structure beneath the anticline, it is difficult to distinguish between slip that is oriented parallel to or cuts across bedding planes.

Seismic vs. Aseismic Fault Slip

The seismic moment for the successful fault models was found to be in the range 6-7 x 10^{25} dyne-cm (6-7 x 10^{18} Nm). The moment could be larger if the fault plane extended farther to the northwest along strike, but it is unlikely to be much smaller. Heaton and Hartzell [1983] calculate M_o = 3.8 x 10^{25} dyne-cm from teleseismic long-period (5 s) compressional waves; Kanamori [1983] determines M_o = 5.4 x 10^{25} dyne-cm from very long period (256 s) surface waves. The cumulative moment of aftershocks does not substantially enlarge the net M_o release. The summed moment of aftershocks with $M_L \geq 4.0$ located by Eaton et al. [1983], excluding the 22 July 1983 M_L = 6.4 rupture on the adjacent Nunez fault, is 0.2 x 10^{25} dyne-cm. The empirical relation of Thatcher and Hanks [1973] is used for this estimation. The fair agreement between geodetic and seismic estimates of M_o implies that most slip was released seismically during the mainshock. Preseismic slip during the decade preceeding the earthquake, and postseismic slip 1-4 months after the earthquake, are therefore too small to be distinguished from the seismic slip.

INTERPRETATION OF PLEISTOCENE DEFORMATION

Surface Folding Caused by Subsurface Fault Slip

The modeling demonstrates that most of the earthquake fault slip associated with the 2 May mainshock was confined to depths greater than 3-5 km. The surface rupture on the Nunez fault associated with the 11 June 1983 M_L = 5.2 and 22 July 1983 M_L = 6.2 earthquakes [Rymer et al., this volume] stands in contrast to the deformation associated with the 2 May mainshock, illustrated schematically in Figures 4a and 4b. Thrust events that do not extend to the surface deform the rocks above the fault into a gentle fold, do not create a fault scarp, and typically result in the deposition of only a thin veneer of superficial sediments (Figures 4c and 4d). Faults can slip repeatedly without reaching the Earth's surface if the stresses at the fault tip and those imposed on the overlying material can relax between earthquakes. These stresses are apparently relieved by creep, by distribution along secondary fractures, or by near-surface splay faults, and so the near-surface rocks do not reach or are not maintained at their failure stress. Yeats [1983] has observed flexural or bedding-plane slip between folded lithic units, and bending-moment faults that accommodate compressional and extensional fiber strains within the units in thoroughly drilled anticlines in California. These faults are seen at the ground surface extending discontinuously to depths of 4 km. Slip on these rootless faults, which do not continue at depth, may relieve the stresses caused by deep-seated events on thrust faults. The diffuse distribution of aftershocks that typifies the Coalinga event and the two other thrust events that will be considered here may be attributable to displacement on these secondary structures. Within the upper surface of an anticline hinge, extensional fiber stress may substantially exceed the regional horizontal compressive stress. Subject to this local stress deviation, unconsolidated near-surface deposits with low cohesive strength may form tensile cracks or grabens atop folds, masking evidence for thrust faulting.

Fault Slip Rate

The profile of the coseismic deformation (Figure 4c) strikingly resembles the structure of Anticline Ridge and the adjacent valley to the southwest. Cumulative subsurface fault slip of at least 2 km during the past 2 m.y., equivalent to 1,000 events with slip similar to the 1983 earthquake, would explain this similarity (Figure 4c).

The earthquake elevation changes are closely correlated with topography (Figure 5a). Geodetic tilt is correlated with the topographic slope in Figure 5b at the 99% level of confidence; the mean tilt is equal to $(1.3 \pm 0.2) \times 10^{-3}$ times the slope [for the details of the correlation method, see Stein, 1981]. Because the largest slope-dependent leveling errors observed in the U.S. reach a magnitude of about 1.5×10^{-4} [Jackson et al., 1980; Stein, 1981], the correlation must reflect the correlation of topography with geologic structure. In addition, these data have been corrected for rod calibration error more rigorously than those for which the large errors had been

reported. After a regional down-to-the-east slope of 6.5×10^{-3} (0.37°) is removed from the leveling route topography (Figure 5a), the gross topographic height is equal to about 300 times the coseismic elevation change. The amplitude of the topography is damped relative to the structural contours, however, by erosion from the ridge crest and deposition into lows. The late Pleistocene beds of the Tulare formation dip 4-16 times more steeply than the topographic slope of the anticline [see Dibblee, 1971]. Thus the minimum cumulative fault slip since deposition of the beds becomes 1.8 m x 300 x 4 = 2 km.

The youngest folded member is the Tulare Formation (Figure 1a), 0.5-2.2 m.y. in age [Lettis, 1982]. Because the base of the Tulare is nearly congruent with the underlying formations, the major episode of folding must postdate initial deposition of the Tulare Formation. This yields a slip rate of about 1-4 mm/yr during the past 1-2 million years, and a repeat time of 500-1500 years if earthquakes are periodic and no shocks larger than the 1983 event have occurred here.

ANALOGUES OF ANTICLINE RIDGE AND THE COALINGA EARTHQUAKE

The 1964 Niigata, Japan, Earthquake

The 1964 Niigata M_s = 7.5 earthquake struck in Japan's most widespread and rapidly deforming fold belt, as measured from historic [Kato, 1983] and Quaternary [Ota, 1980] shoreline deformation. Marine surveys demonstrated that the seabed was upwarped 3-5 m by the reverse dip slip event [Mogi et al., 1964], but the surface deposits were not cut by faults except in a few isolated places (Figure 6). Awashima Island was tilted and uplifted 1.5 m. The sedimentary beds of the island, late Miocene in age, dip 10°-20° [Kawasumi, 1973], about 1,000 times the amount they were tilted during the earthquake. This relation can be explained by progressive uplift and tilt during large slip events on a concealed thrust fault, similar to the style of deformation inferred at Coalinga.

Distinguishing the fault plane from the auxiliary plane for the Niigata earthquake has been difficult for the same reasons it has at Coalinga: the aftershocks clustered without delineating a fault plane [Satake and Abe, 1983], surface breakage was negligable, the sea bottom exhibited a broad uplift [Mogi et al., 1964] over a prominent anticline, and seismic reflection profiles revealed no fault at depths of 0-2 km within the aftershock zone [Marine Safety Agency, 1973] (Figure 6).

The 1,400-year-long historical record of earthquakes in Japan is equally well correlated with active faults and active folds. This is evident when the distribution of energy released by historic earthquakes is compared to the distribution of Quaternary faults and folds [see Figures 5-13 to 5-15 in the Explanatory text of the Quaternary tectonic map of Japan]. Apparently folds provide as good an indicator of earthquake sources as do faults. The Quaternary (2-0 m.y. B.P.) tectonic map of northern Japan [The Research Group for Quaternary Tectonic Map, 1969; The Research Group for Active Faults In and Around Japan, 1980] also exhibits a similar number and distribution of dip-

slip faults and folds (Figure 7). These faults and fold axes are generally parallel to each other and orient normal to the azimuth of maximum compression inferred from horizontal geodetic measurements and by shallow earthquakes. The shortest fold wavelengths (15 km) and highest historic and Quaternary uplift rates (1-3 mm/yr) were measured in areas with the greatest accumulation of Neogene and younger (0-24 m.y.-old) sediments.

Wheeler Ridge and the 1952 Kern County, California, Earthquakes

Anticline uplift occurred at the epicentral (west) end of the 1952 Kern County, California, M_S = 7.3 earthquake whereas the reverse and left-lateral fault ruptured to the surface at the east end of the aftershock zone, (see Figure 8A). The earthquake focus lies beneath Wheeler Ridge, a fold in a 3-km-thick sequence of Pliocene and Quaternary sediments that was upwarped 1.0 m during the earthquake. Models of the horizontal and vertical geodetic data [Dunbar et al., 1980; Stein and Thatcher, 1981] preclude fault rupture through the upper 5 km of sediments at the epicenter (Figure 8B). Geologic correlation suggests that the central section of the fault has slipped at a rate of about 5 mm/yr during the past 2 m.y. [Stein and Thatcher, 1981]. In contrast to the epicentral area, the maximum ground displacement observed at the east end of the fault equals the modeled subsurface fault slip, and abundant fault scarps have formed there, consistent with Figure 4b. In this region, where cretaceous granite is exposed, the top of the fault reaches closer to the ground surface (Figure 8B).

Kettleman Hills Anticline

Unlike Anticline Ridge, which shows stratigraphic evidence for Tertiary uplift followed by more intensive Pleistocene deformation, the Kettleman Hills anticline formed entirely during the Pleistocene [see Woodring et al., 1940, pp. 153-154; Harding, 1976]. Kettleman Hills North Dome anticline shares the assymetry of Anticline Ridge, dipping less steeply on its western flank (Figure 9). Wentworth et al. [1983] find evidence from seismic refraction and reflection data for both a steeply dipping reverse fault and a gently dipping thrust fault beneath the southern end of the Kettleman Hills anticline. Sarna-Wojcicki (in prep.) has dated the Ishi tuff member of the Tuscan formation, immediately beneath the base of the Tulare formation, at 2.4-2.6 m.y. old, using fission track etching of zircons and Potassium-argon dating (Figure 9). Obradovitch et al. [1978] independently obtained a similar age for an ash deposit in approximately the same stratigraphic position. The bed of the Ishi Tuff dips 37°, whereas the depositional dip was less than 1°. This yields a tilt rate of 0.25-0.3 microradian/yr. Since deformation may not have begun immediately after deposition, it is a minimum estimate. This rate is indicative of rapid deformation, equivalent to the horizontal shear strain rate associted with the San Andreas fault. Where the Tulare Formation is traversed by the leveling route on Anticline Ridge (BM's X327-W944, Figure 1a), the beds dip 15-25° [see Dibblee, 1980]. The coseismic tilt there was about 150 microradian (BM's X327-W944; Figure 5b). Repeat of the Coalinga event every thousand years during the last 2.2 m.y. would cause a cumulative tilt of about 20°, consistent with the dip of the beds. The tilt rate at

Coalinga may thus be only 1/2-2/3 of the rate at the Kettleman North Dome.

Dense clusters of small magnitude ($M_L \leq 5$) earthquakes have struck at both ends of the Kettleman North and Middle Domes during the last eight years, a pattern reminiscent of that which preceeded the Coalinga mainshock [see Eaton et al., 1983, Figure 1]. An inspection of the last 50 years of seismicity by Uhrhammer [this volume] reveals a striking alignment of $4.5 < M_L < 5.0$ shocks extending south for 100 km from the Ortigalita fault, passing through Anticline Ridge and the Kettleman Hills. Such an alignment provides permissive evidence for a continuous subcrustal fault beneath the surface monoclines and anticlines. It is thus possible that any portion of the possible subsurface fault is capable of rupturing in a large earthquake.

CONCLUSIONS

The 2 May 1983 Coalinga earthquake most probably ruptured a fault that dips steeply to the northeast beneath Anticline Ridge. Reverse dip slip of 1.8 ± 0.5 m from a depth of 4 ± 1 km to the hypocenter at 10.5 ± 1.5 km provides the fit most compatible with the geodetic and seismic data. A thrust fault dipping gently to the southwest is not precluded by the leveling, but the fit to both the geodetic and seismic data is less satisfactory than for the reverse fault. Folding of Anticline Ridge appears to accompany concealed reverse faulting, most likely because the poorly lithified sediments are too weak to store significant elastic strain, and creep instead.

Thrust earthquakes such as the Coalinga event as well as the Kern County and Niigata shocks leave an incomplete displacement record because slip at the seismic source generally diminishes or disappears at the ground surface. Folds form as a consequence of the diminished surface slip. Although the deformed surface materials can mask active faults, folds also provide evidence to assess the subsurface rate of fault slip.

Folds separating the Coast Ranges from the synclinal San Joaquin Valley share a similar style of deformation and timing, leading to the speculation that they may also be a potential source of large earthquakes, such as at Coalinga. Thrust and reverse faults beneath the Kettleman Hills are revealed by the seismic reflection and refraction profiles. It is nearly certain that concealed faults must also underlie Anticline Ridge and Wheeler Ridge, as both have produced large earthquakes. It is thus an inescapable conclusion that all of the Pleistocene folds in the eastern Coast Ranges should be regarded as possible sites of future large earthquakes. The recent and long-term historical record of earthquakes in Japan, which correlates equally well with the Quarternary folds and faults, lends validity to this argument. This unassessed earthquake hazard demands intensified investigation of deep structures within California fold belts, and study of their contemporary and Quaternary deformation.

REFERENCES

Bull, W. B., 1975, Land subsidence due to ground-water withdrawal in the Los Banos-Kettleman City area, California. Part 2, Subsidence and compaction of deposits: U.S. Geol. Survey Prof. Paper 437-F, 90 p.

Choy, G. L., 1984, Source parameters of the Coalinga, California earthquake of May 2, 1983 inferred from broadband body waves: this volume.

Clark, M., Harms, K., Lienkaemper, J., Perkins, T., Rymer, M., and Sharp, R., 1983, The search for surface faulting, in Borcherdt, R. D., ed., The Coalinga earthquake sequence commencing May 2, 1983: U.S. Geol. Survey Open-File Report 83-5116, p. 8-11.

Conservation Committee of California Oil Producers, 1982 and earlier, Annual review of California oil and gas production: Conservation Committee of California Oil Producers, annual production statistics by fields and pools.

Dibblee, T. W., 1971, Geologic maps of the Coalinga, Joaquin Rodes, New Idria, and Priest Valley 15' Quadrangles, California, U.S.G.S. Open-File Report 71-87.

Dunbar, W. S., Boore, D. M., and Thatcher, W., 1980, Pre-co-, and post-seismic strain changes associated with the 1952 M_L = 7.2 Kern County, California, earthquake: Bull. Seismol. Soc. Am., v. 70, p. 1893- 1905.

Eaton, J., Cockerham, R., and Lester, F., 1983, Study of the May 2, 1983 Coalinga earthquake and its aftershocks, based on the USGS seismic network in northern California, in The 1983 Coalinga, California, Earthquakes, J. H. Bennett and R. W. Sherburne, eds., Calif. Div. Mines & Geol. Spec. Pub. 66, pp. 261-274.

Federal Geodetic Control Committee, 1980, Specifications to support classification, standards of accuracy, and general specifications of geodetic control surveys: National Oceanic and Atmospheric Administration, Rockville, MD, 46 p.

Fielding, E., Barazangi, M., Brown, L., Oliver, J., and Kaufman, S., 1984, COCORP seismic reflection profiles near Coalinga, California: Subsurface structure of the western Great Valley: Geology, v. 12, p. 268-273.

Harding, T. P., 1976, Tectonic significance and hydrocarbon trapping consequences with San Andreas faulting, San Joaquin Valley, California: American Assoc. Petrol. Geol. Bull., v. 60, p. 356-378.

Hart, E. W., and McJunkin, R. D., 1983, Surface faulting northwest of Coalinga, California, June and July 1983, in The 1983 Coalinga, California, Earthquakes, J. H. Bennett and R. W. Sherburne, eds., Calif. Div. Mines and Geol. Special Pub. 66, pp. 201-219.

Hartzell, S. H., and Heaton, T. H., 1983, Teleseismic mechanism of the May 2, 1983, Coalinga, California, earthquake from long period P-waves: in The 1983 Coalinga, California, Earthquakes, J. H. Bennett and R. W. Sherburne, eds., Calif. Div. Mines and Geol. Special Pub. 66, pp. 241-246.

Hill, M. L., 1984, Earthquakes and folding, Coalinga, California, this volume.

Holdahl, S. R., 1981, A model of temperature stratification for correction of leveling refraction: Bull. Geodesique, v. 55, p. 231-249.

Holdahl, S. R., 1982, Recomputation of vertical crustal motions near Palmdale, California, 1959-1975: Jour. Geophys. Research, v. 87, p. 9374-9388.

Ireland, R. L., Poland, J. F., and Riley, F. S., 1982, Land subsidence in the San Joaquin Valley, California as of 1980: U.S. Geol. Survey Open-File Report 82-370, 129 p.

Jackson, D. D., Lee, W. B., and Liu, C., 1980, Aseismic uplift in southern California: An alternate interpretation: Science, v. 210, p. 534-536.

Kamamori, H., 1983, Mechanism of the 1983 Coalinga earthquake determined from long period surface waves, in The 1983 Coalinga, California, Earthquakes, J. H. Bennett and R. W. Sherburne, eds., Calif. Div. Mines and Geol. Special Pub. 66, pp. 233-240.

Kato, T., 1983, Secular and earthquake-related vertical crustal movements as deduced from tidal records (1951-1981): Tectonophysics, v. 97, p. 183-200.

Kawasumi, H., 1973, General Report on the Niigata earthquake of 1964, Tokyo Electrical Engineering College Press, 550 p.

Kukkamaki, T. J., 1938, Uber die nivellitische refraktion: Veroff. Finn. Geodetic Institute, v. 25, p. 26-39.

Lettis, W. R., 1982, Late Cenozoic stratigraphy and structure of the western margin of the central San Joaquin Valley, California: U.S. Geol. Surv. Open-File Report 82-526.

Mansinha, L., and Smylie, D. E., 1971, The displacement fields on inclined faults: Seismol. Soc. America Bull., v. 61, p. 1433-1440.

Marine Safety Agency, Submarine Chart of the Adjacent Seas of Nippon, Marine Safety Agency, Tokyo, 1973.

Mitten, H. T., 1980, Estimated agricultural ground-water pumpage in parts of the San Joaquin Valley, California, 1975-77: U.S. Geol. Survey Open-File Report 80-1281, 11 p.

Mitten, H. T., 1976, Estimated ground-water pumpage in parts of the San Joaquin Valley, California, 1969-71: U.S. Geol. Survey Open-File Report, 7 p.

Mogi, A., B. Kawamura, and Iwabuchi, Y., 1964, Submarine crustal movement due to the Niigata earthquake in 1964: J. Geodetic Society of Japan, v. 70, p. 172-179.

Namson, J. S., Davis, T. L., and Lagoe, M. B., 1983, Thrust-fold deformation style of seismically active structures near Coalinga, California: EOS Trans. AGU, 64, p. 749.

Obradovich, J. D., Naeser, C. W., and Izett, G. A., 1978, Geochronology of late Neogene marine strata in California, Correlation of Tropical through high latitude marine Neogne deposits of the Pacific Basin, Stanford University Publications, Geological Sciences, Vol. XIV, California, pp. 40-41.

Ogilbee, W., and Rose, M. A., 1969, Ground-water pumpage on the west side of the San Joaquin Valley, California, 1962-66: U.S. Geol. Survey basic-data compilation, 7 p.

Ota, Y., 1980, Tectonic landforms and Quaternary tectonics in Japan, Geojournal, v. 4, p. 111-124.

Page, B. M., and Engebretson, D. C., 1984, Correlation between the geologic record and computed plate motions for central California: Tectonophysics, v. 3, pp. 133-156.

Poland, J. F., Lofgren, B. E., and Ireland, R. L., 1975, Land subsidence in the San Joaquin Valley, California, as of 1972: U.S. Geol. Survey Prof. Paper 437-H, 78 p.

Prokopovitch, N.P., and Magelby, D. C., 1968, Land subsidence in Pleasant Valley: American Water Works Assoc. Jour., v. 60, p. 413-424.
Research Group for Active Faults, 1980, Active faults in and around Japan, Univ. of Tokyo Press, Tokyo.
Research Group for Quaternary Tectonic Map, 1969, Quaternary Tectonic Map of Japan, with explanatory text, National Research Center for Disaster Prevention, Tokyo, 167 p.
Rymer, M. J., Harms, K. K., Lienkaemper, J. J., and Clark, M. M., 1984, Rupture of the Nunez fault during the Coalinga earthquake sequence: this volume.
Satake, K., and Abe, K., 1983, A fault model for the Niigata, Japan earthquake of June 16, 1964: J. Physics of the Earth, 31, 217-223.
Savage, J. C., Burford, R. O., and Kinoshita, W. T., 1975, Earth movements from Geodetic measurements: G. B. Oakeshott, Ed., San Fernando, Calif., Earthquake of 9 February 1971, Calif. Div. Mines and Geol. Bull., 196, 175-186.
Segall, P., 1984, Stress and subsidence resulting from subsurface fluid withdrawal in the epicentral region of the 1983 Coalinga earthquake: Jour. Geophys. Res., in press.
Sharp, R. V., 1975, Displacement on tectonic ruptures, G. B. Oakeshott, Ed., San Fernando, Calif., Earthquake of 9 February 1971, Calif. Div. Mines and Geol. Bull., 196, p. 187-194.
Sykes, L. R., 1971, Aftershock zones of great earthquakes, seismicity gaps, and earthquake prediction for Alaska and the Aleutians: Jour. Geophys. Res., v. 76, p. 8021-8041.
Stein, R. S., 1981, Discrimination of tectonic displacement from slope-dependent errors in geodetic leveling from southern California, 1953-1979: in Simpson, D. W., and Richards P. G., eds., Earthquake Prediction, An International Review: Maurice Ewing Ser., v. 4, AGU, Washington, D.C., p. 441-456.
Stein, R. S., and Thatcher, W., 1981, Seismic and aseismic deformation associated with the 1952 Kern County, California, earthquake and relationship to the Quaternary history of the White Wolf fault: Jour. Geophys. Res., v. 86, p. 4913-4928.
Stein, R. S., and King, G. C. P., 1984, Seismic potential revealed by surface folding: 1983 Coalinga, California, earthquake: Science, v. 224, p. 869-872.
Strange, W. E., 1980, The effect of systematic errors in geodynamic analysis: in Lachapelle, G., ed., 2nd International Symposium on problems related to the redefinition of North American vertical geodetic networks: Canadian Inst. Surveying, Ottawa, p. 705-727.
Thatcher, W., 1979, Strain accumulation and release mechanism of the 1906 San Francisco earthquake, J. Geophys. Res., v. 80, p. 4862-4872.
Thatcher, W., and Hanks, T., 1973, Source parameters of southern California earthquakes: J. Geophys. Res., v. 78, p. 8547-8576.
Uhrhammer, R. A., 1984, The May 2, 1983, Coalinga Earthquake and seismicity rates and strain energy in the central Coast Ranges, California: this volume.

Wentworth, C. M., Walter, A. W., Bartow, J. A., and Zoback, M. D., 1983, The tectonic setting of the 1983 Coalinga earthquakes: evidence from deep reflection and refraction profiles across the southeastern end of Kettleman Hills: The 1983 Coalinga, California, Earthquakes, J. H. Bennett and R. W. Sherburne, eds., Calif. Div. Mines and Geol. Special Pub. 66, pp. 113-126.

Whalen, C. T., and Strange, W. E., 1983, The 1981 Saugus to Palmdale, California, leveling refraction test, NOAA Tech. Rpt. Nos. 98NGS27, 13 p.

Woodring, W. P., Stewart, R., and Richards, R. W., 1940, Geology of the Kettleman Hills oil field, California, U.S. Geol. Surv. Prof. Paper 195, 170 p.

Yeats, R. S., 1983, Large scale Quaternary detachments in Ventura Basin, southern California, J. Geophys. Res., v. 88, p. 569-583.

Table 1: Fault Models

Strike/Dip	Slip Direction[1]	Slip m	Vertical Depth To: Top of Fault km	Base of Fault km	Fault Widt km	Moment[2] $M_o 10^{25}$ dyne-cm	Model Fit	Fig.3 Symbol
N53°W67°NE	reverse	1.3	3.0	13.2	11.0	6.5	good	a - - -
N53°W67°NE	reverse	1.8	4.0	11.2	8.0	6.0	good	a ———
N53°W67°NE	reverse	2.3	5.0	10.5	6.0	6.0	good	a ·····
N53°W67°NE	reverse w/ 20°rt-lat	2.2	4.5	11.0	7.0	6.5	good	b ·····
N53°W67°NE	reverse 15°lft-lat.	1.8	4.0	11.5	8.0	7.0	good	b ·····
N53°W23°SW	thrust	2.5	10.5	13.2	10.0	9.0	poor	c — · —
N53°W23°SW	thrust	1.4, top 2.0, base	4.5	7.2	9.0	5.0	good[3]	c ·····
N53°W60°SW N53°W23°SW	reverse thrust	1.0, top 2.0, base	5.0	12.0	11.0	7.5	fair	d ———

Notes: [1]/Strike, Dip, and Slip Direction are constrained by Eaton's [1983] fault plane solution for the 2 May 1983 Mainshock. [2]/Fault length along strike is not well constrained; 14-16 km is used. [3]/Fault lies 6 km above the mainshock hypocenter.

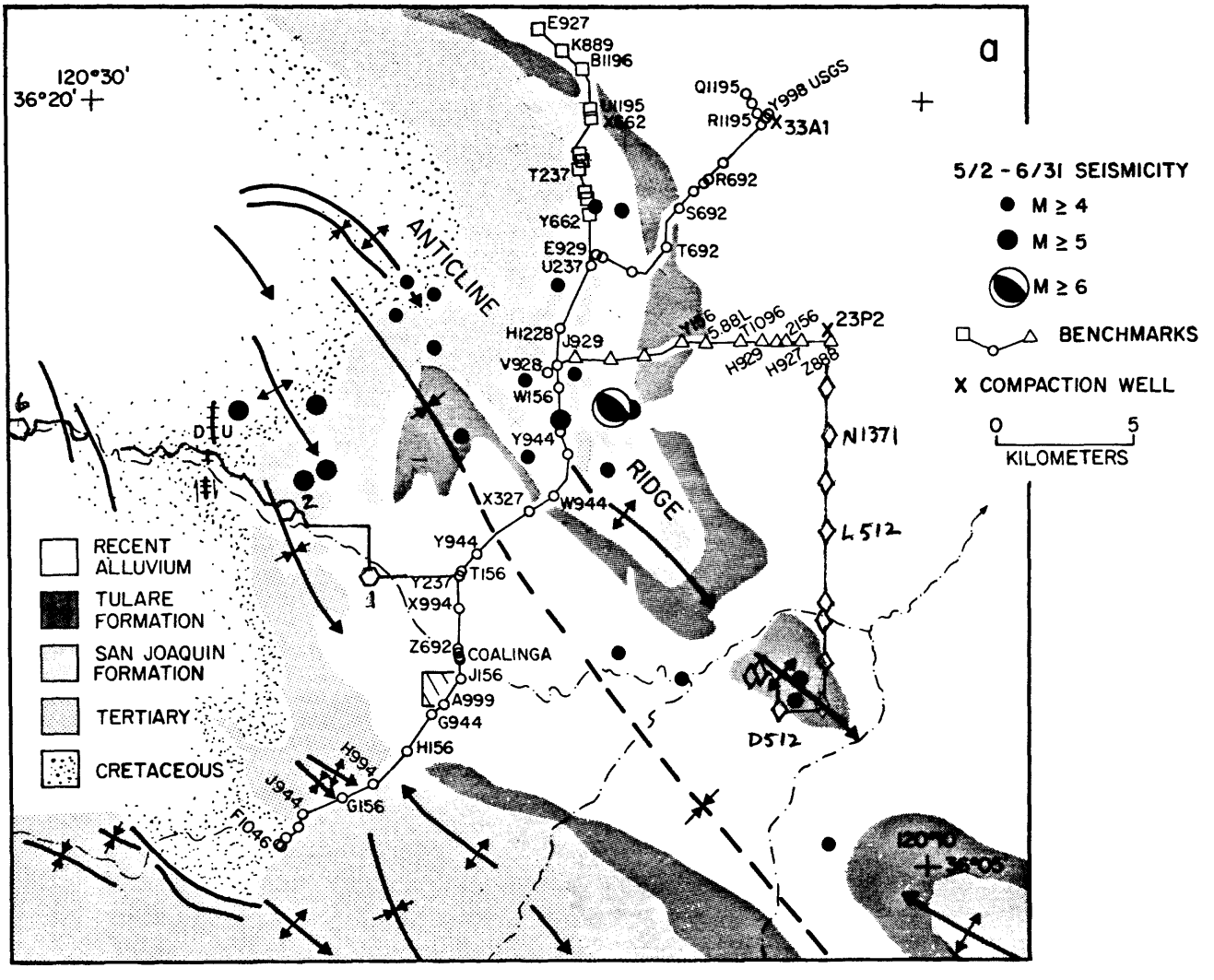

Figure 1. (a.) Map of the leveling route, compaction-recorder wells, and $M_L \geq 4$ aftershocks. Geology and structural features simplified from Fowkes [1982]. (b.) Oil fields, showing the deepest well locations, the Nunez fault surface rupture, and the model fault planes projected to the surface.

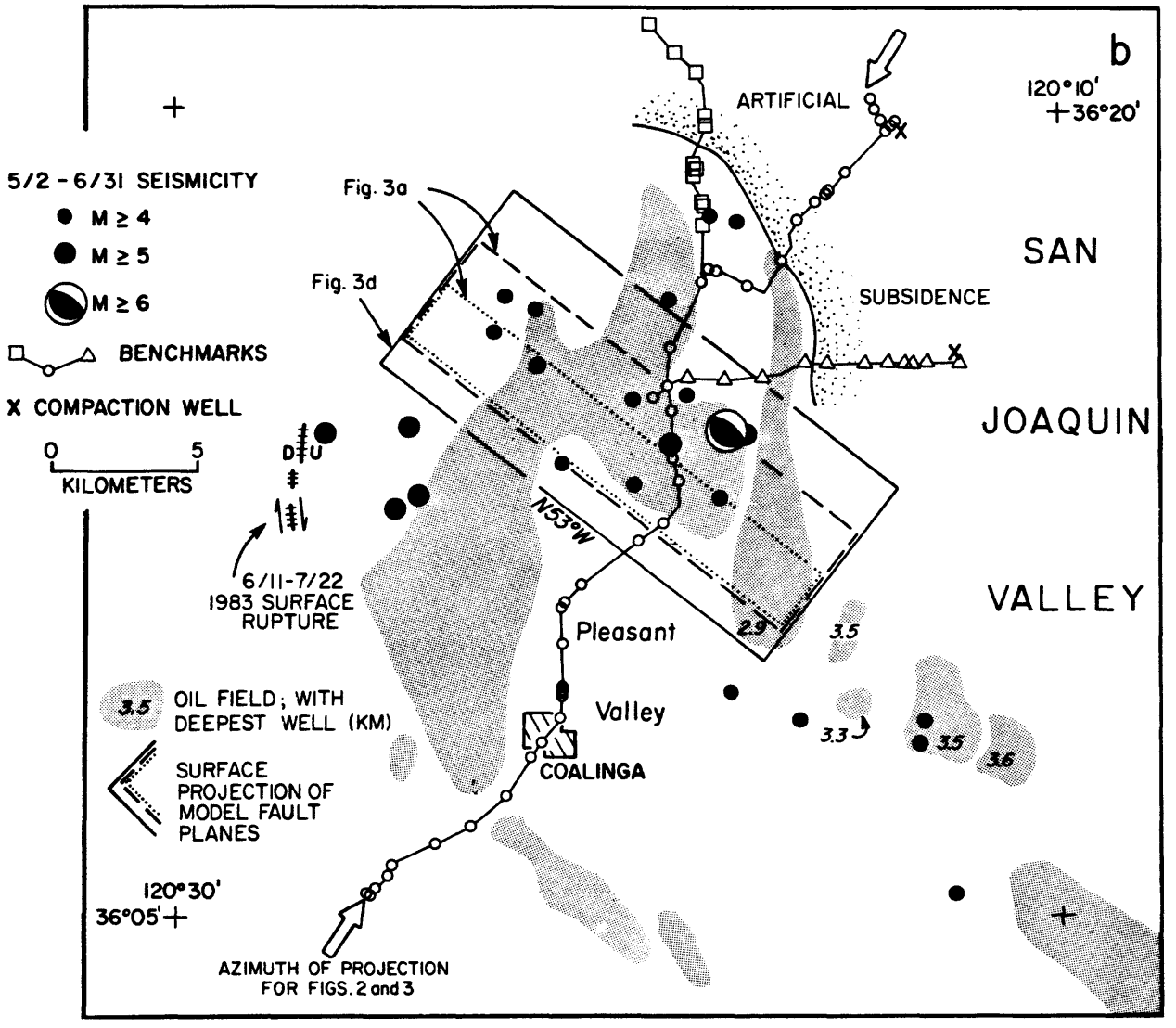

Figure 1. (a.) Map of the leveling route, compaction-recorder wells, and $M_L \geq 4$ aftershocks. Geology and structural features simplified from Fowkes [1982]. (b.) Oil fields, showing the deepest well locations, the Nunez fault surface rupture, and the model fault planes projected to the surface.

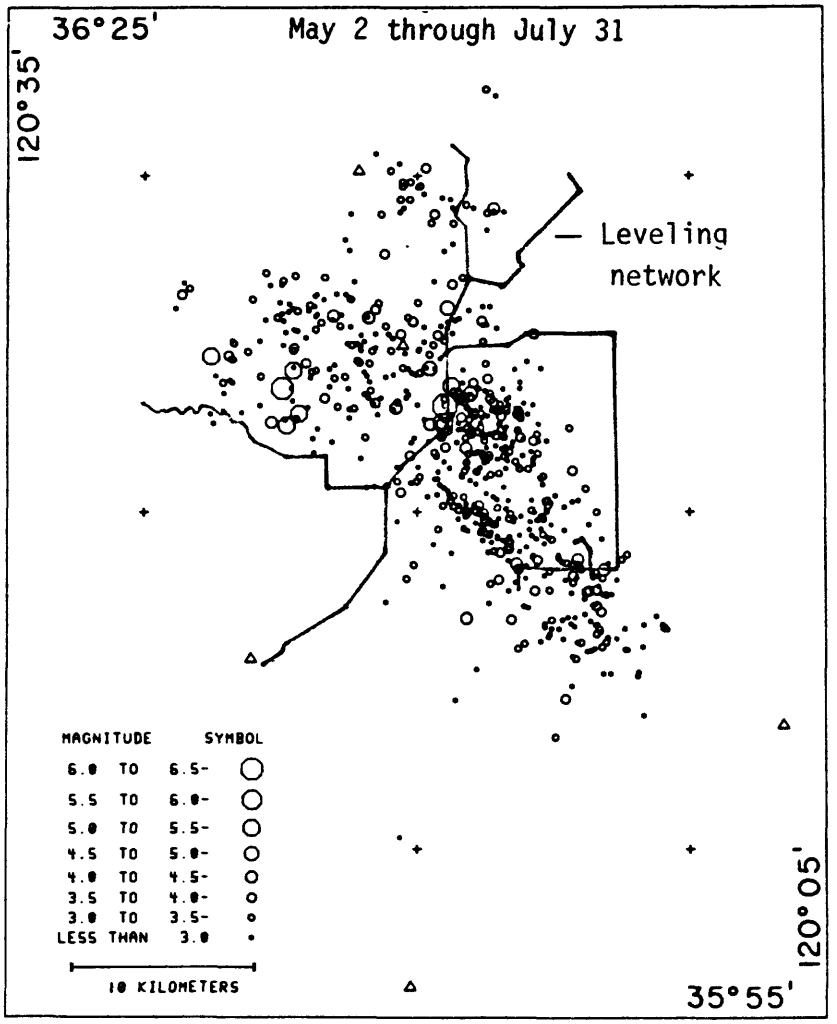

Figure 1c. The leveling network together with aftershocks from 2 May 1983 - 31 July 1983 relocated by Eaton et al. [1983].

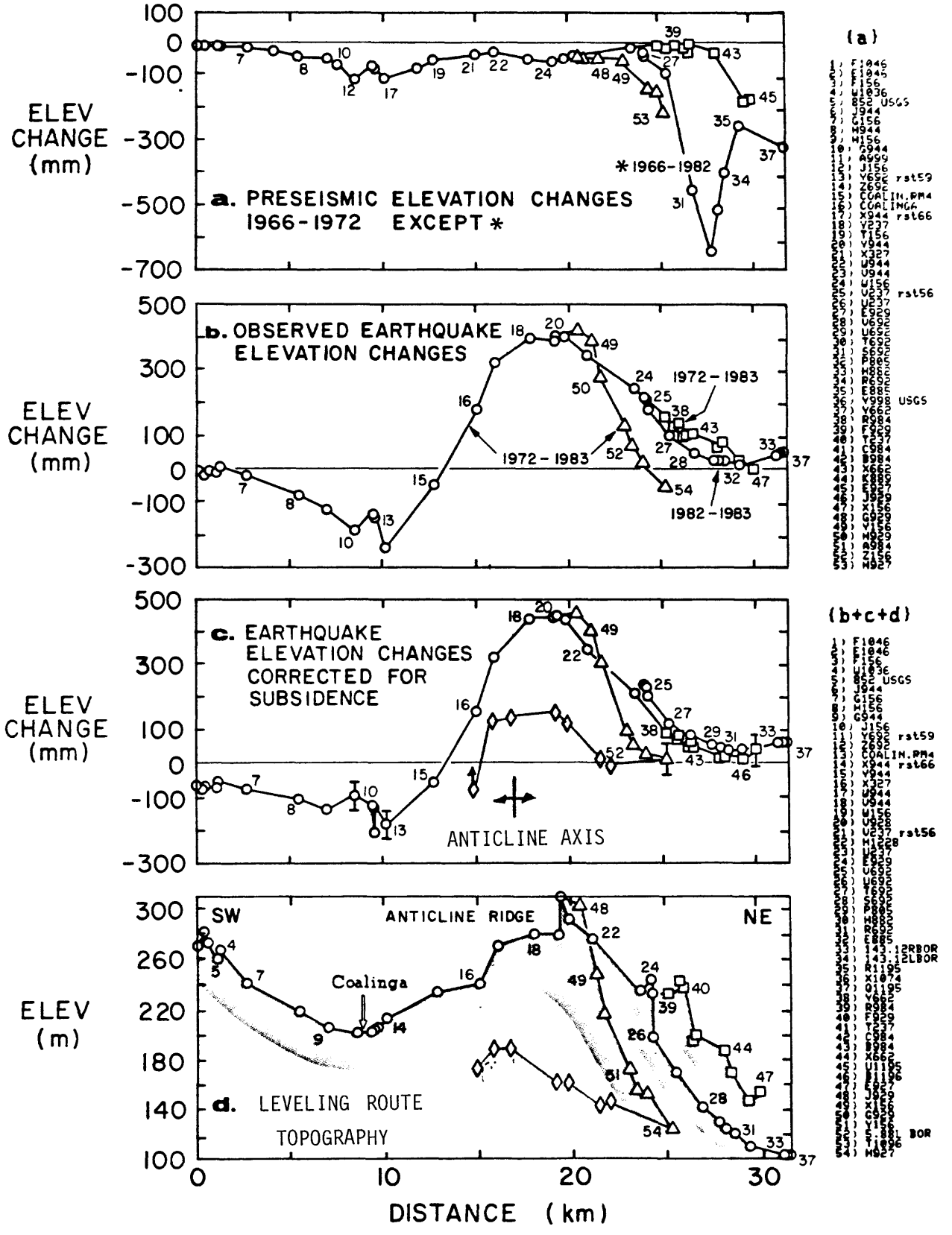

Figure 2. (a.-c.) Profiles of elevation change projected onto an azimuth N37°W, normal to the structural axis. Leveling errors are about equal to the size of the symbols; errors associated with the removal of artificial subsidence are shown by brackets in (c.). (d.) Leveling route topography.

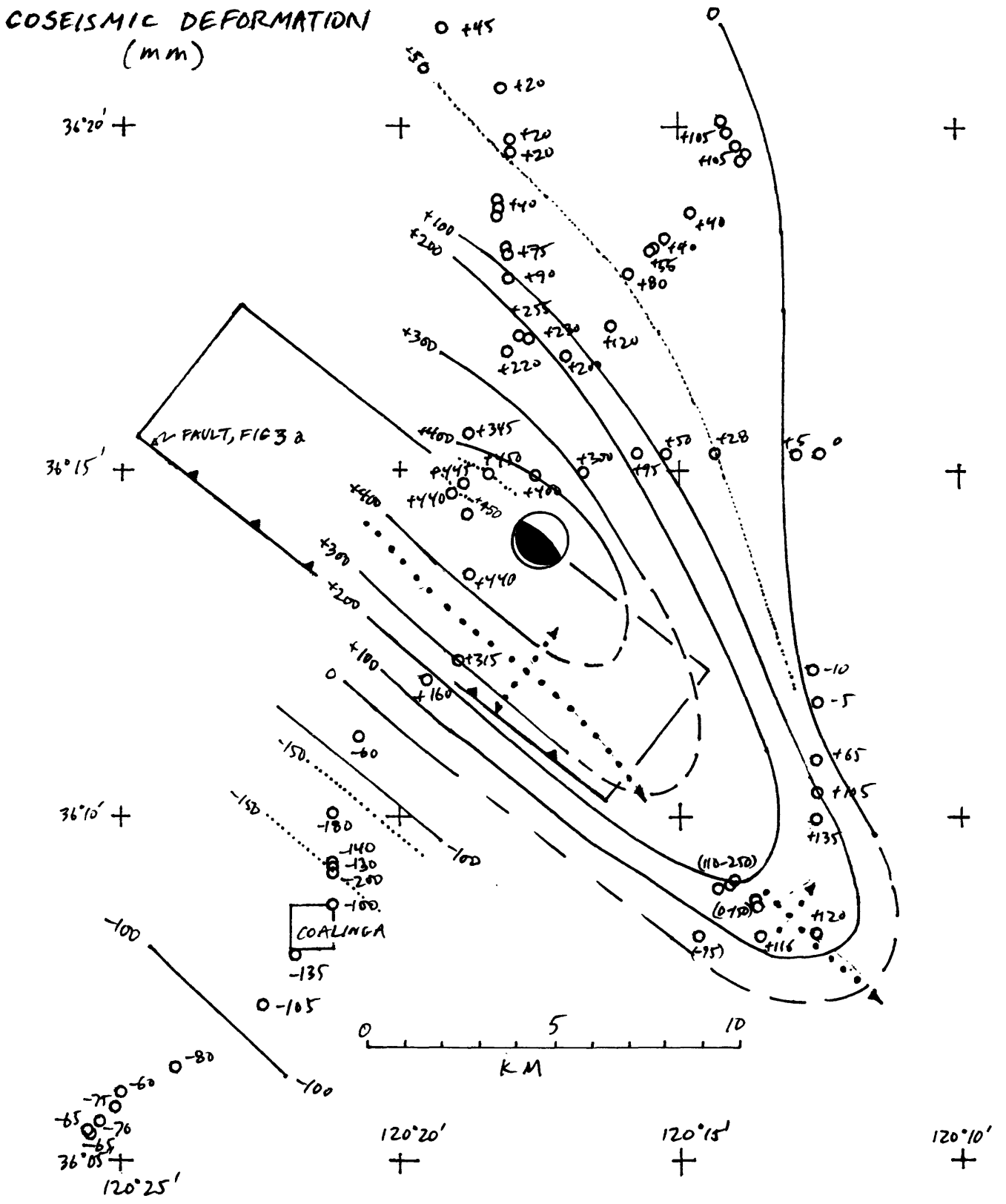

Figure 2e. Map of the coseismic deformation shown in (c), with contours of equal elevation change. Corners of the fault indicated by a solid line in Figure 3a are also shown.

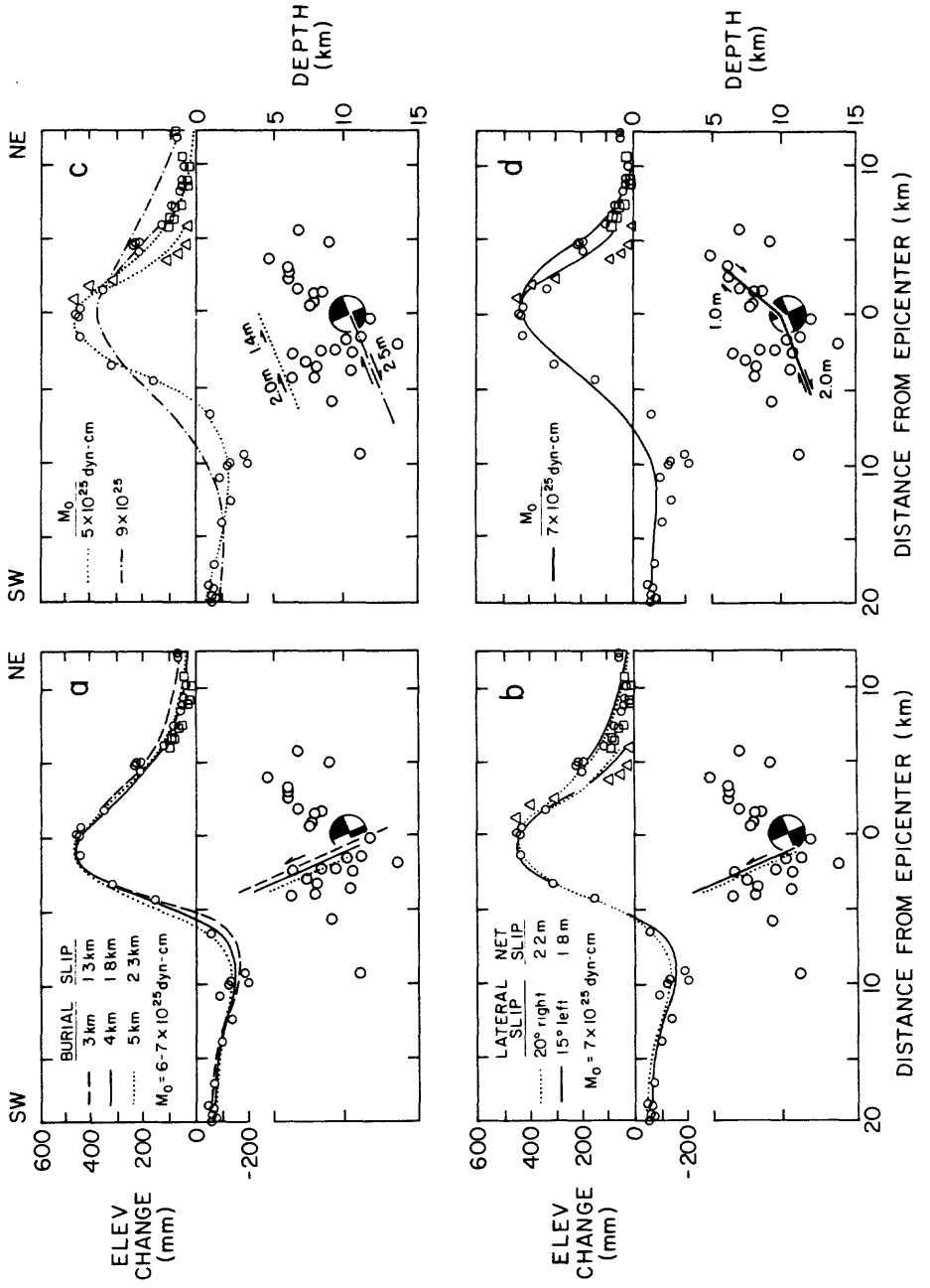

Figure 3. Earthquake elevation changes from Figure 2c compared with predicted deformation, together with a cross-section showing the model faults and the first four days of $M_L \geq 3$ aftershocks, and the mainshock. (a-b) Reverse faults with 67°NE dips. (c-d) Thrust faults dipping 23°SW.

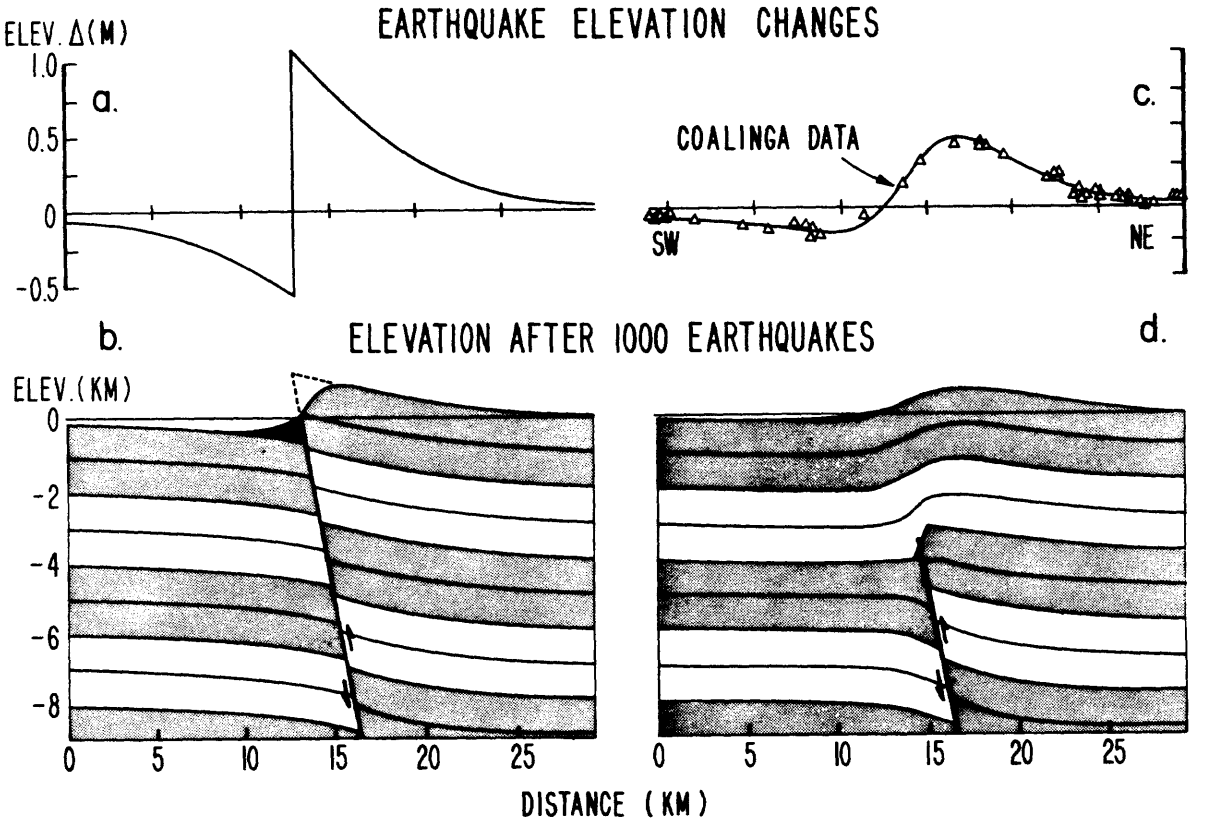

Figure 4. a. Elastic dislocation solution for surface deformation caused by 2 m of reverse dip slip on a fault dipping 65° extending from the ground surface to a depth of 11 km. b. Depth cross section (vertical exaggeration, 2x) after 2 km of cumulative slip, or 1,000 earthquakes. Subsequent to initiation of faulting, erosion of fault scarp (dashed) and deposition into downthrown block (black) occur, which are shown schematically. Remote displacements and interseismic strain release are neglected. c. Fault of a terminated 4 km from the surface, fitted to the observed coseismic elevation changes at Coalinga (1). d. Depth cross section for c. Dip of beds above the top of the fault increases with depth, and near the top of the fault, beds are subject to vertical compression and extension.

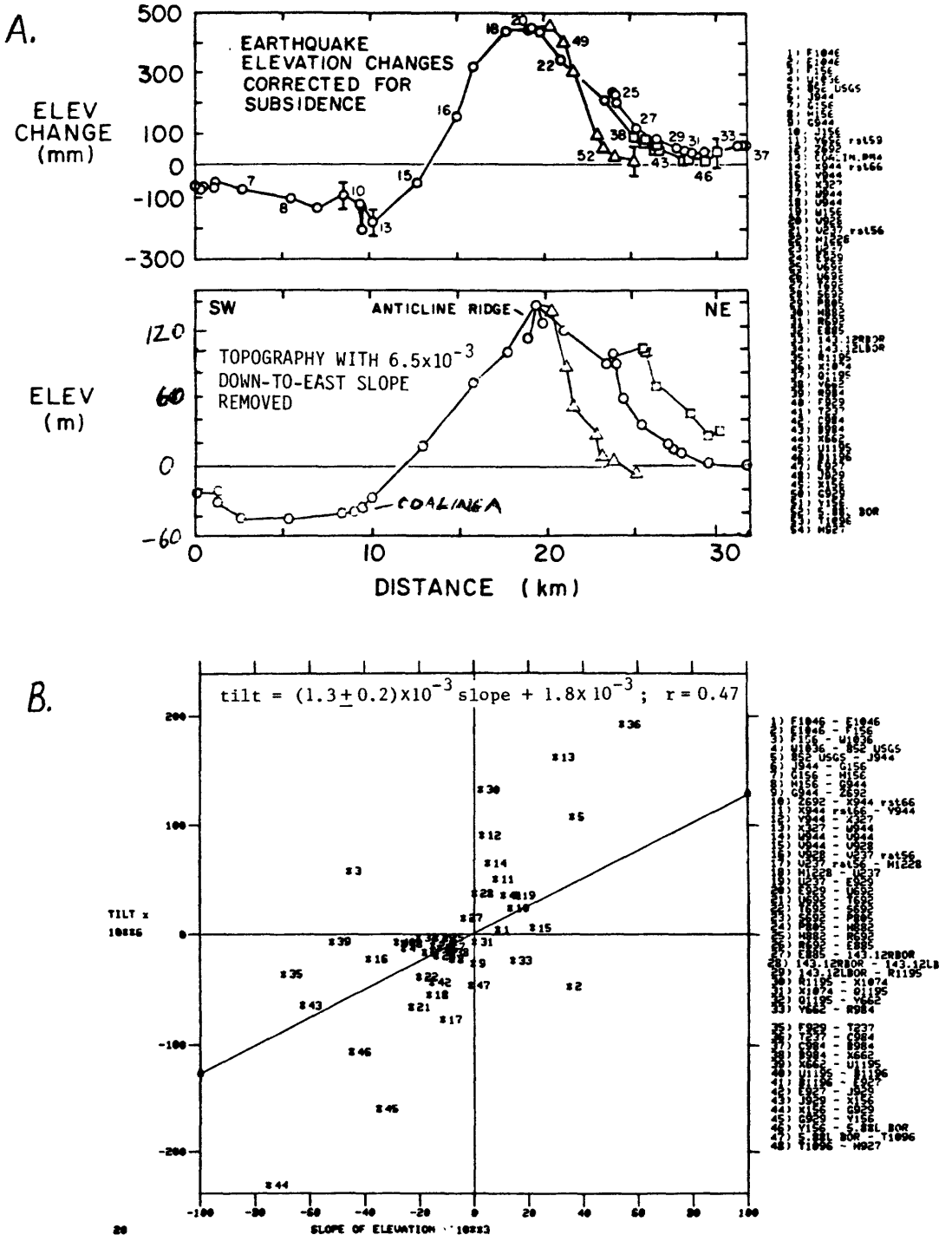

Figure 5. a. Coseismic deformation from Figure 2c (upper box) compared to the topography, after removal of the regional down-to-the-east slope of 37° (6.5×10^{-3}). b. Geodetic tilt (elevation change between successive BM's divided by the distance between them) as a function of topographic slope (elevation difference between successive BM's divided by the distance between them). Tilt is positively correlated with slope at the 99% level of confidence.

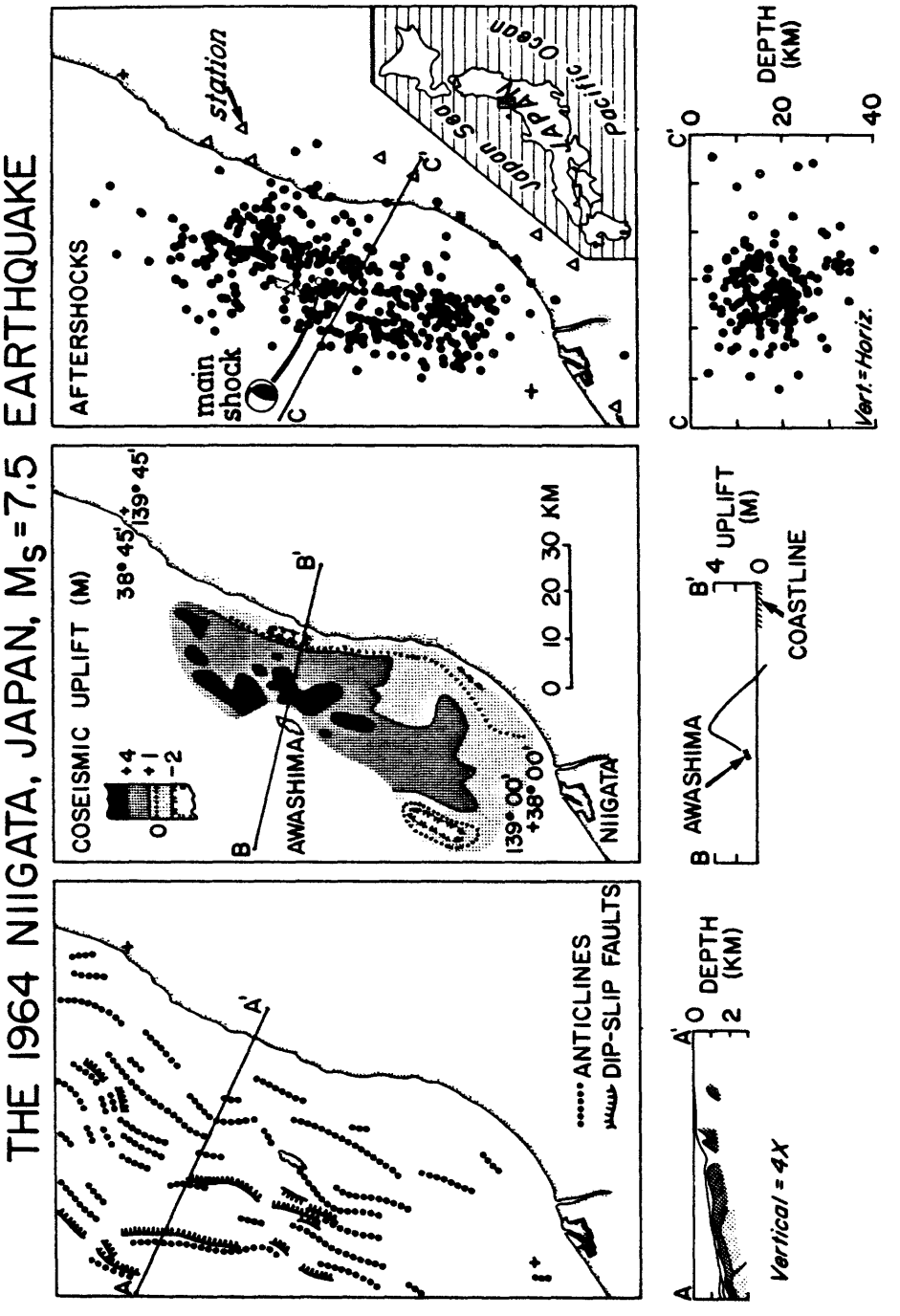

Figure 6. Structural geology, coseismic deformation, and the aftershock distribution for the 1964 Niigata, Japan, earthquake. When the left and center box are superposed, it become evident that the axis of peak earthquake uplift lies atop a major anticline axis. The orientation of the fault plane is disputed.

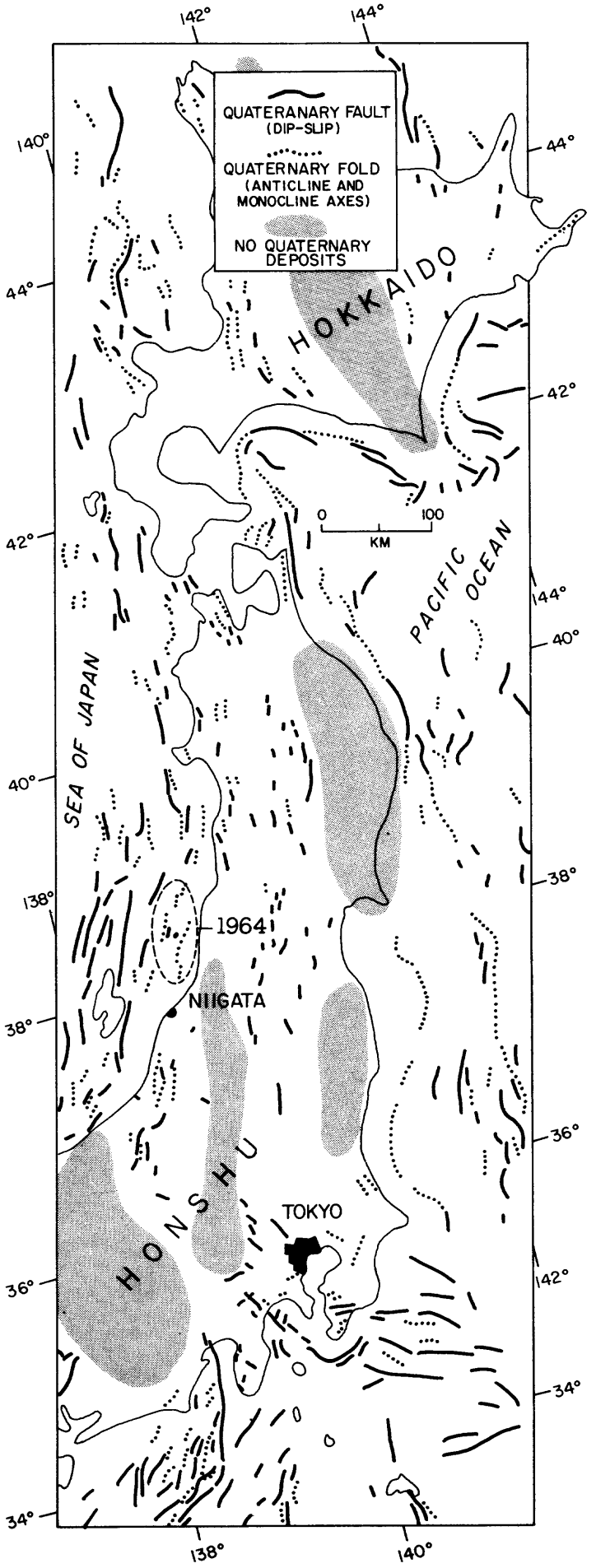

Figure 7. Quaternary tectonic map of northern Japan from Stein and King [1984], showing faults and folds in areas with Quaternary deposits. A dashed line encircles the aftershock zone of 1964 Niigata M_s=7.5 earthquake.

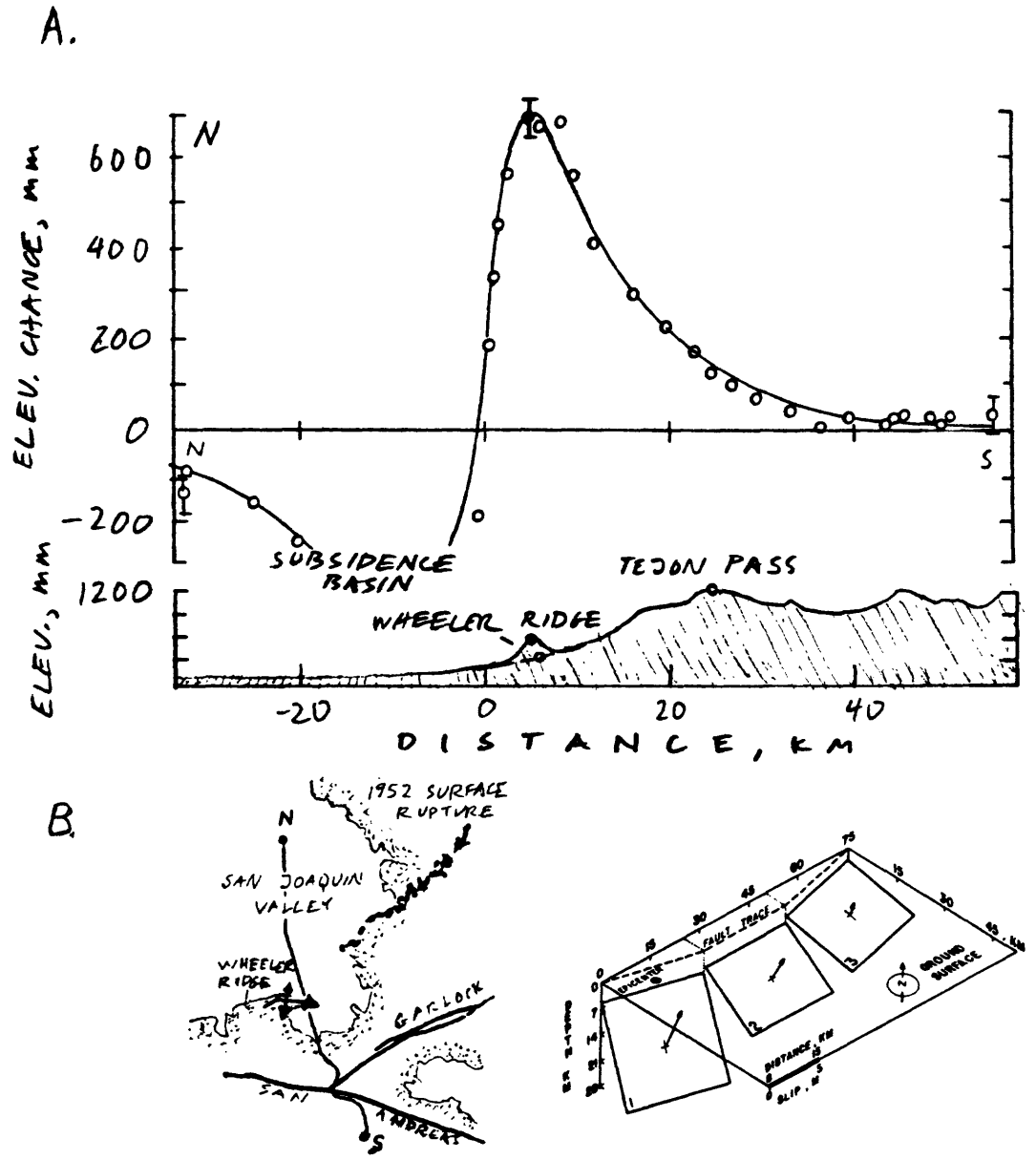

Figure 8. (a) Coseismic deformation associated with the 1952 M_s=7.2 Kern County, California, earthquake boardering the Tehachapi Mountains and the San Joaquin Valley, fit to an elastic dislocation model, with route topography shown below. (b) Map of 1952 surface rupture, Wheeler Ridge anticline, and the leveling route (left), and an isometric diagram of the model fault (right) [Stein and Thatcher, 1981].

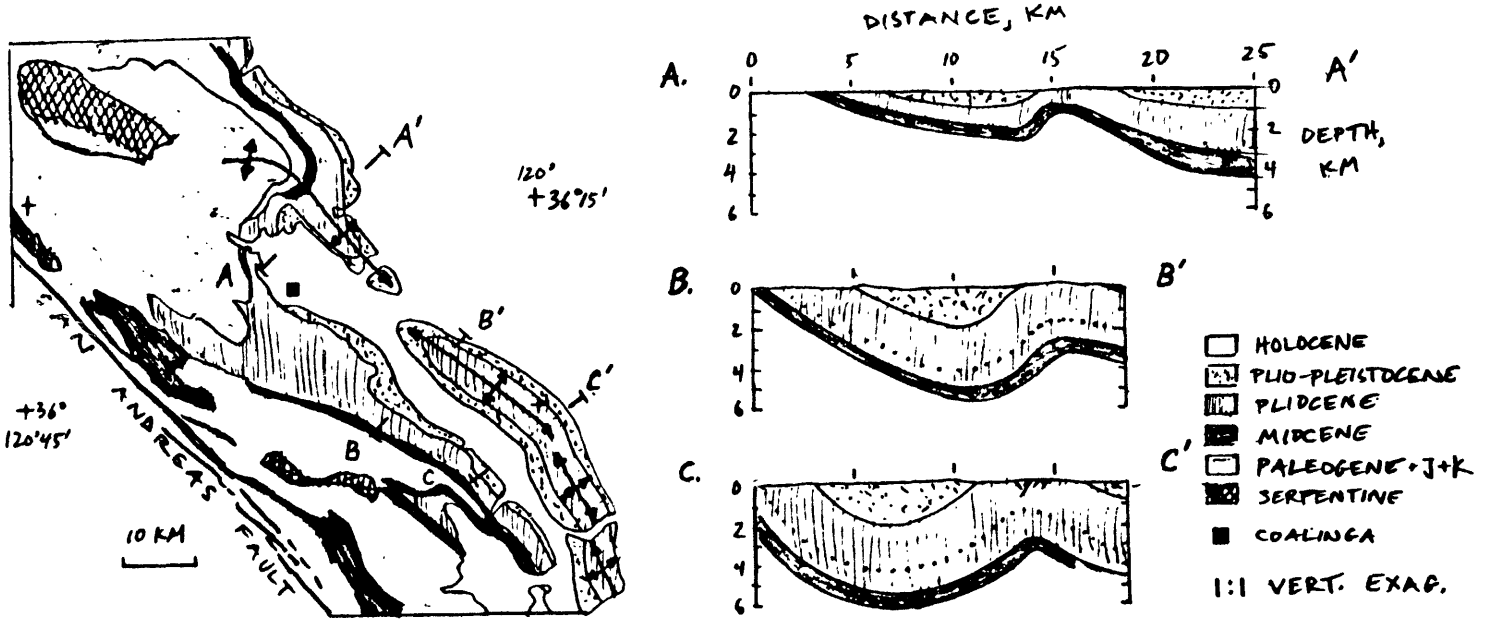

Figure 9. Simplified geology of the Anticline Ridge and Kettleman Hills anticlines and the adjacent Coast Range province. Cross-section's A-A' [Segall, 1983], B-B', and C-C' [Woodring et al., 1940] demonstrate the similar character of the fold. The Kettleman Hills exhibit a thicker Pliocene section and a more tightly folded structure than does Anticline Ridge.

GROUND MOTION PARAMETERS OF THE 1983 COALINGA, CALIFORNIA EARTHQUAKES: IMPLICATIONS FOR CRUSTAL STRENGTH

A. McGarr, C. Mueller, J. B. Fletcher, and M. Andrews

U. S. Geological Survey
345 Middlefield Road, MS/977
Menlo Park, California 94025

ABSTRACT

Using the results of a previous study relating ground motion observations to the crustal environment at the earthquake hypocenter, we develop expressions relating crustal strength to the parameters $\rho R\underline{a}$ and $R\underline{v}$, where $\underline{a}$ is peak acceleration, R is hypocentral distance, $\underline{v}$ is peak velocity, and ρ is density at the hypocenter. These ground motion parameters, as well as the usual seismic source parameters of seismic moment, source radius and stress drop, were determined for 30 events from a large set of digital and analog ground motion data recorded in the epicentral region of the Coalinga sequence. We use these seismic parameters to infer crustal strength and the nature of the seismic deformation process. The inferred crustal strength within the seismogenic zone shows considerable and unexpected variation with several patches of high strength, typical of compressional states of crustal stress elsewhere, surrounded by zones of much lower implied strength.

INTRODUCTION

This paper reports the development of several techniques for estimating crustal strength from peak ground motion parameters in conjunction with seismic source parameters and then the application of these results to attempting to define the distribution of inferred strength within the seismogenic region of the 1983 Coalinga, California earthquake. In addition, a method of estimating the seismic source radius in terms of ground motion parameters plus seismic moment is developed and applied to determine the radius of the Coalinga mainshock of 2 May 1983. For this event the usual techniques (*e.g.*, Brune, 1970, 1971) did not provide definitive results. As will be seen, the crustal strength within the Coalinga seismic zone shows a remarkable and unanticipated variation. In many cases the seismic stress drops (Brune, 1970, 1971) for the Coalinga sequence tend to be unusually high whereas the peak ground motions, both acceleration and velocity, are low relative to expectations based on previous work. Similarly, the inferred crustal strength is, for the most part, considerably below that predicted for a compressive state of stress.

The data used here were collected using both GEOS digital recording systems with force-balance accelerometers (Borcherdt *et al.*, 1983) and SMA-1 accelerometer systems (Maley *et al.*, 1983). These data were then processed to obtain corrected acceleration, velocity, and spectra of displacement at the National Strong Motion Data Center.

Ground motion observations presented by McGarr (1984) indicate that the high-frequency seismic radiation that gives rise to peak acceleration and velocity is determined by the crustal environment at the earthquake hypocenter. Figures 1 and 2 summarize the results of an observational study indicating that the ground motion parameters $\rho R\underline{a}$ and $R\underline{v}$ are strong functions of both the state of stress and the hypocentral depth, where $\underline{a}$ is peak ground acceleration, $\underline{v}$ is peak velocity, R is the distance from the earthquake hypocenter to the recording site and ρ is density of the hypocenter.

The majority of the data in Figure 1 correspond to peak accelerations due to earthquakes in extensional tectonic regimes (normal fault focal mechanisms) and this large subset of the observations was used to define the regression line

$$\rho R\underline{a}\ (\text{extensional}) = -1.08\ MPa + 3.06\ (MPa/km)z \qquad (1)$$

where z is focal depth.

Although the peak acceleration data from thrust or reverse faulting events in tectonic regimes are not nearly as numerous as for the extensional events the compressional values nonetheless indicate that such earthquakes, at a given hypocentral depth, produce ground motion that is typically a factor of about three greater than for shocks in extensional regimes; the data corresponding to the two extreme stress states show a well-defined separation. The compressional data yielded the regression line

$$\rho R\underline{a}\ (\text{compressional}) = 5.65\ MPa + 8.76\ (MPa/km)z \qquad (2)$$

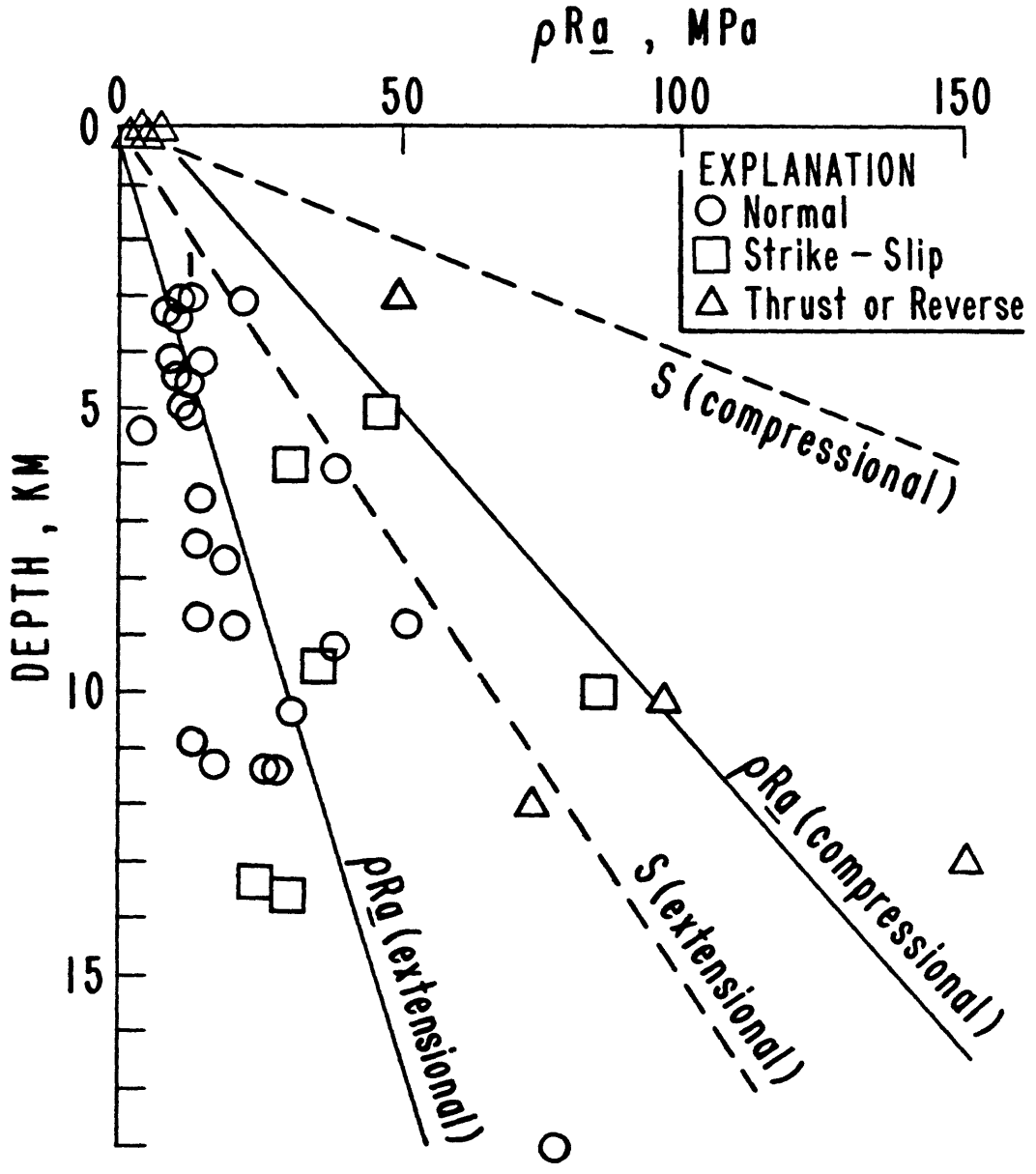

Figure 1. Peak acceleration parameter as a function of focal depth and stress state (from McGarr, 1984). The dashed lines indicate crustal strength S as a function of depth and stress state.

Note that the inferred depth gradient in (2) is about three times that of (1).

Several studies (McGarr, 1984; Hanks and Johnson, 1976) have indicated plausible relationships between the peak acceleration parameter $\rho R\underline{a}$, which from fundamental scaling principles should be independent of earthquake size, and the crustal strength $S(\sigma, z)$, where σ represents the stress state: compressional, extensional or intermediate corresponding to thrust or reverse, normal, or strike-slip faulting respectively.

The strength of the brittle portion of the crust can be calculated with little uncertainty using Byerlee's (1978) law of friction (*e.g.*, Sibson, 1974; Brace and Kohlstedt, 1980). This calculated strength is a function of stress state, depth and pore pressure P. In the present context the strength S is the maximum shear stress that can be sustained in a crustal rock mass assumed to contain a reasonably high density of fault or joint planes of low cohesion. Specifically

$$S = (\sigma_1 - \sigma_3)/2 \tag{3}$$

where σ_1 and σ_3 are the maximum and minimum principal stresses in failure stress state.

For an assumed hydrostatic pore pressure, $S(\sigma, z)$ for the two extreme states of stress is given by (McGarr, 1984)

$$S \text{ (extensional)} \simeq 6.6\ (MPa/km)z \tag{4a}$$

$$S \text{ (compressional)} \simeq 25\ (MPa/km)z \tag{4b}$$

A comparison of these predicted strengths (Figure 1) with the corresponding observations of $\rho R\underline{a}$ led readily to the conclusion that, as theoretically anticipated, the available data are consistent with

$$S(\sigma, z) = K\ \rho R\underline{a}\ (\sigma, z) \tag{5}$$

where K is a constant of the order of 1.

For several reasons the extensional data are better suited than data for the other two stress regimes for estimating K. First, the observations of $\rho R\underline{a}$ for the extensional stress state are especially numerous and represent the broadest range of focal depths. Second, one can be more confident about the assumption of hydrostatic pore pressure in extensional stress states although for one datum in Figure 1 the pore pressure is probably closer to 0 than the hydrostat (the point labeled "1" at a depth of 3 km (McGarr *et al.*, 1975)). In contrast, as will be discussed, compressive stress regimes are sometimes associated with overpressurization; that is P is substantially in excess of the hydrostat, given by P (hydrostat) $= (9.8\ MPa/km)z$.

Thus, a comparison of the extensional peak acceleration regression line (equation (1), Figure 1) with the corresponding crustal strength prediction (4a) yields $K \simeq 2.2$ in (5) or

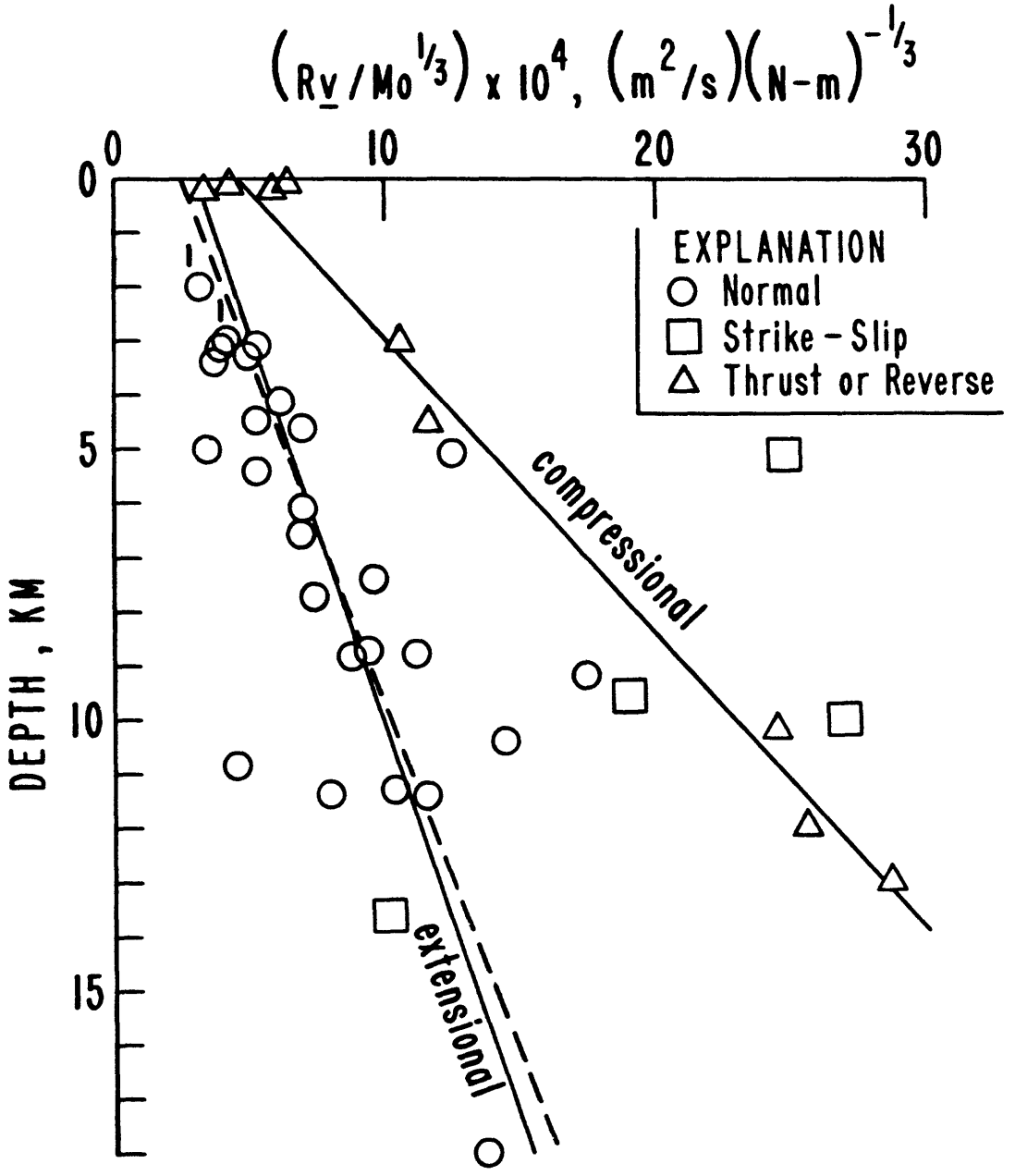

Figure 2. Normalized peak velocity parameter as a function of focal depth and stress state (from McGarr, 1984).

$$S\ (\sigma, z) \simeq 2.2\ \rho R\underline{a}\ (\sigma, z) \qquad (6)$$

Although only the extensional data were used for calibration purposes, it is clear that (6) should apply to any state of stress and pore pressure. In particular, note that the use of (4b) and (6) to predict $\rho R\underline{a}$ (compressional) is entirely consistent with the observations (*i.e.*, $\rho R\underline{a} \simeq 11.4\ (MPa/km)z$ although the predicted depth gradient is about 30% higher than that of the regression line (2). In any case, equation (6) is provisionally used here as a means of estimating crustal strength from peak acceleration in the Coalinga region.

The peak velocity parameter $R\underline{v}$ also shows a well-defined dependence on stress state and focal depth (McGarr, 1984), after the size scaling is taken into account. Specifically, $R\underline{v}/M_o^{1/3}$, where M_o is the seismic moment (Figure 2), varies approximately linearly with depth for a particular stress state. Moreover, at a fixed depth the compressional data are typically a factor of two greater than normal faulting observations. Thus, the dependence on the state of stress is seemingly somewhat weaker than for peak acceleration (Figure 1) but, nonetheless, quite strong. The observation that $R\underline{v}$ is linked to the crustal environment suggests that, as for peak acceleration, crustal strength is the underlying factor in the connection between $R\underline{v}/M_o^{1/3}$ and the hypocentral conditions as defined by depth and stress state. The specific connection is developed later.

It is important to mention that the ground motion data collected during the Coalinga sequence could not have served as a basis for drawing any substantial conclusions regarding the relationships between peak ground motion and crustal strength such as represented by Equation (6). As will be seen, the Coalinga data do not suggest unique relationships between ground motion parameters and hypocentral depth, in contrast to the observations plotted in Figures 1 and 2. Rather than abandoning all of the conclusions presented by McGarr (1984), however, we have adopted the point of view that the previous results are essentially correct but that the crustal strength in the region of Coalinga is anomalous in having considerable variation in strength at a given depth. In-situ pore pressure data compiled by Berry (1973) and, just recently, by Yerkes *et al.* (1984) provide support for this point of view. Specifically, it seems likely, according to Yerkes *et al.*, that many portions of the crust within the zone of Coalinga aftershocks are subjected to superhydrostatic pore pressure which would lead to substantial reductions in strength, as will be discussed.

COALINGA GROUND MOTION DATA

Most of the data analyzed here were recorded using a network of GEOS digital recorders in conjunction with force-balance accelerometers during a period of about four weeks following the mainshock (Borcherdt *et al.*, 1983). The remaining data, including the Coalinga mainshock were recorded using SMA-1 instruments at temporary and permanent sites in and around the aftershock zone (Maley *et al.*, 1983).

A map view of the mainshock and aftershock locations is shown in Figure 3, which also indicates locations of a number of the key ground motion recording sites. Whereas the mainshock was recorded only at several stations co-located at the Pleasant Valley Pumping

TABLE 1

Event	Lat. Degrees	Long. Degrees	Depth[1] km	M_o N-m	r_o km	$\Delta\tau$ MPa	$\underline{Rv}$ m^2/s	$\rho\underline{Ra}$ MPa	$\frac{\underline{Rv} \times 10^4}{M_o^{1/3}}$ $(m^2/s)\ (N\text{-}m)^{-1/3}$	$S(\sigma,z)_{\underline{a}}$, MPa	$S(\sigma,z)_{\underline{v}}$, MPa
4 May 0848a	36.189	120.283	5.7	7.2×10^{12}	0.433	0.04	0.54	0.06	0.28	0.13	0.18
4 May 0848b	36.209	120.255	13.3	6.0×10^{14}	0.532	1.7	16.0	1.2	1.90	2.7	2.4
13 May 1501	36.094	120.209	10.5	2.1×10^{14}	0.437	1.1	7.4	0.58	1.24	1.3	1.2
18 May 2039	36.245	120.350	8.5	4.1×10^{14}	0.508	1.4	18.6	1.2	2.51	2.6	4.5
3 May 2345	36.181	120.423	4.0	2.2×10^{15}	0.600	4.5	58.8	5.0	4.49	11.0	9.6
3 May 1842	36.260	120.275	7.3	5.0×10^{13}	0.241	1.6	6.5	0.84	1.76	1.8	2.1
3 May 1541	36.225	120.278	8.8	4.2×10^{16}	0.897	25.3	725	38.3	20.91	84.3	117.2
9 May 0326	36.210	120.302	10.7	1.8×10^{16}	1.241	4.2	161	9.6	6.09	21.1	18.0
12 May 1341	36.146	120.263	10.8	8.3×10^{15}	0.732	9.3	174	9.9	8.58	21.8	27.6
22 May 0839	36.138	120.219	10.3	1.3×10^{15}	0.561	3.2	38.8	2.9	3.57	6.4	6.8
24 May 0902	36.238	120.326	9.9	2.4×10^{16}	0.740	25.4	280	17.2	9.78	37.8	25.6
4 May 1611	36.263	120.343	13.1	3.5×10^{15}	0.945	1.8	44.5	4.3	2.94	9.5	5.6
9 May 0249	36.229	120.312	12.5	4.2×10^{16}	0.853	30.0	619	36.8	17.74	81.0	79.7
2 May 2342[3]	36.219	120.317	10.2	3.95×10^{18}	(5.4)	11.0	3860	96.2	24.42	211.6	
4 May 0728	36.255	120.330	13.0	2.5×10^{16}	0.814	20.6	396	24.7	13.47	54.3	52.1
9 July 0740	36.237	120.409	9.5	7.6×10^{16}	1.107	24.7	482	32.5	11.35	71.5	34.9
22 July 0239	36.228	120.416	9.2	5.27×10^{17}	1.781	40.8	1720	86.1	21.29	189.4	103.7
22 July 0343	36.210	120.413	9.6	2.5×10^{16}[2]				44.8		98.6	
25 July 2231	36.215	120.406	9.5	6.6×10^{16}[2]				47.8		105.2	
4 May 0246	36.186	120.253	8.9	1.03×10^{14}	0.452	0.49	5.03	0.40	1.07	0.88	1.15
4 May 0818	36.220	120.256	9.34	5.7×10^{13}	0.386	0.43	2.28	0.20	0.59	0.44	0.36
5 May 2246	36.286	120.420	11.09	9.7×10^{13}	0.369	0.84	6.56	0.62	1.43	1.36	1.70
9 May 0312	36.221	120.285	13.02	1.3×10^{14}	0.556	0.33	4.28	0.32	0.84	0.70	0.81

CONTINUED

TABLE 1 CONTINUED

Event	Lat. Degrees	Long. Degrees	Depth[1] km	M_o N-m	r_o km	$\Delta\tau$ MPa	$\underline{Rv}$ m^2/s	$\rho\underline{Ra}$ MPa	$\frac{\underline{Rv} \times 10^4}{M_o^{1/3}}$ $(m^2/s)\ (N\text{-}m)^{-1/3}$	$S(\sigma,z)_{\underline{a}}$, MPa	$S(\sigma,z)_{\underline{v}}$, MPa
9 May 0319	36.222	120.288	13.33	3.60×10^{14}	0.312	5.2	31.8	3.01	4.47	6.62	9.10
18 May 0246	36.184	120.242	8.88	2.06×10^{15}	0.527	6.2	109.0	11.1	8.57	24.4	31.5
12 May 0157	36.108	120.241	9.54	1.11×10^{14}	0.494	0.40	4.20	0.25	0.87	0.55	0.81
9 May 2014	36.208	120.285	8.12	7.6×10^{13}	0.324	0.98	7.02	0.65	1.66	1.43	2.18
9 May 1815	36.169	120.301	10.00	1.31×10^{14}	0.410	0.83	9.70	0.92	1.91	2.02	3.05
5 May 0032	36.211	120.257	9.77	8.0×10^{14}	0.597	1.64	29.5	4.60	3.18	10.1	6.70
8 May 0345	36.249	120.437	2.89	3.19×10^{14}	0.605	0.63	6.33	0.47	0.93	1.03	0.79

Notes:

(1) Locations from Eaton et al. (1983) or from Andrews and Eberhart-Phillips (written communication, 1984).

(2) Moments from Urhammer et al. (1983).

(3) Mainshock, values in parentheses were calculated on basis of equation (11).

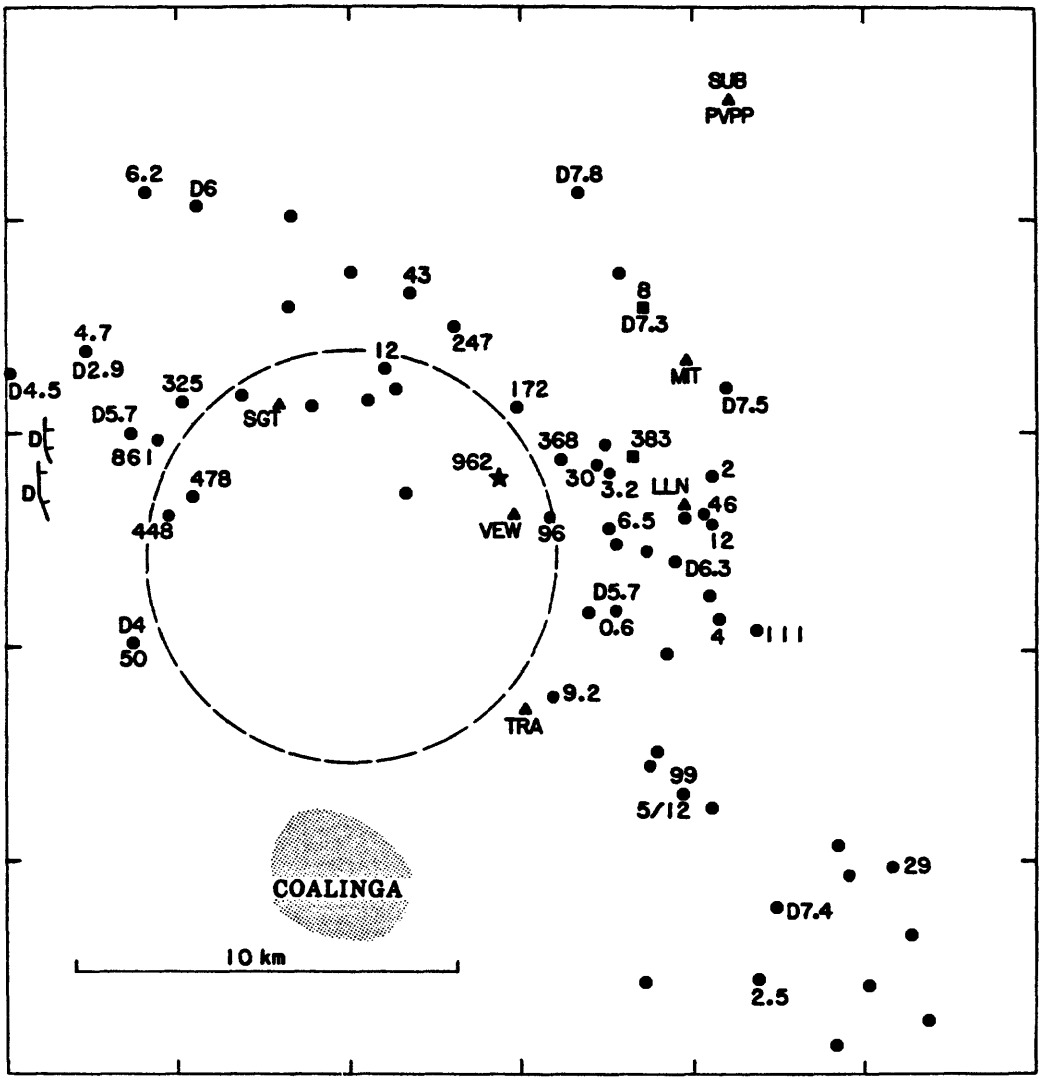

Figure 3. Plan view of epicentral region of Coalinga earthquake. The star indicates the location of the mainshock and the circles correspond to especially well-located aftershocks with magnitudes of 3 or greater. The squares denote less well-located events whose ground motion was analyzed here (Table 1). The locations are from either Eaton *et al.* (1983) or the location files of Andrews and Eberhart-Phillips. Triangles show locations of GEOS stations that provided data for this study. The dashed circle indicates where the mainshock rupture may have occurred. The radius of the circle is about 5.4 km (equation (11), Table 1) and it was drawn to fit within the gap in seismicity outlined by areas of high inferred crustal strength. Numbers by event locations indicate the peak acceleration parameter $\rho R\underline{a}$ in bars (MPa/10). All events shown here were located at depths in excess of 8 km with the exceptions indicated by the letter D followed by the depth in kilometers.

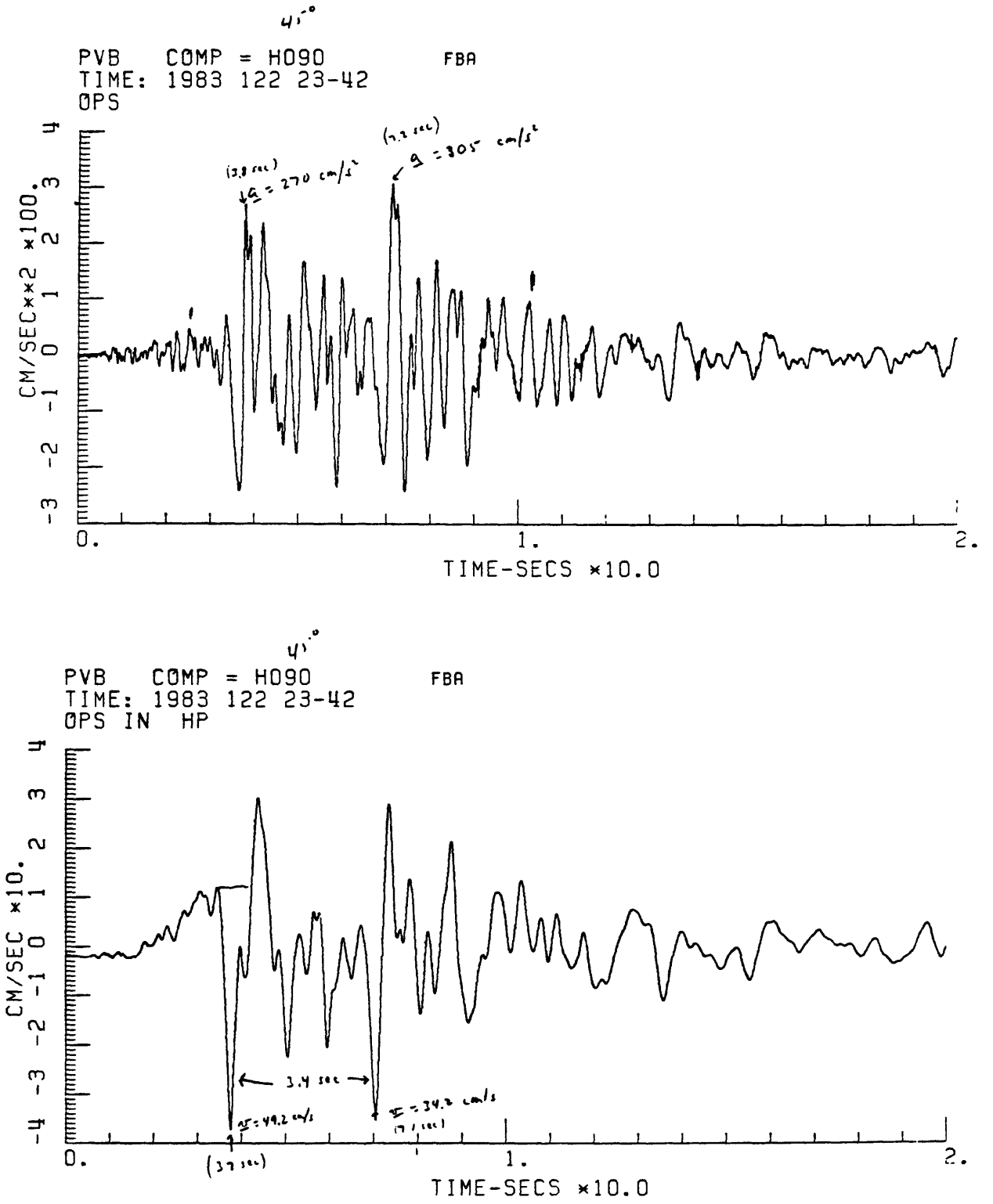

Figure 4. Processed acceleration and velocity from the Coalinga mainshock as recorded in the basement of the Pleasant Valley Pumping Plant (PVPP, Fig. 3). These records show the horizontal component of ground motion in a direction N45°E.

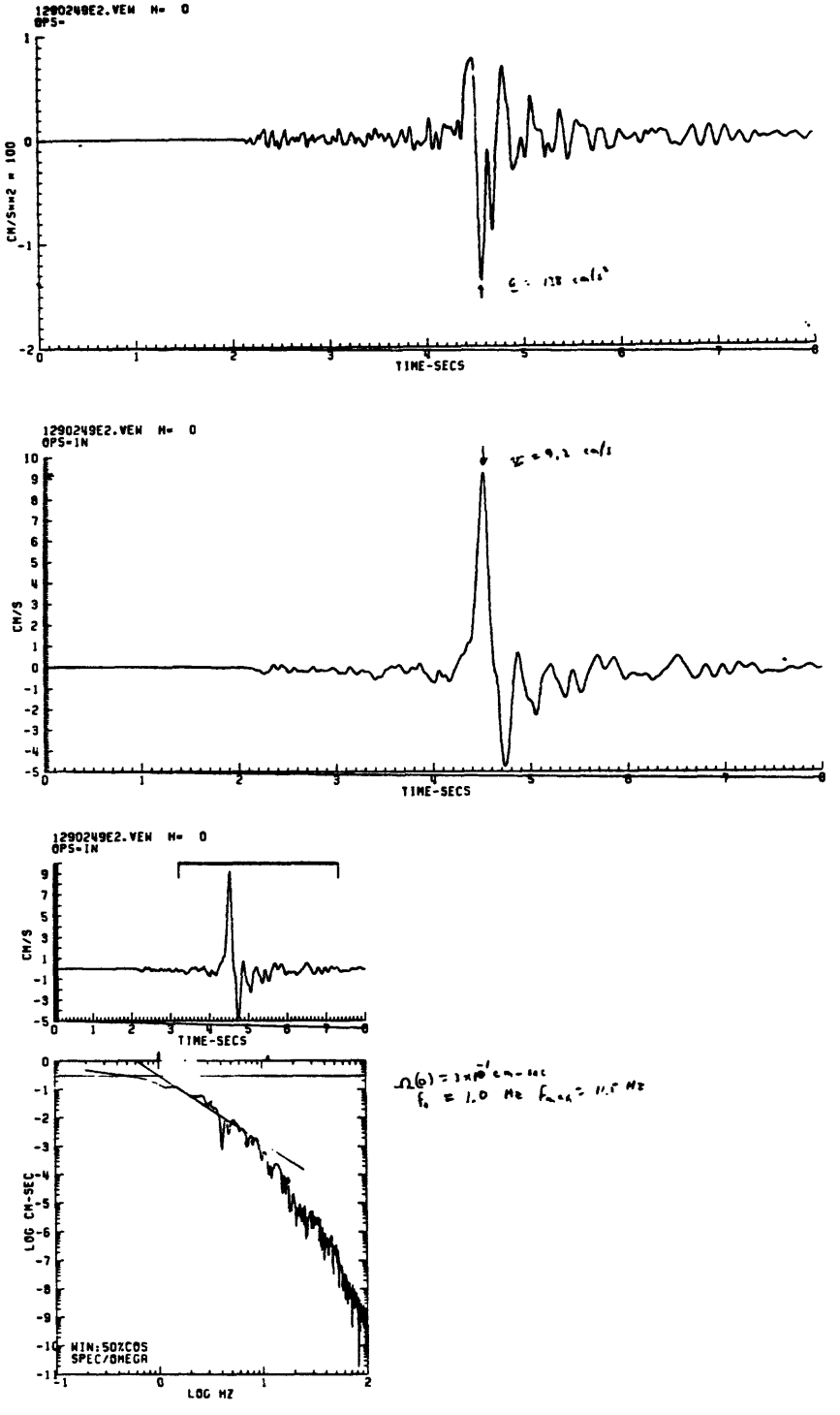

Figure 5. Acceleration, velocity, and spectrum of ground displacement for N-S component recorded at GEOS station VEW (Fig. 3).

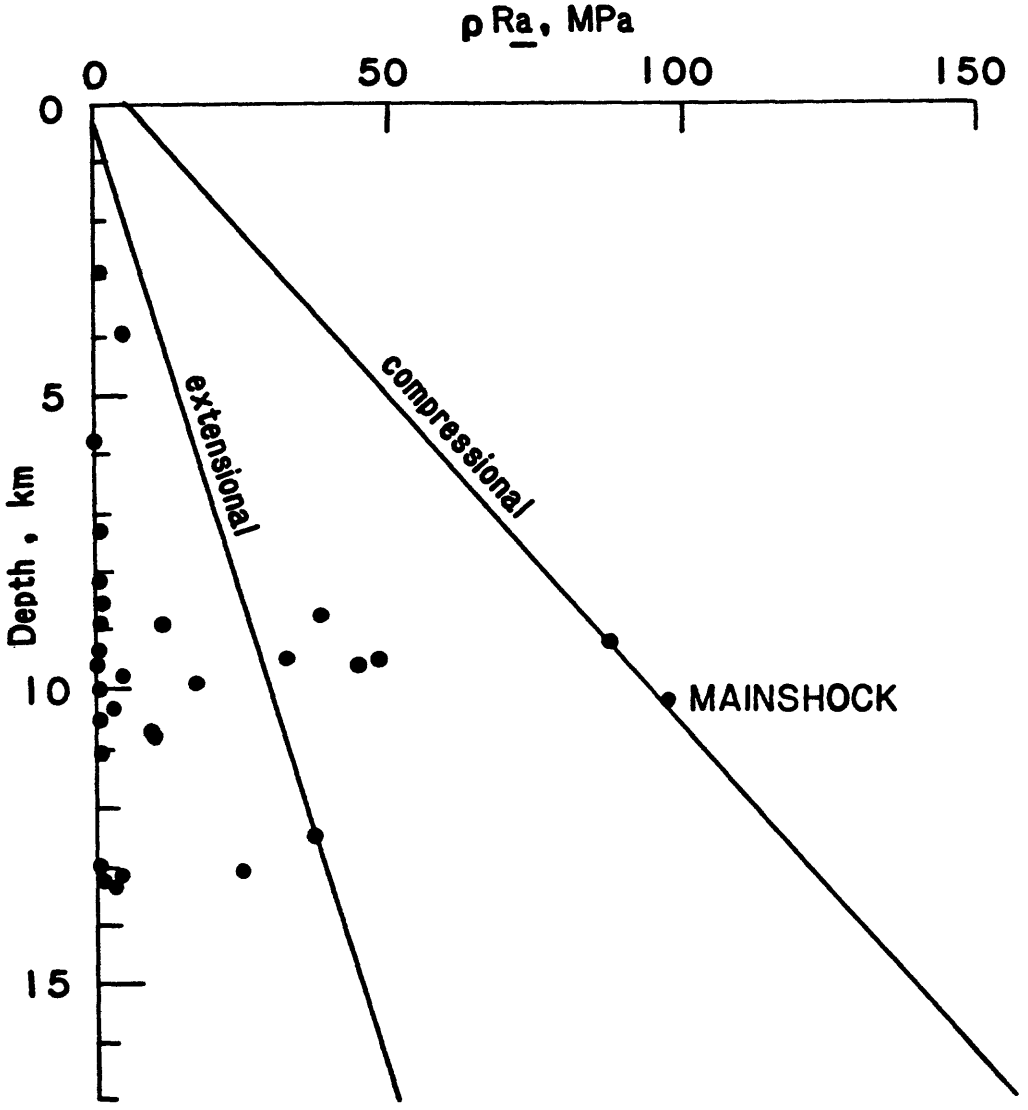

Figure 6. Peak acceleration parameters for Coalinga events (Table 1) as a function of focal depth. Regression lines from Fig. 1 are shown for comparison.

Plant (PVPP) several km to the northeast of the distribution (Figure 3), the aftershocks analyzed here were recorded at multiple sites at typical hypocentral distances of 10 to 15 km.

Table 1 summarizes the results of the analysis of the Coalinga events and Figures 4 and 5 contain examples of the data and analysis leading to the entries in Table 1. The ground motion of the mainshock was analyzed by McGarr (1984) as indicated in Figure 4, which illustrates processed acceleration and velocity traces (Maley *et al.*, 1983) for the $N45°E$ component of ground motion. One notable feature, to be discussed later, is the double-pulse nature of both the acceleration and velocity records. As indicated in the figure the peak ground motion parameters $\rho R\underline{a}$ and $R\underline{v}$ (Table 1) were measured from the first arriving pulse, which, when the other two components of ground motion are taken into account, yielded somewhat larger parameter values than the second pulse. Also note that the duration of high-amplitude ground motion for the mainshock was approximately 5 or 6 seconds.

The best recorded aftershock occurred on 9 May at 0249, a week after the mainshock and produced high-quality ground motion data at six GEOS sites as well as six SMA-1 sites. The ground motion time histories of the aftershocks, as suggested by a comparison of Figures 4 and 5, are much simpler and more compact than that of the mainshock. Another feature common to all of the records analyzed here is the occurrence of the peak acceleration following the peak in velocity (Figures 4 and 5). Thus, peak accelerations appear to be due more to the arrest, rather than initiation, of rupture (*e.g.*, Boatwright, 1980).

It is worth mentioning that although the entries of the event of 9 May 0249 were the result of averaging measurements from 12 sites, six GEOS and six SMA-1, either type of data set considered by itself yields nearly identical results. Thus, systematic calibration problems do not appear to be of any consequence here.

SOURCE PARAMETERS AND PEAK VELOCITY

As outlined by McGarr (1981) the connection of the peak velocity parameter $R\underline{v}$ to seismic source processes necessarily entails the usual seismic source parameters moment M_o, source radius r_o and stress drop $\Delta\tau$, which are related to each other (Brune, 1970, 1971) according to

$$\Delta\tau = \frac{7}{16} M_o / r_o^3 \tag{7}$$

The moment is calculated from the far-field S–wave (Hanks and Wyss, 1972; Spottiswoode and McGarr, 1975) using

$$M_o = \frac{4\pi\beta^3 \rho R \Omega(o)}{0.57} \tag{8}$$

and the source radius is given by (Brune, 1970, 1971)

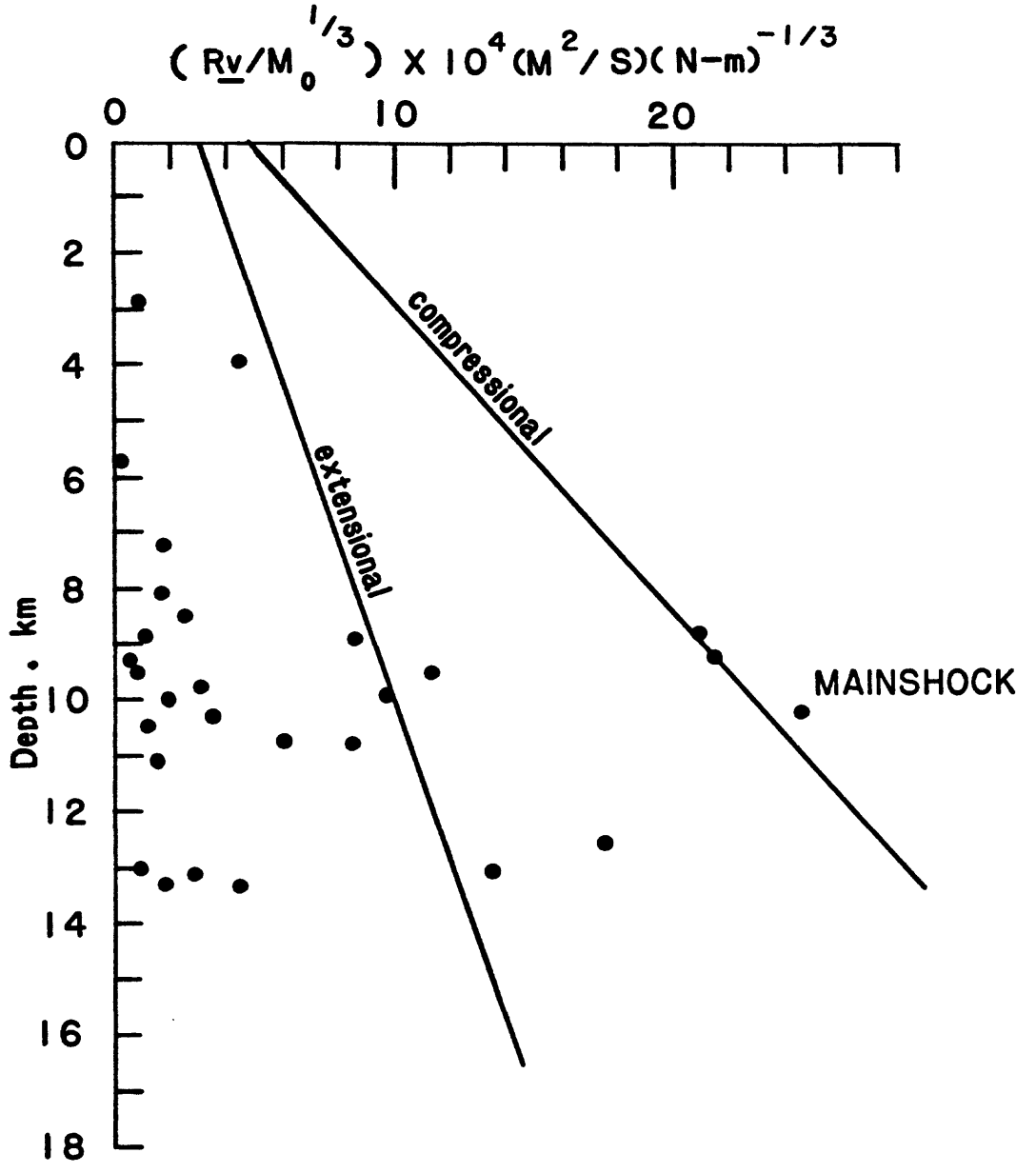

Figure 7. Normalized peak velocity parameter for Coalinga events (Table 1). Regression lines from Figure 2 are shown for comparison.

$$r_o = \frac{2.34\beta}{2\pi F_o} \tag{9}$$

where $\Omega(o)$ is the low-frequency plateau of the spectrum of displacement amplitude and F_o is the corner frequency defined by the intersection of the high and low frequency asymptotes (Figure 5).

A model-dependent relationship between peak velocity and the seismic source processes was presented by McGarr (1981) but, in the meantime it has become clear that such model dependence is not at all essential (*e.g.*, McGarr, 1984). Instead, the observations themselves can be used to develop such a relationship. From equations (19) and (21) of McGarr (1981) we can write

$$r_o = \frac{(\rho R\underline{a})M_o}{c\rho\mu(R\underline{v})^2} \tag{10}$$

where μ is the modulus of rigidity, taken as 3×10^4 MPa. For the specific model of failure considered by McGarr (1981) $c \simeq 69$.

To eliminate the model dependence and empirically determine c, the spectral estimates of r_o (equation (9), Figure 5) were compared to those calculated from (10) using various values of c for the data listed in Table 1 as well as the more extensive data set considered by McGarr (1984). $c = 58$ appears to be the optimum value and thus

$$r_o = \frac{\rho R\underline{a}M_o}{58\rho\mu(R\underline{v})^2} \tag{11}$$

Equation (11) can be used in two ways. First, in the case of earthquakes for which r_o cannot be readily estimated using spectral techniques, (11) provides a means to determine r_o in terms of robust measurements. The mainshock of the Coalinga sequence falls in this category because neither the ground motion data recorded at the Pleasant Valley Pumping Plant (Maley *et al.*, 1983) nor the teleseismic data (*e.g.*, Hartzell and Heaton, 1983) were well suited to estimating the source dimension although numerous estimates of M_o were presented with alacrity (Kanamori, 1983; Urhammer *et al.*, 1983; Rial and Brown, 1983; Hartzell and Heaton, 1983). Thus, equation (11) was used to estimate the source radius of 5.4 km, listed in Table 1.

Alternatively, if r_o is well determined from seismic spectra, as is the case for most of the events listed in Table 1, then equation (11) can be used to relate $R\underline{v}$ to $\rho R\underline{a}$ and thus to the inferred crustal strength by means of (6). That is,

$$S(\sigma, z) = \frac{128\mu\rho r_o(R\underline{v})^2}{M_o} \tag{12}$$

Hence, in the case of events for which M_o, r_o, $\rho R\underline{a}$ and $R\underline{v}$ can all be estimated, equations (6) and (12) provide two independent means of assessing the crustal strength $S(\sigma, z)$.

A result that follows immediately from (12), in comparison to (6), is that $R\underline{v}$ should show a weaker dependence on stress state than $\rho R\underline{a}$. As noted before, a comparison of Figures 1 and 2 shows that the ground motion data tend to support this conclusion. That is, at a fixed focal depth $\rho R\underline{a}$ typically increases by a factor of 3 from extensional to compressional regimes whereas, for a similar transition, $R\underline{v}$ changes by a factor of about 2.

Estimates of $S(\sigma, z)$ calculated using both equations (6) and (12) are listed in Table 1; $S(\sigma, z)_{\underline{a}}$ is from (6) and $S(\sigma, z)_{\underline{v}}$ is from (12). In only one case for which both estimates are available is the disagreement as much as a factor of two. For all of the other events the two estimates are in much better agreement. In any case, note that the inferred crustal strengths in the Coalinga aftershock zone range from about 0 to more than 200 MPa (2 kb) and, moreover, that the mainshock appears to have initiated in the strongest portion of the crust.

For direct comparison with results of the previous study by McGarr (1984) the peak acceleration parameter $\rho R\underline{a}$ is plotted as a function of focal depth in Figure 6. Also shown are the regression lines of Figure 1 (equations (1) and (2)). Except for the mainshock and the largest aftershock of 22 July at 0239 (Table 1), all other values of $\rho R\underline{a}$ are substantially lower than anticipated. That is, because all of these aftershocks occurred in what is clearly a compressional tectonic environment (*e.g.*, Eaton *et al.*, 1983) one would expect the observations of $\rho R\underline{a}$ to plot near the corresponding regression line, whereas, with two exceptions, the peak acceleration data are a factor of two, or more, too small relative to expectations.

The anomalously low values of $\rho R\underline{a}$ are suggestive of either low crustal strength, relative to that expected on the basis of Byerlee's Law and assumed hydrostatic pore pressure (equation (4a)) or substantial attenuation, characterized as $f_{\max}$ by Hanks (1982). For several reasons the latter possibility is improbable. First, $f_{\max}$, typically about 15 Hz, can easily be estimated for each of the recording sites of this study. As shown in Figure 5 the S-wave spectrum of displacement amplitude diminishes as f^{-2} between the corner frequency and $f_{\max}$, which is defined by the position beyond which the spectrum has a substantially higher rate of decay with f. For all of the events of this study (Table 1) there is a generous bandwidth between f_o and $f_{\max}$; *i.e.*, $f_{\max}/f_o \gtrsim 5$ in all cases. Thus, $\underline{a}$ is not likely to have been suppressed due to insufficient bandwidth for the events considered here. Further evidence to this effect comes from the estimates of crustal strength using peak velocity, which is much less affected by limited bandwidth than peak acceleration. The generally good agreement between $S(\sigma, z)_{\underline{a}}$ and $S(\sigma, z)_{\underline{v}}$ (Table 1) tends to support the view that $\underline{a}$ was not suppressed significantly due to limited bandwidth. Thus, it seems likely that much of the crust within the aftershock zone as sampled here is of unusually low strength compared to prior expectations.

Further evidence suggesting low strength is provided in Figure 7 where normalized peak velocity is plotted as a function of depth. The regression lines from Figure 2 have been included for comparison and, as for peak acceleration, we see that with three exceptions the normalized peak velocity is anomalously low.

For purposes of yielding some idea about the spatial distribution of inferred crustal strength, plan and cross section views of hypocenters of events listed in Table 1 along with determinations of $\rho R_{\underline{a}}$ are shown in Figures 3 and 8. Also illustrated are the hypocenters of the exceptionally well-located aftershocks with local magnitudes in excess of 3. In plan it seems that the higher values of $\rho R_{\underline{a}}$ occur mostly in two clusters separated by about 9 km (Figure 3). One cluster includes the mainshock and the other the largest aftershock of 22 July 0239. Outside these two clusters $\rho R_{\underline{a}}$ tends to be much lower, suggestive of reduced crustal strength. Moreover, between the two clusters the level of seismicity is remarkably low. As will be discussed, this gap in seismicity may indicate the zone of rupture that occurred during the mainshock.

Figure 8, a cross section view of the seismicity distribution looking northward, also indicates the two clusters of inferred high crustal strengths, one somewhat east of the center of the distribution and the other near the western edge. Outside the clusters the inferred strengths are exceptionally low.

Several features in the distribution of seismicity and seismic deformation (Figure 8) are immediately apparent. First, the vast majority of hypocenters are in the depth range 8 to 13 km. Even more significantly, nearly all of the major deformation, as indicated by Eaton *et al.*, (1983) originates in a narrower depth range of 9 to 11 km, including the mainshock; one exception to this, at the western boundary of the distribution, is the event of June 11 (Eaton *et al.*, 1983) which was associated with the only surface faulting observed during the sequence, as indicated above the hypocenter (*e.g.*, Hart and McJunkin, 1983; M. Rymer, unpublished report, 1984).

Accepting the generally held notion (*e.g.*, Eaton *et al.*, 1970) that aftershock distributions tend to define planes of earthquake fault slip then one would certainly conclude from the horizontal elongation and the distribution of major event hypocenters in Figures 3 and 8 that the mainshock rupture process took place primarily over a near-horizontal fault plane, presumably the southwest-dipping thrust plane delineated by Eaton *et al.*, (1983).[An argument favoring the reverse, or conjugate, plane was presented by Stein (1983) and Stein and King (1984).]

To pursue this notion further, using the analysis by Fletcher *et al.* (1984) of the 1975 Oroville earthquake as a precedent, we tentatively speculate that the mainshock ruptured within the zone of exceptionally low seismicity bounded by the regions of high inferred crustal strength. Accordingly, a circle with a radius of 5.4 km (from equation (11)) has been drawn in Figure 3 to crudely represent the hypothetical rupture plane. If this model is correct then rupture initiated at the mainshock hypocenter (star) and propagated primarily westward and southward along the thrust plane defined by Eaton *et al.*, and was limited in extent by the regions of high strength, inferred from the aftershock ground motion. This hypothesis can, and will, be tested. For example, it may be possible, using additional ground motion data, to locate the second major pulse of high frequency radiation from the mainshock (Figure 4). The location of this pulse might serve to discriminate between the two possible fault planes.

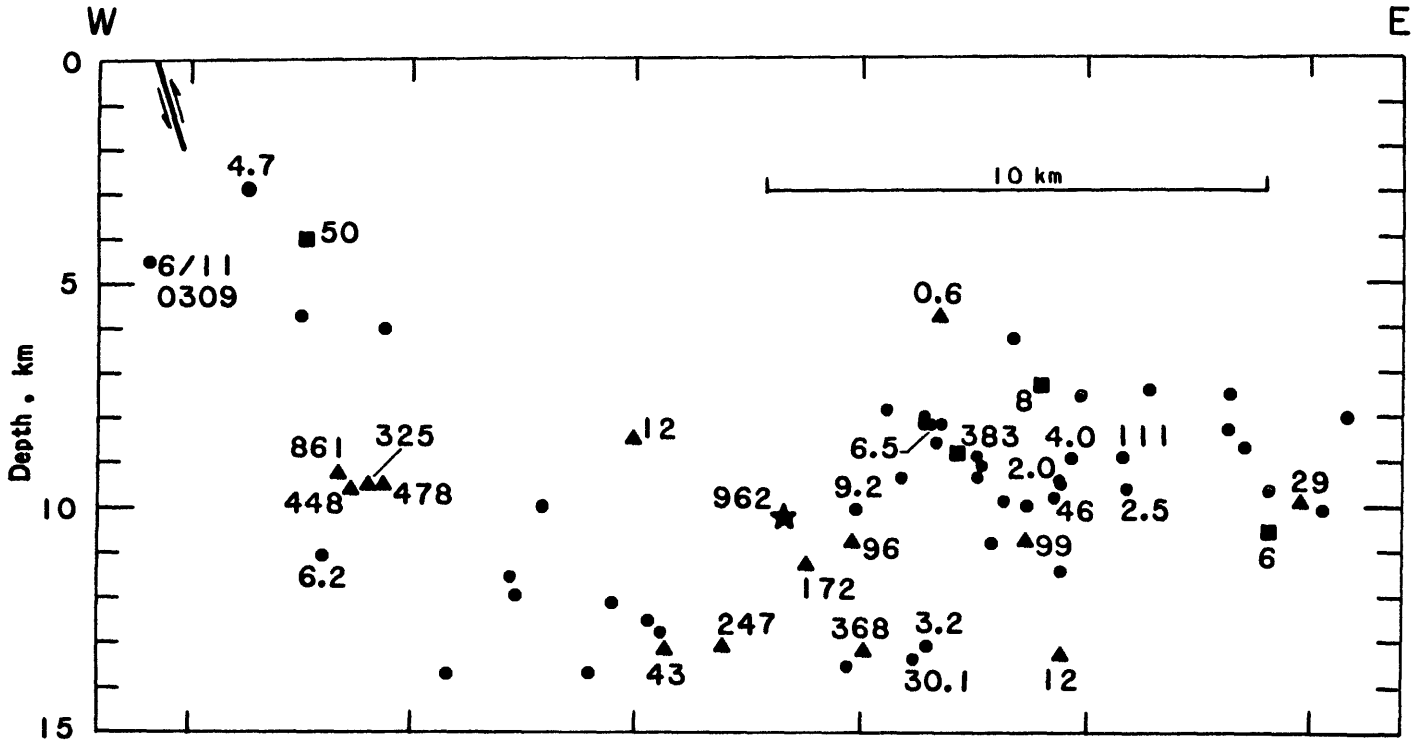

Figure 8. Cross-section view of seismicity, whose epicenters are plotted in Fig. 3. Triangles and squares denote hypocenters of events for which ground motion was analyzed (Table 1), with the squares indicating somewhat uncertain locations, as in Fig. 3. Also indicated is the surface faulting near the western extremity of the aftershock zone. This faulting was associated with the aftershock of 11 June 0309, shown here, and possibly with the large July events indicated as triangles at depths near 10 km and slightly east of the surface faulting. Numbers show values of $\rho R\underline{a}$ in bars.

DISCUSSION

The unanticipated variations in crustal strength inferred from the distribution of the peak acceleration parameter, $\rho R\underline{a}$ in Figures 3 and 8 seem quite enigmatic at this time. Possibly the anomalously low strengths are the result of pore pressure P well in excess of hydrostatic. Evidence that such an effect might be pervasive in the Coalinga area was presented by Berry (1973) and most recently by Yerkes *et al.* (1984). Of particular interest, Yerkes *et al.*, demonstrated on the basis of down-hole data extending to about 6 km depth that $\delta P/\delta z$ tends to increase with depth. Thus, at seismogenic depths of 8 to 13 km it might not be surprising to find pore pressures approaching the lithostatic load. If so then slip across much of the presumed thrust, or planes, at depth involves the failure of material substantially weakened due to greatly enhanced pore pressure, *i.e.*, the Hubbert-Rubey (1959) hypothesis.

At this time there is little justification for attempting to relate the ground motion parameters to hypothetical overpressures in the seismogenic region but in anticipation of more definitive and complete data in the future we indicate here the magnitudes of P necessary to effect specified reductions in crustal strength or corresponding reductions in the ground motion parameters.

Byerlee's Law of friction, in conjunction with the assumption of a faulted or jointed crust (Sibson, 1974; Brace and Kohlstedt, 1980; McGarr, 1984) yields for a coefficient of friction of 0.75

$$\sigma_1 - P = 4\,(\sigma_3 - P) \tag{13}$$

and in a compressional stress state $\sigma_3 = \rho g z$, the vertical stress due to the weight of the overburden, where g is gravity. Combining (3), (6) and (13) gives the crustal strength or peak acceleration as a function of depth and pore pressure

$$S \simeq 2.2\,\rho R\underline{a} \simeq \frac{3}{2}\,(\rho g z - P) \tag{14}$$

We see that as P approaches the lithostat the crustal strength or peak acceleration tends toward zero. In general, then, assuming that the crustal strength at a given depth is uniquely related to the pore pressure, (14) can be used to relate observed ground motion parameters to P. For example, at a depth of 10 km $\rho R\underline{a} = 1000$ bars implies $P \simeq 0.41\,\rho g z$, a near hydrostatic pore pressure which appears to be reached at the mainshock hypocenter (Table 1). If $\rho R\underline{a} = 400$ bars, as for some of the larger aftershocks of the sequence then $P \simeq 0.76\,\rho g z$. For $\rho R\underline{a} = 100$ bars, $P = 0.94\,\rho g z$. Thus, some of the lowest values of $\rho R\underline{a}$ imply near-lithostatic pore pressure conditions (*e.g.*, Figures 6 and 8) if P is, in fact, the factor responsible for the marked reduction in strength. As discussed, the data compiled by Yerkes *et al.*, (1984) tend to argue for such a hypothesis.

With the existing ground motion and pore pressure data it is difficult to demonstrate a convincing relationship between $\rho R\underline{a}$ and P that goes beyond the plausibility argument just

presented. The seismic deformation of the Coalinga sequence occurred almost exclusively below 5 km (Figure 8) whereas the pore pressure data compiled by Yerkes *et al.*, are mostly from the topmost 5 km of the crust. The trend toward increasing overpressurization with depth demonstrated by Yerkes *et al.*, suggests a reasonable likelihood of near-lithostatic values of P at least in certain regions of the seismogenic zone.

Finally, we note that the largest shocks of the sequence involved rupture initiation in what seems to be the strongest regions of the crust, including the mainshock and the largest aftershock (22 July at 0239). This feature of the Coalinga sequence seems to be typical of most, if not all, earthquake sequences (*e.g.*, McGarr *et al.*, 1975; Sibson, 1982) and such effects have been rationalized by Das and Scholz (1983).

ACKNOWLEDGMENTS

J. Boatwright and P. Spudich reviewed an earlier version of this report and provided many helpful suggestions. Discussions with R. Yerkes and M. Rymer were of considerable use in formulating the ideas presented here.

REFERENCES

Berry, F. A. F., High fluid potentials in California coast ranges and their tectonic signficance, *Am. Ass. Pet. Geol. Bull.* **57**, 1219–1249, 1973.

Boatwright, J., Quasi-dynamic models of simple earthquakes: Application to an aftershock of the 1975 Oroville, California earthquake, *Bull. Seismol. Soc. Am.* **71**, 69–94, 1981.

Borcherdt, R., E. Cranswick, G. Maxwell, C. Mueller, R. McClearn, G. Sembera, and L. Wennerberg, Digital strong motion data recorded by the U.S. Geological Survey near Coalinga, California, *U.S.G.S. Open-File Report* **83–511**, 1983.

Brace, W. F. and D. L. Kohlstedt, Limits on lithospheric stress imposed by laboratory experiments, *J. Geophys. Res.* **85**, 6248–6252, 1980.

Brune, J. N., Tectonic stress and the spectra of seismic shear waves from earthquakes, *J. Geophys. Res.* **75**, 4997–5009, 1970; Correction, *J. Geophys. Res.* **76**, 5002, 1971.

Byerlee, J. D., Friction of rocks, *Pure Appl. Geophys.* **116**, 615–626, 1978.

Das, S. and C. H. Scholz, Why large earthquakes do not nucleate at shallow depths, *Nature* **305**, 621–623, 1983.

Eaton, J. P., M. E. O'Neill, and J. N. Murdock, Aftershocks of the 1966 Parkfield-Cholame, Californa, earthquake: A detailed study, *Bull. Seismol. Soc. Am.* **60**, 1151–1197, 1970.

Eaton, J. P., R. Cockerham, and F. Lester, Study of the May 2, 1983 Coalinga earthquake and its aftershocks, based on the USGS seismic network in northern California, *Spec. Pub.* **66**, CDMG, 1983.

Fletcher, J. B., J. Boatwright, L. Haar, T. Hanks, and A. McGarr, Estimation of source parameters for aftershocks of the Oroville, California earthquake, *Bull. Seismol. Soc. Am.* **74**, in press, 1984.

Hanks, T. C., f_{max}, *Bull. Seismol. Soc. Am.* **72**, 1867–1879, 1982.

Hanks, T. C. and M. Wyss, The use of body-wave spectra in the determination of seismic source parameters, *Bull. Seismol. Soc. Am.* **62**, 561–589, 1972.

Hanks. T. C. and D. A. Johnson, Geophysical assessment of peak accelerations, *Bull. Seismol. So. Am.* **66**, 959–968, 1976.

Hartzell, S. H. and T. H. Heaton, Teleseismic mechanism of the May 2, 1983 Coalinga, California, earthquake from long-period P waves, *Spec. Pub.* **66**, CDMG, 1983.

Hubbert, M. K. and W. W. Rubey, Role of fluid pressure in the mechanics of overthrust faulting. I. Mechanics of fluid-filled porous solids and its application to overthrust faulting, *Bull. Geol. Soc. Am.* **70**, 115–166, 1959.

Kanamori, H., Mechanism of the 1983 Coalinga earthquake determined from long period surface waves, *Spec. Pub.* **66**, CDMG, 1983.

Maley, R., G. Brady, E. Etheridge, D. Johnson, P. Mork, and J. Switzer, Analog strong-motion data and processed main event records, *U.S.G.S. Open-File Rept.* **83–511**, 1983.

McGarr, A., Analysis of peak ground motion in terms of a model of inhomogeneous faulting, *J. Geophys. Res.* **86**, 3901–3912, 1981.

McGarr, A., Scaling of ground motion parameters, state of stress, and focal depth, *J. Geophys. Res.*, in press, 1984.

McGarr, A., S. M. Spottiswoode, and N. C. Gay, Relationship of mine tremors to induced stresses and to rock properties in the focal region, *Bull. Seismol. Soc. Am.* **65**, 981–993, 1975.

Rial, J. A. and E. Brown, Waveform modeling of the long period P-waves from the Coalinga earthquake of May 2, 1983, *Spec. Pub.* **66**, CDMG, 1983.

Sibson, R. H., Frictional constraints on thrust, wrench and normal faults, *Nature* **249**, 542–544, 1974.

Sibson, R. H., Fault zone models, heat flow and the depth distribution of earthquakes in the continental crust of the United States, *Bull. Seismol. Soc. Am.* **72**, 151–163, 1982.

Spottiswoode, S. M. and A. McGarr, Source parameters of tremors in a deep-level gold mine, *Bull. Seismol. Soc. Am.* **65**, 93–112, 1975.

Stein, R. S., Reverse slip on a buried fault during the 2 May 1983 Coalinga earthquake: Evidence from geodetic elevation changes, *Spec. Pub.* **66**, CDMG, 1983.

Stein, R. S. and C. King, Seismic potential revealed by surface folding: 1983 Coalinga, California, earthquake, *Science* **224**, 869–872, 1984.

Urhammer, R. A., R. B. Darragh, and B. A. Bolt, The 1983 Coalinga earthquake sequence: May 2 through August 1, *Spec. Pub.* **66**, CDMG, 1983.

Yerkes, R. F., P. Levine, and C. M. Wentworth, Abnormally high fluid pressures and the Coalinga earthquakes—A preliminary review, *This Volume*, 1984.

Finite faulting in three large Coalinga aftershocks

by Charles S. Mueller
U. S. Geological Survey
345 Middlefield Rd. MS 977
Menlo Park, CA 94025

ABSTRACT

For three large Coalinga aftershocks (magnitude $\geq$ 4.5) portable digital seismographs were located near the updip projections of the two candidate fault planes determined by Eaton (this volume). In order to resolve the fault-plane ambiguity for these events, observed seismograms were compared with each other and with synthetic waveforms from four simple faulting models: unilateral updip and downdip rupture on rectangular dislocations corresponding to the two fault planes. Waveform shapes suggest that rupture proceeded southwest from the hypocenter in these events, but cannot unequivocally discriminate between updip rupture on a steeply northeast-dipping plane or downdip rupture on a shallowly southwest-dipping plane. Evidently rupture was more complex than the simple models tested in this study; poor correlation of velocity-seismogram phases at different stations shows the difficulty in constructing complex rupture models from the data.

INTRODUCTION

The fault-plane ambiguity which is discussed in this volume is inherent in the inversion of seismic data for the parameters of an equivalent point source. If the source has sufficient finite extent, this ambiguity can be resolved in practice by analyzing waveforms from stations well distributed over the focal sphere. Simple geometrical considerations show that different finite sources will generally radiate different waveforms, regardless of the details of rupture propagation. Rupture directivity from a propagating fault may be the most prominent effect of finite rupture at some locations (see Boore and Joyner, 1978, for an analysis of directivity in the presence of complex rupture).

During the Coalinga aftershock sequence, over 1100 aftershocks were recorded with portable, digital seismographs deployed in the epicentral area (Mueller *et al.* 1984). In particular, three large aftershocks (magnitude $\geq$ 4.5) with hypocenters near the mainshock hypocenter were recorded: 129 0249, 129 0326, and 144 0902 (Julian day, hour, minute, GMT) referred to hereafter as A1, A2, and A3, respectively (see Table 1). In this paper, using carefully determined magnitudes, hypocenters, and fault-plane solutions as a point of departure (Eaton, this volume), I examine locally recorded waveforms from these three

events in order to distiguish between several simple finite-faulting models.

Fault-finiteness effects are best observed if two or more earthquakes having similar locations, but different rupture styles, are observed at two or more stations located at widely separated azimuths. For example, Bakun *et al.* (1978) and Boatwright and Boore (1982) inferred rupture direction from earthquakes on vertical strike-slip faults by analyzing seismograms from stations located at front- and back-azimuths with respect to the rupture propagation direction. In the case of Coalinga, relatively small and roughly equal ground motions were recorded at stations located northwest and southeast of the aftershocks under study (Figures 1 and 2). This observation suggests that there was no significant component of rupture propagation parallel to strike for these events. It remains to test the proposition that rupture propagation had a significant updip or downdip component. In this situation, the Coalinga fault-plane geometry ensures that stations could not be optimally located in both front- and back-azimuths. However for aftershocks A1 and A2 stations SUB and TRA were located near the updip extensions of the fault-plane candidates. For aftershock A3 stations SUB and VEW were so located. In this configuration, these stations are still sensitive to the effects of finite faulting. In this paper, waveforms recorded at stations SUB, MIT, VEW, and TRA are compared in order to distinguish between simple faulting models. SUB, VEW, and TRA waveforms are compared with synthetic seismograms from finite faults with unilateral updip or downdip rupture.

Initial efforts to model the Coalinga aftershock data made use of fault strike, dip, and rake suggested by first-motion studies and proved encouraging in modeling vertical- and radial-, but not transverse-component displacement pulse shapes. Stations SUB,VEW, and TRA fall near SH-radiation-pattern nodes for the three large aftershocks (Figure 2), so synthetic waveforms at these sites are sensitive to small perturbations in the models. Given the density of recording stations for these events (for example, event A1 was recorded by 10 stations in the USGS digital network alone) a full modeling study should probably make use of a moment-tensor-inversion result as a starting point. This study is more limited in scope. I am simply attempting to distinguish between fault plane candidates by studying plausible models with updip or downdip rupture components. Model parameters were selected using generally accepted source scaling relations for central California; no attempt was made to adjust the models to improve the fit to the data.

DATA

The Coalinga mainshock (122 2342 GMT) and three aftershocks under consideration are described in Table 1. Magnitudes, hypocentral parameters, and the strike and dip of

fault planes are from Eaton (this volume). I calculated the rake angles compatible with the two fault planes for each event. Epicenters and stations are mapped in Figure 1. Nodal patterns from the four focal mechanisms are plotted in Figure 2. In general, each event is characterized by predominantly reverse dip-slip motion on two possible fault planes striking northwest-southeast. Ground acceleration was obtained from three-component force balance accelerometers recorded by GEOS digital event-recording seismographs sampling each component at 200 samples per second (Mueller *et al.* 1984). Velocity and displacement waveforms were obtained by time-domain integrations accompanied by a 5-second zero-phase-shift high-pass filter. The mainshock and large aftershocks were also recorded by a permanent SMA-1 accelerograph cosited with station SUB at the Pleasant Valley Pumping Plant. Events A1 and A2 were recorded by stations SUB, MIT, VEW, and TRA (the EW component at MIT was dead, so radial and transverse components from MIT were not analyzed). Event A3 was recorded by SUB and VEW. All these observations were made at epicentral distances less than one source depth. Simple waveforms recorded from small earthquakes suggest that path or free surface complications will not obscure the observation of source directivity. This observation also justifies the use of a simple wholespace synthetic-seismogram calculation. The effects of attenuation on waveforms appear to be small at the frequencies and distances of interest in this study and have been neglected.

RESULTS

Vertical-component P-wave velocity waveforms for aftershocks A1, A2, and A3 are shown in Figure 3. The initial (hypocentral) P-arrival is aligned at 0.2 s (this arrival is best identified on the acceleration records). In each case, the hypocentral arrival is followed by larger, more energetic phases. Seismograms from 129 0319, a smaller event (magnitude $\approx$ 3.5) with similar hypocenter, show that this complexity is due to the source rather than path or site. If later-arriving phases can be reliably identified, their sources can be located relative to the hypocenter. In Figure 3, I have identified a phase in the A3 records which appears to correlate at SUB and VEW, suggesting that the rupture proceeded relatively toward VEW. This correlation assumes that a radiation-pattern node lies between SUB and VEW for later-arriving energy whereas VEW is nearly nodal for hypocentral P waves (Figure 2). Identification of phases is difficult for aftershocks A1, A2, and 129 0319. This technique can only be applied to P waves because the hypocentral S wave cannot be reliably identified.

It is important to notice that the velocity amplitudes in Figure 3 vary systematically

in a manner that is qualitatively consistent with the radiation patterns suggested by Figure 2. To the extent that radiation pattern strongly influences ground-motion amplitudes, it will be difficult to infer directivity from integral measures of high-frequency ground-motion amplitude (Boatwright and Boore, 1982). In this situation, waveform shape may be a more reliable indicator of directivity than amplitude.

Vertical, radial, and transverse displacement waveforms are shown in Figure 4 for four aftershocks: A1(4a), A2 (4b), A3 (4c), and 129 0319 (4d). Again, 129 0319 is included as an example of a simple event with hypocenter similar to the mainshock and three large aftershocks. Displacement waveforms are simple and one-sided, with the exception of the transverse components for event A1 at VEW and TRA. The complexity of these components is an enigma, because other components suggest that A1 was a simple event (for example, compare the transverse component at SUB with that from 129 0319).

As mentioned earlier, comparison of waveforms at stations to the northwest and southeast of these aftershocks showed roughly equal and relatively small amplitudes, suggesting that there was no significant component of rupture propagation parallel to strike. The simplest faulting models consistent with this observation confine rupture propagation to be updip or downdip on the two candidate fault planes suggested by the first-motion studies. I have calculated synthetic seismograms (using Boatwright and Boore's 1975 simplification of Haskell, 1969) for rectangular faults with length, width, risetime, and dislocation consistent with generally-accepted source-scaling relations for central California (see, for example, Hanks and Boore, 1984):

$$\log M_0 = 1.5M + 16$$

$$r^3 = \frac{7}{16}\frac{M_0}{\Delta\sigma}$$

$$D = \frac{M_0}{\mu \times L \times W}$$

where M_0 = seismic moment, M = local magnitude, $\Delta\sigma$ = stress drop (assume 100 bars), r = source dimension, D = average dislocation, L and W = fault length and width, and μ = shear modulus (assume 3×10^{11} dyn/cm/cm). I have used $L = r$, $W = r/2$, and risetime = W/V_s (for a ramp source-time function) where V_s = shear velocity (assume 3.0 km/s). A rupture velocity of 2.5 km/s was used. These last assumptions cannot be rigorously justified but they seem plausible in the context of this study. Again, the philosophy adopted here is to propose and test the simplest models which incorporate significant updip and downdip rupture components, not to attempt a full modeling study. Two modifications

were made to the whole-space synthetic seismograms. Motivated by the observation that P- and S-wave energy was primarily confined to the vertical and horizontal components, respectively, synthetic vertical and radial components were transformed using the angle-of-incidence at the station (untransformed synthetics exhibited significant vertical-component S and horizontal-component P). Each component was then multiplied by 2 to simulate the free surface. As a further simplification, synthetic seismograms were calculated for fault models with "uprake" and "downrake" propagation from the hypocenter. For the fault geometry under consideration, the difference between updip and uprake or downdip and downrake is a small one; rupture was referenced to the rake direction because this corresponds to purely in-plane rupture propagation. Model parameters are listed in Table 2. (ϕ, θ, and ψ rotate north,east,down coordinates into fault coordinates X_1, X_2, X_3 via three right-handed rotations:

ϕ rotates north into strike (NED $\rightarrow X_1' X_2' X_3'$)
θ rotates X_2' into dip ($X_1' X_2' X_3' \rightarrow X_1'' X_2'' X_3''$)
ψ rotates X_1'' into rake ($X_1'' X_2'' X_3'' \rightarrow X_1 X_2 X_3$).

Then a positive dislocation is in the $+X_1$ direction for a point on the $+X_3$ side of the fault.)

Figure 5 is a schematic cross section showing stations, hypocenter, and the four models to be tested. Radial-component synthetic seismograms are compared with aftershock data in Figure 6. As mentioned earlier, the strong influence of radiation pattern means that waveform shape may be a more reliable indicator of fault finiteness than amplitude in these data. In fact, radial-component amplitudes and polarities are generally well fit, suggesting that the model parameters are grossly correct. Transverse-component data (not shown) are poorly modeled; data are significantly less nodal than transverse components from the models (except for event A2 at SUB which is well fit, at least in amplitude). Observed radial displacement pulses are generally narrower at TRA and VEW than at SUB, favoring Models 1 and 4 in which TRA and VEW are at forward azimuths relative to SUB. Data and synthetics will be compared individually for each event.

129 0249 - A1. The waveform shape at TRA is well fit by Model 1 with rupture updip toward TRA. Decreasing the model moment by a factor of three improves this fit. The waveform at SUB is not well fit by any model but Model 1 is as good as any. At first glance these pulses are simple, but closer inspection reveals some of the complexity which is evident on the transverse components (Figure 4).

129 0326 - A2. This event demostrates clear directivity in both waveform shape and

amplitude. Model 4 with rupture downdip away from SUB gives a good fit to pulse shapes. This interpretation is reinforced by inspection of the narrow, high-amplitude displacement pulses at station ALP (not shown) which was located southeast of TRA and was also near the updip extension of the northeast-dipping plane.

144 0902 - A3. The main displacement pulse is narrower at VEW than SUB. Model 1 with rupture updip toward VEW provides the best fit to these pulse shapes but amplitudes are poorly modeled.

The model-data comparisons suggest that near-field displacements have been faithfully recorded by the force balance accelerometers. This observation is interesting from an instrumentation perspective; these terms do not help distinguish faulting models in the present study.

DISCUSSION AND CONCLUSIONS

Four simple faulting models have been proposed in this study and tested by comparing data and synthetic seismograms from stations most sensitive to fault finiteness. Models were constructed from carefully determined point-source source parameters (strike, dip, rake, magnitude, and hypocenter; Eaton, this volume) and generally accepted scaling relations (fault length, width, risetime, and dislocation). Given the well known tradeoffs involved in such modeling (Anderson and Richards, 1975), the successful fit of a displacement pulse at a single station is relatively insignificant. Nevertheless it is gratifying that displacements are generally well modeled. Rather, it is the comparison of data and synthetic seismograms at two stations that discriminates between the models.

The data suggest that stations TRA and VEW are in forward azimuths relative to SUB for these events and in general Models 1 and 4 fit the data better than Models 2 and 3. Model 1 is preferred for aftershocks A1 (129 0249) and A3 (144 0902) and Model 4 is preferred for aftershock A2 (129 0326), the event demonstrating the strongest directivity. The fits are not compelling, suggesting that these large aftershocks did not rupture with a dominant unilateral rupture component. Observed displacement pulses are simple, but the data do not suggest obvious simple alternative faulting models. Given the complexity of the Coalinga aftershock sequence (Eaton, this volume; Eberhart-Phillips and Reasenberg, this volume) it may not be reasonable to expect simplicity and reproducibility in the large-aftershock faulting. In the absense of strong evidence in favor of a single faulting model, little can be inferred from this study concerning mainshock faulting.

ACKNOWLEDGEMENTS

The following people assisted at various stages of the Coalinga project: E. Cranswick, C. Criley, G. Maxwell, R. McClearn, E. Sembera, and L. Wennerberg. Thanks to J. Boatwright, D. Boore, M. Rymer, and P. Spudich who reviewed this paper. J. Boatwright and D. Boore provided the original synthetic-seismogram program upon which I based my version.

REFERENCES

Anderson, J. G. and P. G. Richards (1975). Comparison of strong ground motion from several dislocation models, *Geophys. Jour. R. Astr. Soc., 42*, 347–373.

Bakun, W. H., R. M. Stewart, and C. G. Bufe (1978). Directivity in the high-frequency radiation of small earthquakes, *Bull. Seism. Soc. Am., 68*, 1253–1263.

Boatwright, J. and D. M. Boore (1975). A simplification in the calculation of motions near a propagating dislocation, *Bull. Seism. Soc. Am., 65*, 133–138.

Boatwright, J. and D. M. Boore (1982). Analysis of the ground accelerations radiated by the 1980 Livermore Valley earthquakes for directivity and dynamic source characteristics, *Bull. Seism. Soc. Am., 72*, 1843–1865.

Boore, D. M. and W. Joyner (1978). The influence of rupture incoherence on seismic directivity, *Bull. Seism. Soc. Am., 68*, 283–300.

Eaton, J. P. *(this volume).* The May 2, 1983 Coalinga earthquake and its aftershocks: a detailed study of the hypocenter distribution and of the focal mechanisms of the larger aftershocks.

Eberhart-Phillips, D. and P. Reasenberg *(this volume).* Hypocenter locations and constrained fault-plane solutions for Coalinga aftershocks, May 2–24, 1983: evidence for a complex rupture geometry.

Hanks, T. C. and D. M. Boore (1984). Moment magnitude relations in theory and practice, *Jour. Geophys. Res., 89*, 6229–6235.

Haskell, N. A. (1969). Elastic displacements in the near-field of a propagating fault, *Bull. Seism. Soc. Am., 59*, 865–908.

Mueller, C. S., E. Sembera, and L. Wennerberg (1984). Digital recordings of aftershocks of the May 2, 1983 Coalinga, California earthquake, *U. S. Geological Survey Open-file Report 84-697.*

TABLE 1. Parameters from first motion study (Eaton, this volume).

Event	Time GMT (day hrmn)	Mag	Latitude	Longitude	Depth (km)	Strike,Dip,Rake
M	122 2342	6.7	36 13.96	-120 18.57	10.01	307,067,090
						127,023,090
A1	129 0249	5.3	36 14.74	-120 17.97	12.04	293,048,073
						136,044,107
A2	129 0326	4.6	36 14.39	-120 17.96	12.43	278,052,077
						119,040,105
A3	144 0902	4.7	36 15.24	-120 19.00	8.86	324,074,084
						166,018,111

TABLE 2. Fault models.

	A1				A2				A3			
Model	1	2	3	4	1	2	3	4	1	2	3	4
ϕ(deg)	293	293	136	136	278	278	119	119	324	324	166	166
θ(deg)	48	48	44	44	52	52	40	40	74	74	18	18
ψ(deg)	-73	107	-107	73	-77	103	-105	75	-84	96	-111	69
Length(km)	1.6	1.6	1.6	1.6	0.70	0.70	0.70	0.70	0.78	0.78	0.78	0.78
Width(km)	0.8	0.8	0.8	0.8	0.35	0.35	0.35	0.35	0.39	0.39	0.39	0.39
Risetime(s)	0.27	0.27	0.27	0.27	0.12	0.12	0.12	0.12	0.13	0.13	0.13	0.13
V. Rup.(km/s)	2.5	2.5	2.5	2.5	2.5	2.5	2.5	2.5	2.5	2.5	2.5	2.5
Disloc.(cm)	-230	230	-230	230	-110	110	-110	110	-120	120	-120	120

FIGURE CAPTIONS

Figure 1. Map of the Coalinga area showing station locations and epicenters. For each earthquake, SUB is near the updip extension of the southwest-dipping fault plane and TRA or VEW is near the updip extension of the northeast-dipping fault plane. Solid line represents bedrock-alluvium contact.

Figure 2. Upper-hemisphere, equal-area focal spheres showing first-motion polarities and nodal patterns for mainshock and three aftershocks (see Table 1).

Figure 3. Vertical-component velocity records for four aftershocks showing emergence and complexity of P-wave phases. The hypocentral P-arrival (best identified on the accelerograms) is aligned at 0.2 seconds. A possible phase correlation is indicated for event A3 (144 0902). 129 0319 records show the simple response of path and site to a small event with similar hypocenter to the three large aftershocks.

Figure 4. Vertical, radial, and transverse component displacement seismograms for four aftershocks. The hypocentral P-arrival is aligned at -1.0 second.

Figure 5. Schematic diagram of the four faulting models in cross section. Actual rupture propagation is "uprake" or "downrake" rather than updip or downdip (see text).

Figure 6. Comparison of models and data: radial-component displacement seismograms for the three large aftershocks. Model patterns are identified in Figure 5. Notice that near-field displacements are recovered from the accelerometer records.

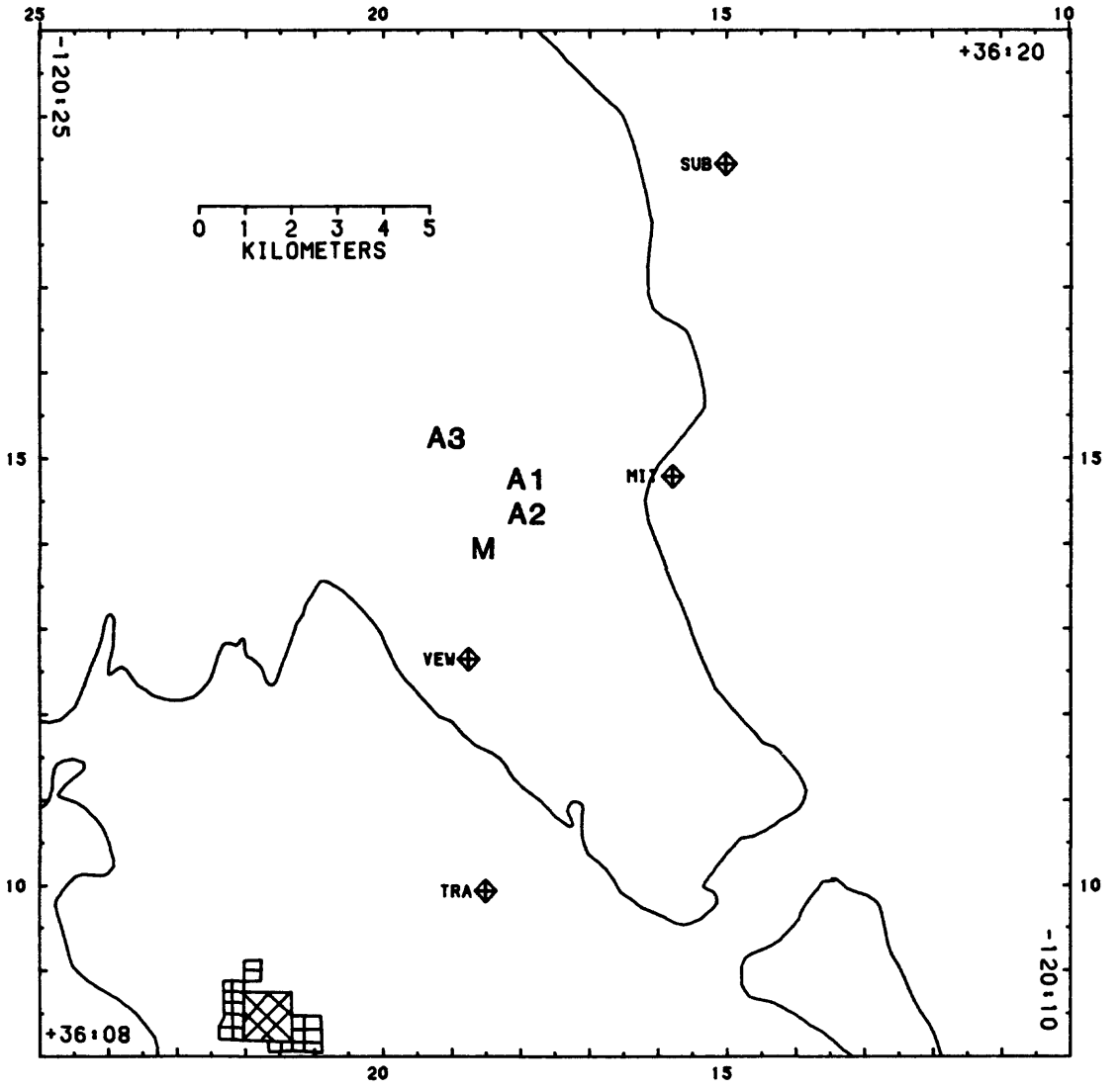
25
20
15
10
-120:25
+36:20
SUB
0 1 2 3 4 5
KILOMETERS
A3
A1
A2
M
MIT
15
VEW
TRA
10
+36:08
-120:10
20
15

Figure 1.

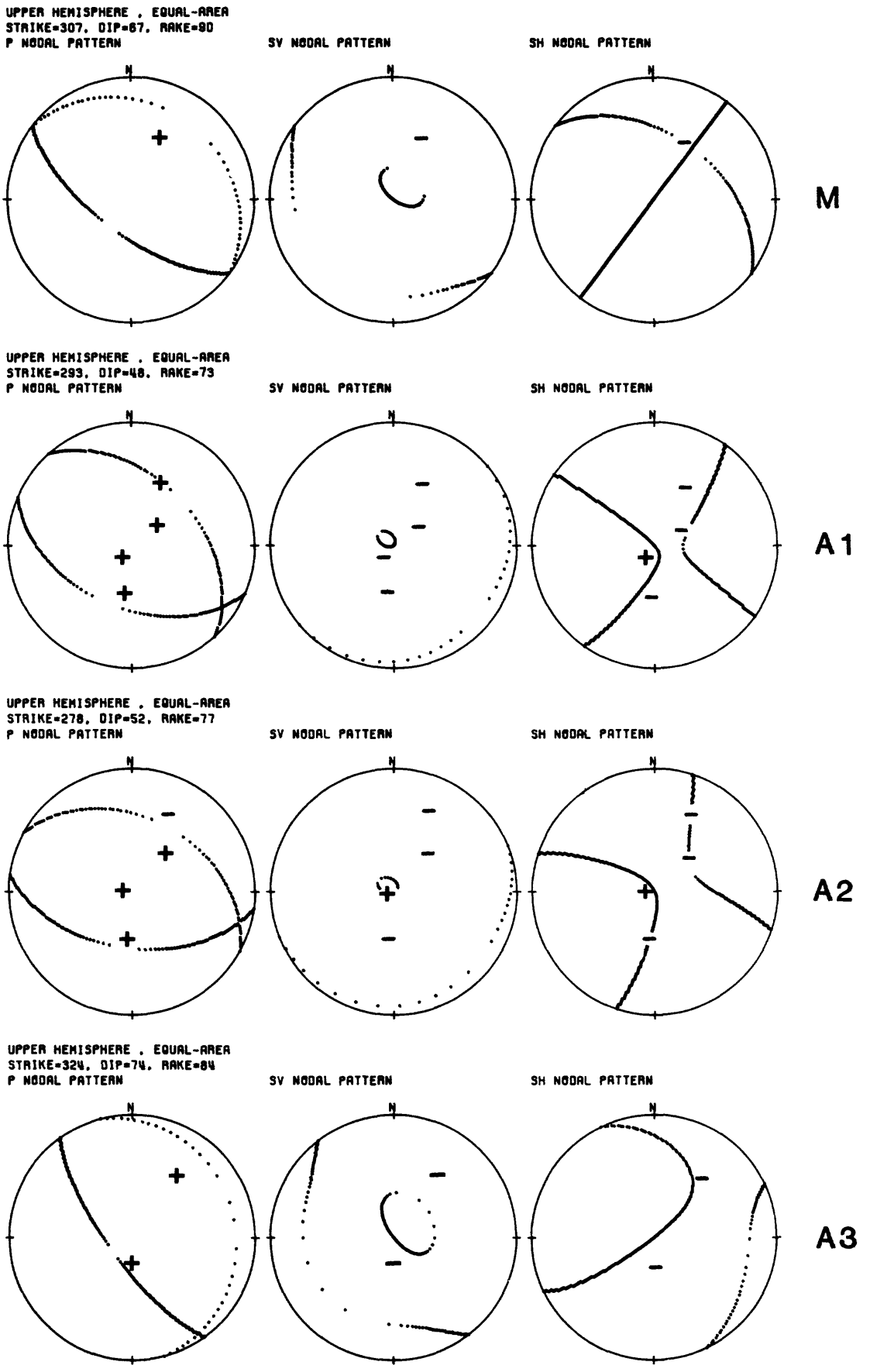
UPPER HEMISPHERE , EQUAL-AREA
STRIKE=307, DIP=87, RAKE=90
P NODAL PATTERN
SV NODAL PATTERN
SH NODAL PATTERN
M
UPPER HEMISPHERE , EQUAL-AREA
STRIKE=293, DIP=48, RAKE=73
P NODAL PATTERN
SV NODAL PATTERN
SH NODAL PATTERN
A1
UPPER HEMISPHERE , EQUAL-AREA
STRIKE=278, DIP=52, RAKE=77
P NODAL PATTERN
SV NODAL PATTERN
SH NODAL PATTERN
A2
UPPER HEMISPHERE , EQUAL-AREA
STRIKE=324, DIP=74, RAKE=84
P NODAL PATTERN
SV NODAL PATTERN
SH NODAL PATTERN
A3

Figure 2.

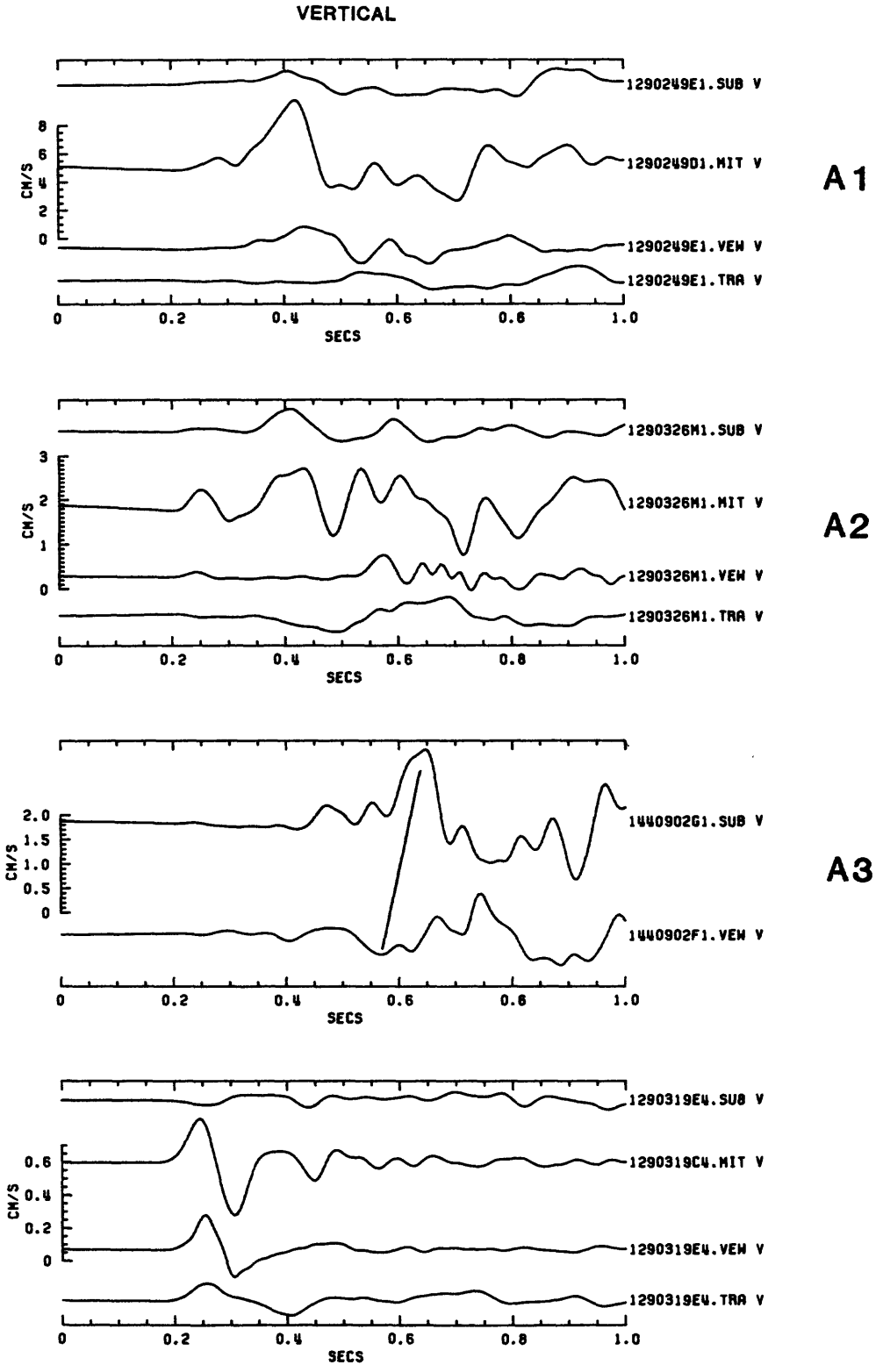
VERTICAL
1290249E1.SUB V
1290249D1.MIT V
1290249E1.VEH V
1290249E1.TRA V
CM/S
SECS
A1
1290326M1.SUB V
1290326M1.MIT V
1290326M1.VEH V
1290326M1.TRA V
A2
1440902G1.SUB V
1440902F1.VEH V
A3
1290319E4.SUB V
1290319C4.MIT V
1290319E4.VEH V
1290319E4.TRA V

Figure 3.

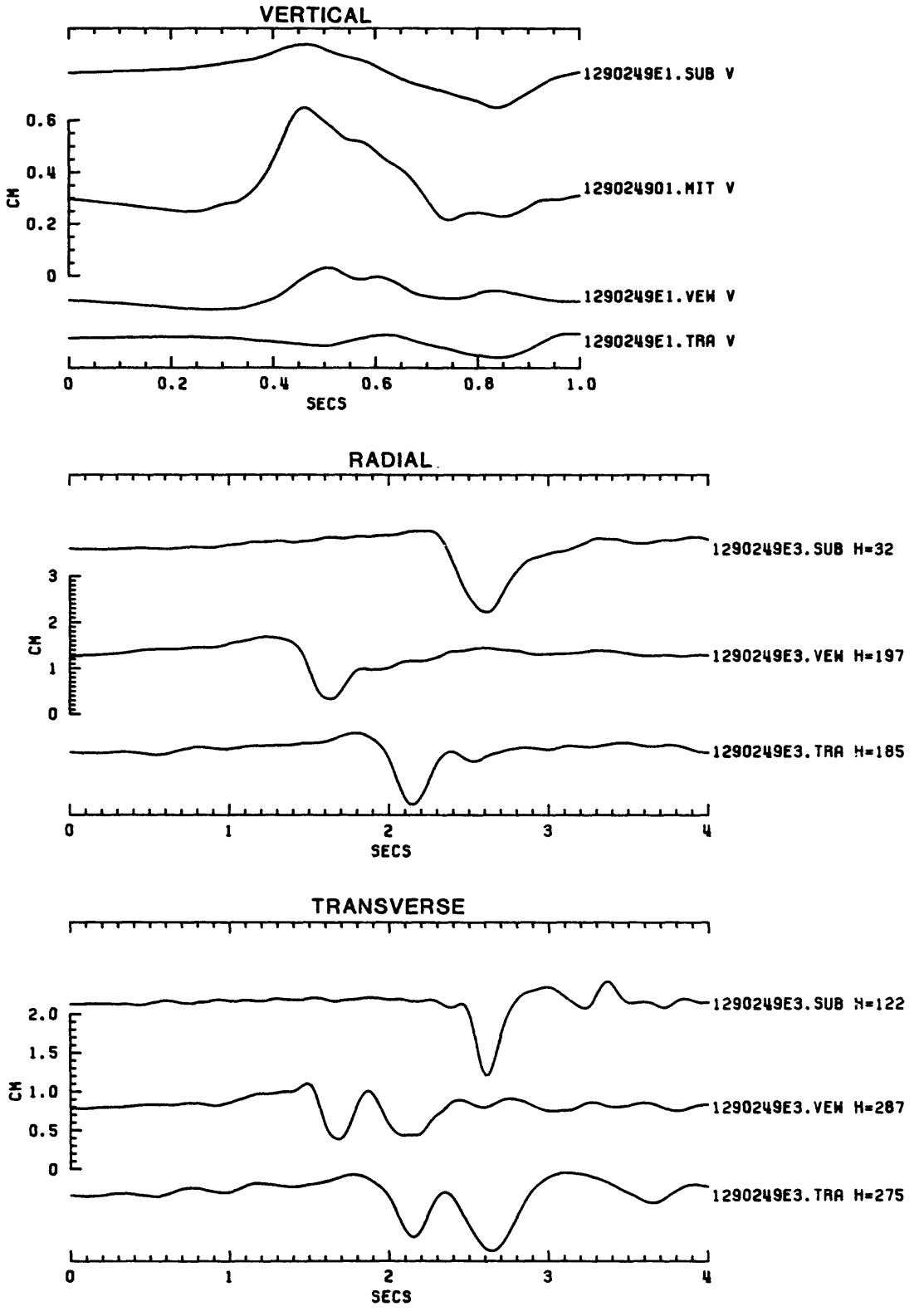
VERTICAL
1290249E1.SUB V
129024901.MIT V
1290249E1.VEH V
1290249E1.TRA V
CM
0.6
0.4
0.2
0
0
0.2
0.4
0.6
0.8
1.0
SECS
RADIAL
1290249E3.SUB H=32
1290249E3.VEH H=197
1290249E3.TRA H=185
CM
3
2
1
0
0
1
2
3
4
SECS
TRANSVERSE
1290249E3.SUB H=122
1290249E3.VEH H=287
1290249E3.TRA H=275
CM
2.0
1.5
1.0
0.5
0
0
1
2
3
4
SECS

Figure 4a.

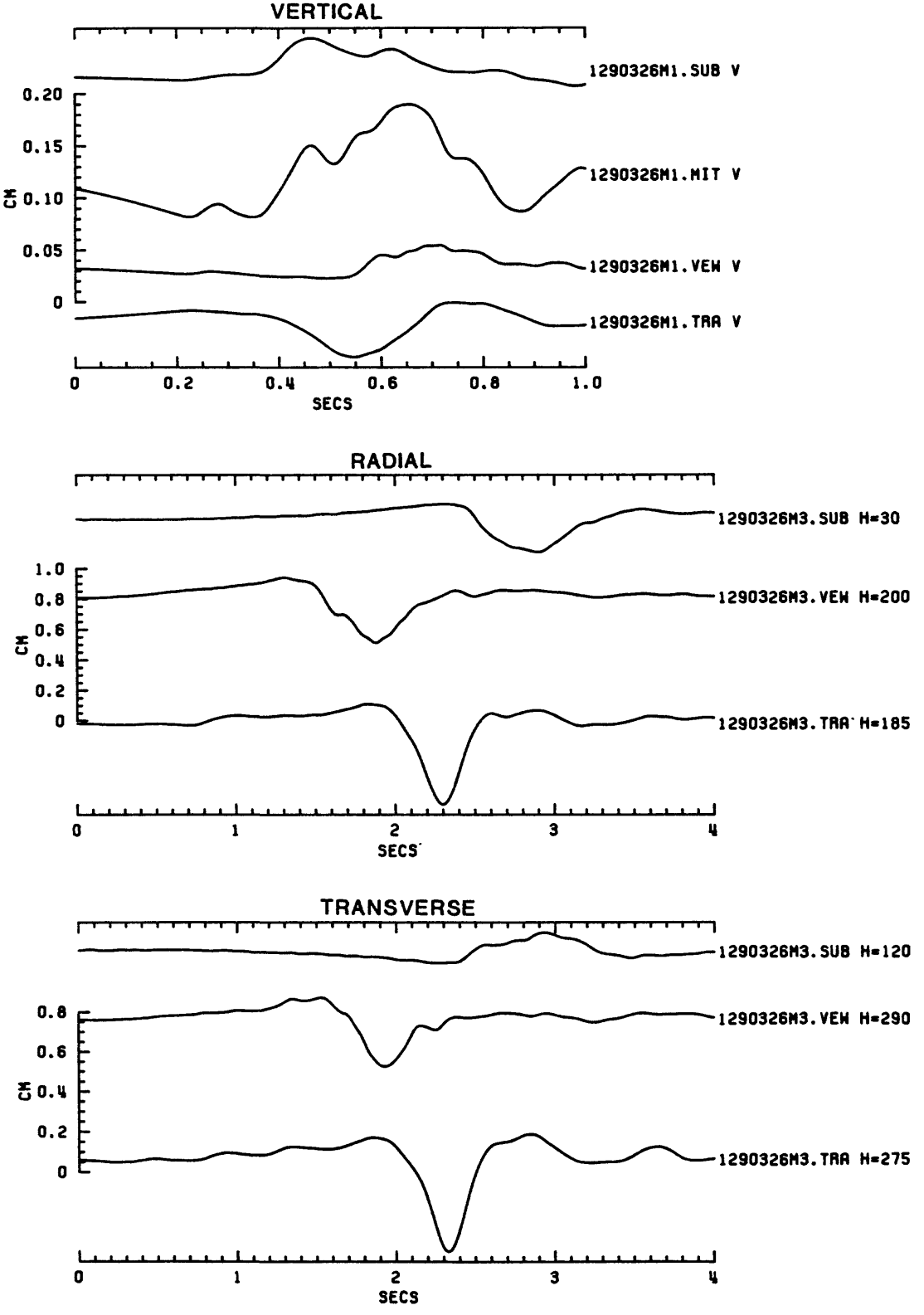
VERTICAL
1290326M1.SUB V
1290326M1.MIT V
1290326M1.VEW V
1290326M1.TRA V
0.20
0.15
0.10
0.05
0
CM
0
0.2
0.4
0.6
0.8
1.0
SECS
RADIAL
1290326M3.SUB H=30
1290326M3.VEW H=200
1290326M3.TRA H=185
1.0
0.8
0.6
0.4
0.2
0
CM
0
1
2
3
4
SECS
TRANSVERSE
1290326M3.SUB H=120
1290326M3.VEW H=290
1290326M3.TRA H=275
0.8
0.6
0.4
0.2
0
CM
0
1
2
3
4
SECS

Figure 4b.

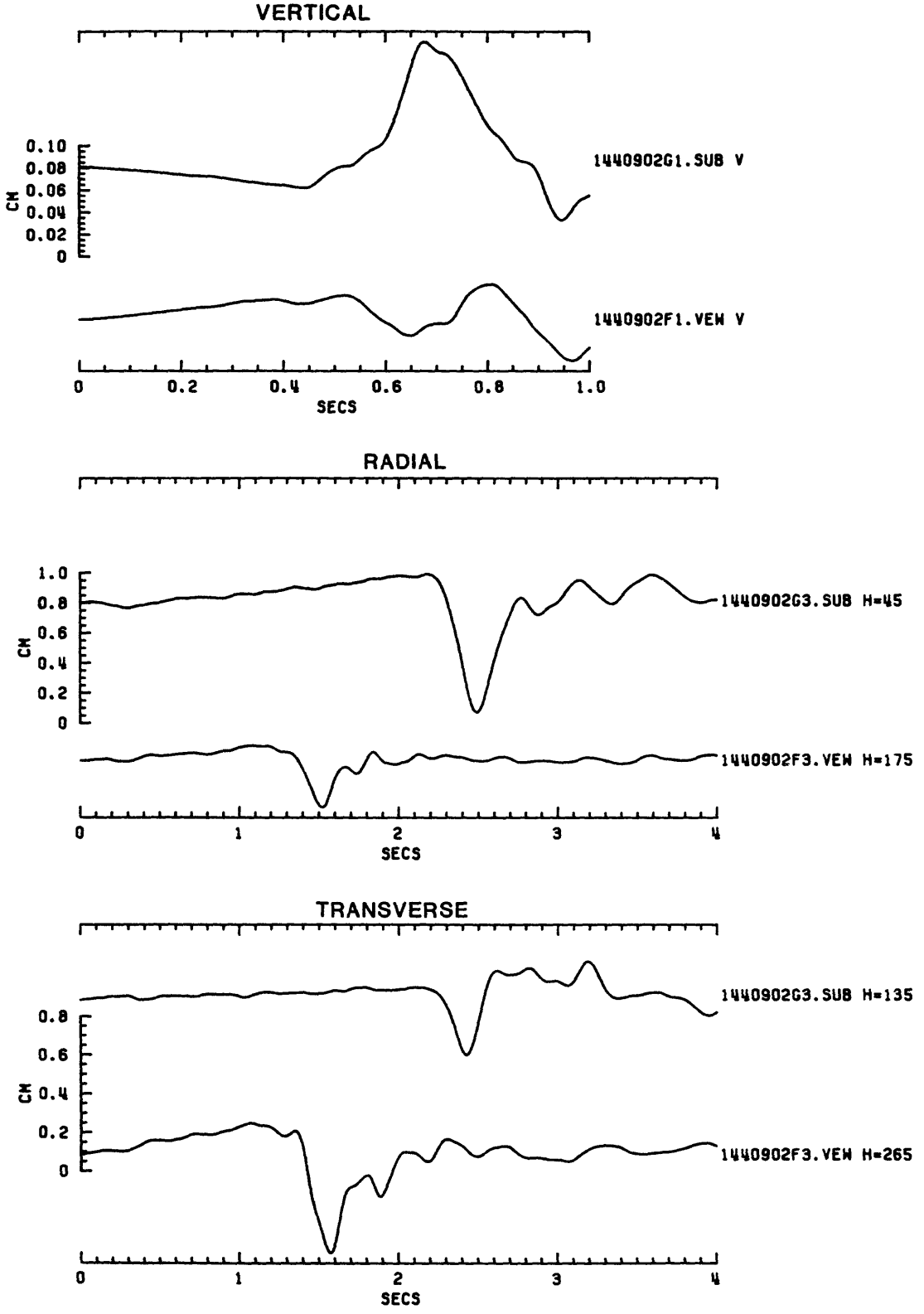
VERTICAL
0.10
0.08
0.06
0.04
0.02
0
CM
1440902G1.SUB V
1440902F1.VEW V
0
0.2
0.4
0.6
0.8
1.0
SECS
RADIAL
1.0
0.8
0.6
0.4
0.2
0
CM
1440902G3.SUB H=45
1440902F3.VEW H=175
0
1
2
3
4
SECS
TRANSVERSE
0.8
0.6
0.4
0.2
0
CM
1440902G3.SUB H=135
1440902F3.VEW H=265
0
1
2
3
4
SECS

Figure 4c.

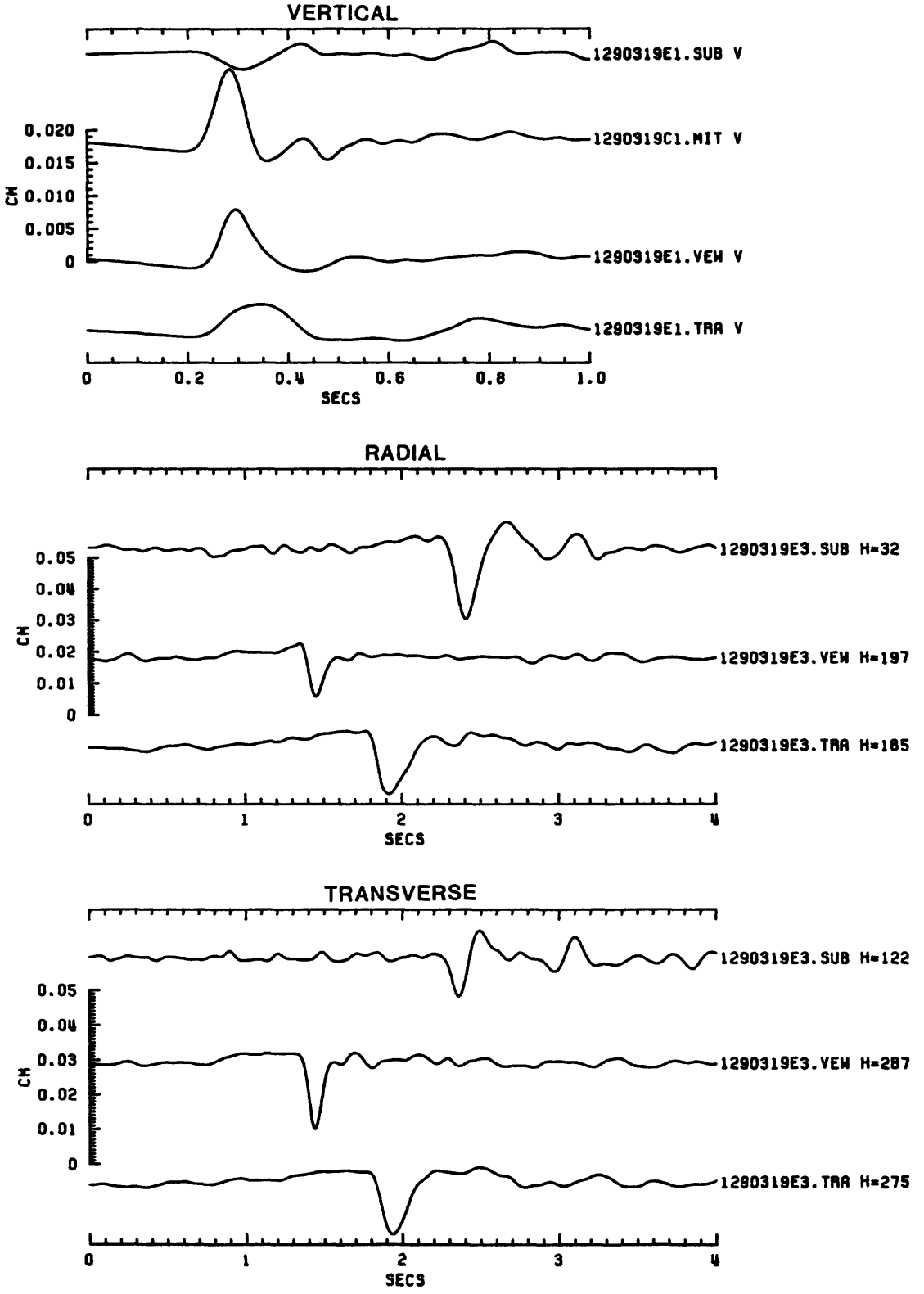
VERTICAL
1290319E1.SUB V
1290319C1.MIT V
1290319E1.VEW V
1290319E1.TRA V
0.020
0.015
0.010
0.005
0
CM
0
0.2
0.4
0.6
0.8
1.0
SECS
RADIAL
1290319E3.SUB H=32
1290319E3.VEW H=197
1290319E3.TRA H=185
0.05
0.04
0.03
0.02
0.01
0
CM
0
1
2
3
4
SECS
TRANSVERSE
1290319E3.SUB H=122
1290319E3.VEW H=287
1290319E3.TRA H=275
0.05
0.04
0.03
0.02
0.01
0
CM
0
1
2
3
4
SECS

Figure 4d.

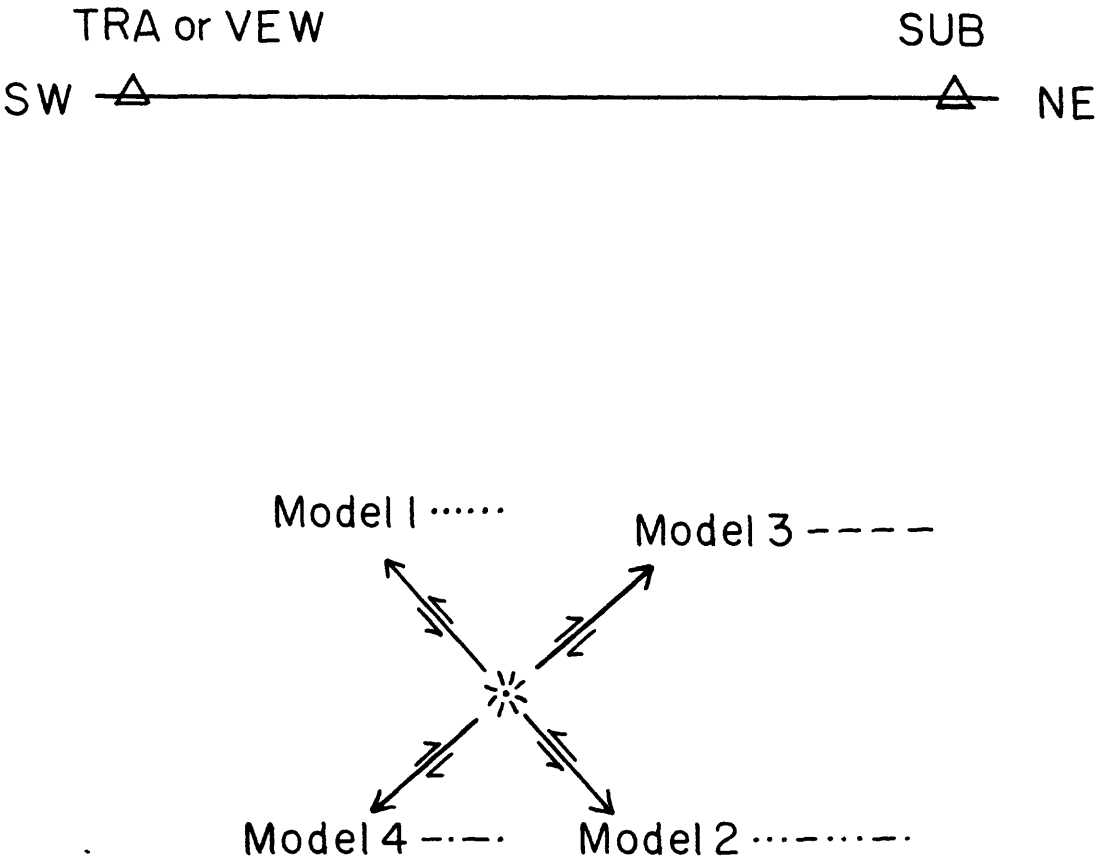

Figure 5.

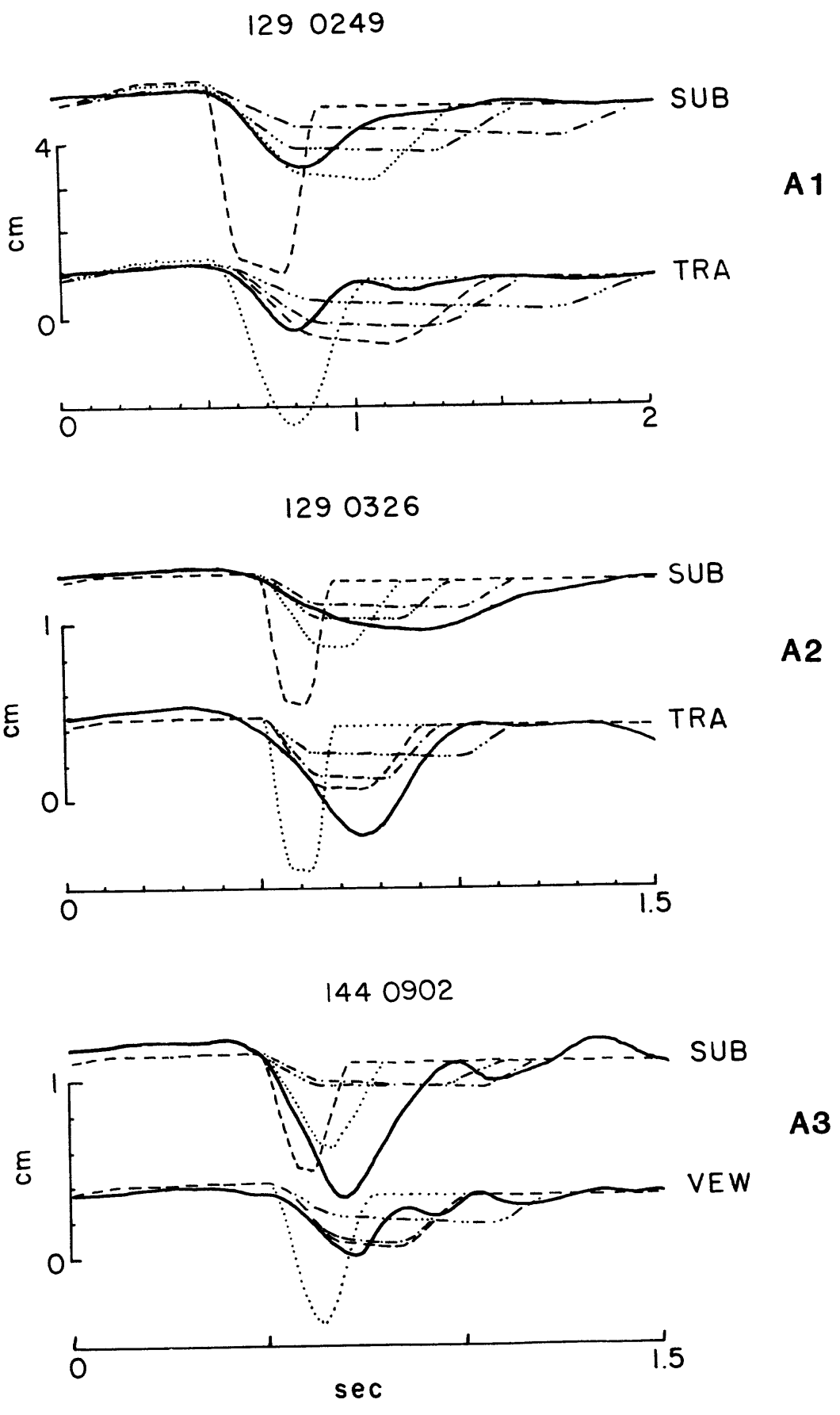
129 0249
SUB
TRA
A1
4
cm
0
0
1
2
129 0326
SUB
TRA
A2
1
cm
0
0
1.5
144 0902
SUB
VEW
A3
1
cm
0
0
1.5
sec

Figure 6.

RUPTURE OF THE NUNEZ FAULT DURING THE COALINGA EARTHQUAKE SEQUENCE

Michael J. Rymer, Katherine K. Harms, James J. Lienkaemper, and Malcolm M. Clark

U.S. Geological Survey
Menlo Park, California 94025

ABSTRACT

A 3.3-km-long right-reverse surface rupture developed along the Nunez fault at the time of a shallow M_L=5.2 earthquake on June 11, 1983. The surface rupture comprised two echelon segments trending about north-south, separated by a 0.4 km gap with a 0.3 km projected right stepover. The north and south segments are approximately 1.3 and 1.6 km long, respectively. Both segments of the Nunez fault dip about 65° to the east throughout most of their length. Displacement along the north segment consisted predominantly of reverse slip, with the east side up, and minor right-lateral components. Maximum reverse and right-lateral components of slip in the north segment were 64 and 20 cm, respectively. In the northern one-fourth of the south segment the relative proportion of slip components were similar to those in the north segment. Farther south in the south segment, however, the reverse component generally diminished and the right-lateral component was commonly dominant. Maximum reverse and right-lateral components of slip in the southern three-fourths of the south segment were 8 and 11 cm, respectively.

Near-field leveling and remeasurements of the fault scarp indicated the presence of afterslip, and indicated renewed rupture associated with at least one of four post-June 11 M_L>5.0 events on the Nunez fault. Cumulative afterslip was greatest near the northern ends of both of the fault segments. The afterslip rate on the north segment greatly diminished after July 27. However, as of May 22, 1984 slip was still occurring on the south segment, possibly compensating for lower coseismic displacement. Afterslip plotted against time on leveling lines near the north ends of the two segments show increased displacement rates or 'jumps' during the interval July 15 to 22, a period which included an M_L=6.0 earthquake, on July 22. We infer that this event was associated with renewed surface displacement greater than the rate of projected afterslip.

The hypocentral location and focal mechanisms of the four M_L>5.0 events after June 11 suggest that the dip of the fault decreases with depth. Aftershocks of the large July 22 event, which also renewed the surface rupture, generally coincide with the dip of the projected Nunez fault, supporting our model of the Nunez fault as a steeply dipping reverse fault which decreases in dip at depth.

INTRODUCTION

A 3.3-km-long right-reverse surface rupture developed along the Nunez fault at the time of a shallow M_L=5.2 earthquake on June 11, 1983. Afterslip and renewed surface rupture associated with at least one of four succeeding shocks (M_L>5.0) increased displacement along the fault. In contrast, no evidence of surface rupture was found for earlier events in the Coalinga earthquake sequence.

Ground and aerial searches immediately after the May 2 main shock (M_L=6.7) revealed cracks and fissures within about 10 km of the instrumental epicenter, but none of these surface breaks appeared to represent movement on deeply rooted fault structures (Clark and others, 1983). A possible exception to the apparent reported absence of surface faulting accompanying the May 2 event is reported by Hart and McJunkin (1983). However, the short length (<10 m) of this compressional feature across an unpaved road suggests that it was probably due to sympathetic movement on a minor fault or along a weakened bedding plane and therefore is not due to deeply rooted faulting. Further investigations of this site on September 29 showed that the road broken by the structure had been regraded and no evidence of fault movement survived.

In this paper we describe surface rupture along the Nunez fault, afterslip on the fault, and the probable configuration of the fault at depth and relations of these data to faulting processes associated with the 1983 Coalinga earthquake sequence. These data provide limitations to speculation on what occurred during the earthquake sequence in the Nunez fault area.

SURFACE FAULTING AND DISPLACEMENT

Coseismic slip associated with the June 11 earthquake is inferred for rupture along at least part of the Nunez fault. Ground breakage was first observed about 20 minuntes after the June 11 M_L=5.2 earthquake, when a local resident drove over the faulted surface of Los Gatos Road (E. J. Fowkes, oral commun., 1983). E. J. Fowkes visited this site about an hour after the event. Fowkes returned the next morning and mapped the rupture in the portion of the south segment north of Los Gatos Road and for about 20 m northwest of Los Gatos Creek. Rupture was first noticed in the north segment on June 12 when V. Birdwell drove over a faulted dirt road surface near the north end of the segment (oral commun., 1984). Rupture south of Los Gatos Creek was first observed on 24 June by J. P. Hughes (written commun., 1983). We searched for ground breaks in that area on June 14-15 but did not notice rupture south of the creek. We did not find the rupture either because of oversight or because the rupture developed after our visit, as afterslip, but before the visit by Hughes.

Figure 2 illustrates the extent of surface faulting discovered in our investigations of the Nunez fault. A 3.3-km segment of the fault broke at the ground surface during the June 11 earthquake. The surface faulting comprises two echelon segments trending about north-south; the north and south segments are approximately 1.3 and 1.6 km long, respectively. These segments are separated by a 0.4 km gap and a 0.3 km projected right stepover (fig. 2). The ruptured segments correspond approximately to the north four-fifths of the known surface expression of the fault, from geologic evidence. Displacement in the north segment of the 1983 rupture consisted dominantly of reverse,

dip-slip, with the east side up, and a minor right-lateral component. Maximum reverse and right-lateral components of slip in the north segment are 64 and 20 cm, respectively (table 1, fig. 3). Slip components in the south segment, but north of Los Gatos Road, were in similar proportions to those in the north segment, that is reverse movement was greater than right-lateral movement. South of Los Gatos Road, however, the dip-slip component generally diminished or vanished and the right-lateral component of surface slip was commonly, though not everywhere, dominant. South of Los Gatos Road the maximum reverse and right-lateral components of slip are 8 and 11 cm, respectively. Surface rupture location and general sense of displacement all along the Nunez fault are consistant with those of earlier faulting episodes, as determined from field relationships in trenches and natural exposures.

The Nunez fault dips steeply to the east throughout most of its length. Dip measurements of about 65° were made in a dry creek bed about 400 m south of the north end of the 1983 rupture, in the roadcut along Los Gatos Road, and in Post Canyon, about 200 m south of 1983 rupture (fig. 2). The predominately steep dip is indicated by the relatively straight course of the fault across topographic irregularities. One possible exception to the steepness of dip is at the north end of the fault. A trench dug approximately 20 m southwest of hill 1534 (fig. 2) revealed a dip of about 45° to the east. Deflection of the fault trace north of this site eastward into a topographic low also indicates a local decrease in dip of the fault plane.

NEAR-FIELD LEVELING

We installed nine leveling lines across the Nunez fault to measure vertical afterslip and possible offset accompanying aftershocks (figs. 2, 3). Lines N1 through N8 comprised brass bench marks attached to 1.5-m-long copper-coated steel rods pounded into the ground. These lines were placed perpendicular to the fault and each consists of six benchmarks, three on each side of the fault. Line N9 consists of 13 nails driven into the pavement on the south edge of the repaved Los Gatos Road; the nails are spread equally across the fault. The lines range in length from 18 to 60 m as constrained by local topography. Time of installation of the lines varied; lines N1 to N6 were installed on July 13-14, line N9 on July 23, and lines N7 and N8 on July 27. A Wild NAK-2 level was used with a fiberglass rod and sighting distances no greater than 25 m. All leveling surveys were conducted under similar climatic conditions. We estimate maximum errors in the relative elevation determined at each station to be $\pm$ 2.0 mm. Local erratic changes in relevelings are probably due to nontectonic processes affecting the ground rather than surveying errors.

For all surveys the same instrument was used; the same rod was used on all but the last survey, but both rods were calibrated. The elevation changes reported here are not fixed to any survey monuments beyond the limits of the lines. We arbitrarily chose the western end points of the lines as fixed datums.

The first releveling, on July 22, following the M_L=6.0 earthquake of that morning, clearly demonstrated that surface displacement had occurred since July 15 (see figs. 3, 4). For simplicity, we define offset to be the relative uplift of the east end of each line above the west end. Offsets were largest near the north ends of the two fault segments, at lines N2 and N6,

measuring 2.2 and 3.1 cm, respectively (fig. 3). A second releveling, on July 27-28, after the July 25 M_L=5.3 event on the Nunez fault, suggested the possibility of small continuing movement, but offsets were near the noise-level for all sites.

The releveling of January 30-31, 1984, showed the most surprising results; six of nine leveling lines clearly showed further slip during a period in which the largest event on the Nunez fault was only M_L=4.1 (September 1, 1983). Lines N3, N4, and N5 along the southern portion of the northern segment of Nunez fault showed negligible change; while N6 near the north end of the north segment showed 0.4 cm. The greatest change, 2.6 cm, occurred on N2, near the north end of the south segment. Lines N1, N9, N7, and N8 showed strong continuing movement elsewhere on the south segment, measuring 1.0, 1.4, 0.9, and 1.1 cm, respectively (fig. 3C).

The greatest accumulated vertical slip since July 15 has occurred near the northern ends of the two segments of the Nunez fault, at lines N6 and N2. Cumulative afterslip as determined by leveling at these two sites is 3.5 and 5.1 cm, respectively. Unfortunately, lines N7 and N8, south of Los Gatos Road were not installed until July 28-29. There, and on line N9, the 1 cm post-July 27-28 movement suggests that these locations may have had earlier offsets similar in size to those at N6 and N2, but we cannot prove this. Nevertheless, the highest rates of vertical slip in this latest period all occurred in the south segment of the Nunez fault, the portion that showed relatively smaller coseismic displacement (fig. 3A).

Timing of afterslip is incomplete, because no leveling data are available for the important June 11 to July 15 interval. If vertical afterslip on the Nunez fault accumulated as a linear function of a logarithm of time (see, for example, Sharp and Lienkaemper, 1982), then the critical period for measuring afterslip was immediately after the June 11 event.

The available leveling does, however, suggest accumulation of afterslip with time. Cumulative offset across three lines with relatively high signal to noise ratio, lines N6, N2, and N1, are shown in figure 4, plotted logarithmically against time. For line N1 the least squares fit to cumulative offset versus time is very strong: correlation coefficient (R) = 0.99, standard deviation (σ) = 1.0 mm. However, the fit of offset from lines N6 and N2 versus time is not as compelling: R = 0.55, σ = 16.7 mm, and R = 0.91, σ = 10.6 mm, respectively. If offset accumulates linearly in proportion to log(time), then the changes measured after the July 22 M_L=6.0 earthquake are clearly much higher (1.5-3 cm) than predicted from the least squares curves of lines N6 and N2 (fig. 4). Line N1, in contrast, shows no deviation from a log(t) relation for that period. The July 25 M_L 5.3 event caused no deviation in slip rates from the least squares relation to log(t) for lines N1, N2, and N6.

Scarp heights near line N2 were remeasured after the July 9 M_L=5.4 earthquake that suggest a small (~1 cm) increase occurred in the intervening period (table 1). Figure 5 shows the combination of the repeated field measurements of the scarp height along with repeated leveling. The validity of fitting afterslip to a log(t)-curve is not contradicted. The behavior of the fault at the site of N2 before June 16 must be inferred from other data; the log(t) curve should not be projected backward in time. At time t = 0.02

days or 29 minutes, the total offset would project to zero; this disagrees strongly with: (1) large pavement offsets at Los Gatos Road (about 300 m to the south of line N2) some 20 minutes after the June 11 M_L=5.2 event, and (2) seismic moments computed from teleseismic data agree with the geometric moment from scarp heights, suggesting a large coseismic slip.

The nature of afterslip in the first 5 days following the June 11 M_L=5.2 event is obscure. Probably a majority of the vertical offset measured on the scarp on June 16 is coseismic. On the leveling arrays for which vertical afterslip was higher than noise level and which have at least three measurements (lines N1, N2, and N6), a logarithmic decline with time appears to be reasonable. Leveling lines at the northern ends of the two segments of Nunez fault show vertical slip during and after the M_L=6.0 earthquake of July 22 which far exceeded a log(t) rate of slip. The afterslip history of the south fault segment south of Los Gatos Road is unknown until 89 days after the June 11 M_L=5.2 earthquake. Since then, slip rates have been higher in the southern segment than at most of the lines across the northern segment, which suggests that slip deficiency in the southern zone is being compensated with afterslip.

SEISMIC MOMENT

Instrumentally determined seismic moment and calculations of seismic moment from surface displacements of the June 11 earthquake bear on the timing of slip on the Nunez fault and the earthquake's relation to the mainshock. The moment of the June 11 event was calculated to be $M_O = 1.7 \times 10^{24}$ dyne-cm from teleseismic long-period (>20 s) compressional waves (USGS, 1983). Uhrhammer and others (1983) calculated a moment of 1.1×10^{24} dyne-cm from broadband displacement seismograms. In the following calculations we use 34 cm as the average surface displacement, the vector sum of the intergrals of both curves in figure 3A. Width of the fault is estimated to be equivalent to the down-dip distance to the hypocentral depth (4.5 km), or about 5.2 km. We assume ruptured fault length is the same as length of surface rupture, 3.3 km. Calculation of moment using the formula $M_O = \mu dlw$, where μ (shear modulus) = 3.0×10^{11} dyne/cm^2, d (average displacement) = 34 cm, w (fault width) = 5.2 km, and l (fault length) = 3.3 km, results in 1.8×10^{24} dyne-cm, which is in close agreement with the seismologically determined values. The agreement of all three values, especially between our value and the long-period determination, implies that most slip was released seismically during the earthquake, which is also suggested by the timing of field observations, discussed above.

In contrast, seismic moment calculations for the May 2 mainshock are, in general, more than an order of magnitude greater than those of the June 11 event. Choy (this volume) determined that the May 2 earthquake was actually a double event, although for the purposes of our comparison, we treat it as a single event; Choy determined a total seismic moment of 2.7×10^{25} dyne-cm. Moment calculations for the May 2 earthquake by other investigators are 6-7 x 10^{25} dyne-cm from geodetic estimates (Stein, this volume), 3.8×10^{25} dyne-cm from teleseismic long-period (5 s) compressional waves (Hartzell and Heaton, 1983), 2.3×10^{25} dyne-cm from broadband displacement seismograms (Uhrhammer and others, 1983), and 5.4×10^{25} dyne-cm from very long period (250 s) surface waves (Kanamori, 1983). Thus the average moment of the June 11 event is about 1/30 of the moment of the May 2 event, even though the June

11 event was apparently the only one to experience deeply rooted surface rupture in the Coalinga sequence.

ORIENTATION OF THE FAULT

In figure 6, the hypocenters of the large post-June 11 events (M_L>5.0) and their focal mechanisms have been projected onto a plane perpendicular to the Nunez fault. We show a 65° dip of the fault at the surface, as measured in the field. At depth, we decrease the dip to accomodate the east-dipping nodal planes, which presumably represent the fault plane. In figure 6 we also show three days of aftershocks of the larger July 22 event (see also fig. 7). The hypocentral distribution of aftershocks shown in figure 7B agrees with a decrease of dip on the Nunez fault at depth and with our choice of the east-dipping nodal plane as the fault plane. Aftershocks from the May 2 main shock in the same area, but before June 11, show a similar albeit more diffuse pattern that generally supports the inferred dip of the fault (fig. 8). Note that the events deeper than our proposed model of the Nunez fault tend to be distributed along a nearly horizontal plane at a depth of 10 to 13 km.

DISCUSSION AND CONCLUSIONS

Mapping of surface rupture and displacement along the Nunez fault after the shallow (~4.5 km depth) June 11 M_L=5.2 earthquake shows that surface rupture occurred on two approximately north-trending en echelon segments that have a total length of 3.3 km (fig. 2). Right-reverse movement occurred, with the east side up relative to the west side. The earthquake and surface rupture are clearly related. The rupture was discovered about 20 minutes after the event and the close agreement of teleseismically and geometrically determined seismic moments suggests predominantly coseismic slip.

Coseismic slip was unevenly distributed along the Nunez fault. In the north segment the reverse component of slip was dominant; the right-lateral component amounted to about one third the reverse component. Maximum values of reverse and right-lateral components measured in the north segment are 64 and 20 cm, respectively. In the portion of the south segment north of Los Gatos Road only reverse components of slip were observed, with maximum slip of 18 cm. In the portion of the south segment south of Los Gatos Road the right-lateral component generally exceeds the reverse component, with maximums of 11 and 8 cm, respectively.

Afterslip is documented on nine leveling lines across the Nunez fault. Cumulative afterslip is greatest near the northern ends of both of the fault segments (fig. 3). Afterslip rate on the north segment has greatly diminished since the July 27 earthquake. However, as of May 22, 1984 slip was still occurring on the south segment, apparently in compensation for lower coseismic displacement (compare fig. 3A with 3C). Afterslip plotted against log(time) on leveling lines N2 and N6 (at the north ends of the two segments) show increased displacement rates or 'jumps' during the interval July 15 to 22, a period which includes the M_L=6.0 July 22 earthquake (fig. 4). We infer that this event was associated with renewed surface displacement greater than the rate of projected afterslip.

Five large events M_L>5.0 have been located in the vicinity of the Nunez fault (Eaton, this volume), and their focal mechanisms suggest that the dip of

the fault decreases with depth. The larger of the July 22 events was associated with renewed surface rupture, and its aftershocks generally coincide with the dip of the Nunez fault plane as we have modeled it. Furthermore, there is little evidence to suggest that activity was along the west-dipping nodal plane. We therefore believe that the Nunez fault is a steeply dipping reverse fault near the ground surface with dip decreasing at depth.

REFERENCES CITED

Clark, M. M., Harms, K. K., Lienkaemper, J. J., Perkins, J. A., Rymer, M. J., and Sharp, R. V., 1983, The May 2, 1983 earthquake at Coalinga, California: The search for faulting, in Borcherdt, R. D., compiler, The Coalinga earthquake sequence commencing May 2, 1983: U.S. Geological Survey Open-File Report 83-511, p. 8-11.

Eaton, J. P, 1984, The May 2, 1983 Coalinga earthquake and its aftershocks: a detailed study of the hypocenter distribution and of the focal mechanisms of the larger aftershocks: this volume.

Choy, L. G., 1984, Source parameters of the Coalinga, California earthquake of May 2, 1983 inferred from broadband body waves: this volume.

Hart, E. W., and McJunkin, R. D., 1983, Surface faulting northwest of Coalinga, California, June and July 1983, in Bennett, J. H., and Sherburne, R. W., eds., The 1983 Coalinga, California earthquakes: California Division of Mines and Geology Special Publication 66, p. 201-219.

Hartzell, S. H., and Heaton, T. H., 1983, Teleseismic mechanism of the May 2, 1983 Coalinga, California, earthquake from long-period P-waves, in Bennett, J. H., and Sherburne, R. W., eds., The 1983 Coalinga, California earthquakes: California Division of Mines and Geology Special Publication 66, p. 241-246.

Kanamori, Hiroo, 1983, Mechanism of the 1983 Coalinga earthquake determined from long-period surface waves, in Bennett, J. H., and Sherburne, R. W., eds., The 1983 Coalinga, California earthquakes: California Division of Mines and Geology Special Publication 66, p. 233-240.

Sharp, R. V., and Lienkaemper, J. J., 1982, Preearthquake and postearthquake near-field leveling across the Imperial fault and the Brawley fault zone, in The Imperial Valley, California, earthquake of October 15, 1979: U.S. Geological Survey Professional Paper 1254, p. 169-182.

Stein, R. S., 1984, Evidence for surface folding and subsurface fault slip from geodetic elevation changes associated with the 1983 Coalinga, California, earthquake: this volume.

Uhrhammer, R. A., Daragh, R. B., and Bolt, B. A., 1983, The 1983 Coalinga earthquake sequence: May 2 through August 1, in Bennett, J. H., and Sherburne, R. W., eds., The 1983 Coalinga, California earthquakes: California Division of Mines and Geology Special Publication 66, p. 221-231.

U.S. Geological Survey, 1983, Preliminary determination of epicenters: Monthly listing, June, 1983: U.S. Geological Survey, National Earthquake Information Service, p. 4.

Table 1. Reverse and right-lateral slip components along the Nunez fault.

Locality (fig. 2)	Distance along Reference line (m) (see fig. 3B)	Slip component (cm) 1/ Vertical 2/	Lateral	Days after June 11
		NORTH SEGMENT		
1	98	20	12	3
2	179	15	--	5
		18-20	--	33
3	252	25	--	6
		25-30	--	33
4	289	15	--	6
		15	--	33
5	300	32	--	6
		48	--	33
6	316	30-40	--	6
7	341	37	--	5
8	354	42-50	4-11	5
		~47	--	35
		64 * 3/	--	35
9	461	12	--	35
10	482	40	--	5
11	678	--	18	5
		5	18	35
12	689	5	4	5
13	711	15	--	5
		18-20	--	35
14	720	40	15	5
15	730	12-13	--	6
		13	--	35
16	782	40	<1	5
		45-50	--	34
17	811	35	--	5
18	887	50	--	5
19	950	10-15	--	6
		16-17	--	34
20	954	--	20	79
21	968	9	17	6
		9	--	34
22	990	35	--	5
23	1018	30	--	6
		45	--	34
24	1034	42-47	--	6
		30-40	--	34
25	1062	8-9	<1	6
		~5	--	34
26	1159	5	--	17
		9-10	--	34
27	1243	10	--	17

Table 1, continued.

Locality	Distance along Reference line (m)	Slip component (cm) 1/ Vertical 2/	Lateral	Days after June 11
		SOUTH SEGMENT		
28	1810	10	--	5
		10-12	--	31
29	1856	15	--	5
		15-16	--	31
30	2025	10	--	5
		10-11	--	31
31	2065	12	--	5
		13	--	31
32	2084	10	--	5
33	2262	<1	1.2	47
34	2345	<1	1.3	47
35	2418	<0.5	2.2	47
36	2823	--	6	48
37	2850	7	8	48
38	2904	5-6	8	48
39	2942	<3	9	48
40	2975	7	6	48
41	3070	5	8-11	47
42	3099	4	1.5	47
43	3136	4	1	47
44	3158	2	2	47
45	3255	1	1	48

Locality	Distance SW of juncture with main fault (m)	Slip component (cm) 1/ Vertical	Lateral	Sense of movement	Days after June 11
		BRANCH FAULT (north segment)			
50	49	17	--	E side up	39
51	92	10	--	W side up	39
52	117	7	--	W side up	39
53	142	<1	--	E side up	39
54	152	4	--	E side up	39
55	209	--	--	3 cm extension	39
56	222	11	--	E side up	39
57	244	6	--	E side up	39
58	281	2	--	W side up	39
59	306	4	--	E side up	39
60	361	<1	--	E side up	39
61	398	<1	--	W side up	39

Table 1, continued.

Locality	Slip component (cm) 1/ Vertical	Lateral	Sense of movement	Days after June 11
	SECONDARY FAULT (south segment)			
75	0.5	0.5	W side up	48
76	2	--	W side up, reverse	48
77	0.5	--	W side up, 3 cm extension	48

1/ Slip components as measured in the field with scale or tape; leveling data (fig. 3C) not included in table.

2/ The reverse component of slip can be derived by multiplying the vertical component of slip as measured in the field by 1/sine of the dip of the fault, where known (reverse component of slip indicated by astrisk (*)).

3/ The 64 cm reverse component is derived from leveling over a 10-m-wide zone across the fault. Vertical slip of 58 cm was determined at this site along with an accurate dip measurement of 65°, resulting in the maximum reverse slip along the Nunez fault.

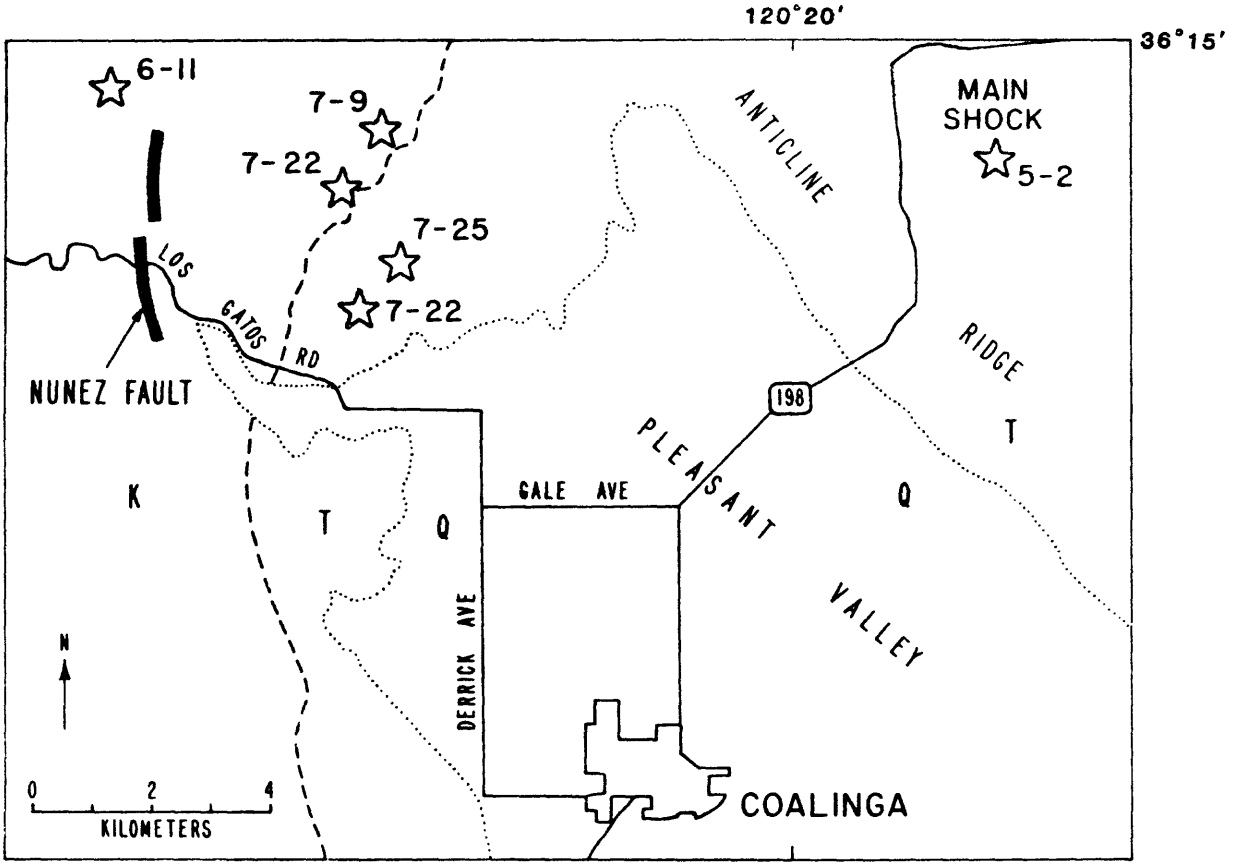

Figure 1. Index map showing location of Nunez fault, which ruptured at the surface in association with an M_L=5.2 earthquake on June 11, 1983. Stars denote location of earthquakes M_L>5.0, with dates, on or near the Nunez fault, solid star denotes location of May 2, 1983 Coalinga mainshock. K = Cretaceous strata, T = Tertiary strata, and Q = Quaternary deposits.

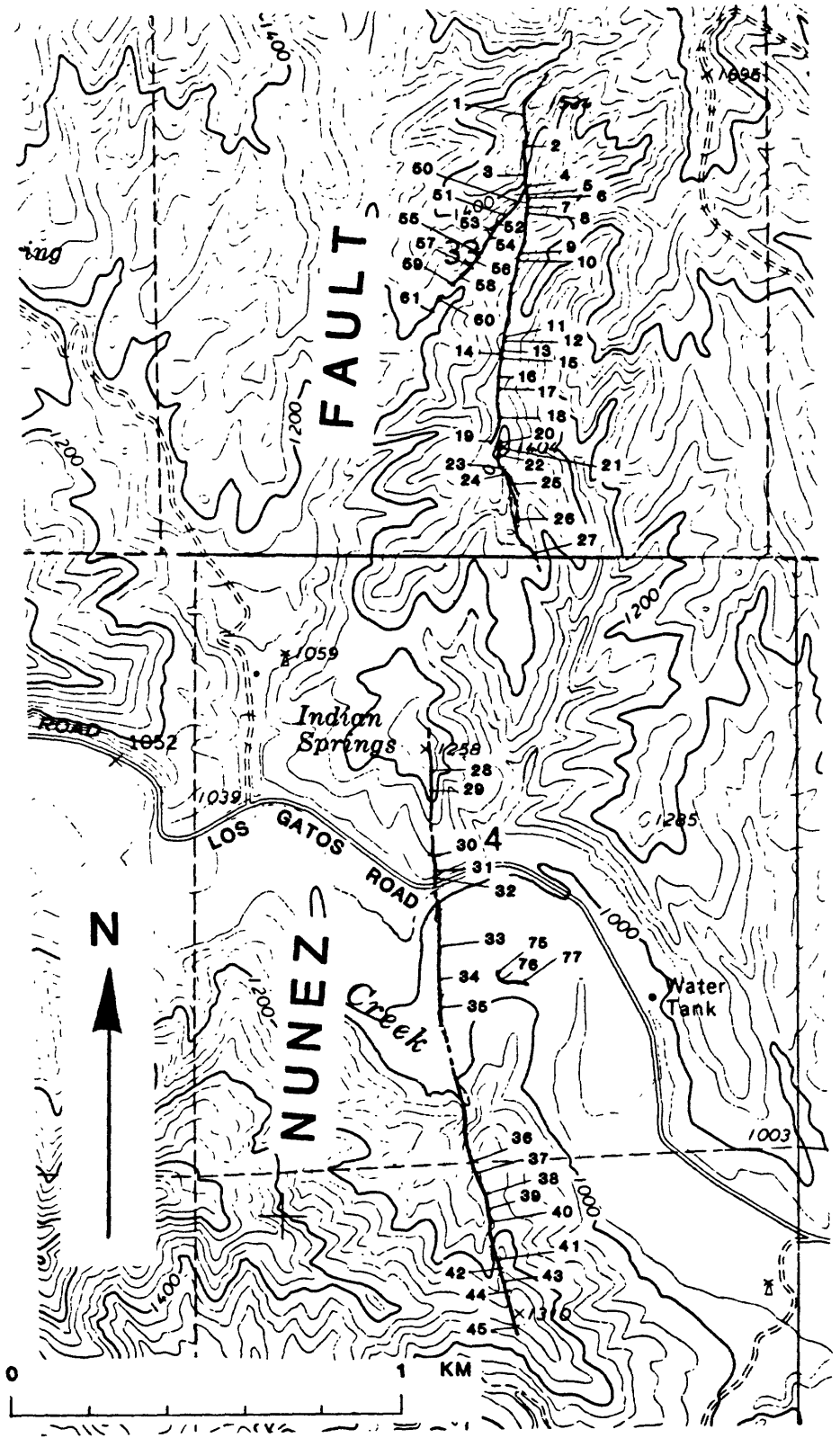

Figure 2. Map showing surface faulting (heavy line) along the Nunez fault associated with the June 11 M_L 5.2 earthquake. Circled numbers indicate locality of measured offset feature, shown in figure 3 and table 1.

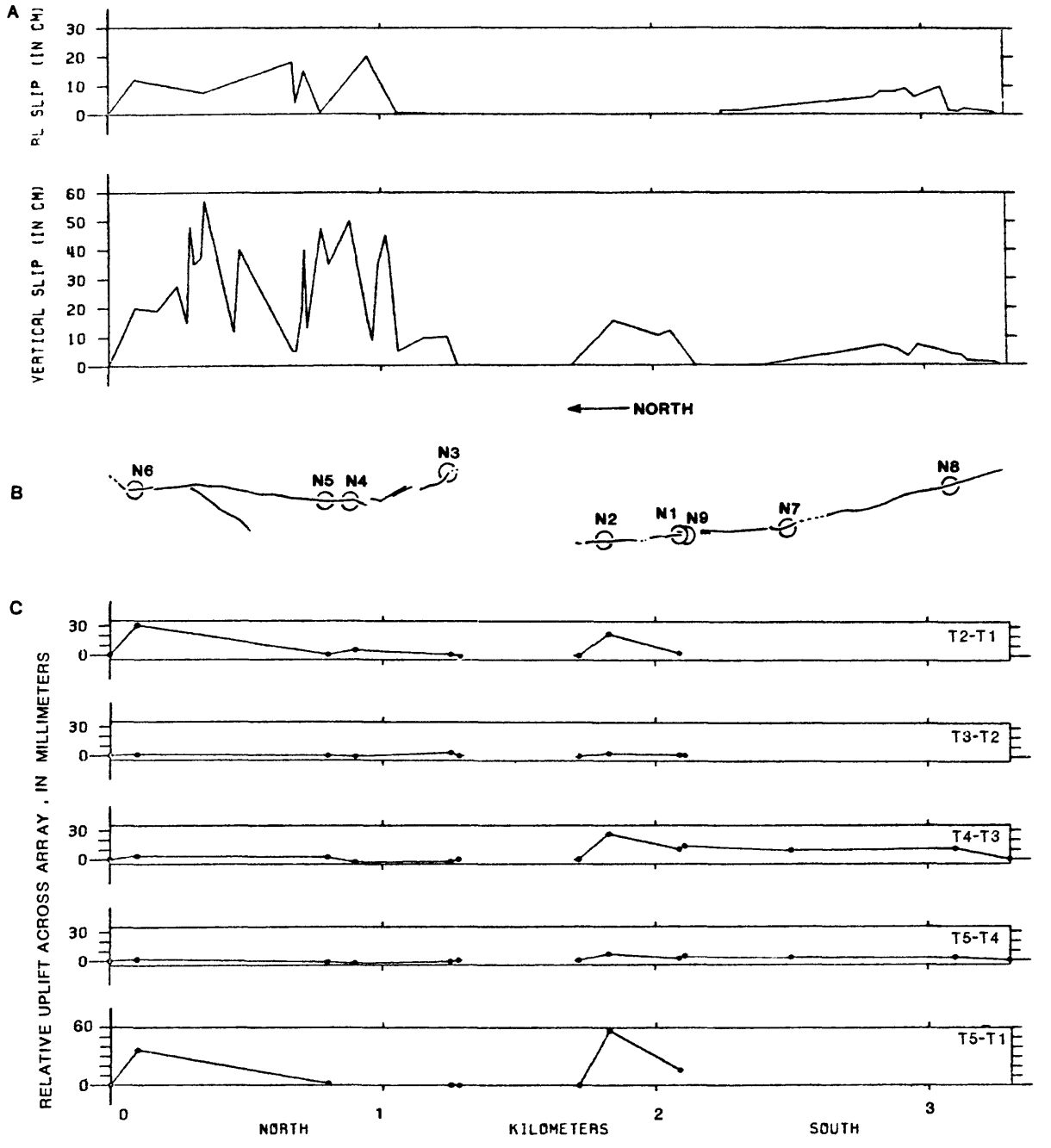

Figure 3. A, cumulative right-lateral and vertical components of slip as a function of distance along the Nunez fault for the 1983 break. Plots of slip do not include displacement on branch and secondary faults and do not include afterslip measured along leveling lines. B, map of surface ruptures. Reference line (see table 1) is an imaginary north-south line with its origin at the north end of 1983 rupture. C, changes in relative elevation measurements along leveling profiles across the Nunez fault for different time intervals (survey time T_1 = July 15, 1983; T_2 = July 22-23; T_3 = July 27-28; T_4 = January 30-31, 1984; and T_5 = May 22). Profiles are labeled on the fault trace as N1 to N9.

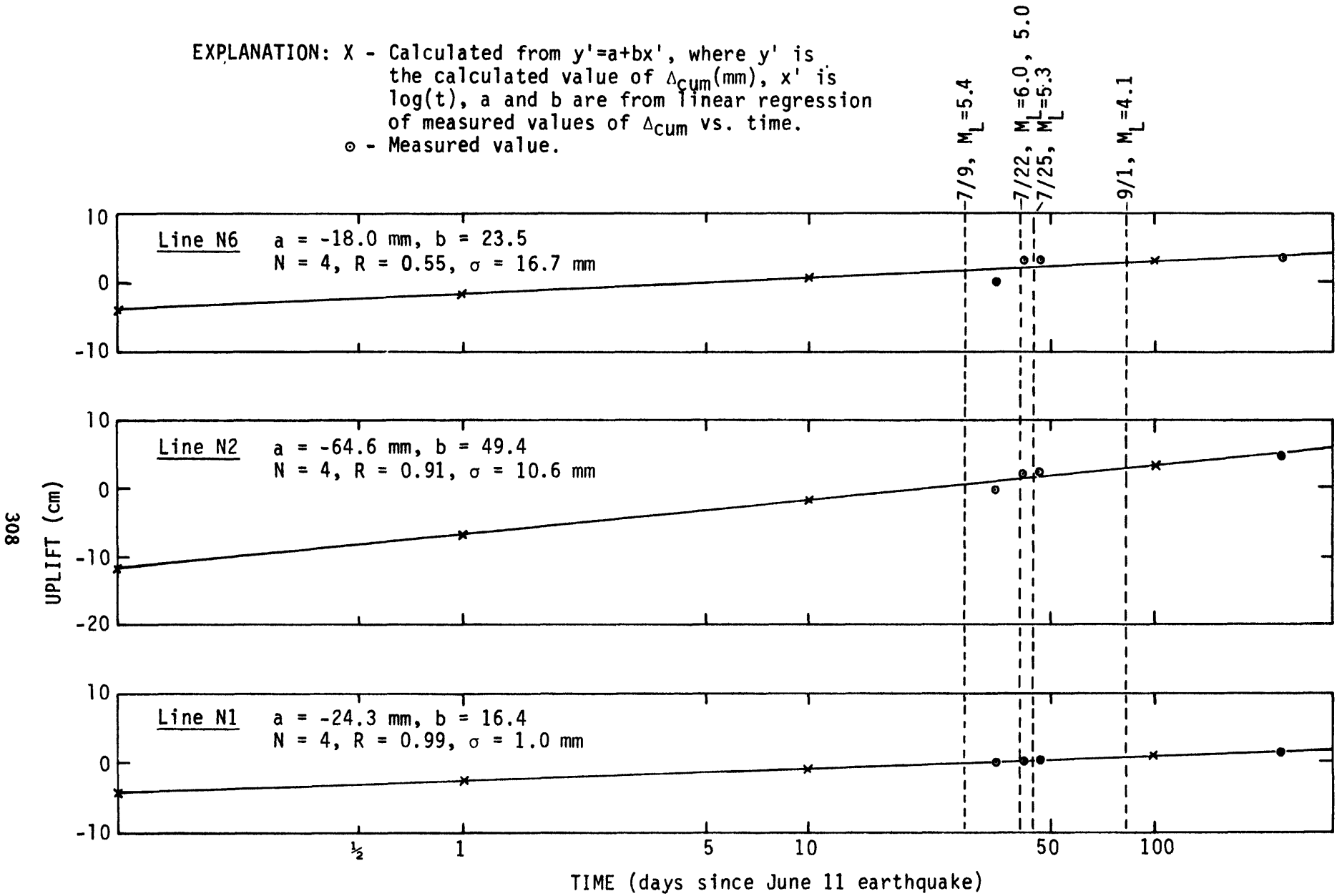

Figure 4. Cumulative vertical displacement as a function of postearthquake time along leveling lines N1, N2, and N6. Solid line is ordinary least squares fit to measurements.

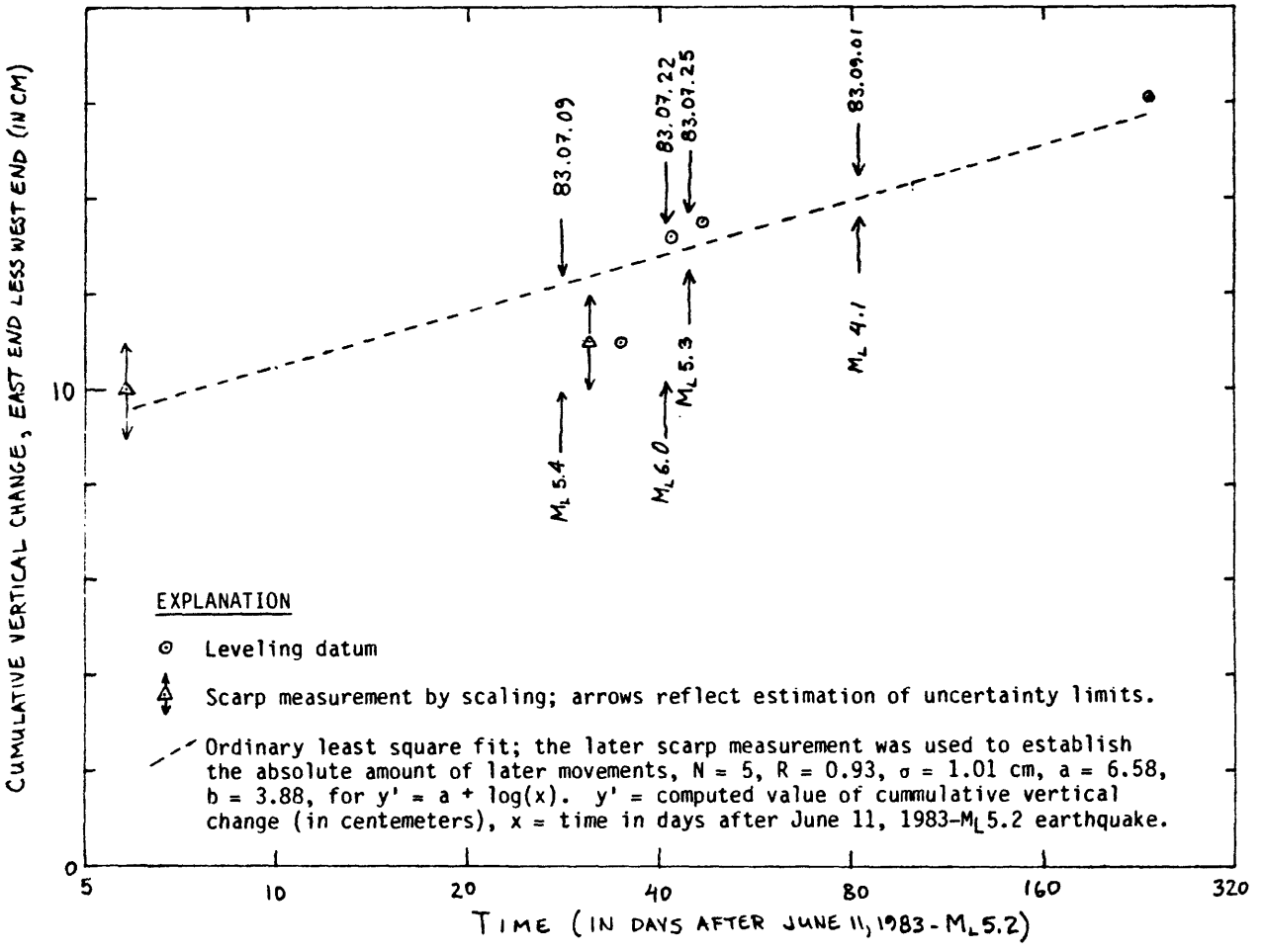

Figure 5. Composite of slip history from direct scarp measurement and leveling along level line N2, see figure 3 for location. Arrows toward dashed line indicate time of large earthquakes on Nunez fault.

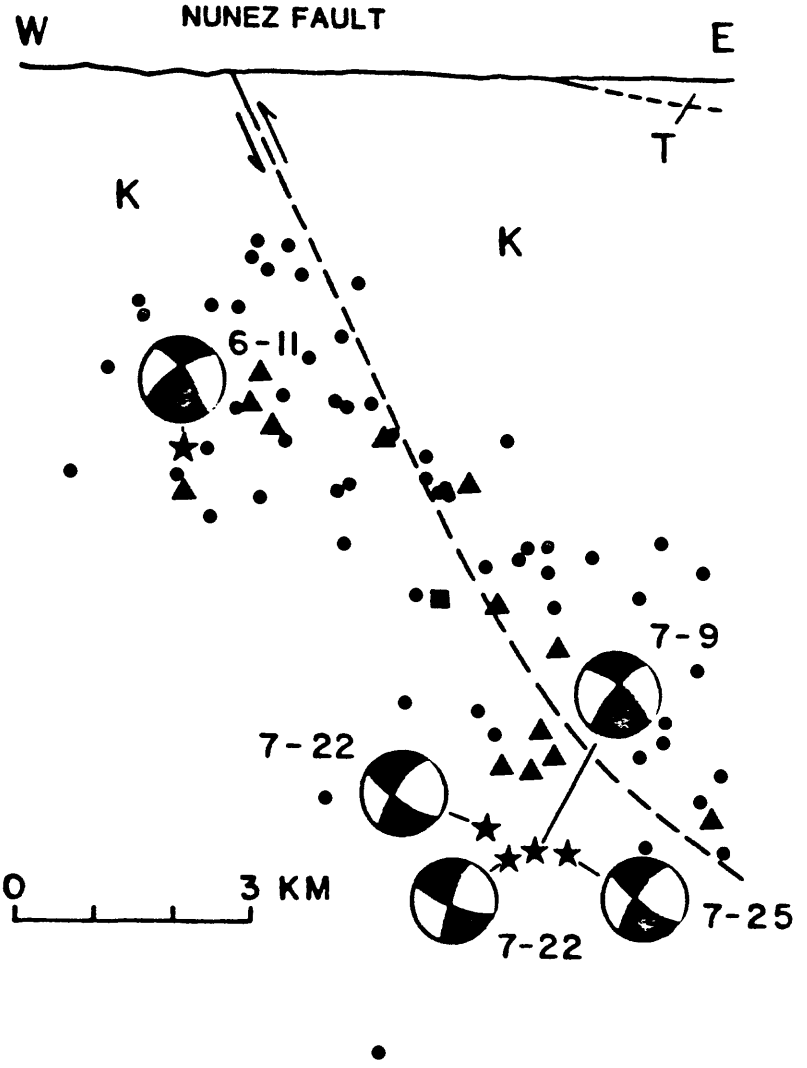

Figure 6. East-west cross section of the Nunez fault (shown as dashed line) showing hypocentral location and focal mechanisms of nearby M_L>5.0 earthquakes (stars) projected to the plane of section. Also plotted are aftershocks (from July 22 to 25 only) of the large event of July 22. These aftershocks are from northern California seismic network (Calnet): dots represent M_L<2.5, triangles, 2.5<M_L<3.5, and square, 3.5<M_L<4.5. Focal mechanisms are shown in cross section, that is, a northern hemisphere projection. The dip of the Nunez fault is shown as 65° near the surface (from field observations) and decreases at depth, as indicated by the east-dipping nodal planes of the M_L>5.0 earthquakes. K = Cretaceous, T = Tertiary; no vertical exageration. (Focal mechanisms modified from Eaton, 1983).

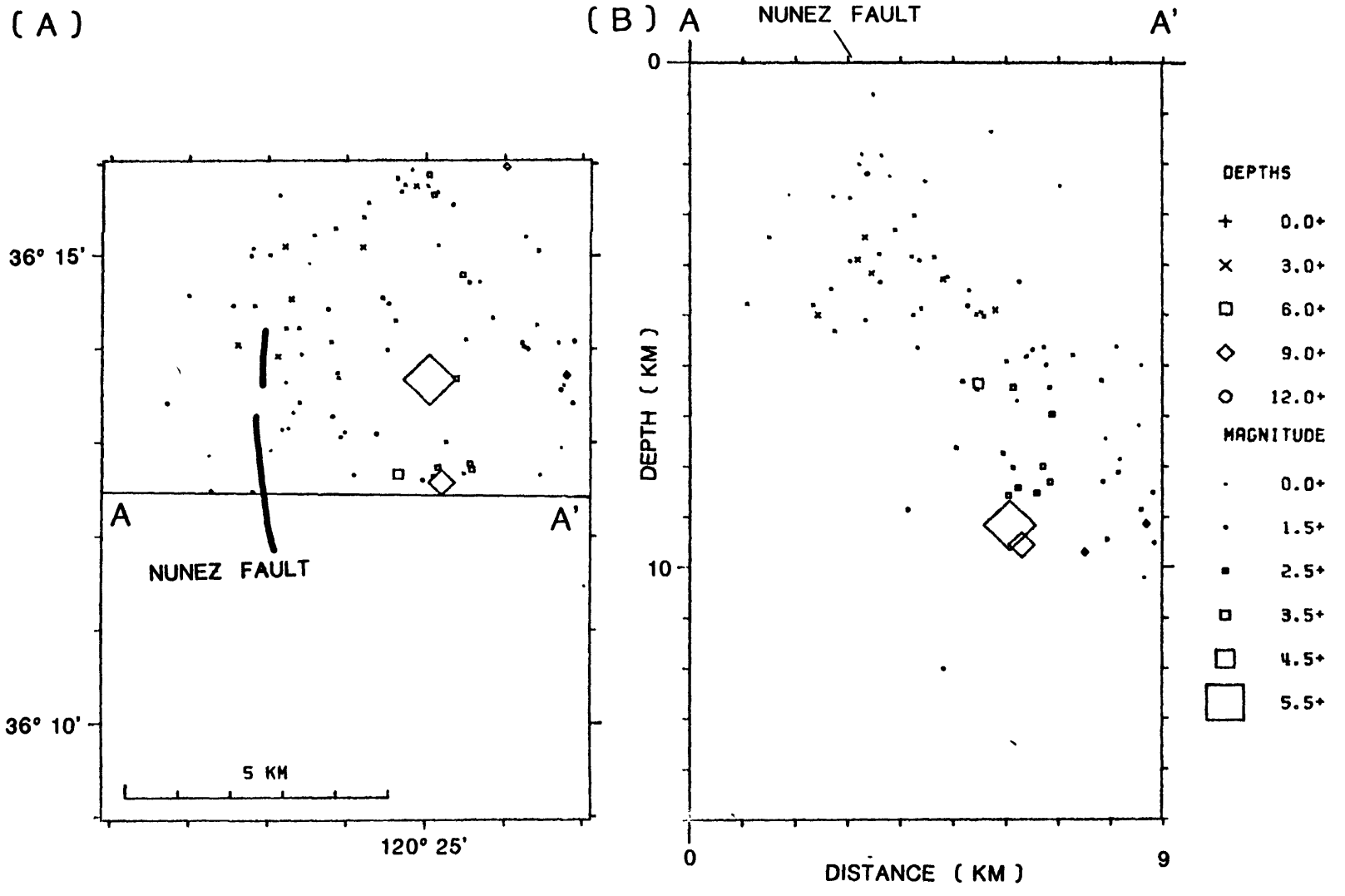

Figure 7. Epicenters (A) and east-west cross section A-A' (B) for area around Nunez fault for interval July 22-25, 1983. Data from Calnet.

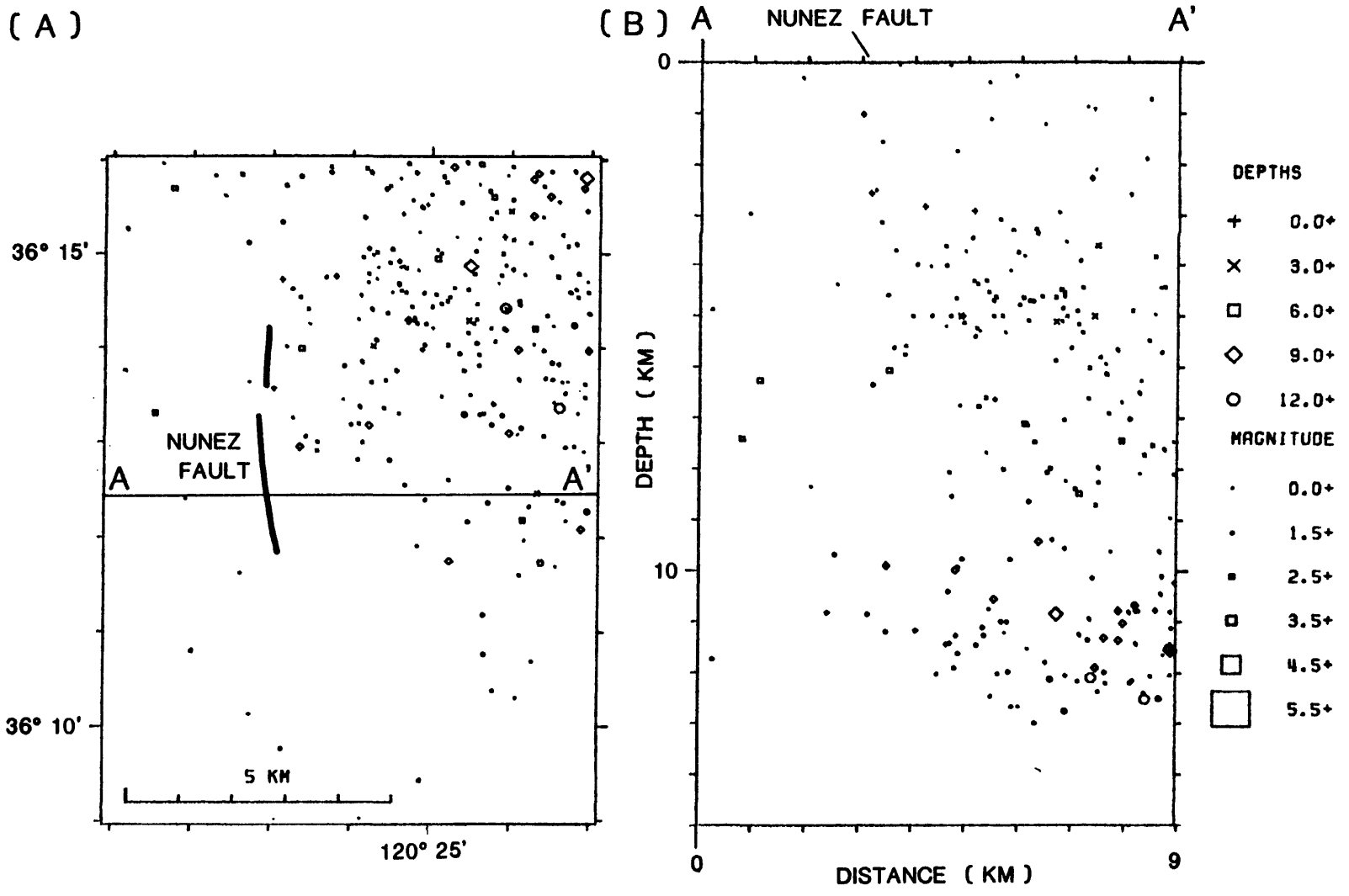

Figure 8. Epicenters(A) and east-west cross section A-A' (B) for area around Nunez fault for interval May 3-June 11, 1983. Data from Calnet.

STRESS AND FLUID PRESSURE CHANGES ASSOCIATED WITH OIL FIELD OPERATIONS: A CRITICAL ASSESSMENT OF EFFECTS IN THE FOCAL REGION OF THE 1983 COALINGA EARTHQUAKE

P. Segall and R. F. Yerkes
U.S. Geological Survey
Menlo Park, California 94025

Abstract

The proximity of the May 2, 1983 Coalinga earthquake to active oil fields on Anticline Ridge led to speculation that the earthquake might have been triggered by oil field operations. Elsewhere, earthquakes have been associated with pore-pressure increases resulting from fluid injection and also with subsidence resulting from fluid extraction. Simple calculations show that shales, which underlie the oil producing strata, hydraulically isolate the oil field from the earthquake focal region. The large volumes of fluid extracted from the oil fields caused a 50 percent decline in reservoir pressures from 1938 to 1983. These observations independently rule out substantial increases in pore pressure at focal depths due to fluid injection. A theoretical method, based on Biot's constitutive theory for fluid-infiltrated elastic media, is used to evaluate the change in stresses acting in the focal region resulting from fluid extraction in the overlying oil fields. As an independent check on the method, the subsidence of the earth's surface in response to fluid withdrawal is calculated and compared with measured elevation changes of Anticline Ridge. The producing horizons are taken to be horizontal permeable layers, bounded above and below by impermeable horizons. Strains within the producing layers are related to extraction-induced changes in pore-fluid mass. Contraction of the producing layers causes the free surface to subside and strains the elastic surroundings. The calculated subsidence rate of Anticline Ridge between 1933 and 1972 is 3 mm/yr, in good agreement with the measured subsidence rate of 3.3 ± 0.7 mm/yr. Calculated pore pressure changes in the deepest producing zone also compare well with observed changes in reservoir pressure. Although the sign of the shear stresses induced by extraction favor reverse slip on either the northeast or southwest dipping nodal plane, the induced normal stresses are compressive, inhibiting fault slip. The driving stress (shear stress minus frictional resistance) acting across the northeast dipping plane increased by 0.1 bar between 4 and 9 km depth, weakly favoring slip, and decreased by 0.05 bar at depths of 9 to 11 km, weakly inhibiting slip. The driving stress on the southwest dipping plane increased by 0.2 bar at 10 km, slightly favoring slip.

INTRODUCTION

Epicenters of the M 6.7 earthquake of May 2, 1983 and its early aftershocks were located along Anticline Ridge, 10 km northeast of Coalinga (Reasenberg *et al.*, 1983; Eaton *et al.*, 1983). Anticline Ridge overlies two active oil fields, one of which has been under production for more than 85 years. The proximity of the earthquake to active oil fields led to speculation that oil field operations might have accelerated the release of stored elastic

strain, thereby triggering the earthquake.

Induced seismicity has been associated with injection of fluids into the shallow crust in a number of other areas, including the Rocky Mountain Arsenal near Denver (Healy *et al.*, 1968), and the Rangely oil field in western Colorado (Raleigh *et al.*, 1972, 1976). Injection-induced seismicity is generally thought to occur when injection increases pore-fluid pressures, thus decreasing the effective confining stress, and allowing fault slip to take place at the existing levels of tectonic shear stress (Raleigh *et al.*, 1972, 1976). The induced earthquakes in the Rangely field had focal depths of less than 4 km, within 2 km of the bottoms of the experimental injection wells (Raleigh *et al.*, 1976).

Induced faulting and seismicity have also been attributed to fluid extraction in oil fields (Yerkes and Castle, 1976). The best documented examples of extraction-induced seismicity occurred in the Goose Creek, Texas oil field (Pratt, 1926) and the Wilmington, California oil field (Kovach, 1974). Most earthquakes previously thought to be associated with fluid extraction had relatively shallow focal depths (Yerkes and Castle, 1976).

We also note that numerous examples of earthquakes induced by filling of reservoirs have been reported, including eight events of magnitude 5 or greater (Simpson, 1976). Although the focal depths of these events are generally not well constrained, the data are consistent with depths comparable to that of the Coalinga earthquake; *i.e.*, 10 km (Gupta and Rastogi, 1976). Reservoir-induced earthquakes are generally considered to have been triggered by increased pore pressures at depth (Bell and Nur, 1978; Zoback and Hickman, 1982) in a manner similar to injection-induced earthquakes.

The main purpose of this paper is to assess the effects of operations in nearby oil fields on the pore-fluid pressures and stresses acting in the focal region of the Coalinga earthquake. Estimates of the magnitude and distribution of pore pressure changes enable us to evaluate whether the Coalinga earthquake is reasonably considered an example of injection-induced seismicity. In a similar fashion, calculations of the fluid pressure and solid stress changes associated with fluid extraction enable us to assess the possibility of extraction-induced seismicity.

RELATIONSHIP OF OIL FIELDS TO THE EARTHQUAKE SEQUENCE

Epicenters of the mainshock and aftershocks during May–July 1983, and their relationship to the Coalinga oil fields, are illustrated in Figure 1. The aftershocks form an elongate zone striking approximately N30°W, parallel to the regional trend of the Coast Ranges and the fold axis of the Coalinga anticline (Eaton *et al.*, 1983). Figure 1 also illustrates P-wave fault plane solutions for $M \geq 5.0$ events. The focal mechanism of the mainshock indicates reverse slip on a N53°W striking fault plane which dips either 67° to the NE or 23° to the SW (Eaton *et al.*, 1983). Coseismic elevation changes analyzed by Stein (1983) favor the steeply northeast-dipping plane, although the shallow plane cannot be ruled out entirely. The elevation changes can be adequately modeled by a single dislocation surface that dips 67° to the NE, and extends from a depth of 4 ± 1 km to 11.2 ± 2 km (Stein, 1983). The earthquake sequence is discussed in considerably more detail elsewhere in this volume.

The geology of the Coalinga region is reviewed by Bartow (this volume). Most of the historic oil production from Anticline Ridge has come from two fields, Coalinga Eastside,

and the Nose area of the Coalinga East Extension (Figure 1). In the Coalinga field, the principal producing horizon is the Miocene Temblor Formation. The Temblor, a pebbly sandstone, has an average thickness of 75 m and occurs at depths of 0.2 to 1.4 km (average depth of 0.6 km). It is capped by shales of the Santa Margarita Formation. The main producing zone in the Coalinga East Extension is the Gatchell sand (of local usage) in the lower Tertiary Lodo Formation. The Gatchell is found at depths of 2.2 to 2.4 km in the Nose area of the Coalinga anticline. The Gatchell grades into the so-called Turritella Silt southwest of the Anticline Ridge, creating a strong permeability barrier to flow from the southwest. The maximum thickness of the Gatchell is 190 m.

A cross section of seismicity through Anticline Ridge (Figure 2) demonstrates that the mainshock and the majority of aftershocks occurred well below the Tertiary oil-bearing formations. With the exception of the June 11 aftershock, the mainshock and $M \geq 5.0$ aftershocks had focal depths of 9 to 12 km. Little is known about the geology at these depths. The deepest wells on Anticline Ridge penetrate upper Cretaceous rocks of the Great Valley sequence, a thick section of which outcrop to the north and west of Anticline Ridge. The Franciscan assemblage, which lies structurally below the Great Valley sequence, is exposed in the cores of anticlines northwest of Coalinga.

The yearly net liquid production (oil + water - returned water) from the oil fields on Anticline Ridge is shown in Figure 3. Since its discovery in 1896, 1.2×10^8 m^3 of liquid has been extracted from the Coalinga Eastside. The average extraction rate from 1905 to 1981 has been 1.6×10^6 m^3/yr (1.0×10^7 bbl/yr). Oil production from the Coalinga East Extension did not begin until 1938, yet this field produced 1.5×10^8 m^3 of liquid. The average rate of liquid extraction from 1940 to 1981 was 3.7×10^6 m^3/yr (2.4×10^7 bbl/yr), as indicated by the dashed line in Figure 3b.

INDUCED FLUID-PRESSURE CHANGES

Records of average reservoir pressure in the Gatchell sand within the Coalinga East Extension field have been maintained by the California State Division of Oil and Gas. The average reservoir pressure from the discovery of the field in 1938 until late 1983, following the earthquake, is shown in Figure 4. The data from 1953 to the present are average pressures, measured in at least two and as many as seven wells, within the gas zone at a depth of 1,980 m. The measurements from 1938 to 1953 are from the oil zone at a depth of 2,060 m. Although various secondary oil recovery projects have involved the injection of gas, water, and polymer solutions into the Gatchell, the net effect of oil field operations between 1938 and 1983 was to reduce the pore pressure by 53 percent, from 23 MPa (3,500 psi) to 11 MPa (1,650 psi). The pressure history is clearly dominated by the large volumes of fluid withdrawn from the reservoir. If the observed decrease in pore pressure was, in fact, transmitted to the focal region of the earthquake, it would have resulted in an increase in effective confining stress, and according to the criteria of Raleigh *et al.* (1972, 1976), a "strengthening" of the fault.

Simple calculations, however, suggest that it is extremely unlikely that any pore pressure changes within the Gatchell (the deepest producing zone at a depth of 2.2 km) could have been transmitted to the focal depth of 10 km in the 45 years between 1938 and 1983. This results primarily from the low permeability of argillaceous rocks which

are known to underlie the Gatchell sand. Permeabilities of shales, measured in laboratory samples and *in situ* (Brace, 1980) are typically 10^{-18} to 10^{-20} m^2 (10^{-6} to 10^{-8} darcy). For flow of water, these permeabilities correspond to hydraulic diffusivities, c, of 10^{-5} to 10^{-7} m^2/s (see below). The penetration depth of a pressure disturbance at time t can be estimated by $\sqrt{ct}$. Taking the larger diffusivity (10^{-5} m^2/s), we find that the pressure disturbance will penetrate 100 m in 45 years ($t \sim 10^9$ s), nearly two orders of magnitude less than the 8 km between the Gatchell and the earthquake focus. This calculation illustrates that even a few hundred meter thick section of shale will be effective in hydraulically isolating the focal region from the oil field. Although one could argue that a highly permeable, fractured zone might link the oil field to the focal region, there is no evidence to support the presence of such a zone. In fact, Cretaceous and lower Tertiary sediments at depths of 3 km and greater in the Coalinga area contain abnormally high fluid pressures. These pressures reach 81–93 percent of the lithostatic pressure (Yerkes and others, this volume). These overpressures attest to the low hydraulic conductivity of the sedimentary rocks below the oil-bearing strata. Finally, we note that even if a highly conductive zone existed, the effect of oil field activities would be to decrease the pore pressure, as discussed above. In sum, all of the available evidence argues against the Coalinga earthquake having been triggered by injection-induced pore pressure changes.

STRESS CHANGES INDUCED BY FLUID EXTRACTION

As discussed in the previous section, the principal effect of oil-field operations has been the removal of large volumes of fluid, and the consequent decline in reservoir pressures. In this section we estimate the stress changes in the focal region resulting from fluid extraction. This discussion summarizes the analysis presented by Segall (1984).

Theory

Stresses induced by fluid extraction arise as the producing rocks contract in response to removal of pore fluid. This process can be understood by considering the simple thought experiment illustrated in Figure 5. The earth's crust is considered to be a uniform, isotropic, fluid-infiltrated half-space, which for simplicity will be assumed to be initially unstressed. Imagine that a small element is cut from the half-space (1 in Figure 5). Because the region is unstressed, this induces no strain in the half-space. Following this, fluid with mass per unit solid volume Δm is uniformly extracted from the pores of the element (2 in Figure 5). This causes the element to undergo a uniform volumetric contraction ϵ^T_{kk}. This 'transformation strain' (Eshelby, 1957) occurs without induced stresses in the solid, and is therefore referred to as a 'stress-free strain.' Because the strain resulting from uniform fluid withdrawal is purely volumetric, the strain in the element is simply

$$\epsilon_{ij} = \epsilon^T_{kk}\delta_{ij}/3 \qquad (i,j,k = 1,2,3) \tag{1}$$

The Kronecker delta, δ_{ij}, is defined by $\delta_{ij} = 1$ for $i = j$, and $\delta_{ij} = 0$ for $i \neq j$.

The magnitude of the transformation strain is related to the change in fluid mass content per unit volume, Δm, through the constitutive equations for the fluid-infiltrated solid. For a linear, isotropic, poro-elastic material (Biot, 1941; Rice and Cleary, 1976) the volumetric strain is related to the mean stress σ_{kk} and change in pore fluid mass content through the relationship given by Segall (1984):

$$\epsilon_{kk} = \frac{\sigma_{kk}}{3K_u} + \frac{B\Delta m}{\rho_o} \tag{2}$$

In eq. (2) K_u is the 'undrained bulk modulus;' that is, the elastic bulk modulus under conditions in which no fluid flow occurs ($\Delta m = 0$). The constant B is 'Skempton's pore pressure coefficient,' and ρ_o is the fluid density in the undisturbed state.

The solid volumetric strain is seen to be composed of two parts: an undrained elastic strain and a strain resulting from change in pore fluid content. For relatively incompressible fluids, such as oil and water, the latter is very nearly $B\Delta v$, where Δv is the change in pore fluid volume per unit solid volume. In this case, B is therefore the ratio of solid volume change to change in pore fluid volume. The range of B is restricted to $0 \leq B \leq 1$; for water saturated soils $B \approx 1$, while for a number of diverse rock types, ranging from sandstones to granites B ranges from 0.5 to 0.9 (Rice and Cleary, 1976). Thus, if water is uniformly withdrawn from a rock with B of 0.8 the volumetric contraction of the rock is 80 percent of the volume of extracted water. For soils, the contraction is nearly 100 percent of the volume of extracted water. Finally we note that Skempton's coefficient is nearly zero when the compressibility of the fluid is very large in comparison to that of the solid (Rice and Cleary, 1976), as would be the case for gas and rock.

Returning to Figure 5, it is now apparent that the stress-free transformation strain resulting from a uniform change in fluid mass content Δm is simply

$$\epsilon^T_{kk} = \frac{B\Delta m}{\rho_o} \tag{3}$$

To restore the element to its initial shape it is necessary to elastically strain the element by $-\epsilon^T_{kk}$ while maintaining the pore fluid mass constant (3 in Figure 5). The elastic straining is achieved by adding tractions T_i to the surface of the element

$$T_i = -K_u \epsilon^T_{kk} n_i \tag{4}$$

where n_i is the unit surface normal.

The element (inclusion) at this stage has no net strain, and therefore fits precisely into the cut in the half-space (matrix). Once the inclusion is reinserted into the matrix, the surface tractions can be relaxed, allowing the inclusion to contract and strain the matrix. If the dimensions of the element are small in comparison to the depth of burial, the stresses due to contraction can be adequately represented by a point center of contraction, or negative center of dilatation. The stresses resulting from the change in fluid mass Δm can be represented by a vertical point force with magnitude Δmg, where g is the acceleration due to gravity.

One can easily show that the stress change due to contraction of the solid dominates the gravitational stress change due to depletion of fluid mass. In fact, for distances from the producing zones of 10 km or less, the stresses due to contraction are at least two orders of magnitude greater than the stresses due to mass depletion (Segall, 1984). Thus, so long as the fluid-depleted zone is elastically coupled to the underlying rocks, the change in gravitational load can be neglected relative to the contraction of the fluid-depleted zone.

The stress and deformation changes resulting from the withdrawal of fluid from a permeable layer embedded in an impermeable, half-space (Figure 6) can be calculated by solving for the change in fluid mass content within the layer, and then summing the stresses due to fluid depletion at each point within the layer. The thickness of the layer, T, is taken to be much smaller than the layer depth, D. This is a reasonable approximation for the oil fields on Anticline Ridge where T/D for the principal producing horizons is of the order of 0.1. The producing layer has permeability k, while the surrounding rocks are assumed to have negligible permeability. As discussed previously, the oil-bearing horizons are stratigraphically bounded by shales, which are likely to be five orders of magnitude less permeable than the producing sandstones (Brace, 1980). Over the 80-year period of oil production the shales are therefore effectively impermeable.

The oil fields are elongate in a NW-SE direction along the axis of the Coalinga anticline. This geometry is idealized as a line of wells extending indefinitely in the z-direction (Figure 6). The fluid flux out of the layer is taken to be independent of position along the z-direction. As fluid is withdrawn from the line of wells, flow is induced in the layer toward the plane $y = 0$. Because the surrounding medium is effectively impermeable, flow occurs only in the y-direction. Finally, note that the model geometry is such that the induced deformation is one of plane strain; that is, there are no displacements in the z-direction.

The governing equation for the alteration in fluid mass content is the homogeneous diffusion equation (Rice and Cleary, 1976), which for one-dimensional flow takes the form:

$$c\frac{\partial^2 \Delta m}{\partial y^2} = \frac{\partial \Delta m}{\partial t} \tag{5}$$

where c is the hydraulic diffusivity of the medium. The hydraulic diffusivity is given approximately by

$$c \cong k/\eta\phi\beta \tag{6}$$

where k is permeability (with units of area), η is the fluid viscosity, ϕ is porosity, and β the fluid compressibility (Rice and Cleary, 1976).

The net mass flux out of the producing zone $-Q$, is taken to be constant for $t > 0$, and 0 for $t < 0$ (the dashed lines in Figure 4). If q is the local fluid-mass flux, then the boundary conditions for flow in an infinite layer are

$$q(y = 0^+) - q(y = 0^-) = -Q \qquad t > 0 \tag{7a}$$

$$q(y = \pm\infty) = 0 \qquad t > 0 \tag{7b}$$

The solution of (5) subject to boundary conditions (7) is (Carslaw and Jaeger, 1959; p. 75)

$$\Delta m(y,t) = -Q\sqrt{\frac{t}{c}}\, ierfc\sqrt{\frac{y^2}{4ct}} \qquad t > 0 \tag{8}$$

where $ierfc(x)$ is the first integral of the complementary error function

$$ierfc(x) = \int_0^x erfc(\xi)d\xi = \frac{e^{-x^2}}{\sqrt{\pi}} - x\, erfc(x) \tag{9}$$

The net flux mass flux $-Q$ is given by

$$-Q = \frac{-\dot{V}\rho_o}{LT} \tag{10}$$

where $\dot{V}/L$ is the average rate of fluid extraction per unit length in the z-direction, and T is the layer thickness.

The vertical displacement of the free surface du_x $(x = 0)$ due to a change in fluid mass Δm at a point along the producing layer $x = D$, $y = \xi$ to $\xi + d\xi$ is that due to a point center of dilatation with strength proportional to the depletion-induced transformation strain at that point

$$du_x(x = 0, y) = \frac{2B(1+\nu_u)T}{3\pi\rho_o}\Delta m(\xi)d\xi\left[\frac{-D}{D^2 + (y-\xi)^2}\right] \tag{11}$$

(Segall, 1984). Here ν_u is the undrained Poisson's ratio. The net displacement $u_x(0, y, t)$ due to distributed fluid depletion along the entire layer is found by substituting (8) and (10) into (11) and integrating with respect to ξ from $-\infty$ to ∞.

$$u_x(x = 0, y, t) = \frac{2B(1+\nu_u)\dot{V}D}{3\pi L}\sqrt{\frac{t}{c}}\int_{-\infty}^{\infty}\frac{ierfc\sqrt{\xi^2/4ct}}{D^2 + (y-\xi)^2}\, d\xi \tag{12}$$

The subsidence is found to increase linearly with the rate of fluid extraction. The subsidence also depends strongly on material properties, including Skempton's coefficient and hydraulic diffusivity. For high diffusivities the fluid depletion is dispersed, the subsidence is spread over a broad area and the peak subsidence is relatively small, whereas for low diffusivities the subsidence is localized and the maximum subsidence is relatively large.

The stress change due to fluid extraction can be calculated in much the same way as the subsidence. The stress change $d\sigma_{mm}$ at a point (x, y) due to an incremental fluid mass change at (D, ξ) is

$$d\sigma_{mn} = \frac{\mu B(1+\nu_u)T}{3\pi\rho_o(1-\nu_u)}G_{mn}(x, y, D, \xi)\Delta m(\xi)d\xi \tag{13}$$

The total stress change due to fluid withdrawal is thus

$$\sigma_{mn}(x,y,t) = \frac{-\mu B(1+\nu_u)\dot{V}}{3\pi(1-\nu_u)L}\sqrt{\frac{t}{c}}\int_{-\infty}^{\infty} G_{mn}(x,y,D,\xi)\, ierfc\sqrt{\frac{\xi^2}{4ct}}\, d\xi \qquad (14)$$

(Segall, 1984), where the Green's functions G_{mn} for the different stress components are

$$\begin{aligned}
G_{xx} &= \frac{(y-b)^2-(x-a)^2}{r_1^4} + \frac{(5x+a)(x+a)-(y-b)^2}{r_2^4} - \frac{16x(x+a)(y-b)^2}{r_2^6} \\
G_{yy} &= \frac{(x-a)^2-(y-b)^2}{r_1^4} + \frac{(x+a)(3a-x)-3(y-b)^2}{r_2^4} + \frac{16x(x+a)(y-b)^2}{r_2^6} \qquad (15) \\
G_{xy} &= \frac{-2(y-b)(x-a)}{r_1^4} - \frac{2(y-b)(3x+a)}{r_2^4} + \frac{16x(x+a)^2(y-b)}{r_2^6}
\end{aligned}$$

It is worth emphasizing at this point that the stress changes discussed here are generated entirely by contraction of the shallow producing horizon. Fluid flow is completely confined to the producing layer. As discussed previously, shales below the producing layer are effectively impermeable so that there is no fluid transport from depth to the producing zone. In this calculation the stresses are transmitted to depth elastically, through the solid rock matrix, without direct fluid transport.

As a final point we calculate the decrease in pore pressure within the producing zone resulting from fluid extraction. In the Biot constitutive theory, the change in pore pressure at a point is simply related to the change in fluid mass content and mean stress at that point. For plane-strain conditions the relation is

$$p(x,y,t) = \frac{(1+\nu_u)B}{3}\left[\frac{2(1+\nu_u)\mu B}{3\rho_o(\nu_u-\nu)}\Delta m(x,y,t) - \sigma_{nn}(x,y,t)\right] \qquad (16)$$

(Rice and Cleary, 1976). The change in mean stress at a point <u>within</u> the producing zone is given by

$$\begin{aligned}
\sigma_{nn}(x,y,t) = \frac{-2(1+\nu_u)\mu B}{3\rho_o(1-\nu_u)}\Bigg\{&\frac{2(1-\nu_u)}{(1-2\nu_u)}\Delta m(x,y,t) \\
&- \frac{2}{\pi}\int_{-\infty}^{\infty}\int_{0}^{\infty}\Delta m(\varsigma,\xi,t)\frac{[(x+\varsigma)^2-(y-\xi)^2]}{[(x+\varsigma)^2+(y-\xi)^2]^2}d\varsigma\, d\xi\Bigg\}
\end{aligned} \qquad (17)$$

(Segall, 1984). This result can be compared with eq. (14), which gives the stresses in the region <u>outside</u> the producing zone $\Delta m(x,y,t) = 0$.

Substituting (8), (10), and (17) into (16), and integrating with respect to ς (note that Δm is non-zero only for $D \leq \varsigma \leq D+T$) results in the following expression for pore pressure change

$$p(x,y,t) = \frac{-2\mu(1+\nu_u)^2 B^2 \dot{V}}{9LT}\sqrt{\frac{t}{c}}\left\{\frac{1-2\nu}{(\nu_u-\nu)(1-2\nu_u)}ierfc\sqrt{\frac{y^2}{4ct}}\right.$$

$$\left. - \frac{2}{\pi(1-\nu_u)}\int_{-\infty}^{\infty}\left[\frac{(x+D)}{(x+D)^2+(y-\xi)^2} - \frac{(x+D+T)}{(x+D+T)^2+(y-\xi)^2}\right] ierfc\sqrt{\frac{\xi^2}{4ct}}d\xi\right\} \quad (18)$$

The pressure change depends on a number of parameters which do not influence the subsidence, namely: shear modulus μ, drained Poisson's ratio ν, and layer thickness T. The pressure change is in fact sensitive to the difference between the undrained and drained Poisson's ratio. In the calculation presented here ν is taken to be 0.2, so that $\nu_u - \nu = 0.13$. Of the three sandstones considered by Rice and Cleary (1976) this difference ranged from 0.13 to 0.19. The pressure change in the Gatchell also depends inversely on layer thickness.

Application of Method to the Coalinga Area

For the purposes of this study there are three principal oil-producing zones: Coalinga Westside, Coalinga Eastside, and the Nose region of the East Coalinga Extension. The geometry adopted to model the effects of fluid extraction in this area is illustrated in Figure 7. The Temblor, which extends between the East and West Coalinga Fields, is located at a depth of 0.6 km, the average depth of the Temblor in the Coalinga Eastside Field (California Division of Oil and Gas, 1973). In the calculation 1.6×10^6 m^3/yr of liquid is extracted from the Eastside beginning in 1905 (refer to Figure 3a). The rate of extraction from the Westside is 1.1×10^6 m^3/yr, also beginning in 1905. The Gatchell, which grades into the Turritella silt southwest of Anticline Ridge, is modeled as a semi-infinite layer located at a depth of 2.3 km. An average of 3.7×10^6 m^3/yr of liquid was extracted from the Gatchell beginning in 1940 (refer to Figure 3b).

The material properties used in the calculation are summarized in Table 1. Thickness, T, porosity, ϕ, and permeability, k, for both Gatchell and Temblor are given by California Division of Oil and Gas (1983). Measured permeabilities of Temblor range from 3×10^{-13} m^2 (300 mdarcy) to 10^{-11} m^2 (10,000 mdarcy); however, 2×10^{-12} m^2 (2,000 mdarcy) is considered to be representative of the entire horizon (Richard Curtain, personal communication, 1983). Oil viscosities are also variable. Oil produced from the Gatchell has a viscosity of approximately 10^{-3} Pa-s (1 cp). Viscosities of Temblor oils, however, range from 10^{-2} Pa-s (10 cp) to 2.5 Pa-s (2,500 cp), (California Division of Oil and Gas, 1983), with an average over the life of the field of 0.15 Pa-s to 0.2 Pa-s (150 cp to 200 cp), (Richard Curtain, personal communication, 1983). Considering that nearly half of net liquid withdrawn from the Temblor is water (Figure 4a),0.1 Pa-s (100 cp) is taken to be a reasonable value for the average liquid viscosity. Using the above values, hydraulic diffusivities calculated from equation (6) are 0.2 m^2/s for the Temblor and 7.0 m^2/s for the Gatchell (Table 1). The uncertainty in permeability and viscosity appropriate for the Temblor zone lead to uncertainties in the calculated diffusivity for the Temblor. It is possible that the actual diffusivity may be as low as 0.02 m^2/s.

Skempton's coefficient and Poisson's ratio under undrained conditions are not routinely measured, and are not available for either the Gatchell or Temblor. The values used in the calculations here (Table 1) are those given by Rice and Cleary (1976) for Berea Sandstone. The shear moduli of the producing rocks have not been reported but can be inferred from bore-hole velocity measurements. Compressional wave velocities in the Gatchell sand average 3.8 km/s. With this data the shear modulus can be calculated from

$$\mu = \frac{(1-2\nu_u)}{2(1-\nu_u)}\rho v_p^2 \tag{19}$$

where v_p is p-wave velocity and ρ is density. Equation (19) gives a value of 8×10^3 MPa for $v_p = 3.8$ km/s assuming ν_u of 0.33 and a density of $2,300$ kg/m^3.

The change in stress acting on the two nodal planes due to liquid extraction was calculated using the methods developed in the previous section. The location and dip of the two model fault planes were chosen to be consistent with the mainshock location and focal mechanism. For the northeast-dipping plane the top of the slipped zone is at a depth of 4.0 km, the base at 11.2 km (Stein, 1983). For the southwest-dipping plane the top of the slipped surface is at a depth of 9.5 km and the base at 13.5 km (Figure 7). The stresses were rotated into the possible fault planes to determine the shear and normal stress acting across these surfaces. The stresses reported here represent the changes in the existing stress state due to extraction of liquid from the Temblor and Gatchell zones. The total stress is the sum of the existing tectonic stress and the stress resulting from extraction.

Northeast Dipping Plane

The change in resolved shear stress on the 67° northeast dipping plane is shown in Figure 8a as a function of depth. Each curve in Figure 8a represents the stress change at a given time following the onset of extraction. The sign convention employed is such that positive shear stresses favor reverse faulting. Note that the shear stresses favor reverse faulting on a high angle fault beneath Anticline Ridge. The magnitudes of the stresses, however, are small: less than 0.4 bar at depths of 8 km or more.

The corresponding changes in normal stress acting across the northeast dipping plane are shown in Figure 8b. The normal stresses are found to be compressive (negative) for all depths and times of interest. In general, the magnitude of the induced compression decreases with depth, and increases at a given depth with time following the onset of extraction.

The change in driving stress $\Delta\sigma_d$ is calculated in order to assess the net effect of changing shear and normal stresses on the fault. The driving stress $\Delta\sigma_d$ is defined as:

$$\Delta\sigma_d = \Delta\sigma_s + f(\Delta\sigma_n + \Delta p) \tag{20}$$

where $\Delta\sigma_s$ and $\Delta\sigma_n$ are the change in shear and normal stress, f is the coefficient of friction, and Δp is the change in pore pressure. Although the calculations involve no fluid transport to or from the fault, there is an undrained, or 'instantaneous,' pore pressure change due to changes in mean stress σ_{nn}. The undrained pressure response is

$$\Delta p = -\frac{(1+\nu_u)B}{3}\Delta\sigma_{nn} \qquad (n=1,2) \tag{21}$$

Substituting equation (21) into (20) yields an expression for the driving stress in the form:

$$\Delta\sigma_d = \Delta\sigma_s + f\left[\Delta\sigma_n - \frac{(1+\nu_u)B}{3}\Delta\sigma_{nn}\right] \tag{22}$$

The change in driving stress acting on the northeast dipping plane is shown in Figure 8c, assuming a coefficient of friction of 0.6. Near the hypocenter, that is for depths greater than 9 km, the increased compression dominates the increased shear stress. The situation reverses at shallow depths after approximately 50 years of extraction. There the increased shear stresses dominate causing an increase in the driving stress. The net effect of fluid extraction is to slightly inhibit slip on the northeast dipping plane in the vicinity of the hypocenter and to slightly favor slip on the same plane at shallow depths.

Southwest Dipping Plane

The change in shear stress acting on the southwest dipping plane as a function of depth is shown in Figure 9a. The sign convention is such that positive shear stresses favor reverse (or thrust) faulting. As is the case for the northeast dipping plane, the shear stresses generated by extraction favor reverse faulting on a deep, low-angle fault beneath Anticline Ridge. The maximum shear stress in this case is slightly less than 0.3 bar. The induced normal stresses acting across the southwest dipping plane (Figure 9b) are compressive, tending to inhibit slip.

The change in driving stress acting across the southwest dipping plane is shown in Figure 9c. In contrast to the result for the steeply-dipping plane, the change in driving stress is of the correct sense to favor reverse motion on the southwest dipping plane. At the time of the earthquake the driving stress increased by nearly 0.2 bars at a depth of 9.5 km and 0.1 bars at 13.5 km.

Subsidence

As an independent check on the analytical methods employed to calculate stress change, the theory can be used to calculate the subsidence of Anticline Ridge resulting from fluid extraction. The calculated subsidence can then be compared with observed elevation changes of benchmarks on Anticline Ridge determined by repeated leveling surveys. The parameters used in this calculation are the same as those employed in the previous stress calculation (Table 1). Three benchmarks on Anticline Ridge (W156, V156, and V237) were chosen for this comparison because they are located on Tertiary rocks, and should not be influenced by soil subsidence related to ground water pumping. All three benchmarks were surveyed in 1960, 1966, 1969, and 1972 (Stein, 1983). In addition, benchmarks W156 and V156 were surveyed in 1933–35 and 1958–59 (Prokopovich and Magleby, 1968).

Elevation changes of the Anticline Ridge benchmarks relative to an assumed stable site on Cretaceous rocks within the Diablo Range west of Coalinga (benchmarks F1046; Stein, 1983, and F156; Prokopovich and Magleby, 1968) are shown in Figure 10. The 1960 to 1972 leveling has been corrected for refraction error (Stein, 1983) using the method of

Holdahl (1981). The 1933–35 and 1958–59 is not corrected for refraction error; however, the reference station is nearly at the same elevation as Anticline Ridge, so that these errors should be less than 15 mm. In fact, the refraction corrections for W156 and V156 between 1960 and 1966 are only 5 mm and 7 mm, respectively. Random errors between the reference station and Anticline Ridge are assumed to be less than 9 mm for first-order leveling (1958–59, 1960, and 1966 surveys) and 19 mm for second-order leveling (1933–35, 1969, and 1972 surveys).

The average subsidence rate of benchmarks W156 and V156 between 1933 and 1972 were 3.2 $\pm$ 0.6 mm/yr and 4.1 $\pm$ 0.4 mm/yr, respectively (Figure 10). Benchmark V237 subsided at a rate of 2.6$\pm$0.1 mm/yr between 1960 and 1972. The mean subsidence rate of Anticline Ridge from these data is 3.3 $\pm$ 0.7 mm/yr. The model subsidence calculated by setting $y = 0$ in equation (12) is also shown in Figure 10. The calculated subsidence is in good agreement with the observed elevation changes. In fact, the subsidence rate between 1933 and 1972 predicted by the model is 3.3 mm/yr. It is worth emphasizing that the model parameters were all estimated from independent data; none of the parameters was adjusted to fit the measured elevation changes. Nevertheless, the material parameters, including hydraulic diffusivity, are imperfectly known. For comparison, the effect of decreasing the diffusivity of the Temblor by one order of magnitude to 0.02 m/s is shown in Figure 10. The average subsidence rate for the same time interval in this case is 6.6 mm/yr, roughly twice the observed rate.

As a further check, the predicted pore-pressure change is compared to the observed pressure decline in the Gatchell sand in Figure 5. The predicted pore-pressure change is found by evaluating equation (18) at $x = D + T/2$ and $y = 0$. Results are shown for thicknesses of the Gatchell of 190 m, 95 m, and 60 m. For a thickness of 190 m, the predicted pressure decline is approximately a factor of two less than observed. This discrepancy could be due to a number of causes. Considering the variable thickness of the Gatchell and the possibility of variable properties within the zone, it is likely that the average thickness of the producing section is somewhat less than 190 m. Decreasing the thickness by a factor of two to 95 m yields a reasonably good fit to the measured pressures (Figure 5). The misfit in calculated pressures might also result from inaccurate estimates of material properties. For example, an equally good fit to the data is obtained by increasing the drained Poisson's ratio from 0.20 to 0.28. Given the simplicity of the model the overall fit to the data is adequate. Of course, the detailed features of the pressure history are not reproduced. This is, in a large part, due to the fact that the actual fluid extraction rate is not constant as assumed in the calculation (see Figure 4b).

DISCUSSION

At the present time stress changes at seismogenic depths resulting from fluid extraction cannot be measured directly, and must therefore be inferred from near surface observations. At first glance it might appear that stresses inferred in this way would be almost entirely unconstrained. On the other hand, the analytical methods used to compute stress can also be used to calculate other quantities, such as surface displacement or reservoir pressure, which can be measured directly. Quantitative agreement between theory and observation would then lend credence to the stresses calculated at depths which are currently inaccessible to direct measurements.

The excellent agreement between calculated subsidence rate and observed rate of elevation change on Anticline Ridge (Figure 10) is therefore particularly significant. The consistency between the calculated decline in reservoir pressure and measured pressures in the Gatchell lends further support to the calculated stresses. The agreement between theory and observation is particularly encouraging because the parameters in the theory are either known from independent observations or can be inferred from measurements on similar rocks.

For a number of reasons estimates of hydraulic diffusivity, particularly of the Temblor, are likely to be accurate only to within an order of magnitude. Decreasing the diffusivity of the Temblor by an order of magnitude was found to increase the predicted subsidence rate from 3 mm/yr to 6 mm/yr, significantly greater than the observed rate of 3.3 ± 0.7 mm/yr. The change in stress acting on the fault also depends non-linearly on diffusivity. Stress changes calculated for a range of diffusivities, assuming only that the diffusivities are known to within an order of magnitude, exhibit somewhat varied behavior. In some cases the changes in driving stress are negative, indicating that extraction inhibits slip. In other cases the driving stress changes are positive. For the northeast dipping plane, the driving stress changes are always less than 0.04 MPa (0.4 bar) at depth of 8 km or more, and less than 0.075 MPa (0.75 bar) anywhere on the fault surface. The change in driving stress acting on the southwest dipping plane tends to be positive for all plausible combinations of hydraulic diffusivities. The magnitudes of the driving stress changes are less than or equal to 0.03 MPa (0.3 bar) at hypocentral depths on the southwest dipping plane.

It is difficult to evaluate the effect of these relatively small stress changes on the stability of a tectonically loaded fault. One possibility is to compare the stress changes resulting from fluid extraction with the stress drop of the Coalinga earthquake. Using the usual relationship for stress drop (Chinnery, 1969), and taking the average slip and fault width to be 1.8 m and 8 km, respectively (Stein, 1983), the stress drop of the mainshock is found to be of the order of 10 MPa (100 bar), the precise value depending on assumptions about the geometry of the fault plane. The change in driving stress due to fluid extraction (Figures 8 and 9) at hypocentral depths (10 ± 1 km) is thus less than 0.2 percent of the stress drop. For the range of diffusivities considered plausible here, the change in driving stress at hypocentral depths is no greater than 0.4 percent of the stress drop.

A second, and perhaps more interesting, comparison is to contrast extraction-induced stresses with stresses resulting from the solid earth tides. Tidal stresses within the crust have amplitudes of the order of 5×10^{-3} MPa (Stacey, 1969). The shear stresses induced by fluid extraction are 3 to 4×10^{-2} MPa, an order of magnitude greater than the tidal stresses. Thus, although extraction-induced stresses are small, they can not be ruled out as a potential triggering mechanism because of their small magnitude.

If the rate of tectonic stress accumulation across the Coalinga fault were known it would be possible to compare the natural stress rate with the stresses induced by extraction. To take a purely hypothetical example, if the rate of tectonic stress accumulation is 0.1 bar/yr, and the mainshock fault surface is the southwest dipping plane (Figure 9), then the effect of fluid extraction might have been to shorten the inter-earthquake time by one to two years. Similarly, if the tectonic stress rate is 0.01 bar/yr, then extraction would be expected to advance the time of the earthquake by one to two decades. If, on the other

hand, the steeply, northeast dipping plane is the mainshock surface (Figure 8), then the most likely effect of extraction would have been to increase the inter-earthquake time by a comparable amount. These examples clearly demonstrate that in order to properly assess the significance of the stress changes calculated here, it will be necessary to determine the tectonic rate of stress accumulation (or the recurrence interval) and to identify which of the two possible planes was the mainshock fault plane.

CONCLUSIONS

The presence of thick argillaceous units below the oil producing horizons is almost certain to have prevented flow of pore fluids between the oil fields and the focal region of the 1983 Coalinga earthquake. In any case, the dominant effect of oil field operations (namely extraction of pore fluids) has been to decrease pore pressures in the producing strata. In the unlikely event that fluid transport occurred between the producing zones and the earthquake focus, the result would have been to diminish pore pressures along the fault zone, thereby inhibiting frictional slip.

Extraction of large volumes of fluid from the oil fields resulted in a 50 percent decrease in pore pressure within the Gatchell sand between 1938 and 1983, and caused Anticline Ridge to subside at approximately 3 mm/yr. Stress changes at hypocentral depths, calculated from a model based on Biot's constitutive theory for fluid-infiltrated, elastic media, are small in comparison to the earthquake stress drop. The calculated driving stress (shear stress minus frictional resistance) depends on the hydraulic diffusivity of the producing rocks and the orientation of the fault plane. For the steeply northeast dipping plane, the driving stress increased by less than 0.1 bars at depths of 4–9 km, weakly favoring slip at shallow depths. At depths of 9–11 km, fluid extraction decreased the driving stress by less than 0.05 bars, slightly inhibiting slip near the earthquake hypocenter. For the shallow, southwest dipping plane the driving stress increased by less than 0.2 bars, slightly favoring fault slip. Although the calculated stress changes are not easily verified by direct measurement, the ability of the theory to quantitatively explain observed changes in the elevation of Anticline Ridge, and reservoir pressures in the Gatchell sand suggest that the method yields reasonable estimates of stress change at depth.

Acknowledgments

We thank Richard Curtain of the California Division of Oil and Gas for providing valuable data on the Coalinga oil fields, R. Stein for assistance in interpreting the leveling data, and D. Eberhart-Phillips and P. Reasenberg for assistance with the aftershock data. J. Walder and R. O. Castle provided helpful comments on the manuscript.

REFERENCES

Bartow, J. A., 1984, Cenozoic stratigraphy and geologic history of the Coalinga region, central California: *this volume.*

Bell, M. L., and A. Nur, 1978, Strength changes due to reservoir-induced pore pressure and stresses and application to Lake Oroville: *Journal of Geophys. Research, v. 83,* p. 4469–4483.

Biot, M. A., 1941, General theory of three-dimensional consolidation: *J. Appl. Phys., v. 12,* p. 155–164.

Brace, W. F., 1980, Permeability of crystalline and argillaceous rocks: *Int. J. Rock Mech. Min. Sci. Geomech. Abstr., v. 17,* p. 241–251.

California Division of Oil and Gas, (unpub. data, 1983), *California Oil and Gas Fields, Volume 1: North and East Central California*: California Division of Oil and Gas, 1973; revised edition.

Conservation Committee of California Oil Producers, 1982, Annual review of California oil and gas production: Cons. Comm. Calif. Oil Gas Prod., 1982 and earlier.

Carslaw, A. R., and C. J. Jaeger, 1982 Conduction of Heat in Solids: Oxford at the Clarendon Press, London.

Chinnery, M. A., 1969, Theoretical fault models, in *A Symposium on Processes in the Focal Region,* K. Kasahara and A. E. Stevens, eds.: Dominion Observatory, Ottawa, p. 211–223.

Eaton, J., R. Cockerham, and F. Lester, 1983, Study of the May 2, 1983 Coalinga earthquake and its aftershocks, based on the USGS seismic network in northern California, in, *The 1983 Coalinga, California Earthquake*: California Division of Mines and Geology Special Publication 66, p. 261–273.

Eshelby, J. D., 1957, The determination of the elastic field of an ellipsoidal inclusion and related problems: *Proc. Roy. Soc. London,* Ser. A *241,* p. 376–396.

Gupta, H. K., and B. K. Rastogi, 1976, Dams and Earthquakes: Elsevier, New York, 229 p.

Healy, J. H., W. W. Rubey, D. T. Griggs, and C. B. Raleigh, 1968, The Denver earthquakes: *Science, v. 161,* p. 1301–1310.

Holdahl, S. K., 1981, A model of temperature stratification for correction of leveling refraction: *Bull. Geodesique, v. 55,* p. 231–249.

Kovach, R. L., 1974, Source mechanisms for Wilmington oil field, California, subsidence earthquakes: *Bull. Seismol. Soc. Am., v. 64,* p. 699–711.

Pratt, W. E., and D. W. Johnson, 1926, Local subsidence of the Goose Creek oil field: *J. Geology, v. 34,* p. 577–590.

Prokopovich, N. P., and D. C. Magleby, 1968, Land subsidence in Pleasant Valley area, Fresno County, Calif.: *J. Amer. Water Works Assoc., v. 60,* p. 413–424.

Raleigh, C. B., J. H. Healy, and J. D. Bredehoeft, 1972, Faulting and crustal stress at Rangely, Colorado, in H.C. Heard, I. Y. Borg, N. L. Carter, and C. B. Raleigh, eds.: *Flow and Fracture of Rocks, Geophysical Monograph Series, American Geophys. Union, Washington, D. C., v. 16,* p. 275–284.

Raleigh, C. B., J. H. Healy, and J. D. Bredehoeft, 1976, An experiment in earthquake control at Rangely, Colorado: *Science, v. 191*, p. 1230–1237.

Reasenberg, P., D. Eberhart-Phillips, and P. Segall,1983, Preliminary views of the aftershock distribution, in R. D. Borcherdt, ed., The Coalinga earthquake sequence commencing May 2, 1983: *U.S. Geological Survey Open-File Report 83-54*, 79 pp.

Rice, J. R., and M. C. Cleary, 1976, Some basic stress diffusion solutions for fluid-saturated elastic porous media with compressible constituents: *Rev. Geophys. Space Phys., v. 14*, p. 227–241.

Segall, P., 1984, Stress and subsidence resulting from subsurface fluid withdrawal in the epicentral region of the 1983 Coalinga earthquake: submitted to *Journal of Geophys. Research.*

Simpson, D. W., 1976, Seismicity changes associated with reservoir loading: *Engineering Geology, v. 10*, p. 123–150.

Stacey, F. D., 1969, Physics of the Earth, J. Wiley & Sons, New York, 324 pp.

State Oil and Gas Supervisor, Annual Reports: California Division of Oil and Gas, 1981 and earlier.

Stein, R. S., 1983, Reverse slip on a buried fault during the 2 May 1983 Coalinga earthquake: evidence from geodetic elevation changes, in, *the 1983 Coalinga, California Earthquakes*: California Division of Mines and Geology Special Publication 66, p. 151–163.

Yerkes, R. F., and R. O. Castle, 1976, Seismicity and faulting attributable to fluid extraction: *Eng. Geology, v. 10*, p. 151–167.

Zoback, M. D., and S. M. Hickman, 1982, In situ study of the physical mechanisms controlling induced seismicity at Monticello, Reservoir, South Carolina: *Journal of Geophys. Research, v. 87*, p. 6959–6974.

	TEMBLOR	GATCHELL
Depth (D)	0.6 km	2.3 km
Thickness (T)	75 m	0–190 m
Rate of Liquid Extraction $(-\dot{V})$	1.6×10^6 m^{3}yr	3.7×10^6 m^3/yr
Year Extraction Begins	1905	1940
Characteristic Length (L) Along Strike	10 km	10 km
Porosity (ϕ)	0.3	0.2
Permeability (k)	2,000 md	420 md
Liquid Compressibility (β)	3×10^{-10}/Pa	3×10^{-10}/Pa
Viscosity (η)	100 cp	1 cp
Diffusivity (c)	0.2 m^2/s	7.0 m^2/s
Skempton's Coef. (B)	0.6	0.6
Poisson's Ratio		
Undrained (ν_u)	0.33	0.33
Drained (ν)	0.20	0.20
Shear Modulus (μ)	8×10^9 Pa	8×10^9 Pa

Table 1: Average Properties Of Producing Horizons

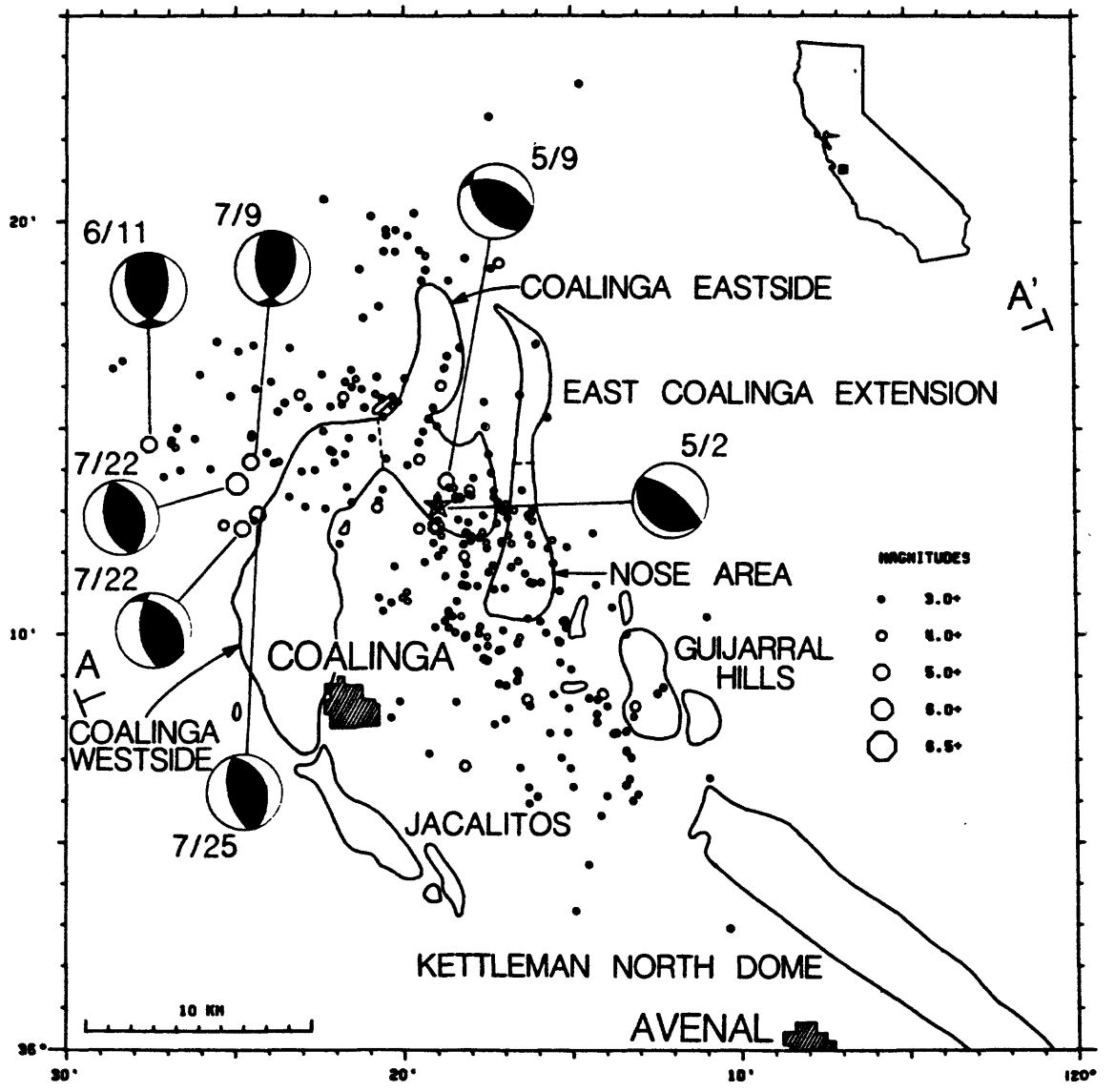

Figure 1. Relationship between Coalinga earthquake sequence and oil fields. Mainshock (star) and M $\geq$ 3 aftershocks are shown for May–July 1983. Focal mechanisms are shown for M $\geq$ 5 events. Outlines of the major oil fields are also shown. (Seismic data is replotted from Eaton *et al.*, 1983).

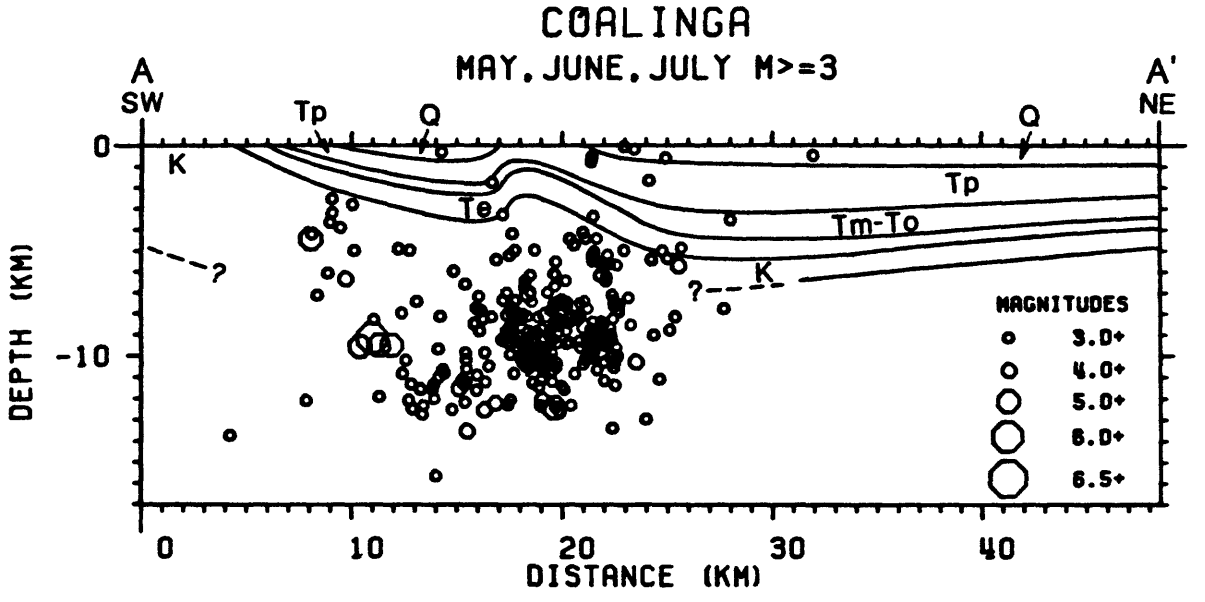

Figure 2. Cross section of seismicity and geology. Mainshock (star) and M $\geq$ 3 aftershocks for May–July 1983 (after Eaton *et al.*, 1983). Mainshock and most large aftershocks have hypocentral depths near 10 km. The principal oil producing horizons have average depths of 0.6 km (Temblor) and 2.2 km (Gatchell). Q: Quaternary; Tp: Pliocene; Tm: Miocene; To: Oligocene; Te: Eocene; K: Cretaceous.

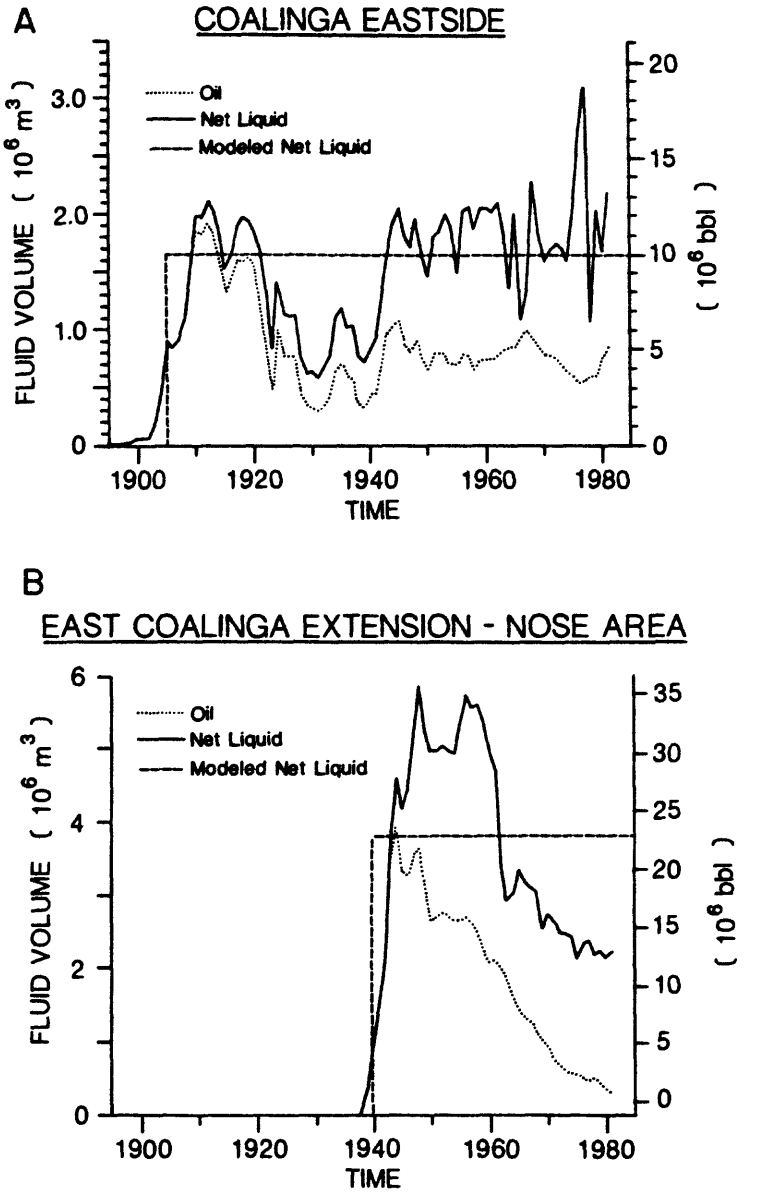

Figure 3. **Production history of Anticline Ridge oil fields. Net liquid is defined as oil + water – returned water. (a) Coalinga Eastside. (b) East Coalinga Extension, nose region. (From Annual Reviews, Conservation Committee, California Oil Producers and Annual Reports, State Oil and Gas Supervisor.)**

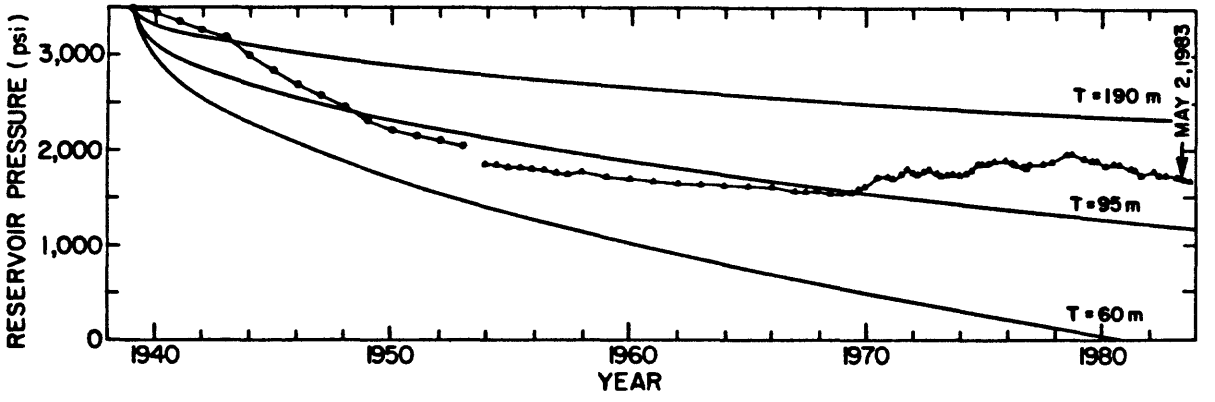

Figure 4. Reservoir pressure with time in the Gatchell sand, Coalinga nose area of the Coalinga East Extension Field. Circles represent pressures measured within the oil zone (2,060 m), triangles are pressures measured within the gas cap (1,980 m). Solid lines are calculated pressure histories assuming fluid withdrawal at a constant rate (see text). *T* is thickness of producing zone.

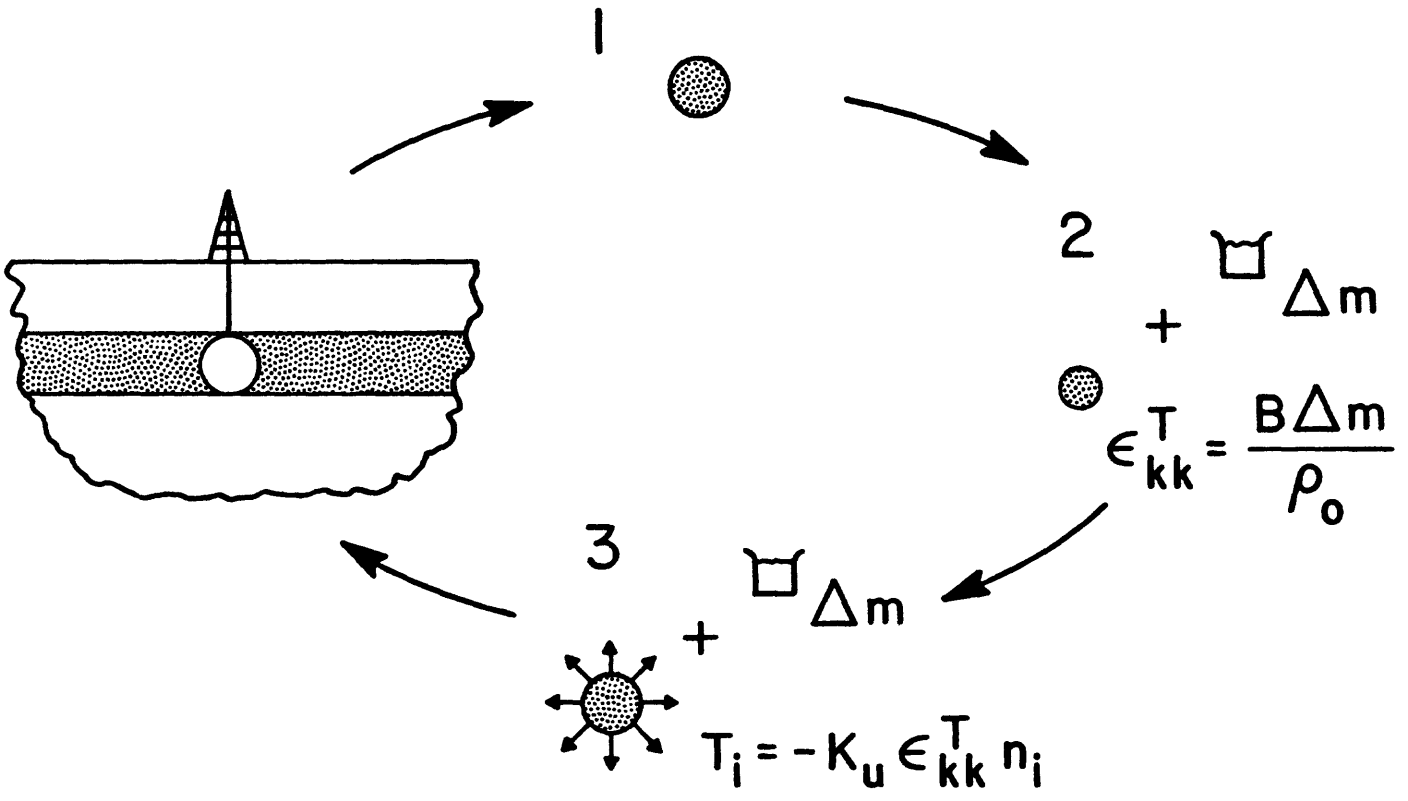

Figure 5. Thought experiment demonstrating effects of fluid extraction: (1) Inclusion is removed from half-space. (2) Fluid with mass Δm is extracted from the inclusion, causing the inclusion to contract. (3) Applied stresses restore the inclusion to its initial shape, allowing it to be reinserted into the half-space.

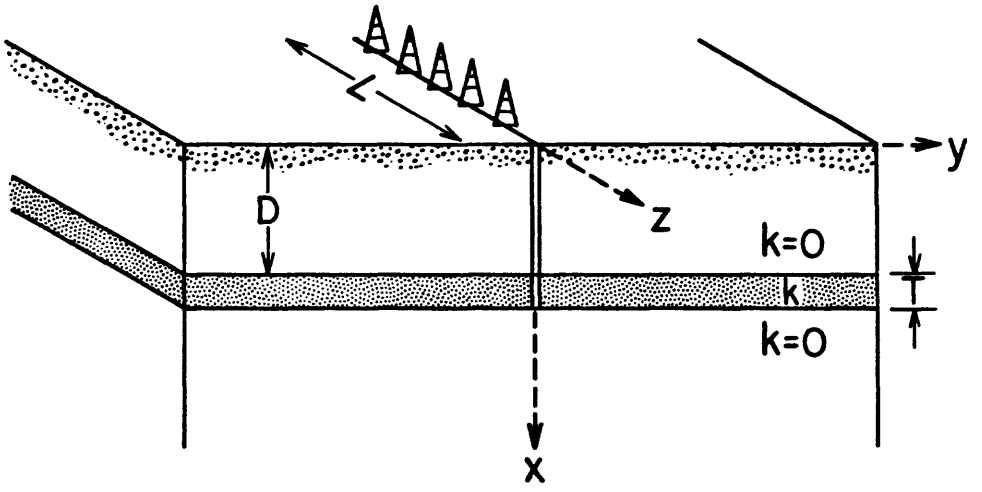

Figure 6. Layer of thickness T, and permeability k buried at a depth D in a fluid-infiltrated, impermeable ($k = 0$), half-space.

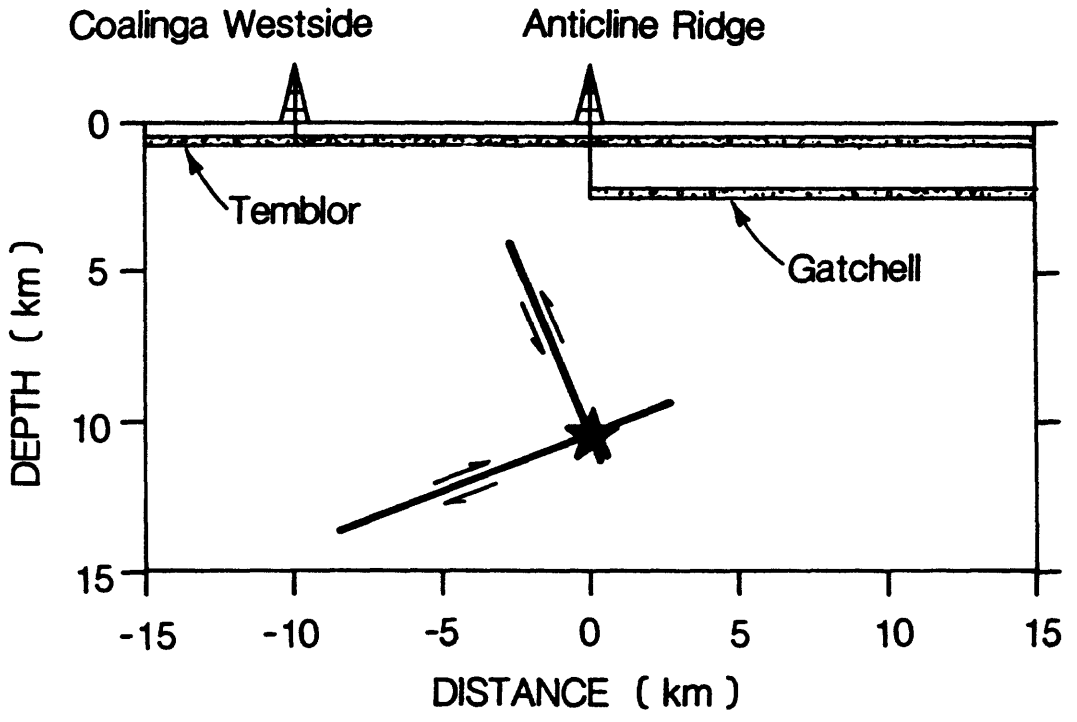

Figure 7. Geometry used to model stress change and subsidence in the Coalinga region.

Figure 8(a)

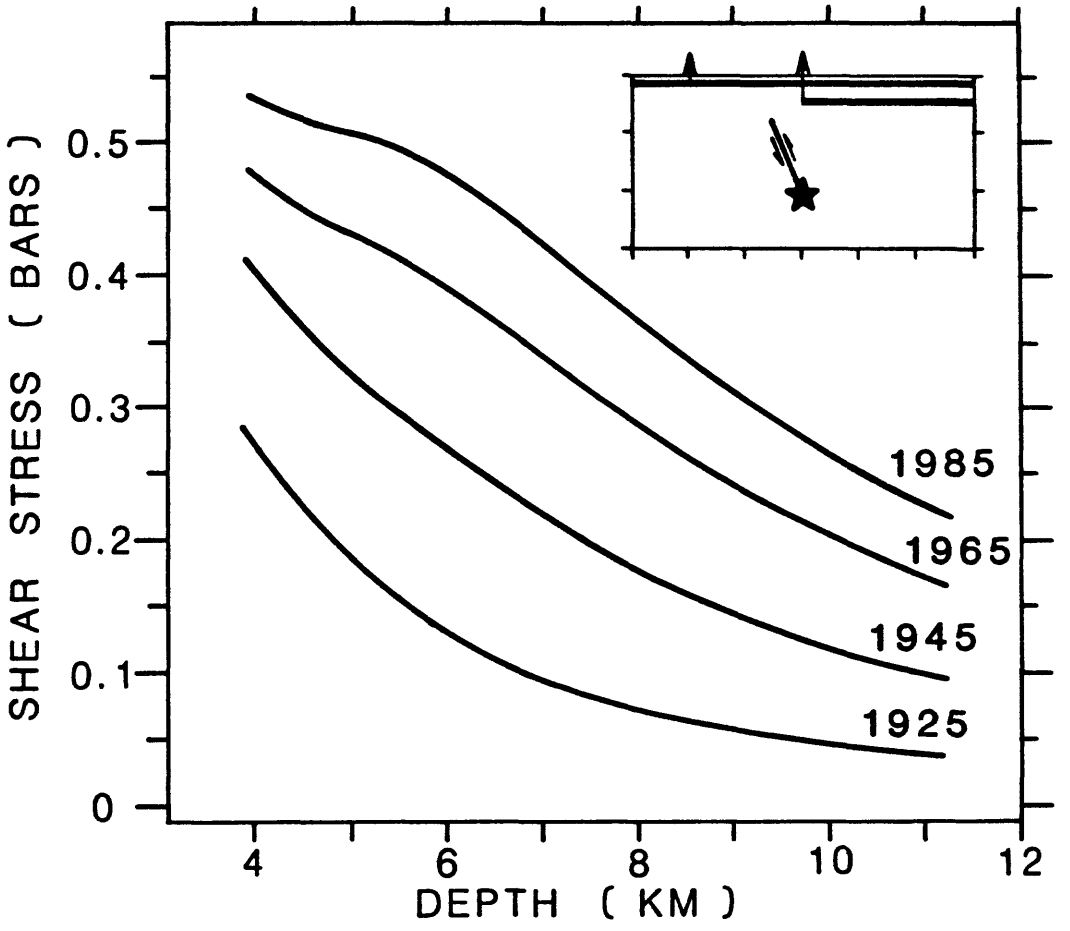

Figure 8. Change in stresses resolved on the northeast dipping plane due to fluid extraction as a function of depth. Stress changes are shown at four different times. Extraction from the Temblor begins in 1905, from the Gatchell in 1940. (a) Change in resolved shear stress. Positive shear stresses favor reverse slip on fault. (b) Change in resolved normal stress. Negative normal stresses indicate compression, which inhibits frictional slip. (c) Change in resolved 'driving stress,' $\Delta\sigma_s + f(\Delta\sigma_n + \Delta p)$. The coefficient of friction f is taken to be 0.6. The pore-pressure change Δp is the undrained or 'instantaneous,' response to changes in mean stress. Positive values of driving stress favor reverse slip, negative values inhibit slip.

Figure 8(b)

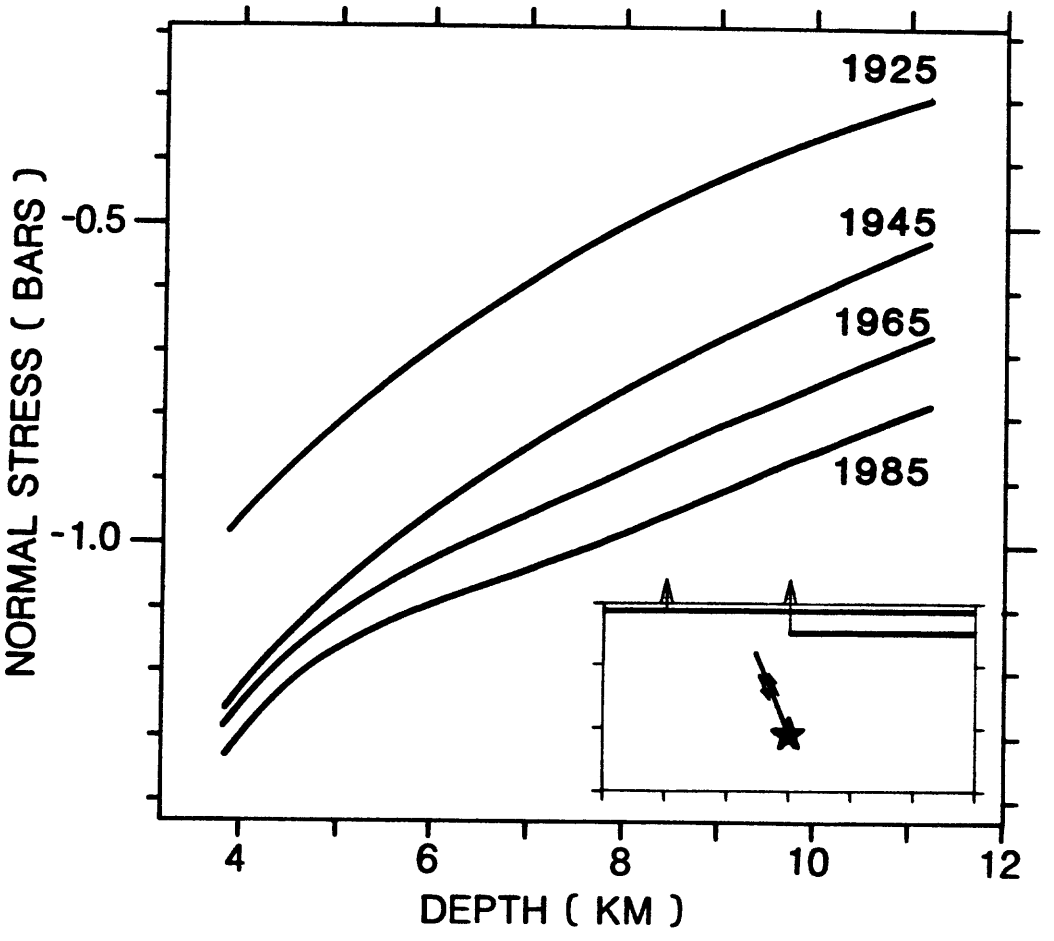
1925
1945
1965
1985
NORMAL STRESS (BARS)
-0.5
-1.0
4
6
8
10
12
DEPTH (KM)

Figure 8(c)

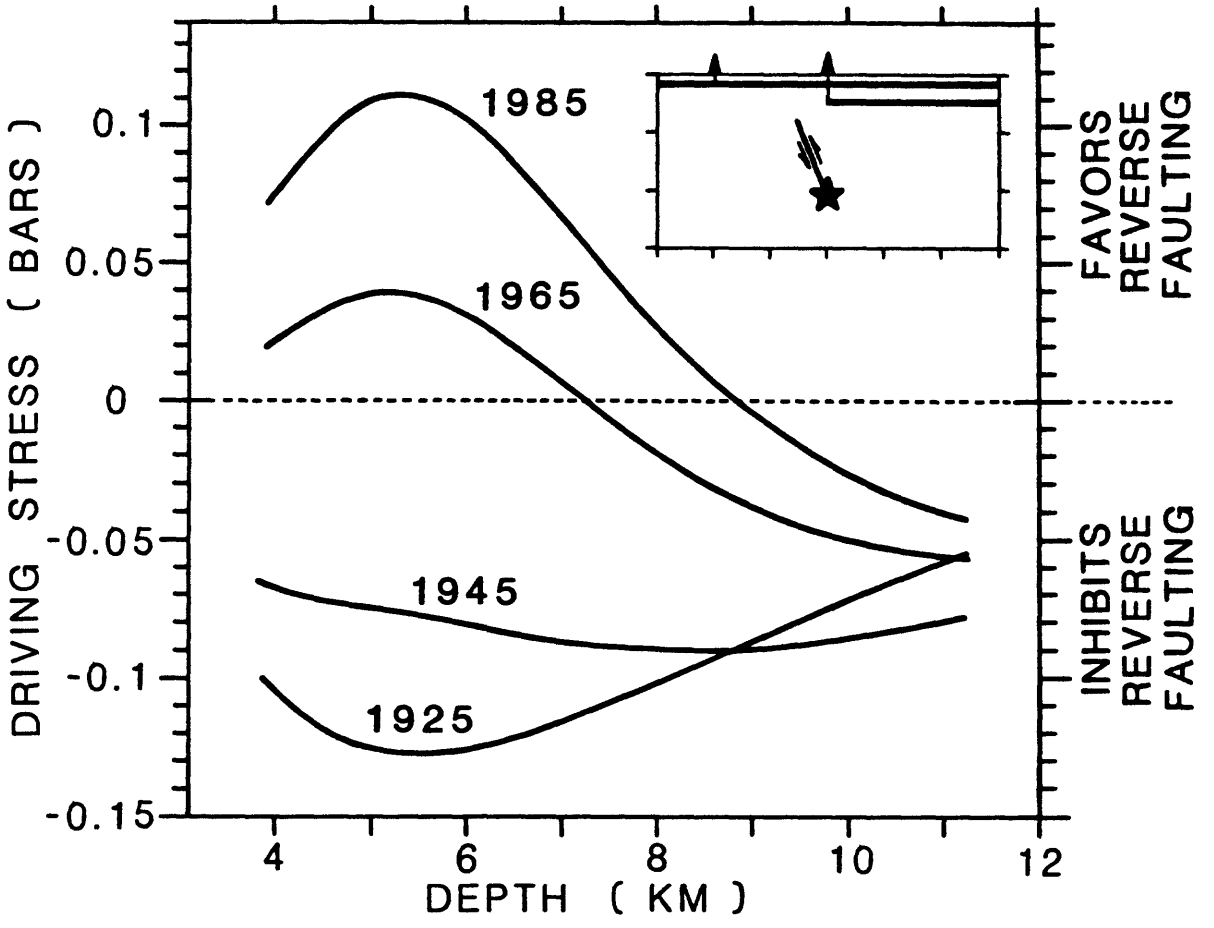
1985
1965
1945
1925
0.1
0.05
0
-0.05
-0.1
-0.15
DRIVING STRESS (BARS)
4
6
8
10
12
DEPTH (KM)
FAVORS REVERSE FAULTING
INHIBITS REVERSE FAULTING

Figure 9(a)

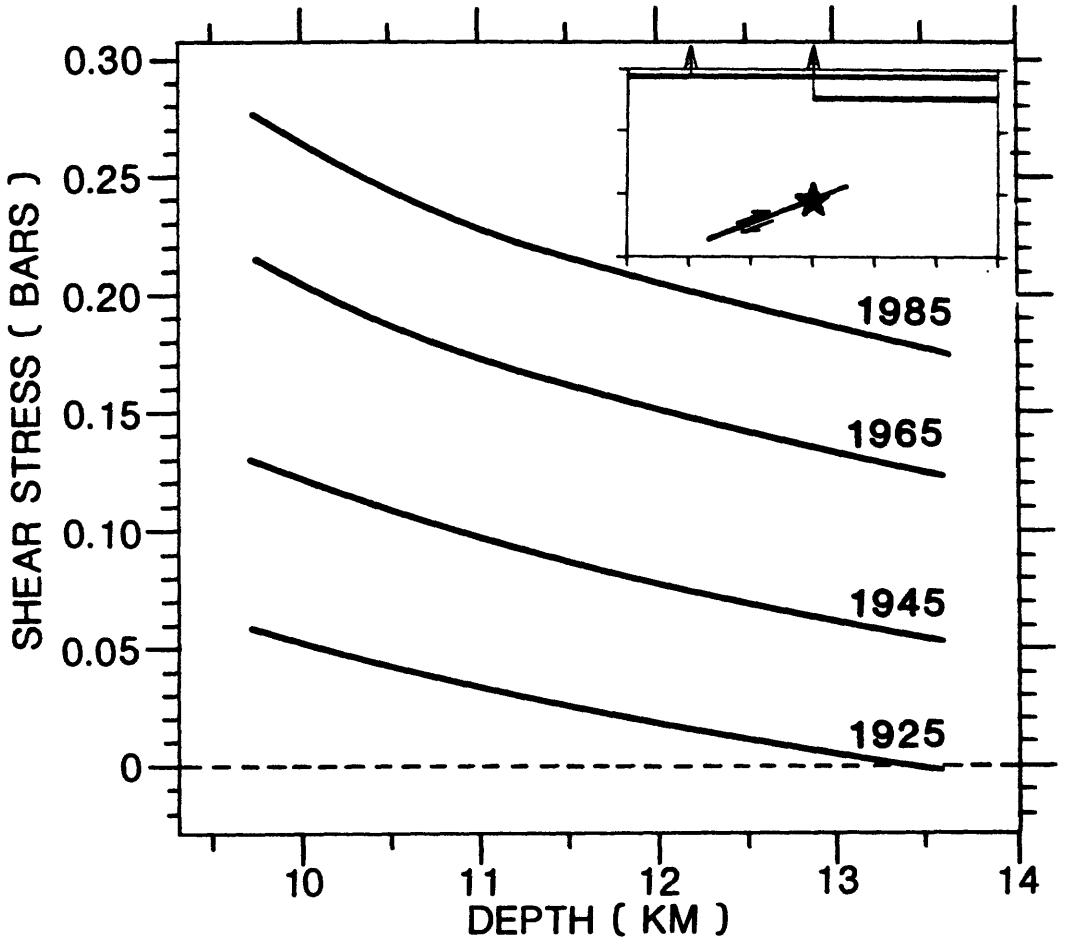

Figure 9. Change in stress resolved on southwest dipping plane. (a) Shear stress. (b) Normal stress. (c) Driving stress. Sign convention is the same as in Figure 8.

Figure 9(b)

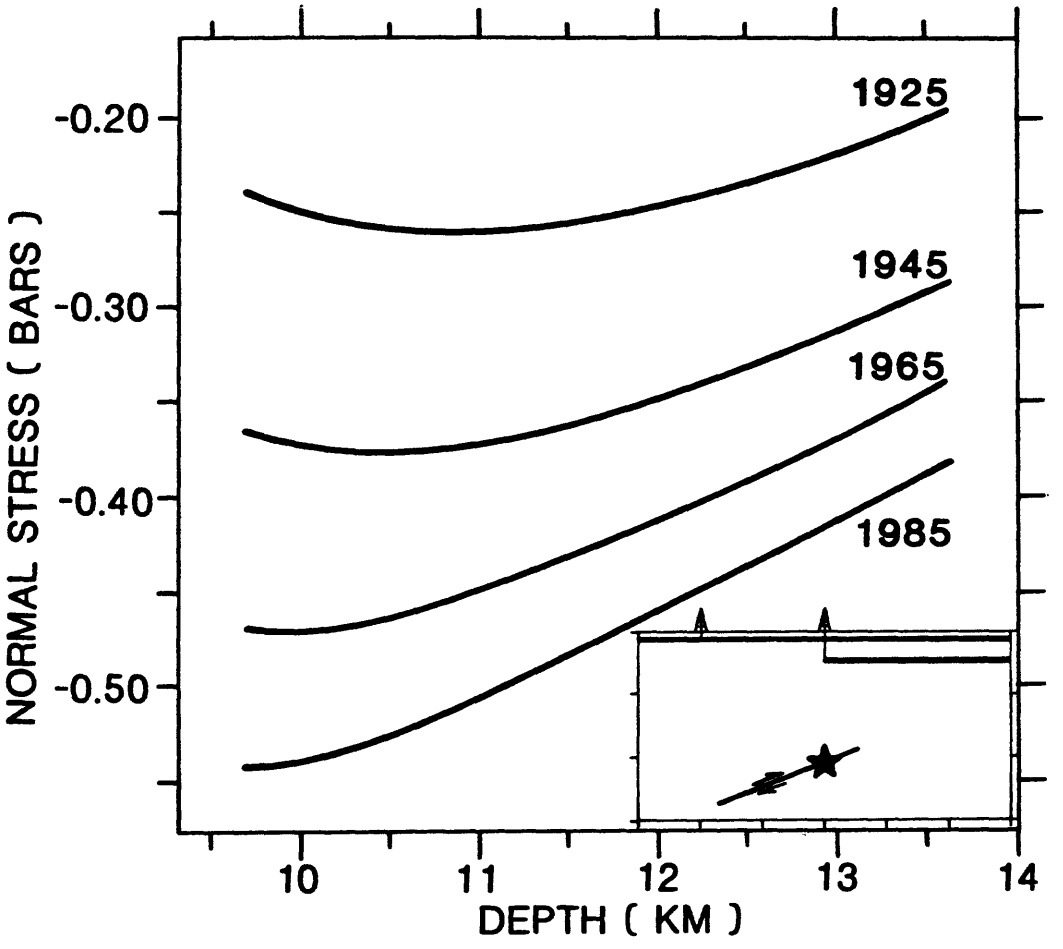
1925
1945
1965
1985
-0.20
-0.30
-0.40
-0.50
NORMAL STRESS (BARS)
10
11
12
13
14
DEPTH (KM)

Figure 9(c)

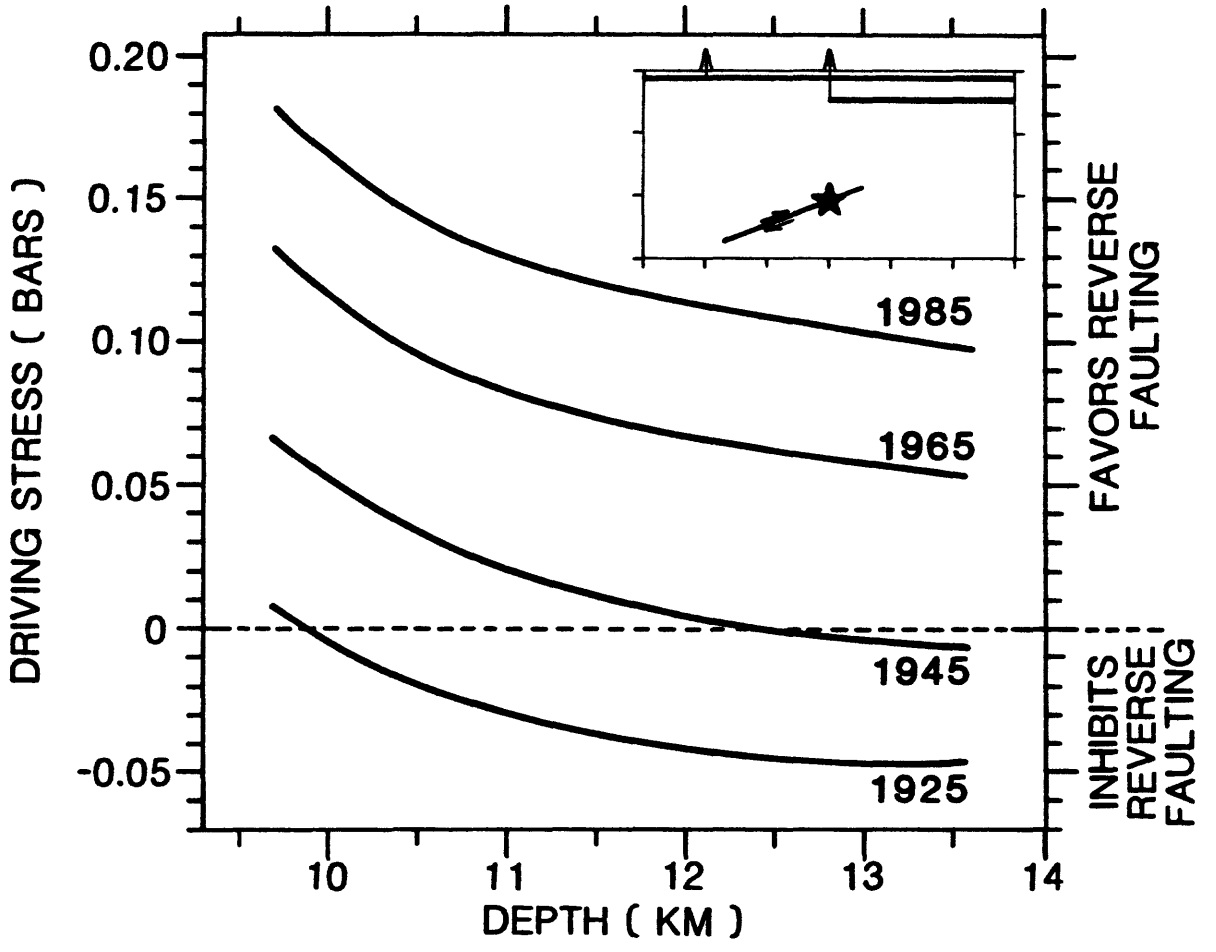
0.20
0.15
0.10
0.05
0
-0.05
DRIVING STRESS (BARS)
1985
1965
1945
1925
FAVORS REVERSE FAULTING
INHIBITS REVERSE FAULTING
10
11
12
13
14
DEPTH (KM)

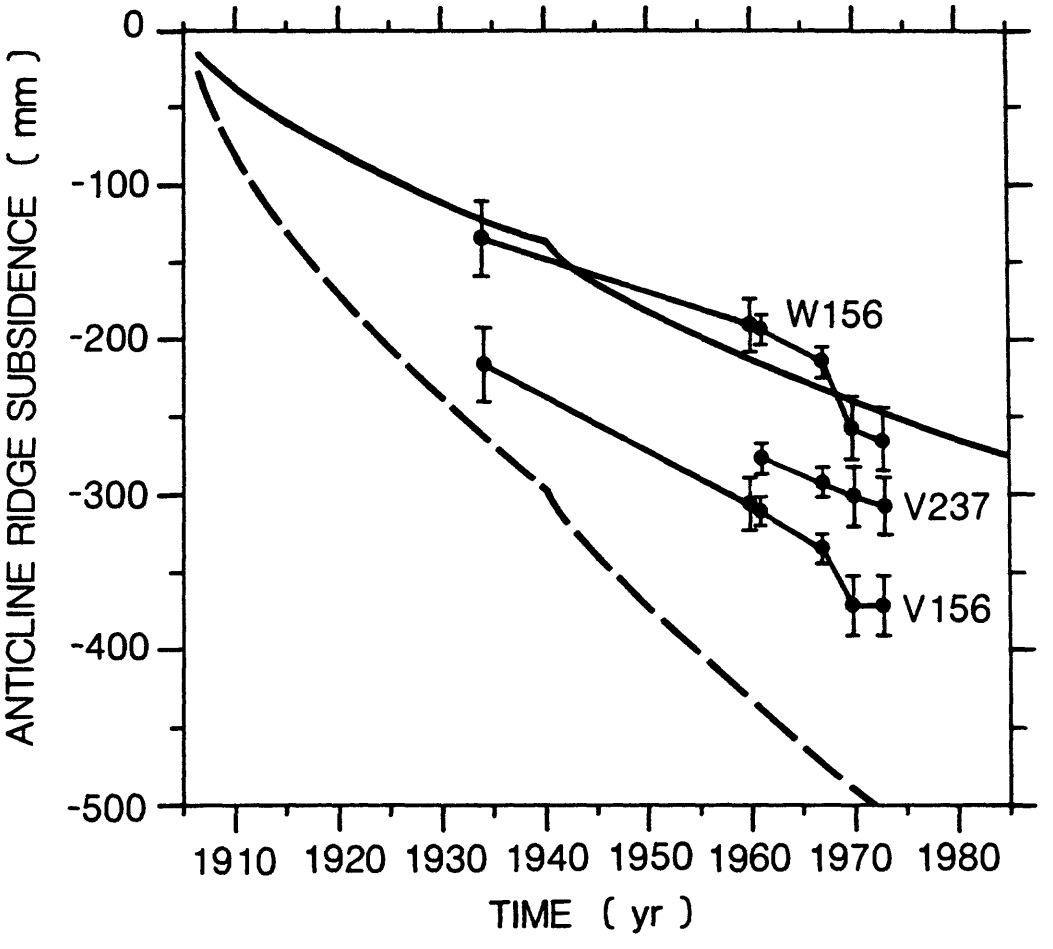

Figure 10. Observed elevation changes of three bench marks (W156, V156, and V237) on Anticline Ridge, compared with vertical displacements calculated from equation (12). The solid curve illustrates subsidence calculated with the hydraulic diffusivity of the Temblor equal to the preferred value of 0.2 m^2/s. The dashed curve illustrates the effect of decreasing this value to 0.02 m^2/s. The diffusivity of the Gatchell is 7.0 m^2/s in both cases.

ABNORMALLY HIGH FLUID PRESSURES IN THE REGION OF THE COALINGA EARTHQUAKES-A PRELIMINARY REPORT

By R. F. Yerkes, Paia Levine, and C. M. Wentworth
United States Geological Survey
345 Middlefield Road
Menlo Park, CA 94025

Abstract

Abnormally high pore-fluid pressures (AHP), through significant reduction of effective vertical stress and rock strength, may have contributed to the Coalinga earthquake sequence. Much of southwest San Joaquin Valley is underlain at shallow depths by deposits with fluid pressure/depth ratios near or above 11.3 kPa/m (0.5 psi/ft); a plot of bottom-hole ratios from about 300 wells averages about 13.6 kPa/m (0.6 psi/ft) and shows an upper bound near 20.4 kPa/m (0.9 psi/ft). The ratios generally increase with depth; below about 3 km the average increases with depth at a rate 22.6 kPa/m (1.00 psi/ft) and the large ratios extend to at least the limit of drilling, about 6.5 km. The ratios at shallow depth along the Lost Hills-Kettleman Hills trend are relatively large; below 3 km AHP probably extends through Coalinga anticline, site of the earthquakes, to Joaquin Ridge on the southeast flank of the New Idria serpentinite. Sonic logs for a few deep modern wells all show abrupt reversals in the velocity/depth gradient at the top of the AHP ($\geqslant$13.8 kPa/m; 0.61 psi/ft) zone; this reversal coincides with the top of a seismic low-velocity zone as determined independently. The sources of the AHP are not known, but all data are consistent with their derivation from metamorphic fluids from Franciscan, Great Valley, and Early Tertiary rocks, supplemented by compaction, and with their presence at depth below Coalinga anticline. Thrusting at rates suggested for the Coalinga earthquake, about 2 mm/yr, may induce AHP in the overridden plate and contribute to renewed thrusting there.

Introduction

Abnormally high pore-fluid pressures (AHP) are directly relevant to the thrust-displacement Coalinga earthquakes because, where present, they counteract the vertical load and significantly reduce the frictional strength of rocks. Well-known examples of such effects are the Denver earthquakes of the early sixties (Healy and others, 1968) and the induced earthquakes of the Rangely oil field (Raleigh and others, 1972). Abnormal fluid pressures are those that depart from hydrostatic; pressures that exceed hydrostatic (superpressures or overpressures) are encountered worldwide. The general upper limit of fluid pressure is the total weight of the overburden, although pressures as great as 140 percent of lithostatic are known to exist locally (Fertl and others, 1976). When the lithostatic gradient is exceeded, the nearby rocks are deformed either by shear failure or hydraulic fracture.

Abnormally high fluid pressures are formed and preserved by pore fluids trapped under stress over geologic time. The inferred causes of overpressures are manifold and complex; in many cases several causes probably are present and impossible to differentiate. In any sealed reservoir containing petroleum fluids, normal pressures in the deepest parts of dipping beds will be transmitted to the shallow parts and result in local overpressures. Petroleum fluids in anticlines thus commonly exhibit locally high pressures, whereas

normal pressures may exist below the oil/water boundary. This circumstance may be indicated in several San Joaquin Valley oil-field wells drilled through the AHP zone at relatively shallow depths. We are concerned here, however, with a regional-scale field of AHP, which in general increases in intensity with depth to the limit of drilling (6.5 km), exists in structural lows such as the Pleasant Valley syncline (as indicated by correlation with independently-mapped seismic low-velocity zones), and is known to be widespread in Great Valley sequence (GVS) and Franciscan rocks in adjoining areas (Berry, 1973).

Phenomena that contribute to large-scale AHP include rapid burial of undercompacted clay and sand sequences, sealed off by natural processes, which then remain undercompacted and overpressured. In addition to mechanical loading, abnormal temperature gradients, diagenesis, generation of petroleum in source rocks, and faulting and folding in compressive terrains have been identified as causes (Fertl and others, 1976; Chapman, 1983).

A brief survey of overpressured terrains is followed by a quantitative description of a discontinuous field of AHP that extends, below about 2 km, over most of the western San Joaquin Valley south of lat 36.80° N.--the north limit of our data. The field is most intense and continuous in the 80 km-long Lost Hills-Kettleman Hills anticlinal trend; from the north part of Kettleman Hills (North Dome), the AHP field probably extends through Coalinga anticline (below 3 km depth) to Joaquin Ridge southeast of the New Idria serpentinite. Although genesis of the AHP is a topic for a separate investigation, we identify a likely operating process, ongoing metamorphism in Franciscan, GVS, and Tertiary rocks, supplemented by compaction; we conclude with consideration of the implications in light of the tectonic setting.

Distribution

Overpressures are found in sedimentary materials world-wide; they are known from all continents, the North Sea, and the eastern Pacific Ocean (see Fertl and others, 1976, Chap. 9, for review). Overpressures occur in Cambrian to Cenozoic deposits, in anhydrite, gypsum, salt, dolomite, and limestone, but perhaps are best known in thick, massive, siltstone-shale sequences such as those of the Gulf Coast. The general range of intensities vs. depth, including San Joaquin Valley examples, is shown in figure 1. In California AHP are known in the east Santa Barbara Channel-Ventura area of the western Transverse Ranges (McCulloh, 1969) and in the Franciscan of the Northern Coast Ranges, are widespread and well developed in GVS of Sacramento Valley, and have been described in some detail in chiefly Tertiary strata of the Lost Hills-Kettleman Hills trend (Berry, 1973).

South San Joaquin Valley

Much of the 14,000 km^2 of San Joaquin Valley south of Panoche Creek (lat 36.80° N.), an area about 250 km long and 55 km wide (fig. 2), is underlain at depths below 1-2 km by deposits with fluid pressure/depth ratios near or above 11.3 MPa/km (0.5 psi/ft). All data come from wells drilled for oil, commonly on structural highs or along their trends. Because oil fields in this area are generally old and most oil-field wells shallow, data for the fields are sparse. Sampling is thus erratic both geographically and vertically, and

about forty percent of the area is not sampled. However, a number of modern, deep wells do sample the AHP field to depths of 5 to 6 km (table 1).

Methods

Equivalent pore-fluid pressures are derived from unit weights of drilling fluid (mud) as determined at the surface. Mud weights are carefully monitored and controlled, especially in overpressured terrain, because of the expense of drill-rig downtime and measures required to correct imbalances. Correction is required when mud is lost by entry into the formation being drilled (mud too heavy or overcompensated for pore-fluid pressure), or when the well "kicks" or "blows out"--the drill string is lifted or pore fluid dilutes the mud--(mud weight undercompensated). In order to avoid such problems, the lightest possible mud, sufficient to balance pore-fluid pressure, is used. Mud weight is adjusted continually as drilling proceeds in order to compensate for normally-increasing bottom-hole pressure. The need for more radical adjustment to compensate for abrupt increases in pore-fluid pressure (the top of the AHP zone) is determined by carefully monitoring the drilling rate, as penetration from normally-pressured to over-pressured beds results in an abrupt increase in drilling rate (Chapman, 1983). Comparison of our derived equivalents with measured formation pressures shows that our estimates are commonly within 10 percent of measured values at a given depth (fig. 3).

Pressure-depth relations

We examined data for about 300 wells to assess relations between mud-weight, equivalent pressures, measured pressures, depth, and stratigraphic level (fig. 4). The results show a regional average pressure/depth ratio of about 13.6 kPa/m (0.6 psi.ft), a lower bound somewhat above the hydrostatic gradient, and an upper bound near 20.4 kPa/m (0.9 psi/ft). The regional average ratio (13.6 K Pa/m; 0.6 psi/ft) is exceeded in at least 75 San Joaquin Valley wells (table 1). Most wells are located on structural highs, and all penetrate thick sedimentary sequences. Most AHP wells are located southwest of a line trending about N. 45^{0} W. near the axis of the valley. The "Sierran" basement surface rises gently northeastward from about 4.5 km depth near this line (fig. 2), from which the sedimentary sequence thins eastward and becomes nonmarine. The AHP zone is generally confined to Miocene and older strata. The top coincides with the top of thick shale/siltstone sequences and locally cuts sharply across stratigraphic boundaries (figs. 3, 6). Although a number of AHP wells penetrate pre-GVS basement rocks, none of these wells is known to bottom in Franciscan rocks.

Profiles of pressure/depth ratio vs. depth for all AHP wells show a relatively abrupt increase of the ratio below a depth of 1.5-2 km. Above this step the ratio is generally uniform in the range 11.3-13.6 kPa/m (0.5-0.6 psi/ft), whereas below it commonly increases to values as large as 20.4 kPa/m (0.9 psi/ft) or even larger. Below the step ($\geq$13.8 kPa/m, 0.61 psi/ft) the average ratio increases with depth at rates greater than 22.6 kPa/m (1.00 psi/ft), as shown by pressure/depth vs. depth plots for individual wells (fig. 5). The Joaquin Ridge well (fig. 5) is modern, and its record shows how carefully mud weight is constantly adjusted to balance pore-fluid presure. All four wells shown (fig.5) had circulation problems, the modern one only at the bottom, the others more frequently at and below the step. Pressure-increase/depth-increase rates ($\Delta P/\Delta D$) of 40.7 kPa/m (1.8 psi/ft) are theoreti-

cally possible in completely closed systems from which fluid cannot escape during rapid burial, and rates greater than 36 kPa/m (1.6 psi/ft) are obtained from Gulf Coast data (Magara, 1978, p. 99).

Pressure vs. sonic velocity

Sonic logs for a number of wells were examined for velocity-pressure relations. In all cases where sonic logs are available, the pressure step (to ratios 13.6 kPa/m) is marked by a sharp reversal in the velocity gradient. Above the step velocity increases with depth at a rate of about 0.5-0.7 km/s/km. The reversal below the step extends over a vertical range of a few tens to about 500 m and involves a reduction in velocity of 15-25 percent. Recovery of a positive trend below the reversal tends toward, but does not attain, the velocity gradient above the step. In one case where seismic velocities were determined independently from reflection and refraction profiles (Wentworth and others, 1983; Walter and Mooney, 1983), a very good correlation is shown between the sonic log and seismic profile-determined velocity gradients, as well as between the top of a low-velocity zone, the reversal on the sonic log, and the pressure step (fig. 7).

Fluid pressures below Coalinga anticline

Well data for Coalinga anticline are limited; (fig. 3); no direct evidence for AHP exists in the epicentral area of the Coalinga main shock above about 3 km depth. However, AHP with pressure/depth ratios $\geq$17.65 kPa/m (0.78 psi/ft) and rates of increase $\geq$22.6 kPa/m (1 psi/ft) are present in GVS beds of the lower plate below 3 km depth both northwest and southeast of Coalinga anticline. In addition, a seismic low-velocity zone, correlated with AHP, exists in dipping GVS beds of the Coalinga anticline-Pleasant Valley area between 3-7 km depth (Walter, this vol.). Once established, AHP zones are barriers to vertical migration of fluid (Chapman, 1973, p. 66). The existence of the thick and extensive LVZ (AHP) in the Coalinga anticline area indicates that any fluids trapped below will add to the total fluid pressure. These data support the assumption of near-lithostatic AHP in GVS-Franciscan rocks at focal depths below Coalinga anticline.

Sources of high fluid pressures

Once sediments are deposited in a basin, several processes may operate to raise fluid pressures if there is containment of the pore fluids (Chapman, 1983). In deep basins compaction of water-rich sediments under increasing overburden can proceed under high enough rates to overtake fluid drainage and place much of the lithostatic load directly on the pore fluid. Diagnetic and metamorphic reactions driven by increasing temperature or chemical disequilibrium between pore fluid and sediment can progressively add water, CO_2, and CH_4 (methane) to existing fluids. Increasing temperature that accompanies burial expands the volume of pore fluid relative to the sedimentary framework. Osmosis across clay-layer membranes can selectively raise pressures. Tectonic deformation can further compress the sedimentary rocks and load the pore fluids.

Berry (1973) attributed the AHP in Tertiary strata of the Lost Hills-Kettleman Hills trend chiefly to transmission of high fluid pressures from the underlying Great Valley sequence, accentuated by gravitational compaction and

regional-scale tectonic compression. Irwin and Barnes (1980) attributed AHP in much of the Coast Ranges to production of CO_2 during metamorphism of Franciscan rocks and/or leakage of CO_2 from mantle rocks. In south San Joaquin Valley, however, neither Franciscan nor GVS rocks are coextensive with the entire region that exhibits AHP, and any general explanation must account for AHP in areas that lack Franciscan and GVS rocks. In our view, a combination of diagenetic/metamorphic reactions, now active in Franciscan, GVS, and Tertiary rocks, supplemented by compaction, can account for the observed distribution of all the abnormal fluid pressures, including the AHP.

A large part of the Cretaceous and Tertiary sequence in south San Joaquin Valley consists of mudstone and siltstone (shale). As noted by Chapman (1983), compaction of a unit volume of water-saturated mudstone from 30 percent to 12.5 percent porosity results in 0.2 volume of expelled water. Compaction, through overburden pressure, decreases shale porosity; and travel time (the reciprocal of sonic velocity) varies directly with porosity. These relations have been quantified for Gulf Coast shales, and reviewed by Chapman (1983, Ch. 3). No comparable studies are available for south San Joaquin Valley, but similar relations are inferred. The recorded increase of velocity with depth above the AHP zone (fig. 7) reflects the general decrease of porosity with increasing overburden load and indicates normal compaction under normal fluid pressure. Where escape of fluid is limited, however, normal compaction is prevented, load is transferred to the pore fluid, an AHP zone is formed because of greater porosity in the undercompacted rock, and velocity decreases (travel time increases).

Once deposited, marine sedimentary rocks such as the Great Valley sequence and overlying Tertiary clastics begin a slow diagenetic and metamorphic progression toward equilibrium. Initially, while large amounts of pore fluid are still present, the clay and/or glass is hydrated in reactions that involve an equilibrium fractionation of deuterium from 0 per mil in sea water (by definition, the zero standard) to δ D of -60 per mil in the water of hydration. Subsequently, at temperatures at least as low as 85^{o} C., metamorphic reactions begin that include conversion of plagioclase to low albite and the clay hydrate to chlorite. These reactions convert the pore fluid to a sodium-calcium-chloride brine and further fractionate the deuterium to -80 per mil in the chlorite and -40 per mil in the brine. Following initial hydration, these reactions consistently produce excess water, which, barring free egress, must raise pore pressure.

Similar reactions are, or recently have been, underway in the GVS and Tertiary marine sediments of south San Joaquin Valley. 1). Natural springs issuing from exposed GVS rocks along the east side of the Diablo Range, including one at elevation 1525 ft on the northeast flank of Coalinga anticline, are consistently Na-Ca-Cl-rich brines with δ D of about -40 per mil (Barnes and others, 1975). 2). Oil-field formation (pore) waters from Eocene and older strata at Kettleman North Dome are characteristically Na-Ca-Cl rich (Kharaka and others, 1981). 3). Extensive examination of x-ray mineralogy of samples from Tertiary and GVS rocks shows the presence of the typical greenschist metamorphic assemblage quartz, chlorite, albite, and calcite (Merino, 1975; I. Barnes, pers. comm.). 4). The burial history of the San Joaquin Valley Cretaceous and Cenozoic sequence, as reconstructed by Zieglar and Spotts (1978), is fully compatible. The reconstruction assumed only a time-constant, linear temperature gradient of 27.2^{o} C./km (15^{o} F. per

thousand ft) (the present-day gradient for the upper 2 km ranges from 27^{o} to 35^{o} C./km; Kron and Stix, 1982) and a linear rate of sedimentation for given time units. The reconstruction shows that GVS beds at and below about 3 km depth in the axial part of the depositional basin attained a temperature of 85 ^{o} C. by about 75 mybp (Late Cretaceous) and about 200^{o} C. by about 55 mybp (early Eocene); these or higher temperatures have persisted to the present day for sediments below 3 km depth.

Organic matter, such as plant fragments, common in Franciscan and other marine sediments, is progressively metamorphosed toward pure carbon (graphite) as the sediment is buried and temperature raised. The process is well established at a temperature of 100^{o} C., and continues on through the blueschist metamorphic facies at 150^{o} C. In rich organic layers these changes transform peat through lignite and bituminous coal to anthracite and ultimately to graphite. As the temperature rises the hydrogen, hydroxyl, and other radicals attached to the basic carbon chains of the organic molecules are driven off, largely in the form of water, CO_2, and methane. Both the water and the gases act to raise pore pressure.

Numerous active springs that issue copious amounts of CO_2 and methane from Franciscan rocks throughout the Coast Ranges, including two at elevation 1600 ft on the northeast flank of Coalinga anticline, indicate that extensive metamorphism of organic matter is underway in Franciscan terrain (Barnes and others, 1975). The carbon in the emerging CO_2 is depleted in ^{13}C ($\delta^{13}C$ of -11 to -17 per mil) relative to CO_2 from the mantle (-7 per mil) or from marine carbonates (0 per mil); organic matter is the only possible source of the methane that accompanies the CO_2 (Ivan Barnes, pers, comm.).

Thus, much of the sequence in the south San Joaquin Valley--Franciscan graywacke, Great Valley strata, and the early Tertiary marine section--have been undergoing diagenetic/metamorphic reactions and compaction that over geologic time have progressively generated excess fluid, both liquid and gas. The potential for AHP has therefore long existed, given only adequate containment. Containment adequate to produce pressure-increase/ depth-increase rates (P/ D) greater than 22.6 kPa/m (1.00 psi/ft) exists over much of the area below depths of 3 km and to at least depths of 6.5 km (fig. 8). We conclude that, assuming hydraulic continuity below 3 km, AHP probably exist in GVS/Franciscan rocks at hypocentral depths (7-14 km) below Coalinga anticline.

AHP and the Coalinga earthquakes

The Coalinga thrust-reverse earthquakes occurred in terrain dominated by north- to northeast-directed compressive stress. The presence of near-lithostatic AHP in Franciscan or GVS beds at hypocentral depths would reduce effective vertical stress by more than 75 percent compared to hydrostatic pressures, would reduce shear strength by more than 65 percent, and thus would greatly enhance the effect of ambient horizontal compressive stress.

High fluid pressures probably exist at hypocentral depths beneath Coalinga anticline. The presence and generation of AHP is documented for Franciscan and Great Valley rocks, one or both of which form the seismogenic zone of the 1983 earthquakes (Walter, this vol.; Wentworth and others, this vol.). The refraction-detected LVZ below the Coalinga anticline area implies an AHP zone and this, in turn, requires containment of excess fluids being

formed below. McGarr and others (this vol.) note that near-lithostatic pore pressures can explain unexpectedly low crustal strengths inferred for the seismogenic zone.

Thrust faulting is a form of tectonic loading and approximately one meter of slip per 500 years (2 mm/yr average), such as estimated for the Coalinga main shock (Stein, this vol.), is comparable to rates inferred for the Rocky Mountain overthrust belt ((Gretener, 1976). At such rates AHP may be induced under the area of maximum loading in the overrridden plate, where a new thrust may develop in the weakened rocks while the older thrust is carried "piggy-back" on the upper plate and is folded or arched in the process, as illustrated in the Canadian Rockies (Gretener, 1972). It is also suggested that, since AHP zones are barriers to vertical migration of fluid, the thrusting process may proceed in a closed system and thus be self-perpetuating (Gretener, 1976).

Acknowledgements

R. F. Curtin and staff of the Coalinga office of the California Division of Oil and Gas were very helpful in gathering and reviewing well data. We greatly appreciate the stimulating discussions of the AHP field and its likely sources and implications with Ivan Barnes, M. C. Blake, T. H. McCulloh, A. F. McGarr, Paul Segall, and M. D. Zoback. McGarr and L. J. P. Muffler kindly read and commented on early versions of the report.

REFERENCES CITED

Barnes, Ivan, Irwin, W. P., and Gibson, H. A., 1975, Geologic map showing springs rich in carbon dioxide or chloride in California: U.S. Geological Survey Water Resources Investigations Open-File Map, scale 1:1,500,000.

Berry, F. A. F., 1973, High fluid potentials in California Coast Ranges and their tectonic significance: American Association of Petroleum Geologists Bulletin, v. 57, no. 7, p. 1219-1249.

Bishop, C. C. and Chapman, R. H., 1980, Bouguer gravity map of California, Santa Cruz Sheet, revised 1980: California Division of Mines and Geology, scale 1:250,00, and explanatory pamphlet.

Bostick, N. H., 1974, Phytoclasts as indicators of thermal metamorphism, Franciscan assemblage and Great Valley sequence (Upper Mesozoic), California: Geological Society of America Special Paper 153, p. 1-17.

Brace, W. F., and Kohlstedt, D. L., 1980, Limits on lithospheric stress imposed by laboratory experiments: Journal of Geophysical Research, v. 85, no. B11, p. 6248-6252.

Chapman, R. E., 1973, Petroleum Geology--A concise study: New York, Elsevier, 304 p.

_____, 1983, Petroleum Geology: Amsterdam, The Netherlands, Elsevier, 415 p.

Church, H. V. Jr., and Krammes, K. F., chm., 1957, Cenozoic correlation section across south San Joaquin Valley from San Andreas fault to Sierra Nevada foothills, California: American Association of Petroleum Geologists Pacific Section, Correlation Section 8.

Church, H. V. Jr., and Krammes, K. F., chm., 1959, Correlation section longitudinally north-south through westside San Joaquin Valley from Coalinga to Midway-Sunset and across San Andreas fault into southeast Cuyama Valley, California: American Association of Petroleum Geologists, Pacific Section, Correlation Section 11.

Fertl, W. H., Chilingarian, G. V., and Rieke, H. H., 1976, Abnormal formation pressures: Amsterdam, The Netherlands, Elsevier, 382 p.

Gretener, P. E., 1972, Thoughts on overthrust faulting in a layered sequence: Bulletin of Canadian Petroleum Geology, v. 20, p. 583-607.

_____, 1978, Pore pressure: fundamentals, general ramifications and implications for structural geology: American Association of Petroleum Geologists, Continuing Education Course Note Series No. 4, 87 p.

Healy, J. H., Rubey, W. W., Griggs, D. T., and Raleigh, C. B., 1968, The Denver earthquakes: Science, v. 161, no. 3848, p. 1301-1310.

Hsu, K. J., 1969, Role of cohesive strength in the mechanics of overthrust faulting and of landsliding: Geological Society of American Bulletin, v. 80, no. 6, p. 927-252.

Irwin, W. P., and Barnes, Ivan, 1980, Tectonic relations of carbon dioxide discharges and earthquakes: Journal of Geophysical Research, v. 85, no. B6, p. 3115-3121.

Kharaka, Y. K., Lico, M. S., Law, L. M., and Carothers, W. N., 1981, Geopressured-geothermal resources in California: Geothermal Resources Council Transactions, v. 5, p. 721-724.

Kron, Andrea, and Stix, John, 1982, Geothermal gradient map of the United States: Natinal Oceanic and Atmospheric Administration, scale 1:2,500,000.

Magara, Kinji, 1978, Compaction and fluid migration practical petroleum geology: Amsterdam, The Netherlands, Elsevier, 319 p.

McCulloh, T. H., 1969, Geologic characteristics of the Dos Cuadras offshore oil field: U.S. Geological Survey Professional Paper 679, p. 28-46.

Merino, Enrique, 1975, Diagenesis in Tertiary sandstones from Kettleman North Dome, California. I. Diagenetic mineralogy: Journal of Sedimentary Petrology, v. 45, no. 1, p. 320-336.

Raleigh, C. B., Healy, J. H., and Bredehoeft, J. D., 1972, Faulting and crustal stress at Rangely, Colorado: American Geophysical Union, Geophysical Monograph Series, v. 16, p. 275-284.

Smith, M. B., 1964, Map showing distribution and configuration of basement rocks in California (South half): U.S. Geological Survey Map OM 215, scale 1:500,000.

Walter, A. W., and Mooney, W. D., 1983, Preliminary report on the crustal velocity structure near Coalinga, California as determined from siesmic refraction surveys in the region: California Division of Mines and Geology, Special Report 66, p. 127-135.

Wentworth, C. M., Walter, A. W., Bartow, J. A., and Zoback, M. D., 1983, Evidence on the tectonic setting of the 1983 Coalinga earthquakes from deep reflection and refraction profiles across the southeastern end of the Kettleman Hills: California Division of Mines and Geology, Special Publication 66, p. 113-126.

Zieglar, D. L., and Spotts, J. H., 1978, Reservoir and source-bed history of Great Valley, California: American Association of Petroleum Geologists Bulletin, v. 62, no. 5, p. 813-826.

Figure Captions

1. Fluid pressure-depth plot for selected fields, showing range of abnormally high gradients. San Joaquin Valley fields shown by heavy lines.

2. Map of southern San Joaquin Valley region showing exposures of Franciscan and Sierran basement rocks, selected faults, oil and gas fields, wells that penetrate zone of abnormally high fluid pressures and/or bottom in basement rocks, fault-plane solutions for earthquakes, lines of structure sections, and contours on top of basement rocks (modified from Smith, 1964). Well data listed in table 1.

3. Structure section along line A-A' (fig. 2) through Lost Hills, Kettleman Hills, and Coalinga anticline to Joaquin Ridge, showing top of zone of abnormally high fluid pressures. Modified from Church and Krammes (1959).

4. Plot of equivalent fluid pressures vs. depth by bottom-hole geology, San Joaquin Valley wells. Well data listed in table 1.

5. Plot of pressure/depth ratio vs. depth for selected wells along Joaquin Ridge-Lost Hills trend, showing intensity of fluid pressures with depth. Well numbers refer to table 1.

6. Structure section along line C-C' (fig. 2) across south San Joaquin Valley, showing top of zone of abnormally high fluid pressures. Modified from Church and Krammes (1957).

7. Sonic velocity, fluid pressure and lithology vs. depth, well 62, western San Joaquin Valley (fig. 2), showing correlation of sonic-log velocities with those from seismic reflection and refraction profiles (Wentworth and others, 1983), and reversal of gradients at top of abnormally high fluid pressure zone at 3.5 km depth.

8. Rate of pressure increase with depth ($\Delta P/\Delta D$) vs. total depth for most "AHP" wells in south San Joaquin Valley (table 1). Line shows least-squares fit.

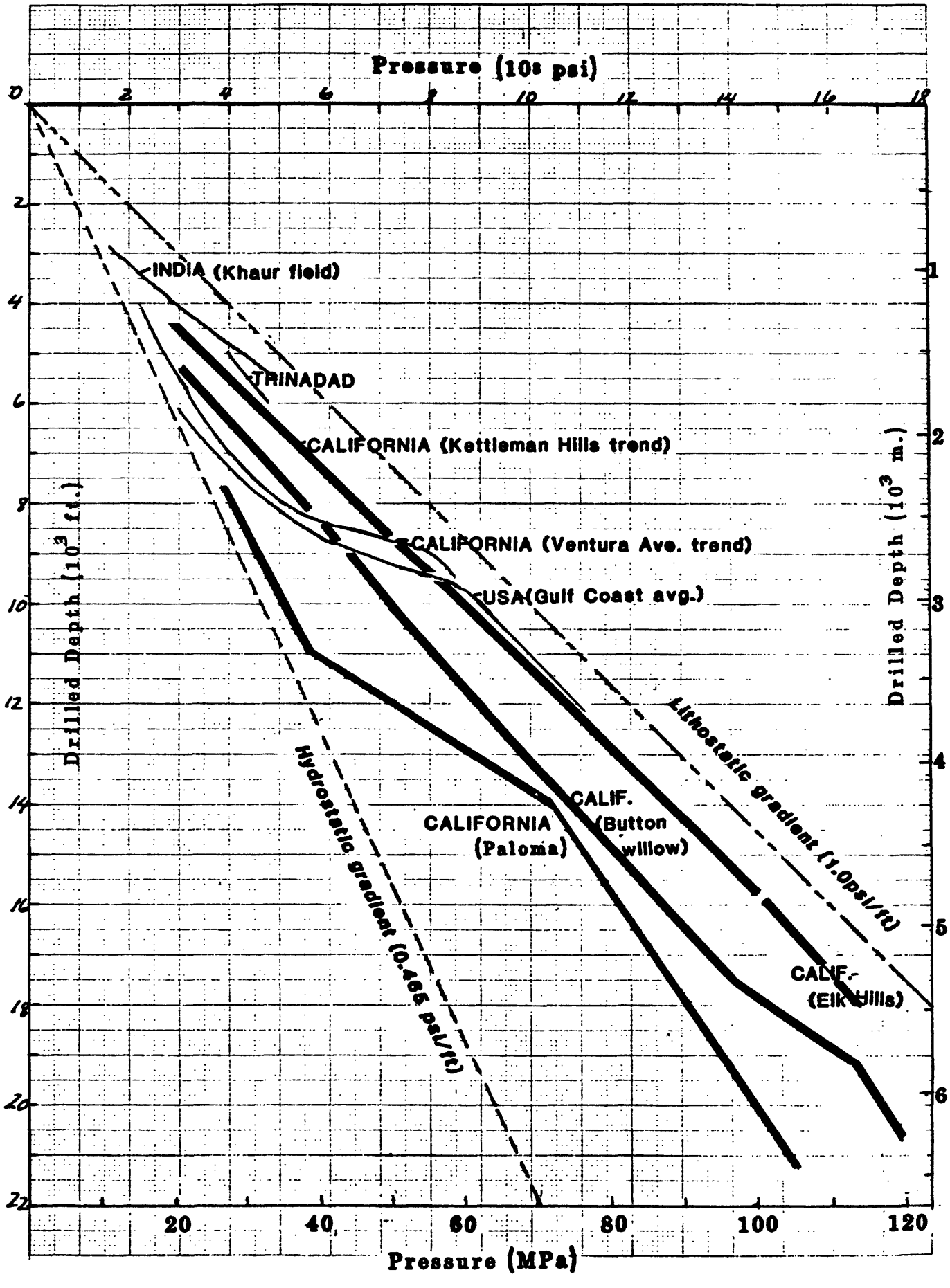
Pressure (10³ psi)
0
2
4
6
8
10
12
14
16
18
INDIA (Khaur field)
TRINADAD
CALIFORNIA (Kettleman Hills trend)
CALIFORNIA (Ventura Ave. trend)
USA(Gulf Coast avg.)
Lithostatic gradient (1.0psi/ft)
Hydrostatic gradient (0.465 psi/ft)
CALIF. (Button willow)
CALIFORNIA (Paloma)
CALIF. (Elk Hills)
Drilled Depth (10³ ft.)
Drilled Depth (10³ m.)
2
4
6
8
10
12
14
16
18
20
22
1
2
3
4
5
6
20
40
60
80
100
120
Pressure (MPa)

Figure 1

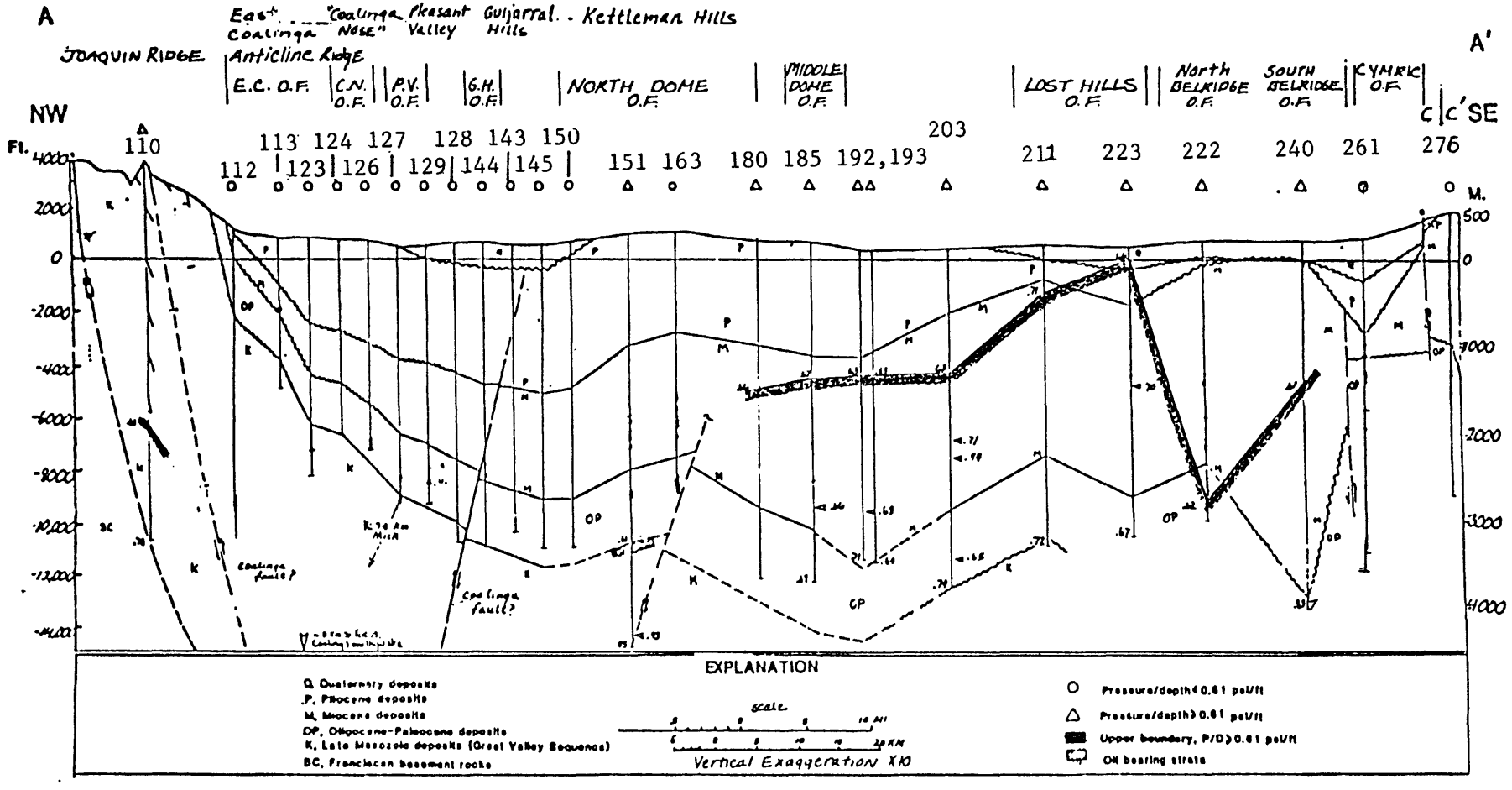
A
A'
NW
SE
C
C'
East Coalinga Nose
"Coalinga" Valley
Pleasant Hills
Guijarral Hills
Kettleman Hills
JOAQUIN RIDGE
Anticline Ridge
E.C. O.F.
C.N. O.F.
P.V. O.F.
G.H. O.F.
NORTH DOME O.F.
MIDDLE DOME O.F.
LOST HILLS O.F.
North BELRIDGE O.F.
South BELRIDGE O.F.
CYMRIC O.F.
Ft.
M.
110
112
113
123
124
126
127
129
128
144
143
145
150
151
163
180
185
192,193
203
211
223
222
240
261
276
coalinga fault?
coalinga fault?
EXPLANATION
Q, Quaternary deposits
P, Pliocene deposits
M, Miocene deposits
OP, Oligocene-Paleocene deposits
K, Late Mesozoic deposits (Great Valley Sequence)
BC, Franciscan basement rocks
scale
Vertical Exaggeration X10
Pressure/depth < 0.61 psi/ft
Pressure/depth > 0.61 psi/ft
Upper boundary, P/D > 0.61 psi/ft
Oil bearing strata

FIGURE 3

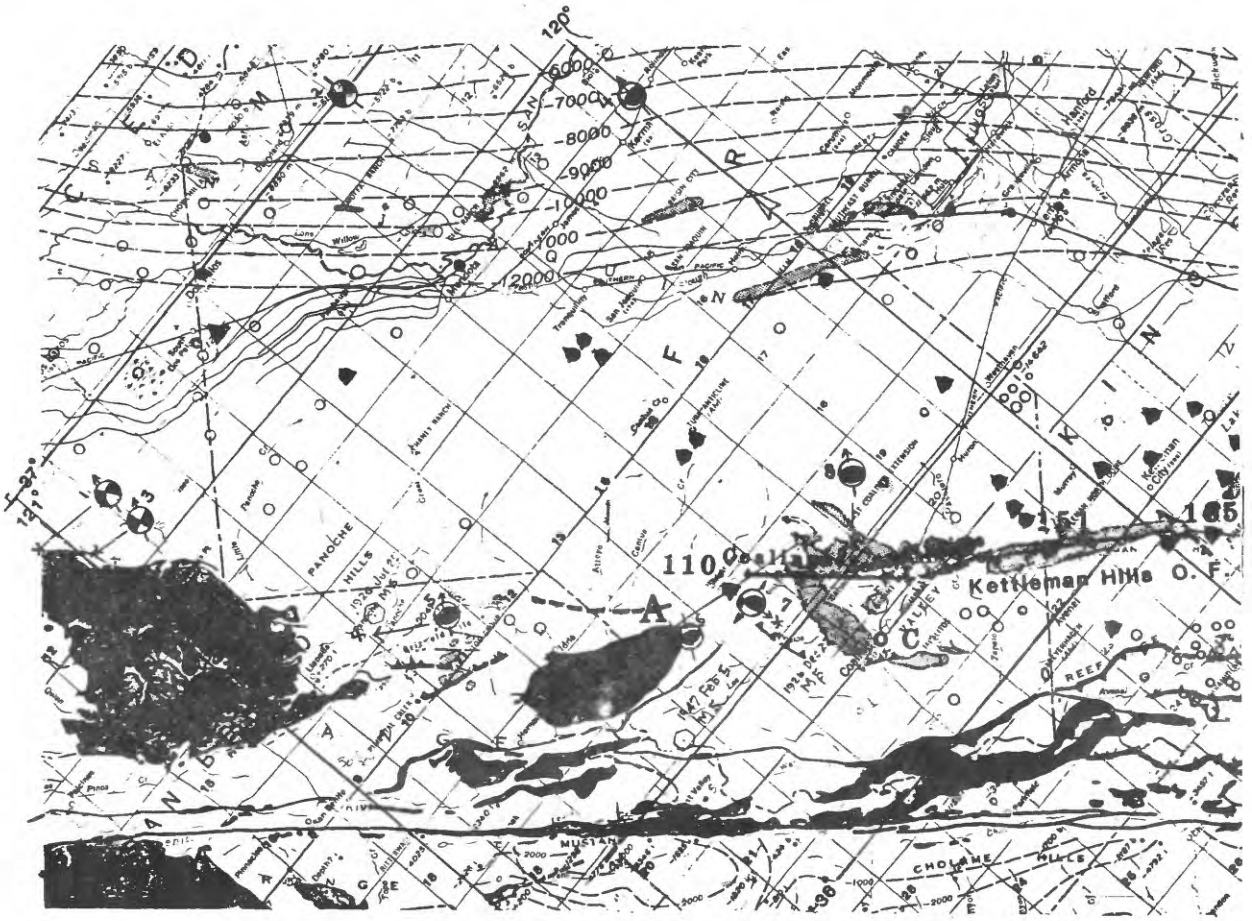

EXPLANATION

Basement rocks (Franciscan, Sierran)

Paloma O.F. Oil or gas field

Fault

Teeth on upper plate of reverse fault: solid, exposed; open, concealed

110 Well penetrates high fluid pressures (≥.61 psi/ft): number refers to table 1

Well bottoms in basement rocks

Other wells investigated

Figure 2

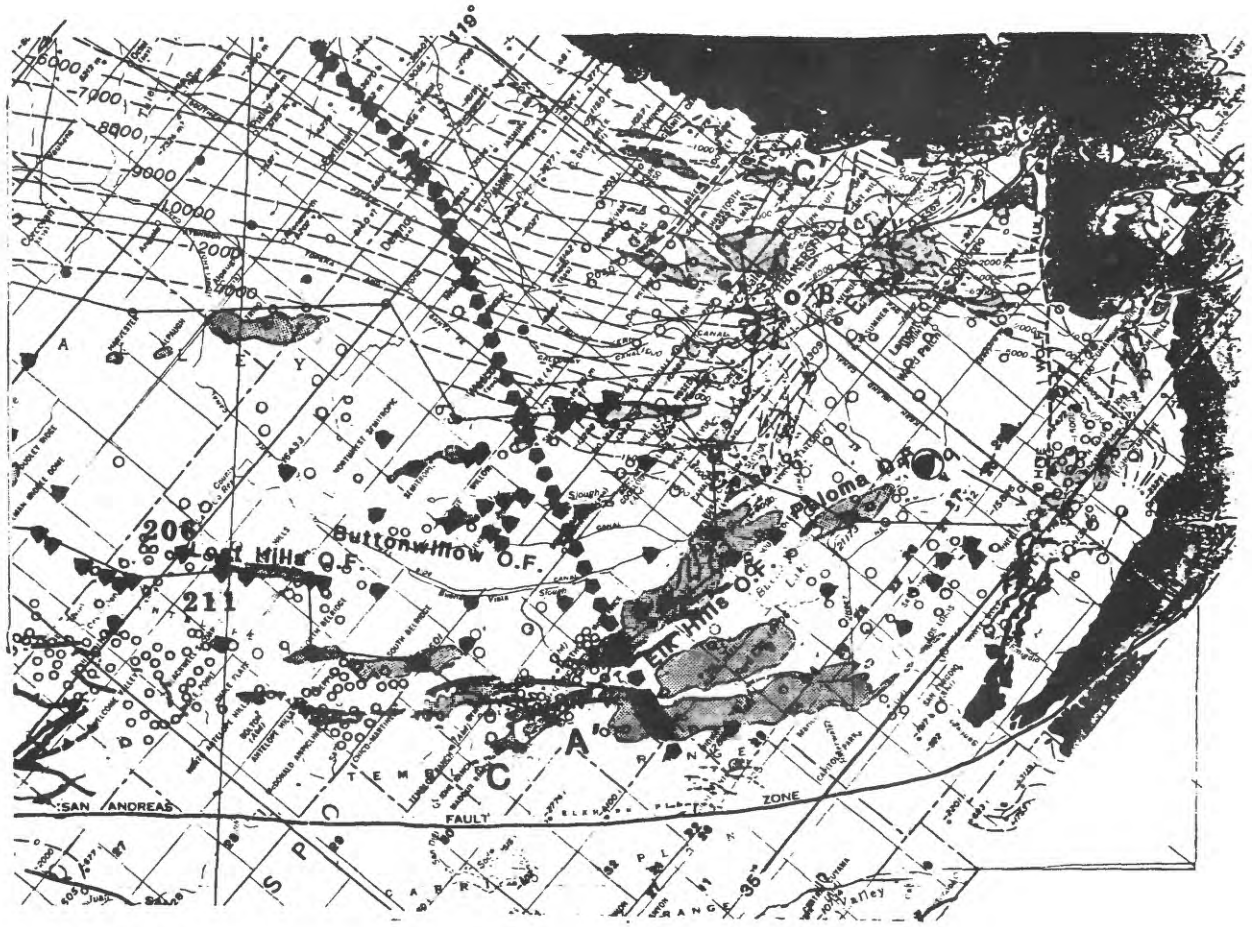

7 8

Fault-plane solution
Showing trend and plunge direction of P axis; lower hemisphere projection, compression quadrants solid; 7, Nunes Canyon, 11 June 1983; 8, Coalinga main shock

A A'

Line of structure section

—— —18000— ——

Contour on top of Sierran basement rocks: datum mean sea level level, contour interval 1000 ft

B, C

B, Bakersfield; C, Coalinga

South edge, Great Valley Sequence

Scale

10 0 10 20 30 40 MI

10 0 10 30 50 70 KM

Figure 2 Cont.

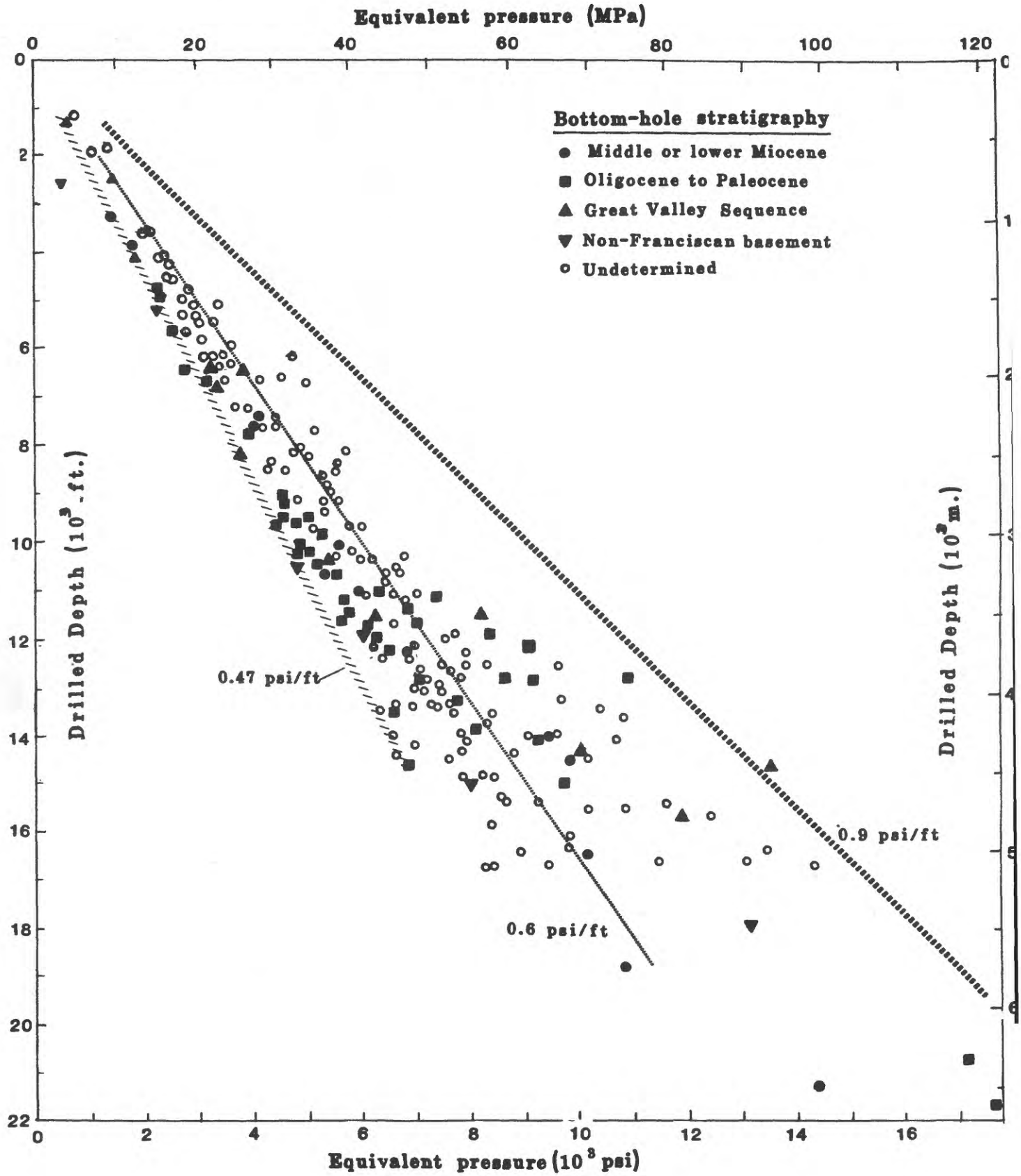
Equivalent pressure (MPa)
0
20
40
60
80
100
120
Bottom-hole stratigraphy
Middle or lower Miocene
Oligocene to Paleocene
Great Valley Sequence
Non-Franciscan basement
Undetermined
Drilled Depth (10^3 ft.)
Drilled Depth (10^3 m.)
0.47 psi/ft
0.9 psi/ft
0.6 psi/ft
2
6
8
10
12
14
16
18
20
22
0
2
4
6
8
10
12
14
16
Equivalent pressure (10^3 psi)

Figure 4

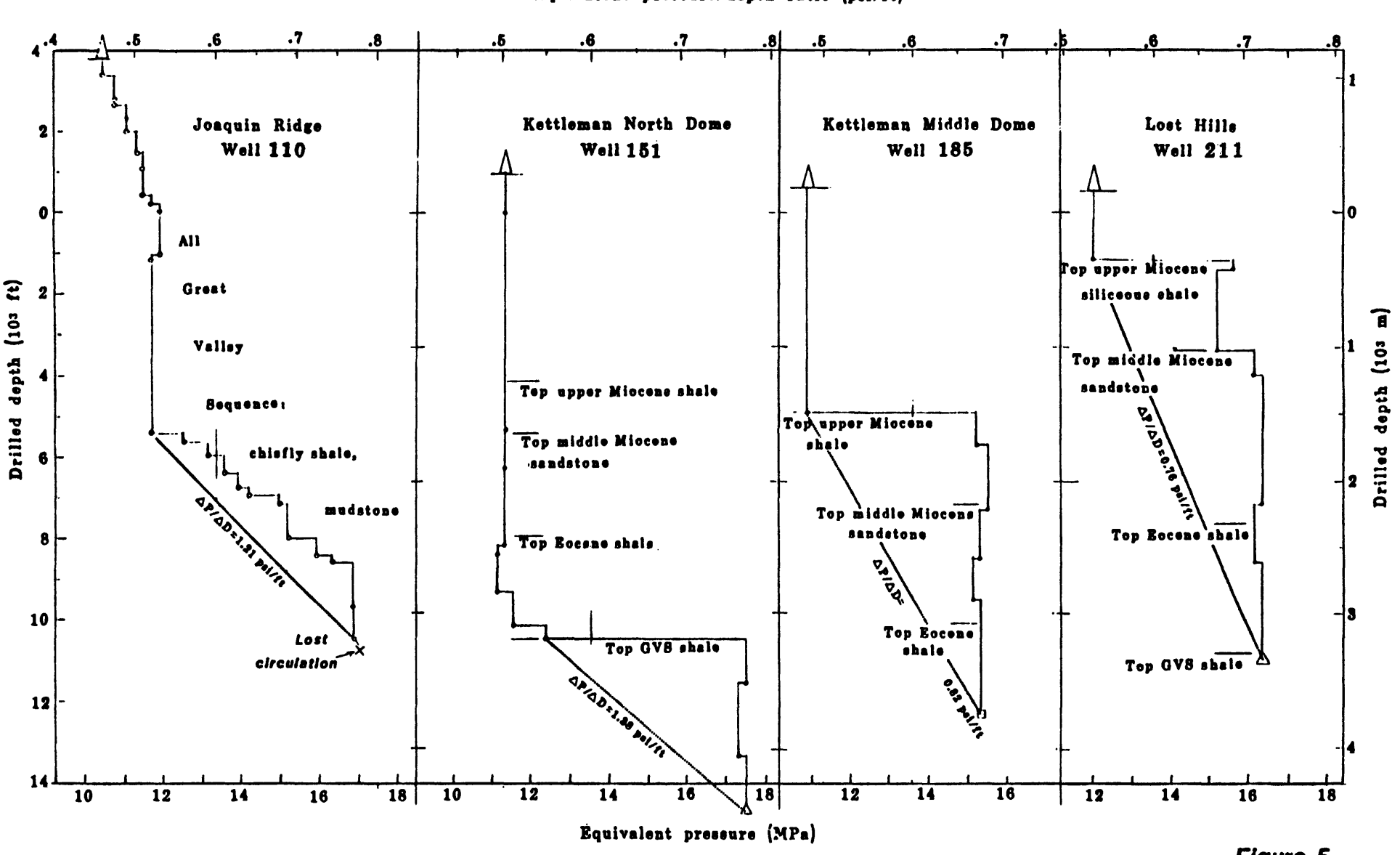
Equivalent pressure/depth ratio (psi/ft)
.4
.5
.6
.7
.8
Joaquin Ridge
Well 110
All
Great
Valley
Sequence:
chiefly shale,
mudstone
ΔP/ΔD=1.21 psi/ft
Lost
circulation
Kettleman North Dome
Well 151
Top upper Miocene shale
Top middle Miocene
sandstone
Top Eocene shale
Top GVS shale
ΔP/ΔD=1.88 psi/ft
Kettleman Middle Dome
Well 185
Top upper Miocene
shale
Top middle Miocene
sandstone
ΔP/ΔD=
Top Eocene
shale
0.82 psi/ft
Lost Hills
Well 211
Top upper Miocene
siliceous shale
Top middle Miocene
sandstone
ΔP/ΔD=0.76 psi/ft
Top Eocene shale
Top GVS shale
Drilled depth (10³ ft)
Drilled depth (10³ m)
10
12
14
16
18
Equivalent pressure (MPa)

Figure 5

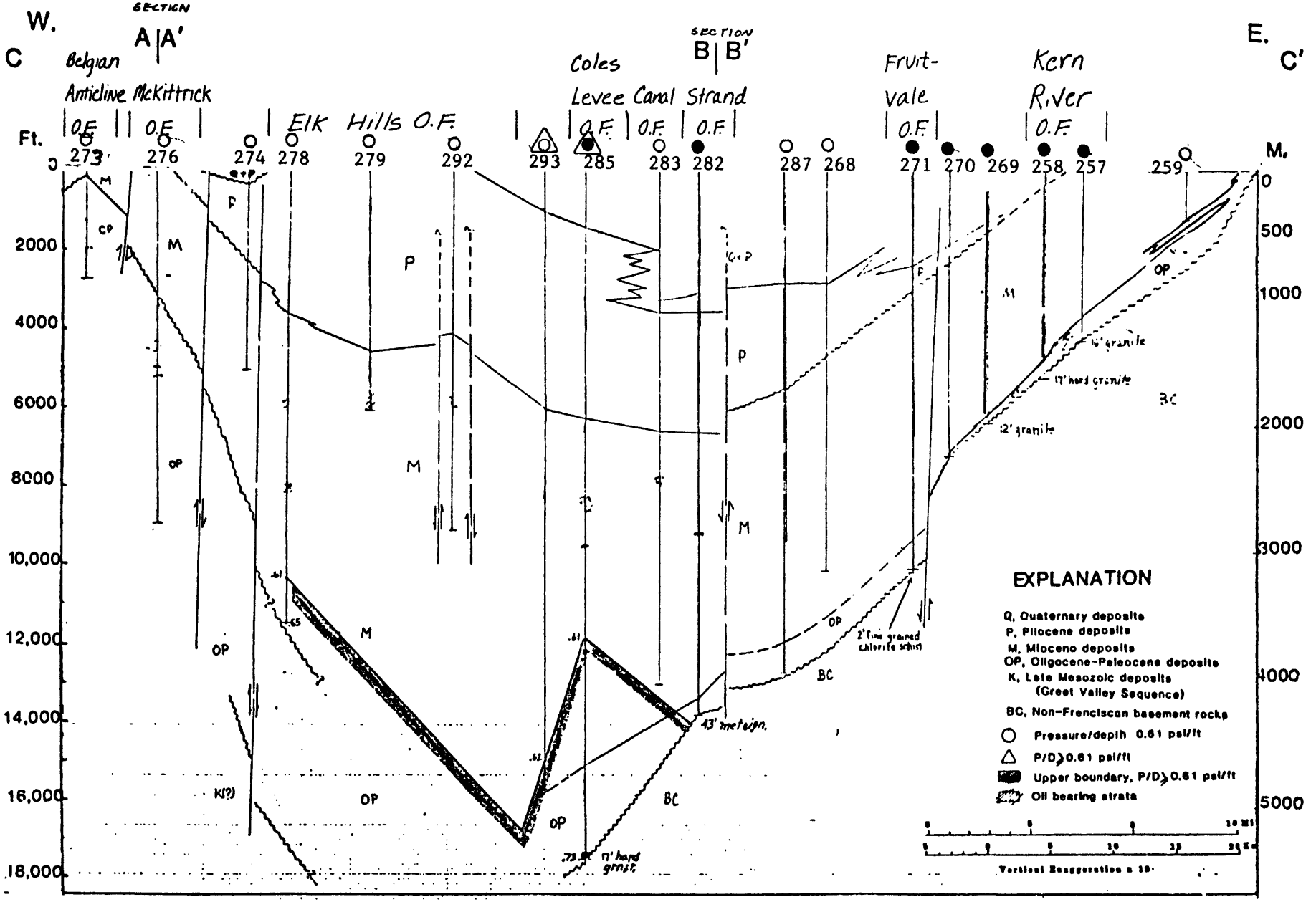
W.
C
SECTION
A | A'
Belgian
Anticline McKittrick
O.F.
O.F.
Elk Hills O.F.
SECTION
B | B'
Coles
Levee Canal Strand
O.F.
O.F.
O.F.
Fruit-
vale
O.F.
Kern
River
O.F.
E.
C'
Ft.
M.
273
276
274
278
279
292
293
285
283
282
287
268
271
270
269
258
257
259
0
2000
4000
6000
8000
10,000
12,000
14,000
16,000
18,000
0
500
1000
2000
3000
4000
5000
P
M
OP
K(?)
BC
43' metsjn.
11' hard grnst.
12' granite
2' fine grained chlorite schist
EXPLANATION
Q, Quaternary deposits
P, Pliocene deposits
M, Miocene deposits
OP, Oligocene-Paleocene deposits
K, Late Mesozoic deposits (Great Valley Sequence)
BC, Non-Franciscan basement rocks
Pressure/depth 0.61 psi/ft
P/D > 0.61 psi/ft
Upper boundary, P/D > 0.61 psi/ft
Oil bearing strata
Vertical Exaggeration x 10

360

FIGURE 6

Velocity-Pressure vs. Depth, Well 206(Elev. 303')

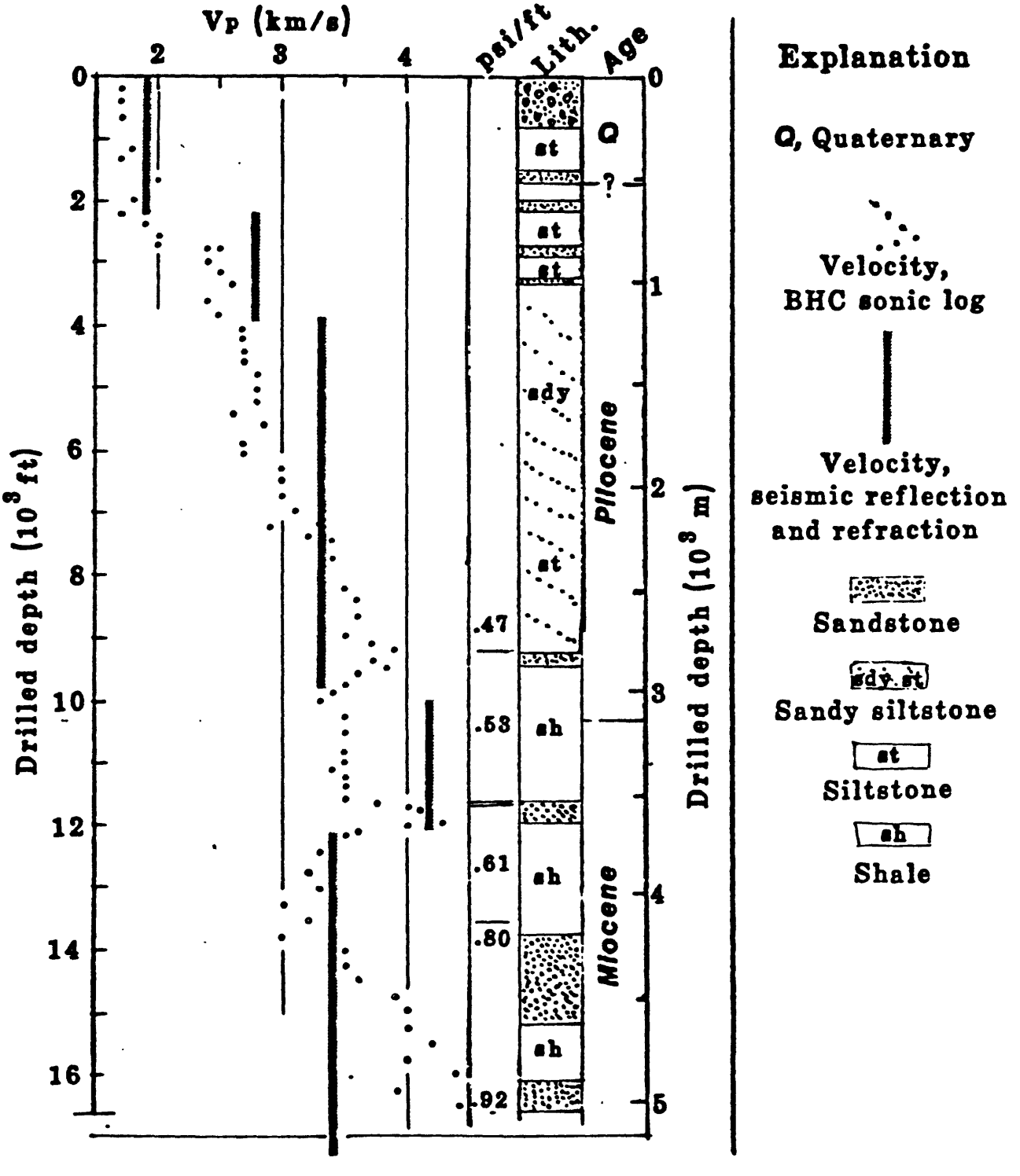

Figure 7

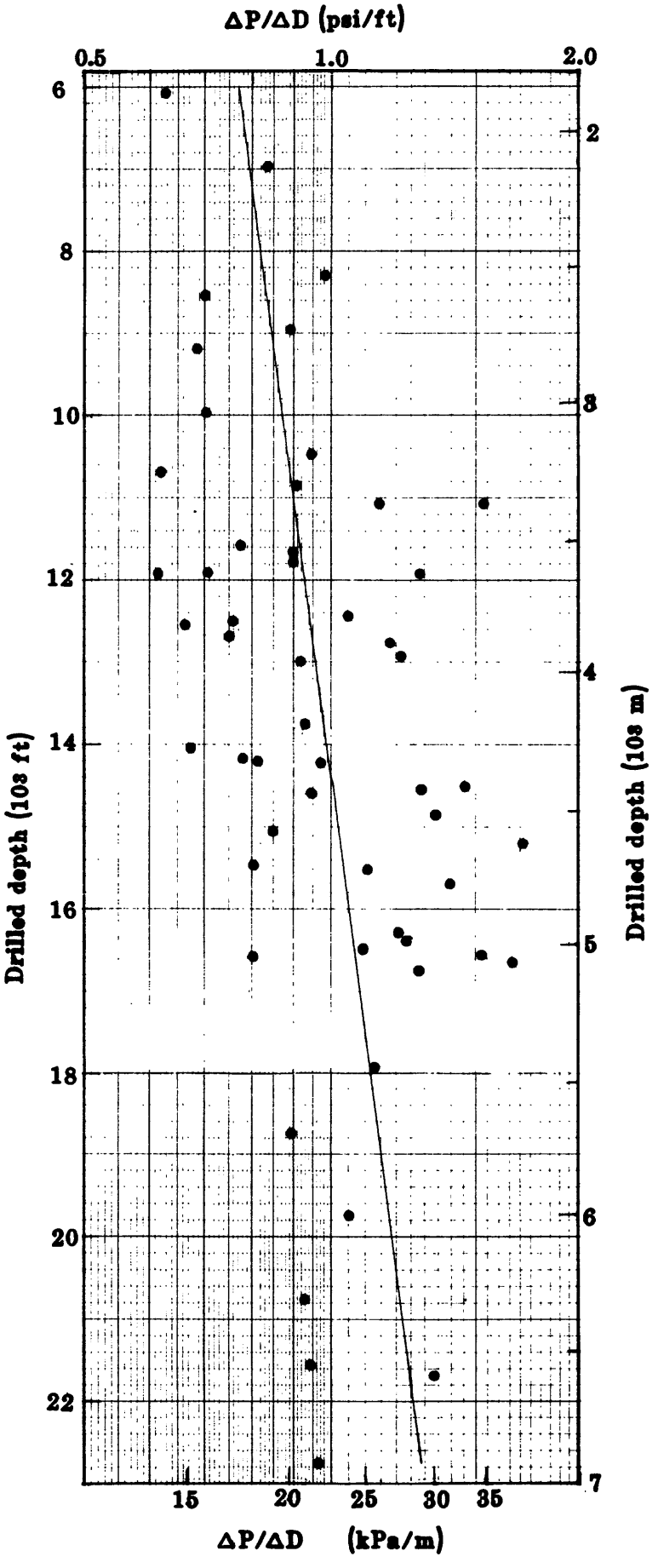
ΔP/ΔD (psi/ft)
0.5
1.0
2.0
6
8
10
12
14
16
18
20
22
Drilled depth (10³ ft)
2
3
4
5
6
7
Drilled depth (10³ m)
15
20
25
30
35
ΔP/ΔD (kPa/m)

Figure 8

No.	T.S.-R.E.-Sec. Year	Operator	Name	Elev. (ft)	Depth to AHP[1/] (ft)	TD (ft)	Bottom Hole Pressure/ Depth (psi/ft)	Bottom Hole Temp. (°F)	Remarks
Mt. Diablo B & M									
1.	10-11-7 1955	Castaic Highlands	Duncan Davis-1	108		6000	.48		
2.	10-11-21 1976	McCulloch	MCO-Makin 1-21	98		7291	.48		
3.	10-12-2 1969	Continental	Fialho	127		10690	.52		
4.	10-12-8 1957	Amerada	Unit-1	117		9004	.51		
5.	10-13-24 1954	Shell	Strat Test 4	136		6000	.47		
6.	10-13-27 1961	Great Basins	S.A.R. 66-27	131		10026	.50	181	
7.	10-14-3 1954.	Shell	Strat Test 11	166		7280	.47		BC at 7260'
8.	10-14-6 1954	Getty	S. Realty 1-6	132		8083	.51		BC at 8182'
9.	10-15-6 1953	Shell	Strat Test 3A	190		6235	.45		
10.	10-15-29 1954	Shell	Strat Test 14A-2	173		7582	.47		
11.	11-10-9 1961	Sun	Escobar	227		9080	.60		
12.	11-11-10 1962	Great Basins	Ambassador-Britto-1	104		9920	.52		
13.	11-12-26 1972	Phillips	Bodfern-1	123	12278	12495	.67	218	
14.	11-12-28 1953	Standard	Radfern-51	131		13005			
15.	11-13-6 1961	Shell	Antelope 3-6	117		12076	.58		BC at 12073', hornblende andesite
16.	11-14-9 1941	Shell	Chowchilla Farms	145		9062	.51		BC at 9038', schist
17.	11-16-31 1953	Shell	Strat Test 7	184		7955	.48		
18.	12-11-22 1969	Continental	Hamburg-1	224		6502	.46		
19.	12-13-6 1973	Arco	Triangle-Radfern-1	136		11522	.51		
20.	12-14-28 1966	McCulloch	Henry Yip-1	145		7512	.50		
21.	12-15-27 1937	Texaco	General Gill-1	168		6438	.47		
22.	13-11-13 1953	Exxon	Stone-1	399		4480	.49		
23.	13-11-28 1958	Bolly	E.S. 28-1	639		3510	.48		
24.	13-12-13 1945	Union	Irvine 65-13	258		6829	.48		
25.	13-12-31 1952	Artnell	Etcheverry	455		5501	.41		

No.	T.S.-R.E.-Sec. Year	Operator	Name	Elev. (ft)	Depth to AHP[1/] (ft)	TD (ft)	Bottom Hole Pressure/ Depth (psi/ft)	Bottom Hole Temp. (°F)	Remarks
26.	13-13-6 1962	Great Basins	Ambassador-Tellee-1	207		9997	.55	194	
27.	13-13-16 1965	Shell	Shaw 1-16	227	13990	16333	.68	290	Bot. in BC, 627' diabase and green-stone
28.	13-13-17 1963	Occidental	Hammond Ranch-1	231		12491	.61	236	
29.	13-14-20 1954	J.K.Hudley	Mendota	225		6615	.47		
30.	13-15-12 1965	Texaco	Gill 86-12	170		6000	.45		
31.	13-15-28 1973	Arco	B.B.Co.-1	180		11567	.50		Top BC at 11522', granite
32.	13-16-19 1957	Shell	Gill 32-19	175		4489	.48		
33.	13-16-27 1973	Atlantic	Gill	193		5950	.47		
34.	13-17-30 1942	Arco	Ponte-1	211		8797	.48		
35.	13-18-6 1959	Hathaway	Slaven	248		5113	.48		
36.	14-12-14 1967	Sun	Giffen Inc.-1	379		4600	.47	129	
37.	14-12-36 1951	Lockhart	Souza 1-36	431		10636	.55	216	
38.	14-13-23 1957	C.L. Caine	-1	342		8430	.45	185	
39.	14-13-31 1973	E.A.Bender	Silver Creek 54-X	405		10387	.53	190	
40.	14-13-33 1964	Arco	Roberts	384		8772	.50		
41.	14-14-22 1954	S. Herndon	Harriette-2	235		8834	.48	171	
42.	14-15-16 1962	Valwood	Starling-Coleman	174		13207	.55		
43.	14-15-26 1968	Valwood 1-A	Sacho-McNear	161		13187	.56	208 at 12701	
44.	14-16-6 1981	Texaco	Sallaberry 1-6	171		10000	.54	182	
45.	14-16-22 1982	Conoco	Earby Prop.-1 62-22	186		10100	.48		
46.	14-16-33 1969	Continental	Young et al-1	160		11941	.53		B.C. at 11912', granodiorite
47.	15-11-25 1958	Panoche Hills	P. Fiorovich et al-1	1151		7025	.50		
48.	15-12-36 1947	Texaco	Lillis 85-36	823		6059	.50		
49.	15-13-22 1942	Union	C.L.C.-1	495		7000	.51		
50.	15-14-24 1950	Shell	Coffin	216		7407	.50		
51.	15-15-22 1942	Shell	Henderson 66-22	186	9992	11946	.70		

No.	T.S.-R.E.-Sec. Year	Operator	Name	Elev. (ft)	Depth to AHP[1/] (ft)	TD (ft)	Bottom Hole Pressure/ Depth (psi/ft)	Bottom Hole Temp. (°F)	Remarks
52.	15-15-23 1962	Shell	Eliason 3-23	187	11430	13010	.64		
53.	15-15-30 1951	Shell	Friis-Hansen 77-30	203		8402	.49	108	
54.	15-15-35 1982	Union	Bravo-1	209	**	**	**		
55.	15-16-23 1983	Home	DiBenedotto-1	165	11320	12399	.63	209	Top BC at 12350', metavolcanics.
56.	15-17-15 1974	Occidental	Noble-1	190	7352	10784	.63		
57.	15-18-19 1969	Morris	SA + FL-1	194		10300	.50	185	
58.	15-18-30 1968	Argosy	Noble 22-30	192		10776	.52	182	
59.	16-13-20 1937	Superior	C.U.P.	2143		6001	.47		
60.	16-13-22 1952	Signal	Glenn-1	1610		7345	.49	161	
61.	16-14-22 1974	Orlando	1-22	429		10358	.68	205	
62.	16-14-27 1969	Rapp	Morris Pucheu 67-27	496		10917	.60		
63.	16-14-36 1959	Hondo	Haber-1	472		10000	.54	190	
64.	16-15-18 1981	Home	Kimberlin	295		8500	.54		
65.	16-15-20 1981	Home	Giffen 20-1	327		8657	.53	178	
66.	16-16-18 1945	Standard	Giffen-74	220		10100	.48	188	
67.	16-16-26 1981	Energy Products	McDonald-1	237		9250	.59	166	
68.	16-16-32 1943	Arco	McDonald Est.-1	258		9315	.51	164	
69.	16-17-19 1968	F + B	Bravo-1	188		8539	.44	165	
70.	16-17-29 1970	Standard	Bravo-41	186		9233	.51	177	
71.	17-11-11 1980	Tannehill	Riccolini	1717		9887	.56		
72.	17-12-5 1957	B.C.B	-1	1869		5540	.51		
73.	17-12-20 1957	Morris	Gonzales	2057		5602	.51		
74.	17-15-14 1969	Standard	Giffen- 67	349	2707	14471	.72		
75.	17-15-15 1944	Getty	Sp-82	368	10240	13019	.78		
76.	17-15-24 1940	Texaco	Everding	345		10307	.51		
77.	17-15-25 1949	Conoco	SP-1	358		10342	.51		

** Information withheld by operator

No.	T.S.-R.E.-Sec. Year	Operator	Name	Elev. (ft)	Depth to AHP[1/] (ft)	TD (ft)	Bottom Hole Pressure/ Depth (psi/ft)	Bottom Hole Temp. (°F)	Remarks
78.	17-15-32 1953	Helm and Sumpf	Indart	487		10500	.52	192	
79.	17-16-5 1955	Burman	Aminoil U.S.A. 77-5	274		10031	.50		
80.	17-16-13 1946	Superior	K.C.D.-1	241		10511	.54	190	
81.	17-16-30 1939	Shell	Port Costa 48-30	330		10711	.51		
82.	17-16-32 1981	Hilliard	Farelli	286		10280	.57	209	
83.	17-17-20 1963	Western-Continental	Everts 72-20	226		10500	.51	181	
84.	17-17-21 1948	Arco	E.M. Buck-1	234		9750	.54		
85.	17-17-32 1968	Shell	Saunders 1-32	238		10930	.57		
86.	17-18-2 1941	Mobil	Burrel-1	210		9400	.50	195	
87.	17-18-16 1973	Amerada	Brix	198		12341	.62	194	
88.	17-18-31 1968	Mohawk	Shell-Bravo	237		9525	.49	165	
89.	17-19-26 1946	Amerada	Lawton 58-26	212		11998	.51		Bot. in BC, Sect. B
90.	18-14-1 1966	Santa Fe	S.P.R.R. 68-1	672		5404	.50		
91.	18-15-4 1959	Shell	Lillis-Christie	485		10320	.49	183	
92.	18-15-23 1951	Exxon	S.P.C.-1	527		10400	.50		
93.	18-16-4 1957	Exxon	C.R. Puck Heber et al	295		11111	.51		
94.	18-16-25 1940	Exxon	S.P.R.R.-1	328		11415	.50		
95.	18-16-32 1976	Natomas	Baird Errea 1-32	374		10210	.52	192	
96.	18-17-2 1969	Shell	1-2 Farry	479		11806	.54		
97.	18-17-5 1968	Shell	1-5 O'Neill	263		11222	.58	188	
98.	18-17-9 1957	Marathon	Citizens' Bank	252		11118	.54	177	
99.	18-17-31 1937	Union	S.P.L.-1	350		11673	.49		
100.	18-18-11 1956	Texaco	S.P.-1	238		10202	.50	175	
101.	18-18-17 1968	Shell	South Lake Farms 1-17	239		10774	.54	180	
102.	18-18-34 1968	Shell	A. King 1-34	254		11733	.56	187	
103.	18-19-1 1956	Malco	Natti Cob	232		8500	.50		

No.	T.S.-R.E.-Sec. Year	Operator	Name	Elev. (ft)	Depth to AHP[1] (ft)	TD (ft)	Bottom Hole Pressure/ Depth (psi/ft)	Bottom Hole Temp. (°F)	Remarks
104.	18-19-4 1955	Geochem	Graeber-Rowen 47-4	221		8860	.48		
105.	18-19-15 1978	Buttes	Union-Texaco-Bezera et al	224		10550	.53	176	
106.	18-20-6 1962	Sun	Borba-1	222		11724	.48	186	BC at 11710'
107.	18-20-27 1948	Getty	Grangeville-1	237		9005			Sect. B
108.	18-20-31 1974	Texaco	Hanes-1	215		10348	.56	166	
109.	18-20-35 1964	R.S. Rheem	Kreyenhagen 23-36	231		9090	.47	145	
110.	19-14-3 1976	Arco	Joaquin Ridge -1	3789	9200	14409	.78	176 at 9040	Sect. A
111.	19-14-25 1954	Holmes and Assoc.	-1	1439		5298	.51		
112.	19-15-15 1952	Shell	363-X	1265		10414	.52	168	Sect. A
113.	19-15-35 1946	Chevron	213	930		5775	.46		Sect. A
114.	19-16-25 1957	Honolulu-Texas-Socal	S.P.L.- 48	416		13394	.58	240	
115.	19-17-8 1955	Getty	Indian-Westates-25	346		12330	.54	200	
116.	19-17-24 1956	Texaco	Rhein-1	340		13437	.53		
117.	19-18-21 1973	North Central	Boston Ranch-1	278	11485	12715	.63	210	
118.	19-19-29 1968	Shell	Willet 1-29	241		13199	.53	204	
119.	19-20-24 1981	Terra	Green	216		10600	48	170	
120.	19-20-26 1982	Terra	Piexoto	234		12850	.45		
121.	19-21-7 1961	Exxon	Capital Co.C-1	244		12816	.49		Top BC at 12695', slate
122.	20-14-25 1962	Standard	S-5 25D	774		1690	.46		
123.	20-15-12 1939	Gulf	Leavitt-Hinta -1	902		8108	.45		Sect. A
124.	20-15-13 1939	Chevron	62-13 C	829		7472	.55		Sect. A
125.	20-16-12 1967	Westates	PVF 11-X-12	430		12150	.44		
126.	20-16-18 1940	Union	68	749		8051	.53		Sect. A
127.	20-16-20 1944	Union	Estrom 84-20	540		9613	.58		Sect. A
128.	20-16-28 1944	Union	Getchell-68	691		11586	.56	211	Sect. A
129.	20-16-29 1943	Chevron	PVF 82-29F	543		9151	.51	190	Sect. A

No.	T.S.-R.E.-Sec. Year	Operator	Name	Elev. (ft)	Depth to AHP[1] (ft)	TD (ft)	Bottom Hole Pressure/ Depth (psi/ft)	Bottom Hole Temp. (°F)	Remarks
130.	20-17-35 1973	Great Basins	H.E. Kettleman 1-35	360	10935	15010	.72	238	
131.	20-18-10 1978	Hilliard	Woods Ranch-1	276		12223	.58	215	
132.	20-18-11 1978	Texaco	Boston Ranch-1	276		13512	.54	214	
133.	20-18-12 1976	Tenneco	Ladd-Westhaven 26-12	275		13308	.60		
134.	20-18-13 1978	Tenneco	Base-Westhaven	275		13303	.58		
135.	20-18-14 1982	Koch	Aqueduct	301		13286	.50	200	
136.	20-18-23 1959	Standard	U.S.A Haven-Boston 813	275		14322	.51	211	
137.	20-19-7 1951	Mobil	S.L.C. -48-7	269		14911	.52	229	
138.	20-20-11 1975	Amshutz	Prietas	202		11495	.44	175	
139.	20-20-22 1979	Conoco	Watson-1	225		12476	.51	190	
140.	20-20-28 1959	R.S. Rheem	Weaver-Lovelace 37-X	188		10720	.51		
141.	20-20-36 1956	Goocham	Campbell 63X-36	209		11711	.50	175	
142.	20-22-16 1979	Union	Salyer	245		11789	.51	188	
143.	21-16-1 1944	Chevron	Bordieu 1-A	583		10868	.49		Sect. A
144.	21-16-1 1944	Sun	Dessel-41	630		11442			Sect. A
145.	21-16-12 1950	Gulf	Orr	563		11449	.54		Sect. A
146.	21-16-20 1956	Texas	Lillis-1 HCT-1	845		10481	.50		
147.	21-16-28 1950	Ohio-Gulf	H.C. Lillis-1	809		11026	.56		
148.	21-17-11 1982	Flynn	Bravo 11-1	400	13200	15200	.71	273 at 14890	
149.	21-17-14 1973	Flynn	Corberry-1	423	1498	13894	.65	243	
150.	21-17-18	Chevron (Kettleman North Dome Association)	4-18-J	658		11746			Sect. A
151.	21-17-34 1955	Chevron	423	981	11400	15693	.85	309 at 15500	Sect. A
152.	21-18-36 1975	Great Basin	81-X	219	3500	14209	.84	250	
153.	21-19-16 1979	Tenneco	API Schutte-1	209	4010	14915	.61	240	
154.	21-19-35 1959	Marathon-Sun	Westlake Farm -1	181	7000	12028	.63	217	
155.	21-20-4 1963	Empire State	Lovelace 56X-4	184		6000	.48	134	

No.	T.S.-R.E.-Sec. Year	Operator	Name	Elev. (ft)	Depth to AHP[1] (ft)	TD (ft)	Bottom Hole Pressure/ Depth (psi/ft)	Bottom Hole Temp. (°F)	Remarks
156.	21-20-22 1978	Gas Producing	Chatom	176		5110	.52	130	
157.	21-21-4 1951	Mobil	Richardson 36-4	202		12064			Bact. B
158.	21-21-10 1959	Getty	Boswell-Richardson-72	199		12701	.50	185	
159.	21-21-24 1956	Gulf	Boswell-1	184		11166	.51	170	
160.	22-15-9 1958	General	Standard 52-9	1046		5258	.51		
161.	22-16-11 1959	McCulloch	Standard-1	802		12226	.57	219	
162.	22-17-24 1974	Standard	DeSmet USL	1033		15073	.55	244	
163.	22-18-7 1939	Chevron (Kettleman North Dome Assoc.)	E-27-7	1049		9855	.50		Sect. A
164.	22-19-4 1979	Baumgartner	A.P.I.-Tadco 2-14	184		13302	.55	217	
165.	22-19-4 1979	Baumgartner	A.P.I.-Tadco 3-4	184		12268	.65	233	
166.	22-19-4 1980	Baumgartner	A.P.I.-Tadco 3A-4	187		13358	.66	250	
167.	22-19-9 1951	American Pacific	Davis Trans-America Corp.-1	182	13400	15555	.75	282	
168.	22-20-8 1982	Husky	KCDC 54-8	180	4179	15131	.72	234	
169.	22-20-17 1967	Tulare Basin Assoc.	Salyer Land Co. 78-17	194		14415	.60		
170.	22-20-28 1942	Shell	Tulare Lake	205	8727	12109	.61		
171.	22-20-29 1978	Hilliard	Sumpf-Williams	211	4605	13932	.69		
172.	22-21-15 1956	Lake	Boswell-1	194		5003	.50	121	
173.	22-21-18 1981	Texaco	Boswell-1	200	4300	15000	.67		
174.	22-22-5 1966	Occidental	Hansen-1	205		14681	.55		Top BC 14662'
175.	22-24-28 1969	Pan	Reese	250		10043			Bot. in BC, weathered granite?
176.	23-17-9 1951	Sun	Lynch-Maureen 68-0	1089	7200	11968	.66	230	
177.	23-17-16 1961	Macpet	Shell Maureen-1	1137		8693	.61	158	
178.	23-17-16 1957	Verde	Maureen 81X-16	1100		10144	.53		
179.	23-17-31 1958	Humble	Avenal Land and Oil	1084		4686	.49		
180.	23-18-1 1941	Chevron (Kettleman North Dome Assoc.)	1-1U	693	5709	12830			Bact. A

No.	T.S.-R.E.-Sec. Year	Operator	Name	Elev. (ft)	Depth to AHP[1/] (ft)	TD (ft)	Bottom Hole Pressure/ Depth (psi/ft)	Bottom Hole Temp. (°F)	Remarks
181.	23-18-2 1935	Getty	73-2u	695	5745	8985	.61		
182.	23-18-12 1976	Sumpf-Williams	Dougherty USL 1-12	605	5485	12628	.71	248	
183.	23-18-12 1981	Sumpf-Williams	Dougherty USL 2-12	585		10656	.56		
184.	23-19-2 1966	Occidental	Howe-1	193	13577	16565	.67	250	
185.	23-19-19 1954	Middle Dome	38-19V	597	5500	12819	.67	248	Sect. A
186.	23-20-13 1982	Terra	Harvester 1-13	209		14800	.52		
187.	23-20-31 1978	American Quasar	Bravo 1-31	252	6200	19996	.87	349	
188.	23-21-25 1982	Terra	Harvester 1-25	218	**	**	**		
189.	23-22-4 1946	Kings	Von Glahn-1	192		13213			Sect. B
190.	23-24-28 1980	General American	Lucy-1	230		11858			Top BC 11800', slate
191.	24-18-20 1955	Reserve	Orchard 48-20	683		5235	.60		
192.	24-19-4 1970	Chevron	SF + FL-68	437	10521	11925	.69	252	Sect. A
193.	24-19-10 1961	Chevron	SF + FL 613-Z	354	6500	11647	.64	220	Sect. A
194.	24-19-27 1961	Occidental	USL 27-27	414	11670	12150	.75	262	
195.	24-19-34 1964	Occidental	SF +FL 123-34	492	11150	11540	.74	246	
196.	24-20-12 1948	Shell	Hacienda-1	200		5015	.49		
197.	24-21-9 1964	E.A. Bonder	Lloyd-51	206		5000	.45		
198.	24-21-20 1966	Sam Manchel	Hacienda Farms 63-20	210		4950	.46		
199.	24-23-22 1940	Nord-Montara	Daniel-35	213		11728	.52		Sect. B
200.	24-23-36 1952	MaGee	Morris-1	222		13480	.50		Sect. B
201.	24-24-20 1970	Chevron	GRI-65	232		12224			Bot. in BC
202.	25-19-2 1963	Occidental	Hallman 131K-2	419	4200	11075	.88	236	
203.	25-19-12 1947	Chevron	SF + FL 4-2	374	5249	12954	.74	265?	Sect. A
204.	25-19-13 1945	Union	South Dome-41	397	2057	8540	.66		
205.	25-19-20 1954	C.W.O.D.	Bates-2	489	5492	9147	.61		

** Information withheld by operator.

No.	T.S.-R.E.-Sec. Year	Operator	Name	Elev. (ft)	Depth to AHP[1/] (ft)	TD (ft)	Bottom Hole Pressure/ Depth (psi/ft)	Bottom Hole Temp. (°F)	Remarks
206.	25-20-22 1967	Shell-Arco	123-22	303	11053	16619	.92	292	
207.	25-21-17 1957	Carl Long	Marie-1	270		4040	.44		
208.	25-22-16 1940	North Kern	Semitropic	248		5310	.50		
209.	25-24-23 1955	Intex	Dearinger 46-23	272		10685	.50		Sect. B
210.	26-20-2 1935	Chevron	United-1	477	1856	6887	.74		
211.	26-20-11 1949	Mobil	Williamson 33-11	481	1800	11553	.72	232	Sect. A
212.	26-20-24 1936	Calif. Lands	Occidental-2	430	2300	8320	.69 at 6449		
213.	26-20-30 1969	King	OLC-1	600		12568	.67	230	
214.	26-20-31 1964	Gulf	Temby OLC-1	615		11904	.53		
215.	26-21-6 1957	Superior	Windmill Shallow-1	283		10511	.50		
216.	26-22-5 1945	Getty	National Royalties-1	235	9435	16668	.83	286	
217.	26-22-9 1968	Occidental	Rouchin	221		10460	.51		
218.	26-22-26 1955	D.D. and Dorothy Dunlap	45-26	268		8500	.49		
219.	26-23-8 1970	Ebert + Brandt	Brandenburger -1	225		5188	.51		
220.	26-23-27 1965	Occidental	Sharples et.al. 1-2	242		14014	.68	248	
221.	26-25-17 1938	TWA	KCL Pond-1	333		9079	.50		
222.	27-20-26 1941	Shell	55	658	10309	10800	.61		Sect. A
223.	27-21-4 1945	Chevron	Cahn 58-4	400	0	11080	.67		Sect. A
224.	27-21-6 1947	Union	Ellis 850-9	375	2309	3500	.62		
225.	27-21-9 1963	Richfield	Buck-1	450		7720	.58		
226.	27-21-36 1948	Chevron	Von Sicklin-45	320	11017	14557	.67		
227.	27-22-10 1972	Great Basin	Tenneco 31x-10	234	12000	21640	.92	374	
228.	27-23-9 1955	Exxon	Arthur E. Conn, et.al.- 1	262	5300	8300	.69		
229.	27-23-25 1944	Chevron	Fullerton-1	291	3946	14770	.61		
230.	27-24-6 1974	Tenneco	Cities-Tenneco -35x	284		16540	.53 at 14224		
231.	27-24-7	Composite: Conoco Meyer-1 + Chevron Mushrush-5		288		15866	.46		Sect. B

No.	T.S.-R.E.-Sec. Year	Operator	Name	Elev. (ft)	Depth to AHP[1/] (ft)	TD (ft)	Bottom Hole Pressure/ Depth (psi/ft)	Bottom Hole Temp. (°F)	Remarks
232.	27-24-30 1956	Exxon	KCL F(11-30)	282	7236	7913	.66	168	
233.	27-24-35 1968	Mobil	KCL 86-35	330		15476	.57	261	Top BC at 15415', 61' hard grnst.
234.	27-25-15 1967	Mobil	Pan KCL 3-15	391		13374	.58	224	Top of BC at 13150', diorite
235.	27-26-12 1941	C.W.O.D	Famosa 12-1	647		6855	.46		
236.	27-26-22 1955	Chevron	C.W.O.D. 87	482		5251	.49		
237.	27-27-4 1953	A. M. Dunn	D.L.K.-1	879		5084	.50		
238.	27-28-9 1956	Shell	Vedder-55	1211		3023	.47		
239.	28-21-19 1975	Chevron	P-554-K-19	599		11853	.60		
240.	28-21-33 1946	Shell	62W-33	603	5622	14104	.67		Sect.A.
241.	28-22-34 1981	Texaco	Bloemhof-1	270		15949	.78		
242.	28-23-5 1949	Chevron	KCL 27-6	294		13614	.76	240	
243.	28-23-6 1958	Texaco	Texas-Standard Stntsman	290	11035	12910	.69	240	
244.	28-23-10 1974	Mobil	Tupman 1	265	5400	20753	.93	354	
245.	28-23-14 1956	Texaco	Breen-1	275	1275	13730	.79	258	
246.	28-23-17 1971	Mobil	Bravo-1	277	6000	15450	.70	270	
247.	28-23-22 1965	Texaco	Superior-Mobil Fee- 1	272	10140	14105	.66	259	
248.	28-23-25 1962	Harcourt	Jacobsen 1	270		6002	.63	147	
249.	28-23-29 1981	Austin	Big Band-1	283		15778	.61		
250.	28-25-7 1944	Getty	86 A-7	328	11095	12630	.61		
251.	28-25-17 1954	Superior	Russel-73	344		15068	.54	245	Bot. in BC, metasediments
252.	28-25-18 1954	Getty-Capitol	54-18	320	6421	12563	.67	203 at 11780	
253.	28-25-20 1958	Gas Chem	Anderson-31	338	9000	12404	.65	203	
254.	28-25-26 1959	Union	Kernco 25X	339	6750	11608	.65	196	
255.	28-25-27 1954	Superior	Weber 3-H	340		11822	.62	210	
256.	28-25-33 1941	Union	Pacific States -21	330		13642	.47		Top BC at 13621', gabbro, Sect.B.
257.	28-28-28 1942	Shell	Parkman-1	934		5254	.46		Bot. in BC, granite, Sect.C.

No.	T.S.-R.E.-Sec. Year	Operator	Name	Elev. (ft)	Depth to AHP[1/] (ft)	TD (ft)	Bottom Hole Pressure/ Depth (psi/ft)	Bottom Hole Temp. (°F)	Remarks
258.	28-28-30 1952	Tenneco	Poe C 74	853		6100	.48		Top BC at 6035', granite, Sect.C.
259.	28-29-17 1946	U.S. Drilling	Olcese-1	1315		2600	.49		Sect.C
260.	29-21-18 1950	Union	Richardson 81-18	864		7710	.60		
261.	29-21-22 1953	Superior	Cymric-1	690		12022	.50		Sect.A
262.	29-22-7 1971	Chevron	So. SMUG 528-7x	493		13541	.79		
263.	29-23-32 1963	Getty	Featherstone	369	1537	15006	.61	200	
264.	29-24-9 1966	Occidental	Root-1	303		15396	.70		
265.	29-24-25 1966	Tenneco-KCL	KCL 122-25	294		11948	.60		
266.	29-25-21 1965	Occidental	Texaco-Sp 15-21	306		10648	.62		
267.	29-26-18 1944	Chevron	KCL 11-44	341		13404	.50		BC at 13127, serpentine, Sect.B.
268.	29-26-36 1941	Marathon	KCL-G-1	373		10595	.52		Sect.C.
269.	29-27-1 1951	Chevron	33-52	578		7014	.46		Bot. in BC, granite, Sect.C.
270.	29-27-11 1948	Superior	KCL-15	447		7724	.44		Bot. in BC Sect. C
271.	29-27-22 1948	Gulf	KCL B-45	402		10591	.49		Bot. in BC, granite, Sect.C
272.	29-27-34 1956	Western Gulf	KCL 33-34	396		11577	.49		Bot. in BC
273.	30-21-21 1954	Superior	Forbes-1	2010		4761	.53		Sect.C
274.	30-22-26 1951	Chevron	Van Wert-68	1038		6098			Sect.C
275.	30-22-29 1948	Texaco	W.P. 15-29	1425		4881	.60		
276.	30-22-30	Composite, Belgian Anticline		1720		10686			Sect.C and A
277.	30-23-25 1977	unnamed	(proprietary)	1181	9050	18761	.83	342	Bot. in BC(?)
278.	30-23-30 1951	Chevron-U.S. NPR 1*	X-55-30R	1341	11710	12856	.61,11710-12944 .55 at TD		Sect.C
279.	30-23-35 1955	Chevron-U.S. NPR 1*	352-35R	1334		7457	.55		Sect.C
280.	30-24-15 1965	Bander	Palm Farms-55	287		11300	.63		
281.	30-24-31 1941	Chevron-U.S. NPR 1*	362-315	1270	6250	9943	.62		
282.	30-25-12 1955	Shell	Posuncula-1	338		14224	.57		Bot. in BC Sect.B and C
283.	30-25-14 1941	Shell	KCL A-44-14	325		13408	.51		Sect.C

* = Unit Operation - Naval Petroleum Reserve

No.	T.S.-R.E.-Sec. Year	Operator	Name	Elev. (ft)	Depth to AHP[1/] (ft)	TD (ft)	Bottom Hole Pressure/ Depth (psi/ft)	Bottom Hole Temp. (°F)	Remarks
284.	30-25-24 1958	Shell	KCL 15x-24	320		15720	.60 at 15405		
285.	30-25-29 1952	Arco	CLA 67-29	311	12265	17895	.73	300	Top BC at 17873' Sect. C
286.	30-25-33 1945	Arco	CLA 21-33	311		13912	.60		
287.	30-26-3 1938	Superior	KCL-12	363		13131	.51		Sect. C
288.	30-26-4 1943	Miller and York	KCL G-1	358		8134	.55		
289.	30-26-30 1947	Shell	KCL A-53-30	329		14224	.49 at 14,000		Sect. B
290.	30-29-10 1971	Atlantic	Comp. -1			5230	.55 at 4,552		Bot. in BC
291.	30-29-20 1957	Shell	45-20	456		8107	.50		Bot. in BC
292.	31-24-4 1947	Chevron-U.O. NPR 1*	343-46	1052		10200	.55		Sect. C
293.	31-25-5 1945	Chevron	KCL 20-13	505	14064	16246	.62		Sect. C
294.	31-25-8 1941	Arco	Feldman U.S. 61-8	403		9346	.60		
295.	31-25-26 1975	Texaco	Elk Vista -1	285	11211	16472	.79	290	
296.	31-26-16 1945	Shell	KCL 45	316		11500	.49		Sect. B.
297.	31-29-10 1968	Termo	Digeorgio-1	500		6419	.50		Bot. in BC
298.	32-23-21 1957	Santa Fe Energy	CHOD 58-21	1654	13615	14504	.62		
299.	32-24-10 1941	Getty	10-25-P	915		14622	.60 at 12,825		
300.	32-25-11 1959	Getty	BVA 22-11	281		11365	.60		
301.	32-25-15 1974	Texaco	Texaco-Tenneco B & M-1	287	14956	16500	.64		
302.	32-26-4 1951	Marathon	KCL A-72-4	309	10900	21482	.72 at 20,008	334	Sect. B
303.	32-26-14 1941	Union	Morgan 51	306		11456	.49		Sect. B
304.	32-28-34 1974	Tenneco	Tenneco-Superior Sandhills 64x	415	18250	22711	.68	320	
305.	32-29-3 1948	Marathon	Mitchell-1	413		13792	.51		Bot. in BC
	San Bernardino B & M								
306.	11-19-3 1954	Socony	Tejon 16-3	592		11963	.57		Bot. in BC
307.	11-20-15 1959	Arco	KCL K22	535		16421	.60	241	

* = Unit Operation - Naval Petroleum Reserve

No.	T.S.-R.E.-Sec. Year	Operator	Name	Elev. (ft)	Depth to AHP[1/] (ft)	TD (ft)	Bottom Hole Pressure/ Depth (psi/ft)	Bottom Hole Temp. (°F)	Remarks
308.	11-20-28 1953	Arco	KCL D-16-28	1477		11816	.60		Sect. B
309.	11-21-5 1960	Arco	KCL Q-841-5	476		13960	.62	199	
310.	11-21-10 1961	Arco	KCL 43-10	536	13436	14499	.61	254	
311.	11-21-15 1958	Arco	KCL 33-15	639	14042	14443	.62		
312.	11-22-8 1948	Conoco	Santiago 1	623		9919	.66		
313.	11-22-12 1951	Gulf	KCL 83-12	319	12172	12172	.61		
314.	10-19-8 1962	Arco	Tejon A 61-8	1239		10462	.60		
315.	10-22-11 1968	Standard	KCL 69-68-11	2207	9509	11069	.60		
316.	10-22-13 1968	Standard	69-29-13	2026	6662	10453	.63		

1/ AHP, zone of abnormally high fluid pressure (P/D 0.61 psi/ft).

Late Cenozoic Structure of the Diablo Range Foothills Near Los Banos, California

William R. Lettis

Bechtel Civil and Minerals, Inc.
San Francisco, California 94105

Abstract

Geologic mapping near Los Banos, California, indicates that the present elevation of the Diablo Range foothills north of Coalinga is the result of late Quaternary deformation. Pliocene and Quaternary deposits were mapped over an area of 1800 km^2 in the foothills and the western San Joaquin Valley. Broad, late Pleistocene pediments veneered by up to 20 m of sand and gravel are preserved across the crest of the foothills. These pediments are warped into a series of gentle north- and northeast-trending folds and are vertically displaced more that 100 m by three northwest-trending fault systems: the Ortigalita, San Joaquin, and O'Neill faults. Elevation of the foothills appears to be the result of vertical displacement along the San Joaquin fault at the foothill-valley margin and by continued uplift and northeastward tilting of the foothills block. The O'Neill fault system is a group of small reverse faults within the foothills whose fault planes coincide with bedding in the northeast-dipping Great Valley sequence. These faults are interpreted to be sympathetic flexural slip displacements associated with the continued northeastward tilting of the foothills. Much of the warping preserved by the pediments may be the result of the differential movement along these bedding-plane faults.

The late Quaternary elevation of the foothills provides a view of the lower crustal structure which may be present beneath Anticline Ridge. The broad Pleistocene folds of the southwestern San Joaquin Valley may be the surficial expression of bedding plane slip faults similar to those in the foothills of the Diablo Range south of San Luis Reservoir.

Introduction

The late Cenozoic tectonic history of the San Joaquin Valley and the Diablo Range is recorded in a thick sequence of upper Cenozoic alluvial-fan and terrace deposits in the western San Joaquin Valley and foothills of the Diablo Range. These deposits have been studied extensively in the west-central San Joaquin Valley near Los Banos (Fig. 1) by Lettis (1982), where their detailed stratigraphy has proved to be a valuable aid in deciphering the late Cenozoic tectonic and climatic history of the region. This report summarizes the structural development of the foothills of the Diablo Range between Little Panoche Creek and San Luis Reservoir approximately 100 km northwest of Coalinga, California (area of Fig. 2 shown on Fig. 1).

LATE CENOZOIC STRUCTURE

Quaternary deformation in the San Joaquin Valley and foothills of the Diablo Range has created a series of northeast- and northwest-trending, broad, gentle folds, which have been displaced vertically and laterally by three northwest-trending fault systems. Faults and folds are concentrated in late Cenozoic deposits and are manifest principally by tilted, warped, and offset Pliocene and Pleistocene terraces, alluvial deposits, and pediment surfaces; very few of the structures are reflected in the attitudes of bedding or in offset of the underlying bedrock.

Folding

Quaternary folds include: (1) a large asymmetric syncline, trending N30°-40°W, underlying the San Joaquin Valley; and (2) many smaller northeast-trending anticlines and synclines, evident in the foothills, and which may project into and slightly deform sediments in the San Joaquin Valley.

The San Joaquin Valley syncline governs the general position and orientation of the valley. This structure exists primarily because of westward tilting of the Sierran block in response to westward expansion of the Basin and Range Province and simultaneous uplift of the Coast Ranges. It has persisted since at least the Miocene, when the Coast Ranges were elevated, eroded, and in places buried beneath the upper Miocene Quien Sabe Volcanics of Taliaferro (1948).

The syncline is best expressed by structure contours on the surface of the Corcoran Clay Member of the Tulare Formation (Lettis, 1982; see also Croft, 1972, and Miller and others, 1971, for contour maps of the Corcoran Clay in the southern San Joaquin Valley). The clay defines an asymmetric trough with a western limb inclined between 1° and 30° NE and an eastern limb dipping less than 1° SW. In the northern and central San Joaquin Valley, the principal line of subsidence lies near the west margin of the valley, generally from 20 to 30 km west of the present courses of the San Joaquin River and Fresno Slough in the valley's topographic axis. Subsurface data indicate that rarely have the structural and topographic axes coincided during the Pleistocene (Lettis, 1982), suggesting that the average rate of deposition from the surrounding mountain ranges has equaled or exceeded the average rate of subsidence.

In the foothills, Quaternary pediments and alluvium are deformed into several broad arches and broad synclinal basins. In the study area, these include the arches over the Panoche, Wisenor, Los Banos, and Laguna Seca Hills, and an unnamed arch north of Quinto Creek. Structural basins include the Little Panoche, San Luis, and Salt Valleys, Carrisalito Flat, and, south of the study area, the Panoche Valley. Figure 2 shows a surface reconstruction of two elevated

pediments in the Laguna Seca Hills area and illustrates the pattern and magnitude of many of these folds. The pediments are veneered by coarse, sandy gravel of the late Pleistocene alluvium of Los Banos (Lettis 1982), indicating that the deformation is late Pleistocene or younger.

If the structures have any significant direction of elongation, it is approximately N 40°-90° E, although the Panoche Hills arch seems to be a simple dome. Folds range from 5 to 20 km in width and have structural relief ranging from 10 to 150 m. The Tulare Formation crops out on their flanks (Lettis, 1982) and dips gently to moderately from less than 5° to 20° NW or SE. The attitude of underlying Cretaceous and Tertiary beds, which strike N 35° to 50° W and dip 30° to 85° NE, typically persists with little change across the Quaternary structures. The single exception is the Los Banos Hills arch (Fig. 2) which has caused a 25° to 35° change in the strike of beds in the underlying Great Valley sequence (Briggs, 1953); this change indicates that deformation in this area probably began before Quaternary time. Based on warping of alluvial deposits, deformation on all the other foothill structures may have begun during the Pleistocene.

The origin of these structures is poorly understood. Briggs (1953) mapped the Wisenor Hills and Los Banos Hills anticlines and suggested that the latter reflects a local intrusion similar in age to the Quien Sabe Volcanics but which has not been exposed by erosion. The Quien Sabe Volcanics, however, were erupted more than 7.5 m.y. B. P. (Snyder and Dickinson, 1979; Garniss Curtis, written commun., 1982), and unequivocal Quaternary deformation of the alluvium of Los Banos over the arch requires an alternative tectonic origin. Based on similar evidence, the other foothill arches cannot be attributed to volcanic intrusion. The general absence of bedrock deformation beneath the Quaternary arches and basins suggests that these structures probably formed by flexural slip along bedding planes in the bedrock in response to continued flexural uplift and tilting of the foothill belt. Buckling under northwest- to southeast-directed compression is unlikely in view of general absence of folds in the underlying bedrock. However, the fold axes are nearly parallel to the least compressive stress axes of focal-plane solutions computed for the San Andreas fault system, including the Ortigalita fault (LaForge and Lee, 1982), suggesting that these folds may represent a response to stress along the San Andreas fault and are simply too broad and gentle to be recognized in the underlying, steeply dipping bedrock. Warping due to extension along en echelon faults (i.e., pullapart basins) would create basins but not the broad uplifted arches that are so prevalent in the foothills south of the San Luis Reservoir.

Faulting

Quaternary deposits are offset by three northwest-trending fault systems, including the Ortigalita fault system, which forms the principal contact between the Franciscan assemblage and the Great Valley sequence; the San Joaquin fault system (Herd, 1979b), which separates the foothills physiographic area from the San Joaquin Valley floor; and the O'Neill fault system, originally named by Herd (1979a) for a small bedding-plane fault near O'Neill Forebay and which is expanded in this report to include all the geologically similar, small bedding-plane faults between the San Joaquin and Ortigalita fault systems (Fig. 2). Figure 3 shows the interpreted position and regional relations of these faults. Geomorphic evidence of late Quaternary faulting includes: (1) linear escarpments separating several levels of foothill pediments veneered by deposits of the late Pleistocene alluvium of Los Banos (Lettis, 1982); (2) lateral continuity of the escarpments across interfluve areas, precluding their origin as fluvial terrace escarpments; and (3) the presence of sag ponds, active springs, drainage reversals, and the development of restricted foothill valleys along the fault traces.

Ortigalita Fault. The Ortigalita fault was first shown by Anderson and Pack (1915) to form the approximate contact between the Franciscan assemblage and Great Valley sequence (Fig. 3). Later workers, including Taliaferro (1943), Leith (1949), Briggs (1953), and Page (1980), described the fault in greater detail and suggested that reverse, thrust, or normal displacement along the Ortigalita and related faults may have elevated the central Diablo Range to its present position during the Pliocene and, possibly, the Pleistocene.

The presence of roughly coeval basalt flows of the Quien Sabe Volcanics at similar elevations on both sides of the fault, however, constrains the timing of this activity. Basalt Hill (south of San Luis Reservoir, Fig. 1) is a small, undeformed outlier of the Quien Sabe Volcanics situated east of the fault. These rocks have a K/Ar date of 9.35 0.1 m.y. old (Garniss Curtis, written commun., 1982) and are interpreted to be a remnant of a basalt flow from the main Quien Sabe volcanic field (Lettis, 1982). The base of the outlier and the main volcanic field are at the same elevation, suggesting that significant uplift of the range relative to the foothills ceased before the late Miocene. Extension of vertically undisplaced embayments of the Tulare Formation and the alluvium of Los Banos into the central Diablo Range across the fault also indicates that little, if any, uplift of the central range relative to the foothills has occurred during the Quaternary.

Quaternary fault activity is, however, indicated by conspicuous morphologic expressions of the fault trace. These include sag ponds, springs, and prominent, weakly dissected escarpments. The presence of these features in late Pleistocene deposits of the

Tulare Formation and alluviums of Los Banos and San Luis Ranch (Lettis, 1982) suggest late Pleistocene activity while local offset of the Holocene alluvium of Patterson, particularly in the headwater area of Little Panoche Creek, suggest Holocene activity.

The sense of Quaternary displacement, although not well understood, clearly differs from the Miocene and earlier vertical displacement that may have elevated the central Diablo Range. Focal-plane solutions (LaForge and Lee, 1982), profiles in trenches (Anderson and others, 1982), and the en echelon character of the fault traces all suggest a significant component of lateral slip.

The extent of Quaternary lateral displacement is not known. The absence of offset ridges or creeks along the fault trace, however, suggests that if major displacement occurred, it happened before the present drainage network of the foothill belt was established duringthe late Pleistocene. The position of the Basalt Hill outlier of the Quien Sabe volcanic field east of the fault and north of the main volcanic field (Lettis, 1982) further suggests that any significant late Cenozoic right-lateral displacement along the Ortigalita fault is not realistic.

San Joaquin Fault System. The trace of the San Joaquin fault system on the foothill-valley margin is marked by a prominent, linear, faceted, east-facing escarpment (Fig. 3) that is especially well-preserved along the front of the Laguna Seca Hills north of Little Panoche Creek (Fig. 2). Although the orientation of the fault plane and the sense of Quaternary displacement are poorly understood, vertical displacement has been reported by Herd (1979b) along an east-dipping fault plane north of the study area near Ingram Creek. The fault plane was not observed during this study but in the context of recent data collected in the Coalinga area may be a steep to shallow southwest-dipping fault. The component of vertical movement, however, is evident along the front of the Laguna Seca Hills (Fig. 2) where the reconstructed pediment surfaces veneered by the alluvium of Los Banos have been truncated. In the Laguna Seca Hills, the alluvium of Los Banos forms a pediment veneer on a surface that at one time was graded to the valley floor, but now projects approximately 140 m above the present valley floor. Using a minimum and maximum probable age of 200,000 to 300,000 yr. for the pediment (Lettis, 1982) this displacement provides an average rate of vertical offset in this area of about 45 to 65 cm per thousand years. The fault trace, however, is overlain by unfaulted alluvium of San Luis Ranch and alluvium of Patterson across the fan heads of the larger Diablo Range drainages, a situation that suggests little activity along the fault during at least the past 40,000 to 60,000 yr.

O'Neill Fault System. The O'Neill fault system includes the zone of numerous small foothill faults between the subparallel to the larger

Ortigalita and San Joaquin faults (Fig. 2,3). These faults trend N 35°-50°W, parallel to the strike of beds in the Cretaceous and Tertiary bedrock, and are evident principally between Little Panoche Creek on the south and San Luis Creek on the north. The faults differ from the larger, bordering faults in that they appear to exhibit predominantly bedding-plane slips in response to continued uplift and tilting of the foothill belt during the Quaternary.

Fault displacement is manifest principally by offset of the broad foothill pediments veneered by the alluvium of Los Banos. Contour reconstruction of these surfaces suggests that vertical displacement ranges from less than 1 to 100 m (Fig. 2). The broad Quaternary folds shown in Figure 2, however, are not displaced laterally, and other evidence of lateral displacement has not been observed. The magnitude of vertical displacement changes not only between individual fault segments but also laterally along each segment. Although maximum vertical offset typically coincides with maximum anticlinal flexure, displacement decreases down the flanks to less than 5 m within most of the synclinal basins.

Available field data suggest that the prinicipal sense of motion in the O'Neill fault system is reverse displacement along east-dipping fault planes. Fault escarpments have a consistent west-facing aspect, and, where the escarpments are traced into the homoclinally east-tilted Cretaceous and Tertiary bedrock, they appear only as sheared shale units between more resistant sandstone beds where the bedding is not displaced.

The apparent reverse displacement on the faults and the absence of disruption in underlying bedrock suggest a sympathetic bedding-plane-slip origin in response to Quaternary flexural folding of the foothill region and (or) fault activity along the larger Ortigalita and San Joaquin faults. The coincidence of maximum displacement with local arching described above suggests, in turn, that the small foothill arches and basins may be a result of bedding-plane slippage.

REFERENCES

Anderson, L. W., Anders, M. H., and Ostenaa, D. A., 1982, Late Quaternary faulting and seismic hazard potential, eastern Diablo Range, California, in, Hart, E.W., Hirschell, S.F., and Schultz, S.S., (eds.) Conference on earthquake hazards in the eastern San Francisco Bay area, Hayward, California: California Division of Mines and Geology Special Publication 62, p. 167-206.

Anderson, R., and Pack, R. W., 1915, Geology and oil resources of the west border of the San Joaquin Valley north of Coalinga, California: U. S. Geological Survey Bulletin 603, 220 p.

Briggs, L. I., 1953, Geology of the Ortigalita Peak Quadrangle, California: California Division of Mines and Geology Bulletin 167, 61 p.

Croft, M. G., 1972, Subsurface geology of the late Tertiary and Quaternary water-bearing deposits of the southern part of the San Joaquin Valley, California: U.S. Geological Survey Water-Supply Paper 1999-H, p. H1-H29.

Herd, D. G., 1979a, Geologic map of O'Neill Forebay, western Merced County, California: U.S. Geological Survey Open-File Report 79-359, scale 1:24,000.

_____ 1979b, The San Joaquin fault zone: Evidence for late Quaternary faulting along the west side of the northern San Joaquin Valley, California: Geological Society of America Abstracts with Programs, v. 11, no. 3, p. 83.

Leith, C. J., 1949, Geology of the Quien Sabe quadrangle, California: California Division of Mines and Geology Bulletin 147, 59 p.

Lettis, W. R., 1982, Late Cenozoic stratigraphy and structure of the western margin of the central San Joaquin Valley adjacent Diablo Range, California: U.S. Geological Survey Open-File Report 82-526, 202 p.

Miller, R. E., Green, J. H., and Davis, G.H., 1971, Geology of the compacting deposits in the Los Banos-Kettleman City subsidence area, California: U.S. Geological Survey Professional Paper 497-E, p. E1-E46.

Page, B. M., 1980, The southern Coast Ranges, in Ernst, W. G., ed., The geotectonic development of California (Rubey volume 1): Englewood Cliffs, N.J., Prentice-Hall, p. 329-417.

Snyder, W. S., and Dickinson, W. R., 1979, Geometry of triple junctions related to San Andreas transform: Journal of Geophysical Research, v. 84, p. 561-572.

Taliaferro, N. L., 1943, Geologic history and structure of the central Coast Ranges of California, in Geologic history and structures, chapter 5 of Geologic formations and economic development of the oil and gas fields of California: California Division of Mines and Geology Bulletin 118, p. 119-163.

_____ 1948, Geologic map of the Hollister quadrangle, California: California Division of Mines and Geology Bulletin 143, scale 1:62,500.

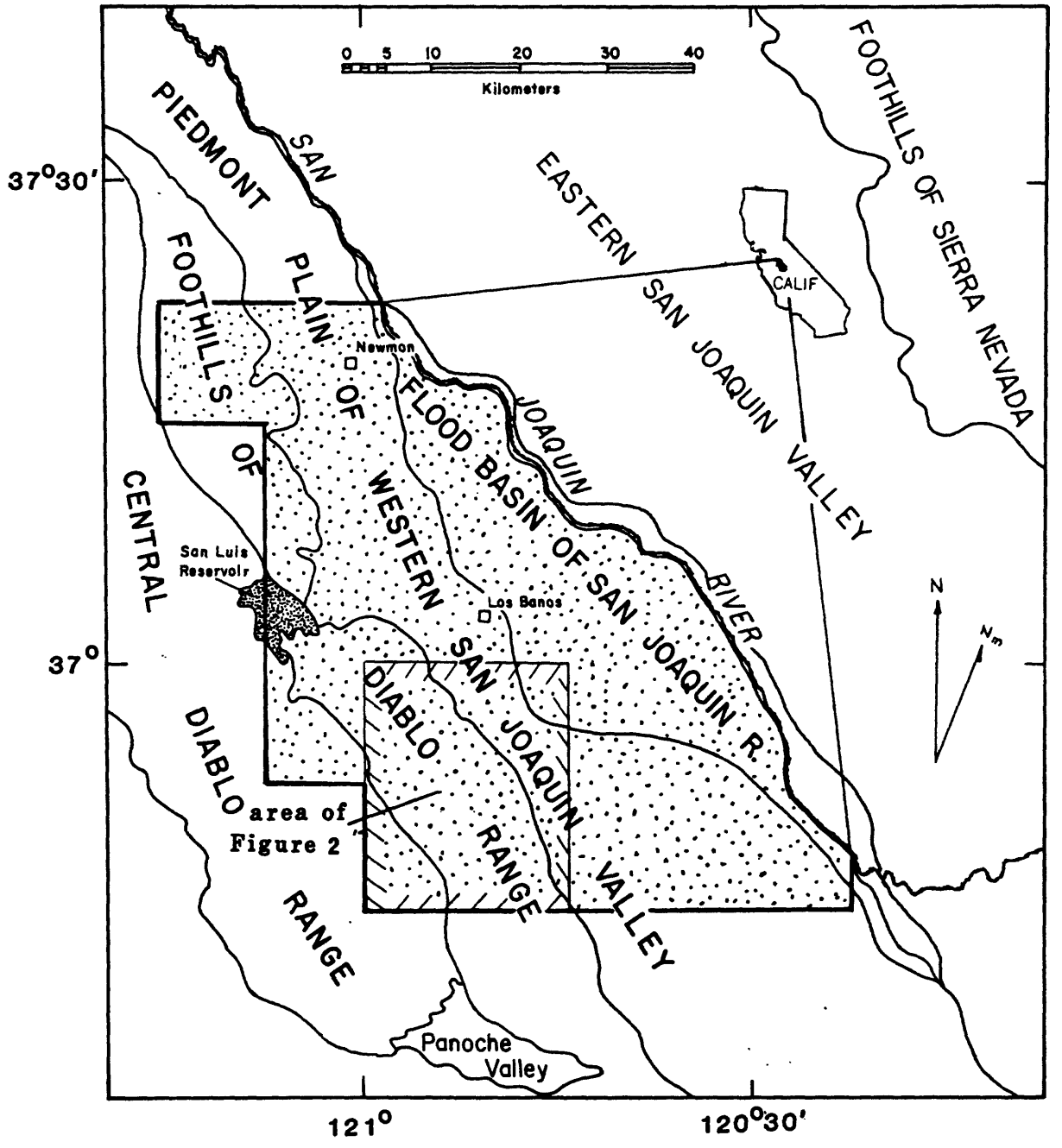

Figure 1. Index map showing location of study area.

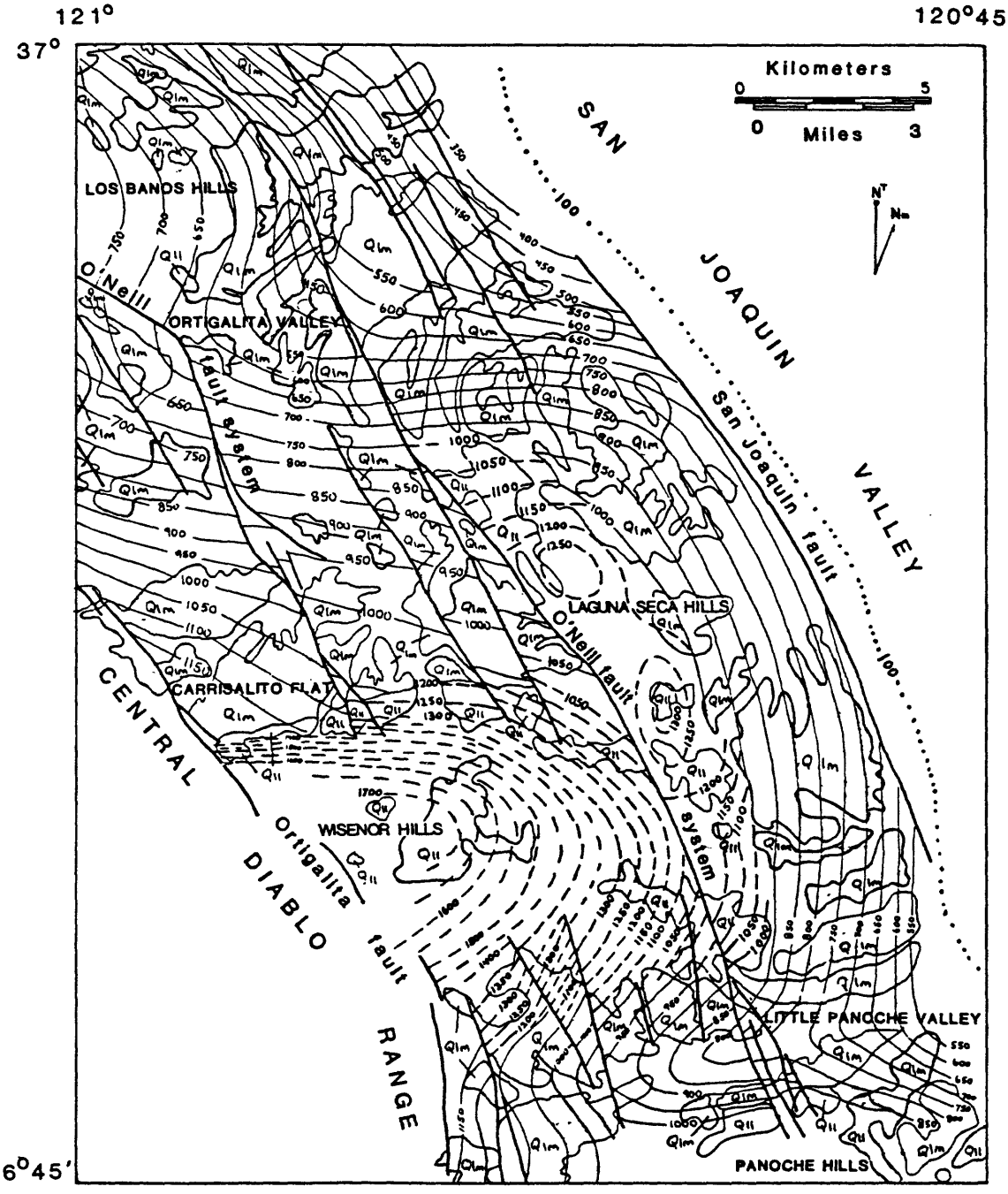

Figure 2. Structure-contour map of reconstruction pediment surfaces in foothills of Diablo Range as recognized by Lettis (1982). Solid contours drawn on middle member (Unit Qlm) of the alluvium of Los Banos; dashed contours drawn on lower member (Unit Q11) of the alluvium of Los Banos: dotted contours drawn on surface of the Corcoran Clay Member of the Tulare Formation. Contour interval, 50 ft. Heavy solid lines, faults. Only generalized outcrops of pediments are shown; pediments typically are veneered by gravelly coarse sand of the alluvium of Los Banos.

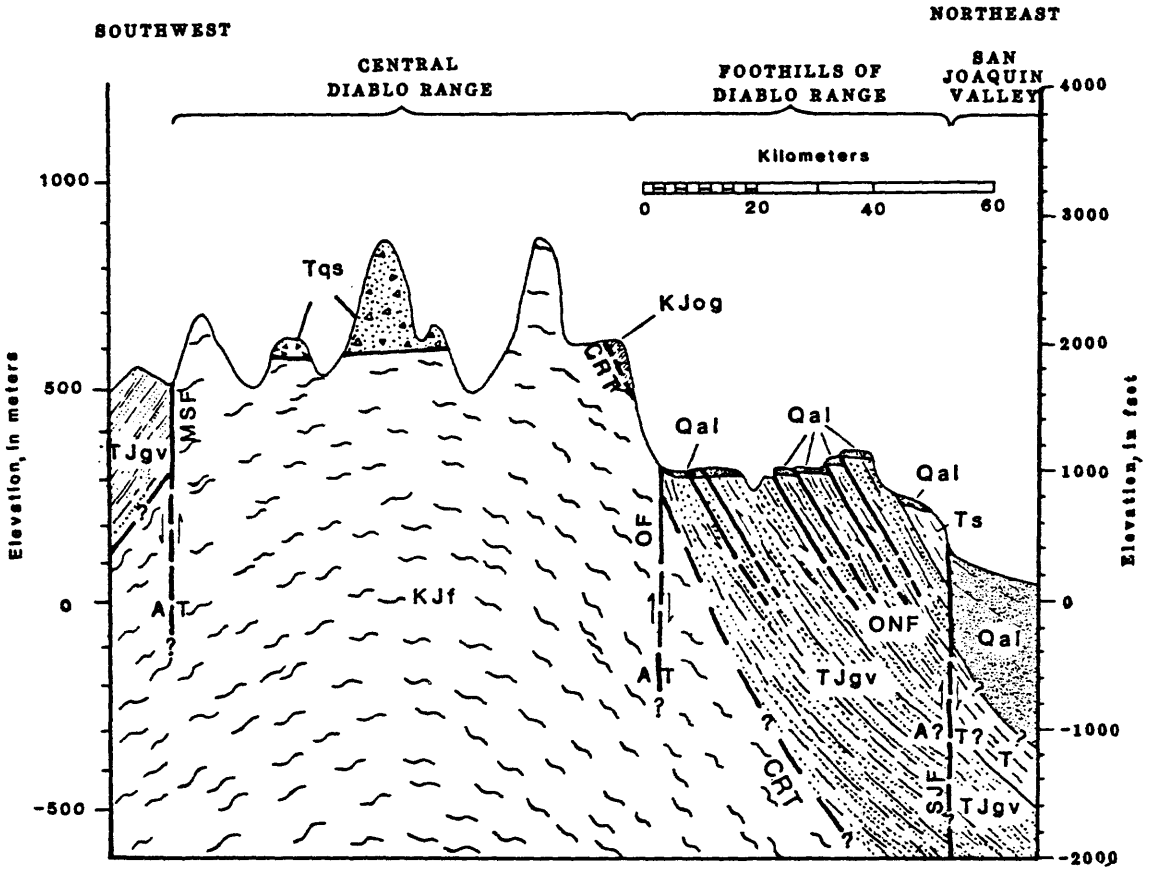

Figure 3. Generalized cross section of Diablo Range at approximately lat 36°50°N, illustrating pertinent lithologic and structural features of central Diablo Range and eastern foothills. Qal, upper Cenozoic alluvium; Tqs, Quien Sabe Volcanics of Taliaferro (1948); Ts, Tertiary marine and nonmarine sedimentary rocks; KJf, Franciscan assemblage; TJgv, Great Valley sequence; Kjog, outlier of basal ophiolite and lower Great Valley sequence, undivided (shown diagrammatically); MSF, Madrone Springs and related faults; OF, Ortigalita fault; ONF, O'Neill fault system; SJF, San Joaquin fault system; CRT, Coast Range thrust. Faults dashed where approximately located; queried where uncertain. A, movement away from observer; T, movement toward observer. Arrows indicate direction of relative movement.

WRENCH-STYLE TRANSFORM TECTONICS AND THE 2 MAY 1983 COALINGA EARTHQUAKE

by

Charles R. Real[1] and David R. Fuller[2]

INTRODUCTION

Since the occurrence of the M6.5 earthquake on May 2, 1983 near Coalinga, controversy has developed over its mechanism and relationship to Coast Ranges and western Great Valley neotectonics. This has been partly because the event was unaccompanied by surface fault rupture, allowing two possible planes of failure as determined from local and teleseismic focal mechanisms (Kanamori, 1983; Hartzell and Heaton, 1983; Eaton et al., 1983), and partly because the region of crustal failure, as defined by aftershocks, coincides with a long-known and well-defined structural feature known as the Coalinga anticline (Stein, 1983; Fuller and Real, 1983). The event was further complicated by an unusually energetic and wide-spread aftershock sequence that included a M5.2 event (June 11) that was accompanied by high-angle reverse faulting along a 3.3 km zone some 10 km west of the mainshock and subparallel to the principal aftershock zone (Hart and McJunkin, 1983). Understanding the origin of this episode of seismic strain release is important not only from an academic point of view, but also for the implications it may have on seismic hazards in other fold belts of a similar tectonic setting.

While arguments have been made for a nearly horizontal southwest-dipping thrust (Eaton et al., 1983), interpretation of subsurface structure (Fuller and Real, 1983) and results of modeling geodetic data (Stein, 1983) and, more recently, seismic reflection profiling (Fielding et al., 1984), favor a northeast-dipping high-angle reverse fault. However, lack of a simple plane as indicated by cross sections through the diffuse aftershock zone (Eaton et al., 1983) suggests a more complicated pattern of failure. M.L. Hill (personal communication, 1983) suggested bedding-plane slip along the flanks of the anticline resulting from flexural-slip folding as a possible cause. Regional patterns of crustal deformation lend further support to the

[1] California Division of Mines and Geology, Sacramento.
[2] California Division of Mines and Geology, Los Angeles.

latter two hypotheses, and it is the inferred style of deformation, namely, wrench tectonics, that we believe is the underlying cause of the Coalinga earthquake. The ideas presented in this paper are based, by-and-large, on the extensive work of R.E. Wilcox and T.P. Harding on wrench-style deformation.

WRENCH-STYLE DEFORMATION

Principal structural features resulting from horizontal shear over a broad region have been described by Wilcox and others (1973) and are collectively the result of what has been termed "wrenching" or "wrench tectonics." These features include synthetic strike-slip faults at a low angle to the shear direction, antithetic strike-slip faulting nearly perpendicular and of opposite sense to the shear direction, and compressional features: en echelon folds, thrusts, and high-angle reverse faults trending at an acute angle to the shear direction. The overall geometry of wrench structures is conveniently described by the wrench strain ellipse (figure 1). Principal wrench styles include: 1) Simple wrenching where crustal blocks move parallel to the wrench fault, 2) convergent wrenching where the crustal blocks move obliquely toward the wrench fault, and 3) divergent wrenching where the crustal blocks move obliquely away from the wrench fault.

Wrench-style deformational patterns have been artificially generated in clay model experiments and have been observed in nature worldwide (Moody and Hill, 1956; Wilcox *et al.*, 1973; Harding, 1974, 1976). Particularly diagnostic are the en echelon fold sets which were originally thought to be directly related to the strike-slip faulting but are now known to develop independently. That is, wrench faulting and en echelon folding are different crustal responses to a common cause; a deep-seated zone of shear. Although simple theory predicts that folds should initiate at an angle of 45° to the direction of shear in a homogeneous medium, clay model experiments and natural occurrences show an average angle of about 30° $\pm$ 15° with variations possible along the same fault trend (Wilcox *et al.*, 1973). A portion, or even most, of the axial extent of such irregular trending folds have even been observed to parallel the wrench fault. Wilcox and others (1973) have concluded that convergence of crustal blocks, changes in wrench fault strike, large vertical displacements, crustal inhomogenaeities, and basement mobility are factors that may influence the form and trend of en echelon fold sets.

Convergent wrenching enhances compressional structures, while divergent wrenching enhances extensional structures. Clay model experiments have shown that a convergence of only 2° significantly enhances the development of folds. Strong or prolonged convergence often leads to secondary faulting of folds. Wrench anticlines are

commonly intensely faulted internally with high-angle reverse, thrust, and even normal faults, resulting from the interplay of the compressional component of convergent wrenching and extensional stresses from flexing (Harding, 1973, 1974).

San Joaquin Valley

The Coalinga anticline is one of many en echelon folds that lie along the western margin of the San Joaquin Valley, an asymmetric Tertiary basin bounded on the east by the Sierra Nevada and on the west by the San Andreas fault. Here, a thick wedge-shaped sequence of oil-bearing Cenozoic sediments unconformably overlie the Mesozoic Great Valley Group and the underthrust Franciscan basement complex of subduction origin. This complex lies juxtaposed to the Salianian block, a portion of the Sierran-Peninsular granitic batholith that has been transported several hundred kilometers northwest in a right-lateral sense since Paleocene. Transport of the Salinian block is a result of relative motion between the Pacific and North American lithospheric plates along the present and ancestral San Andreas fault, as reviewed by Page (1981).

Neogene structural deformation in this region, consequently, is dominated by convergent transform tectonics, characterized by compressional basins, en echelon folds, and northwest-trending strike-slip faults (Page, 1981). Contemporary slip along the San Andreas fault accommodates only about 60 percent of the relative plate motion, with the remainder presumably taken up by slip along other strike-slip faults and plastic deformation over a broad zone tens to hundreds of kilometers wide on either side of the San Andreas plate boundary (Page, 1981). Locally, structural complexity decreases away from the San Andreas fault, reinforcing its importance as the center of structural activity. The well-developed en echelon fold sets, having a basinward plunge and an upward structural trend toward the fault, suggest that vertical deformation along the transform is an additional means of relieving the intense compression across the zone.

The well-developed compressional features along the western San Joaquin Valley are consistent with large-scale oblique convergent wrenching along the San Andreas fault (Harding, 1974, 1976). The direction of relative plate motion is estimated to be N35°W (Minster and Jordan, 1978), while the San Andreas fault trends approximately N40°W in this region, producing a convergence of possibly 5° or more. Such convergence would undoubtedly account for many of the compressional structural features in the region (figure 2).

Although many of the folds along the western San Joaquin Valley can be explained by simple wrench tectonics, Page (1981) has pointed out that the subparallel orientation of some anticlines to the shear zone, such as Kettleman Hills just south of Coalinga anticline, suggest a different origin. This has led some investigators to

speculate on a drape-fold model, formed over pre-existing normal faults that have been reactivated in a reverse sense. Slip along one of these buried faults has been postulated as a cause of the Coalinga Earthquake (Fielding, et al., 1984).

Coalinga Anticline

We believe there is ample evidence that wrenching is a principal cause of deformation throughout the western San Joaquin Valley, including formation of the Coalinga anticline. Geodetic observations made after the earthquake showing continuing growth of the anticline suggest that the Coalinga earthquake sequence is genetically related to wrenching. The en echelon pattern of the Coalinga anticline and adjacent folds, their basinward plunge, their increasing asymmetry, and eventual overturn up-plunge toward the San Andreas fault all bear a striking resemblance to structural characteristics of convergent wrench zones produced in the laboratory and occurring naturally elsewhere in the world. It seems unlikely that drape folds would share this resemblance.

Furthermore, proximity to a major transform, apparent synchroneity between episodes of anticlinal folding and slip along the San Andreas fault since mid-Miocene (Harding, 1976), and space-time correlation between seismicity and anticline growth during this earthquake sequence all suggest a close relationship between wrench deformation and internal failure of the Coalinga anticline. Based on the analysis by Harding (1976), anticlinal folding on the west side of the San Joaquin Valley has occurred contemporaneously with Cenozoic movement on the San Andreas fault, with outward growth and development of structures downplunge away from the fault. The older, more tightly folded portions of anticlines nearest to the San Andreas fault are commonly disrupted by more recent thrusting, interpreted to be a late-stage reaction to prolonged deformation.

Coalinga anticline exhibits these characteristics with simple, gentle, nearly symmetric folding to the southeast, becoming steeper and more asymmetrical toward the northwest until the axial plane is overturned, and the trend of the anticline is bent more toward the northwest, oblique to the shear zone. The 1983 Coalinga earthquake sequence is interpreted as indicating that the older up-plunge portion anticline has been folded beyond the competence of the rock, and has accommodated additional crustal shortening by internal and basement faulting. Although initial failure was apparently high-angle reverse slip, the extended failure pattern is likely to be far more complex as suggested by the aftershock distribution (Eaton et al., 1983) and similar occurrences of faulted wrench anticlines elsewhere (Harding, 1973, 1974).

The subparallel axial trend of the downplunge extremity of Coalinga anticline, and its projection to Kettleman Hills does not preclude a wrench deformation origin as mentioned previously. The strong convergence, crustal heterogeneity, and mobility of the Franciscan basement may account for the irregular axial trend of these structures.

CONCLUSION

The 1983 Coalinga earthquake sequence and associated geodetic changes are a manifestation of continuing fold development in the western San Joaquin Valley. Spatial distribution of the earthquake sequence coincides with the location of the Coalinga anticline, while focal mechanisms and geodetic data indicate compression across the structure. Form, orientation, conformance of the Coalinga anticline with the regional structural pattern of en echelon basins and folds, and synchroneity of episodic fold development with slip on the San Andreas fault suggest that continued growth and internal faulting of the anticline is in response to intense crustal shortening resulting from large-scale oblique convergent wrenching along the Pacific and North American plate boundary.

Transform tectonics has been the dominant mode of deformation in this region since mid-Miocene, and contemporary orientations of plate motion and slip along the San Andreas fault suggest as much as 5^{o} of plate convergence; enough to significantly enhance the development of compressional structures. Although initial failure was apparently high-angle reverse slip along a concealed fault extending from the basement, the complete failure pattern of the anticline is likely to be far more complex as suggested by the aftershock distribution; perhaps including secondary conjugate sets of high-angle reverse, thrust, and even normal faults as has been observed in other faulted wrench anticlines elsewhere.

Future events, similar to the Coalinga earthquake sequence, can be expected to occur in other wrench zones associated with convergence along the San Andreas plate boundary, where tightly folded anticlines are undergoing similar development. This should be considered in future hazard assessments of such regions.

REFERENCES

Eaton, J.P., Cockerham, R., and F. Lester, 1983, Study of the May 2, 1983 Coalinga Earthquake and its Aftershocks, Based on the USGS Seismic Network in Northern California: California Division of Mines and Geology, Special Publication 66, p. 261-274.

Fielding, E., Barazangi, M., Brown, L., Oliver, J., and S. Kaufman, 1984, COCORP Seismic profiles near Coalinga, California: Subsurface structure of the western Great Valley: Geology, v. 12, p. 268-273.

Fuller, D.R. and C.R. Real, 1983, High-Angle Reverse Faulting, A Model for the 2 May 1983 Coalinga Earthquake: California Division of Mines and Geology, Special Publication 66, 177-184.

Harding, T.P., 1973, Newport-Inglewood Trend, California--An Example of Wrenching Style of Deformation: Am. Assoc. Petroleum Geologists, v. 57, n. 1, p. 97-116.

_____, 1974, Petroleum Traps Associated with Wrench Faults: Am. Assoc. Petroleum Geologists, v. 58, n. 7, p. 1290-1304.

_____, 1976, Tectonic Significance and Hydrocarbon Trapping Consequences of Sequential Folding Synchronous with San Andreas Faulting, San Joaquin Valley, California: Am. Assoc. Petroleum Geologists, v. 60, n. 3, p. 356-378.

Hart, E.W. and R.D. McJunkin, 1983, Surface Faulting Northwest of Coalinga, California, June and July, 1983: California Division of Mines and Geology, Special Publication 66, p. 201-219.

Hartzell, S.H. and T.H. Heaton, 1983, Teleseismic Mechanism of the May 2, 1983 Coalinga, California Earthquake from Long-Period P-waves: California Division of Mines and Geology, Special Publication 66, p. 241-246.

Hill, M.L., 1983, (Personal Communication).

Kanamori, H., 1983, Mechanism of the 1983 Coalinga Earthquake Determined From Long-Period Surface Waves: California Division of Mines and Geology, Special Publication 66, p. 233-240.

Minster, J.B. and T.H. Jordan, 1978, Present-Day Plate Motions: J. Geophys. Res. 83, p. 5331-5354.

Moody, J.D. and M.J. Hill, 1956, Wrench-fault tectonics: Geological Society of America, v. 67, p. 1207-1246.

Page, B.M., 1981, The southern Coast Ranges, in Ernst, W.G., ed., The geotectonic development of California: Englewood Cliffs, New Jersey, Prentice-Hall, p. 329-417.

Stein, R.S., 1983, Reverse Slip on a Buried Fault During the 2 May 1983 Coalinga Earthquake: Evidence from Geodetic Elevation Changes: California Division of Mines and Geology, Special Publication 66, p. 151-164.

Wilcox, R.E., Harding, T.P., and D.R. Seely, 1973, Basic Wrench Tectonics: Am. Assoc. Petroleum Geologists, v. 57, n. 1, p. 74-96.

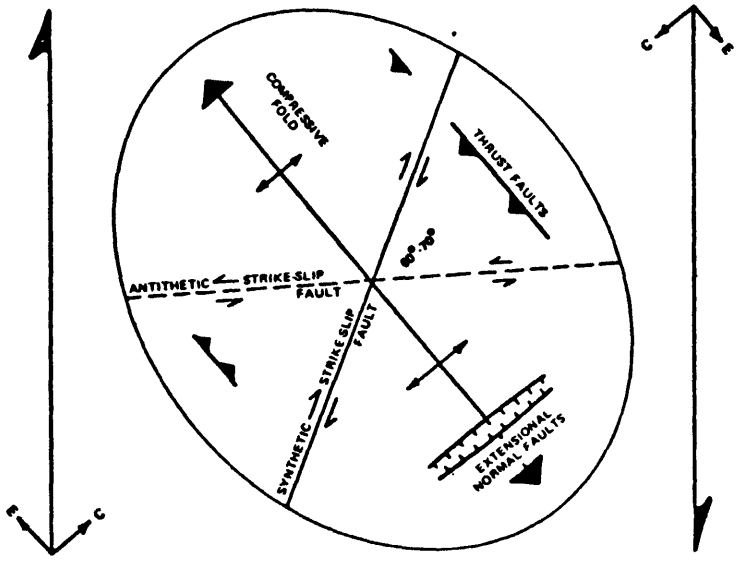

Figure 1. Forces and structures associated with wrenching. Large arrows indicate the direction of principal crustal shear. C is the component of compression derived from wrenching, and E is the component of extension derived from wrenching.

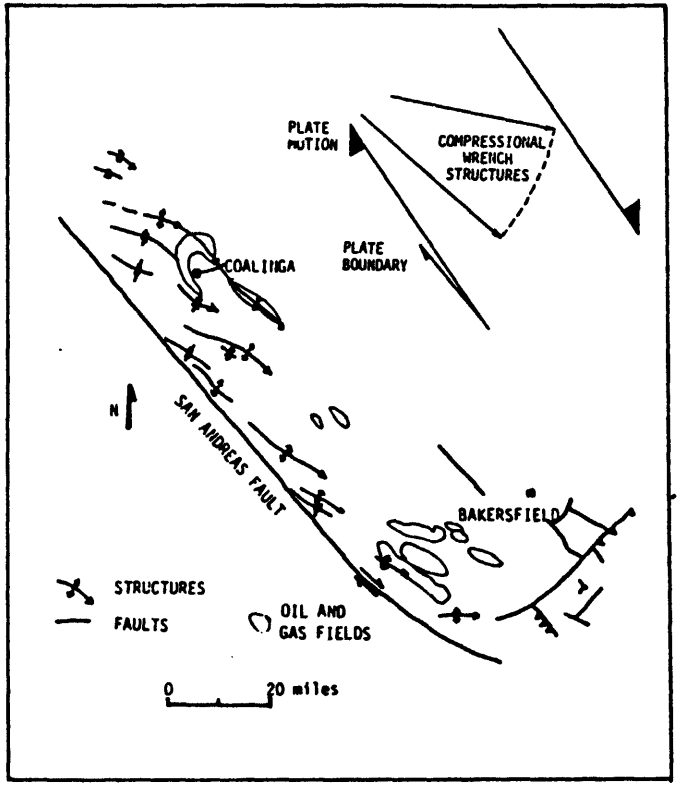

Figure 2. En echelon folds along the western margin of the San Joaquin Valley. The diagram in the upper right shows about 5 degrees plate convergence and range of axial trends of compressional structures associated with wrenching.

EARTHQUAKES AND FOLDING, COALINGA, CALIFORNIA

By Mason L. Hill

14067 E. Summit Drive, Whittier, CA 90602

Abstract

The magnitude 6.6 Coalinga earthquake of May 2, 1983 and most of the other magnitude 4 and greater earthquakes near that town, are tentatively attributed here to flexural-slip on the flanks of growing folds. This explanation apparently conflicts with the 100-year-old theory that all tectonic earthquakes are caused by slip on faults. Perhaps the Coalinga events, in an area where no active faults had been mapped, will serve to suggest another possible mechanism for the generation of some earthquakes. Here the thick stratigraphic section and massive, steeply dipping sandstones on the long southeast trending Coalinga anticline and syncline seem to be conducive to flexural-slip by active concentric folding. The magnitude 2.5 Lompoc earthquake of April 7, 1981 also can be attributed to flexural-slip on the limb of an anticline. Flexural-slip (bedding-plane slip), usually unseen and unmappable, is clearly revealed in the Ojai, Point Conception and Elwood areas. Many small earthquakes may be produced in these and other areas where direct evidence of active flexural-slip by folding is unavailable. The non-linear pattern of epicenters in the Los Angeles basin suggests that a mechanism other than faulting might cause earthquakes. If the May 2 Coalinga earthquake was caused by folding, unusual geologic conditions may be responsible for its high intensity. A reflection seismic line might prove th presence of an appropriate causal fault, or strengthen the possibility that the event was generated by bedding-plane slip. A reanalysis of earthquakes not clearly related to specific faults should be made.

Coalinga Earthquakes

The magnitude 6.6 Coalinga earthquake of May 2, 1983 caused considerable property damage. It came at an unsuspected place, time and strength. The epicenter was located 10 km NNE of the town and the hypocenter was reported to be approximately 10 km deep. Ground rupture, usually occurring with a magnitude 5+ earthquake in California, was not found. Furthermore, surface geologic maps and subsurface data from oil fields in the area, available for many years, do not show faults with earthquake potential (Arnold and Anderson, 1910; Kaplow, 1945; Dibblee, 1971). The absence of known earthquake-generating faults in the area suggests the possibility of another causal mechanism for at least some of the Coalinga earthquakes. Actually, the San Andreas fault 35 km to the SW has been the nearest known significant earthquake generator.

Seismic data gathered in the first 25 hours were presented on May 4 to attendees at geological and seismological meetings in Salt Lake City, Utah. At that time I considered flexural-slip on the Coalinga anticline as a possible cause of the earthquake. This explanation seems to be reinforced by my tentative interpretation of data which have been obtained up to August, 1983. Specifically, nine more seismic events of magnitude 4 to 6.4 which have

occurred in the area have been located, and focal depths and the first motions have been calculated (Eaton et al., 1983). Data on the 10 larger Coalinga earthquakes are shown in table 1. The strike and dip of one of the nodal planes of each of these earthquakes are shown on figure 1.

The hypocenter of the May 2 magnitude 6.6 earthquake is tentatively assumed to be on the NE flank of the Coalinga anticline. This structure is several tens of kilometers long; depth to the base of Cretaceous strata on its flanks probably is at least 12 km; and the massive Cretaceous sandstone units favor a concentric fold mechanism producing flexural-slip. Furthermore, it can be assumed that some of the folds in this region of active tectonism are growing. In fact, a recent leveling survey shows a 40+ cm uplift on the anticlinal ridge (King and Stein, 1983). Therefore, flexural-slip on associated bedding surfaces of large extent, delayed by friction long enough to produce a large elastic rebound, possibly could have generated a 6.6 magnitude earthquake on this structure (event A of fig. 1). In addition, the strike and dip of these Cretaceous beds at hypocentral depth on the NE flank of the Coalinga anticline could be parallel to the steep NE-dipping plane of the first motion solution of the May 2 earthquake and the large aftershocks on May 9 and 24, located about 11 km NNE of Coalinga (events B and D of fig. 1).

The 10 seismic events discussed here are widely separated and non-aligned to indicate more than one causal fault, or other possible sources of energy release (fig. 1). Assumption of the fault model for the May 2 earthquake requires either a SW-dipping thrust or a NE-dipping reverse fault. However, in the absence of a suitable mapped fault, the ambiguity of the first motion solution remains. One interpretation, in my opinion unjustified, provides the NE-dipping reverse fault by recontouring Kaplow's (1945) top Kreyenhagen shale map (Fuller and Real, 1983).

As a working hypothesis, I attribute all of the 10 earthquakes except event E (fig. 1), which was accompanied by 50 cm of surface offset along the newly discovered north-trending Nunez fault (Hart and McJunkin, 1983; Rymer et al., this volume) to flexural-slip on the flanks of folds. For these, I have tentatively chosen one of the nodal planes of the first motion solutions as the earthquake- generating slip zone (table 1 and fig. 1). The 4.3 magnitude earthquake of May 22, 13 km east of Coalinga (C of fig. 1) can be related to reverse-slip on a south-dipping bedding plane between the SE plunge and SW flank of the Coalinga anticline. The magnitude 4 event of June 12, 3 km SSE of Coalinga (F of fig. 1) can be related to reverse-slip on a NE-dipping bedding plane on the SW flank of the Coalinga syncline. The earthquakes which are clustered 9 to 11 km NNW of Coalinga, G, H, I, and J of figure 1, are also tentatively assumed to be caused by flexural-slip on the SW flank of the Coalinga syncline. However, based on the "ruling theory" that tectonic earthquakes are caused by faults, these events have been interpreted as being on the Nunez fault (Hart and McJunkin, 1983; Rymer et al., this volume). On the other hand, I suspect the strike of the reverse-slip planes of these events are probably too divergent from the Nunez fault trend to be on it. However, I realize that if these events, G, H, I, and J (table 1 and fig. 1), are due to flexural-slip on the SW flank of the Coalinga syncline the structure at hypocentral depths would have to diverge from the fold pattern at the surface.

Although we have accepted slip on faults as the explanation of tectonic earthquakes for 100 years (Gilbert, 1884), most of the Coalinga earthquakes

cannot be related to known faults. If the seismic first-motion solutions had indicated strike-slip movements, several subsurface faults would have had to be accepted as generators of the earthquakes. However, with dip-slip nodal planes, an alternative to conventional faulting may be slip on bedding planes. Therefore, flexural-slip on growing folds might be a potential mechanism for most of the Coalinga earthquakes. Furthermore, on the basis of present information, this mechanism may provide a more objective explanation of these earthquakes than resorting to movements on hypothetical reverse or thrust-slip faults.

Considering uncertainties of: 1) epicentral locations and; hypocentral depths, 2) total thickness and depth of the sedimentary section, and 3) shapes and positions of the folds, if any, at depths in excess of 10 km, the flexural-slip model for the generation of the Coalinga earthquakes is in doubt. Obviously, deep reflection seismic control is needed to define the positions of subsurface faults, if any, which could have caused the earthquakes, or if flexural-slip is a possible alternative explanation.

Other Examples of Flexural-Slip

The Coalinga events may indicate that tectonic earthquakes can be generated by bedding-plane slip on concentric folds. If so, some other cases should be found where seismicity results from folding. One such case will be described next, and some other potential ones are suggested.

The Lompoc Event: A magnitude 2.5 earthquake occurred on April 7, 1981 near Lompoc, California (fig. 2). It was related to a ground displacement which extended across the nearly flat floor of a quarry in Miocene diatomite. The event has been ascribed to crustal unloading by quarry operations (Yerkes et al., 1983). A north-facing scarp, as high as 20 cm, was apparently produced at the time of the earthquake. The maximum slip is reported as 23 cm reverse-slip and 9 cm right-slip on bedding surfaces that strike N84°E and dip 39-59°S. The scarp is located approximately 130 m north of the axis of a syncline and 260 m south of an anticlinal axis. The authors expressed surprise at finding a right-slip component of displacement on a fault with this trend in the Transverse Ranges.

According to the tectonic model suggested here for the Coalinga earthquakes, I believe that flexural-slip by folding is the primary cause of the Lompoc displacement. The bedding-plane slip, in a reverse sense toward the axis of the anticline, delayed by friction (reduced by overburden removel), can explain this minor earthquake. A west plunge of the structure at hypocentral depth can be the reason for the right-slip component of movement on the slip-plane.

Oakview-Ojai Area: Bedding-plane slip is revealed in this area by the offset terrace of the Ventura River (fig. 1; Yeats et al., 1981). Here the several faults that offset the terrace extend downward into steeply dipping bedding-planes on the flanks of folds in Miocene sandstone and shale units. They are interpreted as resulting from flexural-slip on these folds, only obvious because they extend upward to offset the flat-lying river terrace. There is no evidence to indicate that these Pleistocene-Holocene movements have produced significant earthquakes.

Flexural-slip near Point Conception: Excavations to study faulting in

this area revealed flexural-slip by the offset of flat-lying marine-continental terrace deposits overlying folded, steeply south-dipping Miocene shale (fig. 2). Arguments developed over whether bedding-plane slip (unmappable without the terrace cover) could cause strong earthquakes (Cluff, et al., 1981).

Flexural-slip on Elwood Anticline: Flexural-slip is revealed in sea-cliff exposures on the south flank of this oil-producing structure by terrace deposits that are offset a few centimeters to a few meters (fig. 2). I have seen and explain these offsets by concentric folding vecause in each case the hanging wall of the reverse fault is toward the south and the fault extends down into bedding of steep south-dipping Miocene shale on the south limb of the Elwood anticline.

Ventura Avenue Anticline: This long (>25 km) oil-producing, east-trending anticline with 40-50° dipping flanks, involving at least 12 km of Cenozoic clastic sediments with many thick sandstone units, is a prime candidate for active fluxural-slip folding (fig. 2). The north-dipping Taylor thrust(s) and the south-dipping Barnard reverse fault(s) may, in my opinion, have been derived from flexural-slip faulting at depth (Hacker, 1969).

Conclusions

At Coalinga, in the absence of known causative faults, flexural-slip on the flanks of folds may be a possible mechanism for most of the earthquakes, although causative subsurface faults might be revealed by seismic surveys. At Lompoc the quarry floor offset is evidence that bedding-plane slip (flexural-slip) caused the 2.5 magnitude earthquake, triggered by removal of overburden. Because most large earthquakes can be related to specific faults, the 6.6 magnitude Coalinga event seems anomalous. In contrast, the 2.5 magnitude earthquake at Lompoc may indicate that many small earthquakes previously assumed to have been caused by elastic rebound on faults are generated by flexural slips on bedding surfaces.

Although bedding-plane slip, required by the kinematics of concentric folding, is a form of faulting (trace-slip) it cannot ordinarily be seen and mapped. Occasionally it becomes obvious, as near Ojai, Point Conception and Elwood, where the slip projects upward to offset unconformably overlying strata, or as at Lompoc where bedding-plane slip offsets the ground surface. Perhaps most concentric-fold bedding-plane slip is by creep, as commonly occurs on faults, because it is likely to be confined to weak argillaceous layers. Therefore, except under very unusual conditions of long and deep fold limbs, as at Coalinga, property-damaging earthquakes due to actively growing folds are unlikely.

Knowing two areas, Coalinga and Lompoc, where earthquakes may have been generated by flexural-slip accompanying folding justifies reviewing earthquakes where there is uncertainty about the causal faults. In the cases described here, the structure, stratigraphy and lithology appear to favor concentric folding on a scale large enough to produce seismic events. Epicenter maps of the Los Angeles basin reveal a shotgun-like pattern which resists correlation with known faults. A reanalysis of these earthquakes might show that many of them are more likely to have resulted from flexural-slip rather than by movements on faults.

I conclude that geologists and geophysicists should combine their talents

and techniques in research on the importance of flexural-slip folding in the generation of earthquakes.

References Cited

Arnold, R., and Anderson, R., 1910, Geology and oil resources of the Coalinga district, California: U.S. Geological Survey Bulletin 398.

Dibblee, T. W., 1971, Geologic map of the Coalinga 15' quadrangle, U.S. Geological Survey, Open-File Report 71-87.

Cluff, L. S., et al., 1981, Seismic safety review of the proposed liquified natural gas facility, Santa Barbara County, California: Report to California Public Utilities Commission by The LNG Seismic Review Panel.

Eaton, J., Cockerham, R., and Lester, F., 1983, Study of the May 2, 1983 Coalinga earthquake and its aftershocks, based on the USGS seismic network in northern California: in The 1983 Coalinga, California earthquakes, California Division of Mines and Geology, Special Publication 66, p. 261-273.

Fuller, D., and Real, R., 1983, High-angle reverse faulting, a model for the 2 May 1983 Coalinga earthquake: in The 1983 Coalinga, California earthquakes, California Division of Mines and Geology, Special Publication 66, p. 177-184.

Gilbert, G. K., 1884, A theory of the earthquakes of the Great Basin: American Journal of Science, v. 27, p. 49-53.

Hacker, R. N., 1969, Ventura oil field: in American Association of Petroleum Geologists, Pacific Section Field guidebook, p. 22-29.

Hart, E., and McJunkin, R., 1983, Surface faulting northwest of Coalinga, California: in The 1983 Coalinga, California earthquakes, California Division of Mines and Geology, Special Publication 66, p. 201-219.

Kaplow, E. J., 1945, Coalinga oil field, California Division of Oil and Gas, v. 31, no. 2.

King, G., and Stein, R., 1983, Surface folding, river terrace deformation rate and earthquake repeat time in a reverse fault environment: The Coalinga, California earthquake of May 1983: in the 1983 Coalinga, California earthquakes, California Division of Mines and Geology, Special Publication 66, p. 165-176.

Rymer, M. J., Harms, K. K., Lienkaemper, J. J., and Clark, M. M., 1984, Rupture of the Nunez fault during the Coalinga earthquake sequence: this volume.

Yeats, R. S., Clark, M. N., Keller, E. A., and Rockwell, T. K., 1981, Active fault hazard in southern California: Ground rupture versus seismic shaking: Geological Society of America Bulletin, v. 92, p. 189-196.

Yerkes, R. F., Ellsworth, W. L., and Tinsley, J. C., 1983, Triggered reverse fault and earthquake due to crustal unloading, northwest Transverse Ranges, California: Geology, v. 11, p. 287-291.

Earthquakes	Dates	Magnitudes	Depths (km)	Selected nodal planes
A	5/2	6.6	10.2	N53W,67NE
B	9	5.2	12.5	N73W,48NE
C	22	4.3	10.3	W,36S
D	24	4.7	9.9	N42W,74NE
E	6/11	5.2	4.5	N13E,54SE
F	12	4.0	13.5	N40W,60NE
G	7/9	5.5	9.5	N24E,41SE
H	22	6.4	9.2	N20W,34NE
I	22	5.0	9.6	N40W,34NE
J	25	5.4	9.5	N20W,36NE

Table 1. Ten Coalinga earthquakes, data from Eaton et al. (1983). The strike and dip of the selected nodal plane of the seismic first motion solutions are shown on Fig. 1.

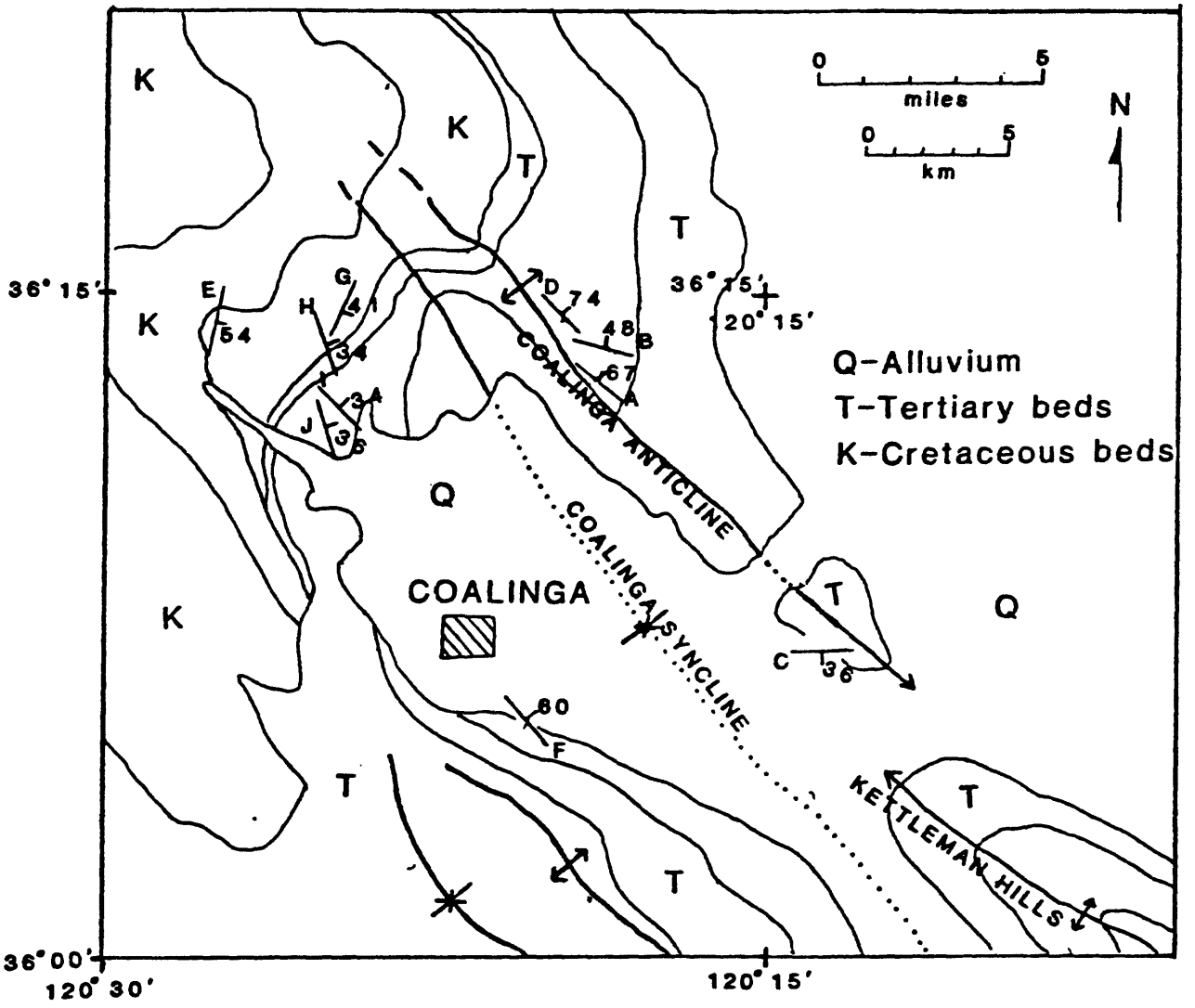

Figure 1. Geologic map showing 10 Coalinga earthquakes and the attitudes of the chosen slip planes from seismic first motion solutions. Data from Eaton et al. (1983).

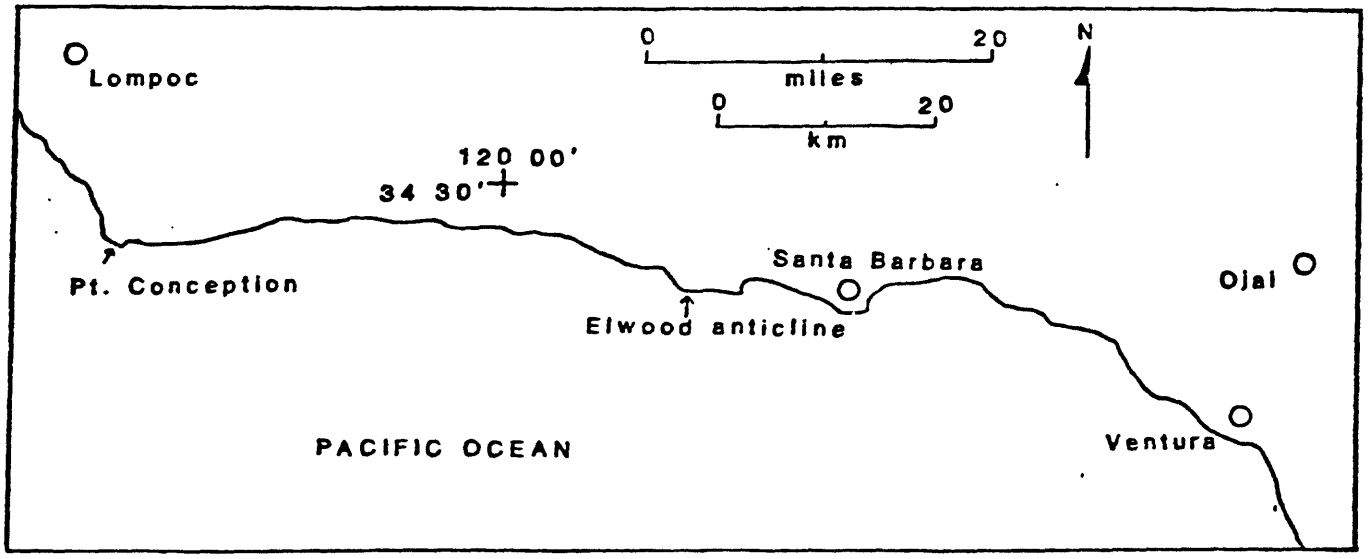

Figure 2. Map showing locations of known and suspected occurrences of flexural slip on growing folds near Santa Barbara, California.

The 1982 New Idria, California, Earthquake Sequence

C. P. Scofield, W. H. Bakun, A. G. Lindh

Abstract

The 1982 New Idria earthquake sequence (main shock magnitude M_L = 5.4 on October 25, 1982 at 2226 UTC) occurred six months before, and on the northwest edge of the source region of the 1983 Coalinga earthquake sequence. The New Idria aftershocks cluster about the main shock hypocenter, with no apparent planar distribution. Focal mechanisms are diverse, with the mechanism for the New Idria main shock requiring oblique thrusting. The New Idria source region lies near the southeast edge of a large ultramafic intrusive body and may be related to the New Idria thrust fault that bounds the northeast edge of the ultramafic outcrop. Although the spatial and temporal relationships of the 1982 New Idria and 1983 Coalinga sequences are clear in hindsight, there are, as yet, no identified characteristics of the New Idria shocks that might have been used to anticipate the Coalinga sequence. In particular, the magnitude and time distributions of the 1982 New Idria earthquakes are consistent with the distributions of comparable aftershock, not foreshock sequences.

INTRODUCTION

On October 25, 1982, a moderate-sized (M_L = 5.4) earthquake occurred 18 km east of the San Andreas fault, about 10 km southeast of New Idria, California (Fig. 1). It was immediately recognized that the New Idria earthquakes were unusual, occurring in an area where earthquakes are infrequent. In order to better locate these shocks, five digital event recorders (DER) were deployed near the New Idria epicentral region (Fig. 1). The data from the DER net complement the central California seismic network (CALNET) data so that more reliable source parameters for the New Idria earthquakes were calculated.

While the 1982 New Idria earthquakes are interesting in themselves, their true significance was only appreciated in May 1983 when the Coalinga earthquake sequence occurred near the southeast edge of the New Idria epicentral area. The spatial and temporal relation of the New Idria and Coalinga earthquake sequences suggests that the New Idria shocks might be considered an early precursor to the larger, more destructive, Coalinga earthquakes. Eaton et al. (1983) suggested that the 1982 New Idria earthquakes, the 1975 Cantua Creek earthquake sequence, the 1976 Avenal earthquake sequence, and other seismic activity in the 1970s east of the San Andreas fault outlined a seismic gap (Mogi doughnut) which was filled by the 1983 Coalinga shocks (e.g., see Fig. 2).

It seems natural to ask whether the most recent seismic activity (i.e., the 1982 New Idria shocks) in this precursory pattern can be discriminated from comparable earthquake sequences not precursory to larger shocks. (An affirmative answer would have important implications for earthquake prediction experiments). Clearly the most obvious earthquake sequences comparable to the 1982 New Idria shocks are the 1975 Cantua Creek (M_L = 4.9 main shock on August 3, 1975) and the 1976 Avenal (M_L = 4.7 main shock on January 14, 1976) earthquakes. In this paper, we describe the source parameters of the New Idria sequence and its relation to the Coalinga earthquakes, and compare characteristics of the Cantua Creek, Avenal, New Idria, and Coalinga earthquake sequences.

HYPOCENTER LOCATIONS

Station coverage in the CALNET was not sufficient in 1982 to provide accurate hypocenters for earthquakes in the New Idria source region. For epicentral distances less than 30 km, the CALNET sampled only a narrow range of azimuths to the south-southwest and north-northwest of the epicenters (see Fig. 1). In order to obtain better azimuthal coverage, five Terra-Technology DCS-302 digital event recorders (DER) with short period (T_0 = 1, $\mathcal{J}$ = 0.7), three-component seismometers were deployed from October 26 to October 31, 198 in the region surrounding the epicenter (see Table 1 and Fig. 1). Seven aftershocks were recorded both by CALNET and DER; P- and S-wave arrivals were recorded on all five DER for two of these aftershocks, the events at 2129 UTC on October 27 and at 0052 UTC on October 29, 1982. Hereafter, these events, marked by asterisks in Table 2a, are referred to as master events. Slopes of Wadati diagrams, determined from a linear regression analysis of the DER data are 0.81 ± 0.11 and 0.81 ± 0.16, respectively, for the two master events. Wadati plot slopes are commonly interpreted to be equal to $\alpha/\beta - 1$, where α and β are the compressional- and shear-wave velocities.

Little is known about the details of the crustal structure near New Idria. The crustal model obtained by Walter and Mooney (1982) for the southern part of the Diablo Range is based on a northwest-striking refraction line that has a southwest terminus about 50 km north of New Idria. The model consists of horizontal layers with uniform velocity gradients. It has been modified in this study to remove the velocity gradients (see Table 3a) so tha the HYPOELLIPSE location algorithm (Lahr, 1980) could be used for the hypocenter determinations described below.

To obtain locations for the master events we used P-arrival times from CALNET stations within 50 km and P- and S-arrival times from the DER net. Al station delays were set equal to zero and α/β = 1.8 was assumed. The resulting travel-time residuals and hypocenter precisions were unacceptably large for the accuracy of the arrival time readings (0.10 s for CALNET, and 0.05 s for the DER). Numerical experiments using different ratios of α to β showed that the rms of the travel-time residuals was minimal for α/β = 1.9, a value allowed by the Wadati diagram analysis. The stability of the location procedure was checked at this point by comparing the results of relocations using P and S arrival times with those using P arrival times only. We concluded that the procedure was stable since the differences for both master events were less than 0.20 min in latitude, 0.10 min in longitude, and 1 km i focal depth. All subsequent relocations were made using P-arrival time data from CALNET stations, P- and S-arrivals from DERs when available, the modifie velocity structure of Walter and Mooney (1982), and α/β = 1.9.

Travel-time corrections were derived in two stages. For stations with Δ<50 km, average residuals from a first set of master event locations became the partial station correction set. Hypocenters were then generated again fo the master events using this incomplete set of station delays. Average residuals for stations with Δ>50 km from this second run became final station corrections, thus completing the set of delays. The entire set of station delays is given in the appendix.

Tests of the relocation procedure for six aftershocks for which abundant DER data are available suggest that CALNET hypocenters are about 2 km farther north, 1 km deeper, and less clustered spatially, than the hypocenters listed in Table 2a. Furthermore, epicenters for these six events obtained using the relocation procedure described above (i.e., the velocity model in Table 3a and the station corrections in the appendix) without the DER arrival times are within 1 km (all but one are within 0.3 km) of the epicenters in Table 2a. Thus, while the DER arrival times were important in defining the station corrections listed in the appendix, the epicenters obtained without these data, that is, most of the aftershocks in Table 2a, are probably reliable to a fraction of a kilometer.

LOCAL MAGNITUDE AND SEISMIC MOMENT

Local magnitude M_L and seismic moment M_0 for all of the events in Table 2a, except the main shock, are estimated from the duration τ of the seismic coda using the formulae of Bakun (1984). Intense aftershock activity precludes any meaningful measurement of τ for the main shock. The M_L=5.4 and log M_0=24.04 values given in Table 2a for the main shock are taken from Uhrhammer et al.(1983).

We used the τ measured for CALNET stations in the routine analysis of central California earthquakes at the USGS in Menlo Park. The practice in late 1982 at the USGS was to measure the durations from 1 in/s playbacks on a digitizing table rather than from develocorder film as prescribed by Lee et al. (1972) and Bakun (1984). These τ are comparable to τ for events randomly selected from Table 2a that were read from develocorder film in the prescribed manner by us.

Each M_L and log M_0 in Table 2a, save those for the main shock, are the mean of the M_L and log M_0 estimates obtained from the number of τ measurements listed in the final column of Table 2a. No station corrections or source-region corrections were used (Bakun, 1984). The uncertainty, given in parentheses, is the standard deviation of the individual measurements.

SEISMICITY

Epicenteral locations for events starting January 1, 1982 and ending May 2, 1983 (the Coalinga main shock) are plotted in Figure 3 and listed in Table 2a. This time period can be divided into three parts: (i) January 1, 1982 to the time of the New Idria main shock on October 25, 1982 at 2226 UTC, (ii) October 25, 1982, 2226 UTC to November 1, 1982, and (iii) November 1, 1982 to the time of the Coalinga main shock on May 2, 1983 at 2342 UTC. While only two earthquakes occurred by October 25 in time period (i), four foreshocks all located near the New Idria main shock hypocenter occurred in the 4 hours before the main shock (see Figure 3). Time period (ii) contains the New Idria main shock and 86 aftershocks. Of these 86 shocks, 65 occurred by the end of October 26. During (iii), seismic activity was sporadic. Clearly, the 1982 New Idria sequence began vigorously and ended quickly.

The aftershocks form a rectangular region about the mainshock (Fig. 3). The longest dimension of this zone is approximately 30 km in a northwest-southeast direction; the shortest dimension is about 20 km. The locations outside this rectangle are poorly constrained solutions. The majority of the epicenters form a tight cluster within 5 km of the mainshock. The New Idria aftershocks cluster in depth as well as in map view. Spatial clustering of the best-located aftershocks is greatest along the east-northeast cross section B-B' in Figure 3.

All aftershocks locate at depths less than 15 km. Those locations which lie only a few kilometers deep probably result from poor depth control. The four foreshocks, the main shock, and the majority of the aftershocks lie at depths between 6 and 10 km. There is no apparent significant dip in the distribution of hypocenters.

FAULT-PLANE SOLUTIONS

P-wave first-motion plots for the main shock and five of the aftershocks recorded on the DER are shown in Figure 4. All first-motion plots were produced using HYPOELLIPSE (Lahr, 1980) and a preliminary velocity model derived by J. Eaton (Table 3b). Eaton's model was constrained so that dilatational and compressional first motions for the New Idria main shock were separate. Differences between Eaton's model and the model derived from Walter and Mooney (1982) are small (see Table 3a and 3b). The focal mechanism for the main shock (constructed by Eaton) is consistent with either oblique thrusting to the north or to the west-southwest (see Fig. 4, upper left).

Fault-plane solutions for the five aftershocks shown in Figure 4 were constructed using DER and CALNET first motions as read from paper playbacks of analog magnetic tape recordings. Whereas the fault-plane solutions of two of the aftershocks requires thrust mechanisms, the other three suggest that normal faulting is appropriate.

EARTHQUAKE FREQUENCY

Plots of earthquake frequency vs. magnitude were obtained for the New Idria, Coalinga, Cantua Creek, and Avenal earthquake sequences (Fig. 5) using the procedure of Richter (1958). Straight lines representing $\log N = a - bM$, where N is the number of shocks of magnitude M or larger, were obtained by inspection. For the New Idria sequence, the preferred line (solid) has a b-value (slope) of 0.97; for the smallest shocks only, $b = 1.46$ (dashed line). If the break in slope for the smaller shocks results from missing events, then the completeness level of the catalog in Table 2a is M_L 1.8. Completeness levels for the Coalinga, Cantua Creek, and Avenal sequences are given in the caption of Figure 5. The b values for the New Idria, Cantua Creek, and Avenal sequences are 0.97, 0.88, and 0.77, respectively, suggesting typical magnitude frequency distributions for these sequences. That is, the b values are not anomalous.

The magnitude frequency distribution for the 1983 Coalinga sequence (Fig. 5b) is not consistent with $\log N = a - bM$ for $M > 3$. The b slope of 1.4 shown in Figure 5b for $3 \leq M \leq 4$ is used here to estimate a completeness threshold of the 1983 Coalinga catalog (Table 2b) of M=3.0. Magnitudes in the 1983 Coalinga earthquake catalog (Table 2b) are based on Eaton's preliminary

analysis; additional work suggests that magnitudes for Coalinga shocks with magnitude ≥ 4 and with magnitude ≤ 4 should be decreased and increased respectively by a few tenths of a magnitude unit (Eaton, personal communication, 1984). These changes would significantly decrease the b value estimate of the Coalinga earthquakes. While Uhrhammer et al.'s (1983) b value of 0.69 is consistent with the $4 \leq M \leq 5$ data in Table 2b and Figure 5b, it was obtained for $M_L > 3$; also, the number of $M_L > 3$ Coalinga shocks to August 1, 1983 obtained by Uhrhammer et al. (1983) is 147, compared with the 318 listed in Table 2b. One explanation for these differences is in that Uhrhammer et al.'s (1983) catalog is complete for magnitude > 3 shocks.

The above catalog differences explain the difference in Uhrhammer et. al.'s (1983) p value for Coalinga and that estimated by us below. Following Liu (1984), earthquake frequencies with time were calculated (see Fig. 6). Liu (1984) found that the coefficient p in $n(t)=n_1 t^{-p}$ typically is < 1 for foreshock sequences and > 1 for aftershock sequences with a single largest (i.e., a main shock) earthquake. $n(t)$ is the daily count of earthquakes and n_1 is the number of earthquakes on the first day following the largest earthquake. That is, Liu found that the activity rates in aftershock sequences change (decrease) more quickly than do the activity rates in foreshock sequences. As noted earlier, the aftershock sequence following the New Idria main shock on October 25, 1982 was essentially finished by November 1, 1982. By all standards, the activity rate decreased very quickly following the New Idria main shock. The p value, obtained using Liu's (1984) techniques, for the New Idria sequence is > 1.5 (Fig. 6a) consistent with the $p > 1$ for aftershocks obtained by Liu (1984). P-values for the Coalinga, Cantua Creek, and Avenal sequences also are > 1.0, suggesting that none of the four sequences has the temporal attenuation characteristics that Liu (1984) associated with foreshock sequences.

DISCUSSION

Although the 1983 Coalinga earthquakes were preceeded by and spatially framed by the 1975 Cantua Creek, the 1976 Avenal, and the 1982 New Idria sequences, their magnitude and temporal frequency distributions are not inconsistent with distributions characteristic of aftershock sequences. Therefore, the filling of the spatial seismic gap by the 1983 Coalinga sequence (Eaton et al., 1983) remains the only identified pattern that might have been used to anticipate the 1983 Coalinga earthquakes. Although the spatial and temporal relationship of the 1982 New Idria and 1983 Coalinga earthquake sequences is clear in hindsight, there is, as yet, no identified anomalous characteristic of the New Idria shocks that signaled the likelihood of the destructive Coalinga earthquakes that started six months later.

The geology of the Coalinga area has been described in detail by Alfors (1983). Of particular interest here is the large ultramafic intrusive body that is bounded on the northeast by the New Idria thrust fault (Fig. 7). The location of the 1982 New Idria earthquakes near the southeast perimeter of this intrusion and the southeast end of the New Idria thrust fault suggests a possible causal relationship of this fault and the 1982 New Idria earthquakes.

REFERENCES

Alfors, J. T., "Regional geology of the Coalinga, California area" in the 1983 Coalinga, California earthquakes, Calif. Div. Mines and Geology Special Publication 66, 1983.

Bakun, W. H., "Magnitudes and moments of duration", Bull. Seismol. Soc. Am., in press, Dec. 1984.

Eaton, J. P., R. Cockerham, and F. Lester, "Study of the May 2, 1983 Coalinga earthquake and its aftershocks, based on the USGS seismic network in northern California," in the 1983 Coalinga, California earthquakes, Calif. Div. Mines and Geology Special Publication 66, 1983.

Lahr, J. C., "HYPOELLIPSE/MULTICS: a computer program for determining local earthquake hypocentral parameters, magnitude, and first motion pattern, U.S. Geol. Survey Open-File Report 80-59, 59 pp, 1980.

Lee, W. H. K., R. E. Bennett, and K. L. Meagher, "A method of estimating magnitude of local earthquakes from signal duration," U.S. Geol. Survey Open-File Report, 28 pp, 1972.

Lee, W. H. K., and J. C. Lahr, "HYPO71 (revised): a computer program for determining hypocenter, magnitude, and first motion pattern for local earthquakes, U.S. Geol. Survey Open-File Report 75-311, 113 pp., 1975.

Liu, Z. R., "Earthquake frequency and prediction, Bull. Seism. Soc. Am. 74, 255-265, 1984.

Richter, C. F., Elementary Seismology, Freeman, San Francisco, 758 pp, 1958.

Uhrhammer, R. A., R. A. Darragh, and B. A. Bolt, "the 1983 Coalinga earthquake sequence: May 2 through August 1" in the 1983 Coalinga, California earthquakes, Calif. Div. Mines and Geology Special Publication 66, 1983.

Walter, A. W. and W. D. Mooney, "Crustal structure of the Diablo and Gabilan Ranges, central California," Bull. Seism. Soc. Am. 72, 1982.

FIGURE CAPTIONS

Figure 1. Map showing the New Idria epicentral area and the locations of seismographic stations in the USGS central California seismic network (CALNET). Five temporary seismic stations (Table 1), shown as open circles, were operated for several days during the New Idria sequence.

Figure 2. Maps of the epicenters of the (a) New Idria, (b) Coalinga, (c) Cantua Creek, and (d) Avenal earthquake sequences listed in Table 2. The dashed line on each map is the perimeter of the concentrated aftershock area of the 1983 Coalinga sequence. The maps show seismicity above the appropriate magnitude completeness threshold (see Fig. 5).

Figure 3. Map (top) and cross sections (bottom) of seismicity for the New Idria earthquake sequence (A and B quality solutions only). The densest spatial clustering of aftershocks lies along the line B-B'. The bold square and solid dots are the hypocenters of the New Idria main shock and its four foreshocks, respectively.

Figure 4. Fault-plane solutions (lower-hemisphere projections) of the New Idria main shock (upper left) and five aftershocks. Date and origin time of each earthquake is given at the upper left. Solid and open circles are compressional and dilatational first motions, respectively. P and T are the directions of the P- and T-axes, respectively.

Figure 5. Cumulative count of earthquakes versus magnitude (Table 2) for the (a) New Idria, (b) Coalinga, (c) Cantua Creek, and (d) Avenal earthquake sequences. The lines represent linear fits obtained by inspection. The dashed line in (a) represents an alternative fit, using $M_L < 2$ shocks only. These plots imply magnitude completeness levels of 1.8, 3.0, 2.8, and 2.0 for the New Idria, Coalinga, Cantua Creek, and Avenal sequences, respectively.

Figure 6. The reduced cumulative earthquake frequency $N_R(t)$ versus time t for the (a) New Idria, (b) Coalinga, (c) Cantua Creek, and (d) Avenal earthquake sequences. p is the coefficient of attenuation with time (Liu, 1984). $N_R(t)$ were calculated using the catalogs in Table 2 and the completeness levels indicated in Figure 5.

Figure 7. Epicenters and fault-plane solutions (lower-hemisphere projections) of selected 1982 New Idria earthquakes relative to the Mesozoic ultramafic intrusive body (hatched area) that is bounded on the north and east by the New Idria thrust fault. Also shown is surface rupture of Nunez fault in association with 1983 Coalinga earthquake sequence. The data used to construct the fault-plane solutions are shown in Figure 4.

Table 1. Temporary station locations.

Station	Lat(°N)	Long (°W)	Elev.(m)	Delay(s)
Kamm Road (KA1)	36 31.91'	120 29.59'	192	0.20
Cantua Creek (CC2)	36 24.06'	120 26.10'	244	-0.17
Oil Field (OF3)	36 17.46'	120 18.48'	265	-0.01
Ackers Road (AR4)	36 13.40'	120 30.15'	381	-0.07
Santa Rita Peak (SR5)	36 23.56'	120 40.96'	1483	-0.28

Table 2a. 1982 New Idria earthquakes 1/

DATE	HRMN	SEC	LATITUDE	LONGITUDE	DEPTH	NO	GAP	D3	RMS	MAGNITUDE	LOG M_o	NO	DUR
820305	0805	59.02	36N19.48	120W35.49	12.01	17	136	22.0	0.13	2.62(0.19)	19.88(0.23)		43
820530	0605	59.59	36N20.51	120W27.16	00.00	6	217	33.0	0.01	2.02(0.12)	19.17(0.14)		6
821025	1834	53.02	36N18.14	120W30.77	7.73	11	185	24.0	0.13	1.91(0.12)	19.03(0.14)		11
821025	2037	32.68	36N17.72	120W31.62	7.27	14	179	24.0	0.07	3.02(0.18)	20.36(0.21)		54
821025	2049	49.63	36N17.59	120W31.32	6.09	14	137	23.0	0.10	2.38(0.14)	19.59(0.17)		33
821025	2051	02.77	36N18.04	120W30.86	7.13	16	142	24.0	0.09	2.51(0.17)	19.74(0.20)		48
821025	2226	04.35	36N17.82	120W31.21	7.29	17	139	24.0	0.03	5.40	24.04		
821025	2234	32.45	36N17.58	120W31.71	4.27	12	177	25.0	0.07	3.14(0.20)	20.50(0.24)		22
821025	2237	46.65	36N16.63	120W29.78	1.74	9	186	21.0	0.08	1.87(0.13)	18.99(0.15)		7
821025	2238	16.15	36N17.54	120W30.60	9.82	10	194	23.0	0.08	1.90(0.13)	19.03(0.15)		8
821025	2239	13.23	36N19.22	120W30.60	2.95	15	193	26.0	0.12	2.75(0.12)	20.03(0.14)		28
821025	2240	02.57	36N16.72	120W31.44	7.94	12	170	22.0	0.06	2.37(0.06)	19.58(0.08)		3
821025	2243	02.87	36N17.88	120W30.16	9.42	5	224	23.0	0.03	2.11(0.10)	19.28(0.12)		10
821025	2243	43.26	36N17.43	120W32.01	7.78	10	175	24.0	0.10	2.01(0.11)	19.16(0.13)		6
821025	2244	44.29	36N18.44	120W31.35	0.73	7	186	27.0	0.05	1.91(0.04)	19.04(0.04)		4
821025	2246	30.24	36N15.90	120W30.94	2.93	7	264	25.0	0.14	2.12(0.13)	19.28(0.15)		9
821025	2247	12.97	36N17.68	120W31.41	4.32	7	179	24.0	0.11	1.93(0.15)	19.07(0.18)		5
821025	2249	33.41	36N17.07	120W32.28	6.62	10	171	23.0	0.08	1.96(0.10)	19.10(0.12)		12
821025	2250	36.84	36N17.14	120W30.92	7.16	9	175	25.0	0.08	2.01(0.11)	19.16(0.14)		9
821025	2251	51.42	36N16.45	120W30.60	0.20	6	169	26.0	0.12	1.91(0.17)	19.04(0.20)		6
821025	2255	26.33	36N17.06	120W31.71	6.93	13	132	23.0	0.10	2.13(0.07)	19.30(0.08)		12
821025	2259	28.72	36N17.47	120W32.14	7.80	15	175	24.0	0.11	2.30(0.14)	19.50(0.16)		30
821025	2308	33.33	36N18.78	120W28.03	6.36	5	303	32.0	0.01	2.17(0.13)	19.35(0.16)		19
821025	2309	30.56	36N16.83	120W29.63	7.95	12	175	21.0	0.09	2.21(0.11)	19.39(0.13)		18
821025	2311	26.25	36N16.22	120W27.76	11.47	4	254	25.0	0.03	2.02(0.09)	19.16(0.11)		9
821025	2312	13.75	36N16.35	120W28.89	8.95	7	200	20.0	0.06	4.38(0.14)	21.96(0.16)		46
821025	2315	54.09	36N20.41	120W32.54	13.57	5	151	35.0	0.01	4.14(0.14)	21.68(0.17)		51
821025	2325	43.01	36N17.04	120W31.80	6.44	11	172	24.0	0.08	2.08(0.10)	19.24(0.12)		11
821025	2330	01.00	36N16.87	120W30.64	7.56	9	173	25.0	0.11	2.16(0.10)	19.34(0.12)		11
821025	2332	03.80	36N17.82	120W31.40	7.47	16	139	24.0	0.07	3.44(0.19)	20.84(0.22)		24
821025	2334	05.13	36N16.86	120W31.04	6.47	13	172	22.0	0.10	2.32(0.09)	19.52(0.10)		7
821025	2334	36.72	36N16.57	120W28.63	0.73	11	174	13.0	0.07	2.13(0.13)	19.29(0.16)		8
821025	2335	20.75	36N17.14	120W31.15	1.68	15	134	25.0	0.07	3.04(0.19)	20.37(0.23)		40
821025	2337	44.27	36N18.51	120W31.93	3.39	6	266	27.0	0.06	2.07(0.08)	19.23(0.10)		5
821025	2351	07.95	36N17.70	120W44.60	0.65	9	241	17.0	0.15	2.14(0.12)	19.31(0.14)		15

DATE	HRMN	SEC	LATITUDE	LONGITUDE	DEPTH	NO	GAP	D3	RMS	MAGNITUDE	LOG M_O	NO	DUR
821025	2357	57.26	36N16.19	120W31.00	8.59	12	165	21.0	0.10	2.23(0.14)	19.41(0.17)		23
821025	2359	23.19	36N15.01	120W34.43	2.11	8	202	21.0	0.10	2.09(0.15)	19.25(0.18)		12
821026	0014	12.09	36N17.09	120W29.44	9.15	10	178	22.0	0.07	2.34(0.14)	19.55(0.17)		16
821026	0040	05.88	36N15.71	120W32.36	5.29	8	217	24.0	0.05	2.15(0.10)	19.32(0.12)		4
821026	0045	55.26	36N17.81	120W31.61	7.72	9	180	26.0	0.04	1.90(0.15)	19.02(0.18)		8
821026	0051	08.87	36N17.35	120W30.07	7.84	10	179	22.0	0.05	1.92(0.11)	19.05(0.13)		6
821026	0051	50.78	36N17.68	120W31.21	6.46	12	233	26.0	0.07	1.92(0.06)	19.05(0.07)		5
821026	0104	52.79	36N15.55	120W32.39	8.02	11	157	21.0	0.14	2.01(0.18)	19.16(0.21)		8
821026	0117	54.62	36N18.12	120W30.15	11.41	9	186	24.0	0.07	1.89(0.09)	19.01(0.11)		7
821026	0146	58.89	36N17.09	120W28.93	8.86	10	179	22.0	0.09	2.27(0.15)	19.46(0.18)		21
821026	0155	37.97	36N17.89	120W28.95	9.05	9	200	23.0	0.05	1.91(0.07)	19.03(0.08)		6
821026	0157	01.18	36N18.27	120W31.68	6.49	15	183	25.0	0.07	2.50(0.17)	19.73(0.20)		40
821026	0204	20.62	36N16.93	120W31.25	7.13	13	172	22.0	0.12	2.24(0.15)	19.43(0.18)		26
821026	0213	34.29	36N16.47	120W29.73	8.46	10	171	24.0	0.05	1.99(0.20)	19.13(0.24)		7
821026	0220	40.51	36N12.69	120W30.16	14.27	4	329	34.0	0.12	1.78(0.11)	18.89(0.12)		5
821026	0304	56.85	36N18.10	120W29.22	10.05	9	237	28.0	0.08	2.66(0.18)	19.93(0.22)		41
821026	0310	56.54	36N18.57	120W31.16	7.38	11	234	27.0	0.03	2.53(0.16)	19.77(0.19)		24
821026	0352	40.89	36N17.47	120W30.63	9.22	14	179	23.0	0.11	2.31(0.17)	19.51(0.20)		28
821026	0401	37.93	36N15.98	120W27.68	2.97	4	271	37.0	0.03	1.94(0.15)	19.07(0.18)		9
821026	0418	53.30	36N16.64	120W30.91	12.57	13	170	22.0	0.06	1.89(0.05)	19.01(0.05)		5
821026	0429	05.68	36N18.93	120W31.99	8.50	13	144	26.0	0.13	2.52(0.18)	19.76(0.22)		42
821026	0455	16.04	36N18.48	120W30.56	2.11	12	187	25.0	0.15	2.18(0.16)	19.36(0.19)		23
821026	0518	38.73	36N14.73	120W26.40	2.92	4	306	32.0	0.01	2.11(0.17)	19.28(0.21)		11
821026	0533	59.21	36N16.66	120W35.19	7.29	12	161	22.0	0.05	2.08(0.13)	19.24(0.16)		16
821026	0551	23.18	36N16.82	120W28.75	5.35	9	177	21.0	0.06	1.96(0.13)	19.10(0.16)		11
821026	0602	45.79	36N11.62	120W21.98	10.36	4	317	39.0	0.10	1.79(0.07)	18.90(0.08)		4
821026	0752	05.07	36N18.60	120W31.67	6.25	10	186	25.0	0.02	2.07(0.16)	19.22(0.19)		11
821026	0758	44.36	36N18.76	120W31.57	7.75	10	235	26.0	0.03	1.75(0.07)	18.84(0.09)		6
821026	0816	25.22	36N17.40	120W31.15	7.19	12	177	23.0	0.06	2.21(0.17)	19.39(0.20)		23
821026	0926	30.00	36N16.71	120W28.91	7.53	11	175	21.0	0.08	2.02(0.15)	19.17(0.18)		17
821026	1222	08.28	36N34.30	120W39.30	0.00	4	306	100.0	0.08	1.57(0.01)	18.64(0.02)		5
821026	1222	11.03	36N18.99	120W31.96	7.20	6	190	26.0	0.01	1.96(0.04)	19.10(0.05)		3
821026	1324	14.99	36N17.08	120W32.58	7.40	16	130	23.0	0.10	2.93(0.22)	20.24(0.17)		69
821026	1548	43.78	36N17.89	120W30.42	10.15	13	183	24.0	0.06	3.13(0.22)	20.48(0.26)		60
821026	1743	10.61	36N16.90	120W28.04	8.48	10	180	21.0	0.06	1.97(0.10)	19.11(0.12)		13
821026	2042	30.74	36N18.30	120W32.44	9.05	15	139	25.0	0.06	2.89(0.20)	20.20(0.24)		50
821026	2115	11.12	36N19.08	120W31.23	5.21	7	192	27.0	0.06	1.97(0.14)	19.11(0.16)		10
821027	0853	03.89	36N17.71	120W34.54	9.37	11	219	23.0	0.10	1.76(0.14)	18.99(0.17)		17
821027	1602	27.33	36N17.25	120W32.84	0.01	13	172	24.0	0.12	2.14(0.15)	19.31(0.18)		19
*821027	2129	39.79	36N18.43	120W31.58	7.53	15	142	25.0	0.08	3.13(0.21)	20.48(0.24)		61

DATE	HRMN	SEC	LATITUDE	LONGITUDE	DEPTH	NO	GAP	D3	RMS	MAGNITUDE	LOG M_o	NO	DUR
821028	0344	43.16	36N18.87	120W30.97	0.06	10	191	26.0	0.06	2.10(0.14)	19.26(0.16)		15
821028	1717	49.21	36N17.95	120W32.33	6.16	19	111	19.0	0.09	2.80(0.18)	20.09(0.21)		46
821028	1858	39.89	36N17.52	120W28.89	9.69	9	184	22.0	0.03	1.99(0.15)	19.13(0.18)		10
*821029	0052	11.16	36N18.90	120W31.47	8.08	25	58	17.0	0.12	3.33(0.17)	20.72(0.20)		55
821029	0959	34.96	36N17.33	120W32.21	6.36	10	174	24.0	0.11	2.03(0.14)	19.18(0.16)		11
821029	1306	56.06	36N18.16	120W31.28	7.51	13	183	24.0	0.09	2.27(0.15)	19.47(0.18)		33
821029	1417	07.53	36N10.42	120W45.99	0.30	4	183	34.0	0.01	2.36(0.14)	19.57(0.16)		19
821029	1607	29.24	36N19.19	120W31.44	11.96	14	119	20.0	0.12	2.71(0.17)	19.98(0.20)		51
821030	0908	49.89	36N18.86	120W31.42	7.55	23	74	12.0	0.07	2.47(0.15)	19.70(0.18)		41
821030	0916	59.25	36N16.98	120W32.62	0.55	19	170	16.0	0.18	2.59(0.17)	19.84(0.20)		38
821030	1122	35.78	36N16.67	120W33.19	0.65	10	165	23.0	0.07	2.17(0.08)	19.35(0.09)		14
821030	1301	43.63	36N18.66	120W31.69	5.88	12	186	26.0	0.09	2.00(0.15)	19.15(0.18)		15
821030	1556	35.47	36N16.90	120W33.90	0.82	13	168	23.0	0.11	2.38(0.12)	19.60(0.14)		25
821030	2335	45.47	36N16.17	120W34.83	2.40	12	208	22.0	0.09	2.09(0.14)	19.25(0.17)		12
821030	2343	37.25	36N16.86	120W32.72	0.28	10	168	23.0	0.11	2.12(0.15)	19.29(0.18)		15
821031	0410	15.19	36N16.97	120W32.79	0.10	7	169	24.0	0.08	2.02(0.16)	19.17(0.19)		10
821031	1008	01.09	36N21.65	120W35.34	14.31	11	147	25.0	0.09	1.87(0.14)	18.99(0.17)		17
821031	1554	26.00	36N16.73	120W32.85	0.08	10	167	23.0	0.07	2.57(0.15)	19.82(0.17)		33
821101	0913	23.71	36N12.93	120W31.47	1.82	5	307	37.0	0.01	1.95(0.10)	19.09(0.12)		12
821101	2035	55.02	36N17.02	120W32.65	2.29	9	170	24.0	0.07	1.98(0.10)	19.12(0.11)		8
821102	1540	15.63	36N17.12	120W33.02	0.56	11	170	23.0	0.13	2.26(0.17)	19.46(0.20)		11
821103	2138	50.56	36N13.69	120W27.88	0.45	13	141	21.0	0.13	2.06(0.12)	19.21(0.14)		17
821103	2147	32.19	36N13.78	120W28.64	1.70	14	142	21.0	0.10	2.15(0.08)	19.32(0.10)		13
821104	0159	32.91	36N17.18	120W32.79	0.12	9	171	24.0	0.10	1.94(0.12)	19.07(0.14)		7
821104	0747	22.25	36N18.43	120W32.35	8.19	10	184	25.0	0.19	1.88(0.11)	19.00(0.13)		9
821105	1824	31.90	36N14.39	120W26.97	0.35	8	259	23.0	0.05	2.04(0.14)	19.19(0.17)		6
821109	1225	17.44	36N17.69	120W26.18	11.33	10	208	22.0	0.09	1.94(0.15)	19.07(0.17)		7
821113	0720	51.57	36N18.31	120W31.65	6.46	11	233	26.0	0.05	2.00(0.15)	19.14(0.17)		22
821113	2226	13.68	36N18.94	120W31.24	7.85	12	147	26.0	0.07	2.37(0.14)	19.59(0.17)		35
821115	0812	18.75	36N18.52	120W31.62	6.19	13	185	25.0	0.12	2.18(0.12)	19.35(0.14)		27
821119	1238	15.15	36N17.70	120W33.40	0.96	15	174	23.0	0.13	2.17(0.15)	19.34(0.18)		27
821120	0639	18.03	36N17.75	120W34.56	10.02	17	129	22.0	0.11	2.33(0.12)	19.53(0.15)		35
821120	1352	25.07	36N16.90	120W37.54	6.28	16	117	20.0	0.17	1.96(0.14)	19.10(0.16)		19
821122	0817	48.35	36N18.46	120W34.27	11.57	15	134	23.0	0.17	2.19(0.14)	19.37(0.16)		33
821129	1215	38.49	36N17.61	120W32.06	11.71	10	177	25.0	0.10	2.02(0.13)	19.16(0.15)		20
821201	0447	00.98	36N20.50	120W36.48	14.59	9	175	22.0	0.10	1.90(0.18)	19.02(0.22)		14
821201	1411	28.40	36N21.83	120W34.15	14.59	12	153	24.0	0.13	2.00(0.09)	19.14(0.11)		22
821208	0221	03.00	36N16.80	120W28.55	9.31	11	233	26.0	0.05	2.21(0.14)	19.39(0.17)		22
821222	0339	51.90	36N18.80	120W31.16	5.13	14	146	26.0	0.07	2.25(0.12)	19.44(0.14)		23
821223	1550	56.48	36N17.47	120W32.57	8.26	12	183	25.0	0.06	2.23(0.16)	19.42(0.19)		19

DATE	HRMN	SEC	LATITUDE	LONGITUDE	DEPTH	NO	GAP	D3	RMS	MAGNITUDE	LOG M_o	NO	DUR
821225	0145	12.42	36N18.25	120W33.36	2.10	10	195	26.0	0.12	2.13(0.13)	19.30(0.15)		17
821225	0626	19.59	36N15.74	120W31.81	8.86	13	219	24.0	0.09	2.21(0.16)	19.39(0.19)		22
821230	2222	45.24	36N17.51	120W21.58	13.57	5	264	40.0	0.02	2.05(0.12)	19.20(0.14)		10
830101	1106	41.51	36N17.19	120W31.19	1.40	10	189	25.0	0.06	2.00(0.12)	19.15(0.14)		13
830104	2145	39.91	36N15.66	120W34.74	0.00	7	244	21.0	0.08	1.92(0.05)	19.05(0.06)		5
830113	0625	57.60	36N16.76	120W32.87	8.52	15	181	23.0	0.06	2.65(0.16)	19.91(0.19)		42
830113	0712	47.56	36N17.41	120W25.11	8.02	13	241	29.0	0.06	3.02(0.21)	20.35(0.25)		46
830114	0250	23.08	36N17.76	120W33.31	9.30	14	224	25.0	0.07	2.75(0.40)	20.03(0.48)		57
830201	1500	20.38	36N15.15	120W37.33	4.31	6	147	18.0	0.03	2.01(0.12)	19.16(0.15)		16
830214	1317	03.50	36N16.19	120W29.68	2.63	12	225	24.0	0.05	2.09(0.10)	19.25(0.12)		11
830227	0126	08.01	36N16.72	120W28.28	2.75	12	177	26.0	0.08	2.36(0.14)	19.57(0.17)		24
830305	1948	08.27	36N17.03	120W31.20	0.00	11	173	22.0	0.14	2.00(0.10)	19.15(0.12)		8
830419	1959	12.98	36N18.80	120W31.18	5.11	13	146	26.0	0.06	2.11(0.10)	19.27(0.12)		10
830424	0149	00.25	36N16.17	120W23.56	1.13	8	189	35.0	0.05	2.00(0.07)	19.14(0.08)		6

1/ Locations obtained using HYPOELLIPSE (Lahr, 1980). D3 = epi. dist. (km) to the third closest station. Magnitudes and log M_o are determined from the number of coda durations (NO DUR) listed using Bakun (1984). The uncertainties in M_L and log M_o given in parentheses, are the standard deviations of the individual M_L and log M_o estimates.

Table 2b. 1983 Coalinga earthquakes.[1/]

DATE	HRMN	SEC	LAT (°N)	LONG (°W)	DEPTH	MAG	NO	GAP	DMIN	RMS
830502	2342	37.76	36-13.15	120-18.99	10.24	6.7	42	206	4.0	0.07
830502	2347	28.01	36-12.65	120-19.05	10.21	5.6	13	201	4.8	0.13
830502	2355	29.62	36- 6.34	120-16.30	5.00	3.4	20	223	20.2	0.19
830503	0 8	7.13	36-10.59	120-18.69	9.02	3.02	11	279	43.7	0.10
830503	0 9	22.81	36- 7.98	120-16.99	9.37	3.8	9	211	34.1	0.03
830503	0 9	30.72	36-15.39	120-53.33	16.17	3.24	11	142	7.4	0.19
830503	013	18.76	36-10.39	120-21.66	13.01	3.1	11	231	38.0	0.07
830503	014	48.11	36-12.27	120-23.03	12.52	3.2	22	200	41.5	0.06
830503	015	36.69	36- 4.47	120-14.52	9.98	3.73	13	234	28.8	0.05
830503	017	59.06	36-12.60	120-19.54	7.96	4.3	8	210	42.1	0.09
830503	022	12.14	36-15.73	120-20.64	8.84	3.4	17	241	40.9	0.10
830503	025	49.27	36-11.21	120-33.24	12.70	3.1	11	192	21.9	0.22
830503	028	16.24	36-15.55	120-22.17	7.87	3.0	19	208	38.6	0.22
830503	030	41.55	36-17.95	120-20.73	8.57	3.1	23	215	41.4	0.12
830503	032	36.52	36-15.60	120-34.87	12.13	3.0	7	282	19.9	0.16
830503	036	55.83	36-13.26	120-20.73	10.52	3.1	34	163	3.1	0.09
830503	039	45.76	36-13.09	120-20.78	12.57	4.0	37	208	25.0	0.10
830503	047	30.90	36-12.11	120-15.72	9.98	3.7	26	219	8.9	0.07
830503	050	22.66	36-12.80	120-18.99	8.98	3.8	20	212	27.7	0.20
830503	057	43.79	36-16.05	120-18.89	8.62	4.5	33	216	3.2	0.13
830503	1 3	7.75	36-15.95	120-21.25	10.86	3.1	14	222	37.3	0.09
830503	1 3	39.45	36-11.19	120-18.12	5.00	3.0	17	226	28.5	0.20
830503	1 4	24.05	36-10.40	120-16.32	10.88	3.2	17	231	27.5	0.17
830503	1 6	56.69	36-10.83	120-19.88	10.94	3.2	27	207	27.6	0.05
830503	111	5.55	36-11.56	120-16.04	13.50	3.2	16	232	40.2	0.23
830503	112	3.40	36- 7.05	120-15.33	7.51	3.1	13	214	21.9	0.14
830503	116	40.34	36-13.04	120-17.06	8.40	3.1	32	217	6.3	0.15
830503	118	57.48	36-13.25	120-17.19	0.54	3.56	14	217	55.6	0.18
830503	123	4.53	36-10.32	120-15.95	7.43	3.20	26	216	27.4	0.12
830503	131	46.63	36-16.19	120-21.41	9.02	3.1	35	192	2.7	0.14
830503	133	4.94	36-15.60	120-17.38	0.08	3.1	11	244	52.8	0.17
830503	133	53.83	36-10.17	120-18.67	7.37	3.1	18	242	13.9	0.18
830503	134	0.38	36- 9.40	120- 9.76	6.65	3.1	6	247	51.5	0.06
830503	136	19.67	36-13.95	120-17.40	4.43	3.5	30	217	29.8	0.19
830503	138	55.93	36-16.62	120-28.34	7.14	3.2	26	152	12.1	0.17
830503	141	45.76	36- 7.65	120-13.69	8.73	3.9	31	216	17.0	0.10
830503	155	46.38	36-12.81	120-18.39	7.85	3.8	33	211	5.1	0.13
830503	158	7.98	36-10.26	120-18.53	0.47	3.5	13	243	26.7	0.26
830503	158	18.25	36-46.92	121-30.70	9.12	3.16	11	174	5.8	0.17
830503	2 3	5.70	36-15.59	120-21.82	1.77	3.2	11	245	39.1	0.13
830503	211	49.47	36-13.99	120-26.63	6.07	3.1	25	213	16.0	0.24
830503	215	14.74	36-13.42	120-18.07	8.25	3.9	31	215	32.6	0.07
830503	217	40.91	36-15.66	120-17.62	11.39	3.6	27	240	29.3	0.16
830503	218	54.10	36-12.49	120-18.17	11.23	3.2	25	210	5.8	0.19
830503	222	1.30	36-15.82	120-16.54	1.68	3.0	16	244	30.9	0.19
830503	226	8.63	36-16.31	120-22.43	9.89	3.2	42	172	3.8	0.11
830503	236	24.28	36-11.07	120-15.37	7.11	3.16	12	225	10.5	0.18
830503	236	39.08	36-12.15	120-15.17	0.19	3.0	12	220	31.0	0.14
830503	238	19.06	36-11.26	120-16.15	10.12	3.0	26	217	29.0	0.16
830503	242	59.01	36- 8.39	120-18.45	8.27	3.10	16	234	23.3	0.22
830503	244	26.06	36-16.13	120-21.73	3.30	3.37	13	239	23.2	0.18
830503	252	25.47	36-16.21	120-19.97	6.15	3.1	30	214	2.5	0.11
830503	258	19.33	36- 9.92	120-18.18	9.01	3.0	20	242	14.3	0.13
830503	3 3	12.47	36- 7.15	120-19.25	0.31	3.1	12	248	43.9	0.16
830503	322	1.75	36-13.23	120-21.53	12.21	3.62	33	142	3.5	0.07
830503	328	40.34	36-16.46	120-18.79	3.37	3.43	36	217	22.8	0.16
830503	336	52.77	36- 9.69	120-17.84	9.12	3.3	28	211	25.7	0.05
830503	338	52.01	36-13.36	120-18.99	12.37	3.02	36	209	3.7	0.12
830503	340	25.16	36-12.30	120-15.59	0.06	3.40	25	219	8.9	0.20
830503	359	4.49	36-14.95	120-19.43	9.91	3.04	31	214	19.9	0.06
830503	4 2	24.39	36-10.82	120-18.43	10.06	3.08	25	215	29.4	0.22
830503	4 2	46.22	36-17.04	120-16.07	4.88	3.01	12	255	31.8	0.10

Table 2b. 1983 Coalinga earthquakes (continued)

DATE	HRMN	SEC	LAT (°N)	LONG (°W)	DEPTH	MAG	NO	GAP	DMIN	RMS
830503	431	11.44	36-16.86	120-24.91	11.57	3.32	41	202	18.6	0.08
830503	432	30.46	36-19.01	120-17.16	5.72	4.41	3	258	45.5	0.01
830503	433	36.59	36-17.00	120-24.46	15.66	3.46	16	204	19.3	0.06
830503	443	28.86	36-14.78	120-21.63	11.24	3.21	37	207	18.2	0.10
830503	455	17.44	36-12.21	120-16.20	9.10	3.51	36	218	8.2	0.10
830503	458	12.72	36-12.78	120-16.19	10.57	3.38	29	233	7.6	0.12
830503	5 1	59.81	36- 9.94	120-16.56	8.45	3.35	26	208	11.0	0.19
830503	533	49.87	36-12.28	120-17.10	9.62	3.67	33	216	7.1	0.12
830503	542	15.08	36-14.40	120-21.74	11.64	3.18	39	106	2.1	0.10
830503	546	27.57	36-13.04	120-16.94	9.23	3.14	32	217	6.4	0.11
830503	554	23.88	36-15.96	120-24.39	12.76	3.16	23	173	6.1	0.08
830503	558	29.04	36-12.42	120-16.89	9.39	3.59	35	217	7.2	0.10
830503	6 4	45.92	36-14.87	120-24.51	10.85	3.99	18	218	34.9	0.10
830503	612	50.24	36-14.20	120-23.70	7.44	3.31	42	111	5.0	0.15
830503	621	47.38	36-14.13	120-19.90	9.65	3.2	33	202	1.8	0.13
830503	628	38.51	36-19.86	120- 4.94	0.46	3.17	17	275	49.0	0.21
830503	635	2.98	36-11.91	120-18.21	12.09	4.07	37	204	6.6	0.07
830503	659	8.51	36-14.28	120-20.52	9.94	3.07	39	169	1.2	0.09
830503	728	19.26	36-20.23	120-19.68	5.00	3.61	34	221	9.8	0.16
830503	728	34.54	36- 5.96	120-19.39	3.01	3.47	8	216	41.3	0.18
830503	733	55.91	36-11.74	120-15.56	10.11	3.18	29	219	9.5	0.09
830503	735	25.01	36- 7.63	120-13.77	9.38	3.53	35	215	16.9	0.08
830503	757	12.55	36- 6.36	120-14.98	9.22	3.13	23	228	27.7	0.13
830503	759	18.84	36-16.24	120-20.79	7.45	3.39	11	213	2.4	0.04
830503	814	38.86	36-14.19	120-22.05	11.39	3.00	30	205	34.8	0.10
830503	826	34.98	36- 3.34	120-14.91	7.68	3.02	29	223	15.9	0.11
830503	842	35.33	36-14.40	120-17.47	8.38	3.13	36	217	4.7	0.17
830503	855	1.46	36- 8.45	120-16.34	8.07	4.2	25	213	23.9	0.07
830503	924	16.57	36-11.45	120-18.76	9.06	3.19	28	211	33.7	0.05
830503	939	45.91	36-13.37	120-18.46	10.35	3.78	14	242	43.8	0.20
830503	1035	20.35	36- 9.62	120-17.18	8.93	3.43	34	212	15.3	0.07
830503	1041	28.83	36- 9.80	120-16.62	9.41	3.28	37	206	11.2	0.14
830503	1120	21.60	36-11.66	120-16.81	9.30	3.16	27	215	8.2	0.11
830503	1135	49.41	36-11.29	120-16.24	8.74	3.12	35	216	9.3	0.12
830503	1156	1.30	36-13.17	120-18.97	11.47	3.14	33	207	4.0	0.09
830503	1257	4.90	36- 7.04	120-13.24	10.34	3.59	36	219	18.2	0.08
830503	13 9	13.83	36-11.23	120-14.29	12.98	3.72	15	246	29.7	0.15
830503	1320	28.98	36-15.83	120-20.83	6.72	3.12	28	211	40.6	0.13
830503	1347	28.74	36-15.61	120-23.52	10.68	3.15	40	144	4.7	0.11
830503	1348	52.31	36-12.84	120-16.91	9.77	3.51	26	232	31.7	0.13
830503	1413	40.70	36-12.74	120-18.09	8.44	3.0	34	214	5.5	0.09
830503	1414	54.52	36- 3.43	120-26.68	13.92	3.54	7	184	14.8	0.12
830503	1420	22.38	36-16.95	120-23.38	10.62	3.31	38	171	5.7	0.08
830503	1426	55.41	36-15.28	120-20.60	8.02	3.74	31	211	24.9	0.09
830503	1437	41.48	36-11.77	120-19.38	8.08	3.18	32	187	6.1	0.13
830503	1450	46.61	36-10.03	120-17.78	10.27	3.67	38	197	10.0	0.19
830503	15 4	2.44	36-13.31	120-18.30	8.01	3.50	39	214	4.5	0.10
830503	1510	35.70	36-16.00	120-21.53	8.83	3.81	40	184	2.5	0.09
830503	1527	54.29	36-15.77	120-20.34	8.19	3.24	37	212	1.5	0.19
830503	1541	41.24	36-13.52	120-18.04	8.22	4.6	34	215	4.6	0.13
830503	16 2	8.40	36-12.29	120-18.01	6.10	3.00	31	210	6.2	0.15
830503	1611	17.92	36-13.58	120-18.50	8.28	3.15	36	214	3.9	0.12
830503	1617	0.99	36- 8.57	120-15.56	9.38	3.66	33	208	13.9	0.15
830503	1622	37.52	36-12.12	120-17.53	6.43	3.30	32	214	6.9	0.13
830503	1655	12.70	36-10.19	120-19.07	8.18	3.19	35	184	9.1	0.11
830503	17 1	29.25	36-12.37	120-18.02	8.56	3.74	35	211	6.1	0.10
830503	17 9	36.21	36-10.49	120-18.67	9.37	3.21	31	190	8.7	0.15
830503	1735	57.94	36-10.05	120-15.79	10.18	3.27	34	213	11.5	0.08
830503	1744	38.03	36-15.08	120-19.01	7.59	3.19	36	215	2.3	0.10
830503	1841	30.73	36- 8.73	120-12.29	5.36	3.44	25	228	16.9	0.16
830503	1850	18.84	36- 9.50	120-19.23	7.75	3.42	38	180	10.3	0.13
830503	1948	32.25	36-10.12	120-17.06	9.06	3.04	24	203	10.3	0.11
830503	2036	40.62	36-10.69	120-13.83	5.44	3.02	35	221	12.8	0.18
830503	2056	52.34	36- 7.90	120-14.27	10.67	3.39	37	213	16.0	0.14

Table 2b. 1983 Coalinga earthquakes (continued)

DATE	HRMN	SEC	LAT (°N)	LONG (°W)	DEPTH	MAG	NO	GAP	DMIN	RMS
830503	2136	57.48	36- 8.90	120-16.62	10.73	3.71	31	201	12.6	0.11
830503	2229	44.27	36-11.68	120-20.27	7.18	3.50	24	172	6.1	0.10
830503	2345	46.90	36- 7.68	120-13.41	7.58	3.51	9	258	19.4	0.08
830503	2345	55.88	36-15.28	120-15.71	0.59	3.62	12	251	47.7	0.10
830503	2346	3.02	36- 7.22	120-22.29	1.06	3.76	10	209	39.2	0.13
830503	2357	12.52	36-13.85	120-21.30	5.55	3.18	23	251	7.3	0.07
830504	127	21.64	36-10.44	120-11.00	3.54	3.00	8	254	16.5	0.10
830504	127	33.88	36-14.41	120-24.05	5.00	3.05	16	300	40.3	0.15
830504	246	9.15	36-11.50	120-16.39	9.10	3.08	33	209	8.9	0.10
830504	424	20.83	36-13.54	120-20.62	5.44	3.10	9	176	2.6	0.15
830504	541	41.94	36-12.20	120-18.23	9.70	3.02	25	206	6.1	0.11
830504	739	7.72	36-16.95	120-18.33	7.64	3.22	38	210	4.9	0.09
830504	818	8.06	36-13.52	120-16.48	5.69	3.46	31	210	20.5	0.13
830504	825	46.06	36-12.22	120-16.80	9.67	3.04	37	209	7.5	0.10
830504	848	27.60	36-12.24	120-17.09	7.51	3.48	21	222	7.2	0.12
830504	848	52.96	36-11.84	120-18.01	12.10	3.32	17	213	40.9	0.05
830504	859	1.56	36- 6.01	120-13.21	8.75	3.23	30	215	19.3	0.07
830504	10 2	43.36	36- 9.18	120-15.04	5.05	3.00	21	239	17.8	0.16
830504	12 0	26.55	36-11.23	120-18.26	6.99	3.01	33	201	7.7	0.11
830504	1226	8.98	36-11.73	120-18.13	8.74	3.20	33	205	16.4	0.06
830504	1325	6.73	36-15.54	120-20.32	10.34	3.00	33	204	20.3	0.08
830504	1329	15.70	36- 5.66	120-14.16	7.43	3.49	35	206	17.9	0.08
830504	1557	12.88	36-12.92	120-17.65	4.72	3.00	24	210	18.5	0.17
830504	1559	13.77	36-13.83	120-17.93	8.09	3.60	33	210	4.4	0.07
830504	1611	19.46	36-15.76	120-21.78	12.26	4.0	43	161	2.4	0.06
830504	1836	35.48	36- 9.43	120-17.63	9.48	3.19	30	195	11.1	0.12
830504	1945	2.52	36- 6.81	120-16.54	8.39	3.62	34	195	16.2	0.09
830504	2119	56.89	36-14.02	120-25.73	5.00	3.11	24	159	8.0	0.11
830504	22 3	42.68	36-11.79	120-16.60	7.77	3.17	33	210	8.3	0.16
830505	013	6.19	36-13.04	120-16.71	8.58	3.09	29	212	6.7	0.14
830505	027	50.62	36-13.02	120-17.04	9.89	3.53	35	209	6.3	0.09
830505	032	11.15	36-13.07	120-16.17	7.93	3.39	32	212	20.2	0.10
830505	156	42.23	36-12.25	120-17.55	9.45	3.44	34	207	17.7	0.12
830505	331	8.56	36-11.11	120-17.31	10.56	3.01	36	206	16.6	0.11
830505	437	48.36	36- 7.21	120-13.40	9.28	3.74	35	213	17.8	0.07
830505	554	32.02	36-13.19	120-16.96	8.76	3.04	36	210	6.3	0.11
830505	643	32.33	36- 2.91	120-10.34	21.99	3.26	30	219	23.3	0.10
830505	8 6	26.46	36- 8.11	120-14.27	8.45	3.67	34	211	15.7	0.08
830505	939	32.79	36- 7.86	120-17.30	12.32	3.06	14	244	13.8	0.10
830505	1020	43.90	36-15.81	120-23.07	11.55	4.3	33	144	4.1	0.06
830505	1133	40.41	36-14.44	120-22.10	11.22	3.49	43	100	2.5	0.06
830505	1150	49.76	36- 9.73	120-17.51	9.54	3.37	40	198	10.7	0.07
830505	1242	15.42	36-14.42	120-24.07	12.10	3.66	36	116	5.4	0.07
830505	1440	7.93	36-12.43	120-16.30	6.44	3.37	35	210	7.9	0.07
830505	1550	9.55	36- 8.24	120-15.12	8.31	3.34	30	209	14.8	0.13
830505	2246	12.20	36-17.08	120-25.54	10.23	3.29	42	147	8.5	0.10
830506	431	25.15	36-19.33	120-19.54	7.40	3.08	34	210	43.4	0.14
830506	457	9.20	36-11.20	120-17.82	10.34	3.32	41	102	8.0	0.07
830506	943	38.73	36-10.58	120-20.62	12.56	3.60	44	96	8.1	0.06
830506	1151	44.16	36-15.51	120-22.82	11.20	3.32	44	124	3.6	0.07
830506	1831	10.18	36-15.52	120-19.12	4.44	3.29	39	128	21.1	0.12
830506	2142	49.75	36-16.42	120-21.55	4.20	3.13	32	202	21.1	0.18
830506	2328	43.54	36- 8.03	120-13.19	8.56	3.39	32	135	16.9	0.12
830507	017	15.10	36-16.75	120-18.71	8.61	3.7	24	176	20.9	0.20
830507	515	2.03	36- 8.89	120-16.63	9.16	3.26	38	116	12.6	0.08
830507	543	57.07	36-13.36	120-17.31	9.38	3.56	39	116	5.6	0.08
830507	728	32.13	36- 6.14	120-13.97	8.13	3.07	34	141	18.2	0.07
830507	732	32.95	36-15.51	120-21.15	12.09	3.11	41	125	1.4	0.07
830507	1143	42.40	35-32.81	120- 8.90	13.77	3.01	28	177	13.2	0.19
830507	1242	30.33	36-16.96	120-25.13	13.15	3.58	22	202	37.3	0.06
830508	120	14.43	36-11.92	120-18.97	8.30	3.52	61	39	3.6	0.14
830508	123	3.82	36-12.42	120-18.00	12.15	3.05	24	110	6.0	0.11
830508	147	25.61	36-11.53	120-17.48	7.42	3.04	56	42	3.0	0.17
830508	345	33.64	36-14.73	120-26.88	2.55	3.40	57	32	5.8	0.24

Table 2b. 1983 Coalinga earthquakes (continued)

DATE	HRMN	SEC	LAT (°N)	LONG (°W)	DEPTH	MAG	NO	GAP	DMIN	RMS
830508	738	11.29	36-15.06	120-17.58	5.22	3.34	61	38	3.7	0.16
830508	1037	20.79	36-12.21	120-21.91	11.03	3.33	65	32	5.4	0.13
830508	1523	32.51	36-10.90	120-20.74	5.98	3.38	59	39	5.4	0.16
830508	1542	12.91	36-13.59	120-18.65	6.69	3.33	13	117	3.8	0.17
830508	1542	31.14	36-10.79	120-20.37	11.14	3.18	16	205	33.7	0.19
830508	1918	24.01	36-16.44	120-28.62	12.12	3.58	47	121	12.4	0.09
830508	2025	39.67	36-12.42	120-18.89	6.18	3.50	37	110	16.6	0.12
830509	249	11.28	36-13.75	120-18.74	12.46	5.24	48	62	3.5	0.05
830509	312	45.36	36-13.39	120-17.99	12.34	3.3	39	116	4.8	0.09
830509	319	11.00	36-13.36	120-18.34	12.68	3.36	41	116	4.4	0.05
830509	326	36.67	36-12.63	120-19.08	7.11	4.1	36	105	4.8	0.24
830509	330	40.62	36-13.30	120-18.46	12.43	3.2	38	206	4.3	0.06
830509	1118	23.07	36-10.34	120-18.79	9.26	3.03	41	103	8.9	0.08
830509	1324	33.45	36-11.15	120-17.00	8.82	3.29	40	105	8.8	0.08
830509	1815	44.23	36-10.45	120-18.57	8.58	3.03	29	108	22.0	0.07
830509	2014	35.72	36-12.37	120-17.77	7.32	3.00	29	110	19.8	0.20
830510	1326	29.50	36-18.85	120-19.35	8.26	3.9	43	146	7.4	0.12
830510	1345	47.67	36-13.59	120-19.47	5.65	3.09	39	211	6.9	0.11
830510	15 4	41.94	36- 9.34	120-15.36	9.19	3.34	25	213	12.9	0.14
830510	1522	42.56	36-19.68	120-20.51	0.77	3.45	15	128	16.5	0.19
830510	1620	18.95	36-19.19	120-19.35	7.86	3.05	33	148	22.9	0.09
830510	1711	48.90	36-19.13	120-18.17	5.42	3.03	16	145	15.1	0.11
830510	19 0	28.84	36-18.58	120-18.67	7.26	3.28	37	75	7.3	0.12
830511	814	47.96	36- 8.87	120-16.30	10.37	3.60	37	67	12.9	0.22
830511	2049	25.16	36-16.25	120-21.17	9.00	3.49	38	60	2.6	0.21
830511	2335	52.71	36-10.95	120-21.05	6.15	3.08	45	49	7.4	0.30
830512	157	22.58	36- 6.80	120-15.05	8.90	3.08	39	69	14.0	0.11
830512	642	7.58	36-14.79	120-20.94	9.16	3.10	41	79	0.7	0.09
830512	1341	6.53	36- 9.12	120-16.62	10.16	3.5	39	65	12.3	0.07
830512	1434	24.88	36-15.41	120-23.73	11.36	3.03	45	60	4.9	0.10
830512	1956	6.64	36-18.88	120-17.40	8.78	3.09	37	121	7.4	0.17
830513	1422	15.63	36- 6.53	120-13.30	9.53	3.38	43	79	11.4	0.11
830513	1440	3.26	36- 7.67	120-15.14	8.45	3.39	36	71	14.9	0.11
830513	15 1	10.42	36- 4.93	120-10.90	5.00	3.60	4	347	84.2	0.09
830513	1859	6.05	36-12.09	120-18.82	8.15	3.00	10	100	5.9	0.05
830514	5 2	2.94	36-15.25	120-19.25	11.44	3.69	41	117	10.0	0.06
830514	1715	16.74	36-10.20	120-17.74	10.18	3.60	33	60	9.7	0.07
830515	034	29.64	36- 6.15	120-13.06	6.25	3.10	22	78	10.8	0.15
830516	131	37.37	36- 7.65	120-15.67	10.72	3.56	41	68	15.3	0.07
830516	1217	42.56	36- 6.39	120-13.41	5.55	3.47	14	143	11.5	0.06
830516	1421	48.07	36- 8.79	120-16.95	9.30	3.71	38	110	12.6	0.06
830516	1452	33.42	36- 8.83	120-17.16	8.91	3.06	36	62	12.4	0.08
830516	1826	59.62	36- 9.87	120-15.40	9.20	3.12	16	159	12.1	0.16
830516	1840	15.81	36- 9.94	120-18.16	7.36	3.13	37	59	9.9	0.13
830516	19 9	37.28	36-10.01	120-18.16	7.39	3.33	34	59	14.4	0.14
830517	742	11.11	36-14.95	120-22.39	9.88	3.06	41	54	2.8	0.08
830517	2222	12.96	36-13.07	120-22.31	8.12	3.41	40	95	13.1	0.07
830518	222	26.98	36- 9.38	120-17.50	6.44	3.10	31	111	11.3	0.11
830518	246	57.73	36-34.50	120-52.34	24.18	3.65	5	121	19.6	0.02
830518	2039	32.09	36-14.49	120-22.18	6.57	3.38	35	71	2.6	0.17
830519	723	39.02	36-16.13	120-23.94	9.69	3.14	39	74	5.6	0.11
830519	11 5	29.85	36-12.91	120-16.31	13.41	3.57	30	65	7.3	0.06
830519	2326	6.53	36-14.76	120-26.20	2.82	3.41	38	59	8.5	0.18
830520	11 1	41.05	36-12.50	120-17.67	7.73	3.39	34	60	6.2	0.15
830520	1222	34.01	36-10.35	120-15.22	9.26	3.01	42	72	11.6	0.13
830521	10 5	40.80	36-10.33	120-15.28	10.33	3.24	40	72	11.6	0.08
830521	20 0	23.37	36-10.06	120-18.48	7.01	3.01	33	57	9.5	0.12
830522	839	21.42	36- 8.28	120-13.14	10.30	4.27	47	86	13.0	0.09
830523	1327	10.17	36-11.48	120-18.19	8.85	3.12	41	57	7.3	0.13
830524	9 2	17.38	36-14.27	120-19.54	9.94	4.69	49	73	1.9	0.07
830524	1146	19.76	35-58.98	120- 5.36	8.85	3 07	6	240	22.1	0.19
830524	1147	41.31	36-12.72	120-17.23	10.40	3.36	23	208	40.7	0.15
830524	1226	7.46	36-10.45	120-18.30	9.69	3.22	37	104	9.0	0.08
830525	1645	14.19	36- 8.48	120-14.51	6.18	3.35	33	76	14.9	0.10

Table 2b. 1983 Coalinga earthquakes (continued)

DATE	HRMN	SEC	LAT (°N)	LONG (°W)	DEPTH	MAG	ND	GAP	DMIN	RMS
830526	854	54.86	36-13.52	120-17.31	9.11	3.23	40	65	5.5	0.12
830526	952	1.70	36- 6.57	120-10.92	8.15	3.01	31	99	8.5	0.12
830527	2040	49.02	36-13.37	120-23.39	12.52	3.60	36	69	5.2	0.08
830529	124	3.24	36-13.12	120-22.91	12.35	3.46	39	42	4.9	0.09
830529	147	26.47	36-22.56	120-17.43	7.74	3.21	37	91	8.3	0.20
830529	149	0.08	36-23.35	120-14.75	0.48	3.15	16	236	47.3	0.20
830530	131	16.60	36- 9.81	120-15.36	10.13	3.12	38	72	12.3	0.16
830530	321	52.23	36-13.97	120-23.03	11.60	3.34	40	41	4.2	0.07
830530	13 8	8.25	36- 8.01	120-20.39	11.60	3.04	34	55	9.6	0.08
830530	16 1	16.35	36-10.18	120-15.19	11.18	3.00	32	73	17.7	0.08
830531	231	43.75	36- 6.11	120-16.05	8.13	3.38	24	211	15.1	0.09
830531	441	1.07	36- 5.96	120-16.29	5.22	3.41	22	68	14.7	0.20
830601	5 6	39.41	36- 8.41	120-20.13	12.03	3.10	37	65	10.3	0.10
830601	16 8	58.74	36-11.28	120-15.92	8.77	3.00	35	67	9.7	0.09
830606	16 6	48.64	36-10.01	120-13.40	9.01	3.39	38	84	14.1	0.11
830607	516	36.67	36- 8 30	120-13.98	8.99	3.00	39	80	14.1	0.10
830607	518	37.49	36- 8.59	120-14.10	10.07	4.1	43	79	14.5	0.08
830607	1827	14.66	36-11.70	120-17.35	11.60	3.14	41	158	7.7	0.11
830611	3 9	52.05	36-14.62	120-27.55	4.45	5.22	53	65	10.6	0.19
830611	548	30.84	36-14.54	120-26.77	3.21	3.11	39	61	9.4	0.18
830611	1427	5.28	36-13.84	120-27.12	4.23	3.18	47	59	10.1	0.13
830611	23 2	19.65	36-14.65	120-26.90	3.66	3.6	44	62	9.6	0.16
830612	131	27.15	36- 6.85	120-18.19	13.53	4.04	49	55	12.1	0.12
830612	658	53.05	36-11.05	120-19.91	8.82	3.02	39	97	7.3	0.09
830614	1410	25.92	36-16.30	120-26.05	11.92	3.18	43	68	8.6	0.13
830615	044	15.40	36-14.16	120-23.85	11.34	3.14	36	77	5.2	0.13
830615	9 2	11.88	35-48.28	120-30.24	7.23	3.20	6	303	66.8	0.05
830616	1737	23.34	36-13.60	120-21.69	10.20	3.40	38	94	3.0	0.08
830619	1328	19.89	36- 9.07	120-16.58	6.98	3.36	36	65	12.4	0.09
830620	1033	43.77	36-12.49	120-14.40	5.00	3.22	36	72	10.2	0.15
830620	2313	7.57	36-39.64	121-17.92	10.22	3.40	24	80	5.7	0.17
830624	1047	34.53	36-33.97	121-12.46	6.89	3.19	42	33	1.9	0.22
830629	145	35.57	36-22.76	120-43.54	23.49	3.08	10	149	16.6	0.88
830629	641	7.57	36- 8.58	120-12.48	11.10	3.47	39	136	16.3	0.08
830630	23 6	53.73	36-14.01	120-22.64	10.82	3.13	40	46	3.6	0.07
830702	1312	45.47	36-19.29	120-20.25	5.47	3.16	37	146	8.0	0.17
830704	2119	25.26	36-19.29	120-20.59	4.12	3.18	41	80	17.1	0.15
830705	2210	14.26	36-19.69	120-19.88	5.63	3.24	42	80	3.5	0.20
830706	17 9	18.63	36-14.67	120-19.54	9.75	3.06	41	82	1.6	0.09
830707	015	59.67	36-15.01	120-26.73	3.91	3.02	35	187	17.4	0.14
830707	030	33.44	36-12.49	120-18.13	10.46	3.55	19	255	44.3	0.06
830709	740	50.94	36-14.20	120-24.54	9.51	5.49	53	47	6.2	0.11
830714	1525	35.44	36-12.25	120-19.12	8.63	3.56	37	56	5.4	0.10
830717	2158	8.04	36-15.65	120-20.16	11.13	3.60	24	244	1.4	0.09
830718	1841	5.65	36- 9.64	120-17.11	9.61	3.14	26	201	11.1	0.10
830718	1928	5.21	36- 9.96	120-17.53	11.28	3.84	26	199	10.3	0.06
830722	239	53.74	36-13.67	120-24.94	9.18	6.40	50	48	7.0	0.12
830722	249	9.60	36-12.66	120-25.34	6.36	4.0	39	101	8.4	0.12
830722	258	35.94	36-19.81	120-20.24	5.55	3.1	38	82	9.0	0.16
830722	3 3	41.23	36-12.77	120-24.43	8.31	3.2	39	67	7.1	0.08
830722	3 8	12.76	36-20.15	120-20.96	4.41	3.3	38	86	1.7	0.19
830722	311	48.76	36-17.66	120-21.18	10.58	3.5	18	234	40.6	0.08
830722	343	0.66	36-12.57	120-24.79	9.57	5.03	49	44	7.8	0.11
830722	427	40.64	36-20.56	120-22.37	8.78	3.20	39	148	28.1	0.12
830722	430	26.90	36-19.81	120-20.53	5.19	3.34	42	83	2.5	0.17
830722	712	10.34	36-15.77	120-25.13	4.91	3.36	42	60	7.1	0.12
830722	2152	32.43	36-14.79	120-24.52	8.00	3.08	42	49	6.0	0.10
830725	2231	39.22	36-12.92	120-24.33	9.53	5.35	49	42	6.8	0.10
830731	1643	52.27	36-12.88	120-16.30	10.01	3.40	41	104	7.4	0.07
830731	1724	9.86	36- 8.45	120-14.26	9.39	3.28	41	130	15.3	0.09
830731	1754	20.04	36-12.97	120-16.22	9.59	3.15	42	65	7.4	0.07

1/Locations obtained using HYPO71 (Lee and Lahr, 1975). DMIN = epi. dist. (km) to the nearest station. MAG are coda-duration magnitudes M_D: routine CALNET estimates if precision = 0.01; estimated by J.P. Eaton from coda durations at nearby low-gain CALNET stations if precision = 0.1.

Table 2c. 1975 Cantua Creek earthquakes.[1/]

DATE	HRMN	SEC	LAT (°N)	LONG (°W)	DEPTH	MAG	NO	GAP	DMIN	RMS
750803	635	16.87	36-25.13	120-23.36	6.66	4.87r48	116	38.8	0.26	
750803	647	32.53	36-27.33	120-24.49	8.19	3.02 45	70	37.9	0.29	
750803	648	45.68	36-27.51	120-24.48	6.88	3.12 35	174	38.0	0.26	
750803	649	31.62	36-25.15	120-22.39	8.06	2.85r39	73	40.3	0.25	
750803	711	36.54	36-26.09	120-24.34	5.49	2.94 41	116	37.7	0.23	
750803	727	13.26	36-26.55	120-23.09	8.79	3.21 42	72	39.6	0.26	
750803	838	0.89	36-24.30	120-23.59	12.15	3.55r51	116	38.3	0.27	
750803	9 0	30.87	36-24.11	120-24.10	12.71	3.50r46	115	37.5	0.27	
750803	957	5.56	36-26.51	120-22.91	7.45	3.36 47	117	39.9	0.27	
750803	0759	41.07	36-26.30	120-23.61	5.62	2.80 38	117	38.8	0.24	
750803	1014	2.64	36-25.53	120-25.02	12.23	2.97 41	115	36.5	0.23	
750803	1346	58.44	36-25.72	120-24.41	7.73	3.03 42	116	37.4	0.25	
750803	14 1	49.16	36-25.96	120-23.34	6.25	2.82 39	117	39.1	0.25	
750803	1658	36.02	36-25.96	120-24.73	8.84	3.15 47	116	37.0	0.26	
750804	714	48.43	36-24.67	120-23.70	8.67	3 29r52	116	38.2	0.26	
750805	0944	9.36	36-27.02	120-23.05	5.41	2.87 42	118	39.9	0.29	
750807	2142	1.36	36-25.70	120-22.52	6.35	2.96 45	117	40.2	0.21	
750807	2146	2.69	36-25.45	120-22.81	8.18	3.43 50	117	39.7	0.24	
750808	628	14.91	36-25.96	120-22.68	7.16	3.20 54	117	40.0	0.23	
750808	2223	44.13	36-27.56	120-22.39	6.05	3.19 46	118	41.1	0.28	
750815	2227	52.33	36-26.91	120-25.54	9.89	4.53r37	125	36.2	0.29	
750817	852	53.09	36-26.52	120-23.24	7.32	2.89 35	117	39.4	0.29	
750818	835	55.07	36-27.89	120-24.72	6.31	2 81 33	117	37.9	0.26	
750829	752	43.26	36-27.35	120-25.61	10.66	3 79r66	116	36.3	0.23	
750829	830	41.21	36-28.00	120-25.29	5.36	3.48 50	125	37.1	0.33	
750830	548	15.08	36-27.44	120-25.61	7.58	3.36 39	116	36.3	0.30	
751229	15 7	32.18	36-47.30	121- 8.19	7.08	3.38r66	77	6.9	0.20	

[1/] Locations obtained using HYPO71 (Lee and Lahr, 1975). DMIN = epi. dist. (km) to the nearest station. MAG and M_L (Univ. of Calif. Berkeley) if followed by an "r", otherwise MAG are CALNET coda-duration magnitudes M_D.

Table 2d. 1976 Avenal earthquakes.[1]/

DATE	HRMN	SEC	LAT (°N)	LONG (°W)	DEPTH	MAG	NO	GAP	DMIN	RMS
760114	2144	0.09	36- 5.18	120-16.64	8.58	4.71r	42	79	14.2	0.44
760114	2148	53.63	36- 4.17	120-12.45	6.27	2.49	17	238	19.2	0.23
760114	22 6	55.23	36- 5.85	120-12.90	3.46	2.05	12	256	19.8	0.16
760114	2227	54.31	36- 5.91	120-14.15	5.32	2.28	14	232	17.9	0.19
760114	2236	47.97	36- 4.71	120-11.93	0.22	2.21	23	240	20.5	0.27
760114	2318	26.70	36- 5.16	120-13.68	6.19	2.50	29	177	18.6	0.25
760114	2340	17.70	36- 5.38	120-14.07	9.07	3.45r	40	81	18.0	0.29
760115	0 9	36.61	36- 5.73	120-13.95	9.39	3.48r	34	93	18.2	0.29
760115	1155	57.31	36- 5.24	120-12.62	6.25	2.14	26	237	20.2	0.21
760115	1826	51.91	35-47.28	119-54.76	19.63	2.29	22	177	40.1	0.23
760116	511	33.21	36- 5.36	120-13.18	6.74	2.85	37	178	19.4	0.25
760116	515	33.45	36- 5.15	120-13.90	5.54	2.12	24	230	18.3	0.26
760116	617	25.61	36- 5.71	120-13.40	6.06	2.51	33	139	19.0	0.29
760116	7 6	54.52	36- 5.53	120-12.73	7.45	2.99	34	179	20.0	0.27
760117	016	1.20	36- 5.67	120-13.18	5.35	2.45	30	95	19.4	0.23
760118	2126	37.44	37- 4.71	121-14.59	4.89	2.34	77	61	2.1	0.19
760119	1151	2.67	36- 5.34	120-14.29	5.61	2.10	18	228	17.7	0.19
760119	1335	44.16	36- 6.14	120-12.68	4.31	2.06	19	124	20.1	0.26
760120	836	29.82	36- 4.62	120-14.11	5.27	2.03	16	228	18.1	0.23
760120	1427	30.33	36- 5.32	120-12.32	6.53	2.05	23	238	20.7	0.24
760122	17 5	28.20	36- 4.19	120-11.50	7.93	2.55	21	186	20.2	0.19
760122	2043	45.63	36- 4.42	120-11.53	6.17	2.01	14	243	20.5	0.20
760124	238	49.41	36- 5.60	120-13.14	6.77	2.12	15	235	19.4	0.19
760126	2330	27.22	37- 3.12	121-13.18	7.37	2 24	51	76	2.5	0.21
760128	2325	11.60	36-52.95	120-58.06	4.43	2.43	65	84	13.5	0.20
760209	2328	42.27	36-26.49	120-21.62	6.93	2 64	36	118	21.4	0.28
760209	2331	47.82	36-26.12	120-21.57	11.54	2.70	34	118	20.7	0.19
760210	0 0	50.38	36-27.03	120-21.52	5.28	2.60	37	119	22.4	0.29
760210	133	32.52	36-26.43	120-21.65	10.87	2.60	33	122	21.3	0.19
760307	1324	25.96	36-29.44	120-49.27	7.00	2.69	46	61	13.1	0.26
760317	4 1	52.60	36-49.14	121- 8.01	8.58	4.32r	69	77	7.2	0.19
760317	1442	27.57	36-49.13	121- 7.82	7.13	2.26	54	59	7.5	0.18
760318	155	14.19	36-48.64	121- 7.82	5.47	2.71	55	76	7.8	0.19
760320	1038	10.65	36-31.66	120-43.26	5.03	3.12	48	72	16.3	0.25
760320	1050	42.17	36-32.14	120-43.50	5.37	3.42	54	72	15.3	0.29
760403	2140	10.24	36- 1.40	120- 4.68	6.69	2.30	14	271	25.5	0.21
760409	4 9	39.59	36-32.11	120-45.68	5.58	2.40	28	122	14.5	0.24
760415	2157	37.87	36- 1.74	120- 6.66	6.04	2.36	14	146	23.1	0.22
760416	919	2.05	36- 1.34	120- 5.44	4.57	2.98	31	147	24.4	0.21
760416	17 7	31.28	36-32.73	120-41.39	6.50	3.14	52	127	15.9	0.23
760416	1710	44.12	36-32.30	120-42.52	8.90	2.01	18	182	15.7	0.17
760426	037	4.02	36-43.83	120-47.00	8.29	2.82	45	70	7.5	0.21
760505	18 1	43.94	36-11.84	120-12.36	8.12	2.36	33	119	13.5	0.20
760523	1739	39.65	36-28.40	120-32.01	7.60	3.33	50	141	27.9	0.23
760610	132	8.71	36-12.08	120-15.76	11.37	2.24	28	195	8.9	0.21
760610	632	14.50	36-12.28	120-14.58	12.15	2.10	22	147	10.2	0.22
760620	15 7	45.24	36-48.92	121- 7.77	5.42	2.53	61	55	7.7	0.16
760703	022	51.55	36-43.50	121- 6.43	6.34	2.18	43	86	7.1	.12
760706	032	38.87	36-43.46	121- 6.49	5.58	2 24	45	60	7.1	.14
760709	9 2	16.59	36-26.25	120-40.93	9.73	2.06	19	167	26.9	0.17
760724	333	59.93	36-44.30	120-43.27	6.06	2.65	45	136	10.5	0.20
760729	1358	48.19	36- 6.31	120- 9.14	2.17	2.55	22	189	23.4	0.11
760809	446	51.79	36-37.02	120-44.71	4.04	2.08	30	170	6.6	.19
760810	2015	15.67	36-27.31	120-54.42	13.43	2.05	19	115	10.5	.14
760811	1453	9.86	36-36.09	120-46.07	.29	2.13	30	171	7.2	.16
760901	7 8	12.22	36-31.03	120-55.68	11.08	2.12	32	83	12.0	0.16
760912	1135	27.38	36-26.03	120-20.93	3.50	2.30	23	180	20.5	0.27
760926	622	54.67	36-50.40	120-40.18	5.44	2.11	34	157	13.8	0.15
761018	349	30.48	36-24.06	120-43.01	12.30	2.13	31	128	9.6	0.20
761019	1836	40.89	36-47.38	120-51.99	6.22	2.65	56	124	15.6	0.15
761024	1250	44.81	36-21.67	120-43.82	12.41	2.67	36	61	17.2	0.16
761114	2113	9.05	36-46.74	120-53.07	4.63	2.03	37	111	9.1	0.18
761115	1811	17.39	36-23.49	120-23.53	6.15	2.99r	43	72	16.4	0.24
761128	434	17.24	36-49.29	120-34.31	5.98	2.05	32	128	22.6	0.18
761128	7 7	40.08	36-49.14	120-34.15	3.43	2.01	43	92	22.9	0.21
761208	546	49.93	36- 4.43	120- 8.10	6.54	2.22	15	258	24.1	0.20

[1]Locations obtained using HYPO71 (Lee and Lahr, 1975). DMIN = epi. dist. (km) to the nearest station. MAG are M_L (Univ. of Calif. Berkeley) if followed by an "r" otherwise MAG are CALNET coda-duration magnitudes M_D.

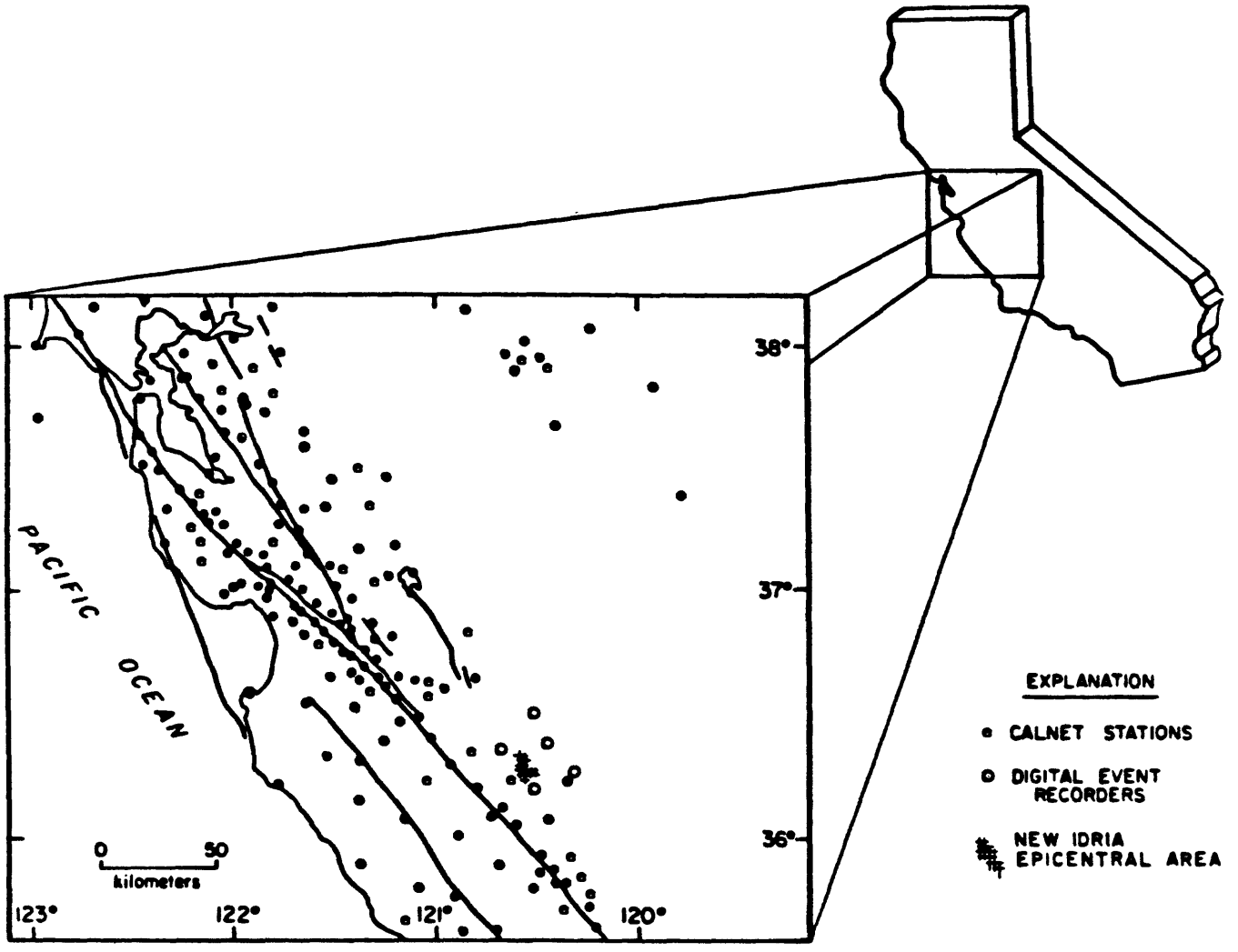

Figure 1. Map showing the New Idria epicentral area and the locations of seismographic stations in the USGS central California seismic network (CALNET). Five temporary seismic stations (Table 1), shown as open circles, were operated for several days during the New Idria sequence.

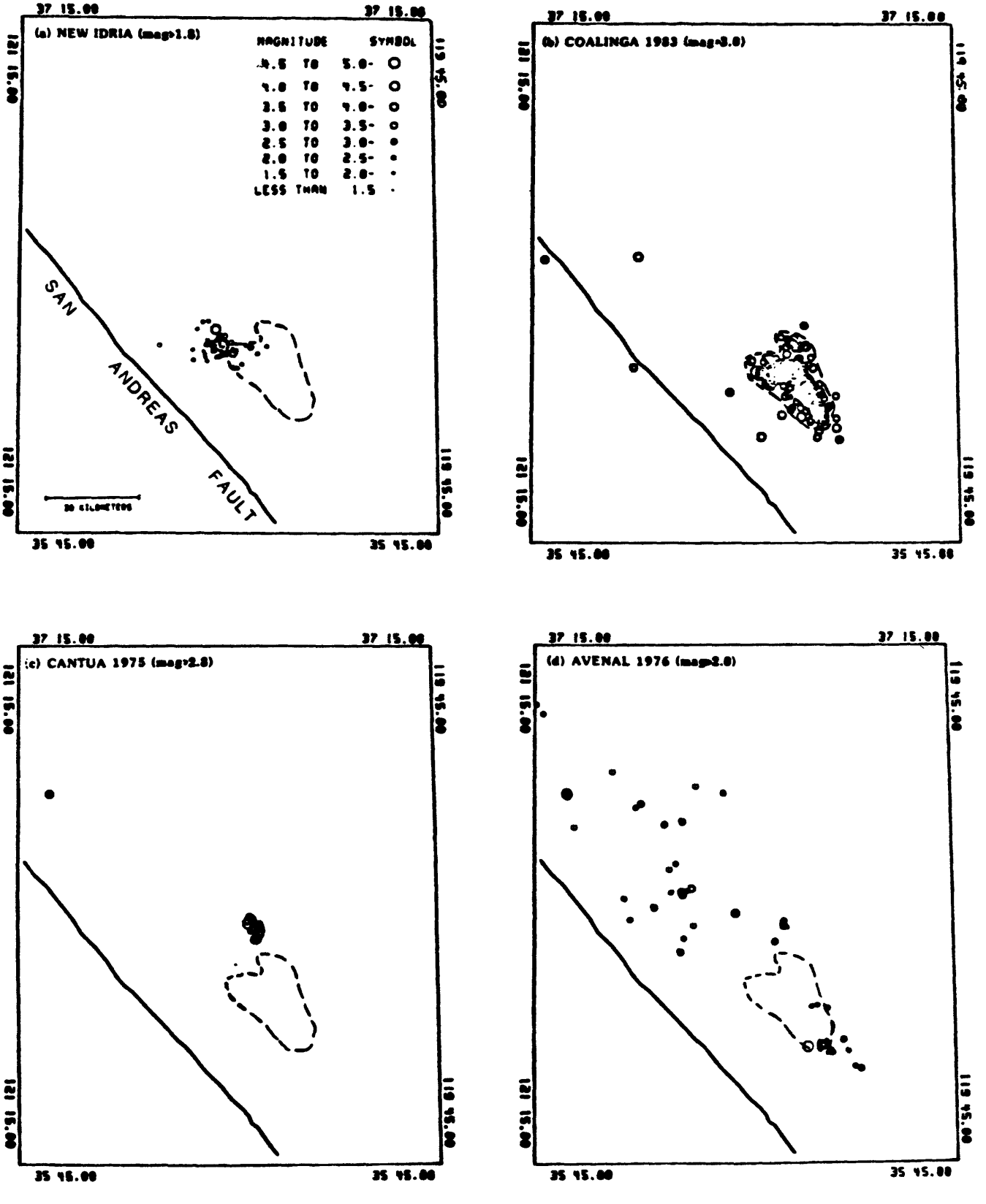

Figure 2. Maps of the epicenters of the (a) New Idria, (b) Coalinga, (c) Cantua Creek, and (d) Avenal earthquake sequences listed in Table 3. The dashed line on each map is the perimeter of the concentrated aftershock area of the 1983 Coalinga sequence. The maps show seismicity above the appropriate magnitude completeness threshold(see figure 5).

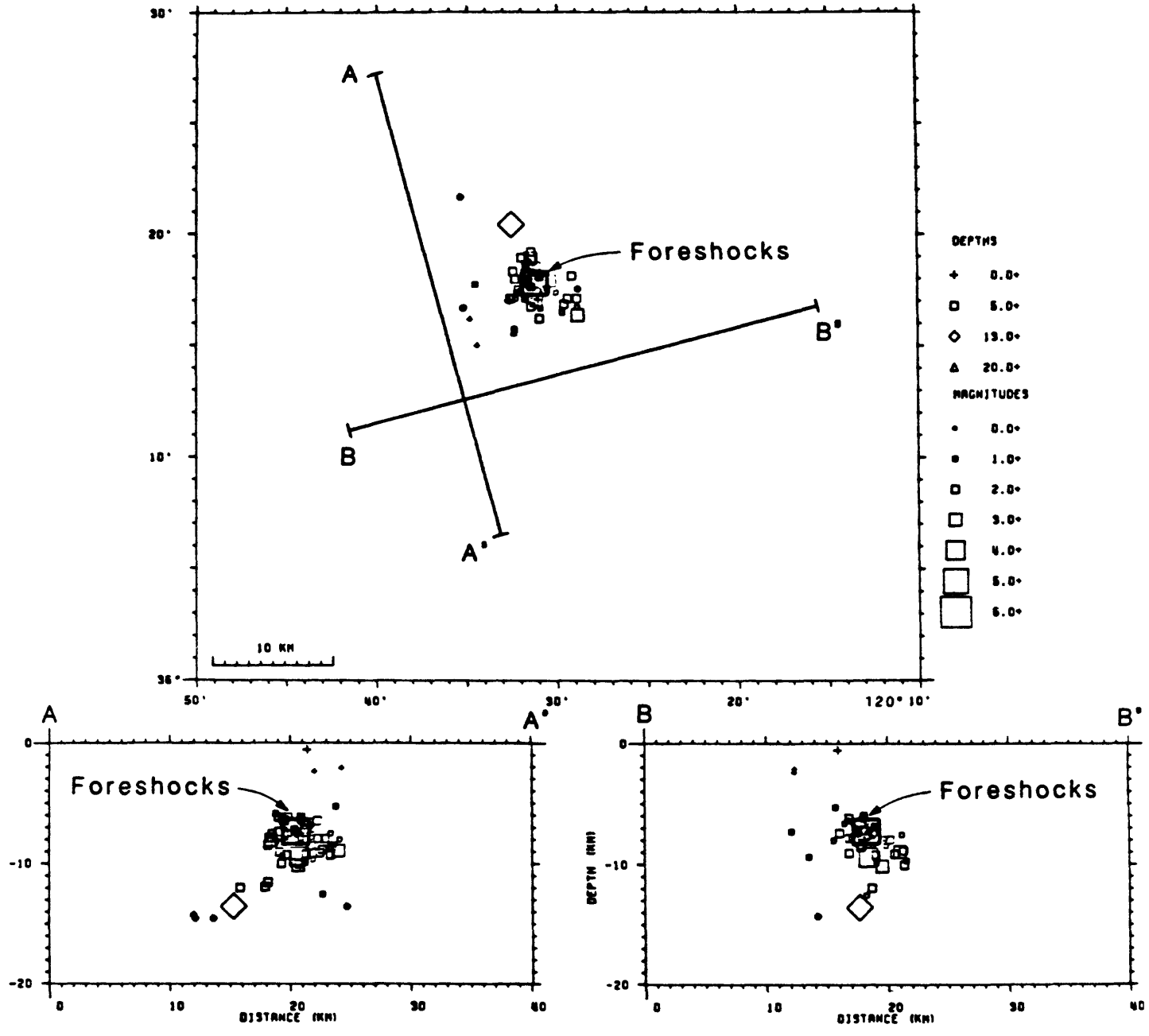

Figure 3. Map (top) and cross sections (bottom) of seismicity for the New Idria earthquake sequence (A and B quality solutions only). The densest spatial clustering of aftershocks lies along the line B-B'. The bold square and solid dots are the hypocenters of the New Idria main shock and its four foreshocks, respectively.

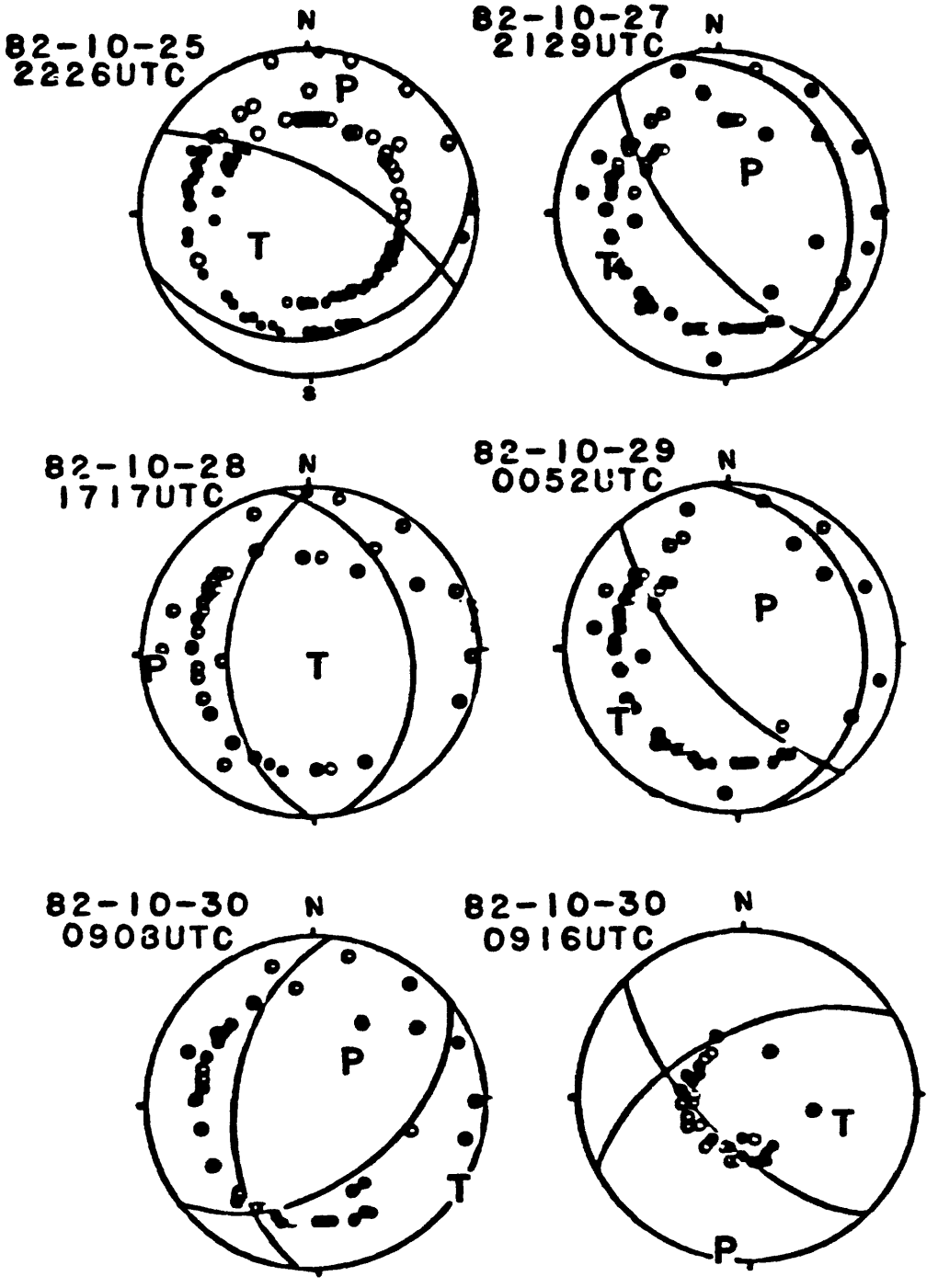

Figure 4. Fault-plane solutions (lower-hemisphere projections) of the New Idria main shock (upper left) and five aftershocks. Date and origin time of each earthquake is given at the upper left. Solid and open circles are compressional and dilatational first-motions, respectively. P and T are the directions of the P- and T-axes, respectively.

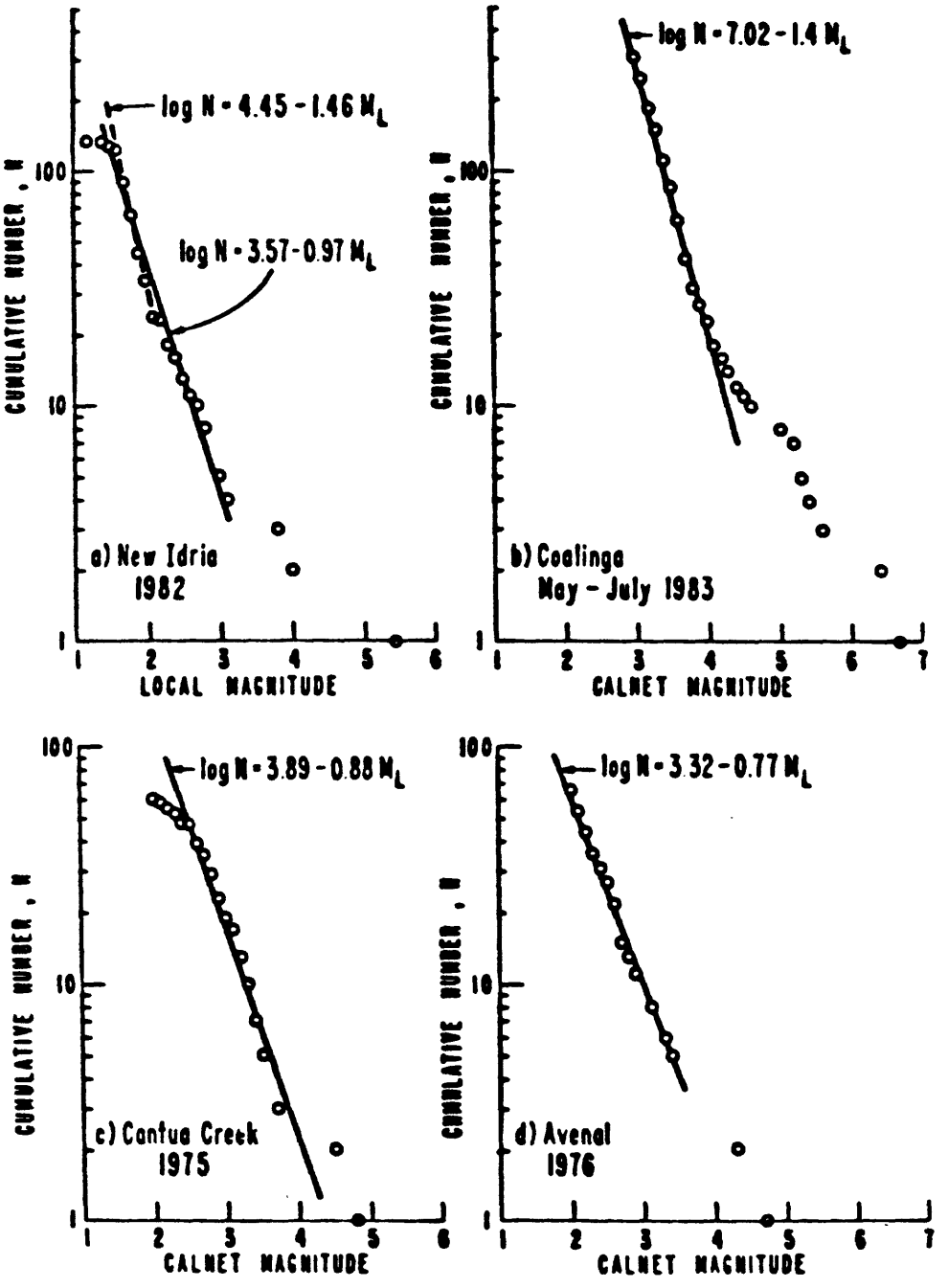

Figure 5. Cumulative count of earthquakesversus magnitude(Table 3) for the (a) New Idria, (b) Coalinga, (c) Cantua Creek, and (d) Avenal earthquake sequences. The lines represent linear fits obtained by inspection. The dashed line in (a) represents an alternative fit, using $M_L < 2$ shocks only. These plots imply magnitude completeness levels of 1.8,3.0,2.8, and 2.0 for the New Idria, Coalinga, Cantua Creek, and Avenal sequences, respectively.

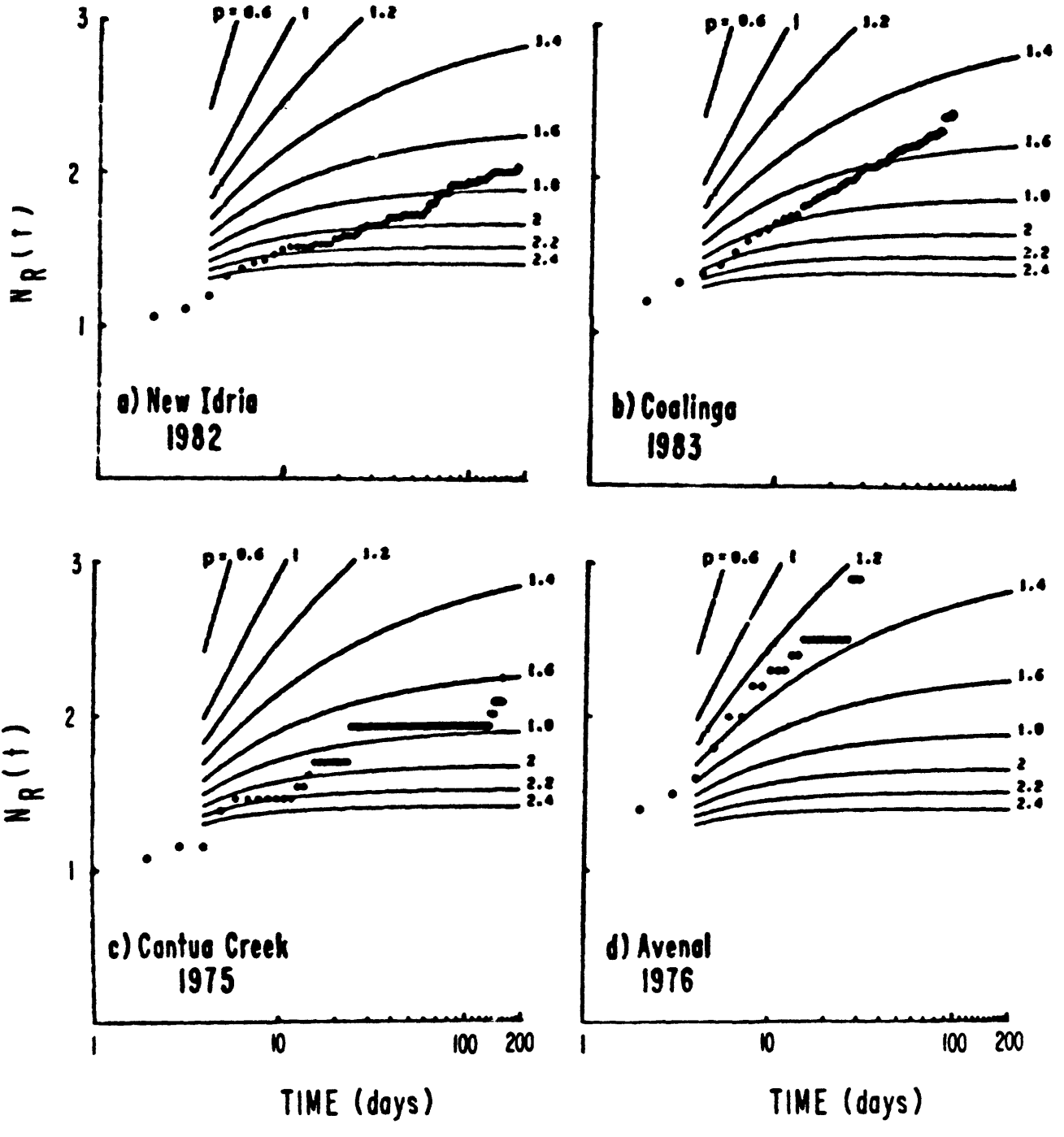

Figure 6. The reduced cumulative earthquake frequency $N_R(t)$ versus time t for the (a) New Idria, (b) Coalinga, (c) Cantua Creek, and (d) Avenal earthquake sequences. p is the coefficient of attenuation with time (Liu, 1984). $N_R(t)$ were calculated using the catalogs in Table 2 and the completeness levels indicated in figure 5.

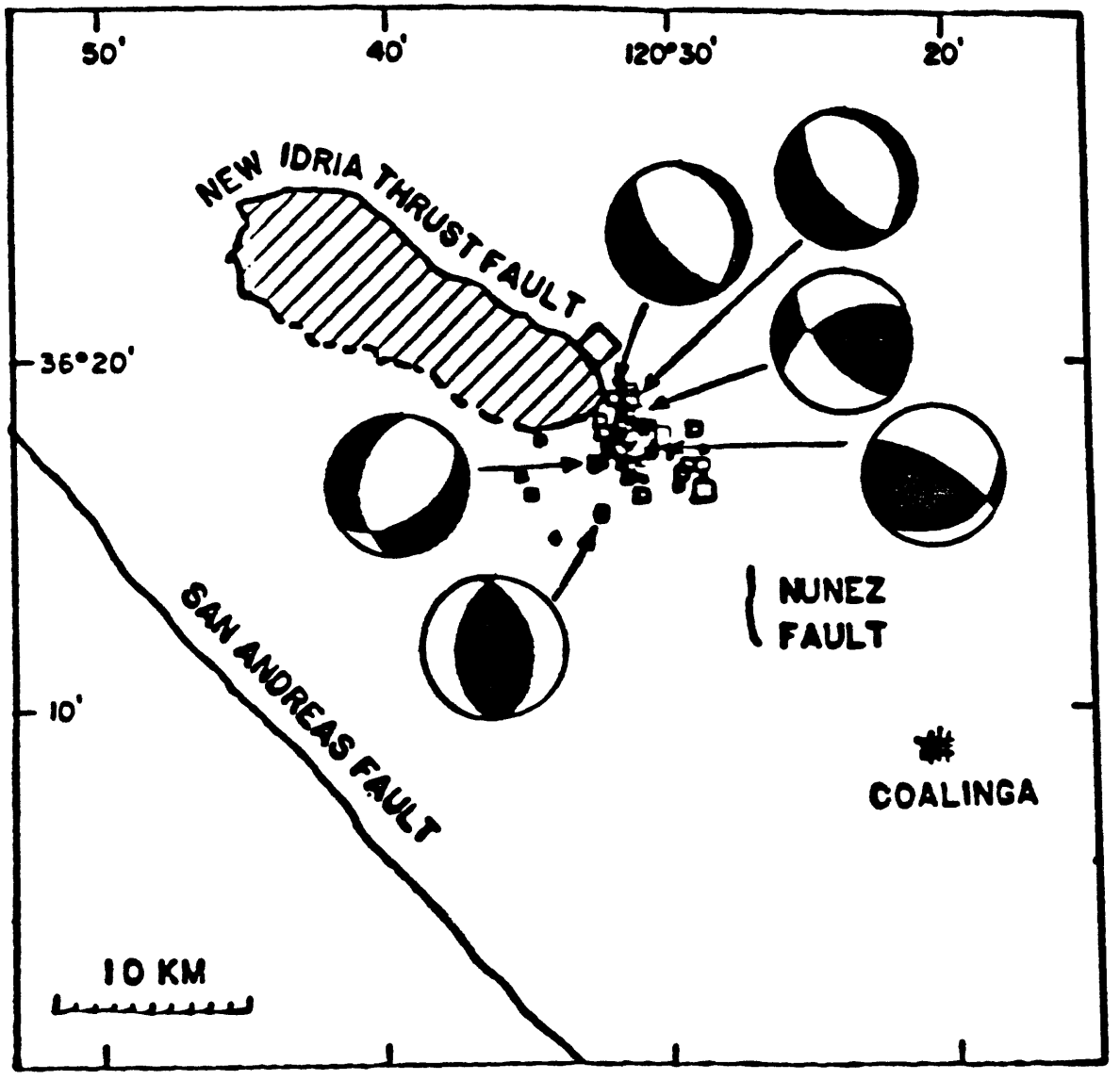

Figure 7. Epicenters and fault-plane solutions (lower-hemisphere projections) of selected 1982 New Idria earthquakes relative to the Mesozoic ultramafic intrusive body (hatched area) that is bounded on the north and east by the New Idria thrust fault. Also shown is surface rupture of Nunez fault in association with 1983 Coalinga earthquake sequence. The data used to construct the fault-plane solutions are shown in Figure 4.

APPENDIX. STATION DELAYS (SEC) +

STA**	DELAY	STA**	DELAY	STA**	DELAY	STA**	DELAY
PMC	-0.28	BSR	-0.64	PAR	0.12	PRC	-0.01
AR4	-0.07(0.04*)	BVL	-0.74	PBR	-0.18	PRI	-0.05
BAV	-1.0	BVY	-0.54	PBW	-0.19	PSA	-0.46
BBG	-0.44	CC2	-0.17(0.24*)	PBY	-0.36	PSH	-0.20
BBN	-0.44	HCP	-0.96	PCA	0.13	PSM	0.35
BCG	-0.20	HCR	-0.72	PCR	-0.41	PSR	-0.02
BEH	-0.49	HDL	-0.28	PGH	-0.36	PST	0.20
BHS	-0.52	HFE	-0.40	PHA	-0.24	PTR	-0.59
BJC	-0.98	HPH	-0.68	PHC	-0.24	PWK	-0.02
BLR	-0.02	HFP	-0.74	PHG	0.05	SRS	-0.28(0.73*
BMS	-0.57	HJG	-0.88	PHR	-0.24	TYG	-0.72
BPC	-0.25	HJS	-0.26	PIV	-0.09		
BPF	-0.66	HLT	-0.47	PJL	-0.53		
BPI	-1.0	HOR	-0.36	PLO	-0.62		
BPP	-0.51	HQR	-0.60	PMC	-0.28		
BRM	-0.58	KA1	0.20(0.01*)	PMG	-0.80		
BRV	-0.34	OF3	-0.01(0.15*)	PMP	0.09		
BSC	-0.56	PAD	-0.33	PMP	-0.78		
BSG	-0.98	PAG	-0.66	PPF	0.26		
		PAN	-0.56	PPR	-0.38		
		PAP	-0.38	PPT	0.13		

\+ P wave additive station correction used with crustal model (Table 2a) derived from Walter and Mooney (1982).

** Station code adopted by CALNET.

* S wave station correction. See +.

CORRELATION BETWEEN SEISMICITY ON THE COAST RANGE - SIERRAN BLOCK BOUNDARY ZONE AND GREAT INTERPLATE EARTHQUAKES ON THE SAN ANDREAS FAULT SYSTEM

by Paul Somerville
Woodward-Clyde Consultants
566 El Dorado Street
Pasadena, CA 91101

This paper examines the temporal and spatial correlation between intraplate seismicity along the boundary between the Coast Range and the Sierran Block (termed the "Boundary Zone") and the occurrence of great interplate earthquakes on the San Andreas fault. The purpose in examining this correlation is to evaluate the manner in which stress across the plate boundary is transmitted into the adjacent interior of the North American plate, and to search for indications in this intraplate seismicity that may be precursors to great interplate earthquakes.

A clear temporal correlation between intraplate seismicity in Japan and great interplate subduction zone earthquakes in the adjacent trenches has been noted by Shimazaki (1976, 1978). The occurrence of large intraplate earthquakes in the few years or few decades preceding great interplate subduction earthquakes is believed to be triggered by the increase in tectonic stress that precedes the interplate earthquake. Shimazaki (1978) has proposed a model, described by Figure 1, to explain this triggering effect. An intraplate earthquake occurs when the local intraplate stress, which grows at rate (a), reaches the crustal strength. One sawtooth-shaped cycle is shown in Figure 1. The interplate earthquake cycle modulates the local intraplate stress buildup with a higher frequency sawtooth having period (T) and local rate of stress increase (b). For a period of time (Tp) preceding the interplate earthquake, the intraplate stress is elevated above its previous maximum level (which was reached at the time of the previous interplate earthquake). The interplate cycle thereby regulates the timing of intraplate earthquakes that occur within a given interplate cycle, making them more likely to occur during the period (T_p) preceding the interplate earthquake.

Triggering of intraplate seismicity might also be expected in regions adjacent to impending great interplate transform earthquakes such as those on the San Andreas.

The occurrence of large intraplate earthquakes following great subduction zone earthquakes is attributed by Shimazaki to stress concentration near the base of the interface between the oceanic and continental plates, which underlies the seismically active intraplate region. Because of geometrical dissimilarities, this kind of intraplate seismicity would not be expected to follow great interplate transform earthquakes.

Shimazaki (1976, 1978) found that the duration of the period of increased intraplate seismicity preceding great interplate earthquakes was quite different between northeastern and southwestern Japan, being 5 years and 40 years respectively. He attributed this difference to differences in the rate of intraplate strain accumulation, which are presumably attributable to the distinct differences between these two subduction zones. It is not known whether such differences exist

between the northern and south-central segments of the San Andreas. If there is any difference, it would tend to be a greater rate of intraplate strain accumulation in south-central California than in northern California, leading to a longer period of intraplate seismicity prior to great interplate earthquakes there.

The historical seismicity and tectonics of the Boundary Zone have been described by Wong and Ely (1983). The precise nature of the Boundary Zone is not pursued further here. For our purposes, it is sufficient to regard the Boundary Zone as a pre-existing zone of weakness within the North American plate along which intraplate deformation is concentrated.

A general view of seismicity preceding and following great San Andreas earthquakes has been provided by Ellsworth et al. (1981, 1982). In the following, the seismicity of the Boundary Zone preceding and following great San Andreas earthquakes by a few decades will be examined.

1. The 1857 earthquake on the south-central San Andreas

The available seismicity data do not resolve whether there was intraplate seismicity along the Boundary Zone in south-central California preceding or following the 1857 earthquake. No other earthquakes are reported in this region during the period 1850-1879 by Toppozada et al. (1981). However, the detection threshold preceding 1857 was about M 6 1/2, and did not decrease to M 6 until about 1870 (Toppozada et al., 1981). Thus it is possible that intraplate events as large as M 6 to 6 1/2 were undetected during this period. As noted by Sieh (1978a), several M 5 to 6 foreshocks of the 1857 earthquake could have occurred as far east as the Boundary Zone.

2. The 1906 earthquake on the northern San Andreas

A significant sequence of earthquakes occurred in the vicinity of the Boundary Zone in northern California during the two decades preceding the 1906 earthquake (Figure 2). It has been suggested by Wong and Ely (1983) that these earthquakes may have been associated with the Boundary Zone. The sequence includes events of M 6.2 in 1889 near Antioch, M 6.2 in 1892 near Allendale, M 5.5 in 1902 near Elmira, M 4.5 in 1903 near Willow, and M 4.5 in 1904 near Woodland. The M 6.0 earthquake of 1881, which was felt most strongly in Modesto, may also have occurred on the Boundary Zone (Wong and Savage, 1978). These events are distributed along a 170-km-long segment of the Boundary Zone that lies adjacent to the central half of the 1906 San Andreas rupture zone. The activity of such a long segment of the Boundary Zone is most easily understood as resulting from a broadly distributed change in stress, such as that due to loading of the adjacent plate boundary.

The earthquake detection threshold in this region of California was fairly uniform from 1850 to the early 1900s, allowing us to infer that the Boundary Zone activity began abruptly a few decades prior to the 1906 earthquake. There was no significant activity along this segment of the Boundary Zone following the 1906 earthquake. This pattern of activity coincides with the pattern expected from the comparison with Japan described above. We hypothesize that the enhanced seismicity of the Boundary Zone in northern California during the two decades preceding the 1906 earthquake on the San Andreas was due to changes in stress associated with the occurrence of the 1906 earthquake.

Using the model presented by Shimazaki (1978) illustrated in Figure 1 and assuming a long-term recurrence time (T) of 150 years for great earthquakes on the San Andreas and an active preseismic intraplate period (Tp) of 20 years on the Boundary Zone, we find that the rate of stress increase (b) along the Boundary Zone due to loading of the San Andreas is approximately six times greater than the long-term average rate of stress increase (a) along the Boundary Zone.

3. The coming earthquake on the south-central San Andreas

A significant sequence of earthquakes has occurred in the vicinity of the Boundary Zone in central California during the past decade (Eaton et al., 1983), of which the most recent event is the 1983 Coalinga earthquake. During that decade, the rate of occurrence of moderate magnitude earthquakes (M 5 or greater), four in the decade, has been approximately four times greater than the average rate during the preceding four decades. A detailed view of the seismicity in the Coalinga area during the period 1953-1982 is given by Uhrhammer, 1984, this volume, Figure 1.

Based on the hypothesized relation of Boundary Zone seismicity to the 1906 San Andreas earthquake in northern California, it appears possible that the Boundary Zone seismicity in south-central California may continue for another decade or so and may represent a long-term precursor to the next great earthquake on the south-central San Andreas. As was discussed previously, the duration of active seismicity on the south-central California segment of the Boundary Zone is expected to be the same as or longer than the period of several decades that the northern California segment experienced prior to the 1906 earthquake.

The Boundary Zone activity in northern California was adjacent to the central part of the rupture segment of the 1906 earthquake, while that in central California lies at the northern end of the expected rupture segment of the next south central San Andreas earthquake. It is possible that the Boundary Zone sequence tends to be concentrated in the region adjacent to the epicenter of the San Andreas event. If this is the case, the current Boundary Zone seismicity in south-central California might be expected to eventually migrate southward.

A contrast in Boundary Zone seismicity levels between the northern California and central California segments is evident in Figure 3, which shows seismicity from 1930 to 1976. The pattern of relatively high seismicity along the Boundary Zone in south central California during this period, in contrast with relatively low seismicity along the Boundary Zone in northern California, is the reverse of the pattern for the earlier period (1850-1929) shown in Figure 2. This reversal lends further weight to the hypothesis that the seismicity of the individual Boundary Zone segments is correlated with the phase of the seismic cycle in the adjacent segment of the San Andreas fault.

A large variety of evidence, independent of that considered here, has been used in support of the hypothesis that the next great earthquake on the south-central segment of the San Andreas fault is imminent (Lindh, 1983). The evidence presented here contributes a more location-specific criterion for precursory activity than the expectation of a generally higher level of seismicity in southern California. The temporal criterion presented here is in good agreement with estimates based on paleoseismology (Sieh, 1978b). However, the criteria are based on only one precedent, drawn from an adjacent segment of the Boundary

Zone - San Andreas system, and for which only historical seismicity data are available.

References

Eaton, J., R. Cockerham, and F. Lester, 1983. Study of the May 2, 1983, Coalinga earthquake and its aftershocks, based on the U.S.G.S. seismic network in northern California, in The 1983 Coalinga, California, Earthquakes, C.D.M.G. Special Publication 66, pp. 261-273.

Ellsworth, W. L., A. G. Lindh, W. H. Prescott, and D. G. Herd, 1981. The 1906 San Francisco earthquake and the seismic cycle, in Earthquake Prediction, an International Review, D. W. Simpson and P. G. Richards, eds., American Geophysical Union, Washington, D.C., p. 126-140.

Ellsworth, W. L., A. G. Lindh, and B. L. Moths, 1982. Regional seismicity and great earthquakes: implications for the San Andreas system, California. Terra Cognita, 2, p. 171 (abstract).

Lindh, A., 1983 . Preliminary assessment of long term probabilities for large earthquakes along selected segments of the San Andreas fault system in California. U.S.G.S. OFR 83-63, 15 pp.

Shimazaki, K., 1976. Intra-plate seismicity and inter-plate earthquakes: historical activity in southwest Japan. Tectonophysics, 3, 33-42.

Shimazaki, K., 1978. Correlation between intraplate seismicity and interplate earthquakes in Tohoku, northeast Japan. Bull. Seism. Soc. Am., 68, 181-192.

Sieh, K. E., 1978a. Central California foreshocks of the great 1857 earthquake. Bull. Seism. Soc. Am., 68, 1731-1749.

Sieh, K. E., 1978b. Pre-historic large earthquakes produced by slip on the San Andreas fault at Pallett Creek, California. J. Geophys. Res., 83, 3907-3939.

Toppozada, T. R., C. R. Real, and D. L. Panke, 1981. Preparation of isoseismal maps and summaries of reported effects for pre-1900 California earthquakes. C.D.M.G. Open File Report 81-11, 78 p.

Wong, I. G., and R. W. Ely, 1983. Historical seismicity and tectonics of the Coast Ranges - Sierran Block Boundary: Implications to the 1983 Coalinga, California, Earthquakes, in The 1983 Coalinga California Earthquakes, C.D.M.G. Special Publication 66, pp. 89-104.

Wong, I. G., and W. U. Savage, 1978. Epicentral location bias based on maximum intensity in the western San Joaquin Valley, California: Earthquake Notes, 49, 26-27.

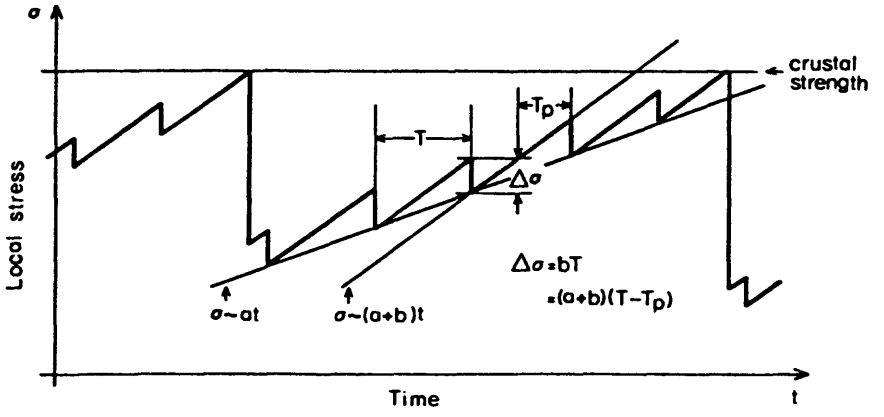

FIG. 1. Hypothetical change in local stress in time (see text).

(Source: Shimazaki, 1978)

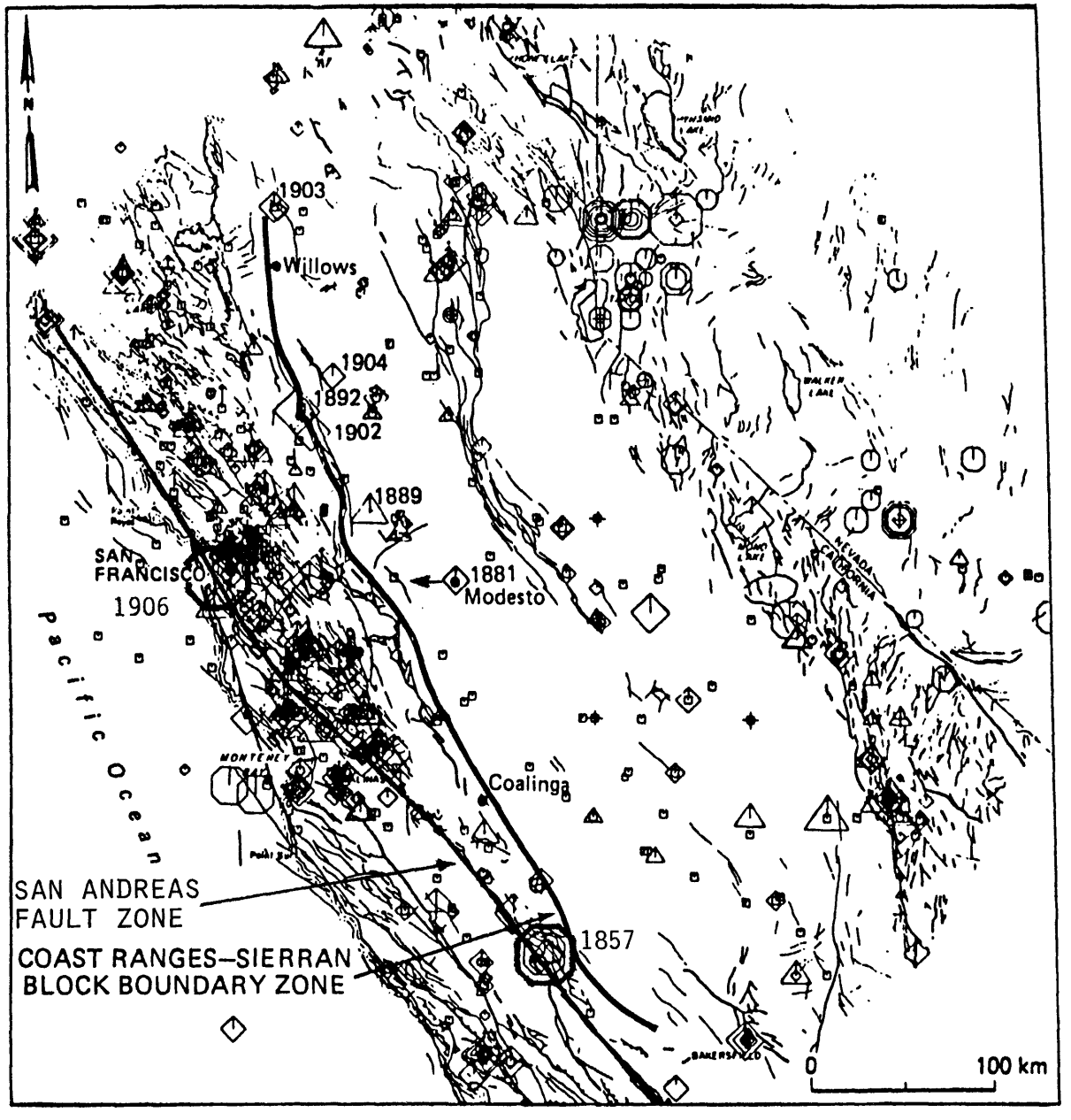

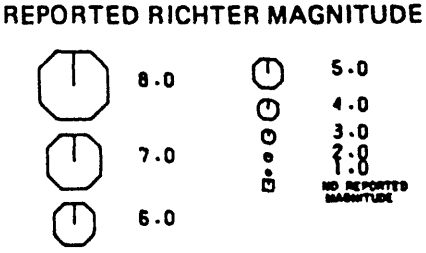

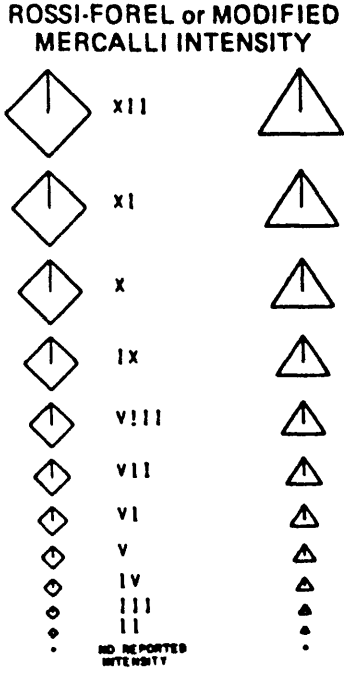

Figure 2. Historical seismicity of the Coast Ranges–Sierran block boundary zone and adjacent regions, 1850 to 1929.

(Source: Wong and Ely, 1983)

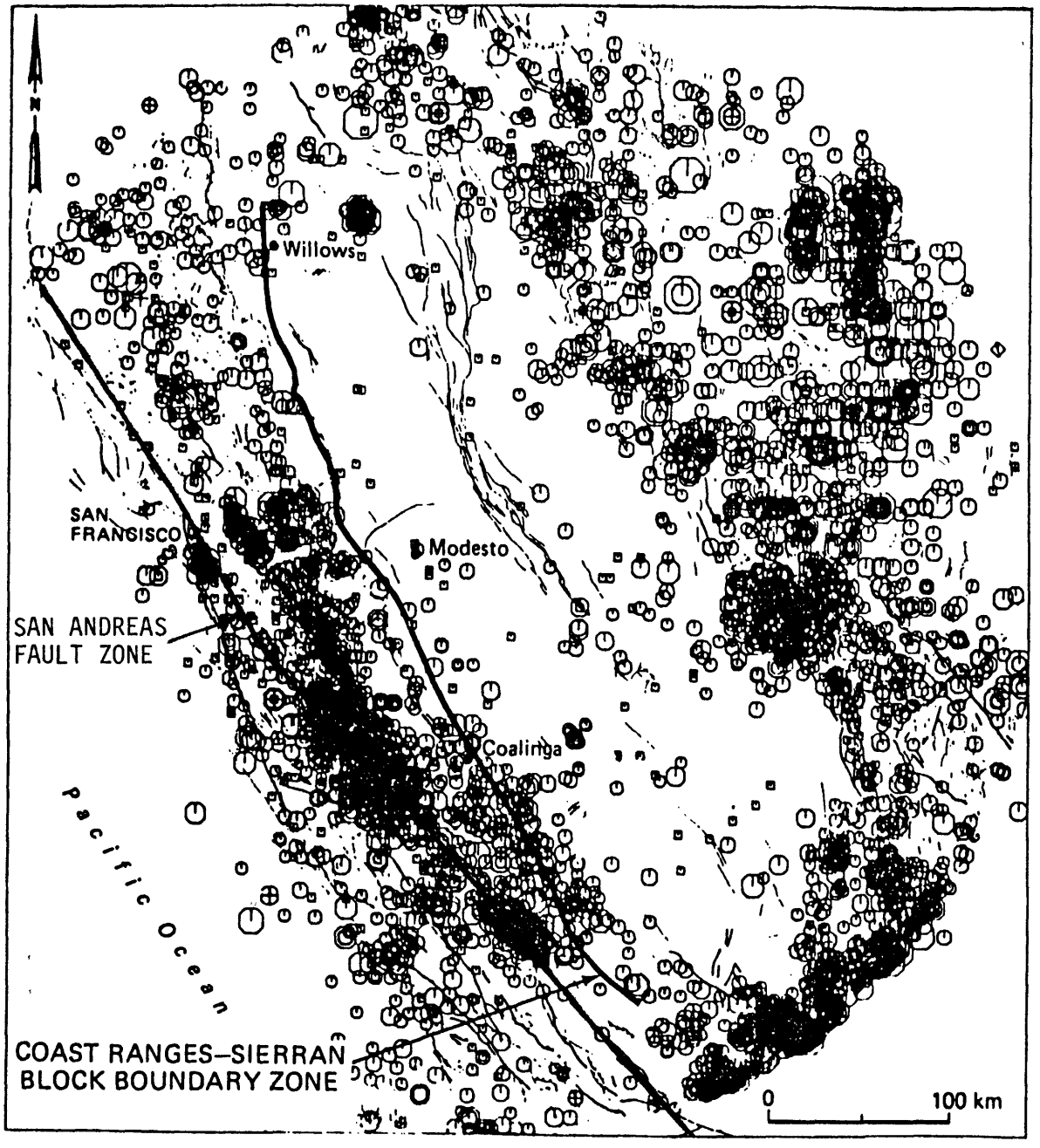

REPORTED RICHTER MAGNITUDE

8.0
7.0
6.0
5.0
4.0
3.0
2.0
1.0
NO REPORTED MAGNITUDE

Figure 3. Historical seismicity of the Coast Ranges–Sierran block boundary zone and adjacent regions, 1930 to 1976 .

(Source: Wong and Ely, 1983)